

Lecture Notes in Mechanical Engineering

Y. V. D. Rao · C. Amarnath ·
Srinivasa Prakash Regalla ·
Arshad Javed ·
Kundan Kumar Singh *Editors*

Advances in Industrial Machines and Mechanisms

Select Proceedings of IPROMM 2020



Lecture Notes in Mechanical Engineering

Series Editors

Francisco Cavas-Martínez, Departamento de Estructuras, Universidad Politécnica de Cartagena, Cartagena, Murcia, Spain

Fakher Chaari, National School of Engineers, University of Sfax, Sfax, Tunisia

Francesco Gherardini, Dipartimento di Ingegneria, Università di Modena e Reggio Emilia, Modena, Italy

Mohamed Haddar, National School of Engineers of Sfax (ENIS), Sfax, Tunisia

Vitalii Ivanov, Department of Manufacturing Engineering Machine and Tools, Sumy State University, Sumy, Ukraine

Young W. Kwon, Department of Manufacturing Engineering and Aerospace Engineering, Graduate School of Engineering and Applied Science, Monterey, CA, USA

Justyna Trojanowska, Poznan University of Technology, Poznan, Poland

Francesca di Mare, Institute of Energy Technology, Ruhr-Universität Bochum, Bochum, Nordrhein-Westfalen, Germany

Lecture Notes in Mechanical Engineering (LNME) publishes the latest developments in Mechanical Engineering—quickly, informally and with high quality. Original research reported in proceedings and post-proceedings represents the core of LNME. Volumes published in LNME embrace all aspects, subfields and new challenges of mechanical engineering. Topics in the series include:

- Engineering Design
- Machinery and Machine Elements
- Mechanical Structures and Stress Analysis
- Automotive Engineering
- Engine Technology
- Aerospace Technology and Astronautics
- Nanotechnology and Microengineering
- Control, Robotics, Mechatronics
- MEMS
- Theoretical and Applied Mechanics
- Dynamical Systems, Control
- Fluid Mechanics
- Engineering Thermodynamics, Heat and Mass Transfer
- Manufacturing
- Precision Engineering, Instrumentation, Measurement
- Materials Engineering
- Tribology and Surface Technology

To submit a proposal or request further information, please contact the Springer Editor of your location:

China: Ms. Ella Zhang at ella.zhang@springer.com

India: Priya Vyas at priya.vyas@springer.com

Rest of Asia, Australia, New Zealand: Swati Meherishi

at swati.meherishi@springer.com

All other countries: Dr. Leontina Di Cecco at Leontina.dicecco@springer.com

To submit a proposal for a monograph, please check our Springer Tracts in Mechanical Engineering at <http://www.springer.com/series/11693> or contact Leontina.dicecco@springer.com

Indexed by SCOPUS. All books published in the series are submitted for consideration in Web of Science.

More information about this series at <http://www.springer.com/series/11236>

Y. V. D. Rao · C. Amarnath ·
Srinivasa Prakash Regalla · Arshad Javed ·
Kundan Kumar Singh
Editors

Advances in Industrial Machines and Mechanisms

Select Proceedings of IPROMM 2020



Springer

Editors

Y. V. D. Rao

Department of Mechanical Engineering
Birla Institute of Technology and Science
Pilani-Hyderabad Campus
Hyderabad, Telangana, India

Srinivasa Prakash Regalla

Department of Mechanical Engineering
Birla Institute of Technology and Science
Pilani-Hyderabad Campus
Hyderabad, Telangana, India

Kundan Kumar Singh

Department of Mechanical Engineering
Birla Institute of Technology and Science
Pilani-Hyderabad Campus
Hyderabad, Telangana, India

C. Amarnath

Department of Mechanical Engineering
Indian Institute of Technology Bombay
Mumbai, Maharashtra, India

Arshad Javed

Department of Mechanical Engineering
Birla Institute of Technology and Science
Pilani-Hyderabad Campus
Hyderabad, Telangana, India

ISSN 2195-4356

Lecture Notes in Mechanical Engineering

ISBN 978-981-16-1768-3

<https://doi.org/10.1007/978-981-16-1769-0>

ISSN 2195-4364 (electronic)

ISBN 978-981-16-1769-0 (eBook)

© The Editor(s) (if applicable) and The Author(s), under exclusive license to Springer Nature Singapore Pte Ltd. 2021

This work is subject to copyright. All rights are solely and exclusively licensed by the Publisher, whether the whole or part of the material is concerned, specifically the rights of translation, reprinting, reuse of illustrations, recitation, broadcasting, reproduction on microfilms or in any other physical way, and transmission or information storage and retrieval, electronic adaptation, computer software, or by similar or dissimilar methodology now known or hereafter developed.

The use of general descriptive names, registered names, trademarks, service marks, etc. in this publication does not imply, even in the absence of a specific statement, that such names are exempt from the relevant protective laws and regulations and therefore free for general use.

The publisher, the authors and the editors are safe to assume that the advice and information in this book are believed to be true and accurate at the date of publication. Neither the publisher nor the authors or the editors give a warranty, expressed or implied, with respect to the material contained herein or for any errors or omissions that may have been made. The publisher remains neutral with regard to jurisdictional claims in published maps and institutional affiliations.

This Springer imprint is published by the registered company Springer Nature Singapore Pte Ltd.
The registered company address is: 152 Beach Road, #21-01/04 Gateway East, Singapore 189721,
Singapore

Contents

Compliant Mechanism

Jacobian-Based Inverse Kinematics Analysis of a Pneumatic Actuated Continuum Manipulator	3
Mrunal Kanti Mishra, Sambaran Ghosal, Arun Kumar Samantaray, and Goutam Chakraborty	
Path Curvature Theory: A Classic and Effective Design Tool	15
Mattia Cera, Marco Cirelli, Ettore Pennestrì, Pier Paolo Valentini, and V. R. Shanmukhasundaram	
Recent Developments in Higher Path Curvature Analysis	27
Mattia Cera, Marco Cirelli, Ettore Pennestrì, Pier Paolo Valentini, and V. R. Shanmukhasundaram	
Jump Phenomena in a Motor-Driven Quick-Return Mechanism that Excites the Base of a Vibrating Structure	39
Anubhab Sinha, Saurabh Kumar Bharti, Arun Kumar Samantaray, and Ranjan Bhattacharyya	
Real-Time Trajectory Estimation of a Ball Moving in a 3D Space	51
Dheeraj Bhogisetty, Sai Surya Srinivas Kunapuli, and Shital S. Chiddarwar	
Design and Trajectory Optimization of Delta Robot	61
Kunal Nandanwar and B. K. Rout	
Sustainable Model for Mechanization of Peppermint Oil Extraction Plants for Rural India	73
Mohd Anas, M. Abdullah Mujeeb, and Anurag Sharma	
Vibration Isolation in Six Degrees of Freedom Using Combined Passive and Active Isolation Technique	83
T. Akshay Kumar and B. Santhosh	

Evolution of Three Hold-Down Configuration for Large Antenna Mounted on a Dual Axes Steerable Mechanism	91
Saurabhkumar H. Patel, V. Sri Pavan Ravichand, Anoop Kumar Srivastava, S. Narendra, A. Shankara, and H. N. Suresha Kumar	
Workspace Analysis of a 5-Axis Parallel Kinematic Machine Tool with 3-RRS Parallel Manipulator	101
Anshul Jain and H. P. Jawale	
Four-Bar Linkage Mechanism in Papermaking and Its Replacement by Direct Servo Drive Technology in Roll to Sheeting Lines in a Paper Mill—Converting House	113
Muralidhar Ekambaram	
Robotics, Industrial CAD/CAM Systems, Mechatronics	
Two Degree-Of-Freedom Omni-Wheel Based Mobile Robot Platform for Translatory Motion	125
Uday Manne, Raghuveer Maddi, Dimple Dannana, Devasena Pasupuleti, and Rajeevlochana G. Chittawadigi	
Kinematic Error Modeling of a Parallelogram Arm of the Delta Robot and Its Dimensional Optimization	137
Venkata Sai Prathyush Idumudi and Arshad Javed	
Design and Control of Mobile Robots with Two and Four Independent Rotatable Power Wheels	149
Divyansh Khare, Kausadikar Varad Prashant, and Santhakumar Mohan	
Analysis of a 4-DOF 3T1R Parallel Robot for Machining Applications: A Stiffness Study	161
Paulo Rossi, Roberto Simoni, and Andrea Piga Carboni	
Modelling and Simulation of Industrial Robot Using SolidWorks	173
Chinmaya Sabnis, N. Anjana, Amit Talli, and Arunkumar C. Giriyapur	
Machinery Associated with Manufacturing	
Long-Range Drilling System with Constrained Tool Path Based on Scissor-Like Elements	185
Juan G. Grijalva, Edson R. De Pieri, and Daniel Martins	
Development of an Automatic Thread Tension Adjusting Device for Single Needle Lock Stitch Machine	195
Bhaskar Guin and Rohan Roy	
Bearing Fault Diagnosis in Induction Motor Using Modified AlexNet Algorithm	205
Swapnil K. Gundewar and Prasad V. Kane	

Improved Design and Development of Crop Conveying Mechanism in Reaper Machine	219
Anand Kumar Jangir, Narendra Achera, Saurav Khandelwal, Chirag Gupta, Himanshu Chaudhary, and N. R. N. V. Gowripathi Rao	
Ergonomic Workstation Design for Welding Operation—A Case Study	229
T. A. Madankar, P. V. Kane, D. Agrawal, and S. V. Kedar	
Prediction of Torque and Cutting Speed of Pedal Operated Chopper for Silage Making	243
Pravin B. Khope and Sagar D. Shelare	
Finite Element Modeling and Parametric Investigation of Friction Stir Welding (FSW)	251
K. S. Mehra, S. Kaushik, G. Pant, S. Kandwal, and A. K. Singh	
Wear Analysis of Polytetrafluoroethylene (PTFE) Reinforced with Carbon and Bronze	261
Prasun Kumar Pandey, S. Thirumalini, R. Padmanaban, and G. Jayashankkar	
Modelling of a Porous Functionally Graded Rotor-Bearing System Using Finite Element Method	273
Aneesh Batchu, Bharath Obalareddy, and Prabhakar Sathujoda	
Influence of Workpiece Mating Gap on Friction Stir Welding of 316L for Fixture Design on a Machine	285
B. Raghu Prem, Kundan K. Singh, and Ravi Shanker Vidyarthi	
Integration of IoT and Industry 4.0 in Mechanism and Machines	
Physics-Driven Process Digital Twins to Aid Pharma and Specialty Material Manufacturing	299
Jenil P. Dedhia and Ravichandra Palaparthi	
EEG-Based Hand Movement Recognition: Feature Domain and Level of Decomposition	311
Nabasmita Phukan, Nayan M. Kakoty, Nipun Gupta, and Neelanjana Baruah	
Burr Registration Using Image Processing	321
Anup Pillai, Shital Chidderwar, M. R. Rahul, and Mohsin Dalvi	
LoRa-Based Infrastructure for Medical IoT System	331
P. Muthu Subramanian and A. Rajeswari	
A Robust Image Analysis Method for Cutting Tool Wear Monitoring in High-Speed Micromilling Process	339
Aman Sharma, Vaibhav Rathore, Brajesh Panigrahi, and Kundan K. Singh	

Space Applications and Modern Structures

Behavior Study of Tape Springs for Space Deployment Applications	349
Rutvik Dangarwala, Hemant Arora, Shashikant Joshi, and Sudipto Mukherjee	
Parametric Optimization of Joints and Links of Space Deployable Antenna Truss Structure	363
Hemant Arora, Vrushang Patel, B. S. Munjal, and Sudipto Mukherjee	
Response of a Vibratory System Under Impact Using Contact Force Models	375
Deepak Maslekar, Anirban Guha, and Sriprya Ramamoorthy	
Failure Behaviour of a Thin Domed Steel Disc with and without Scores Under a Pressure Impulse	385
K. Gopinath, V. Narayananamurthy, and Y. V. D. Rao	
Development of Shape Memory Alloy (SMA) Based Hold-Down and Release Mechanism for Space Applications	393
Harshkumar Patel, Hemant Arora, Shashikant Joshi, and Sudipto Mukherjee	
Applicability of Low-Cost Duct-Shaped Wind Turbine for Domestic Purpose and Low Wind Speed	405
S. V. S. K. Prasad Raju, M. Govindaraju, and T. Satish Kumar	
Bio-medical Devices and Bio-mechanisms, Devices for Aerospace, Automobile and Railways	
Novel CAM Mechanism-Based Life-Support Ventilators in Animal Healthcare	417
Prem Dakshin and Shashank Khurana	
Multi-body Topology Optimization of Connecting Rod Using Equivalent Static Load Method	427
G. Lakshmi Srinivas and Arshad Javed	
Challenges in the Design of a Laparoscopic Surgical Forceps	437
Md. Abdul Raheem Junaidi, Harsha Sista, Y. V. Daseswara Rao, and K. Ram Chandra Murthy	
Improvement in Wear and Friction Properties of Heat-Treated Steel Using Micro-grooved Patterns	451
Nikhil More and S. S. Lakade	
Force Optimization for an Active Suspension System in a Quarter Car Model Using MPC	459
Jayesh Narayan, Saman Asghari Gorji, and Mehran Motamed Ektesabi	
Mobility Analysis of Coupled System of Upper Limb Exoskeleton and Human Arm	475
Macha Vidyaaranya, Sakshi Gupta, and Ekta Singla	

Pressure Vessels, Acoustics and Noise Control, Mechanical and Electro-Mechanical Systems of Modern Machinery

- AHP Integrated TOPSIS Methodology for Selection of Non-Conventional Machining Process for Micro-Drilling** 489

Pranav Vijay Deosant, Ashish Ravindra Lande,
Anurag Gopal Vishwakarma, and Hemant P. Jawale

- Design and Development of Acoustic Metamaterial and Micro-Perforated Panel by Using 3D Printing** 501

Atharva R. Kshirsagar, D. Job Sandeep Rajprian, and J. Jeyanthi

- Study of Effect of Angle of Contact and Angle of Extension of Wear Plate on Maximum Stress Induced in Horizontal Pressure Vessel** 511

Aniruddha Nayak and Pravin Singru

- Effect of Number of Stiffening Rings, Their Position and Cross Section on Stress Concentration Near Saddle Support in Horizontal Pressure Vessels** 521

Aniruddha Nayak and Pravin Singru

- Water Wave Interaction with Very Large Floating Structures** 531

Kottala Panduranga and Santanu Koley

- Annual-Averaged Performance of Oscillating Water Column Wave Energy Converter Devices in Real Sea Conditions** 541

Kshma Trivedi and Santanu Koley

Material Handling and Automated Assembly

- Inverse Kinematic Model of a Cable-Driven Continuum Manipulator** 553

Vipin Pachouri and Pushparaj Mani Pathak

- Task Space Reconstruction in Modular Reconfigurable Manipulation System** 565

Athul Thaliyachira Reji, Anubhav Dogra, Shashi Shekhar Jha,
and Ekta Singla

- Design Analysis and Experimental Validation of Modular Handling System for Satellite Ground Application** 575

G. A. Srinivasa, Shashank Srivastava, and Saurabh Chandraker

- Numerical Investigation on Dynamic Stability of a Pick and Place Robot Arm** 587

B. Upendra, B. Panigrahi, K. Singh, and G. R. Sabareesh

- A Method for Evaluation of Welding Performance of SMAW Electrodes** 597

Brajesh Asati and Ravi Shanker Vidyarthi

Modeling and Kinematic Analysis of a Robotic Manipulator for Street Cleaning Applications Using Screw Theory	609
Neel Gandhi, Garlapati Nagababu, and Janardhan Vistapalli	
Hybrid Electric Vechicle and Electric Vechicle Mechanisms	
Dynamics and Isolation Capabilities of a Magnetic Spring-Based Quasi-Zero Stiffness Vibration Isolation Mechanism for Passenger Vehicle Seat Isolation	621
Prajapati Brijeshkumar and B. Santhosh	
Vertical Vibrations of the Vehicle Excited by Ride Test	631
Massimo Cavacece, Giorgio Figliolini, and Chiara Lanni	
Investigation of Dynamic Forces and Moments in the Neck Region of the Driver of a Vehicle	643
Raj Desai, Anirban Guha, and P. Seshu	
Analysis of Design of Head Restraints of Car Seat Considering Indian Anthropometry	653
Radhika Tekade, Girish Ramteke, and P. V. Kane	
Novel Method for BSR Test Cycle Generation	665
K. J. Sarat and C. Lakshmikanthan	
Feasibility of Adoption of Double-Crank Inversion of Four-Bar Chain as a Substitute for a Gear Box	675
Akshay Anant Pachpor, Jayant Pandurang Modak, and Prashant Brajmohan Maheshwary	
Structural Synthesis and Classification of Epicyclic Gear Trains: An Acyclic Graph-Based Approach	683
V. R. Shanmukhasundaram, Y. V. D. Rao, S. P. Regalla, D. Varadaraju, and E. Pennestrì	
Fuel Economy and Drivability Trade-Off for Mild Hybrid Electric Vehicle Architectures	709
Neeraj Shidore, Norman Bucknor, and Madhusudan Raghavan	

About the Editors

Prof. Y. V. D. Rao is currently an Associate Professor at the Department of Mechanical Engineering, Birla Institute of Technology and Science (BITS), Pilani, Hyderabad campus. He obtained his B.Tech. (Mechanical Engineering) from National Institute of Technology, Surathkal (Known that time as Regional Engineering College); M.Tech. (Design Eng.) from the Indian Institute of Technology, Delhi (IITD); and Ph.D. from the Government College of Engineering, Raipur (Known now as NIT Raipur). His major areas of research interest include topological synthesis and analysis of Gear trains and Robotic structures, Robot-Assisted Incremental Sheet Metal Forming, Vibration and Shock Isolation, Robotic Dental Implantation, and Crashworthiness in automobile vehicles under axial impacts. He has published 18 papers in peer-reviewed international journals. He has so far published 40 plus research works in national and international conferences.

Prof. C. Amarnath is a Mechanical Engineering Graduate of 1968. After earning his Ph.D in the area of Mechanism Synthesis and Design, he joined IIT Bombay as a faculty member and has held several senior positions like Head of Dept. and Dean at IITB. He was heading SINE, the Innovation, Entrepreneurship, and Incubation Centre, at IIT Bombay till his retirement from service in 2012. Prof. Amarnath has several publications to his credit and has established the Robotics Lab, the Textile Lab, and the Innovation Centre at IITB. He is a consultant to several industries like L&T, Godrej, BHEL, and Nuclear Power Corporation. Major projects undertaken by him (some as member of a team) include a Spiral Heat Exchanger Mfg. Machine (L&T), Push-Pull Mechanism for NPC, Six legged walking machine (BRNS-BARC), and a Remotely Operated Robot for the Army Technology Board. Prof. Amarnath was instrumental in establishing and is the current President of the Association for Machines and Mechanisms. He was recently bestowed the Distinguished Service award by IFToMM, the International Federation.

Prof. Srinivasa Prakash Regalla is currently a Professor at the Department of Mechanical Engineering, Birla Institute of Technology and Science, Pilani, Hyderabad campus. He obtained his B.Tech. (Mech.) from Kakatiya University, Warangal; M.Tech. (Mech.) from the Indian Institute of Technology, Kanpur; and Ph.D. from the

Indian Institute of Technology, Delhi. His major areas of research interests include computer-aided mechanical design, additive manufacturing, tribology in sheet metal forming, biomechanics, and design of medical devices. He has published 50 papers in respected international journals and two books on product design. Dr. Regalla received the BIRAC-BIG grant award in 2014 for prosthetic design and distinguished alumni award from his B.Tech. college.

Dr. Arshad Javed is currently an Assistant Professor at the Department of Mechanical Engineering, Birla Institute of Technology and Science, Pilani (BITS Pilani), Hyderabad Campus. He obtained his B.Tech. (Mechanical Engg.) from BIET Jhansi(UP) and M.E. (Mechanical Engg.) and Ph.D. from BITS Pilani, Pilani Campus. His teaching and research interests include Topology Optimization, Robotics, Mechatronics, Automation, and Microfluidic systems. He has published 15 papers in respected international journals and presented several research works in National and International conferences.

Dr. Kundan Kumar Singh is currently an Assistant Professor at the Department of Mechanical Engineering, Birla Institute of Technology and Science, Pilani (BITS Pilani), Hyderabad Campus. He obtained his B.Tech. (Mechanical Engg.) from JGEC Jalpaiguri (WB); MME (Mechanical Engg.) from Jadavpur University, Kolkata (WB); and Ph.D. from Indian Institute of Technology Bombay, Mumbai, India. His teaching and research interests include machine tool dynamics, manufacturing automation, micro manufacturing, surface metrology, data analysis, and condition monitoring. He has published 9 papers in reputed international journals and presented several research works in National and International conferences.

Compliant Mechanism

Jacobian-Based Inverse Kinematics Analysis of a Pneumatic Actuated Continuum Manipulator



Mrunal Kanti Mishra , Sambaran Ghosal, Arun Kumar Samantaray , and Goutam Chakraborty

1 Introduction

Continuum manipulators are biologically inspired manipulators. These draw inspiration from a variety of biological species such as snakes [1], octopus arms [2], or elephant trunks [3]. They have gathered huge research interests in the past decades owing to the inherent flexibility of their designs. These manipulators are day by day finding new application areas especially in the fields where rigid link manipulators are not feasible, i.e., in workspaces with a large number of barriers or obstacles. The development of closed-form models for these kinds of manipulators is a challenge.

Over the past decades, numerous planar and spatial kinematics models are developed for continuum manipulators. Some of these include the Cosserat Rod model [4], Elastic Beam theory [5], or even a lumped model [6]. For instance, as a planar forward kinematics model, a serpentine curve is designed which closely matches the kinematics of a snake's body in two dimensions as it crawls across the ground [1]. On the other hand, Chirikjian [4] fitted a mathematical curve to a high degree of freedom hyper-redundant manipulator. However, due to computational complexity, a few continuum robots match the proposed curve. Jones and Walker [5] used an Elastic Beam theory to develop an FK model and validated it on a multi-section continuum manipulator. Giri and Walker [6] discretized a continuum arm to a three-module lumped element model and studied FK. Escande et al. [7] studied the FK of a multi-section bionic manipulator with the help of the triangulation method. They

M. K. Mishra · S. Ghosal · A. K. Samantaray · G. Chakraborty
Indian Institute of Technology Kharagpur, Kharagpur 721302, West Bengal, India
e-mail: mrunkanti@gmail.com

A. K. Samantaray
e-mail: samantaray@mech.iitkgp.ac.in

G. Chakraborty
e-mail: goutam@mech.iitkgp.ac.in

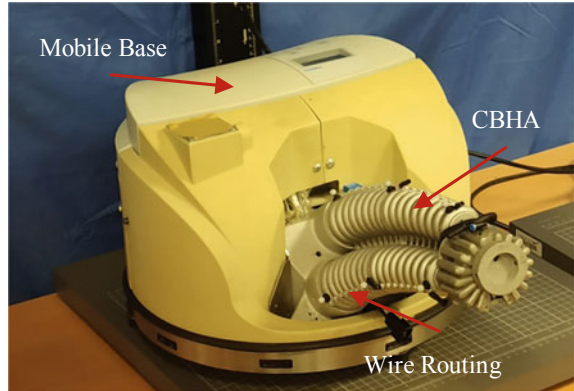
have validated the developed method by coupling the continuum manipulator along with six degrees of freedom conventional rigid manipulator. Mishra et al. [8] developed a closed-form solution for a single segment continuum manipulator using an elliptical integral approach. The model approximates an Euler–Bernoulli beam as a continuum manipulator in planar space. A geometrical approach-based FK is also developed which relates between actuator zone-based parameters and the pose of the manipulator, which assumes the section to be a constant cross-section. As a result, the deflected manipulator takes a circular shape with a constant radius of curvature, and so the model is named as constant curvature model [9]. This model is proved a remarkable approach across a wide variety of continuum manipulator designs due to its analytical attractiveness.

Continuum manipulators are those having infinite degrees of freedom, involving more flexibility and reachability of targets. This redundancy can be exploited for the avoidance of obstacles, elimination of singularities, and as well as for smooth motion tasks realizing. Inverse kinematics modelling of continuum manipulators remains difficult to obtain because they are under-determined systems with a high number of unknown parameters. Moreover, most of the governing IK equations are highly nonlinear in nature, which does not even have closed-form solutions. The inability to solve these high nonlinear equations leads most of the researchers towards numerical methods or model-free methods. Neppalli et al. [10] developed the IK for a continuum manipulator using the geometrical approach. They tried to find the solutions by inverting the continuum curvature model for a single section only. However, this method fails to determine the solutions for multi-section manipulator. Chirikjian [11] proposed an IK model using a backbone curve. The same authors also developed a modal approach to calculate actuator zone parameters [12]. This method gives a very accurate result, but because of its complicity, it is very difficult to use. Braganza et al. [13] used a feed-forward neural network to control nine degrees of freedom OctArm -V. Similarly, Li et al. [14] used a model-free method based on the Kalman filter to control a continuum manipulator.

Most of the aforementioned IK models either fail to describe the pose in closed form or computationally complex to solve. This in turn implies an inability to develop an effective model-based controller in real time. Therefore, in this paper, we use the constant curvature model to arrive at the FK equations. After the FK model, we develop the IK solutions for the manipulator by using the pseudo-Jacobian method. The developed method is validated on Robotino-XT (see Fig. 1), which consists of a two-segment continuum manipulator named as CBHA.

The outline of the paper is organized as follows. A brief introduction on the kinematics of different kinds of continuum robots is provided in Sect. 1. In Sect. 2, the forward kinematics using Continuum Curvature Model along with the proposed Jacobian-based inverse kinematics model is presented. The proposed model is applied on a serially connected two-stage bionic continuum manipulator and the results for the same are given in Sect. 3. Finally, in Sect. 4, some concluding comments are specified.

Fig. 1 Robotino-XT: CBHA with a mobile base



2 Kinematic Modelling

2.1 Forward Kinematics

Forward Kinematics of bending sections of continuum manipulators is widely developed under the constant curvature assumption [9]. This model is particularly based on two different assumptions. Firstly, the entire manipulator is separated into multiple numbers of segments. This approximation allows converting the infinite degrees of freedom system to a finite one. Secondly, the shape of a bending section is to be a perfect arc of a circle or the curvature radius is constant throughout the length. This approximation has the advantage to simplify the model formulations for some continuum manipulators and allow easy formulations of matrix transformation.

Continuum Curvature model is obtained by using two independent mappings as shown in Fig. 2. The explicit mapping is varied from manipulator to manipulator and mostly depends on the number of actuators per segment. This mapping maps actuator zone parameters (length of the actuators) to configuration zone parameters (segment arc parameters). On the other hand, the typical mapping is applied to all types of

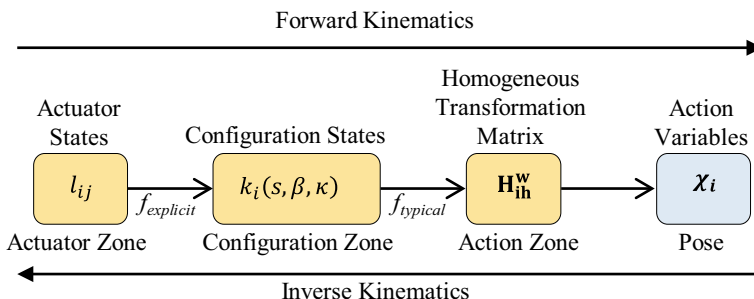


Fig. 2 Systematic model procedure for forward and inverse kinematics

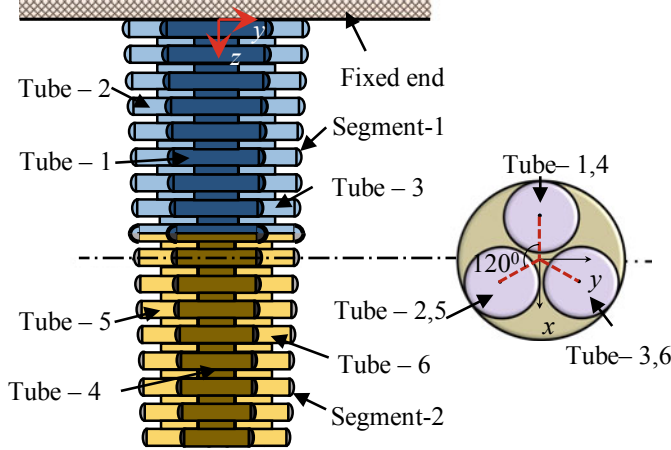


Fig. 3 Two-segment manipulator with cross-section

continuum manipulators, regardless of lengths and orientation. This mapping maps configuration zone parameters to action zone parameters, i.e., manipulator pose.

A continuum manipulator segment can be actuated by j —number of actuators. However, for several reasons, three actuators per segment with 120° actuator spacing type continuum manipulator is best suitable to move a manipulator spatially [9]. These kinds of manipulators are energy efficient and have great manoeuvrability than other choices of actuator numbers and actuator spacing. So, in this paper, a two-segment continuum manipulator along with three actuators per segment having 120° actuator spacing is considered. The manipulator along with its cross-sectional area is shown in Fig. 3. The mapping between the actuator lengths (l_{ij}) and the segment arc parameters ($\mathbf{k}_i(s_i, \beta_i, \kappa_i)$) for three actuators per segment with 120° actuator spacing is determined as [5]

$$\begin{aligned} s_i(l_{ij}) &= \frac{l_{i1}+l_{i2}+l_{i3}}{3} \\ \beta_i(l_{ij}) &= \text{atan2}\left(\sqrt{3}(l_{i3}-l_{i2}), l_{i2}+l_{i3}-2l_{i1}\right) \\ \kappa_i(l_{ij}) &= \frac{2\sqrt{l_{i1}^2+l_{i2}^2+l_{i3}^2-l_{i1}l_{i2}-l_{i2}l_{i3}-l_{i3}l_{i1}}}{(l_{i1}+l_{i2}+l_{i3})r_{s_i}} \end{aligned} \quad (1)$$

and the mapping between the arc parameters and the manipulator pose of a segment is determined by a transformation matrix as [9]

$$\mathbf{H}_{ih}^{ib} = \begin{bmatrix} \cos \kappa_i s_i \cos \beta_i & -\sin \beta_i & \sin \kappa_i s_i \cos \beta_i & \frac{\cos \beta_i (1-\cos \kappa_i s_i)}{\kappa_i} \\ \cos \kappa_i s_i \sin \beta_i & \cos \beta_i & \sin \kappa_i s_i \sin \beta_i & \frac{\sin \beta_i (1-\cos \kappa_i s_i)}{\kappa_i} \\ -\sin \kappa_i s_i & 0 & \cos \kappa_i s_i & \frac{\sin \kappa_i s_i}{\kappa_i} \\ 0 & 0 & 0 & 1 \end{bmatrix} \quad (2)$$

where s is the segment length, β is the segment angle, κ is the segment radius of curvature, l is the length of the actuator for i th segment and j th actuator, r_s is the radius of each segment, and \mathbf{H}_{ih}^{ib} is the homogeneous matrix for i th segment. Note that, under the same actuation to the actuators of a section, the lengths of the actuators are the same, resulting in the orientation of the segment to a null matrix and the head frame position of the segment to $[0 \ 0 \ s_i]^T$.

Using the relations from (1) and (2), the tip rotation matrix and position vector of a two-segment continuum manipulator with respect to the world frame is given as

$$\mathbf{H}_{2h}^w = \mathbf{H}_{1b}^w \prod_{s=1}^2 \left(\mathbf{H}_{sh}^{sb} \mathbf{H}_{(s+1)b}^{sh} \right), \quad \mathbb{R} \in [4 \times 4] \quad (3)$$

where $\prod(\cdot)$ calculates product summation of the transformation matrices. Note that, in the end section of the manipulator, $\mathbf{H}_{(s+1)b}^{sh}$ is an $[4 \times 4]$ identity matrix. From (3), the pose of the tip of a segment in the Cartesian frame is portrayed by

$$\chi = [\theta_x \ \theta_y \ \theta_z \ x \ y \ z]^T \quad (4)$$

where $\theta_x = \text{atan}2(-\mathbf{H}_{2h}^w(2, 3), \mathbf{H}_{2h}^w(2, 4))$, $\theta_y = \text{atan}22(-\mathbf{H}_{2h}^w(1, 3), \mathbf{H}_{2h}^w(3, 3))$, $\theta_z = 0$, $x = \mathbf{H}_{2h}^w(1, 4)$, $y = \mathbf{H}_{2h}^w(2, 4)$, $z = \mathbf{H}_{2h}^w(3, 4)$. Note that p, q of $\mathbf{H}(p, q)$ are matrix row and column, respectively. The rotation of the manipulator along the central axis (θ_z) is equal to zero, because the manipulator is only allowed to a two-way bending, and no torsional moment is allowed. Therefore, we will omit θ_z from our further derivation and consider the pose of the manipulator tip to be five degrees of freedom.

2.2 Differential Kinematics

Differential kinematics of a continuum manipulator can be determined by applying the first derivative with respect to time to forward kinematics relation. Therefore, applying first time derivative to (4) results,

$$\dot{\chi} = \mathbf{J}(l)\dot{l}(t), \quad \mathbb{R} \in [5 \times 1] \quad (5)$$

where $\mathbf{J}(l)$ is the Jacobian matrix and can be determined by applying chain rule as

$$\mathbf{J}(l) = \frac{\partial \chi}{\partial l} = \frac{\partial \chi}{\partial \mathbf{H}} \frac{\partial \mathbf{H}}{\partial k} \frac{\partial k}{\partial l}, \quad \mathbb{R} \in [5 \times 3n]. \quad (6)$$

From (6), it can be checked that $\frac{\partial \chi}{\partial \mathbf{H}} \in \mathbb{R}^{(5 \times 16)}$ is independent of a number of segments of the manipulator. However, for instance, for a two-segment manipulator, $\frac{\partial \mathbf{H}}{\partial k} \in \mathbb{R}^{(16 \times 6)}$ and $\frac{\partial k}{\partial l} \in \mathbb{R}^{(6 \times 6)}$ depend on the number of segments of the manipulator.

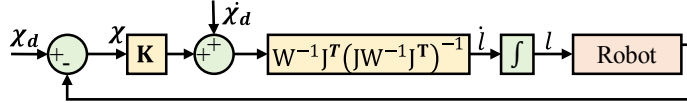


Fig. 4 Block diagram for inverse kinematics using Jacobian

2.3 Inverse Kinematics

In order to move the manipulator pose in a certain trajectory, it is essential to find actuator zone parameters from the action zone parameters. Thus, it is crucial to develop inverse kinematics solutions correctly. To develop a model-based controller for a class of continuum manipulator, in this paper, a Jacobian matrix is developed using the differential kinematics equation as of (6). However, no direct procedure is available to invert the rectangular Jacobian matrix. So, a weighted matrix is used for pseudo-Jacobian inverse (\mathbf{J}^\dagger), where $\mathbf{J}^\dagger = \mathbf{J}^T(\mathbf{J}\mathbf{J}^T)^{-1}$. So, using resolved rate algorithm, a weighting matrix [15], and a gain matrix, the actuator state velocities $\dot{l}(t)$ can be determined as

$$\dot{l}(t) = \mathbf{W}^{-1}\mathbf{J}^T(\mathbf{J}\mathbf{W}^{-1}\mathbf{J}^T)^{-1}(\dot{\chi}_d + \mathbf{K}(\chi_d - \chi)) \quad (7)$$

where the weighting matrix is a diagonal matrix and is defined as

$$\mathbf{W} = \text{diag}(w_1 \ w_2 \ \dots \ w_n), \ \mathbb{R} \in [3n \times 3n] \quad (8)$$

where the weight values are chosen in such a way to avoid joint limits. In addition, the gain matrix is defined by

$$\mathbf{K} = \text{diag}(\kappa_1 \ \kappa_2 \ \dots \ \kappa_5), \ \mathbb{R} \in [5 \times 5] \quad (9)$$

where the gain values are chosen as positive values. This matrix is usually a diagonal matrix, which reduces the tracking errors between actual χ and desired χ_d . Additionally, integration of the actuator zone velocities $\dot{l}_{ij}(t)$ is performed to find actuator zone parameters/trajectory $l_{ij}(t)$. The block diagram for IK is given in Fig. 4.

3 Results and Discussion

The developed kinematics formulations can be verified on a n -segment continuum manipulator. However, for simplicity, the effectiveness of the developed model is validated on Robotino-XT, which contains a CBHA attached to a mobile base with 48° angle as shown in Fig. 1. The mobile base of Robotino-XT can move and rotate individually on a horizontal surface and the CBHA is a two-stage pneumatic actuated

continuum manipulator. Each manipulator segment consists of three flexible tubes with 120° spacing and each tube is attached with a flexible string. The strings help to measure the length of the tubes at any stage. The flexible tubes are actuated by an external compressor with a maximum allowable pressure of 2 bar. The differential pressures of the tubes of each segment ultimately help the manipulator to bend about a certain axis. The tubes are made of flexible material, namely polyamide. The geometric parameters of the manipulator are provided in Table 1.

The workspace of the Robotino-XT depends on the individual actuation of the mobile base and CBHA. The mobile base can move horizontally to any position in any direction, whereas the CBHA can move spatially depending upon the actuation pressure. Therefore, the workspace of the Robotino-XT is assumed as a *rectanguloid* of a certain height. In this paper, only pneumatic actuation is supplied to the CBHA and the actuation of the mobile base is given zero. The lengths of each tube of the actuated CBHA is measured by the attached strings and by using the Continuum Curvature model, the workspace of the manipulator is determined in local coordinate as shown in Fig. 5 [8].

The desired trajectory is required to validate the derived formulations from the workspace of the continuum manipulator. Therefore, within the workspace of the CBHA, the reference trajectory for a circle is chosen as

Table 1 Geometric parameters of a two-segment continuum manipulator

Symbol	Unit	Range
Tube length (actuator length)	(mm)	90–125
Tube volume	(10^5 mm 3)	1.52–2.046
Average segment diameter	(mm)	107.8

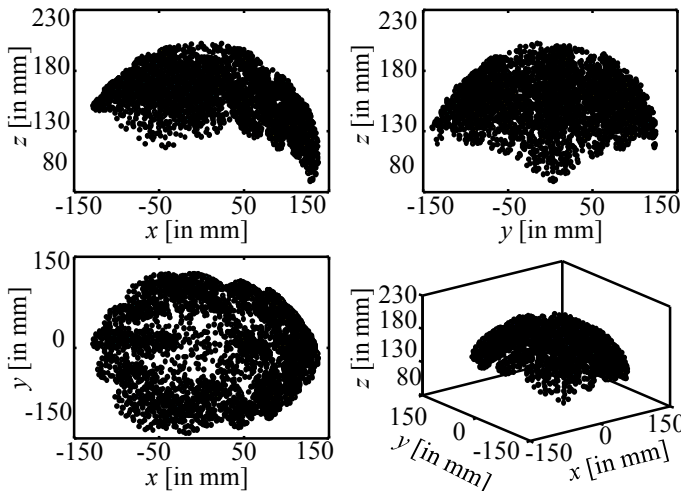


Fig. 5 Workspace of CBHA

$$\begin{aligned}x(t) &= 90 \cos 0.52t \text{ (mm)} \\y(t) &= -5 + 90 \sin 0.52t \text{ (mm)} \\z(t) &= 180 \text{ (mm)}\end{aligned}\quad (10)$$

where $x(t)$, $y(t)$, $z(t)$ are the required trajectory for the pose of the manipulator end effector. The tip orientation is omitted from the current analysis. The accuracy of the actual trajectory mentioned in (10) is verified by comparing the output of the inverse kinematics solution (obtained using (7)) by inserting it into the forward kinematics model and observing the differences in the trajectories. In Fig. 6, the weight matrix values are kept constant for all manipulator trajectories, whereas the gain values are varied suitably to improve the accuracy. It is found that an increase in the gain values increases the accuracy significantly. A detailed inspection shows that only by changing the third and the fourth gain values, the accuracy changes. This is because we have considered $x(t)$, $y(t)$ as variables and $z(t)$ as constant. Moreover, any changes in the first and second gain values do not affect the trajectory, because the tip orientations have no specific significance for the trajectory pose.

We defined the period to complete the desired circle to be 12 s and set the weighting matrix $\mathbf{W} = \text{diag}(1, 1, 1, 0.5, 1, 1)$, and gain matrix $\mathbf{K} = \text{diag}(0.005, 0.005, 10, 10, 0.05)$. During this time, the manipulator end-effector pose is varied sinusoidally as shown in Fig. 7. From the figure, it is seen that the x , y tip coordinates approximately achieved the desired trajectory. However, a significant error occurred in z coordinate as the trajectory tracking progresses. This can be further improved by improving the gain values.

Fig. 6 A circular Desired trajectory versus Actual trajectory

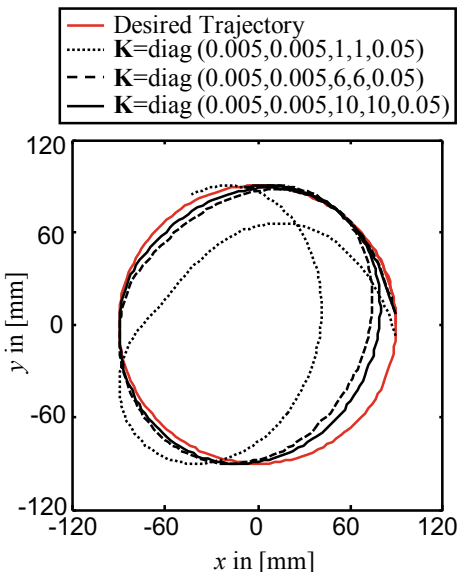
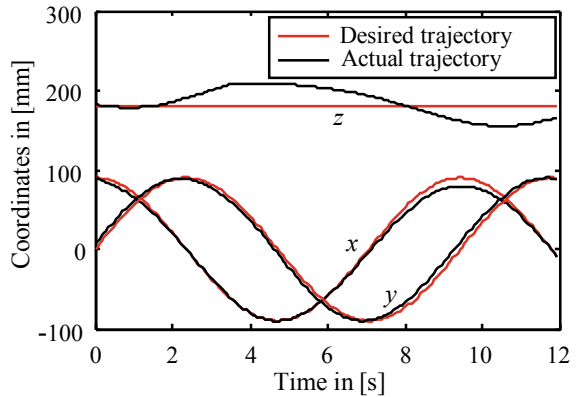


Fig. 7 Manipulator tip position over the period of time

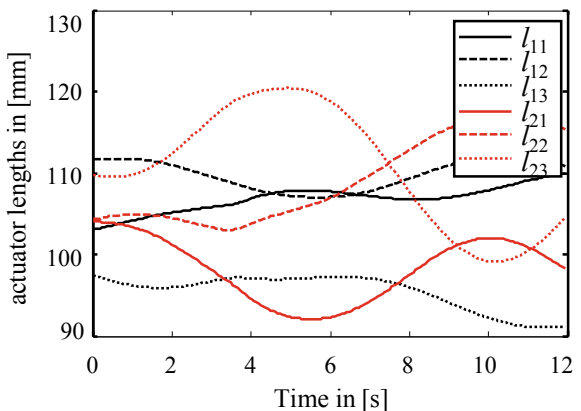


The average positional error of the manipulator tip for optimized weight and gain values is compared with previously developed inverse kinematics methods as shown in Table 2. Previously developed methods are based on model-free techniques whereas the current method is based on model-based techniques. For the desired trajectory, the lengths of all the six actuators are determined from the proposed model in Fig. 4. The length variation of the actuators is displayed in Fig. 8.

Table 2 Error comparison of different methods

Authors	Manipulator	Method	Error (mm)
Braganza et al. [13]	OctArm-V	Feed-forward neural network	30
Li et al. [14]	Pneumatic actuator muscle	Adaptive Kalman filter	2.31
Present method	Two-stage Elephant trunk like manipulator	Resolved rate algorithm	3.51

Fig. 8 Actuator length variation according to differential kinematics



4 Conclusion

In this paper, a closed-form inverse kinematics model is developed using the pseudo-Jacobian inverse method and applied on CBHA of Robotino-XT, which is a two-segment continuum manipulator. A circular trajectory is chosen from the workspace of the manipulator to validate the proposed model. The method discussed above assumes a suitable weighting matrix and a gain matrix. The weighting matrix helps in weight distribution to the actuators, so that inverse of the diagonal Jacobian matrix can be performed. However, changing the values does not help to increase accuracy. The gain matrix tracks the error in the desired and current pose of the manipulator and helps to increase the tip positional accuracy. It is observed that, with an increase in certain gain values, the manipulator pose accuracy increases. In future, the proposed model-based method can help to develop an effective real-time controller to manoeuvre the manipulator smoothly.

References

1. Hirose, S.: Biological Inspired Robots, Snake-Like Locomotors and Manipulators. Oxford University Press, Oxford (1993)
2. Kang, R., Branson, D.T., Guglielmino, E., Caldwell, D.G.: Dynamic modeling and control of an octopus inspired multiple continuum arm robot. *Comput. Math Appl.* **64**(5), 1004–1016 (2012)
3. Mishra, M.K., Samantaray, A.K., Chakraborty, G., Jain, A., Pathak, P.M., Merzouki, R.: Dynamic modelling of an elephant trunk like flexible bionic manipulator. In: International Mechanical Engineering Congress & Exposition 2019, vol. 4, pp. 1–9. ASME, Salt Lake City (2019). <https://doi.org/10.1115/IMECE2019-11113>
4. Chirikjian, G.S.: Hyper-redundant manipulator dynamics: a continuum approximation. *Adv. Robot.* **9**(3), 37–41 (1995)
5. Jones, B.A., Walker, I.D.: Kinematics for multisection continuum robots. *IEEE Trans. Robot.* **22**(1), 43–55 (2006)
6. Giri, N., Walker, I.D.: Three module lumped element model of a continuum arm section. In: IEEE/RSJ International Conference on Intelligent Robots and Systems 2011, pp. 4060–4065. IEEE, San Francisco (2011)
7. Escande, C., Chettibi, T., Merzouki, R., Coelen, V., Pathak, P.M.: Kinematic calibration of a multisection bionic manipulator. *IEEE/ASME Trans. Mechatron.* **20**(2), 663–674 (2015)
8. Mishra, M.K., Samantaray, A.K., Chakraborty, G., Pachouri, V., Pathak, P.M., Merzouki, R.: Kinematics model of bionic manipulator by using elliptic integral approach. In: 4th International and 19th National Conference on Machines and Mechanisms. Springer, Mandi (2019)
9. Webster III, R.J., Jones, B.A.: Design and kinematic modeling of constant curvature continuum robots: a review. *Int. J. Robot. Res.* **29**(13), 1661–1683 (2010)
10. Neppalli, S., Csencsits, M.A., Jones, B.A., Walker, I.D.: Closed-Form inverse kinematics for continuum manipulators. *Adv. Robot.* **23**, 2077–2091 (2009)
11. Chirikjian, G.S.: A general numerical method for hyper-redundant manipulator inverse kinematics. In: IEEE International Conference on Robotics & Automation 1993, pp. 107–112. IEEE, Atlanta (1993)
12. Chirikjian, G.S., Burdick, J.W.: A modal approach to hyper-redundant manipulator kinematics. *IEEE Trans. Robot. Autom.* **10**(3), 346–354 (1994)

13. Braganza, D., Dawson, M.D., Walker, I.D., Nath, N.: A neural network controller for continuum robots. *IEEE Trans. Rob.* **23**(5), 1270–1277 (2007)
14. Li, M., Kang, R., Branson III, D.T., Dai, J.S.: Model-free control for continuum robots based on an adaptive kalman filter. *IEEE/ASME Trans. Mechatron.* **23**(1), 286–297 (2018)
15. Chan, T.F., Dubey, R.V.: A weighted least-norm solution based scheme for avoiding joint limits for redundant joint manipulators. *IEEE Trans. Robot. Autom.* **11**(2), 286–292 (1995)

Path Curvature Theory: A Classic and Effective Design Tool



Mattia Cera, Marco Cirelli, Ettore Pennestrì, Pier Paolo Valentini,
and V. R. Shanmukhasundaram

1 Introduction

The planar path curvature analysis is a well-known classic topic in kinematics. Two centuries of scientific investigations created a formidable cultural heritage, as well as a great source of knowledge and inspiration for mechanical engineers. This paper has the purpose to discuss applications of this theory to three industrial cases: the stability of lifting rigs, the design of centrifugal dampers, and the analysis of compliant linkages. These topics seem more related to dynamics and elasticity than to curvature kinematics.

The first part is dedicated to the modeling of a body resting on two curves [1]. When the curves are circles, this model reproduces the dynamics of a four-bar coupler subjected to the weight force. A geometric criterion for the stability analysis of lifting rigs will be established. The second part is dedicated to the computation of tautochrone oscillation period T of a particle moving along an epicycloid and subjected to a centrifugal force field. The derivation of an analytical expression of T is based on a novel application of the fundamental formulas of Cesàro's intrinsic geometry. The obtained result is meaningful for the tuning of centrifugal dampers [2, 3]. The last application regards an application of Euler–Savary equation to compliant linkages.

M. Cera · E. Pennestrì (✉) · P. P. Valentini
University of Rome Tor Vergata, 00133 Rome, Italy
e-mail: pennestri@mec.uniroma2.it
URL: <https://www.uniroma2.it>:

M. Cirelli
Niccolò Cusano University, 00166 Rome, Italy
e-mail: marco.cirelli@unicusano.it

V. R. Shanmukhasundaram
Birla Institute of Technology and Science, Department of Mechanical Engineering, Pilāni, India

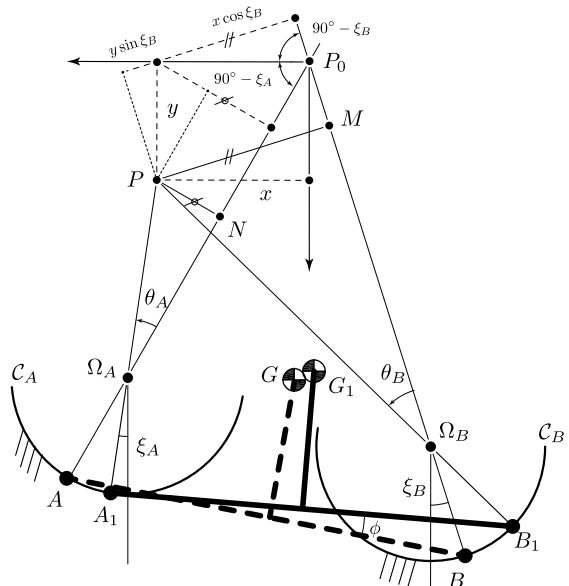
2 Oscillations of a Body Resting on Two Curves

As depicted in Fig. 1, a body with two points A and B is sliding without friction along the curves C_A and C_B , respectively. The body is initially in equilibrium under the gravity force. Our purpose is to obtain the period T of small oscillations. In this section, it will be demonstrated how such period is related to the system geometric parameters. It will be also discussed how the theory of planar curvature offers a concise solution to the final result.

The following nomenclature is adopted:

- A_1, B_1 positions of points A and B after a body rotation;
- g acceleration of gravity;
- G and G_1 initial and final positions of the center of mass, respectively;
- k_G radius of gyration;
- L_{eq} length of equivalent simple pendulum;
- M and N orthogonal projections of P and P_0 along directions $\Omega_B P_0$ and $\Omega_A P = 0$, respectively;
- m mass of the moving cylinder;
- I_G body moment of inertia about center of mass G ;
- P_0 and P initial and final positions of the velocity pole, respectively;
- x, y coordinates of P in a Cartesian system of coordinates with origin in P_0 and axes along horizontal and vertical directions;
- ϕ infinitesimal rotation angle of bar AB ;
- Ω_A, Ω_B centers of curvature of trajectories of A and B , respectively;

Fig. 1 Oscillations of a body resting on two curves



- θ_A, θ_B infinitesimal angles of rotations of segments Ω_AA and Ω_BB , respectively;
- ξ_A, ξ_B angles formed by segments Ω_AA and Ω_BB with vertical direction, respectively.

From the system geometry, the following equalities can be deduced:

$$\widehat{AA_1} = \Omega_AA \cdot \theta_A = P_0A \cdot \phi \quad (1a)$$

$$\widehat{BB_1} = \Omega_BB \cdot \theta_B = P_0B \cdot \phi \quad (1b)$$

$$\widehat{G_0G} = P_0G_0 \cdot \phi \quad (1c)$$

Moreover, the lengths of infinitesimal arcs \widehat{MP} and \widehat{NP} are

$$\widehat{MP} = \Omega_BP \cdot \theta_B, \quad \widehat{NP} = \Omega_AP \cdot \theta_A \quad (2)$$

For the equilibrium, the distance x is required. This distance will be computed solving the system

$$\begin{cases} x \cos \xi_B + y \sin \xi_B = \Omega_BP \cdot \theta_B \\ x \cos \xi_A - y \sin \xi_A = \Omega_AP \cdot \theta_A \end{cases} \quad (3)$$

or

$$x = \frac{\Omega_BP \cdot \theta_B \sin \xi_A + \Omega_AP \cdot \theta_A \sin \xi_B}{\sin(\xi_A + \xi_B)} \quad (4)$$

The Aronhold-Kennedy theorem yields

$$\theta_B = \frac{P_0B}{\Omega_BB} \phi, \quad \theta_A = \frac{P_0A}{\Omega_AA} \phi \quad (5)$$

The substitution of (5) into (4) gives

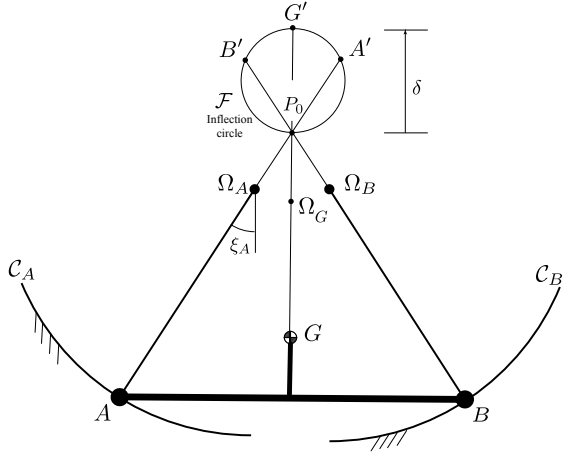
$$x = \frac{\frac{\Omega_BP_0 \cdot P_0B}{\Omega_BB} \sin \xi_A + \frac{\Omega_AP_0 \cdot P_0A}{\Omega_AA} \sin \xi_B}{\sin(\xi_A + \xi_B)} \phi \quad (6)$$

Taking the moments about P , we have the governing differential equations of motion

$$(k_G^2 + P_0G^2) \frac{d^2\phi}{dt^2} + g(G_0G + x)\phi = 0 \quad (7)$$

Since $G_0G = P_0G\phi$, the length of an equivalent pendulum can be expressed as

Fig. 2 Equivalent symmetric four-bar linkage



$$\frac{k_G^2 + P_0 G^2}{L_{eq}} = P_0 G + \frac{\Omega_B P_0 \cdot P_0 B}{\Omega_B B} \frac{\sin \xi_A}{\sin (\xi_A + \xi_B)} + \frac{\Omega_A P_0 \cdot P_0 A}{\Omega_A A} \frac{\sin \xi_B}{\sin (\xi_A + \xi_B)} \quad (8)$$

To gain insights, it is useful to particularize the previous equation for the case of a point mass ($k_G = 0$) on the coupler of a symmetric four-bar linkage (see Fig. 2) such that $\xi_A = \xi_B$, $\Omega_{AA} = \Omega_{BB}$, $P_0A = P_0B$.

Under these conditions, Eq. (8) simplifies into

$$\frac{P_0 G^2}{L_{eq}} = P_0 G + 2 \frac{\Omega_B P_0 \cdot P_0 B}{\Omega_B B} \frac{\sin \xi_A}{\sin 2\xi_A} \quad (9)$$

One can verify that¹

$$G'P_0 = P_0B \frac{\Omega_B P_0}{\Omega_B B \cos \xi_A} \quad (10)$$

Therefore, from Eq. (9), we can conclude that

$$L_{eq} = \frac{P_0 G^2}{P_0 G + G'P_0} = \frac{P_0 G^2}{G'G} = \Omega_G G \quad (11)$$

The result confirms that in some cases, the theory of curvature offers a concise solution for preliminary stability and natural frequency analysis of one degree of freedom mechanical systems. An application is the test of the stability of suspension

¹Considered that $P_0G' \cos \xi_A = P_0B'$, the proportion (10) gives

$$(\Omega_B P_0 - \Omega_B B) : \Omega_B B = (P_0 B' - P_0 B) : P_0 B$$

This leads to the second form of the Euler–Savary equation $P_0 B^2 = \Omega_B B \cdot B'B$ specialized for point B .

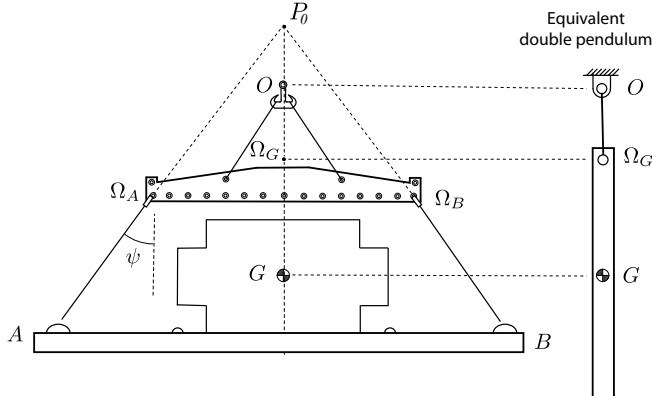


Fig. 3 Stability of lifting rigs

rigs [4, 5]. With reference to Fig. 3, the stability for small oscillations about the equilibrium position of the suspended load requires the position of center of curvature Ω_G to lie between suspension point O and center of mass G :

$$\therefore P_0O < P_0\Omega_G < P_0G \quad (12)$$

In particular, the beam mass is assumed negligible and the system motion can be considered as that of a double pendulum suspended at O , with $O\Omega_G$ the first massless bar and Ω_GG the second bar. In terms of readily measured segment lengths, after Euler–Savary equation:

$$\frac{1}{P_0O} > \frac{1}{P_0G} + \left(\frac{1}{P_0A} - \frac{1}{P_0\Omega_A} \right) \cos \psi \quad (13)$$

3 Curvature Theory and Design of Centrifugal Dampers

Centrifugal dampers are key components of modern internal combustion engines with a reduced number of cylinders and increased energy output at lower engine speeds [2]. In Ref. [6], a kinematic equivalence between a four-bar linkage and the new generation of centrifugal dampers has been established. The main components are counterweights where their centers of mass are constrained to move along given tautochrone² trajectories (e.g., cycloids or epicycloids) [3, 7]. In this section, we will

²Given a field of forces F , a curve C is said to be *tautochrone* with respect to a point O if a particle starting from rest, moving along C under the action of F , arrives at point O after an interval of time T which is independent from the point starting position.

investigate the relationship between path curvature kinematics and the tautochronism for the case of a point moving on epicycloid and subjected to a centrifugal force field. This condition applies to the case of centrifugal damper design where the counterweight oscillation period is tuned with the rotor oscillation frequency that needs to be reduced.

Early centrifugal dampers design relied upon the hypothesis of isochronism of simple pendulum small oscillations. The advantage of using tautochrone trajectories is due to the independency between natural period and oscillation amplitude. For this reason, tautochrone oscillation is an important feature of centrifugal dampers.

The analytical derivation to obtain the period of oscillation of a mass along a cycloid subjected to a gravitational field is well known in the literature. However, less common is the case of a particle oscillating along an epicycloid and subjected to a centrifugal force field. In the following, two different approaches will be proposed.

From elementary differential equations theory, the oscillation of a point with unit mass is tautochrone about an equilibrium position when the governing differential equation has the form

$$\ddot{s} = F_t \quad (14)$$

where the tangential force acting on the unit mass particle has the form

$$F_t = -k^2 s \quad (15)$$

with k a constant and s the curvilinear abscissa. The tautochrone property is maintained also when a linear viscous damping is applied [1], but to minimize algebra, we will consider the absence of energy losses.

Let us consider a mass particle sliding along a smooth epicycloidal path under the action of a repulsive force F , linearly varying with the distance from center O and directed along OM . Hence, when the force is at M , the force module $F = \mu OM$, with μ a constant.

The length of curvilinear abscissa is

$$s = \frac{4b(a+b)}{a} \cos \frac{\tau}{2} \quad (16)$$

where

- a, b the radii of the fixed and moving circles, respectively;
- τ the angle of moving circle rotation.

From the geometry of Fig. 4, the component of F along tangent t is

$$F_t = -\mu KM = -\mu a \cos \frac{\tau}{2} \quad (17)$$

The combination of (16) with (17) yields

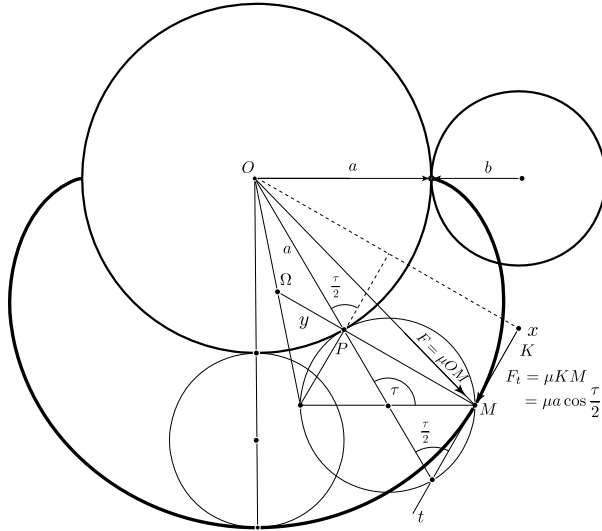


Fig. 4 Tautochronism of oscillations of a particle with epicycloidal path under a centrifugal field force F proportional to OM

$$F_t = -\mu \frac{a^2}{4b(a+b)} s \quad (18)$$

For a unit mass, the equation of motion of the mass particle is

$$\ddot{s} + \mu \frac{a^2}{4b(a+b)} s = 0 \quad (19)$$

The period of tautochrone motion is

$$T = \frac{2\pi}{a} \sqrt{\frac{4b(a+b)}{\mu}} \quad (20)$$

Since centrifugal dampers counterweights are subjected to a centrifugal force field, the epicycloidal path ensures tautochronism of oscillation. The previous analytical result can be proved independently making use of the Cesàro's fundamental equations [8, 9]:

$$\frac{dx}{ds} = \frac{y}{\rho} - 1, \quad \frac{dy}{ds} = -\frac{x}{\rho} \quad (21)$$

We start by solving the following problem:

Find the intrinsic equation of a curve such that the projection of the radius vector along the tangent is proportional to the curvilinear abscissa.

Since the abscissa axis of the intrinsic coordinate system coincides with the tangent t , the previous requirement is analytically expressed by the condition

$$x = ks \quad (22)$$

where k is a constant.

From the first of (21) follows

$$y = (k + 1)\rho \quad (23)$$

Moreover, from the second of (21), follows

$$ydy = -k(k + 1)sds$$

or

$$y^2 = -k(k + 1)s^2 + C \quad (24)$$

with C integration constant. The combination of (23) and (24) gives the intrinsic equation of the curve satisfying the requirement:

$$ks^2 + (k + 1)\rho^2 = C \quad (25)$$

We observe that the case of $C = 0$ corresponds to a logarithmic spiral, otherwise the following cases hold:

- $k > 0$, epicycloid;
- $k < 0$, hypocycloid;
- $0 < k < -1$, pseudocycloid.

The intrinsic equation of an epicycloid is [8]:

$$\frac{s^2}{A^2} + \frac{\rho^2}{B^2} = 1 \quad (26)$$

with

$$A = \frac{4b(a + b)}{a}, \quad B = \frac{4b(a + b)}{a + 2b} \quad (27)$$

therefore

$$k = \frac{4b(a + b)}{a^2}, \quad C = 4b(a + b) \quad (28)$$

Since $F_t = -\mu x$, the period of oscillation is easily computed.

4 A Four-Bar Linkage with Flexure Hinges

Four-bar linkages with flexure hinges (see Fig. 5), made of two crossed cantilever leaf springs with their free ends connected through a rigid bar (the coupler), are often used instead of four bars with revolute joints. Because of its lack of hysteresis, friction, and backlash, this embodiment is advantageous for use in high-precision applications.

In this section, on the basis of results presented in [10], we will deduce the diameter of the inflection circle for the coupler absolute motion. It is assumed a moment bending load on a flexure hinge.

Since

$$O_A A = O_B B = L \quad (29)$$

$$PA = \frac{b}{2 \cos \psi} \quad (30)$$

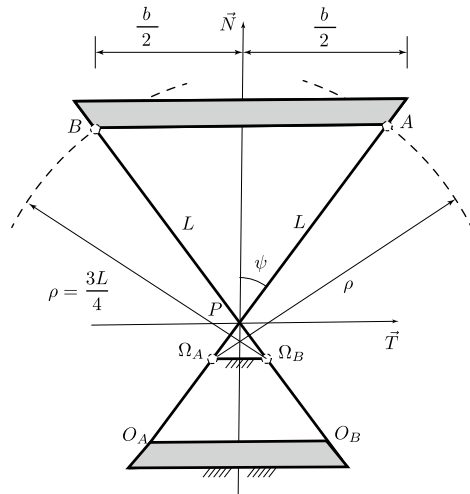
$$P\Omega_A = PA + A\Omega_A = \frac{b}{2 \cos \psi} - \frac{3L}{4} \quad (31)$$

The Euler–Savary equation

$$\left(\frac{1}{PA} - \frac{1}{P\Omega_A} \right) \cos \psi = \frac{1}{\delta}$$

particularizes into

Fig. 5 Four-bar with flexure hinges: nomenclature



$$\frac{1}{\delta} = \left(\frac{\frac{1}{b}}{\frac{2 \cos \psi}{3L}} + \frac{\frac{1}{b}}{\frac{4}{6L \cos^3 \psi}} \right) \cos \psi \quad (32)$$

or

$$\delta = b \frac{3L \cos \psi - 2b}{6L \cos^3 \psi} \quad (33)$$

If $\psi = 45^\circ$ and $b = L \frac{\sqrt{2}}{2}$, then

$$\delta = \frac{L\sqrt{2}}{6}, \quad |r| = |r'| = L \frac{\sqrt{2}}{2} \quad (34)$$

Moreover, if $3L \cos \psi - 2b = 0$, then $\delta = 0$ and $PA = PB = \frac{3L}{4}$, and all points on the coupler trace approximate circles centered at P .

The synthesis of a compliant four-bar mechanism for prescribed finite coupler motion is discussed by Valentini and Pennestrì [11, 12]. The numerical value of δ confirms the findings reported in the previously cited references.

A review of contributions about flexure-based hinges and compliant microgrippers is presented by Verotti et al. [13].

5 Conclusions

Three applications of path curvature analysis have been presented. The dynamics of a body resting on two curves has been initially investigated and particularized into one of a four-bar linkage. It was shown how Euler–Savary equation allows the development of a criterion for the stability of small coupler oscillations. An application of such a criterion regards the stability of lifting rigs. The second topic is the derivation of an equation for computing the tautochrone period of oscillation of a mass particle along an epicycloid path and subjected to a centrifugal field. The derivation makes use of the fundamental formulas of Cesàro’s intrinsic geometry. This formula can be used for the tuning of a tautochrone centrifugal damper. The third application confirms the possibility of a second-order approximation of point paths in compliant linkages.

References

1. Routh, E.J.: Dynamics of a System of Rigid Bodies. Dover Publications Inc. (1960)
2. Kooy, A.D., Seebacher, R.: Best-in-class dampers for every driveline concept. In Schaeffler Kolloquium 2018 (2018)

3. Cirelli, M., Capuano, E., Valentini, P.P., Pennestrì, E.: The tuning conditions for circular, cycloidal and epicycloidal centrifugal pendula: a unified Cartesian approach. *Mech. Mach. Theory* **150**, 20 (2020)
4. Longman, R.W., Freudenstein, F.: The stability analysis of lifting rigs - part1: necessary and sufficient conditions. *ASME J. Eng. Ind.* **97**(2), 532–536 (1975)
5. Kaps, H.: Stability of cargo suspension arrangements (2013)
6. Cirelli, M., Gregori, J., Valentini, P.P., Pennestrì, E.: A design chart approach for the tuning of parallel and trapezoidal bifilar centrifugal pendulum. *Mech. Mach. Theory* **140**, 711–729 (2019)
7. Shaw, S.W., Schimitz, P.M., Haddow, A.G.: Tautochronic vibration absorbers for rotating systems. *ASME J. Comput. Nonlinear Dyn.* **1**(4), 283–293 (2006)
8. Cesàro, E.: *Lezioni di geometria intrinseca*. Tipografia della Reale Accademia delle Scienze, (in Italian) edn. (1896)
9. Cesàro, E.: *Vorlesungen über natürliche Geometrie*. Teubner, Leipzig (1901)
10. Sieker, K.-H.: *Getriebe mit Energiespeichern*. Akademische Verlagsgesellschaft Geet & Portig K.-G. (1952)
11. Valentini, P.P., Pennestrì, E.: Compliant four-bar linkage synthesis with second-order flexure hinge approximation. *Mech. Mach. Theory* 225–233 (2018)
12. Valentini, P.P., Cirelli, M., Pennestrì, E.: Second-order approximation pseudo-rigid model of flexure hinge with parabolic variable thickness. *Mech. Mach. Theory* **136**, 178–189 (2019)
13. Verotti, M., Dochshanov, A., Belfiore, N.P.: A comprehensive survey on modern microgrippers design: Mechanical structure. *ASME J. Mech. Des.* **139**(6) (2017)

Recent Developments in Higher Path Curvature Analysis



Mattia Cera, Marco Cirelli, Ettore Pennestrì, Pier Paolo Valentini,
and V. R. Shanmukhasundaram

1 Introduction

The mechanical generation of curves is the main task for kinematic synthesis. The mainstream of investigations of the so-called Burmester theory focused toward the search of loci of points whose path approximates circles and straight lines solely. In comparison, less attention was initially devoted to the approximate mechanical tracing of other curves such as cycloids and parabolas.

References [1, 2] offer a systematic presentation of linkages for the exact generation of plane curves. However, in many cases, such linkages do not match the requirement of a simple kinematic structure. Often approximate, but simple solutions are better appreciated in engineering. For these reasons, the availability of kinematic synthesis methods, for accurate approximate solutions, has been always appreciated by practitioners and engineers. The kinematic synthesis of linkages, for the mechanical generation of curves with infinitesimally close positions, is herein discussed. In this case, the motion requirements are often expressed in terms of the radius of curvature and its derivatives with respect to plane rotation angle. Similarly to the Taylor series, the higher the number of differential coefficients matched, the smaller the difference between the ideal function and the approximated one.

The intrinsic geometry of the Italian geometer Cesàro [3, 4], where the curves are defined in terms of the radius of curvature ρ and curvilinear abscissa s , demonstrated an almost natural tool to establish important analytical relationships.

One of the earliest contributions to the generalization of the classical Burmester theory for the search of loci of points tracing different curves is due to Freudenstein

M. Cera · E. Pennestrì (✉) · P. P. Valentini
University of Rome Tor Vergata, 00133 Rome, Italy
e-mail: pennestri@mec.uniroma2.it
URL: <https://www.uniroma2.it>

M. Cirelli
Niccolò Cusano University, 00166 Rome, Italy
e-mail: marco.cirelli@unicusano.it

V. R. Shanmukhasundaram
Department of Mechanical Engineering, Birla Institute of Technology and Science, Pilāni, India
© The Author(s), under exclusive license to Springer Nature Singapore Pte Ltd. 2021 27
Y. V. D. Rao et al. (eds.), *Advances in Industrial Machines and Mechanisms*,
Lecture Notes in Mechanical Engineering,
https://doi.org/10.1007/978-981-16-1769-0_3

[5]. He deduced the loci of moving plane points tracing curves with prescribed differential features. Denoted with ρ_1 and ρ_2 the radii of curvature of evolute and that of the evolute of evolute, one can define the curvature ratios:

$$\lambda_1 = \frac{\rho_1}{\rho}, \quad \lambda_2 = \frac{\rho_2}{\rho} \quad (1)$$

In a general planar motion,

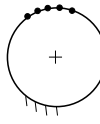
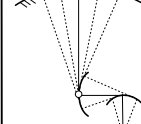
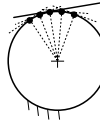
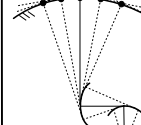
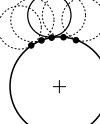
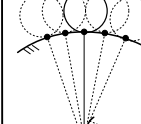
- the locus of points whose path is characterized by a given value of λ_1 is the quartic of curvature derivative, with double points in the pole velocity P_0 and at points of infinity;
- there are only five points (the generalized Burmester points—GBPs) whose path is characterized by given values of λ_1 and λ_2 .

Since their definition, the location of the generalized Burmester points for the most general plane motion had some difficulties. Freudenstein located them only for some particular cases, such as the motion of a coupler four-bar in the symmetric position [5]. Pennock and Rizq [6] attempted their location through the iterative solution of a system of nonlinear equations formed by the loci of points with given values of λ_1 and λ_2 . However, they could not detect all the points, and the iteration often converged in the velocity pole. Pennestrì and Belfiore [7], making use of B-invariants and computer algebra, deduced the coefficients of a quintic polynomial whose solution allowed the location of the generalized Burmester points for the planar link motion of a linkage. The main inconvenience was that the algebraic expression of each coefficient was too long to be printed. The current viable solution is the one proposed in 2018 by Cera and Pennestrì [8]. The main equations required to compute the generalized Burmester points will be presented in this paper with some numerical examples.

It should be acknowledged that the mechanical generation/approximation of curves through the trajectories of points on the moving plane is not the only solution approach. Envelopes of straight lines and other curves on the moving plane offer alternative ways of solution. Likely the theory about this approach started with the contribution of Camus [9]. Early contributions are due to Aronhold [10], Müller [11], and Bereis [12]. Figure 1 and the following list both summarize the extensions of infinitesimal Burmester theory toward the mechanical generation of planar curves with fourth-order accuracy.

1. Generation of circles using a point trajectory. This is called the *classic Burmester problem*. The *classic Burmester points* have trajectories with five points in common with a circle (e.g., [13–15]).
2. Generation of circles employing straight-lines envelope. A line with five positions tangent to a circle is herein denoted as the *classic Burmester line*. For a general motion, its existence is not guaranteed [16–18].
3. Generation of a circle through the envelope of five positions of a moving circle is denoted as the *classic Burmester circle*.

Fig. 1 Extensions of Burmester theory for infinitesimally separated positions [18]

		Geometric entity approximated	
		Circle	Curve with prescribed higher curvature
Tracing geometric entity	Point		
	Straight-line		
	Circle		

4. Generation of a curve with prescribed curvature ratios λ_1 and λ_2 by means of a point trajectory. The point with such capability is denoted as the *generalized Burmester point* [5–8].
5. Generation of a curve with prescribed curvature ratios λ_1 and λ_2 using a straight-line envelope. The straight line with such capability is denoted as the *generalized Burmester line* [16, 18].
6. Generation of a curve with prescribed curvature ratios λ_1 and λ_2 through a circle envelope. The circle with such capability is denoted as the *generalized Burmester circle*.

In industrial applications, where an accurate generation of paths of curves with prescribed differential properties is required (e.g., devices based on tautochrone motions, grinding of optical lenses), the importance of this theory is appreciated.

Thanks to the recent extension of the intrinsic geometry [3, 4] to the planar motion kinematics [8, 17, 18], progress has been made regarding the mechanical generation of curves by point paths tracing or through envelopes of lines and curves. This paper summarizes the previous developments with some applications to the generation of tautochrone motions.

2 Outlines of Intrinsic Geometry

The *fundamental formulas* of Cesàro's intrinsic geometry are [3] (see Fig. 2)

$$\frac{dX}{ds} = \frac{dx}{ds} - \frac{y}{\tilde{\rho}} + 1, \quad \frac{dY}{ds} = \frac{dy}{ds} + \frac{x}{\tilde{\rho}} \quad (2)$$

where (X, Y) and (x, y) are the Cartesian coordinates of P in the fixed and moving canonical systems, respectively. For a point P fixed under an infinitesimal displacement, $\frac{dX}{ds} = \frac{dY}{ds} = 0$.

Thus, the following conditions of stationarity are deduced from (2):

$$\frac{dx}{ds} = \frac{y}{\tilde{\rho}} - 1, \quad \frac{dy}{ds} = -\frac{x}{\tilde{\rho}} \quad (3)$$

2.1 Motion Polodes

Equations (2) and (3) can be applied to motion polodes. The canonical systems (fixed and moving) are overlapped with the intrinsic ones referred to polodes.¹ Thus, the origin M of the intrinsic system coincides with pole velocity P_0 , as depicted in Fig. 2. Since the points on the moving plane do not change their position with respect to the moving polode, the stationarity conditions (3) are specialized for the moving plane as follows:

$$\left(\frac{dx}{ds} \right)_p = \frac{y}{\rho_p} - 1, \quad \left(\frac{dy}{ds} \right)_p = -\frac{x}{\rho_p} \quad (4)$$

where ρ_p is the radius of curvature of the moving polode.

Similarly, the variation of coordinates in the fixed plane are expressed by (2), written for this plane:

$$\left(\frac{dX}{ds} \right)_\pi = \left(\frac{dx}{ds} \right)_\pi - \frac{y}{\rho_\pi} + 1, \quad \left(\frac{dY}{ds} \right)_\pi = \left(\frac{dy}{ds} \right)_\pi + \frac{x}{\rho_\pi} \quad (5)$$

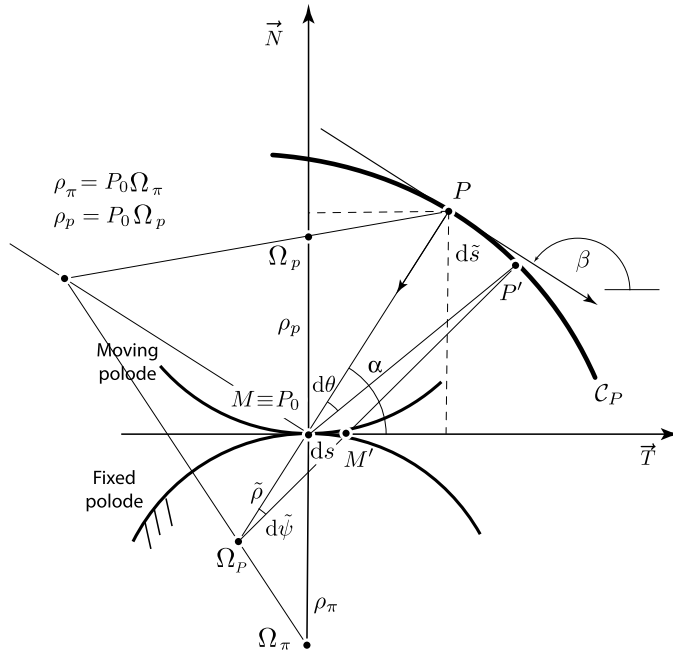
where ρ_π is the radius of curvature of the fixed polode.

Because of the pure rolling between the polodes (i.e., no sliding occurs), the following equalities hold:

$$ds = (ds)_p = (ds)_\pi. \quad (6)$$

Substituting (4) into (5) and taken into account (6) follows:

¹Subscripts p and π refer to moving and fixed polodes, respectively.

**Fig. 2** Nomenclature

$$\frac{dX}{ds} = \frac{y}{\delta}, \quad \frac{dY}{ds} = -\frac{x}{\delta} \quad (7)$$

where δ is the inflection circle diameter. Equation (7) give the differential transform from moving to fixed coordinates.

Assuming

$$h = P_0 P = \sqrt{x^2 + y^2} \quad (8)$$

follows

$$\frac{d\tilde{s}}{ds} = \chi = -\frac{h}{\delta} \quad (9)$$

where $d\tilde{s}$ is the arc on the point P trajectory.

Taking into account (9), the following equalities are established:

$$d\tilde{s} = h d\theta = \tilde{\rho} d\tilde{\psi} = \chi ds \quad (10)$$

2.2 Intrinsic Equation of a Point Path Curve

Let us denote with (M, N) and (m, n) the direction cosines of tangent t_p to path \mathcal{C}_P in P , respectively, in the canonical systems $P_0 - XY$ (fixed) and $P_0 - xy$ (moving). Taking into account (4), the differentiation of (m, n) with respect to polodes arc length $s = s_p = s_\pi$ yields

$$\frac{dm}{ds} = \frac{x}{h} \left(\frac{y}{h^2} - \frac{1}{\rho_p} \right), \quad \frac{dn}{ds} = \frac{y}{h} \left(\frac{y}{h^2} - \frac{1}{\rho_p} \right) \quad (11)$$

By means of (5), (11) is transformed into the $P_0 - XY$ coordinate system:

$$\frac{dM}{ds} = \frac{dm}{ds} - \frac{n}{\rho_\pi}, \quad \frac{dN}{ds} = \frac{dn}{ds} + \frac{m}{\rho_\pi} \quad (12)$$

For the direction cosines, the following identity holds:

$$\left(\frac{dM}{d\tilde{\psi}} \right)^2 + \left(\frac{dN}{d\tilde{\psi}} \right)^2 = 1 \quad (13)$$

After some algebraic manipulations involving (10)–(12), an equation somewhat related to the second form of Euler–Savary equation is deduced:

$$\tilde{\rho} = \frac{h^3}{h^2 - \delta y} \quad (14)$$

The combination of (14) with

$$\tilde{s} = - \int \frac{h}{\delta} ds \quad (15)$$

gives the intrinsic equation $f(\tilde{s}, \tilde{\rho}) = 0$ of the point P trajectory.

3 Quartic of Curvature Derivative

The quartic of curvature derivative is obtained through the differentiation of Euler–Savary equation (14) with respect to s

$$\frac{d\tilde{\rho}}{ds} = -\frac{\tilde{\rho}^2}{h^3} \left[(\epsilon + 1)x - \delta_1 y - 3\delta \frac{xy}{h^2} \right] \quad (16)$$

where $\epsilon = \frac{\delta}{\rho_p}$ and $\delta_i = \frac{d^i \delta}{ds^i}$, $i = 1, 2, \dots$

The quartic of curvature derivative can be expressed in Cartesian coordinates and in terms of the curvature ratio $\lambda_1 = \frac{d\tilde{\rho}}{ds}$.

Taken into account (10) and substituting (14) into (16), follows

$$\lambda_1 (x^2 + y^2 - \delta y)^2 - \delta (x^2 + y^2) [(\epsilon - 1)x - \delta_1 y] + 3\delta^2 xy = 0 \quad (17)$$

If we impose $\lambda_1 = 0$ in Eq. (17), the cubic of stationary curvature is deduced

$$(x^2 + y^2) [(\epsilon - 1)x - \delta_1 y] - 3\delta xy = 0 \quad (18)$$

4 The Generalized Burmester Points

The GBPs are determined by solving the system composed of Eq. (16) and its derivative.

Introducing the parameters

$$\tau = \frac{h}{\tilde{\rho}}, \quad \nu = \frac{y}{x} \quad (19)$$

Equation (16) can be rewritten in the form

$$\lambda_1 = \frac{1 - \tau}{\nu \tau^2} [(\epsilon + 1) - \delta_1 \nu - 3(1 - \tau)] \quad (20)$$

Then, from the differentiation of Eq. (20) w.r.t the angle $\tilde{\psi}$, one obtains

$$\begin{aligned} & \left((\lambda_2 - 3\lambda_1^2 - 3) \tau^3 + (\delta_1 \lambda_1 - 4\epsilon + 8) \tau^2 + (\delta \delta_2 - \epsilon^2 + 7\epsilon - 7) \tau - \delta \delta_2 + \epsilon^2 - 3\epsilon + 2 \right) \nu^2 \\ & + \left(-7\tau^3 \lambda_1 + 6\tau^2 \lambda_1 + (1 - \tau)(\epsilon_1 \delta + \epsilon \delta_1 - \delta_1) \right) \nu - (\tau - 1)\tau(6\tau + \epsilon - 5) = 0 \end{aligned} \quad (21)$$

in which the following identities have been established

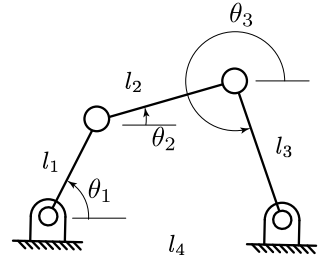
$$\frac{d\lambda_1}{d\tilde{\psi}} = \lambda_2 - \lambda_1^2, \quad \epsilon_1 = \frac{d\epsilon}{ds}$$

Solving Eq. (20) in terms of ν

$$\nu = -\frac{\epsilon \tau + 3\tau^2 - \epsilon - 5\tau + 2}{\tau^2 \lambda_1 - \tau \delta_1 + \delta_1} \quad (22)$$

and substituting this expression (22) into Eq. (21), a polynomial of 5th degree, with τ as unknown, is deduced

Fig. 3 Four-bar linkage:
nomenclature



$$n_5\tau^5 + n_4\tau^4 + n_3\tau^3 + n_2\tau^2 + n_1\tau + n_0 = 0 \quad (23)$$

where

$$\begin{aligned} n_5 &= 9\lambda_2 - 12\lambda_1^2 - 27 \\ n_4 &= 6(\epsilon - 2)(\lambda_2 - 2\lambda_1^2 - 9) \\ n_3 &= (-3\lambda_1^2 + \lambda_2 - 36)\epsilon^2 + (4\delta_1\lambda_1 + 12\lambda_1^2 - 4\lambda_2 + 171)\epsilon - 6\delta_1^2 \\ &\quad + 7\delta_1\lambda_1 + (3\epsilon_1\lambda_1 + 9\delta_2)\delta - 12\lambda_1^2 + 4\lambda_2 - 171 \\ n_2 &= -10\epsilon^3 + (2\delta_1\lambda_1 + 87)\epsilon^2 + (-4\delta_1^2 - \delta_1\lambda_1 - 201 + (\epsilon_1\lambda_1 + 6\delta_2)\delta)\epsilon \\ &\quad + 14\delta_1^2 + (-3\epsilon_1\delta - 6\lambda_1)\delta_1 + 134 + (-2\epsilon_1\lambda_1 - 21\delta_2)\delta \\ n_1 &= -\epsilon^4 + 17\epsilon^3 + (\delta\delta_2 - \delta_1^2 - 69)\epsilon^2 + (-\delta\delta_1\epsilon_1 - 10\delta\delta_2 + 7\delta_1^2 + 104)\epsilon \\ &\quad + 5\delta\delta_1\epsilon_1 + 16\delta\delta_2 - 10\delta_1^2 - 52 \\ n_0 &= -(\epsilon - 2)(-\epsilon^3 + 5\epsilon^2 + (\delta\delta_2 - \delta_1^2 - 8)\epsilon - \delta\delta_1\epsilon_1 - 2\delta\delta_2 + \delta_1^2 + 4) \end{aligned}$$

Hence, the GBPs in canonical system coordinates are given by

$$x_{GB} = \frac{\rho_0\tau}{\sqrt{1+\nu^2}}, \quad y_{GB} = \frac{\rho_0\tau\nu}{\sqrt{1+\nu^2}} \quad (24)$$

where $\rho_0 = \frac{\delta\nu}{\tau(1-\tau)\sqrt{1+\nu^2}}$ manipulating Euler–Savary equation (14).

5 Numerical Example

The discussed results will be applied toward the mechanical generation of a cycloid using a coupler point path of a four-bar linkage.

The adopted four-bar nomenclature is shown in Fig. 3, while the geometrical data for the given configuration of the four-bar are collected in Table 1.

The following synthesis procedure has been applied:

Table 1 Four-bar configuration

Links (mm)		Angles ($^{\circ}$)	
l_1	300	θ_1	33.557
l_2	400	θ_2	180.000
l_3	300	θ_3	326.443
l_4	100		

Table 2 Four-bar invariants

Invariants			
δ (mm)	86.835	$\epsilon(-)$	-0.400
δ_1 (-)	0.000	ϵ_1 (mm $^{-1}$)	0.000
δ_2 (mm $^{-1}$)	$-1.263 \cdot 10^{-2}$		

Table 3 Generalized Burmester point

Generalized Burmester Point			
τ (-)	0.714	x_{GB} (mm)	0.000
ν (-)	$-\infty$	y_{GB} (mm)	303.198

1. From the intrinsic equation of the cycloid

$$\rho(s)^2 = \rho_0^2 - s^2 \quad (25)$$

the curvature ratios are evaluated for the given design position $s = 0$

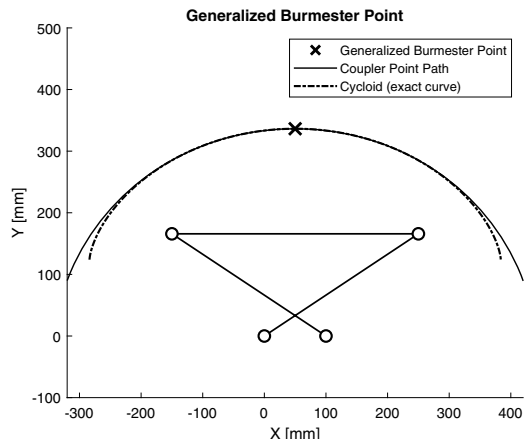
$$\lambda_1 = \frac{\rho_1}{\rho} = \frac{d\rho}{ds} = -\frac{s}{\sqrt{\rho_0^2 - s^2}} \Big|_{s=0} = 0$$

$$\lambda_2 = \frac{\rho_2}{\rho} = \frac{d\rho_1}{ds} = -1$$

2. The kinematic analysis of the four-bar up to the fourth order is carried out in order to compute the invariants δ , ϵ , δ_1 , δ_2 , ϵ_1 ² (Table 2).
3. By means of Eqs. (22) and (23), τ and ν are obtained, then the GBPs are calculated in canonical system coordinates through Eq. (24) (Table 3).
4. GBPs absolute coordinates in the four-bar reference system, the geometry of the system, and the comparison between the ideal curve and the approximated coupler point path are depicted in Fig. 4.

²For further details about invariants expressions, see [18].

Fig. 4 Generalized Burmester point
 Burmester point
 $X_{GB} = 50.000 \text{ mm}$,
 $Y_{GB} = 336.365 \text{ mm}$



It is worthy to note that for a symmetrical application, there are at most three symmetrical solutions [18]. For this particular case, only one solution is real, and the other two are complex.

6 Conclusion

Infinitesimal Burmester theory is a classic topic in kinematic synthesis. This paper summarized some recent progress in the computation of generalized Burmester points as well as the mechanical approximation of curves by means of mechanisms.

References

1. Dobrowolski, W.W.: Theorie der Mechanismen zur Konstruktion Ebener Kurven. Akademie-Verlag, Berlin (1957)
2. Artobolevskii, I.I.: Mechanisms for the Generation of Plane Curves. The Macmillan Company (1965)
3. Cesàro, E.: Lezioni di geometria intrinseca. Tipografia della Reale Accademia delle Scienze, (in Italian) edn. (1896)
4. Cesàro, E.: Vorlesungen über natürliche Geometrie. Teubner, Leipzig (1901)
5. Freudenstein, F.: Higher path-curvature analysis in plane kinematics. ASME J. Eng. Ind. **87B**, 184–190 (1965)
6. Pennock, G.R., Rizq, Q.N.: Application of generalized Burmester theory to the analysis and synthesis of planar mechanisms. In: Proceedings 3rd National Applied Mechanics & Robotics Conference, November 1993, Paper AMR-93-058, Cincinnati, OH (1993)
7. Pennestrì, E., Belfiore, N.P.: On the numerical computation of generalized Burmester points. Meccanica **30**, 147–163 (1995)

8. Cera, M., Pennestrì, E.: Generalized Burmester points computation by means of Bottema's instantaneous invariants and intrinsic geometry. *Mech. Mach. Theory* **135**, 225 (2019). November
9. Camus, C.E.L.: Sur la figure des dents des roues et des ailes des pignons pour rendre les horloges plus parfaites. *Mémoires de l'Academie des sciences de l'Institut de France*, pp. 117–197 (1733)
10. Aronhold, S.H.: Grundzüge der kinematischen Geometrie. *Verhandlungen des Vereins zur Beförderung des Geweberfleisses in Preussen* **52**, 129–155 (1872)
11. Müller, R.: Konstruktion der Krümmungsmittelpunkte der Hüllbahnevoluten bei starren ebenen Systemen. *Z. Math. Phys.* **36**, 257–266 (1891)
12. Bereis, R.: Über die Geraden-Hüllbhanen bei der Bewegung eines starren ebenen Systems. *Österreichisches Ingenieur-Archiv* **9**(1), 45–55 (1955)
13. Burmester, L.: Lehrbuch der Kinematik. Verlag von Arthur Felix (1888)
14. Allievi, L.: Cinematica della Biella Piana. Tipografia Francesco Giannini (1895)
15. Eren, K., Ersoy, S.: Revisiting Burmester theory with complex forms of Bottema's instantaneous invariants. *Complex Var. Elliptic Equ.* **62**(4), 431–437 (2017)
16. Soni, A.H., Siddhanty, M.N., Ting, K.L.: Higher-order planar tangent-line envelope curvature theory. *ASME J. Mech. Des.* **101**, 563–568 (1979)
17. Cera, M., Pennestrì, E.: Higher-order curvature analysis of planar curves enveloped by straight-lines. *Mech. Mach. Theory* **134**(4), 213–233 (2018)
18. Cera, M., Pennestrì, E.: The mechanical generation of planar curves by means of point trajectories, line and circle envelopes: a unified treatment of the classic and generalized Burmester problem. *Mech. Mach. Theory* **142**, 103580 (2019)

Jump Phenomena in a Motor-Driven Quick-Return Mechanism that Excites the Base of a Vibrating Structure



Anubhab Sinha, Saurabh Kumar Bharti, Arun Kumar Samantaray,
and Ranjan Bhattacharyya

1 Introduction

A quick-return mechanism is a mechanical setup that converts rotary motions into reciprocating motions, with unequal durations for the forward and return strokes. The forward stroke is usually designated as the working stroke, whereas the return stroke is the useless/idle stroke. The setup is so named because the return stroke is made quicker than the working stroke, which vastly improves the economy of the machining process. The time taken for the useless stroke is known as the non-machining time or the idle time [1]. The mechanism and its variations are frequently used in applications where the action is required in one direction of motion only, such as—shapers, planers, power saws, impact presses, mechanical actuators, and revolver technology [2, 3].

The rotary motions of the quick-return mechanism are usually generated from an electrical motor. However, a real-world motor is a non-ideal drive. A non-ideal drive refers to a power source whose energy supply is insufficient. The dynamics of a non-ideal drive is cross-coupled with the load acting on it and hence, a non-ideal drive is inherently load dependent [4–6]. The Sommerfeld effect is the nonlinear jump phenomenon that affects rotating machineries powered by non-ideal drives. It is characterized by a sequence of prolonged capture at resonance, followed by a sudden release from there. In addition to wastage of costly energy, the continued capture at resonance despite increasing input power is detrimental to any appliance with respect to its health, performance, and sustainability aspects. The investigation

A. Sinha (✉) · S. K. Bharti · A. K. Samantaray · R. Bhattacharyya
Indian Institute of Technology Kharagpur, Kharagpur 721302, West Bengal, India

A. K. Samantaray
e-mail: samantaray@mech.ittkgp.ac.in

R. Bhattacharyya
e-mail: rbmail@mech.ittkgp.ac.in

of jump phenomena as well as recognizing ways to tackle it has received significant attention in recent years [7–12]. In view of that, the present paper attempts to study the jump phenomena characteristics for a motor-driven quick-return mechanism, whose slider end is connected to a vibrating body. The subsequent discussions are strictly based on steady-state analysis of the dynamical system.

1.1 Mechanical Model

Figure 1a shows a quick-return mechanism powered by a permanent magnet DC motor. The operator regulates the source voltage V_s . The motor generates output torque T_m on crank AB, rotating about point A (with rotation angle θ). A large flywheel is also mounted at A. The sleeve collar B slides on the arm OC, which oscillates around pivot point O (with oscillating angle ϕ). Rigid link CD connects the oscillating arm OC with the horizontally reciprocating slider. Note that the slider end is linearly connected to a vibrating block (with coupling parameters K and C). The nomenclature and values of the related parameters are detailed in Table 1.

Figure 1b shows the two extreme positions of the oscillating arm OC. The extremities occur when crank AB is perpendicular to arm OC. Let lines OB₁C₁ and OB₂C₂ represent the two extremities. Accordingly, the return stroke angle θ_r of the quick-return mechanism is given by minor angle B₁AB₂, while its corresponding major angle gives the forward stroke angle θ_f . From Δ OB₁A, one obtains $\theta_r = 2 \cos^{-1}(r/p)$ and $\theta_f = 2\pi - 2 \cos^{-1}(r/p)$. With ω as the operating motor speed, the time taken for forward stroke (t_f) and return stroke (t_r) motions are now given as

$$t_f = \{2\pi - 2 \cos^{-1}(r/p)\}/\omega \quad (1)$$

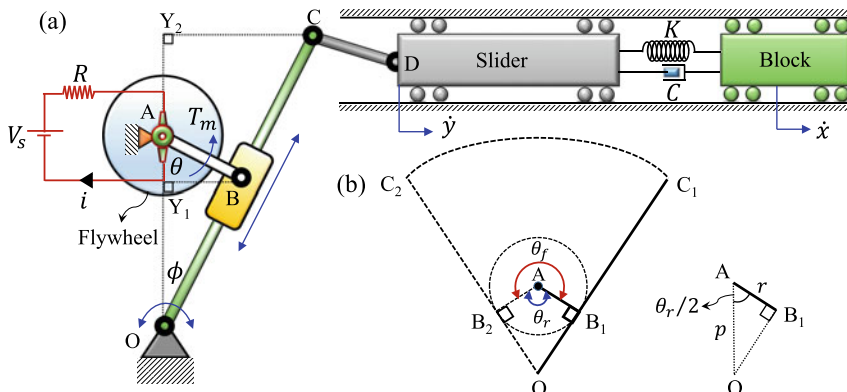


Fig. 1 **a** Schematic of the mechanism; **b** geometrical configuration at extremities

Table 1 Parameters

Notation	Description	Value
V_s	Source voltage	<Variable>
μ_m	Motor constant	0.9 Nm/A
R	Resistance	0.08 Ω
ω	Motor speed	–
p	Distance OA	0.115 m
q	Arm length OC	0.145 m
r	Radial length AB	0.090 m
θ_f	Forward stroke angle	283°
θ_r	Return stroke angle	77°
K	Spring stiffness	4800 N/m
C	Viscous damping	11 Ns/m
M	Block mass	3 kg
ω_0	Fundamental frequency	40 rad/s
ξ	Damping factor	0.046

$$t_r = \{2 \cos^{-1}(r/p)\}/\omega \quad (2)$$

Obviously, for constant ω , t_f is greater than t_r .

2 Analytical Formulation

From ΔAY_1B in Fig. 1a,

$$AY_1 = r \cos \theta \quad (3)$$

$$BY_1 = r \sin \theta \quad (4)$$

In ΔOBY_1 , substituting Eqs. (3) and (4), one obtains

$$\tan \phi = (r \sin \theta)/(p - r \cos \theta) \quad (5)$$

From ΔOCY_2 ,

$$CY_2 = q \tan \phi \quad (6)$$

The horizontal slider displacement (y) is directly related to the instantaneous perpendicular distance CY_2 . With the crank angle $\theta = \omega t$, substituting Eq. (5) in Eq. (6), one obtains the slider displacement as

$$y(t) = \{e_c \sin(\omega t)\}/\{p - r \cos(\omega t)\} \quad (7)$$

where $e_c = qr$ is the eccentricity parameter for the mechanism. For constant ω values, the slider motions are periodic in nature. Thus, the slider displacement $y(t)$ from Eq. (7) can be alternatively expressed as a general Fourier series of the form

$$y(t) = \sum_{n=0}^{\infty} \{p_n\} \cos(n\omega t) + \sum_{n=0}^{\infty} \{q_n\} \sin(n\omega t) \quad (8)$$

with (p_n, q_n) as the Fourier coefficients, where $p_n = (1/\pi) \int_0^{2\pi/\omega} \{y(t)\omega \cos(n\omega t)\} dt$ and $q_n = (1/\pi) \int_0^{2\pi/\omega} \{y(t)\omega \sin(n\omega t)\} dt$. The corresponding slider velocity is obtained as the time derivative of Eq. (8)

$$\dot{y}(t) = \sum_{n=0}^{\infty} \{n\omega q_n\} \cos(n\omega t) + \sum_{n=0}^{\infty} \{-n\omega p_n\} \sin(n\omega t) \quad (9)$$

The equation of motion for the SDoF vibrating block along with the slider base (we assume $M \gg m_s$ where m_s is the slider mass) is written as

$$M\ddot{x}(t) + C\dot{x}(t) + Kx(t) = C\dot{y}(t) + Ky(t) \quad (10)$$

with $x(t)$ as the displacement of the block mass M . The slider is considered to be lightweight in comparison with the mass of the vibrating block. Defining parameters $\omega_0 = (K/M)^{0.5}$ as the undamped fundamental frequency component and $\xi = C/(2M\omega_0)$ as the damping factor, Eq. (10) is further rewritten as

$$\ddot{x}(t) + 2\xi\omega_0\dot{x}(t) + \omega_0^2x(t) = \sum_{n=0}^{\infty} \{P_n\} \sin(n\omega t) + \sum_{n=0}^{\infty} \{Q_n\} \cos(n\omega t) \quad (11)$$

where coefficients $P_n = -np_n 2\xi\omega_0\omega + q_n\omega_0^2$ and $Q_n = nq_n 2\xi\omega_0\omega + p_n\omega_0^2$.

The particular integral of Eq. (11) yields the steady-state solutions (i.e., solutions as $t \rightarrow \infty$) of the vibrating block ($x_{ss}(t)$), which is obtained as

$$x_{ss}(t) = \sum_{n=0}^{\infty} \{u_n - v_n\} \cos(n\omega t) + \sum_{n=0}^{\infty} \{e_n + f_n\} \sin(n\omega t) \quad (12)$$

with $u_n = (a_n Q_n)/D$, $v_n = (b_n P_n)/D$, $e_n = (a_n P_n)/D$, $f_n = (b_n Q_n)/D$, $a_n = \omega_0^2 - n^2\omega^2$, $b_n = 2n\xi\omega_0\omega$, and $D = (a_n^2 + b_n^2)$. Subsequently, the steady-state block velocity is obtained by time differentiating Eq. (13) as

$$\dot{x}_{ss}(t) = \sum_{n=0}^{\infty} \{n\omega e_n + n\omega f_n\} \cos(n\omega t) + \sum_{n=0}^{\infty} \{n\omega v_n - n\omega u_n\} \sin(n\omega t) \quad (13)$$

For the undamped system, resonance occurs when $a_n = 0$. So, the mechanism enters resonance whenever motor speed ω approaches the values ω_0/n (with $n = 1, 2, 3, 4$, and so on).

The power input from the DC motor is $P_m = T_m\omega$, where torque generated by the non-ideal motor is given by $T_m = \mu_m(V_s - \mu_m\omega)/R$ [4, 5]. On substitution, one writes

$$P_m = \mu_m\omega(V_s - \mu_m\omega)/R \quad (14)$$

When the dynamics attain steady equilibrium conditions, the power supplied (P_m) to the mechanical system will equalize the power dissipated (P_d) from it. By equating P_m and P_d and substituting Eq. (14) thereof, one obtains an expression of V_s as

$$V_s = (P_d R)/(\mu_m\omega) + \mu_m\omega \quad (15)$$

Note that dissipated power P_d in Eq. (15) can be written as

$$P_d = (\omega/2\pi) \int_0^{2\pi/\omega} C\{\dot{x}_{ss}(t) - \dot{y}(t)\}^2 dt \quad (16)$$

With the help of Eqs. (9) and (13), Eq. (16) is further expanded as

$$P_d = (C/2) \left\{ \sum_{n=0}^{\infty} (g_n^2 + h_n^2) \right\} \quad (17)$$

with coefficients $g_n = n\omega(e_n + f_n - q_n)$ and $h_n = n\omega(v_n - u_n + p_n)$.

3 Results and Discussions

Two response plots are shown in Fig. 2, using Eqs. (12), (15), and (17). Figure 2a shows the output motor speed (ω) against input voltage V_s and Fig. 2b shows the same for the coexisting vibration amplitudes of the block mass M (the amplitudes are calculated as the mean values of the displacement response from Eq. (12)).

Notice that in Fig. 2a, when operator starts increasing the source voltage for starting the mechanism (*run-up* condition), the resulting speed response is not linear throughout. In fact, from point a onwards, the speed progress is more and more disproportionate. The actual speed trajectory can be traced as follows— $o \rightarrow a \rightarrow b \rightarrow c \rightarrow d \rightarrow e \rightarrow f \rightarrow g \rightarrow h \rightarrow i$ and so on, which clearly demonstrates that responses for the quick-return mechanism are discontinuous. The reason being that when the motor speed approaches some resonance zone, the non-ideal motor lacks sufficient power to make smooth transit through that zone. Under resonance,

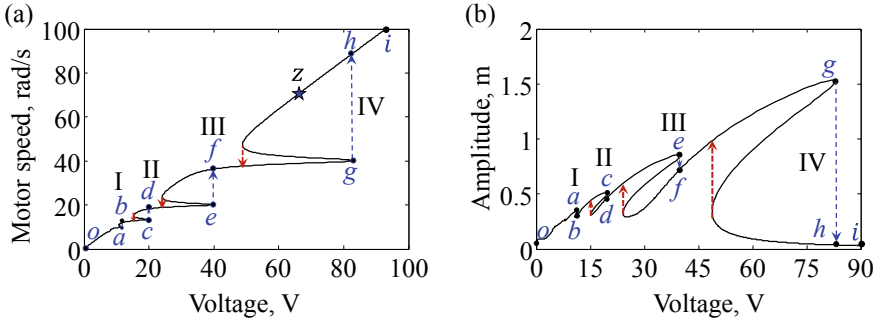


Fig. 2 Response plots—**a** speed response; **b** amplitude response at steady state

the vibrating block withdraws much of the motor power and oscillates with growing amplitudes (refer Fig. 2b). This effectively leaves lesser power to be available for operating speed and hence, speed increment at this stage is withheld even for large changes in voltage values. This indicates that the quick-return mechanism is captured at resonance. And since the mechanism is unable to speed up, getting captured at lower speeds involves a larger average time for the return strokes (recall that from Eq. (2), t_r increases if ω is small). This lead to a net increase in the non-machining/idle time; thus, effectively lowering machine productivity. In Fig. 2a and b, the capture zones are marked by sections $b \rightarrow c$, $d \rightarrow e$, and $f \rightarrow g$.

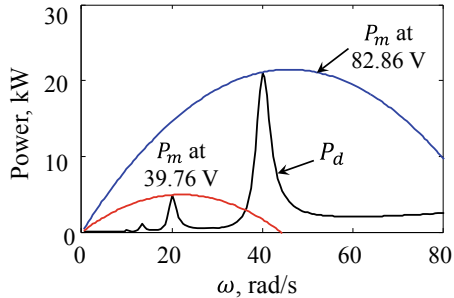
Afterward, when necessary input power is provided, the ‘capture phases’ cease to exist and each capture zone culminates with a distinct ‘jump’. In Fig. 2a and b, there are four such consecutive jumps (I, II, III, and IV) corresponding to four resonance zones. These are marked by dotted blue arrows for sections $a \rightarrow b$, $c \rightarrow d$, $e \rightarrow f$, and $g \rightarrow h$, respectively. During the run-up, the speed response displays a jump-up in values, while the corresponding amplitude response shows a jump-down in values. The series of jumps is actually indicative of the sequential escape from each successive resonance zone. The details of the jump segments are given in Table 2. Observe that the jump sizes keep on increasing as we move on to higher speeds, with jump IV being the largest one.

On the other hand, if the operator reduces voltage for shutting down the mechanism (*run-down* condition), the transitioning jump points are found to be different from those experienced during run-up. Moreover, the average size of the run-down jumps

Table 2 Run-up jump segments (refer Fig. 2a)

Jump	Path	Initiating voltage (V)	Speed transition (rad/s)
I ($\sim \omega_0/4$)	$a \rightarrow b$	11.50	10.1–11.8
II ($\sim \omega_0/3$)	$c \rightarrow d$	19.71	13.4–18.2
III ($\sim \omega_0/2$)	$e \rightarrow f$	39.76	20.1–36.3
IV ($\sim \omega_0$)	$g \rightarrow h$	82.86	40.2–88.9

Fig. 3 Power requirements—Motor power P_m and dissipated power P_d against speed ω



(marked with dotted red arrows in Fig. 2a and b) is relatively smaller. Note that during run-down, the speed response records a jump-down, while the vibrations experience a corresponding jump-up.

We now check for the necessary power requirements that allow the machine to avoid the resonance capture. Figure 3 shows the P_d curve, which has two major resonance peaks (ω_0 and $\omega_0/2$ peaks) alongside few minor ones. Two separate P_m curves for two distinct voltages are also added to the same plot. Recall that from Eqs. (14) and (17), P_d depends on ω but not on V_s ; unlike P_m which depends on both ω and V_s . To ascertain whether a particular V_s can generate adequate motor power to avoid capture—consider whether the P_m curve for that voltage can overshoot the P_d peaks; failing which, the mechanism gets stuck perpetually. Notice that P_m for 39.76 V tangentially overshoots the $\omega_0/2$ peak (at 20 rad/s), but fails to do so for the ω_0 peak. That means generated power at 39.76 V can successfully evade the $\omega_0/2$ resonance zone, but not the ω_0 zone. To entirely avoid the resonance capture, the minimum voltage requirement is 82.86 V. This is evident from the P_m curve for 82.86 V, which is shown to surpass all possible peaks. Indeed, as per Table 2, 39.76 V and 82.86 V are the respective initiating voltages for Jumps III and IV.

Now, suppose there is a need to run the machine at 70 rad/s (point z in Fig. 2a). Then, the conventional way of start-up will most certainly ensure capture at some resonance. To avoid that and opt for a safer way to acquire that speed, voltage regulation must be done judiciously. At first, full power above the critical value (i.e., 82.86 V) must be provided, so that none of the resonances are encountered. That way, all jumps are averted, and the machine directly acquires 90 rad/s (i.e., point h or above). From there on, gradually reducing voltage and allowing a motor run-down (via backwards path $h \rightarrow z$) gets the machine to safely run at 70 rad/s.

Nonetheless, it must be pointed out that the machine cannot avail all possible speed ranges, no matter how carefully voltage is regulated. This is particularly true for the negative slopes in Fig. 2, which indicate unstable solutions [4, 6, 8]. Wherever negative slopes exist (in Fig. 2a and b), the corresponding speed or amplitude values are not feasible in practice. The mechanism cannot be made to operate at these speeds and so, these speed ranges are termed ‘inoperable/missing’.

Figure 4a demonstrates how the eccentricity parameter e_c affects the power requirements. From Eq. (7), eccentricity e_c depends on both the crank radius AB

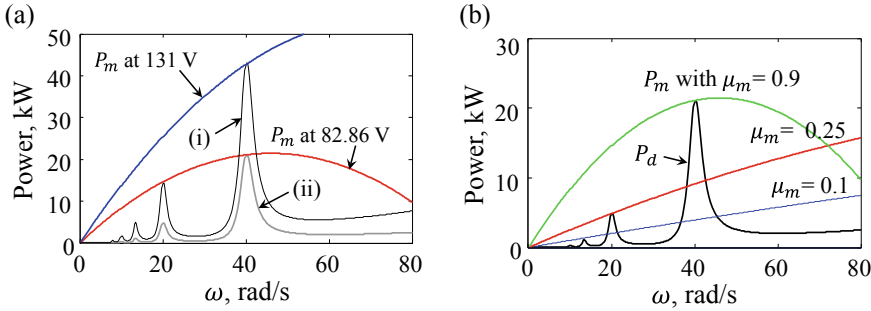


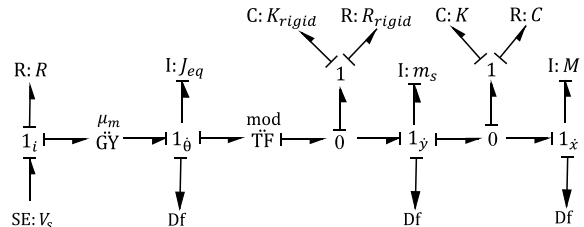
Fig. 4 Power characteristics—Influence of **a** eccentricity e_c and **b** motor constant μ_m

(r) as well as the arm length OC (q). Notice that curve (ii) is the old P_d curve with $e_c = 0.013$ ($q = 0.145$ m and $r = 0.09$ m). The critical voltage requirement was 82.86 V. Now, let's increase OC by 2.5 cm and AB by 1 cm. So, the new e_c value is 0.017 ($q = 0.170$ m and $r = 0.1$ m). Curve (i) represents the new P_d curve for $e_c = 0.017$. We observe that with the increase in the e_c value, the peak power demand for the ω_0 resonance zone is almost doubled. Hence, traversing the resonance would now be twice as difficult as before. The new critical voltage requirement to do so has now increased to 131 V (with the same motor).

As for the motor drive, Fig. 4b shows the effect of motor constant μ_m on the power characteristics. The plot in Fig. 4b includes P_m curves for three distinct μ_m values, alongside the old P_d curve. Note that all three P_m curves are generated at 82.86 V. It is observed that with $\mu_m = 0.1$ Nm/A, even at 82.86 V, the P_m curve only manages to surpass the $\omega_0/3$ peak, but none of the remaining peaks. Next, with $\mu_m = 0.25$ Nm/A, the $\omega_0/2$ peak is cleared off but the ω_0 peak still remains unsurpassed. It finally takes a motor with μ_m as high as 0.9 Nm/A to successfully power through the dominant resonant peak (ω_0) and all remaining peaks by default. It must be pointed out here that had the resonances occurred at higher speeds (i.e., if the peaks were shifted to the right), the motors with lower μ_m values would better serve the purpose.

The discussions so far have focused only on steady-state analysis, which often shows the most critical aspects of the jump phenomena. However, to confirm that, we now take up simulated responses obtained from a Bond Graph (BG) model of the mechanical system. In the BG model shown in Fig. 5, the source element SE: V_s

Fig. 5 Bond graph model of the quick-return mechanism



provides power to the 1_i junction (which models the current flowing through the motor circuit); the element R: R is the armature resistance attached to this 1_i junction. The Gyrator element GY of modulus μ_m converts the 1_i junction (electrical domain) into $1_\dot{\theta}$ junction (mechanical domain). At the $1_\dot{\theta}$ junction, the inertial I: J_{eq} element represents the rotary inertia J_{eq} (which is the combined rotary inertia of the motor, crank, and the flywheel at A). Next, the transformer TF element transforms the $1_\dot{\theta}$ junction (crank rotations) into $1_\dot{y}$ junction (slider motions); the expression for the TF modulus *mod* is obtained by differentiating Eq. (7). The slider mass is modeled as I: m_s attached at the $1_\dot{y}$ junction. To avoid differential causality, padding elements C: K_{rigid} and R: R_{rigid} are inserted between the $1_\dot{\theta}$ and $1_\dot{y}$ junctions, via a 0-junction. The inertial I: M element, which models the mass of the vibrating block, is attached to the 1_x junction (block motions). The elements C: K and R: R represent the coupling parameters between the slider and the block. The three Df elements record the corresponding flow variables at their respective 1-junctions.

Note that for numerical simulations (Fig. 6), two additional inertia parameters are involved—the rotary inertia J_{eq} and the slider mass m_s . The values are taken as $J_{eq} = 3.2 \text{ kgm}^2$ and $m_s = 0.8 \text{ kg}$. The high rotary inertia limits the large speed fluctuations that occur due to unequal stroke durations and swift motion reversals at the end of each stroke. The padding parameters are taken as $K_{rigid} = 1e8 \text{ N/m}$ and $R_{rigid} = 1000 \text{ Ns/m}$. To properly witness the jumps, we slowly increase the voltage from 1 to 83 V over a long time span of 5000 s. This slow voltage increment helps to slow down the angular accelerations so that the simulation mimics the steady-state analysis.

It is observed that in spite of the high rotary inertia, speed fluctuations still persist. However, all four jumps are detected, with Jumps III and IV being the most visible ones due to their large sizes. In between Jumps I–IV, on account of successive resonance captures, the amplitudes of the vibrating block continue to grow alarmingly. And a sudden decline in the amplitudes occurs only after Jump IV, which basically implies that the resonance conditions are finally over. The respective initiating voltages for jumps I, II, III, and IV are calculated as 11.10 V, 18.91 V, 39.40 V, and

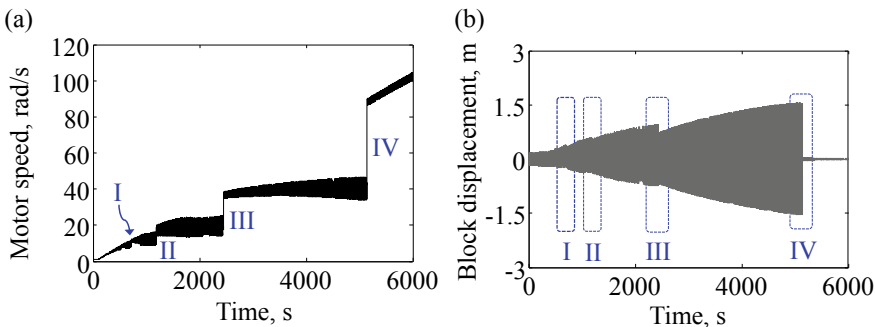


Fig. 6 Bond graph simulated responses—**a** motor speed; **b** block displacement

82.80 V. Notice that the simulation jumps occur slightly before the theoretically predicted values (as per Table 2) due to persistent speed fluctuations and unsteady angular accelerations.

4 Conclusions

The jump phenomena for the quick-return mechanism manifest as a series of separate jumps, which are each preceded by periods of prolonged capture at multiple resonance zones. During resonance capture, escape from resonance becomes a struggle and the mechanism has difficulty acquiring target speeds or even reaching higher speed regimes, unless additional motor power is inputted. The process is economically disadvantageous because costly motor power is wasted on machine vibrations, whereas speed progression takes a backseat. Besides, if resonance is encountered at lower speeds, the total idle time of the quick-return mechanism increases. Also, once the capture phases are terminated and the jumps take place, some speed ranges are rendered inoperable due to discontinuities. The jump phenomena thus present a number of hurdles for the mechanism by reducing its efficiency, performance as well as machine productivity. To tackle the peak power demands during the resonance period, the power characteristics of the system are discussed—with special mention to the influence of eccentricity and motor parameters. The criteria for power requirements can lead to important design considerations, which must be accounted for when designing the mechanism or deciding on a suitable motor. Since steady-state analysis often outlines the most extreme characteristics, a design based on that can be arguably considered both safe and conservative.

References

1. Ghosh, A., Mallik, A.K.: Theory of Mechanisms and Machines. Affiliated East-West Press, New Delhi (1976)
2. Hsieh, W.H., Tsai, C.H.: A study on a novel quick return mechanism. *Trans. Can. Soc. Mech. Eng.* **33**(3), 487–500 (2009)
3. Monkova, K., Monka, M., Hloch, S., Valicek, J.: Kinematic analysis of quick-return mechanism in three various approaches. *Tech. Gaz.* **18**(2), 295–299 (2011)
4. Cveticanin, L., Zukovic, M., Balthazar, J.M.: Dynamics of Mechanical Systems with Non-Ideal Excitations. Springer, Berlin (2017)
5. Sinha, A., Samantaray, A.K., Bhattacharyya, R.: Self-synchronization of two unbalanced DC motor-driven rotors on a common movable platform. In: Badodkar, D., Dwarakanath, T. (eds.) *Machines, Mechanism and Robotics. Lecture Notes in Mechanical Engineering*. Springer, Singapore (2019)
6. Sinha, A., Bharti, S.K., Samantaray, A.K., Bhattacharyya, R.: Self-synchronization in a class of motor driven reciprocating mechanisms. In: Proceedings of the ASME 2019 International Mechanical Engineering Congress and Exposition. Salt Lake City, Utah, USA. ASME (2019)

7. Hu, W.H., Thöns, S., Rohrmann, R.G., Said, S., Rücker, W.: Vibration-based structural health monitoring of a wind turbine system. Part I: resonance phenomenon. *Eng. Struct.* **89**, 260–272 (2015)
8. Jansen, C.: The “Sommerfeld” effect - saving energy through vibration reduction. KÖTTER Consulting Engineers GmbH, Rheine **8**, 1–2 (2019)
9. Sinha, A., Bharti, S.K., Samantaray, A.K., Chakraborty, G., Bhattacharyya, R.: Sommerfeld effect in an oscillator with a reciprocating mass. *Nonlinear Dyn.* **93**(3), 1719–1739 (2018)
10. Piccirillo, V., Tusset, A.M., Balthazar, J.M.: Dynamical jump attenuation in a non-ideal system through a magneto-rheological damper. *J. Theor. Appl. Mech.* **52**(3), 595–604 (2014). Warsaw
11. Jha, A.K., Dasgupta, S.S.: Attenuation of Sommerfeld effect in an internally damped eccentric shaft-disk system via active magnetic bearings. *Meccanica* **54**(1–2), 311–320 (2019)
12. Chakraborty, P., Chakraborty, G., Bhattacharyya, R.: Elimination of Sommerfeld effect in non-ideal systems using dry friction. In: Proceedings of the ASME 2019 International Mechanical Engineering Congress and Exposition. Salt Lake City, Utah, USA. ASME (2019)

Real-Time Trajectory Estimation of a Ball Moving in a 3D Space



Dheeraj Bhogisetty, Sai Surya Srinivas Kunapuli, and Shital S. Chiddarwar

1 Introduction

Humans have the ability to infer information from the motion of objects. For example, consider a ball thrown in the air. We can track and estimate the trajectory of an object instinctively based on intuition. It is possible because of the inherent knowledge we possess about the physics governing the motion, the environment, and the type of object. With the help of computer vision, this ability can be given to robotic systems. This paper discusses an algorithm for detecting and tracking a thrown ball in real-time using a stationary depth camera. The task of estimation of the 3D trajectory of a thrown ball can be divided into three subtasks: (1) Ball detection, (2) Estimation of 3D world coordinates of the ball, and (3) 3D Trajectory estimation. The thrown ball remains in the air roughly for about 0.8–1.2 s and covers an average distance of 4 m. So, the vision system should be fast enough to detect and track the ball and estimate its trajectory.

Detection of the thrown object is the first and most crucial subtask. The thrown ball is segmented by background subtraction method using Gaussian Mixture Model (GMM) [1]. In background subtraction, the changes in light intensity or motion changes due to sudden disturbances to camera or camera oscillation result in a change in the background model. This leads to the detection of unwanted motion giving noisy and erroneous results. So, for robustness and accurate results, the Gaussian Mixture Model (GMM) is used for modeling the background. After the successful segmentation of foreground objects, the ball centroid coordinates are obtained using blob analysis. The determination of the 3D coordinates of the ball is challenging. Using a monocular system, the 2D coordinates of the ball can be directly obtained. The third coordinate can be solved for certain cases, where the motion is limited to a plane, with the help of a pin-hole camera model. But in this case, the motion of the

D. Bhogisetty (✉) · S. S. S. Kunapuli · S. S. Chiddarwar
Mechanical Engineering, VNIT Nagpur, Nagpur, India

ball is not confined to a single plane. It can be solved using a monocular system by developing nonlinear estimation models, [2–6], but they are complex. Though this can be solved using a stereo camera system, [7] and [8], the requirement of multiple cameras, sophisticated hardware, and the calibration of these cameras increase both cost and complexity. This is where Kinect is useful. Using both the sensors in Kinect, RGB camera, and depth sensor, a 3D point cloud can be generated from which the 3D world coordinates can be obtained [9]. Using the 3D coordinates, the trajectory can be estimated.

The 3D trajectory estimator is based on the time-series analysis. Time-series analysis deals with series of data which are recorded or measured at discrete time intervals. As the data obtained from the camera is discrete, it can be used for the trajectory estimation case. The ball is considered to be a projectile and the only force acting on the ball is the gravity. The forces due to air drag are considered negligible and hence ignored for simplicity. Using the least-squares method, the estimator fits a parabola. This estimation is refined as more coordinates are obtained in subsequent frames. The overview of the algorithm is shown in Fig. 1.

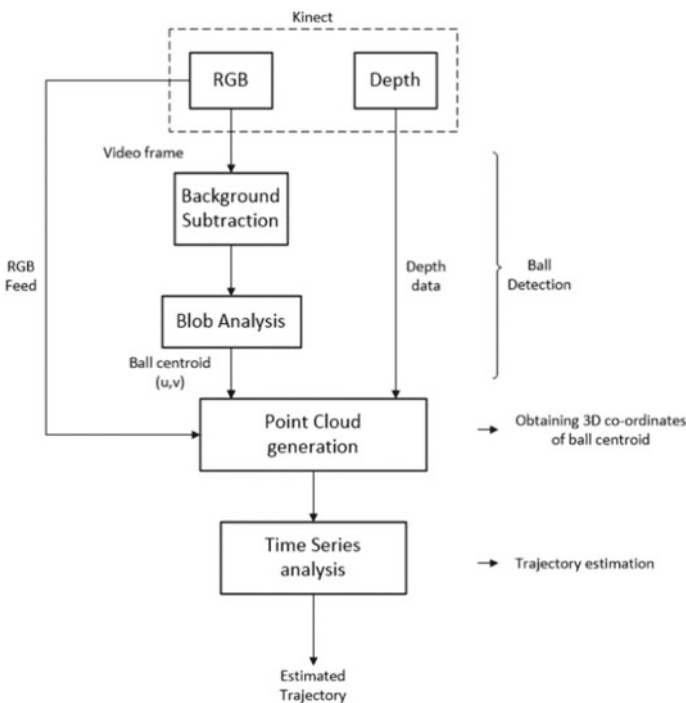


Fig. 1 Algorithm flowchart

2 Related Work

Most of the work related to the estimation of projectile motion is found in the work related to the ball-catching task. From the literature survey, it is evident that in most of the works, monocular systems [2–4, 6], and stereo camera systems [7, 8] are used. Monocular systems have easy calibration procedures, but more effort has to be put into the 3D reconstruction of the scene. Whereas for stereo systems, 3D reconstruction is easy using the triangulation method but requires accurate calibration and complex elaboration hardware. Different from the conventional approach, the algorithm proposed in this paper uses the depth camera.

In [2–4], an eye-in-hand 3D monocular robotic ball-catching system is proposed. In this configuration, the camera is not stationary and moves with the robot end-effector following the ball. For ball detection, an equalized color-based clustering in the Hue–Saturation–Lightness (HSL) color space is used in [2–4]. An iterative trajectory estimator is used in [2, 3]. First, a linear estimator is used for estimating the trajectory in order to provide an initial baseline for the camera and later a nonlinear estimator is used to refine the linear estimation of the trajectory over time. In [4], the ball trajectory is estimated as a parabola. In [5], an expectation–maximization algorithm is used to detect objects on parabolic trajectories in a video over short time periods. Regions of interesting motion are detected using size, speed, and compactness criteria. The 3D positions and velocities of projectiles are estimated from monocular views using a robust nonlinear optimization-based formulation in [6]. A theoretical formulation is developed with minimum conditions for the existence of a unique solution.

In [7], a robotic ball catcher is proposed where a stereo camera system is used for visual tracking. The ball is detected by segmentation based on difference images, similar to background subtraction. An Extended Kalman Filter (EKF) is used for predicting the trajectory also considering air drag. A humanoid with stereo vision is considered in [8]. The ball is detected using a novel circular gradient method which is robust to change in lighting conditions and size of the ball. A Multi Hypothesis Tracker (MHT) with Kalman Filter is used to predict one or more trajectories from the set of detected circles.

In [10], an algorithm was developed for detection of aerial balls in an MSL context. The point cloud obtained from Kinect was voxelized in an occupancy voxel space rather than considering the whole point cloud, for ball detection which reduced the computation. Once the ball coordinates were detected, Singular Value Decomposition was used to compute a parabolic equation that best fits the coordinates for estimating the trajectory.

3 Ball Detection

The brightness and clarity of the input video also play a role while detecting the ball. Less brightness and clarity can cause difficulty while detecting the ball, which may result in false detection. The compactness ratio of the ball obtained from the video may be different from the actual one and the object with the next least compactness ratio might get detected. The algorithm requires a minimum clarity and brightness such that it can distinguish the moving objects from the stationary ones, and different shapes. The use of Kinect in an environment with an ambient lighting ensures that those requirements are met.

3.1 Background Subtraction Using GMM

The thrown ball is segmented from its background using the background subtraction model as the camera is stationary. In background subtraction, subsequent frames are subtracted, and the change in the image is obtained. The difference image is then thresholded. As a result, the stationary objects are eliminated, and only the objects which are moving are obtained. As proposed in [1], Gaussian Mixture Models are used to model the background. This model adapts to changes in the background and gives accurate results improving robustness.

Gaussian Mixture Models (GMM)

A gaussian mixture model is a parametric probability density function $p(x)$,

$$p(x) = \sum_{i=1}^K \phi_i N(x|\mu_i, \sigma_i) \quad (1)$$

The Gaussian function is $N(x|\mu_i, \sigma_i)$. K is the number of mixture components. Mixture component weights ϕ_i are constrained such that $\sum_{i=1}^K \phi_i = 1$ so that the total probability distribution normalizes to 1. Initially, a set of frames have to be given to this model for training to be trained to learn the weights ϕ_k .

3.2 Blob Analysis

After thresholding the difference image, a binary image containing blobs is obtained and among them, the ball has to be detected. Difficulties arise in detecting the ball due to its small size, low resolution, background clutter, and noise. Due to its small size, the ball has a low compactness ratio (compactness ratio is the ratio of area to the perimeter of the ball in the image) [5]. Using the blob analysis and compactness

ratio, moving objects other than the ball are eliminated from consideration. The image coordinates of the centroid of the ball are obtained and the ball is detected.

3.3 Results

The ball detection part was implemented in MATLAB using real-time feed from the RGB camera of Kinect with 480×640 resolution @30 fps. The number of initial video frames given for training the background model is 100, the learning rate is chosen as 0.005 with adaptive learning, and the number of Gaussian modes in mixture model is 7 with other parameters remaining default. The results of ball detection in a random frame during the ball's flight are shown below (Fig. 2).

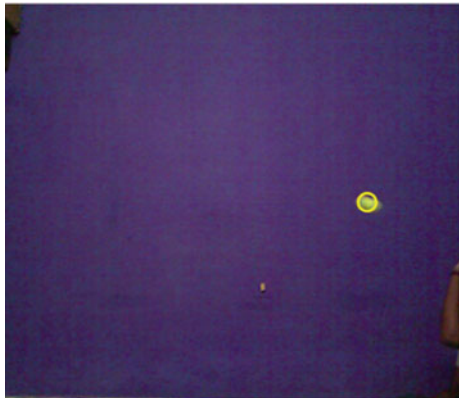
In Fig. 3, we can see that multiple blobs are detected, one of the ball and others of a human hand moving in the frame. The blobs are separated and the ball is detected using compactness ratio (Fig. 4).

Fig. 2 Actual image



Fig. 3 Mask after background subtraction



Fig. 4 Ball detected

4 Trajectory Estimation

After detecting the ball using background subtraction and compactness ratio, we need to estimate the trajectory of the ball. This needs the 3D coordinates of the ball. We obtained these values from the point cloud generated using the Kinect camera.

4.1 Point Cloud Analysis

Point clouds are a set of data points which when combined represent a particular object or an entire scene. These points represent the X, Y, and Z geometric coordinates of a single point on an underlying sampled surface. Point clouds are generated by combining a large number of single spatial measurements. Point clouds are generally 3D, and adding information about the color makes them 4D. 3D laser scanners are the most common devices which are used to generate point clouds. Here, we used Kinect integrated with MATLAB to generate the point cloud of the scene.

The real-world X, Y, and Z coordinates of each pixel in the image are stored in three 3D matrices of size $480 \times 640 \times n$ each, where ‘n’ represents the number of frames in the feed and 480×640 is the resolution of the camera. The coordinates are then extracted from these matrices, using the ball’s position in the pixel domain which are obtained from the detection part. The coordinates obtained are then used for the trajectory estimation. The point cloud generated by the Kinect camera, of a scene, is shown below (Figs. 5 and 6).

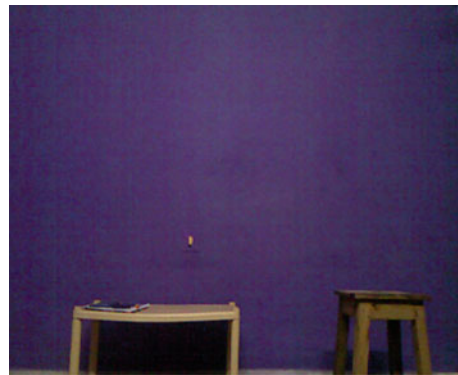


Fig. 5 Actual image of the scene

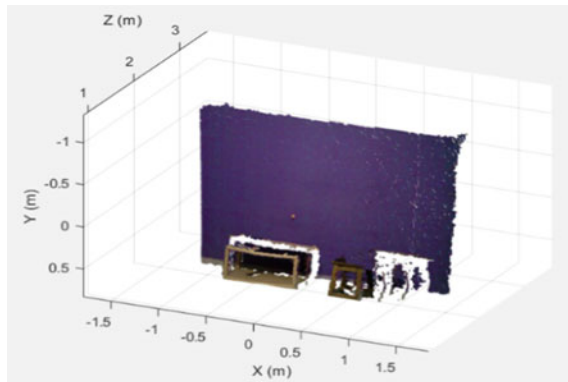


Fig. 6 Point cloud of the scene

4.2 Time-Series Analysis

Time-series analysis is a collection of methods used to extract meaningful statistics and other useful information from time-indexed data. Time-series forecasting, one of the methods in time-series analysis, is used here to predict future values based on previously observed values, using a model that defines the system. One disadvantage of this analysis is that the model is estimated based on the time-series data which might be influenced by some external factors. These factors may not be the same after some time. But we can assume the effect of these factors to be negligible because the time window for our calculations is small and the measurements are taken in a controlled environment.

Time-series analysis in MATLAB

To implement the time series in MATLAB, we need more data compared to the actual data we get during the 0.8–1.2 s of the flight of the ball. As the data we get is discrete, it is interpolated to get more data points than we have before resulting in better output. This time-domain data is now used to estimate a state-space model defined by the equations below.

$$\dot{x}(t) = Ax(t) + Bu(t) + Ke(t) \quad (2)$$

$$y(t) = Cx(t) + Du(t) + e(t) \quad (3)$$

where A, B, C, D, and K are state-space matrices, u(t) is the input, e(t) is the disturbance, y(t) is the output, and x(t) is the vector of three states. In our case, the output is the ball coordinates. This model can now be used to forecast the position of the ball using already measured data.

4.3 Results

Below are the results after applying this method. This data is fitted into a parabola using the least-squares method and the final 3D trajectory is plotted (Figs. 7 and 8).

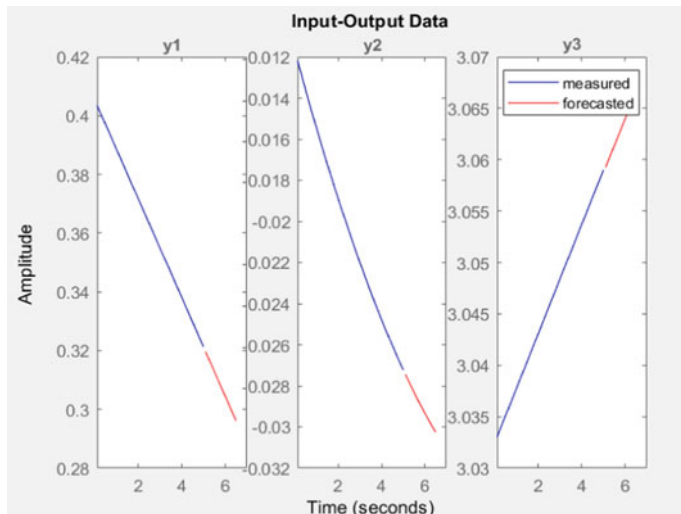


Fig. 7 Measured and forecasted values using time-series analysis in 3D, where y1, y2, and y3 are X, Y, and Z coordinates, respectively

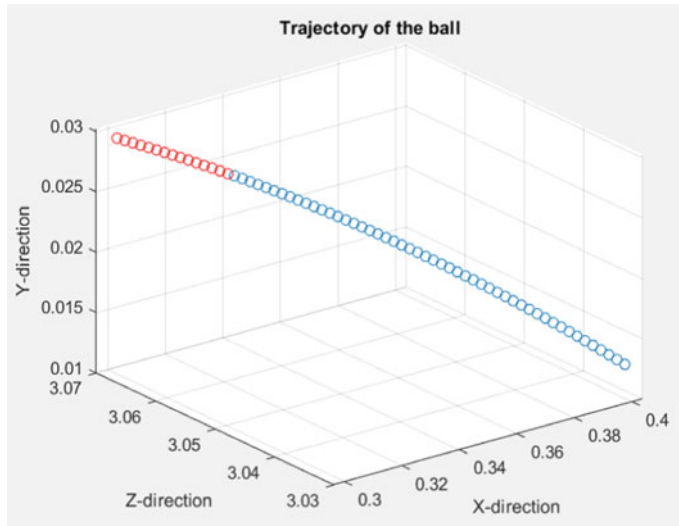


Fig. 8 3D plot of measured (blue) and forecasted values (red)

5 Conclusion

The main goal of estimating the trajectory of the ball was achieved. The method discussed here gives a relatively simpler approach to the trajectory estimation problem. Background subtraction and compactness ratio used for the detection of the ball gave results that are accurate and more robust to the environmental conditions like scene lighting and color of the ball. The use of time-series analysis for trajectory estimation is a slight deviation from its general use for statistics, signal processing, etc. Nevertheless, the method gave good results, thus encouraging its use in the computer vision domain.

References

1. Aslam, N., Sharma, V.: Foreground detection of moving object using Gaussian mixture model. In: 2017 International Conference on Communication and Signal Processing (ICCP), Chennai, pp. 1071–1074 (2017). <https://doi.org/10.1109/iccp.2017.8286540>
2. Lippiello, V., Ruggiero, F., Siciliano, B.: 3D monocular robotic ball catching. Robot. Auto. Syst. **61**(12), 1615–1625 (2013)
3. Lippiello, V., Ruggiero, F.: 3D monocular robotic ball catching with an iterative trajectory estimation refinement. In: Proceedings of IEEE International Conference on Robotics and Automation, May 2012, Saint Paul, MN, USA, pp. 3950–3955 (2012)
4. Lippiello, V., Ruggiero, F.: Monocular eye-in-hand robotic ball catching with parabolic motion estimation. In: Proceedings of 10th International IFAC Symposium on Robot Control, Dubrovnik, Croatia, pp. 229–234 (2012)

5. Ribnick, E., Atev, S., Papanikolopoulos, N., Masoud, O., Voyles, R.: Detection of thrown objects in indoor and outdoor scenes. In: Proceedings of IEEE/RSJ International Conference on Intelligent Robots and Systems, October/November 2007, San Diego, CA, USA, pp. 979–984 (2007)
6. Ribnick, E., Atev, S., Papanikolopoulos, N.: Estimating 3D positions and velocities of projectiles from monocular views. *IEEE Trans. Pattern Anal. Mach. Intell.* **31**(5), 938–944 (2009)
7. Frese, U., Bauml, B., Haidacher, S., Schreiber, G., Schaefer, I., Hahnle, M., Hirzinger, G.: Off-the-shelf vision for a robotic ball catcher. In: IEEE/RSJ International Conference on Intelligent Robots and Systems, Maui, HI, pp. 1623–1629 (2001)
8. Birbach, O., Frese, U., Bauml, B.: Real-time perception for catching a flying ball with a mobile humanoid. In: IEEE International Conference on Robotics and Automation, Shanghai, PRC, pp. 5955–5962 (2011)
9. Zhang, Z.: Microsoft kinect sensor and its effect. *IEEE Multimedia* **19**(2), 4–10 (2012). <https://doi.org/10.1109/MMUL.2012.24>
10. Dias, P., Silva, J., Castro, R., Neves, A.J.R.: Detection of aerial balls using a kinect sensor. In: RoboCup 2014. Lecture Notes in Computer Science, vol. 8992. Springer, Cham (2015)

Design and Trajectory Optimization of Delta Robot



Kunal Nandanwar and B. K. Rout

1 Introduction

Delta Robot is a 4-degree of freedom (DOF) parallel robot. The first 3-DOFs are meant for translations in XYZ directions and fourth leg is used to control a single rotational DOF at the end-effector platform. The robot consists of three arms connected to universal joints at the base and provides the three translational DOFs. The mechanism of the robot can be treated as a spatial generalization of a four-bar linkage (Fig. 1).

The delta robot use parallelograms which restrict the movement of the end platform to pure translation. The robot's base is mounted above the workspace and all the actuators are located on it. From the base, three middle jointed arms extend. The ends of these arms are connected to a small triangular platform. Actuation of the input links will move the triangular platform along the X, Y, or Z direction. The delta robot is extensively used for pick-and-place jobs in the chocolate industries, desktop haptic robot devices, sketching industries, and packaging industries, which has high precision during assembly operations in electronics and 3-D printers as discussed in [1–3]. These are closed-loop manipulators which have the capability of high-speed operations.

Romdhane designed a 6-DOF hybrid serial–parallel manipulator. It was made of a base and two platforms in series [4]. Huang et al. proposed a 3-DOF parallel mechanism module which formed the main body of a reconfigurable hybrid robot. The Tricept robot used widely is a hybrid system with a 3-DOF parallel mechanism and a 2-DOF serial mechanism. The parallel part of Tricept robot is formed by ball screws,

K. Nandanwar (✉) · B. K. Rout
Birla Institute of Technology & Science, Pilani, India
e-mail: f2015430p@alumni.bits-pilani.ac.in

B. K. Rout
e-mail: rout@pilani.bits-pilani.ac.in

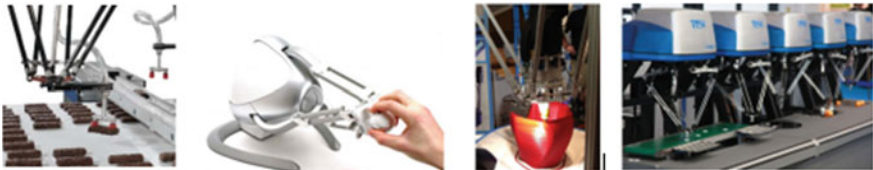


Fig. 1 Applications of delta robots [1–3]

which makes the mechanism huge [5]. Liang and Ceccarelli designed a waist–trunk system. The waist–trunk system consisted of a 3-legged parallel platform and a 6-legged parallel system. The two platforms were connected in a serial architecture. The system was designed for humanoid robots which have high payload capacity, high stiffness, and accuracy, but the structure was too complicated [6, 7]. ABB Flexible Automation launched a 4-DOF delta robot, under the name IRB 340 FlexPicker. The IRB robot has more flexibility and larger scope of application in comparison with the delta robot. FANUC Robotics developed two types of delta robots, M-1iA and M-3i, with 4 or 6 DOFs. The FANUC delta robots provide motion flexibility of a human wrist, fast cycle times, ultracompact arm, and precision [8]. Energy used by these mechanisms plays a vital role in the selection process. The literature reviewed rarely discusses aspects related to energy consumption or synthesis of mechanism to traverse a path. Current paper deals with the energy aspects of the delta robot without considering its rotational DOF of base to simplify the kinematic and dynamic model and minimize the computational time.

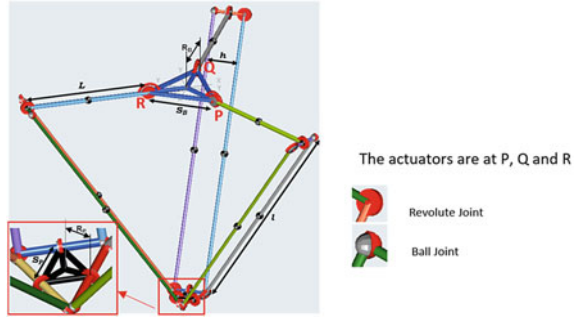
The paper is organized in the following sections. Section 2 discusses the kinematic model used for the delta robot. The dynamic model of the robot is presented in Sect. 3. The steps used for path and trajectory optimization are discussed in Sect. 4. Lastly, the steps used for the optimal design of the above robot are discussed in Sect. 5. Finally, the results are summarized in Sect. 6.

2 Model Building and Validation

For the considered problem, a virtual delta robot is developed using the student version of Altair HyperWorks [9]. The dimensions used for the model and kinematic analysis are provided in Table 1. It should be noted that the local reference frame has been referred to as ‘Marker’ in this paper. The three parallelograms were defined using two revolute joints at one diagonal and two ball joints at the other. Ideally, the model could be correctly represented with all joints as revolute joints, but this will lead to an over-constrained model. Here, over-constraints scenarios are avoided by using ball joints. The dimensions associated with the model are presented in Fig. 2 which consist of 17 links, 15 revolute, 6 spherical joints, and 3 actuators. The current model has required 3-DOF and not over-constrained. To verify the design of the above model, the Inverse Position Kinematics (IPK) and Forward Position Kinematics

Table 1 Delta robot dimensions

Label	Meaning	Value
S_B	Base Equilateral Triangle Side	288
S_P	Platform Equilateral Triangle Side	76
L	Upper Legs Length	524
L	Lower Legs Parallelogram Length	1244
H	Lower Legs Parallelogram Width	131

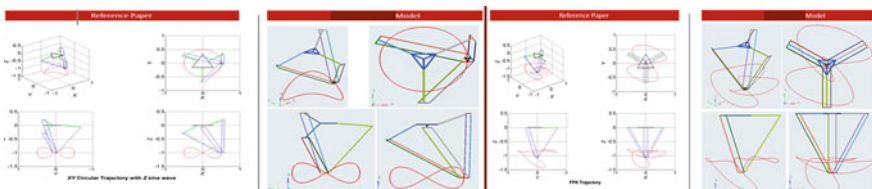
Fig. 2 Representative model of delta robot

(FPK) results are matched which are available in [10]. This step is implemented essentially to validate whether the delta robot is modeled correctly.

Inverse Position Kinematics. In inverse position kinematics, the input motion is cartesian coordinate position of the end-effector platform with respect to time and determine the joint angles at base, i.e., P, Q, and R as outputs. The cartesian trajectory to be followed by the end-effector is given in (1)

$$\begin{aligned} X \text{ mm} &= 500 \cos((2\pi/5)t) \\ Y \text{ mm} &= 500 \sin((2\pi/5)t) \\ Z \text{ mm} &= -1000 + 200 \sin((4\pi/5)t) \end{aligned} \quad (1)$$

The results obtained from simulation for 5 s [10] available in Fig. 3 show the trajectories and configurations of the two models at time $t = 0$ and $t = 5$. This shows

**Fig. 3** Trajectories and configurations after IPK (left), FPK (right)

that the model is correct for inverse position kinematics. Similarly, the results are compared for forward position kinematics.

Forward Position Kinematics. In forward position kinematics, the input motion is rotation of the upper links that is known and the cartesian (xyz) coordinates of end-effector platform is the output to be determined. For correct comparison, the same data set available in [10] has been used and Eq. (2) is taken as the input for FPK:

$$\begin{aligned}\theta_P \text{ deg} &= 45 \cos((2\pi/5)t) \\ \theta_Q \text{ deg} &= 45 \sin((4\pi/5)t) \\ \theta_R \text{ deg} &= 45 \sin((6\pi/5)t)\end{aligned}\quad (2)$$

The simulated results are obtained for 5 s. Figure 3 shows the trajectories and configurations of the two models at time $t = 0$ and $t = 5$ s. Therefore, it can be concluded that the model is kinematically correct and the dynamics of the robot should be developed to determine the torque and subsequently energy requirement. Thereafter, an optimization problem can be formulated to obtain optimal dimensions. Figure 6 FPK: trajectories and configurations.

3 Dynamic Model for the Delta Robot

The aim here is to develop the dynamic model which provides torque for known motion. In this case, inverse and forward dynamics concepts are used to verify the model. For mass values, the density of steel was chosen and the diameters of all the links were the same, which can be concluded that mass was proportional to length. The torque applied with respect to time as input at the base actuators is available in (3). The torque inputs at joints are given by

$$\begin{aligned}\tau_P &= 400 \sin((2\pi/5)t) \\ \tau_Q &= -500 \sin((2\pi/5)t) \\ \tau_R &= 300 \sin((3\pi/10)t)\end{aligned}\quad (3)$$

These torque inputs to the model produced the following displacement profile presented in Fig. 4.

However, in both the optimization problems, the path is given as input and work done needs to be calculated. For this model, the torques needed are computed as output. Now, the displacement curves shown above were given as input to the platform. But the software was not aware of the source of motion, i.e., where the motors are located which are giving rise to this motion. Hence, the need for feedback controllers was realized.

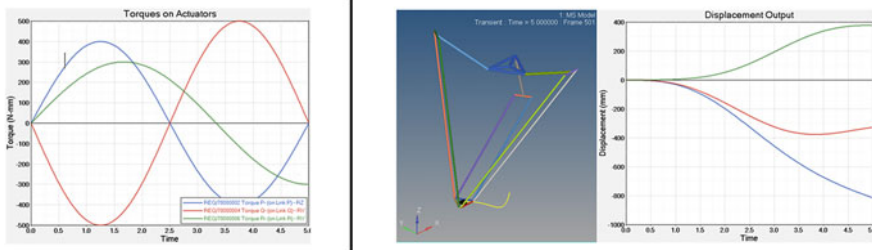


Fig. 4 Torque input to the joints of delta robot (left), displacement output at the joints (right)

Implementation of Controller. The controller will find out the input required to generate the given path. For the feedback controller, the target value is chosen, and input value and the difference between these two as error term are computed. The controller will feed this error multiplied by a gain to the actuator as input and the input will be such that the error is minimized. To work with the controller, displacement error is used along with proportional feedback to get the torque curves with proportional gain (K_P) as 10^{-5} . These values were fed to the torque inputs at three base joints (P, Q, and R). The torque output from the solver is presented in Fig. 5 (left).

It can be observed that the torque outputs are approximately the same as the input curves. However, there are some deviations present in the profiles. To obtain smoother curves, Integral and Differential terms of error are used to reduce accumulated error and rate of change of error. The integral gain (K_I) is chosen 10 times of proportional gain (K_P) and differential gain (K_D) was taken as 0.1 times proportional gain (K_P) following the thumb rule of PID controllers. PID controller with velocity as proportional error provided the best results. The output of this model is presented in Fig. 5 (right) and observed that Fig. 4(left) has very negligible differences with the curves.

The torque profiles can be used to compute the energy consumed. The aim of the work is to compute the energy consumed by taking the dynamics of the robot into

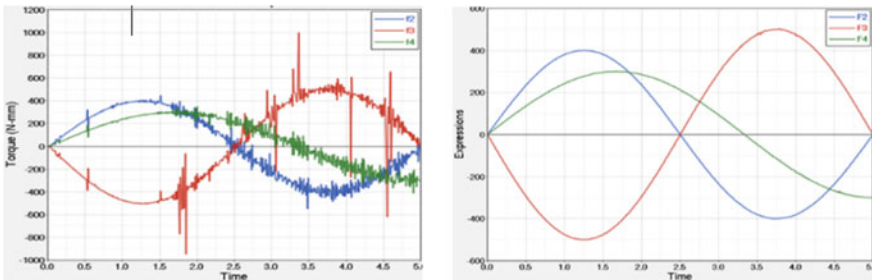


Fig. 5 Torque output from joints of delta robot, displacement controlled (left), performance with PID controller (right)

considerations. Current analysis does not consider the heat loss, frictional resistance at motors or joints, or any other loss. Here, torques and change in velocity are responsible for energy consumption. The energy is obtained by considering the area under a curve which would be helpful in easily setting up the optimization problem. Hence, it was decided to take energy output as the area under the (Torque \times Angular Velocity) versus Time curve. Here, the absolute value of torques and angular velocities are used thus the value of (Torque \times Angular Velocity) will always be positive.

4 Path Optimization

In this problem, the starting point and the goal point of the delta robot platform are given, and the optimal path needs to be obtained which consumes the least amount of energy. For the path optimization, the points in the model, parameters, spring damper constants, forces, inertia properties, etc. are considered as design variables. Objectives and constraints were added and results in form of output plots are obtained.

4.1 Problem Specific Modifications to the Model

A goal point (B) and a marker were defined with origin at the start point (A) and X-axis in the direction of the goal point (B). The platform is initially at A and needs to travel to B. Velocity in the X direction of new marker was kept constant to ensure that the platform accurately reaches the point B in a given time even if the path is changed in Y and Z directions. The path was kept designable in the YZ plane of the new marker.

4.2 Attempt I: Sine Curves

Initially, the path is designed as a sine curve with its amplitude as design variable. The sine curve path ensures the goal location of the platform at B. The dataset values are set up as amplitude of ‘sine’ in both y and z directions of the marker. And, the motion input is given as per the demand variable discussed in Sect. 4.1. Thus, the desired initial path equation with path equations are

$$\begin{aligned} Y &= (\text{Amplitude}_Y \sin((\pi/5)t)) \\ Z &= (\text{Amplitude}_Z \sin((\pi/5)t)) \end{aligned} \quad (4)$$

The velocity-controlled PID controllers are used where input is velocities. Hence, the above expressions were first differentiated with respect to time and then fed to

Table 2 Simulated results from optimizer

Energy	Sine Curve	Bezier Curve
Energy consumed with the initial design (J)	75.810	71.916
Energy consumed with the optimized design (J)	36.960	33.289
% reduction in energy	51.21%	53.71%
Time (s)	49	80.04

the demand variables. The Amplitude_Y and Amplitude_Z are taken as variables and initial values are chosen as 150 mm.

Optimization Setup.

Design Variables. Amplitude_Y, Amplitude_Z (Initial Values = 150 mm for both)

Response Expression.

$$\text{Minimize } C = \tau_P \omega_P + \tau_Q \omega_Q + \tau_R \omega_R \quad (5)$$

Constraints.

$$-300 < \text{Amplitude}_Y < 300, -300 < \text{Amplitude}_Z < 300$$

Objective.

Minimize area under the curve ‘Torque × Angular Velocity versus Time’

After application of the optimization routine, there is a reduction in energy and it reduces energy by 51.21% (Table 2). However, the major disadvantage in using a sine curve as the path is that the shape of the path is not changeable. It will always remain as a sine curve. This restricts the freedom of movement of the platform in one plane. Thus, a path that can provide more flexibility during optimization is required.

4.3 Attempt II: Bezier Curve Method

A Bézier curve is a parametric curve frequently used in computer graphics and related fields. The curve is parameterized using control points. The resulting curves are smooth and less volatile as compared to standard polynomial curve parameterized by its constants. The mathematical basis for Bézier curves is the Bernstein Polynomial [11]. This polynomial is used in the algorithm to generate the Bezier curves (Fig. 6).

More number of control points will give more flexibility to the path and better results. In this problem, the fifth degree Bezier curve is selected that has 6 control points. Out of the 6 points, the first and the last points are kept constant since the start and goal points are fixed. So, there are 4 designable control points in each Y and Z direction which means there are 8 design variables.

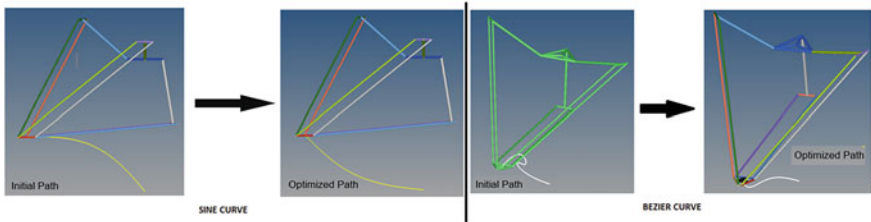


Fig. 6 Initial path versus optimized path

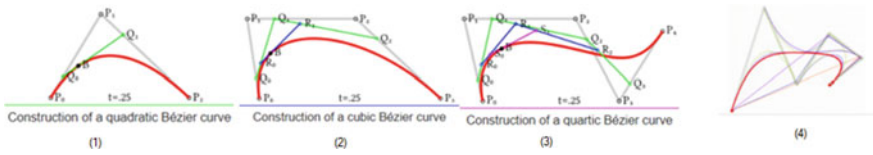


Fig. 7 Bezier curves ($P_0, P_1 \dots$ are control points), fifth degree Bezier curve (image 4)

In the model, Bezier curves are used by implementing an algorithm directly in the Python script that takes Y and Z coordinates of the control points with respect to time as inputs and generates the required number of curve points as outputs. To begin with, 501 points are generated. The points are in the form (p, q) , where p is time and q is y coordinate in points and z coordinate in points_2. These Y and Z coordinates are with respect to the marker defined in Fig. 7. Except for the start and goal point, all other points are the design variables (dv). As discussed in the previous sections, velocity is needed as input. Hence, the curves obtained are differentiated and fed as input to the demand variables.

Optimization Setup.

Design Variables. dv0 to dv7, Initial values are assigned at random with values varying between the limits: $[-400, 400]$

Response Expression.

$$\text{Minimize } C = \tau_P \omega_P + \tau_Q \omega_Q + \tau_R \omega_R \quad (6)$$

Objective.

Minimize area under the curve ‘Torque \times Angular Velocity versus Time’

Table 3 provides the optimized values of design variables (control points) (dv0 to dv3 represent the Y coordinates in the reference marker, and dv4 to dv7 represent the Z coordinates in the reference marker). From the optimization routine, the design that uses the lowest energy is obtained.

Table 3 Optimized values of design variables

DV	Lower bound	Upper bound	Initial value	Optimized value
dv0	-4.0000e+02	4.0000e +02	+3.9000e +02	+1.3941e +02
dv1	-4.0000e +02	4.0000e +02	+3.0000e +02	+8.2232e +01
dv2	-4.0000e +02	4.0000e +02	-3.0000e +02	+7.3540e-01
dv3	-4.0000e +02	4.0000e +02	+2.0000e +02	-1.3440e +01
dv4	-4.0000e +02	4.0000e +02	-3.6000e +02	-8.1464e +01
dv5	-4.0000e +02	4.0000e +02	-2.3000e +02	-6.4326e +01
dv6	-4.0000e +02	4.0000e +02	-2.0000e +02	-1.4115e +02
dv7	-4.0000e +02	4.0000e +02	+3.9900e +02	-8.4577e +01

4.4 Methods Attempted

The following steps were used for optimization before finalizing the Bezier curves method. (i) Major problem was to ensure that the platform reaches the goal point accurately. Thus, the frequency of the sine curve was introduced as the design variable to provide flexibility in design. Constraints for the position were also introduced but the results obtained were not satisfactory. (ii) The curve points are made designer specific and ten points were chosen in each Y and Z direction which led to 20 design variables. This step increased the computation time and level of curve approximation and provided good results. However, results were not comparable with the sine curve model. (iii) The polynomial expressions are fed as input and the coefficients are kept as design variables. This approach failed and the polynomials used are too sensitive to the changes in coefficients, i.e., even a small change in their value led to a drastic change in path. The optimizer could not evaluate such a path and the optimization failed. (iv) Lastly, the Bezier curve method with more control points is used. Here, 18 designer-specific control points are used to make the Bezier curves instead of 8 as discussed in Sect. 4.3. It was observed that the computation time increased by 5–6 times. The optimal results are nearly the same as the earlier case when 501 control points were used. This result indicates that more control points will increase computation time and will not be feasible for this delta robot model.

5 Design Optimization

Here, the path to be followed is already specified, and there is a need to change the link lengths, initial angle, distance between base and platform, etc. to obtain an optimal configuration that consumes minimum energy. Thus, link length, initial angle with horizontal, width of the parallelogram, and size of the platform and base are parameterized which has five design variables: (i) Length of the Upper Link; (L) (ii) Initial Angle of the Upper Link with horizontal. The links shown in the figure

Table 4 Bounds for design variables

Variable	Lower bound	Nominal value	Upper bound
Length (mm)	200.00	524.00	800.00
Angle* (radian)	-0.50	0.00	1.00
RB (mm)	120.00	165.00	250.00
RP (mm)	30.00	50.00	100.00
Half-Width of Parallelogram (mm)	40.00	65.50	90.00

are horizontal. Hence, the angle is zero-degree; (iii) Base Radius (RB); (iv) Platform Radius (RP); (v) Parallelogram width (h). PID controllers are used to generate torques that drive the three motors along a given path. The maximum angles of the upper legs with horizontal are restricted to 1 rad and chosen as constraints.

The delta robot model is parameterized in such a way that (i) The lengths of the base triangle remain equal during every iteration, (ii) The lengths of the triangle representing the end-effector remain equal during every iteration, (iii) The lengths of the upper legs are equal, and (iv) The width of the three parallelograms are equal.

Optimization Setup.

Design Variables. (Angle in ‘radians’ others in ‘mm’) (Table 4)

Response Expression.

Exp_1: Torque × Angular Velocity

Exp_2: Angle of ‘Link P’ with horizontal

Exp_3: Angle of ‘Link Q’ with horizontal

Exp_4: Angle of ‘Link R’ with horizontal

Objective. Minimize area under the curve ‘Torque × Angular Velocity versus Time’

Constraints. Angle of ‘Link P’ ≤ 1.0 , Angle of ‘Link Q’ ≤ 1.0 , Angle of ‘Link R’ ≤ 1.0 (Fig. 8).

The result for energy is:

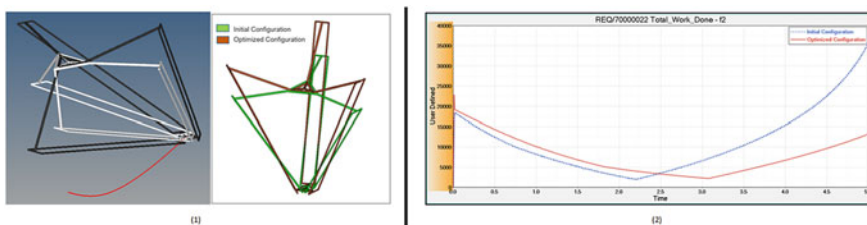


Fig. 8 (1) Initial versus optimal config. (2) Energy curves for initial and optimized config.

- Initial Cost (Area under the curve) = 55.989 J
- Final Cost (Area under the curve) = 38.921 J
- Cost reduction = 30.484%

These results can be considered appropriate as the design is feasible and there is a significant reduction in energy. If the robot links have adjustable lengths, then changing the link lengths for a particular job might save a considerable percentage of energy. The same optimization was attempted for more paths, and all the attempts provided satisfactory results.

6 Summary

In the paper, a virtual model of the delta robot is developed and PID controllers are used to drive the end-effector along a chosen path. To use a designable path, Bezier curves are used. The control points of the Bezier curve are designated as design variables. The output from the Bezier curve is used in splines which are in turn used in PID controllers to modify the path of the end-effector. In this paper, eight control points are defined as design variables to ensure a smooth path. The ‘Finite Differencing’ is chosen as the option in the software for computation of sensitivities in a Sequential Least Squares Quadratic Programming (SLSQP) based optimization. The optimizer provided a design that reduces energy consumed by 53% with the optimal path. In addition, design optimization problem of the delta robot was dealt. Similarly, energy consumed by the three motors is chosen as the cost function. With the ‘Finite Differencing’ option and SLSQP-based optimization, the optimized design reduced total energy consumption by 30%.

References

1. <https://www.sti.epfl.ch/>. Accessed July 2016
2. www.images.bit-tech.net. Accessed May 2016
3. www.robot.fanucamerica.com. Accessed Mar 2019
4. Romdhane, L.: Design and analysis of a hybrid serial-parallel manipulator. *Mech. Mach. Theory* **34**(7), 1037–1055 (1999)
5. Huang, T., Li, M., Zhao, X.M., et al.: Conceptual design and dimensional synthesis for a 3-DOF module of the TriVarianta novel 5-DOF reconfigurable hybrid robot. *IEEE Trans. Robot.* **21**(3), 449–456 (2005)
6. Liang, C., Ceccarelli, M.: Design and simulation of a waist-trunk system for a humanoid robot. *Mech. Mach. Theory* **53**, 50–65 (2012)
7. Liang, C., Ceccarelli, M., Carbone, G.: Experimental characterization of operation of a waist-trunk system with parallel manipulators. *Chin. J. Mech. Eng.* **24**(5), 713–722 (2011)
8. Poppeova, V., Uricek, J., Bulej, V., et al.: Delta robots—robots for high speed manipulation. *Tehnicki vjesnik* **18**(3), 435–445 (2011)
9. <https://altairuniversity.com/free-altair-student-edition/>

10. Williams II, R.L.: The delta parallel robot: kinematics solutions, October 2016. Ph.D. thesis, Ohio University (2016)
11. <https://www.sciencedirect.com/topics/engineering/bernstein-polynomial>. Accessed May 2019

Sustainable Model for Mechanization of Peppermint Oil Extraction Plants for Rural India



Mohd Anas M. Abdullah Mujeeb, and Anurag Sharma

1 Introduction

Peppermint oil, extracted from *Mentha piperita*, has main ingredients as menthol (45%) and menthone (22%). Farmers prefer to cultivate peppermint plant because its cultivation gives a high profit in the least time of cultivation. The crop takes 3.5 months of time and is ready by May for oil extraction. As the weather in northern India is quite sunny; therefore, proper irrigation is required during its cultivation. The oil when sold gives high profit. One of the products of peppermint is Synthetic menthol, which is sold at very high rates by retailers.

It is used in a wide range of cosmetics like soaps as it possesses a fresh, minty and cooling effect due to the presence of menthol [1]. Due to its pleasant fragrance, peppermint is in chewing gums, toothpastes, etc. It has wide medicinal applications.

India shares its peppermint cultivation with other countries such as USA, Japan, Brazil, China and Thailand. [% cultivated in India]. Different types of peppermint plants cultivated in India are Peppermint, spearmint, Bergamot mint and Japanese mint. In India, presently Japanese mint is cultivated on about 60,000 hectares of land with the estimated production of 12,000 tonnes of mint oil which accounts for about 75% of total menthol mint being produced in the world.

The traditional methods adopted for peppermint oil extraction in most part of Uttar Pradesh is complex, least profitable and not safe for workers and farmers. Several visits/surveys were conducted in various districts of Uttar Pradesh like Bahraich, Barabanki, Ramnagar, Sitapur, Lakhimpur, etc. The workers have complained about

M. Anas · M. A. Mujeeb · A. Sharma
Integral University, Lucknow 226026, India
e-mail: anas@iul.ac.in

A. Sharma
e-mail: anuragsa@student.iul.ac.in

the complications that occur during peppermint oil extraction [2]. The major problems discussed were the long time taken to fill peppermint leaves into the boiler drum, drum lid opening and closure problem, compression of leaves and the hazardous removal of burnt leaves and its scattering.

So far different methods have been developed; however, they cannot replace the traditionally existing method because such models developed were not sustainable. Some of the developed models were highly motorized and some were of high technology, which were least accepted by Indian farmers. Most of high tech models failed due to non presence of electricity in rural India.

This depicts that there is a need to develop farmer-friendly sustainable model which would be safe and easily operated without electricity (Fig. 1).

M. Anas and Abusad have discussed in detail the existing problems in traditional method of peppermint extraction oil plant. The major problem being the unsafe removal of used leaves after steam distillation. The other problems discussed are problems related to filling the drums with leaves, compression of the leave, removal of lid and fire ashes, heating efficiency problems and overall slow and inefficient management [2] (Fig. 2).

Beyond all, the safety of farmer is of prior consideration. The three major problems discussed in detail were as follows.

1. When Farmers/labours jump into the drum to compress the peppermint leaves, the irritation of the skin occurs. The smell is highly unpleasant and one cannot easily smell at that spot. The removal of boiled leaves is manual and highly



Fig. 1 View of a peppermint oil extraction plant



Fig. 2 Manual removal of burned leaves

risky. There are chances of getting the hot steam on the face and body and the farmers may fall from the edge of the drum.

2. It is seen that too much time is consumed to compress the dry peppermint leaves in the drum. A good mechanism can save human effort and minimize the time of preparing stacks of peppermint plants or leaves. Several labour put effort to cover the drum with its lid, which hardly fits accurately at the first attempt. Only a mechanized model can make the work easy and save time (Fig. 3).
3. One drum takes 5 h to boil for extraction. Large time is spent in compressing the leaves, filling the drum and removal of leaves. Preheat system with the extra drum will save time. All such steps need to be managed in order to optimize efficiency.

2 Literature Survey

A mechanical system to extract and separate lemon grass oil was designed by Braimah, S. R., Andoh, P.Y., and the design analysis was performed for the fabrication. Tests were performed to find machine performance and quality of the oil produced. The prototype machine developed was used to extract lemon grass oil from the leaves [3].



Fig. 3 Labour filling the drum and pressing it with their foot

Several post harvesting techniques have been presented and analysed by various authors [4–6].

Hesham H. A. Rassem et al. have worked with a set-up that comprises of a condenser and a decanter to collect the condensate and to separate essential oils from water, respectively. The principle of extraction is based on isotropic distillation [7]. K. Satish Kumar, 2010, has adopted a method and mechanism for easy extraction of essential oils. He has concluded that the method of extraction depends on the extraction method employed [8].

However, most of the post harvesting techniques adopted are not found to be farmer-friendly, in terms of ease of work with simple machines economical for Indian farmers. The basic need for the Indian sub-continent is to design a model that would work without electricity as most of the rural areas do not have power supply. Virendra P. S. in 2006 has mentioned that the Steam Distillation method for extraction is the cheapest way for the extraction of oils from the different parts of the plants [9].

Some authors have worked on modern methods of extraction. Seid Yimer has mentioned in his research work, in which Eucalyptus leaves are extracted for essential oil by the steam distillation process. Such a process was complex [10]. Alina Kunika, 2014, has worked on ultrasound-assisted machine for the extraction of essential oil from waste carrot seeds where essential oil yield increased by approx. 33% [11]. Gomez has used microwave protocol to extract lipophilic substances. Statistical analysis shows that the reproducibility of the modified method is high. Several samples can be run within an hour with this method. However, such methods are very expensive and require technical skills [12].

No definite research is available about peppermint plant industries of rural India. The mechanized models so far made are not accepted by our farmers because of complex mechanism of handling, high installation cost and least profit. As a result, we see the models have not replaced the old traditional methods of extraction of peppermint oil. The present mechanized model has very less installation cost, can be easily handled and besides that double the existing efficiency will be obtained when implemented. The mechanization of the plant will not only make the process faster but also will be very safe to operate.

3 Proposed Mechanized Model for Rural Areas of Indian Context

As mentioned above, the survey of peppermint oil extraction plants was done in different villages and towns of state called Uttar Pradesh (India). People working in those plants were quarried and the existing traditional system was analysed. It was found that the plants were run without electricity. Models are also proposed keeping in view the rural areas not having power supply. Modern methods if proposed and adopted against the traditional system would yield high profit and would provide ease of work. One of the mechanized models proposed to work at the commercial level is the Three-Dimensional Non-Electric Mechanized System. The different stages of working of the model are shown in Figs. 4, 5 and 6.

In this method, one chain pulley arrangement is used to lift up and drop down the stakes of leaves. The entire pulley is mounted on a beam that moves to the plane. Thus, the stakes of leaves will be able to move in three directions. It also has a mechanism of compressing the leaves and fastening it in wires. For all such movements, the manual power is used. Hence, there is no need of electric power supply.

The main stages of working mechanisms are as follows:

1. Leave collection: The leaves are collected in a net of wire in a drum of the size of the boiler drum.
2. Leave compression: The compressed leaves are stacked by a simple hook with a circular net at the base. The wheel moves down to compress the leaves. The circular net at the base keeps the compressed raw leaves intact and prevents them from scattering (Fig. 5).

Fig. 4 Collection of leaves

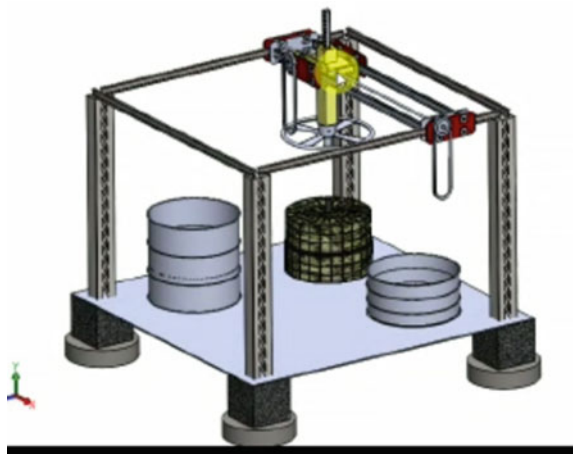
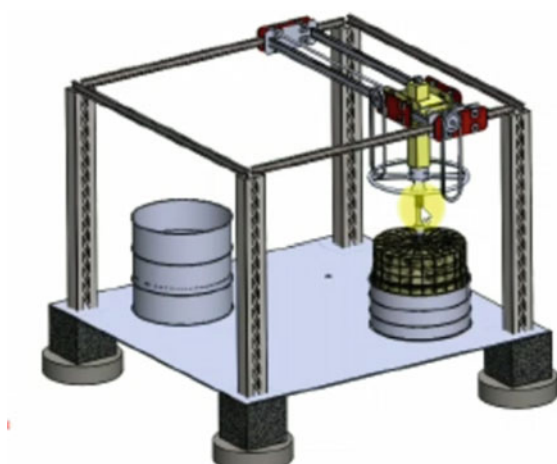


Fig. 5 Compression of leaves



3. Stack/Leave transfer: The stacks from the stack collection area are transferred into the boiler (drum) by chain pulley arrangement. The chain pulley arrangement can be very well fitted in the beam structure at a height of 20 ft above the ground. Stakes are pulled by chain pulley arrangement (as in Fig. 6) and collected one above the other at the stack collection area. The chain pulley arrangement is used to carry stacks in two dimensions. It rests on beams of I cross-section.
4. Removal of the burned leaves: The drum lid is fixed over the drum (boiler) by chain pulley arrangement and then it is fastened by nut bolts. The boiler is heated at the base, containing 300 mm water depth. The steam so produced extracts the oil from the peppermint leaves. The oil is separated from steam when it is condensed in the condenser and the oil is collected in a container.

Fig. 6 Transfer of compressed leaves

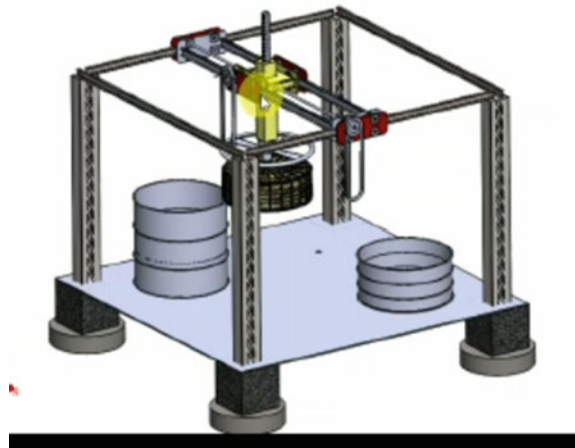
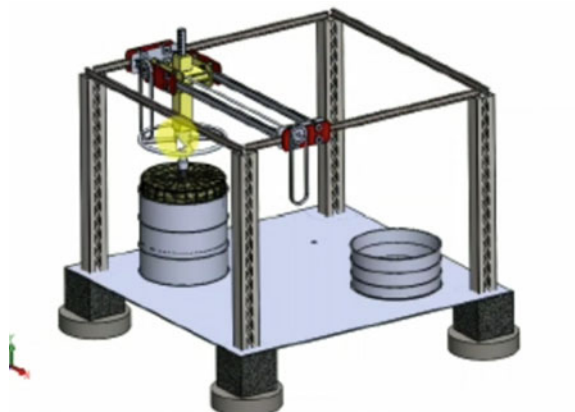


Fig. 7 Filling the drum with stakes of leaves



The cover is unfastened and opened by chain pulley arrangement. The chain pulley arrangement further removes the stakes of burnt leaves one by one and is kept over the smoke emission chamber (drier unit) for faster cooling and drying (Figs. 7 and 8).

4 Results and Discussion

The traditional method adopted in various places is surveyed and it is found that farmers use various sizes of the drum (Boiler). However, the preferred size of drum and other details related to the plant are as follows:

The working area for the entire plant is $5.5 \times 5.5 \text{ m}^2$.

The plant has the following major elements:

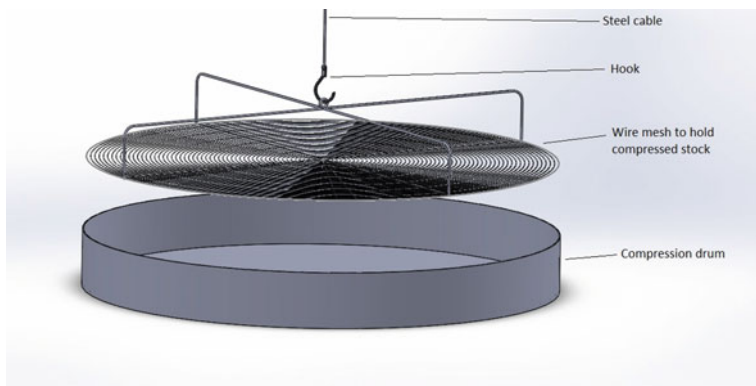


Fig. 8 The net to carry the stakes of leaves

Drum (boiler) is of diameter = 182 cm and height = 152 cm (available data, obtained from the survey at various sites).

Drum (open) of diameter = 182 cm and height = 35 cm.

The comparison of traditional plant and mechanized plant is presented in Table 1.

The proposed three-dimensional model satisfies the need of farmers. The step wise mechanism is shown in Figs. 4, 5 and 6. It is depicted from Table 1 that the existing system is very slow and takes a lot of time for filling the leaves in the boiler. The leaves preparation, i.e. compression in the old traditional method takes 3 h whereas it takes 1 h in the mechanized system. However, the installation cost and profit are high in the mechanized plant. Thus, the mechanized plant is very efficient and profitable.

Table 1 Comparison of Mechanized model with Existing model

S No	Description	Existing plant	Mechanized plant
1	Installation cost	2,20,00	4, 85,000
2	Working area covered	$5.5 \times 5.5 \text{ m}^2$	$5.5 \times 5.5 \text{ m}^2$
3	Raw material preparation Time	2 h	1 h
4	Time required for removal of burnt leaves and their scattering	3 h	1 h
5	Burning time	4.5 h	4.5 h
6	Peppermint plant weight in 1 tank	4 quintal	4 quintal
7	Labour	4	2
8	Labour cost	Rs 1600/day	Rs 800/day
9	Total tank used in 1 day	02	05
10	Earning per day of the plant@Rs1000/tank	Rs 2000/day	Rs 5000/day

5 Conclusions

Various mechanized models are proposed and presented in Sect. 3. These mechanized models are helpful to overcome the uneasy, hazardous, non profitable, complex and highly laborious methods of our old traditions. The Non-Electric Mechanized 3D System works in all dimensions. The movement is not limited. Large space is required. Installation cost is high. It is highly profitable. No power supply is required.

The proposed mechanized model is able to function properly. The major conclusions are as follows:

- a. It saves time for removal of leaves.
- b. It saves time for filling the leaves.
- c. It provides safety to the farmers.
- d. It provides ease of work.
- e. It is environment-friendly.

References

1. Sugiura, T., Uchida, S., Namiki, N.: Taste-masking effect of physical and organoleptic methods on peppermint-scented orally disintegrating tablet of famotidine based on suspension spray-coating method. *Chem. Pharm. Bull.* **60**(3), 315–324 (2012)
2. Anas, M., Abusad: Mechanization of peppermint oil extraction plant of rural India. In: Proceedings, iNaCoMM2019, Paper 195, IIT Mandi, Mandi (2019)
3. Braimah, S.R., Andoh, P.Y., Tawiah, P.O.: Designing a mechanical system that will be used to extract and separate lemon grass oil. *Int. J. Sci. Technol.* **5**(3), 01–11 (2016)
4. Khan, F., Dwivedi, A.K.: A review on techniques available for the extraction of essential oils from various plants. *Int. Res. J. Eng. Technol.* **05**(05), 1100–1103 (2018)
5. Suryawanshi, M.A., Mane, V.B., Kumbhar, G.B.: Methodology to extract essential oils from lemongrass leaves: Solvent extraction approach. *Int. Res. J. Eng. Technol.* **03**, 1776–1788 (2016)
6. Rozzi, N.L., Phippen, W., Simon, J.E., Singh, R.K.: Supercritical fluid extraction of essential oil components from lemon-scented botanicals. *Lebensm Wiss. U. Technol.* **35**, 319–324 (2002)
7. Rassem, H.H.A., Nour, A.H., Yunus, R.M.: Techniques for extraction of essential oils from plants: a review. *Aust. J. Basic Appl. Sci.* **10**(16), 117–127 (2016)
8. Satish Kumar, K.: Extraction of essential oil using steam distillation, Thesis, NIT Rourkela, India (2010)
9. Virendra, P.S., Rao, D.P.: Extraction of essential oil and its application, Project 2006-07. NIT Rourkela, India (2007)
10. Yimer, S., Manoharan, S.O.: Extraction of essential oil from eucalyptus leaves as antibacterial application on cotton woven fabric. *Int. J. Bacteriol. Virol. Immunol.* **1**(1), 001–007 (2014)
11. Majewska, M., Kunika, A., Gruska, R.: The effect of ultrasound-assisted maceration on the bioactivity, chemical composition and yield of essential oil from waste carrot seeds (*Daucus Carota*). *J. Essential Oil Bear. Plants* **17**(6), 1075–1086 (2014)
12. Gomez, N.E., Witte, L.: Simple method to extract essential oils from tissue samples by using microwave radiation. *J. Chem. Ecol.* **27**(11), 2351–2360 (2001)

Vibration Isolation in Six Degrees of Freedom Using Combined Passive and Active Isolation Technique



T. Akshay Kumar and B. Santhosh

1 Introduction

Vibrations that are undesirable in many applications must be isolated to avoid performance degradation of systems. Linear vibration isolators are effective when the ratio $\frac{\omega}{\omega_n} > \sqrt{2}$, where ω is the excitation frequency and ω_n is the natural frequency. Isolation of low-frequency vibrations using passive linear isolators is limited. It is possible to develop low-frequency vibration isolation system using the concept of quasi zero stiffness (QZS), and the isolator falls under the category of high static and low dynamic stiffness (HSLDS) isolators [1]. There are different ways to obtain the QZS conditions in practical systems which include oblique springs [2], cam roller mechanisms [3], Euler buckled beam [4], and using magnetic springs [5]. Among these, the magnetic spring-based isolators gained attention due to the fact that there are no contact elements and the chance of occurrence of contact nonlinearity such as friction and backlash can be avoided. The QZS isolator system based on the concept of negative stiffness is essentially a nonlinear system and can exhibit different dynamic phenomena when excited externally [6]. Therefore, it is necessary to take good care when designing such systems for practical applications.

The QZS isolators are mainly designed to isolate vibration in one direction. But there are applications where vibration isolation in multi directions is important. Some examples include multi-direction vibration isolation for high-resolution cameras on the spacecraft and vehicles moving in terrain and in ships. Multi-direction isolation can be generalized as six degrees of freedom isolation. The Stewart platforms are generally employed for six degrees of freedom vibration isolation using passive or active isolation techniques [7]. The kinematic relations between the upper and lower plates of the Stewart platform are complicated. There is a specific configuration for the Stewart platform known as the cubic configuration which simplifies the kinematic relationships [7].

T. Akshay Kumar · B. Santhosh (✉)

Department of Mechanical Engineering, Amrita School of Engineering, Amrita Vishwa Vidyapeetham, Coimbatore, India
e-mail: b_santhosh@cb.amrita.edu

In this work, a Stewart platform in the cubic configuration with its struts designed to have negative stiffness based on magnetic springs is used to study the vibration isolation characteristics. This study is in line with Zheng et al. [8]. The dynamic equations of motion are nonlinear and can be simplified based on some assumptions to reduce the computational effort involved in the solution. The isolation characteristics of the passive system are investigated using transmissibility plots and compared with linear isolator to highlight the low-frequency vibration isolation. Active vibration isolation is employed in the simplified model using force and integral force feedback to increase the isolation range and to reduce the amplitude of vibration. It is found that the hybrid system with passive and active isolation techniques improves the performance of the isolator.

The paper is organized as follows. The kinematic and dynamic relationships of the Stewart platform in the cubic configuration with the negative stiffness elements are briefly discussed in Sect. 2. The transmissibility plots for the simplified dynamic models are compared with the linear isolator in Sect. 3. The active isolation technique along with the results are presented in Sect. 4. Important conclusions from the study are provided at the end.

2 Kinematics and Dynamics of the Stewart Platform in Cubic Configuration

The Stewart platform in its cubic configuration is shown in Fig. 1 which consists of upper plate, lower plate, and six struts. The struts are to be replaced with magnetic spring-based negative stiffness elements to achieve the QZS condition which results in enhanced low-frequency vibration isolation. The kinematic relationship between the deformation of the struts and the coordinates of the upper plate is derived in [8]. The deformation of the struts is given by the vector $\mathbf{q} = [q_1 \ q_2 \ q_3 \ q_4 \ q_5 \ q_6]^T$. The motion of the upper plate is represented by the coordinates $\mathbf{X}_p = [x \ y \ z \ \alpha \ \beta \ \gamma]^T$. The rate of deformation of the struts and the velocity vector of the upper plate are related through

$$\dot{\mathbf{q}} = \mathbf{J}(\mathbf{X}_p)\dot{\mathbf{X}}_p \quad (1)$$

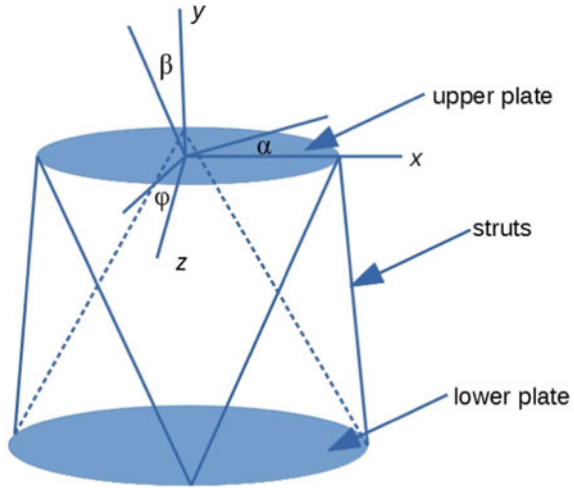
where $\mathbf{J}(\mathbf{X}_p)$ is the Jacobian matrix which is a function \mathbf{X}_p . The derivation and the structure of the same can be found in [8]. The simplification of the Jacobian matrix is done under the assumption of small vibrations.

2.1 Dynamic Equations and Its Simplification

The dynamic equation of motion for the system considering all nonlinear effects are derived in [8] and is given below

$$\mathbf{M}(\mathbf{X}_p)\ddot{\mathbf{X}}_p + \mathbf{C}(\mathbf{X}_p)\dot{\mathbf{X}}_p + \mathbf{J}^T(\mathbf{X}_p)\mathbf{F}_R(\mathbf{q}) + \mathbf{N}(\mathbf{X}_p, \dot{\mathbf{X}}_p) = \mathbf{F}_{ext} \quad (2)$$

Fig. 1 Stewart platform in cubic configuration



The mass, damping, and restoring forces are functions of \mathbf{X}_p . The vector $\mathbf{N}(\mathbf{X}_p, \dot{\mathbf{X}}_p)$ is the centrifugal force vector which will be neglected in the further analysis when the assumption of small vibration is taken into account. The restoring force vector is defined by modeling the struts of the isolator based on a negative stiffness concept and employing the magnetic springs [5]. The expressions for the damping and restoring force are given below

$$\mathbf{C} = c \mathbf{J}^T \mathbf{J} \quad (3)$$

$$\mathbf{F}_R = (k_e + k_0) \mathbf{q}_i + \frac{k_1}{3} \mathbf{q}_i^3 \quad (4)$$

where c is the damping coefficient, k_e is the stiffness of vertical spring used for load carrying, and k_0, k_1 are the linear and cubic stiffness terms of the magnetic spring obtained by a curve fitting of the restoring force expression derived by modeling the magnetic spring characteristics using the FEMM (Finite Element Method Magnetic) software.

Equation of motion given in Eq. (2) can be simplified based on the following assumptions to reduce the computational effort involved in solving the equation of motion and make it amenable to apply analytical and semi-analytical methods of solution. Equation (2) is a fully nonlinear model with geometric and stiffness nonlinearity. The mass, damping, and stiffness terms are functions of \mathbf{X}_p and need to be updated in every iteration when performing numerical simulations and thus become computationally expensive. The first simplification is based on the assumption that under a low vibration environment, the strut deformation is small compared to the stroke length. The effect of geometric nonlinearity can thus be neglected. The mass, damping, and stiffness matrices thus become independent of the coordinate \mathbf{X}_p . The effect of centrifugal force can also be neglected. The equation of motion can now be rewritten as

Table 1 Parameters used for simulation

m (kg)	c (Ns/m)	k_e (N/m)	k_0 (N/m)	k_1 (N/m 3)
2.6	1.34	5931	-5552	2.71×10^7

$$\mathbf{M}\ddot{\mathbf{X}}_p + \mathbf{C}\dot{\mathbf{X}}_p + \mathbf{J}^T \mathbf{F}_R(\mathbf{q}) = \mathbf{F}_{ext} \quad (5)$$

The second assumption is that the deformation of the magnetic springs are small and limited within the linear regime, and the effect of stiffness nonlinearity can be neglected. The system thus becomes linear and Eq. (2) can be modified as

$$\mathbf{M}\ddot{\mathbf{X}}_p + \mathbf{C}\dot{\mathbf{X}}_p + \mathbf{K}\mathbf{X}_p = \mathbf{F}_{ext} \quad (6)$$

The nonlinear equation (5) and the linear equation (6) are solved numerically to estimate transmissibility in all six directions and also to estimate the vibration isolation capability under low-frequency vibration environment.

3 Transmissibility Plots for Six Degrees of Freedom Isolator

In this section, the transmissibility plots for the linear six degrees of freedom isolator without negative stiffness is compared with the two simplified six degrees of freedom vibration isolation system with negative stiffness element. The transmissibility plots are obtained by numerically integrating the equations of motion with the parameters given in Table 1 [8]. The transmissibility plots are obtained by numerically solving the equations of motion for harmonic excitation with an excitation amplitude of 0.2 N in translational directions and 0.02 N/m in the rotational directions. The transmissibility plots in the translational directions (x, y, z) and angular directions (α, β, ϕ) are shown in Fig. 2a-f.

The transmissibility plots are generated for the linear system without negative stiffness isolator, the linear system with negative stiffness isolator given by Eq. (6), and for the nonlinear system given by Eq. (5). It is clearly visible from the plots that the introduction of negative stiffness provides good isolation at a lower frequency compared to the conventional linear system in all three directions. The transmissibility plots in z and ϕ directions have only a single peak due to the non-existence of coupling in that direction. The nonlinear system transmissibility plots show the existence of superharmonic peaks and jump phenomenon. The study needs to be further extended using analytical methods to understand the complete nonlinear dynamics of the system. Also, bifurcation diagrams can be generated to understand the qualitative behavior of the system under harmonic excitation.

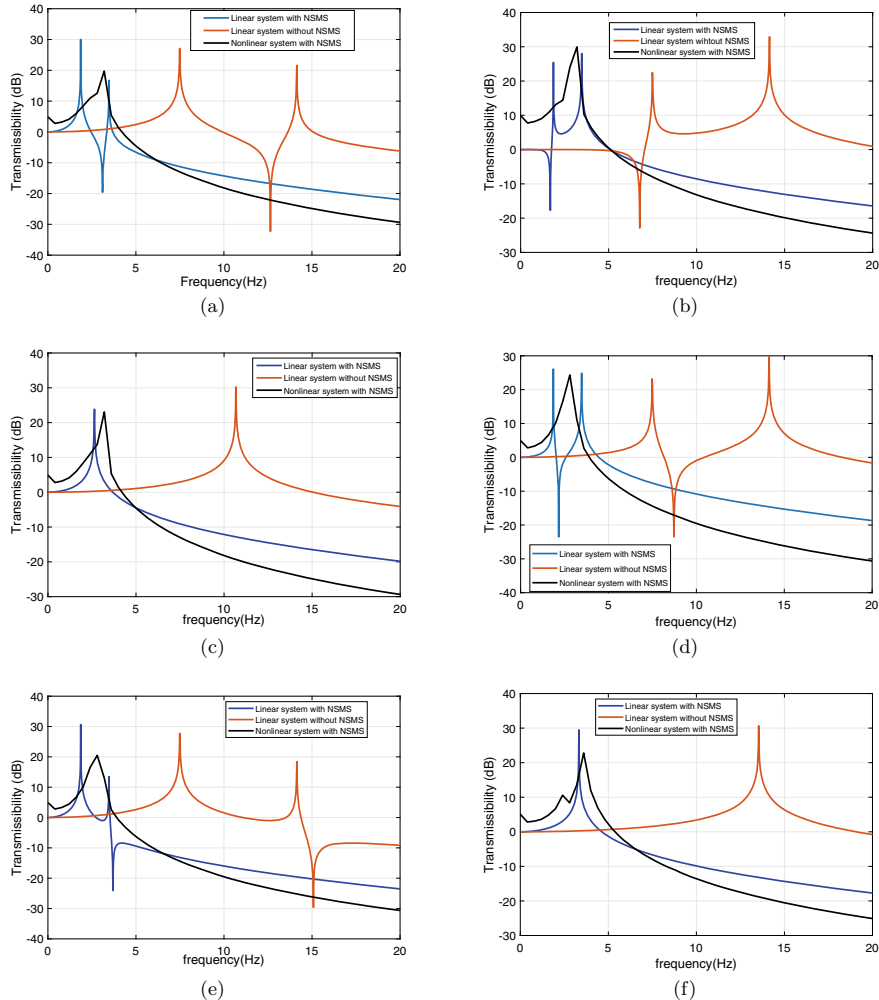


Fig. 2 Transmissibility plots in **a** x direction, **b** y direction, **c** z direction, **d** α direction, **e** β direction, and **f** ϕ direction

4 Active Vibration Control

Active vibration control is employed in the linear system equations of motion Eq. (6) to reduce the resonant amplitude. The active control is employed with force and integral force feedback [9]. For a linear undamped single degree of freedom system, the equations of motion and the transmissibility in the Laplace domain are given below

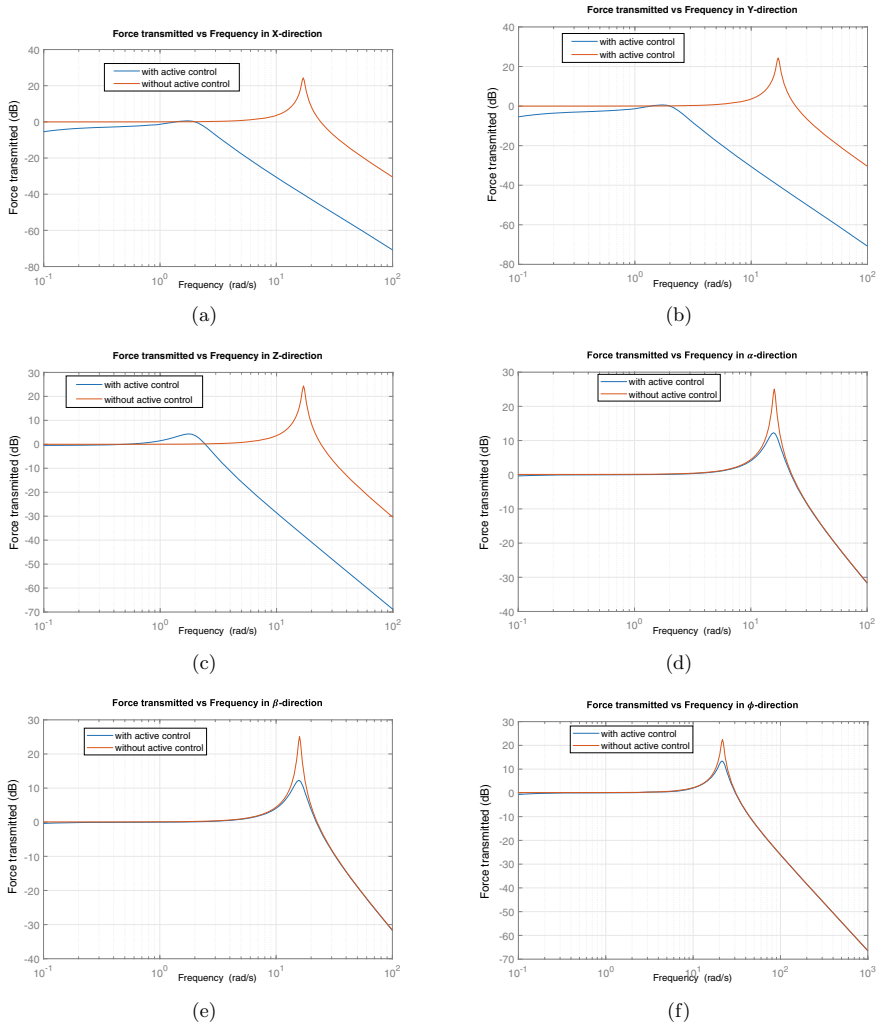


Fig. 3 Vibration isolation with active control **a** x direction, **b** y direction, **c** z direction, **d** α direction, **e** β direction, and **f** ϕ direction

$$m\ddot{x} + kx = F(t) \quad (7)$$

$$TR = \frac{F_t(s)}{F(s)} = \frac{G(s)}{1 + H(s)G(s) - H(s)} = \frac{k}{ms^2(1 - K_p) - mK_i s + k} \quad (8)$$

where $H(s) = K_p + \frac{K_i}{s}$ is the controller transfer function with K_p and K_i as the proportional and integral gains. The Nyquist plots are used to select control parameters ensuring that all poles lie on the left side for stability of the system. Converting into time domain and considering steady state $s = j\omega$

$$TR = \frac{1}{-\frac{\omega^2}{\omega_n^2}(1 - K_p) + 1 - j\omega_n K_i} \quad (9)$$

From the above equation, as the value of K_p decreases, there is an increase in low-frequency isolation region, and as the value of K_i decreases, it induces damping in the system and decreases the resonant amplitude.

The active vibration control strategy is implemented in the six degrees of freedom linear model considered in this paper with the same parameter values used in the simulation. The vibration isolation capability in all six directions is plotted in Fig. 3a-f and compared with that of the linear system without active control.

Vibration amplitude reduction is observed in all six directions. An improvement in low-frequency vibration is also observed for the x , y , and z directions. The active control methodology is thus effective in reducing the vibration amplitude at resonance and also to improve the vibration isolation at low-frequency ranges.

5 Conclusions

In this study, six degrees of freedom vibration isolation using passive and active techniques are studied using the Stewart platform mechanism in the cubic configuration. For passive vibration isolation, the struts of the Stewart platform are replaced with a magnetic spring-based negative stiffness isolator to get the high static low dynamic stiffness (HSLDS) condition to ensure low-frequency vibration isolation. The equations of motion for the system considering the three-dimensional kinematics are found to be a nonlinear equation with both stiffness and geometric nonlinearities. The model is simplified to a system with stiffness nonlinearity and also to a linear system. The equations of motion are numerically solved to obtain the transmissibility plots. It is found that the addition of negative stiffness improves the low-frequency isolation in all six directions. The active vibration control is based on a force and integral force feedback in the linearly approximated system. It is found that the active vibration control reduces the resonant amplitude in all six directions and improved low-frequency isolation in the translational directions. The above study will help to develop a hybrid six degrees of freedom vibration isolation system combining both passive and active control techniques.

References

1. Carella, A., Brennan, M.J., Waters, T.P.: Static analysis of a passive vibration isolator with quasi-zero-stiffness characteristic. *J. Sound Vib.* **301**, 678–689 (2007)
2. Carella, A., Brennan, M.J., Waters, T.P., LopesJr, V.: Force and displacement transmissibility of a nonlinear isolator with high-static-low-dynamic-stiffness. *Int. J. Mech. Sci.* **55**, 22–29 (2012)

3. Zhou, J., Wang, X., Xu, D., Bishop, S.: Nonlinear dynamic characteristics of a quasi-zero stiffness vibration isolator with cam roller spring mechanisms. *J. Sound Vib.* **346**, 53e69 (2015)
4. Huang, X., Liu, X., Sun, J., Zhang, Z., Hua, H.: Vibration isolation characteristics of a nonlinear isolator using Euler buckled beam as negative stiffness corrector: a theoretical and experimental study. *J. Sound Vib.* **333**, 1132e1148 (2014)
5. Zheng, Y., Zhang, X., Luo, Y., Yan, B., Ma, C.: Design and experiment of a high-static-low-dynamic stiffness isolator using a negative stiffness magnetic spring. *J. Sound Vib.* **360**, 31–52 (2016)
6. Santhosh, B.: Dynamics and performance evaluation of an asymmetric nonlinear vibration isolation mechanism. *J. Braz. Soc. Mech. Sci. Eng.* **40**(4), 169 (2018)
7. Geng, Z., Haynes, L.S.: Six-degree-of-freedom active vibration isolation using a Stewart platform mechanism. *J. Robot. Syst.* **10**(5), 725–744 (1993)
8. Zheng, Y., Li, Q., Yan, B., Luo, Y., Zhang, X.: A Stewart isolator with high-static-low-dynamic stiffness struts based on negative stiffness magnetic springs. *J. Sound Vib.* **422**, 390–408 (2018)
9. Preumont, A., Horodinca, M., Romanescu, I., De Marneffe, B., Avraam, M., Deraemaeker, A., Bossens, F., Abu Hanieh, A.: A six-axis single-stage active vibration isolator based on Stewart platform. *J. Sound Vib.* **300**(3–5), 644–661 (2007)

Evolution of Three Hold-Down Configuration for Large Antenna Mounted on a Dual Axes Steerable Mechanism



Saurabhkumar H. Patel, V. Sri Pavan Ravichand, Anoop Kumar Srivastava, S. Narendra, A. Shankara, and H. N. Suresha Kumar

1 Introduction

Deployable appendages like antennae on spacecraft are compactly stowed to meet two basic requirements, viz. space constraint in launch envelope and higher natural frequency to sustain launch accelerations. Conventionally, hold-down mechanisms are used to meet the above two requirements of satellite missions. There are different types of hold-down mechanisms based on the type of restraint and actuation used for rigidly stowing the antenna onto spacecraft during launch and subsequently deploying the antenna on orbit to respective functional location. The type of hold-down being incorporated is beyond the scope of this paper. The hold-down interfaces, size, and footprint are simulated for various analytical studies. The challenge is to devise an optimized configuration for this hold-down system to cater to large antennae so that during stowed position, the system should ensure stowed stiffness specifications of satellite and after deployment, the components of hold-down mounted on

S. H. Patel (✉) · V. Sri Pavan Ravichand · A. K. Srivastava · S. Narendra · A. Shankara · H. N. S. Kumar

Spacecraft Mechanisms Group, URSC, ISRO, Bangalore, India
e-mail: spatel@ursc.gov.in

V. Sri Pavan Ravichand
e-mail: sripavan@ursc.gov.in

A. K. Srivastava
e-mail: akrs@ursc.gov.in

S. Narendra
e-mail: naren@ursc.gov.in

A. Shankara
e-mail: ashan@ursc.gov.in

H. N. S. Kumar
e-mail: hns@ursc.gov.in

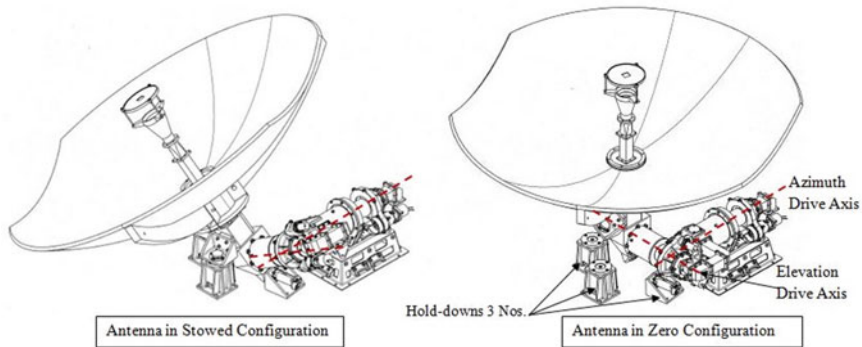


Fig. 1 Antenna and hold-down assembly

spacecraft should not hinder nominal motion of appendages. The design of hold-down system presented in this paper is related to steerable parabolic antenna, which has 1-meter aperture diameter and 7.5 Kgs of mass (Fig. 1).

2 Requirements

- Antenna deployment mechanism with hold-down system should have stowed natural frequency greater than 60 Hz.
- Hold-down system should be designed so as to ensure sufficient clearance after release.
- After deployment on orbit, a nominal movement of $\pm 30^\circ$ in azimuth and $\pm 10^\circ$ in elevation directions need to be ensured for antenna without physical hindrance.
- Design margins of greater than 1.5 to be ensured for critical elements of the drive mechanism like bearing, motors, etc., against the launch acceleration loads.

3 Literature Studies

Several large size antenna mechanisms called as High Gain Antenna have been flown in various space missions. The scope of the present literature study is limited to the hold-down mechanisms for dual axis steerable high gain antenna of size approximately 1–2 m. Moreover, the type of the mechanism of hold-down is also not included in the scope.

Self-Restrained, High Torque, Dual Gimbal Mechanism for Antenna pointing [1] shows the existing design of self-restraint kind of dual gimbal antenna Mechanism.

Mass of the antenna is very small in this case so that it does not require any hold-down. Hold-down configuration and design should be done in addition to the existing design of dual gimbal mechanism to accommodate large size antenna.

High gain antenna on Rosetta mission [2] also incorporated 3 hold-downs for arresting the large antenna of 2.2 m diameter. The mechanism was tripod based and the 2 hold-downs were mounted on the tripod joints and not on the antenna ribs. The third hold-down was mounted on the deck and the location was adjusted using an in situ potting bracket on the antenna rib. Hold-down and release axis for all the three hold-downs is kept same. The hold-downs are also spanned from each other by a distance of 700 mm.

Solar Observatory had 1.1 m diameter High Gain Antenna [3] which was also steered along 2 axes, had 4 hold-downs for arresting the antenna. All the four hold-downs were mounted on the deployable arm which is used for compactly stowing the antenna on the spacecraft deck. No hold-downs were mounted on the antenna ribs. The axis of the hold-down and release mechanism is kept same.

In case of World Space Observatory [4], a three hold-down system was incorporated for 1 m diameter antenna. The drive in this case is adopted from the Rosetta mission and hold-downs are Pyro based. All the three hold-downs are mounted on the antenna rib and axis is kept the same.

The mechanism presented in this paper is a modification of the existing dual gimbal mechanism [1] with two hold-downs mounted normal to the spacecraft deck and one hold-down mounted parallel to the deck to resist the launch load. It also ensures clear release without hindrance. Thus, mechanism presented provides an optimized solution with only three hold-downs in a compact volume and meeting the stiffness requirements of the spacecraft. Moreover, this configuration can be extended for a larger size of antenna also without changing the hold-down configuration.

4 Studies Carried Out

4.1 FEA Approach

Finite Element Analysis (FEA) Study. During the parametric study with respect to hold-down configuration, finite element method has been used considering the complex geometry of the mechanism which is difficult to analyze analytically. The elements used are of h-version, as it enables better stress distribution at intricate geometrical locations, and the convergence of the response characteristics has been ensured by increasing the number of elements.

Modeling. Tetrahedron element shape is chosen for analysis along with 10 nodded types as this enables to capture the stress distribution effectively in intricate geometric parts. The element size has been chosen as 0.018 based on stress convergence for

the hold-down unit. The standard package used for this is MSC/PATRAN as pre-processor and post processor with MSC/NASTRAN as solver. This modeling procedure has been adopted based on the experience gained during analysis of spacecraft mechanisms [5].

Convergence Study. Initially the number of TET10 elements used in the analysis of hold-down unit was 3410 and the stress distribution has been evaluated. Then the number of elements was varied and the convergence with regard to the peak stress has been observed at 9784 and it has been chosen for parametric studies. The corresponding CPU time required on a Dell work station was about 12 min.

4.2 Two Hold-Down Configuration

The objective of any hold-down system configuration study is to ensure stiffness requirements of antenna mechanism system with minimum hold-down mass. Thus, the starting point is one hold-down configuration. But, to hold a one-meter antenna by only one hold-down while meeting the requisite stowed frequency, the hold-down should be near to C.G. of antenna. This is not possible for such big antennae owing to large distributed inertia of system. Also, movement of the holding point away from C.G. will create large moments during launch which the motor drive units cannot withstand. Thus, two hold-down configurations become inevitable to balance these large moment loads. Two options of such two hold-down configuration have been studied.

- Two Hold-downs mounted directly on Antenna rib
- Two Hold-downs mounted on Antenna Arm connecting Antenna to Drive mechanism.

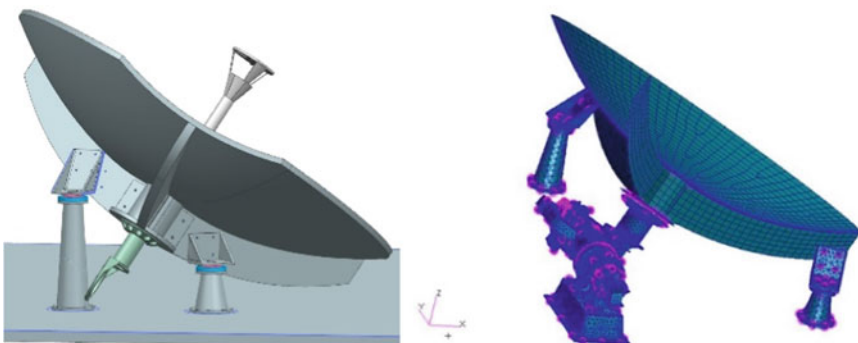


Fig. 2 Two hold-downs directly mounted on antenna rib—CAD model & FE model

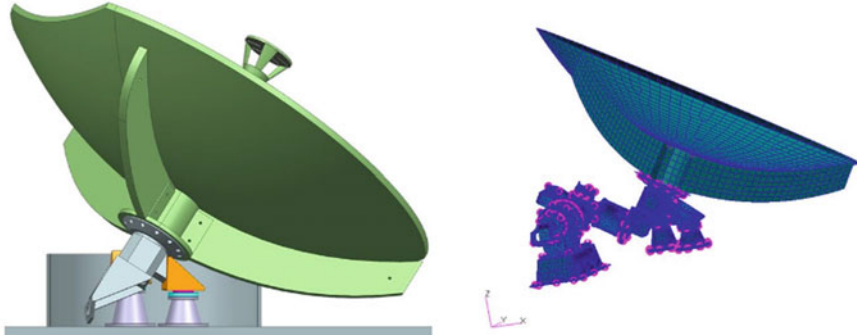


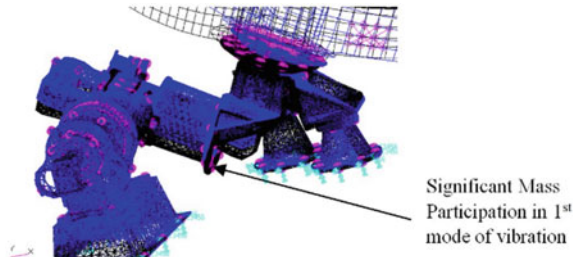
Fig. 3 Two hold-downs directly mounted on antenna arm—CAD model & FE model

Two Hold-down Directly Mounted on Antenna Rib. As shown in Fig. 2, Two Hold-downs have been fixed directly on antenna ribs. Finite Element model has been generated for this configuration so as to evaluate the frequency results for different relative positions of the two hold-downs on the antenna ribs. It has been found that the fundamental frequency for the case of farthest relative position between the two ribs, as shown in Fig. 2, is 43 Hz and the corresponding value for the minimal relative position is found to be 32 Hz. Also, the maximum moment along the two orthogonal drive axes for the above two cases are 1.92 Nm and 1.38 Nm, respectively. Thus, the frequency specifications are not being met in this case.

Two Hold-down Directly Mounted on Antenna Arm. As shown in Fig. 3, two Hold-downs have been fixed directly on antenna arm which lead to the change in the geometric configuration of the antenna arm. Finite Element model has been generated for the above configuration and natural frequency of system has been estimated using normal mode analysis. It has been found that the first mode of vibration is 28 Hz, which is much lower than the required frequency. The maximum moment along the two orthogonal drive axes for this configuration is found to be 1.13 Nm. Thus, the frequency specifications are not being met in this case as well. But this configuration is desirable, in comparison to that described earlier, from strength and assembly point of view.

Various iterations for different mounting configuration with two Hold-downs have been tried but none of these configurations have been able to meet natural frequency requirement. One more exercise was carried out by assigning large elastic modulus for the hold-down elements to get the upper bound of frequency possible using 2 hold-downs. This also did not give promising results. Option of mounting third hold-down on antenna rib was not explored because of space constraints and it was hindering the clear release of hold-down.

Fig. 4 Mode shape for hold-down mounted on antenna arm configuration



4.3 Evolution of Three Hold-Down Configuration

Based on analysis results of mechanism as mentioned in Sect. 4.1, it is necessary to introduce third hold-down. The best place to locate third hold-down is derived based on mode shapes of previously analyzed two Hold-down configurations. Based on comparison of the two configurations of two hold-downs, presented in Sect. 4.1, it has been decided to explore hold-down mounting on antenna arm and not on antenna ribs. The antenna FE model with base mount gives a frequency of greater than 100 Hz. Fixing of hold-downs on the ribs would change the load path and lead to reduction in frequency.

Figure 4 shows the 1st mode shape of the FE model analyzed for two hold-downs configuration mounted on antenna arm. It can be observed that if the marked area, where significant mass is participating in 1st mode of vibration, is arrested using 3rd hold-down, significant improvement in natural frequency can be achieved. But holding at the shown point in vertical direction (i.e. direction of existing hold-down) is found to be difficult. The placement of the hold-down from kinematic movement point of view should be such that it offers clear release without any obstruction. The standard practice of making conical spigots also requires a suitable wedge angle lesser than 40° for taking the in-plane loads. Details for finding the spigot angles are explained in the next section.

4.4 Geometric Method for Finding the Spigot Angles

The following steps are adopted for finding the spigot angle of the hold-down suitable for clear hold-down release.

- Step 1: A line is drawn connecting the drive center and the hold-down spigot extreme point.
- Step 2: An arc is traced with this line as radius and drive center as origin.
- Step 3: A tangent is drawn on this arc and its angle (θ_1) with the vertical is noted.

The spigot angle (θ_2) thus selected should be more than the angle arrived in step 3 (θ_1) to ensure clear release. Figure 5 show that the wedge angle required (θ_1) for

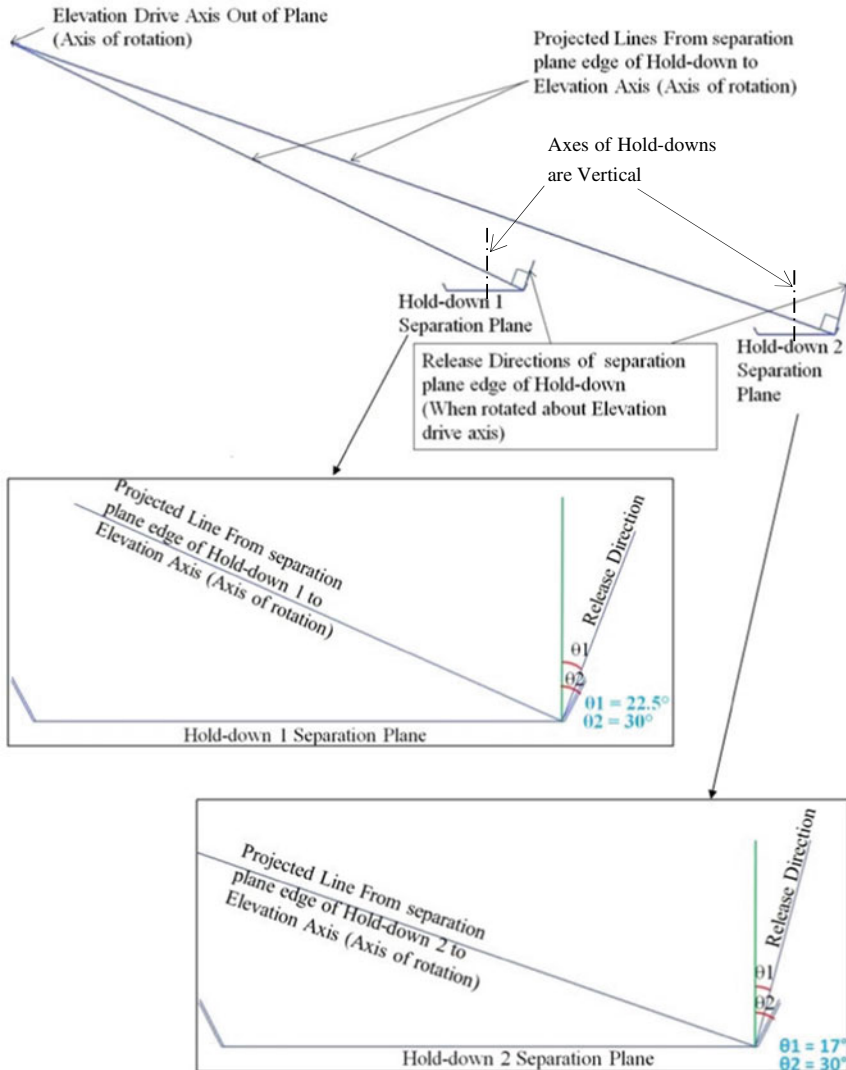


Fig. 5 Projected sketch of hold-down release direction w.r.t. separation plane

hold-down 1 and 2 were 22.5° and 17° respectively. Thus to maintain modularity of spigots 30° wedge angle (θ_2) was selected for both.

4.5 Third Hold-Down Placement Study

In order to accommodate the third hold-down same consideration of clear release and no hindrance during rotation had to be met. Various options were studied for the placement of the third hold-down along the same axis as the previous two. Configuration options which are meeting spigot angle requirement less than 40° were leading to obstruction during rotation. One configuration option was giving clear movement of antenna after release, but having spigot release angle requirement more than 56° as shown in Fig. 6 denoted by “ α ”. If hold-down axis is rotated orthogonally, spigot release angle requirement will be 34° in place of 56° . Thus, the hold-down axis was rotated to make it parallel to the horizontal plane and normal to the axis of the other two hold-downs. In this configuration wedge angle of 34° could be accommodated for the third hold-down spigot. Figure 6 shows the line sketch for arriving at the

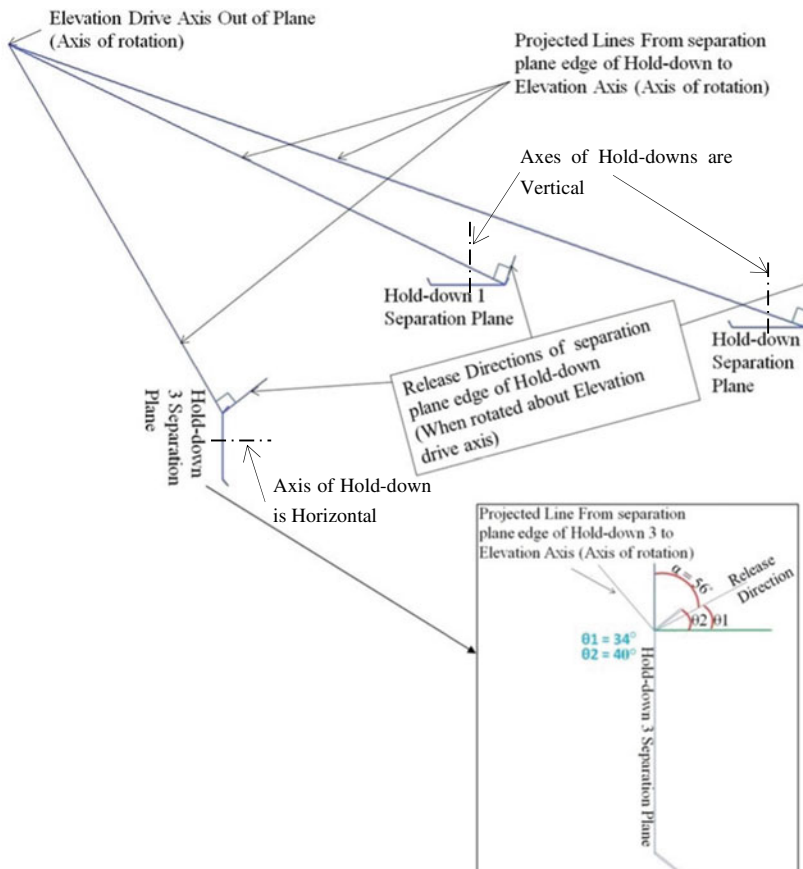


Fig. 6 Projected sketch of hold-down release direction w.r.t. separation plane for third hold-down

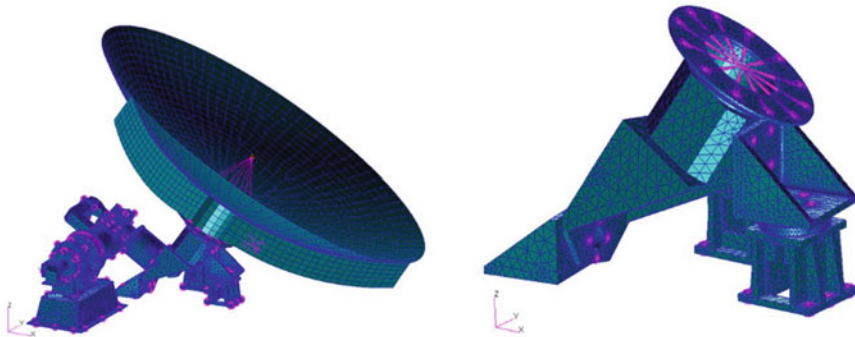


Fig. 7 FE Model for three hold-down configuration mounted on antenna arm

Table 1 Analysis result for three hold-down mounted on antenna arm

Mass (Kg)	Mode	Frequency	T1	T2	T3	R1	R2	R3
14.1	1	6.72E + 01	0.475	3.29	0.0005	0.675	0.119	2.90
	2	7.79E + 01	1.52	0.219	0.755	0.473	1.76	0.069
	3	1.08E + 02	0.027	0.015	0.0013	0.047	0.042	0.161

wedge angle of the third hold-down. Wedge angle required (θ_1) for hold-down 3 was 34° . Spigots 40° wedge angle (θ_2) was selected for hold-down 3.

So with this configuration all the requirements like the introduction of third hold-down at the separation plane, clear movement of hold-down elements after release and accommodation could be met.

4.6 Frequency Analysis with Three Hold-Downs

Normal mode frequency analysis was carried out for above three hold-down configurations with FE model shown in Fig. 7 and result are shown in Table 1.

It can be seen that first mode of vibration is **67.2 Hz**, which is meeting the specification value of > 60 Hz.

Hence this three Hold-down configuration meets all the requirements listed in Sect. 2.

5 Conclusion

This paper presents a systematic approach for the selection of the number and placement of the hold-downs for rigidly holding a large $\phi 1$ m antenna on a dual axis drive mechanism. It presents a chronological order of hold-down mounting configurations

supported by analysis for achieving the required stowed frequency. The study also illustrates step by step procedure for the finalization of the spigot wedge angles in the hold-down. The FE analysis in each case study has been presented and an optimized solution is proposed with three hold-downs mounted along 2 axes. The paper will serve as benchmark for the finalization of the hold-downs required for large diameter antenna on a dual axis drive mechanism.

It must be noted that the performance of the mechanism is always mission critical for all satellites. Accommodation of an optimized resolution which leads to high stowed frequency is very important as it determines the load regime also.

References

1. Srivastava, A.K., Kamboj, A., Sharma, G., Nagraj, B.P., Shankara, A., Suresha Kumar, H.N., Keshava Murthy, K.A.: An innovative, self-restrained, high torque, dual gimbal mechanism for antenna pointing. *Satellite Technology Day* (2017)
2. Pereira, C.: Mechanisms of the Rosetta high gain antenna. In: *Proceedings of the 9th European Space Mechanisms and Tribology Symposium*, 19–21 September 2001, Liège, Belgium. Compiled by R.A. Harris. ESA SP-480, pp. 83–90. ESA Publications Division, Noordwijk, Netherlands (2001). ISBN 92-9092-761-5
3. Web page link of SENAR, Solar Orbiter. <https://www.aeroespacial.sener/en/products/solar-orbiter-high-antenna-subsistem>
4. Wamsteker, W.: *ESA/VILSPA/SCI-SA, Study Manager. Assessment Study Report*, WSO/UV, World Space Observatory, p. 64
5. Sri Pavan RaviChand, V., Srivastava, A.K., Kumar, A., Suresha Kumar, H.N., Keshava Murthy, K.A.: Analytical approach to develop a robust mechanism for on-orbit gimbaling of satellite antenna. In *ICAME-2020 (International Conference on Advances in Mechanical Engineering-2020)* (2020)

Workspace Analysis of a 5-Axis Parallel Kinematic Machine Tool with 3-RRS Parallel Manipulator



Anshul Jain  and H. P. Jawale

1 Introduction

The popularity of PMs has increased considerably in recent years since they offer better rigidity, enhanced agility, higher accuracy and high load-carrying capacity over their serial counterparts [1]. These features allow PMs to be applicable in various fields like parallel kinematic machine tools, industrial robots, telescopes and so on [2]. PMs with less than 6-DoF have attracted a lot of attention in the research fraternity because of their simple architecture and low cost of design and manufacturing [3]. PKMs based on variable geometry truss structures opened a new domain in the machine tool industry after NC machines in recent years [4]. The 3-RRS Spatial Parallel Manipulators (SPMs) are generally used in machining devices, coordinate measuring machines, telescope positioning and in simulating motions [5]. It is also used as a substructure in hybrid manipulators [6]. Srivatsan and Bandyopadhyay [7] defined the safe working zone of PM while Tetik [8] obtained the reachable workspace and safe working zone of 3-RRS PM.

In order to optimize the dimensions and design of robot manipulators, workspace analysis is always considered as an important criterion. This paper presents a 5-DoF PKM tool architecture based on 3-DoF 3-RRS SPM and two additional DoF of the movement of the base in the X- and Y- direction. A quantitative improvement in reachable workspace over conventional 3-DoF PKM is presented, which enables the tool to cover more space beneficial in complex machining operations and industrial applications. Along with this, its rigidity also increases because of the gantry structure.

The paper is organized as follows: Sect. 2 presents a description of a 3-RRS PM with complete notations. Section 3 deals with the mobility analysis of the manipulator.

A. Jain  · H. P. Jawale
Visvesvaraya National Institute of Technology, Nagpur 440010, India

In Sect. 4, Parallel Kinematic Machine is discussed. Section 5 deals with position level kinematic analysis followed by workspace analysis in Sect. 6. Section 7 focuses on conclusions and results.

2 Description of a 3-RSS Parallel Manipulator

The architecture of the 3-RSS PM used in this study is shown in Fig. 1. It consists of a fixed base, a moving platform and three identical limbs. Fixed base and moving platform are of triangular shapes. The input angles (active angles) are θ_i and the passive angles are ϕ_i , respectively, and measured from the axis of the revolute joints up to the limbs. They are considered as (-) if measured from outside and (+) if measured from inside.

Active revolute joints are at the base at points P_i , passive revolute joints are at points Q_i and passive spherical joints S are at points R_i on moving platform, where $i = 1, 2, 3$ for three limbs, respectively. O -XYZ is a fixed coordinate frame attached on the base and M -UVW is attached on the moving platform. O and M are chosen as centres of fixed base and moving platform, respectively.

X-axis is along vector $\overrightarrow{OP_1}$ and Z-axis is perpendicular to the plane of the platform. Also, U-axis is along vector $\overrightarrow{MR_1}$ and W-axis is perpendicular to the plane of the

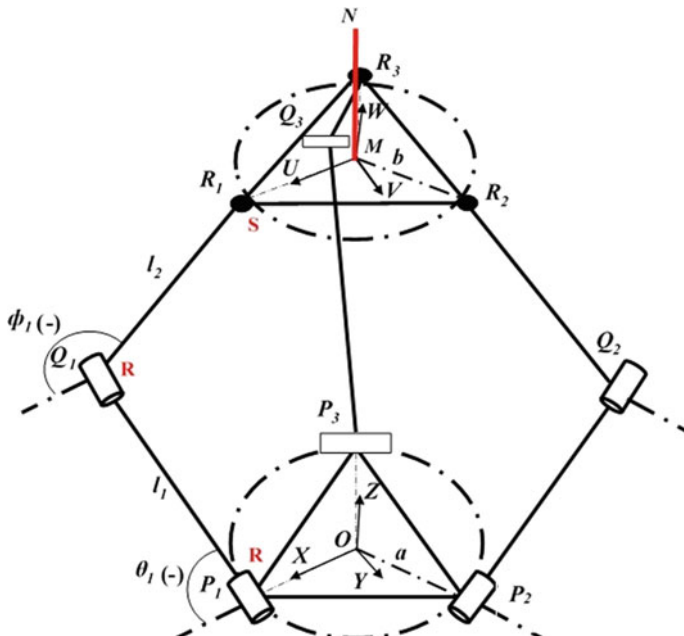


Fig. 1 Kinematic sketch of 3-RSS PM

platform. The radius of base platform is denoted by a , i.e., $\overline{OP}_1 = \overline{OP}_2 = \overline{OP}_3 = a$, and the radius of the moving platform is denoted by b , i.e., $\overline{MR}_1 = \overline{MR}_2 = \overline{MR}_3 = b$.

Lengths of lower and upper links are denoted by l_1 and l_2 , respectively, for all three limbs. MN is an End-Effector (EE) of length 500 mm attached (or whose origin is) at point M .

3 Mobility Analysis of Manipulator

This manipulator consists of a total of six revolute and three spherical joints ($j = 9$) and eight number of links ($n = 8$).

According to the general Grubler–Kutzbach criterion, the DoF of any mechanism can be calculated as

$$F = \lambda(n - j - 1) + \sum f_i \quad (1)$$

Here, $n = 8$, $j = 9$, and $\sum f_i = 6 \times 1 + 3 \times 3 = 15$.

Also, since spatial manipulator, $\lambda = 6$.

From Eq. (1), $F = 6(8-9-1) + 15 = 3$.

Therefore, 3-DoF is obtained for the moving platform of this manipulator with 1T2R type of motion (T = Translation, R = Rotation). The vertical movement of the manipulator along the Z-axis is denoted by M_z , and the rotational movement of the manipulator about X and Y axes is denoted by α_x and α_y , respectively.

4 Description of Parallel Kinematic Machine

This PKM basically consists of a workbench, the frame structure of the machine tool and a 3-DoF 3-RRS PM as shown in Fig. 2. It is designed to have a total of 5-DoF, which includes 3-DoF of manipulator which slides on the frame structure of machine tool along X-direction and Y-direction providing extra 2-DoF. M_x , M_y , M_z , α_x , α_y are the respective five axis motions of the machine tool in which M_x , M_y , M_z are the positioning parameters and α_x , α_y are the orientation parameters. More precisely, $(M_z, \alpha_x, \alpha_y)$ are for moving platform of manipulator because of 1T2R type of motion characteristic and M_x , M_y are for the translation of the manipulator on the frame structure along X and Y directions. Reachable workspace of the machine was enhanced appreciably because of the sliding motion of the PM along X and Y directions.

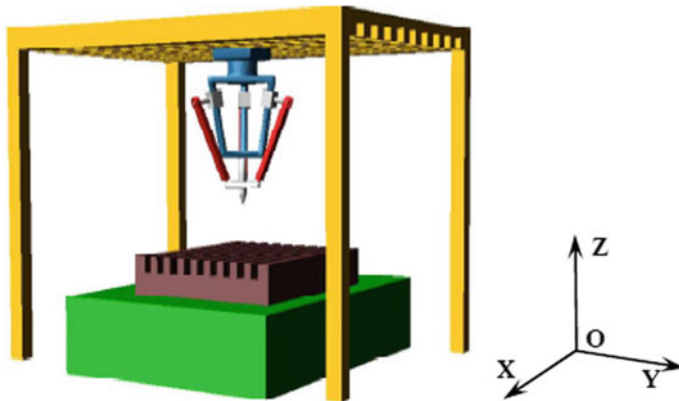


Fig. 2 5-axis Parallel Kinematic Machine [4]

5 Position Level Kinematic Analysis

It consists of two types of analyses: (i) Inverse Kinematics (IK) and (ii) Forward Kinematics (FK).

In IK, location (position and orientation) of moving platform is known in the form of independent pose parameters M_z , α_x , α_y and the input angles θ_i are to be determined.

In FK, the location of the moving platform is obtained from the known input angles.

The position of the origin of the moving platform with respect to $O\text{-}XYZ$ is defined as follows:

$$\overline{M} = [M_x \ M_y \ M_z]^T \quad (2)$$

The constraint equations for 3-RRS PM can be given similar to [9] as

$$M_y = -u_y b \quad (3)$$

$$M_x = b(u_x - v_y)/2 \quad (4)$$

$$u_y = v_x \quad (5)$$

The rotation matrix for the moving coordinate frame $M\text{-}UVW$ with respect to the fixed frame $O\text{-}XYZ$ be

$$R = \begin{bmatrix} u_x & v_x & w_x \\ u_y & v_y & w_y \\ u_z & v_z & w_z \end{bmatrix} \quad (6)$$

where

$$\begin{aligned} u_x &= c_y c_z & v_x &= c_y c_z & w_x &= s_x \\ u_y &= c_z s_x s_x + c_x s_z & v_y &= c_x c_z - s_x s_x s_z & w_y &= -s_x c_y \\ u_z &= s_x s_z - c_x s_y c_z & v_z &= s_x c_z + c_x s_x s_z & w_z &= c_x c_y \end{aligned} \quad (7)$$

and s and c stand for *sin* and *cos*, respectively. Also, subscripts *x*, *y* and *z* stand for rotation angles α_x , α_y and α_z , respectively.

Considering the workspace of the given manipulator, the choices for the suitable workspace parameters are M_z , w_x and w_y .

For given w_x and w_y , from Eq. (7), α_x and α_y can be obtained as

$$\alpha_y = \sin^{-1}(w_x) \quad (8)$$

$$\alpha_x = \sin^{-1}(-w_y/c_y) \quad (9)$$

Also, using Eqs. (5) and (7), the only unknown parameter in the rotation matrix α_z can be obtained as

$$\alpha_z = \tan^{-1}(-s_x s_y / (c_x + c_y)) \quad (10)$$

Complete mathematics and formulations to obtained IK and FK are given in [10]. Some of the final results are highlighted below as

$$\text{active (input) angles } \theta_i = 2 \tan^{-1} \left[-B_i \pm (A_i^2 + B_i^2 - C_i)^{0.5} \div (C_i - A_i) \right] \quad (11)$$

$$\text{passive angles } \phi_i = \text{atan2}(\cos \phi_i, \sin \phi_i) \quad (12)$$

where,

$i = 1, 2, 3$ and

$$A_i = 2I_1 \cos \mu_{1i} (a \cos \mu_{1i} - B_{i,x}) \quad (13)$$

$$B_i = 2I_1 B_{i,z} \cos^2 \mu_{1i} \quad (14)$$

$$C_i = B_{i,x}^2 - 2a B_{i,x} \cos \mu_{1i} + \cos^2 \mu_{1i} (a^2 + I_1^2 - I_2^2 + B_{i,z}^2) \quad (15)$$

and $\mu_{12} = 0^\circ$ $\mu_{12} = 120^\circ$ and $\mu_{13} = 240^\circ$.

Also,

$$M_z + b u_z = -I_2 \sin \phi_1 - I_1 \sin \theta_1 \quad (16)$$

$$M_z - 0.5 b u_z + 0.866 b v_z = -I_2 \sin \phi_2 - I_1 \sin \theta_2 \quad (17)$$

$$M_z - 0.5 b u_z - 0.866 b v_z = -I_2 \sin \phi_2 - I_1 \sin \theta_3 \quad (18)$$

After getting all the important results, it should be noted that Eq. (11) gives the solution for IK and Eqs. (8), (9) and (16), (17), (18) give a solution for FK. In PMs, IK is always considered easier to execute than FK.

It is important to state that the solution of FK is considered one of the major challenges in PMs because of the mathematical complexity involved in it. A 16th order polynomial in terms of a tangent of the half of one of the passive joint angles is obtained while doing formulations [10]. This 16th order polynomial gives 16 solutions for the moving platform in which some are real with the physical limitations of the robot while some are imaginary or beyond the reach of the robot.

For complete analysis to be carried out, one has to consider only real values out of those 16 values and discard imaginary ones for further calculations. Out of the number of sets obtained in FK depending upon the number of real values, only one set matches with the independent pose parameters used in the IK and then it can be said that the kinematic analysis that has been done for the given manipulator is correct.

In this paper, workspace analysis is carried out by considering the link proportions with respect to a as $l_1 = l_2 = 1.6*a$ and $b = 0.7*a$. Considering $a = 500$ mm, we have, the lengths of lower and upper links as $l_1 = l_2 = 800$ mm and $b = 350$ mm. As a random, position level kinematic analysis is carried out to verify the above-mentioned formulations. Let us consider $M_z = 1371$ mm, $\alpha_x = -29.83^\circ$ and $\alpha_y = 16.07^\circ$ as independent pose parameters given in IK. Using Eq. (11), input angles θ_i are obtained as -60° , -60° , -90° , respectively.

Now, for FK, considering these input angles as input, and using Eqs. (8), (9), (16), (17) and (18), a 16th order polynomial is obtained in terms of a tangent of half of one of the passive joint angles which give 8 real solutions as shown in Table 1.

As mentioned earlier, only one set matches with the independent pose parameters used in the IK and for this case, 3rd set of solution matches as shown in Table 1. Thus, our position level kinematic analysis is verified.

6 Workspace Analysis

Workspace analysis in this paper is carried out by calculating the reachable workspace of the manipulator which is defined as one reached by the origin of the end-effector [11]. As already mentioned in the previous section, workspace analysis is carried

Table 1 Eight real solutions

Sr. no	M_z (mm)	α_x (deg.)	α_y (deg.)
1	1347.36	-28.56	-33.44
2	1347.36	-28.56	-33.44
3	1371.06	-29.83	16.07
4	79.72	9.10	5.27
5	189.14	51.15	-17.78
6	189.14	51.15	-17.78
7	283.10	76.63	29.35
8	1103.9	-74.30	-29.10

out by considering the link proportions with respect to a as $l_1 = l_2 = 1.6*a$ and $b = 0.7*a$. Considering $a = 500$ mm, we have the lengths of lower and upper links as $l_1 = l_2 = 800$ mm and $b = 350$ mm.

Reachable workspace in this paper is obtained by varying the input angles for the three limbs from 0° to -90° (from outward to inward) as shown in Table 2.

Now, from the above table, it is apparent that 6 sets of input angles θ are considered to obtain the reachable workspace which covers almost all ranges of input angles from 0° to -90° . These 6 sets of input angles for three limbs lead to their 6^3 combinations resulting in 216 different poses of moving platform for estimations. It should be noted that the number of combinations that can be increased up to any value apparently will improve the workspace profile but will also lead to mathematical and programming complexity.

For 216 combinations of input angles, 3456 solutions are obtained initially. Considering only real values out of those and discarding imaginary values, IK is performed for each set of output parameters M_z , α_x , α_y and the final values obtained are used to plot the reachable workspace of the manipulator as shown in Fig. 3. The highest reach achieved by the manipulator as obtained from mathematical formulations is 1585.67 mm.

From Fig. 3, it is seen that for the given inputs, the EE is capable of reaching any point within the shown work volume.

By considering an incremental mode of motion of individual limbs, another interpretation of reachable workspace can be obtained. By keeping any two limbs in the

Table 2 Sets of θ_i

Sr. no	θ_1 ($^\circ$)	θ_2 ($^\circ$)	θ_3 ($^\circ$)
1	-0.01	-0.01	-0.01
2	-20	-20	-20
3	-40	-40	-40
4	-60	-60	-60
5	-80	-80	-80
6	-90	-90	-90

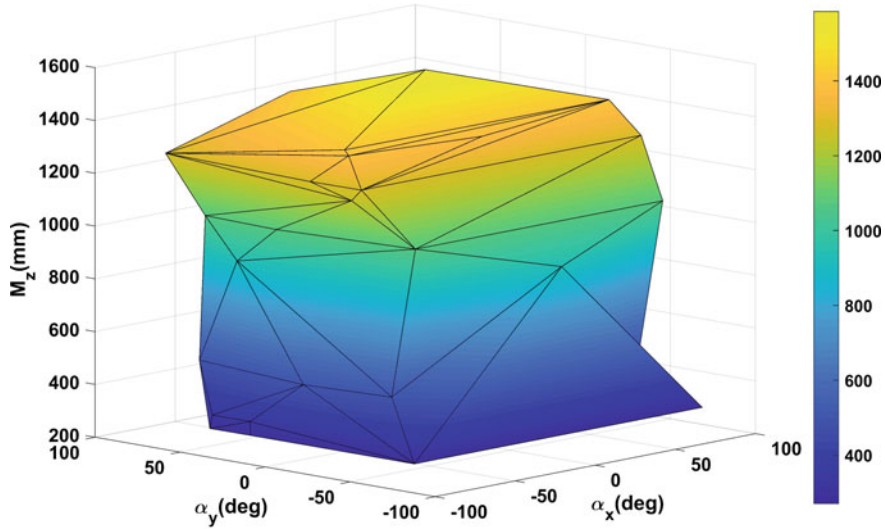


Fig. 3 Reachable workspace plot for origin of EE

locked position and actuating the remaining link within extreme possible ranges, a reachable workspace can be obtained. This procedure must be done for all three limbs to obtain the position and orientation of the movable platform. The extreme ranges of points R_1, R_2, R_3 as shown in Fig. 1, will give the total reach of the movable platform and its respective plot of reachable workspace is shown in Fig. 4.

Locking R_2 and R_3 will give the locus of point R_1 from R_1 to R_1^1 . Similarly, locking R_1 and R_3 will give the locus of point R_2 from R_2 to R_2^1 and locking R_1 and

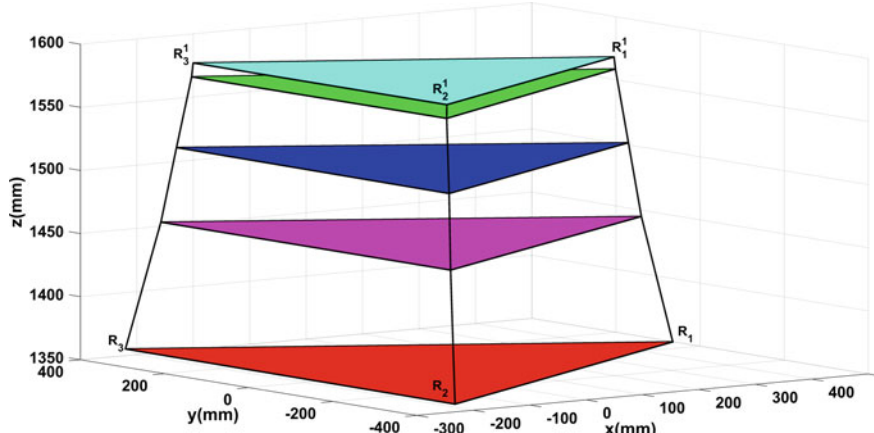


Fig. 4 Reachable workspace plot for points R_1, R_2 and R_3 for input angles -80°

R_2 will give locus of point R_3 from R_3 to R_3^1 . This procedure is carried out for $\theta_1 = \theta_2 = \theta_3 = -80^\circ$.

The range of possible motion of respective input obtained for three input angles is θ^{-60° to θ^{-90° . Similar work can also be done for other combinations of input angles.

Now, in PKM as shown in Fig. 2, manipulator is attached upside down. Base platform of the manipulator is attached to the frame structure and translates along X and Y directions while the moving platform carrying the EE is facing towards the workbench. In a stationary position of the manipulator, the pattern of the reachable workspace following the same procedure of incremental mode of motion of individual limbs as mentioned above for $\theta_1 = \theta_2 = \theta_3 = -80^\circ$ is shown below in Fig. 5. Note that the different colours shown are just for different positions of the platform.

Now, it has been said that the manipulator slides on the frame structure along X and Y directions providing an extra 2-DoF. In this paper, it has been considered that the manipulator is moving 500 mm in X and Y directions. Figure 6 shows the complete pattern of work volume of the manipulator for $\theta_1 = \theta_2 = \theta_3 = -80^\circ$ thereby presenting more usefulness and effectiveness of the mechanism over conventional PKM by showing the increment in the reach of the tool. This increment is essential to execute complex machining operations.

The workspace shown in red colour is for the original position of the manipulator while that shown in green colour and blue colour are when the manipulator is translated 500 mm along X-direction and Y-direction, respectively. Figure 7 shows the top view of the same.

From Figs. 6 and 7, it can be seen that the reach of the moving platform increases in both directions, which in turn increases the reach of the EE or tool certainly helpful in complex industrial applications and machining operations. It should be noted that, in this paper, translation of the manipulator is considered as 500 mm as a random value, however, can be increased or decreased depending upon the requirements.

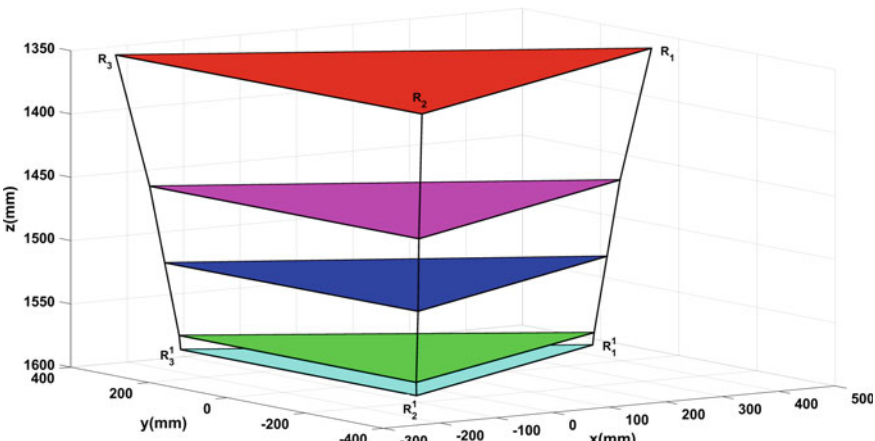


Fig. 5 Reachable workspace plot of manipulator attached to PKM

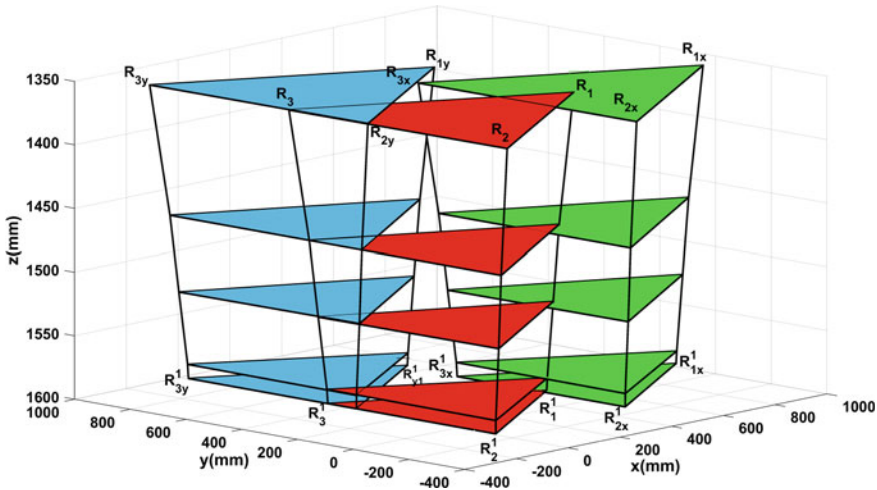


Fig. 6 Complete work volume of manipulator after translation along X and Y directions

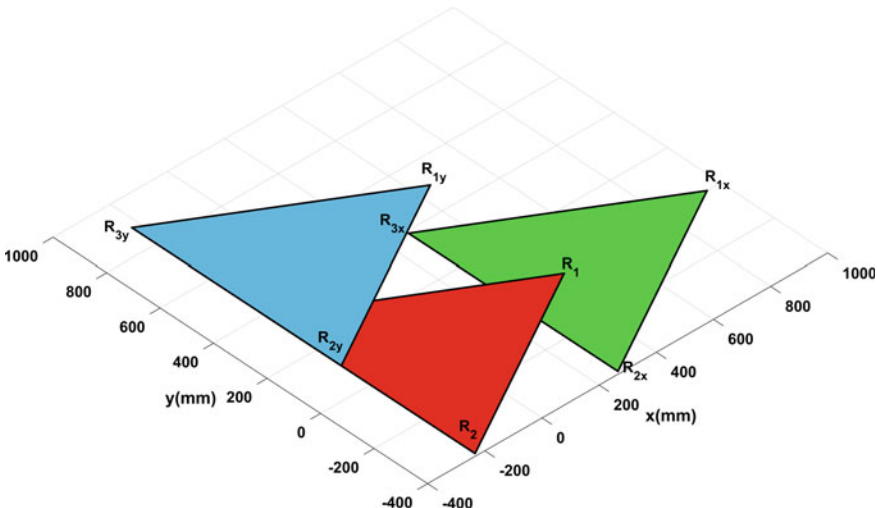


Fig. 7 Top view of the complete work volume of the manipulator

7 Conclusions and Results

Complete work on the position level kinematic analysis and the workspace analysis is carried out. The major challenge in this work lies in the solution of FK which results in 16th degree polynomial for a single combination of input angles and in this paper, it is carried out for 216 combinations. Workspace analysis in the form of

reachable workspace is carried out and found that the EE is capable of reaching any point within the shown work volume for the given inputs.

A new configuration of 5-DoF PKM is suggested which consists of 3-DoF of the manipulator which slides on the frame structure of the machine tool along X-direction and Y-direction providing extra 2-DoF. A quantitative improvement in reachable work volume over conventional 3-DoF PKM is presented. The new configuration proposed has a larger workspace and higher rigidity than many of its other counterpart configurations. Translation of the manipulator over the frame structure along X and Y directions significantly increases its reach and so the movement of the tool thereby increasing its utility.

After obtaining the reachable workspace for the mechanism, effects of link tolerances and joint clearances are under investigation and their results can be obtained in the future. Prototype fabrication for the same is also under consideration as future work.

References

1. Wang, J., Gosselin, C.: A new approach for the dynamic analysis of parallel manipulators. *Multibody Sys. Dyn.* **2**, 317–334 (1998)
2. Zhang, Y., Ting, K.: Design and analysis of a spatial 3-DOF parallel manipulator with 2T1R-type. *Int. J. Adv. Robot. Syst.* **10**(5), (2013)
3. Fan, C., Liu, H., Zhang, Y.: Type synthesis of 2T2R, 1T2R and 2R parallel mechanisms. *Mech. Mach. Theory* **61**, 184–190 (2013)
4. Chen, W., Zhao, L., Zhang, J.: A 3-DOF parallel manipulator based 5-axis parallel kinematics machine tool. In: Advanced Materials Research, vol. 317, 319th edn, pp. 698–702 (2011)
5. Li, Q., Herve, J.M.: 1T2R parallel mechanisms without parasitic motion. *IEEE Trans. Robot.* **26**(3), 401–410 (2010)
6. Li, J., Wang, J., Chou, W., Zhang, Y., Wang, T., Zhang, Q.: Inverse kinematics and dynamics of the 3-RS parallel platform. In: Proceedings of the IEEE International Conference on Robotics & Automation. <https://doi.org/10.1109/ROBOT.2001.932999> (2001)
7. Srivatsan, A., Bandyopadhyay, S.: Determination of the Safe Working Zone of a Parallel Manipulator, vol. 15, pp. 201–208. Computational Kinematics, Springer (2014)
8. Tetik, H.: Modelling and control of a 3-RS parallel manipulator. MSc Thesis, Izmir Institute of Technology (2016)
9. Tsai, L.W. (ed.): Robot Analysis: The Mechanics of Serial and Parallel Manipulators. Wiley (1999). ISBN 978-0-471-32593-2
10. Tetik, H., Kalla, R., Kiper, G., Bandyopadhyay, S.: Position Kinematics of a 3-RS Parallel Manipulator, ROMANSY 21-Robot Design, Dynamics and Control, vol. 569, pp. 65–72. CISM, Springer (2016)
11. Merlet, J.P.: Parallel robots: open Problems. In: 9th International Symposium of Robotics Research, pp. 27–32. Snowbird, USA (1999)

Four-Bar Linkage Mechanism in Papermaking and Its Replacement by Direct Servo Drive Technology in Roll to Sheeting Lines in a Paper Mill—Converting House



Muralidhar Ekambaram

1 Introduction

Application Engineering plays a very important role in the development of any technology. I would like to quote Mr. Herbert Kroemer, the Nobel Laureate here. He stated that “Certainly when I thought of the heterostructure laser, I did not intend to invent CD Players. I could not have anticipated the tremendous impact of fiber optic communications. The person who comes up with applications thinks differently than the scientist who lays the foundation”. This gives us insight that both the fundamental researcher and the Application Engineer complement each other in making any device/idea/law invented/discovered by the scientists succeed or apply appropriate device/idea for any specific application [1]. The application of the Grashof criterion is also one such standing example of how the law has been successfully deployed in improving one of the papermaking processes.

Till Grashof law was deployed in a Roll to sheet converting equipment in a Paper mill, the sheets used to be manufactured with single rotary cutters/guillotine shearing machines at very low speeds and with low accuracies of cut lengths and diagonal lengths resulting in Parallelogram formation of sheets. To overcome these shortcomings and for increasing the productivities of these converting machines, engineers started deploying Grashof law in the cutting section of these converting machines bringing about a revolution in cutting technology with Dual rotating cutters achieving exactly the desired cut length and diagonal accuracies. After successfully deploying the law practically and achieving results exactly in line with requirements, the advances in DC and AC servo motor and controller technologies ensured the improvements in machine performances in multifold. These servo technologies were employed directly coupling the motors to load shafts removing the in-between

M. Ekambaram (✉)
Adeptus Servo-Mechatronics Private Limited, Hyderabad, India
e-mail: ekambaram@servomechatronics.in

Mechanical variations, Double draglink transmissions thereby avoiding the typical mechanical wear out and backlash—Maintenance problems.

The paper discusses and analyses the merits and demerits of three suitable cam profile motions for the application.

2 The Application

2.1 Principle of Operation—Dual Rotating Knives Cutter

A rotary cutter generally includes a pull roll or draw roll section, doctor board systems, a cutting head assembly, and a drive system that varies the cut length. The draw roll section consists of a rubber-covered squeeze roll spring loaded or pneumatically loaded against a steel draw drum. These two rolls pinch the web and “draw” it into the cutter rig (Figs. 1, or 2).

In rotary cutters, two basic design principles are employed. By far the most common and simplest design is the rotary/stationary bed knife, or “conventional” cutter (Fig. 1). The bottom knife blade is mounted on stationary support with the top blade mounted on a rotating cylinder. The “fly” knife strikes the stationary bed knife, severing the web that passes between the two blades.

With the appropriate approach angles and knife grinds, the stationary bed knife cutter can cut board grades up to 0.016" thick (325 gsm) cleanly. As the web bulk

Fig. 1 Single
rotary/stationary bed knife
[2]

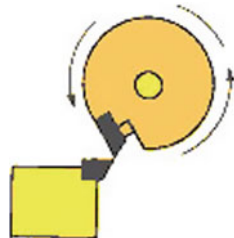
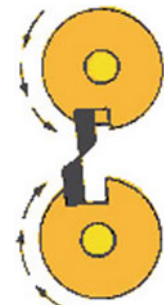


Fig. 2 Rotary cutter with
dual rotating knives [2]



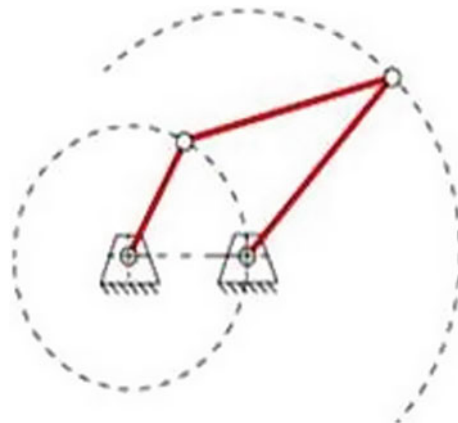


Fig. 3 Double crank mechanism with trajectories of input and output links [3]

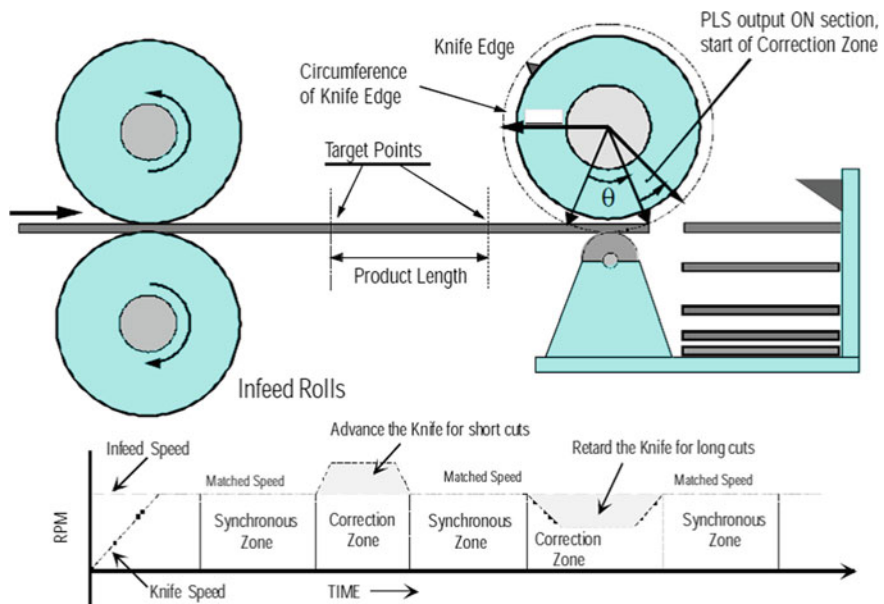


Fig. 4 Illustration of paper roller and cutter [4]

thickens, the cleanliness of the cut (absence of loose fibers, hair, or dust) deteriorates and the leading edge of the sheet develops a perceptible skived tip [2].

The dual knife/rotary cutter (Fig. 2) provides the cleanest, quietest, and highest quality and capacity cutting action available. In this design, both top and bottom blades are mounted in rotating cylinders. The upper and lower cylinders are generally coupled together by anti-backlash gearing. The web of material passes between the

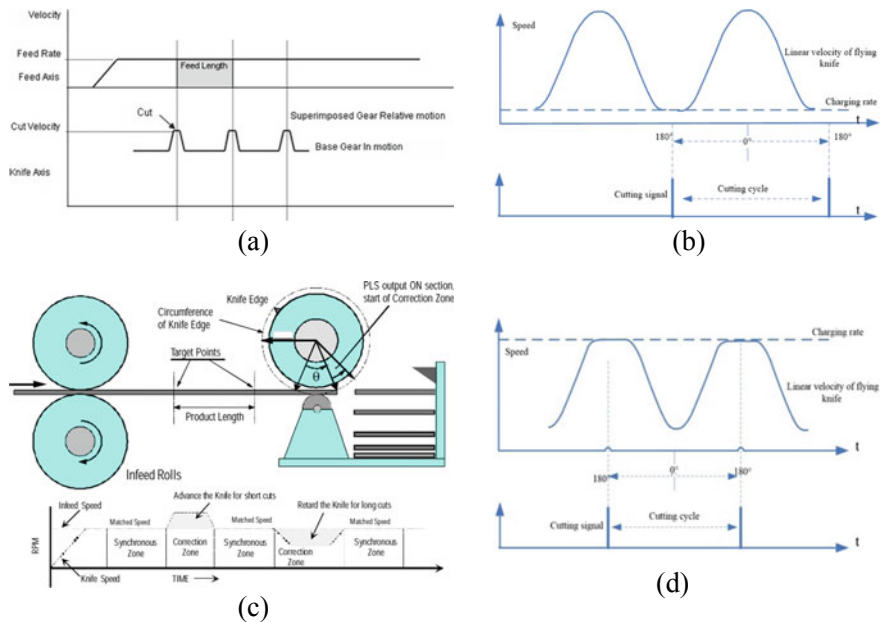


Fig. 5 Cutter motion profiles: **a** Triangular [5]; **b** Sinusoidal for cut lengths < circumference of the cutter drum [6]; **c** Trapezoidal; **d** Sinusoidal for cut lengths > circumference of the cutter drum

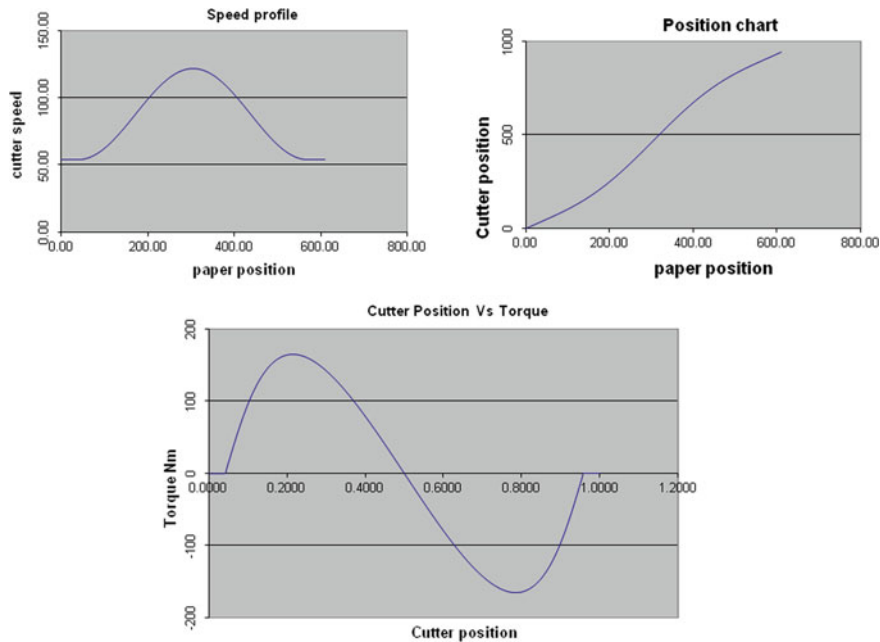


Fig. 6 Graph plots detailing the cutter speed, position, and torque characteristics [7]

two cylinders and the resulting scissors-like action provides the cleanest, quietest cutting action available.

For the cutter to perform properly, the peripheral speed of the knives must equal the speed of the material at the time of cut (Fig. 5b and d). Since the knife speed and web speed are identical at the time of cut, the dual knife rotary design has the additional benefit of not requiring an adjustment for squareness (diagonal accuracy) when changing sheet length. The manner in which the knives' speed matches the web speed has evolved over the years.

2.2 Grashof Law and Criterion

The Grashof's law states that for a four-bar linkage system, if the short link is a fixed link, the sum of the shortest and longest link of a planar quadrilateral linkage is less than or equal to the sum of the remaining two links, ($s+l \leq p+q$) then both the links can rotate fully but the output crank rotating with varying rotating speed [8].

Consider a four-bar linkage. Denote the smallest link by S, the longest link by l and adjacent to S, and the other two links by P and Q. In the double crank mechanism, the shortest link 'S' is a ground link. Both input crank and output crank rotate 360° —full rotation.

This phenomenon was identified as an answer to achieving the motion profile required for Dual rotating Cutter Equipment and employed with detailed engineering. Thus, Draglink employed machines that started producing results with cut length and diagonal accuracies better than ± 0.5 mm at speeds above 100 mtrs/min. As the years progressed, market demands increased multifold both inaccuracies and productivity, it was compelling technologists to improve upon drives employed. Initially, mechanical variators in conjunction with drag link transmissions (Four-bar linkages) were employed [9].

A crank link rotates at constant rotational speed, while the driven link varies its rotational speed within a single rotation. By selecting the individual link lengths, the requirement of synchronizing speed at the time of cutting is met with and balance part of a rotation, the rotational speed of the driven link is varied compensating for the time available to achieve different cut lengths as required by the market. This equation has dwelled in detail at a later part of the paper.

- It is defined that Format length = Circumference of the cutter drum
- If cutter blade tip radius = r
- Format length = $2\pi r$
- If Paper speed = v
- Cutter rotational speed during cutting = $v/2\pi r$
- Say Cutter angle of rotation during cutting = 10°
- Therefore, in the remaining 350 degrees the speed of the cutter is adjusted and varied to follow in the position of feeding paper to achieve the cut length set

- For cut lengths > Circumference of cutter the cutting is at high speeds and after cutting the speed is decreased and increased again to synchronous speed for the next cutting
- For cut lengths < Circumference of cutter, the cutting is at low speeds and after cutting the speed is increased and brought down again to synchronous speed for the next cutting.

2.3 Application Concept and Paper Cutter Motion Profile Requirement [10]

2.4 Application Technology Progress

As the Drag link technology started getting employed in the cut to length application, initially the technology progressed with the deployment of mechanical variator like Kopp variator, flywheel, Drag link transmission with linkage length adjustment through a motorized actuator to control the machine and set the cut lengths through pushbuttons. Subsequently, with the advent of DC motor Thyristor drives in the 1960s, the mechanical variators were done away with replaced by DC Motors and drives paving way for further improvements in the electrical drives deployed.

3 Motion Control Servo Technology

3.1 Electronic Cam Profile Drives and Developments

From the 1980s when Servo drives with DC Servomotors had evolved, the same was extensively employed in the application throughout the world. Subsequently with AC Servo technology progress since the millennium year, AC Servo drive with AC Servo motors are employed in every present-day built machine. This has assisted the machines to achieve accuracies better than ± 0.38 mm at speeds above 350 mtrs/min.- such unthought-of exemplary performances.

3.2 The Cutter Motion Profile Variants

Triangular, Sinusoidal, and Trapezoidal speed profile graphs for the application are illustrated below (Fig. 5):

3.3 Graphical Presentation of Required Cutter Speed, Position, and Torque Profiles (Fig. 6)

3.4 Moment of Inertia and Selection of Servo Drives

There is a finite relationship between the Load moment of inertia and the source moment of inertia. Earlier around 30 years back it used to be Source MOI/Load MOI $>1/2$ till simple PID controls were used and presently the same $>1/15$ or $1/20$ by employing feed forward feedback trim control algorithms.

In addition to the above, the selection of a Motor rating is based on the following procedure.

- (1) Calculate the MOI of the load.
- (2) Mechanical transmission ratio between the Motor shaft to load shaft = N:1
- (3) Load MOI reflected on the motor(GD^2) = Load MOI/ N^2 + Mech. Transmission MOI as reflected at the input + Motor MOI
- (4) Calculate the average speed (N_a) of the cutter drum required at min. cut length in the cut length range = Max. Paper speed/Cut length at corresponding max. Machine designed paper speed at min. cut length (cut length in mtrs and paper speed in mtrs/min.)
- (5) Calculate the synchronous speed (n_s) = Paper speed/circumference of cutter drum = $v/2\pi r$ where r is the radius of cutter drum and v is the paper speed.
- (6) Peak speed required on load shaft(N_p) = $2 \times$ Average speed—Synchronous speed (n_s)
- (7) Max. Speed range (N_r) for min. cut length = $2 \times$ Average speed— $2 \times$ Synchronous speed
- (8) Time for each cut = $1/\text{Average speed } (N_a)$ in min.
- (9) If 15 degrees is needed for cutting, Balance time is required for acceleration and deceleration.
- (10) Then balance time = $15/360 \times (N_a) = t_{ns}$ = Nonsynchronous motion time/cycle
- (11) Half of the Nonsynchronous motion time (t_{ns}) approximately taken for acceleration
- (12) Now we have Total MOI, Speed change, and time for acceleration, and conventionally calculating Torque can be calculated T_a in Kg M = $4 \times GD^2 \times N_r / (375 \times t_{ns}/2)$
- (13) Min. rated speed required on the motor = peak speed required = N_p
- (14) The selected motor should be capable of transmitting the T_a with rated speed $>N_p$.
- (15) The Load MOI /Motor MOI < 15 only if Feed forward controls are employed.

Table 1 The performance of Different parameters with respect to their profiles [7]

Comparison of cutter motion profiles				
S. no	Parameter	Trapezoidal profile	Triangular profile	Sinusoidal profile
1	Acceleration	Least constant throughout speed change	Higher than trapezoidal and constant throughout speed	Varying continuously and highest peak
2	Speed transition points	Abrupt to introduce smoothening formula at transition point	Abrupt to introduce smoothening formula at transition point	Naturally smooth
3	Peak speeds	Higher than triangular	Least among the profiles	Highest among the profiles
4	Mechanical transmission suitability	Fairly ok	Highest stress of transmission	Lowest stress of transmission

3.5 Comparison of Cutter Motion Profiles (Table 1)

3.6 Feed Forward Control Servo Algorithms

Feed forward augmentation is a prediction technique that estimates the output from a proportional-integral-derivative (PID) control algorithm without waiting for the PID algorithm to respond. Feed forward reduces the error faster or keeps the error smaller than relying on the PID algorithm alone.

With the above control philosophy, the system is very near to where it should be with respect to Speed, Torque, and Position at any specific point of operation and the PID controls only trims the system for any small errors that might have crept in due to any empirical conditions, thereby any system oscillations that invariably occur in a pure PID control algorithms are avoided totally.

This yields the main advantage in Servo motor selection as the MOI mismatch between Loads to Motor can be as high as 15 or even greater up to 20. This feature facilitates the deployment of PMSM (Permanent Magnet Synchronous Motors) for the application that too without any gear transmissions in-between motors and the load.

3.7 Successful Deployment Examples

A 1960 Vintage 3.2 mtr/120 mpm Jagenburg make Duplex Paper board sheeter was recently refurbished and retrofitted with 180 kW/500 rpm Servomotor directly

driving the cutter section by removing the Double Drag Link transmission achieving cut length and diagonal length inaccuracies within ± 0.5 mm and also increasing the productivity by approx. 20% for cut length range between 400–1600 mm. The video of the installation is as per hyperlinked video employing exactly the technology explained above [11].

Also, the same technology has found inroad S into another associated industrial vertical—Corrugation—Multiply high speed Corrugation machine. One can watch the application in the video in the link [12].

Since the application is for manufacturing 5 ply Corrugation sheets meant for the packaging industry, the targeted accuracies are within ± 1 mm.

The same Servo Motion control technology is also employed in the Steel sheets manufacturing process in the steel mills.

In all the above applications, it was found that the speeds of the machine can be increased multifold and accuracies of cut length and diagonal lengths achieved are phenomenally high, Machine uptime availability is increased many points, job change over times are reduced to 1 or 2 min as compared to earlier very long change over times with draglink transmissions and in addition the desired cut length accuracies are achieved in machines ramp up/downtimes as achieved during machine stable running conditions.

4 Conclusion

With the above in view, it is confirmed that any theoretical laws/criteria/rules/discoveries can be applied gainfully if properly identified and if the application targets to achieve the technological philosophies in letter and spirit with adjusting the applications to suit the empirical conditions. This paper is an endeavor to highlight how application engineering played an important role in the growth of technologies.

References

1. Ekambaram, M.: In: Growth, Developments and Future Prospects of Solid State Switching Devices IE Annual Conference, Hyderabad (2002)
2. Maxsons Automatic Machinery company, Sheeter manufacturers from 1906
3. Maqsood, S.: Theory of machines: kinematics and machines
4. ORMEC Application Highlights, Rotary Knife Cutoff
5. Application building block by ORMEC
6. Study on control strategy of the rotary synchronous fixed-length cutting system—Huazhu Wu1, Naihao Luo2, Changyou Wang, 1, 2, 3 Dalian Jiaotong University, Dalian, China
7. Practical experiences of Author in Dynaspede Integrated systems Pvt. Ltd and Walmsleys India Pvt. Ltd. in 2004 and 2017
8. <https://www.youtube.com/watch?v=xFg8WQRfHHo>
9. <https://www.youtube.com/watch?v=SLgKmlFrCf8>

10. <https://drive.google.com/file/d/1rxFE19heJrXAnRVpJcE7DThTGJAK8yrA/view?usp=sharing>
11. https://drive.google.com/file/d/1kkdcRPdislofyoNyeHj_TuVJ9KAQO4_8/view?usp=sharing
12. <https://drive.google.com/file/d/1Ieu2EhzHkT8ztQ3ygCTd9NbXx90Knifm/view?usp=sharing>
13. Astro system, Automation Applications Handbook
14. Boulter, B.T.: Solutions, AIC, IEEE IAS Annual Meeting. Part III Position Regulation, Applying Drive Specifications to Systems Applications (2002)
15. Motion control—Application note—RotaryCutter AN00226–003 by ABB

Robotics, Industrial CAD/CAM Systems, Mechatronics

Two Degree-Of-Freedom Omni-Wheel Based Mobile Robot Platform for Translatory Motion



Uday Manne , Raghuveer Maddi , Dimple Dannana ,
Devasena Pasupuleti , and Rajeevlochana G. Chittawadigi

1 Introduction

Mobile wheeled robots are used to carry out a variety of tasks in industries and other places. A rectangular platform with two wheels on two opposite sides is one of the standard configurations of such wheeled robot. In such a case, the wheel rotation is typically achieved using motors, which translate the robot in the forward and backward directions. If opposite sense rotation is given on the two opposite sides, rotation about a vertical axis (zero turning radius) can be achieved or can steer the robot along a curved path. Mecanum wheels can be used in place of conventional wheels to achieve motion in a transverse direction as well, thus avoiding the explicit rotation of the platform. Hence, these can be used for easy movement of the robot in any direction on a plane [1].

Mecanum wheel has a set of rollers on its tread and the axes of the rollers are usually 45° or 135° with the axis of the wheel. Hence, two possibilities of wheel design are generally used which mirror each other. When a wheel is rotated by coupling with a motor mounted on the platform, only one roller at the bottom is in contact with the ground and exerts a force on the platform in a direction along the axis of the bottom-roller and is dependent on the rotation sense of the wheel. Layout of four wheels in a Mecanum Wheel Robot (MWR) can be done on a rectangular or a square shaped platform. A detailed study of their analysis is provided in [2, 3]. For a rectangle shaped platform, a XY coordinate frame is assumed to be fixed at its center when looked from the top such that X is towards the right side and Y is towards the front of the platform, when looked from the top. When a wheel is looked from the top, if the axis of the top-roller is making 45° with respect to the X axis,

U. Manne · R. Maddi · D. Dannana · D. Pasupuleti · R. G. Chittawadigi ()

Department of Mechanical Engineering, Amrita School of Engineering, Amrita Vishwa Vidyapeetham, Bengaluru, India

e-mail: rg_chittawadigi@blr.amrita.edu

the bottom-roller would be making 135° , because of the geometry of the Mecanum wheel.

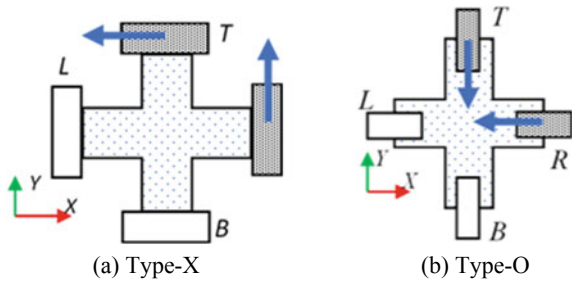
The two most common layouts have the diagonal pair of wheels with the same kind of rollers on them. In the top view, if the top-roller's axes of the four wheels form an X-shape, it is referred to as Type-X [2]. In this case, the bottom-rollers' axes of the neighboring wheels intersect outside the rectangular platform, forming a rhombus. Hence, the direction of contact forces is along the edges of the rhombus. Similarly, if the top view has the top-rollers' axes along a rhombus, the bottom-rollers' axes form an X-shape and so will be the contact forces. This is referred to as Type-O. Of the two, Type-X is analytically found to have a better capability of carrying out omnidirectional motion (translations and rotation) [2, 3] and is the preferred layout for MWR.

Type-O MWR can also be built on a square shaped platform. In that case, the forces on the platform intersect at its center and hence does not result in any moment about the vertical axis. This ensures that the platform cannot have any yaw rotation about the vertical axis. This concept has been extended in this paper for a meaningful application.

The rollers of the Mecanum wheels can be aligned such that the axis of each roller is orthogonal to the axis of the wheel [4]. By doing so, if the wheel is driven, it causes the bottom-roller to have contact force along its axis. If the wheel is moved (using other wheels) such that it has a motion along its axis, the bottom-roller on the tread rotates about its own axes, without causing any rotation of the wheel, thus achieving the omnidirectional capability. These special categories of Mecanum wheels are known as "omni-wheels". Considering omni-wheels as relatively inexpensive, many robots have been developed using them. Omni-wheels are easier to use as compared to Mecanum wheels. The forces acting on them are easier to analyze and the resulting mobile robots are simpler to control. One such attempt by the authors with three omni-wheeled based mobile platform is discussed in [5], in which the robot has been controlled using Bluetooth-based mobile application and also integrated with Leap Motion device for intuitive control using gestures of a human user.

Of the many applications of the omnidirectional wheel based robots, transporting items is one of the common applications. In some scenarios, the robots move in orthogonal directions and do not require any rotation about the vertical axis (yaw). In fact, any possible rotation may result in moving away from the desired path or trajectory, due to any inaccuracies. Hence, it is desired to have only translation in the forward-backward, transverse, and diagonal directions. To achieve only translation on a plane, only two degrees-of-freedom (DOF) are sufficient. A square shaped Type-O variant of the MWR can be used for the same. However, the desired translation can only be achieved if all the four wheels are powered (active), thus increasing the cost and complexity of the robot. In the literature, few have achieved translation using two DOFs, i.e., using only two motors. OmBuRO [6] has one wheel with a set of active rollers on its tread. It can translate to balance like an inverted pendulum, moving on a floor. In this paper, the authors propose simpler layouts of four omni-wheel based robots with two motors, which are compared, and one of the layouts is proposed to be suitable for the intended applications.

Fig. 1 Proposed 2-DOF omni-wheel based layouts



2 Proposed Layouts of 2-DOF Translating Robots

The authors propose two layouts, as illustrated in Fig. 1. The omni-wheels have rollers on their circumference which are perpendicular to the axis of rotation of the hub, therefore, the axes of top and bottom rollers are parallel, unlike in Mecanum wheels [4]. When an omni-wheel is powered by a motor, the wheel exerts a force on the plus (which can be assumed to be a square rotated virtually by 45° about the vertical axis) shaped platform, similar to what a conventional wheel would have, i.e., it would be along the axis of the bottom-roller. Hence, Type-X (of Mecanum wheel layout) is equivalent to the layout shown in Fig. 1a. Similarly, Type-O equivalent layout is shown in Fig. 1b. This understanding is then used to differentiate between the configurations, and therefore, perform the force analysis. Both the proposed layouts are provided with two wheels which are coupled to motors, and hence referred to as active wheels, and two passive wheels are provided to support the platform. Their positions and orientation ensure that the platform looks symmetric when looked from the above.

The wheels are labeled as T (Top), R (Right), B (Bottom), and L (Left). Here, both T and R are considered to be active whereas B and L are passive. Sample forces of the active wheels in both Type-X and Type-O layouts are shown using blue arrows. Another point to observe is that the line of action (LOA) of these forces intersect outside the plus-shape in case of a Type-X, whereas for the Type-O, they intersect at the center of the platform, which is consistent with the Mecanum wheel based Type-X and Type-O layouts, respectively [3].

3 Type-X Layout

In this section, the motion and dynamic analysis on a Type-X layout platform is reported. The applied force on the platform can be depicted using a blue colored arrow as shown in Fig. 2. The applied force can be considered as an equivalent force-moment system, where a parallel force with the same magnitude can be considered to be acting through the centroid of the platform and a moment with a magnitude of the

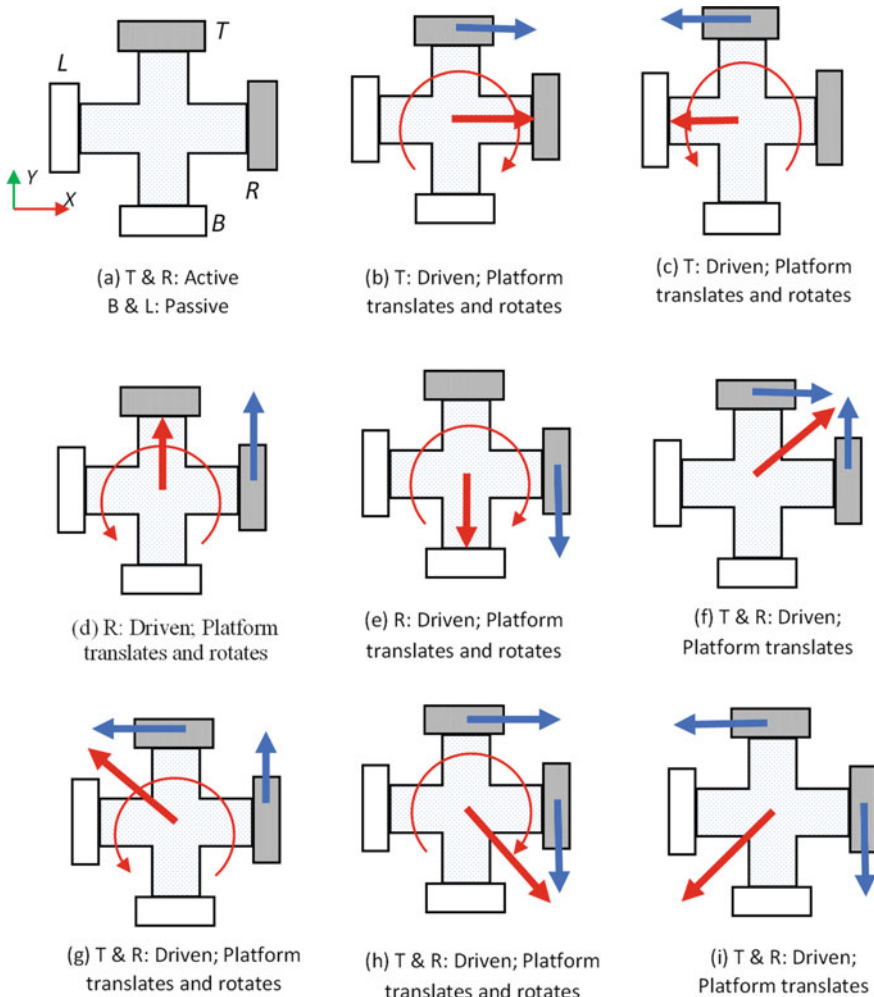


Fig. 2 Type-X mobile platform with two active omni-wheels

(force)*(perpendicular distance), acting along the vertical direction. The equivalent force-moment is shown in the red color.

The active wheels when not provided any input, do not cause any movement of the platform, as shown in Fig. 2a. When T is actuated with a force along $+X$ direction, the corresponding equivalent force-moment is illustrated in red color in Fig. 2b. Therefore, the platform has a tendency to move towards the right (when looked from the top) along $+X$ direction and also has a clockwise moment which causes a rotation of the platform, which may not be desired.

When T is actuated in the $-X$ direction, the force acting on the platform is depicted by the blue arrow as illustrated in Fig. 2c. The equivalent force that acts on the centroid

of the platform is shown by the red arrow and due to this, the platform translates in the $-X$ direction and also has a tendency to rotate in the anticlockwise direction when looked from the top. When R is actuated in the $+Y$ direction, the blue arrow indicates the force acting on the platform as shown in Fig. 2d. The red arrow depicts the equivalent force acting at the centroid of the platform. The platform tends to translate in the $+Y$ direction with a rotation in the anticlockwise direction about the Z axis.

The platform has a tendency to translate with a moment in the clockwise direction about the Z axis, when R is actuated in the $-Y$ direction, as illustrated in Fig. 2e. In Fig. 2f, both T and R are actuated to apply the forces as shown. The equivalent system through the centroid only has a resultant vector without any moment, which is the desired motion for pure translation. However, if the direction of the rotation of T is reversed, the applied force direction reverses, as shown in Fig. 2g. In this case, the equivalent system has a resultant force and moment at the centroid. Similarly, when the direction of R is reversed, as shown in Fig. 2h, translation of the platform, as well as moment in the clockwise direction, is observed. When T and R are actuated to obtain forces, as shown in Fig. 2i, a resultant force in the third quadrant (between $-X$ and $-Y$ axes) achieves pure translation. As the proposed plan is to achieve only translation of the platform without any yaw rotation (about Z axis), the scenarios in Fig. 2f and Fig. 2i are the only desired scenarios. Hence, Type-X configuration with only two actuated wheels is not a feasible solution. In literature, Type-X using omni-wheels is generally driven by four actuators and hence the moments get neutralized and a pure translation of the platform is possible, at the cost of two extra actuators.

4 Type-O Layout

The limitations in the Type-X configuration can be overcome by aligning the wheels so that they are radially outward along the $+X$, $+Y$, $-X$, and $-Y$ axes. This configuration is referred to as Type-O and is shown in Fig. 3a. The actuation of the R results in the force acting on the platform in blue color, shown in Fig. 3b. Since this force passes through the origin of the platform, there is no moment caused due to it, and hence the force can be repositioned at the origin and acting in the same direction. Thus, the platform moves in the direction of $+X$. Similarly, when R is actuated in the opposite direction, the force is as shown in Fig. 3c, and the equivalent force acts on the platform in the $-X$ direction. The robotic platform translates in the $-X$ direction. When T is actuated, as seen in Fig. 3d, the blue color arrow represents the force acting on the platform. The equivalent force acts on the centroid of the platform as shown by the red arrow and this force tends to propel the platform in the $+Y$ direction. The opposite effect is seen when the force is reversed, as illustrated in Fig. 3e, and the platform moves in the $-Y$ direction due to the equivalent force acting at the centroid of the platform. For the actuation of T and R in Fig. 3f the forces pass through the origin and the resultant force causes the platform to move in the diagonal direction in the first quadrant (between $+X$ and $+Y$ axes). If the direction of the R is reversed, the resultant force

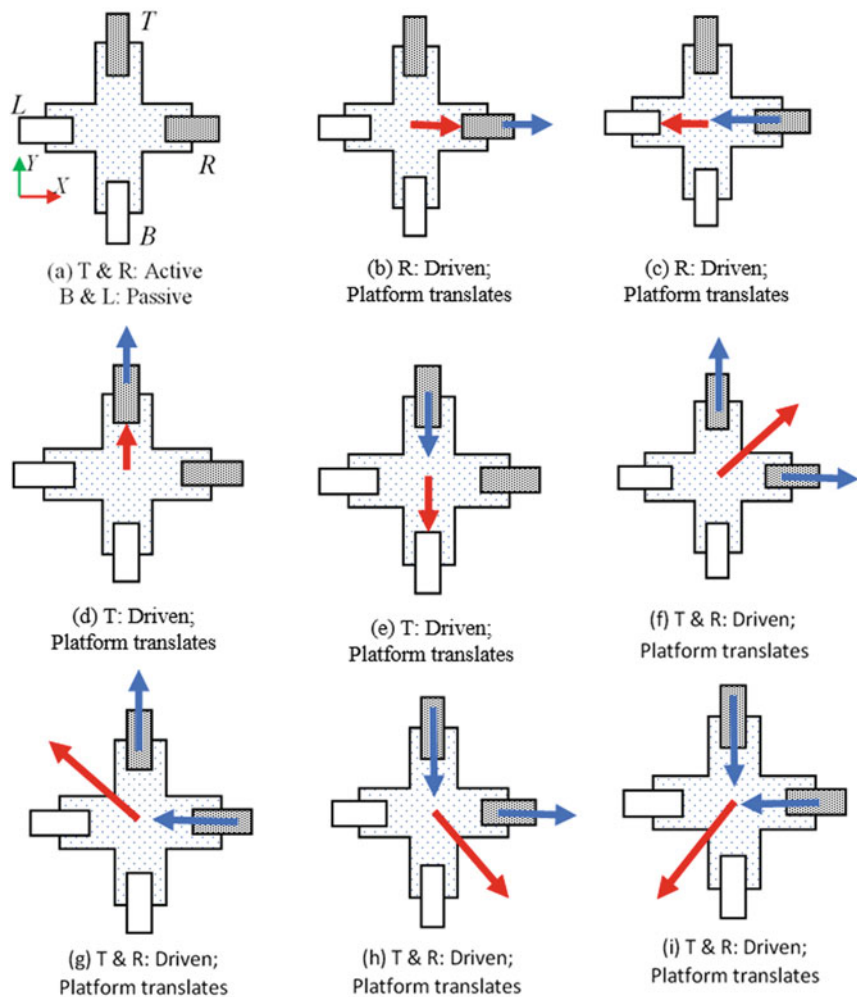


Fig. 3 Type-O mobile platform with two active omni-wheels

is along the diagonal in the second quadrant (between $+Y$ and $-X$ axes) and the platform moves in that direction (Fig. 3g). The resultant force acts along the diagonal in the fourth quadrant (between $+X$ and $-Y$ axes), when the forces are in the directions as illustrated in Fig. 3h. The robotic platform translates in the direction of the diagonal in the third quadrant, when the traction forces, as shown in Fig. 3i act on the robotic platform. Thus, proving that Type-O is the ideal platform for 2DOF applications.

5 Simulation in V-REP

The Coppelia robot simulator also known as V-REP, is centered on a distributed control architecture. V-REP, the Virtual Robot Exploration Framework, has the capability to model, modify, program, and simulate a robot. The robot could be of serial or parallel architecture with fixed or moving base. Similarly, mobile robots can be simulated with much ease. In the work carried out and reported in this paper, the academic version of V-REP, available for free, has been used.

Firstly, a virtual model of a robot has to be modeled in any 3D CAD design software according to the required dimensions. Thereafter, the assembled model has to be exported in the CAD software as '*stl*' format. The files are then imported in V-REP by selecting 'File-Load Model-Browse-Saved.*stl* file'. For the proposed robots, similar steps were carried out in Autodesk Inventor software. The characteristics of the body and the wheels are set, which is reported in detail in [5], another work by the same authors. V-REP automatically detects the wheels in the model, giving the wheels the dynamic nature of the revolving joint between the body and the wheels. LUA Script, which is the default scripting language in V-REP, was used to write the program to provide input motions to the motors or wheels. When the program was executed, the virtual model moved, based on the solver that was available in the V-REP software. The virtual model of the Type-X and Type-O layout robots modeled in Autodesk Inventor and later imported in V-REP are shown in Figs. 4 and 5, respectively.

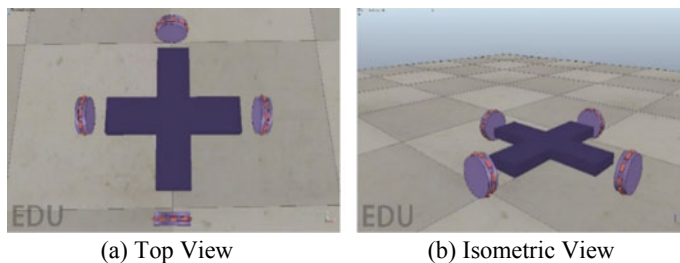


Fig. 4 Model of Type-X layout robot in V-REP

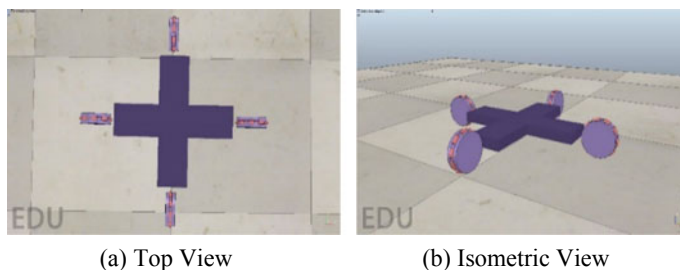


Fig. 5 Model of Type-O layout robot in V-REP

For the motion, plots are available in V-REP software. The plots as illustrated in Fig. 6, show the trace of the path of the virtual models when X v/s Y is plotted to understand the translation of the platform and yaw v/s time is plotted to understand the change in the orientation. Yaw angle is an inbuilt data stream present in V-REP. The data of the simulated motions obtained in V-REP was exported to a.csv file and then imported into MATLAB software to draw multiple plots together for easier comparison. The data denotes the relative position and orientation of the Center of Gravity (CG) of the object at an instant of time. In Fig. 6, the left block shows the X – Y plot for the forward motion of Type-X platform, Type-O, and the ideal or desired motion. It is observed that the Type-X plot is nearly straight up to a certain distance and then deviates due to the change in orientation as observed by the variation in the yaw v/s time plot, in the right block. The forward motion of the Type-O platform is observed to be linear as the orientation of the platform remains almost constant during the movement.

The yaw v/s time plot of the rightward motion of the Type-X platform shows much more variation than Type-O, which validates that there is orientation change during translation as illustrated in Fig. 7a. The plots for forward-right motion (first quadrant diagonal), as shown in Fig. 7b, are close to the ideal translatory motion. Figure 7c, shows the plots for forward-left motion (second quadrant diagonal), where it is observed that Type-X does not translate entirely but rotates significantly as seen in the yaw v/s time plot. Upon examination of the graphs, it can be concluded that

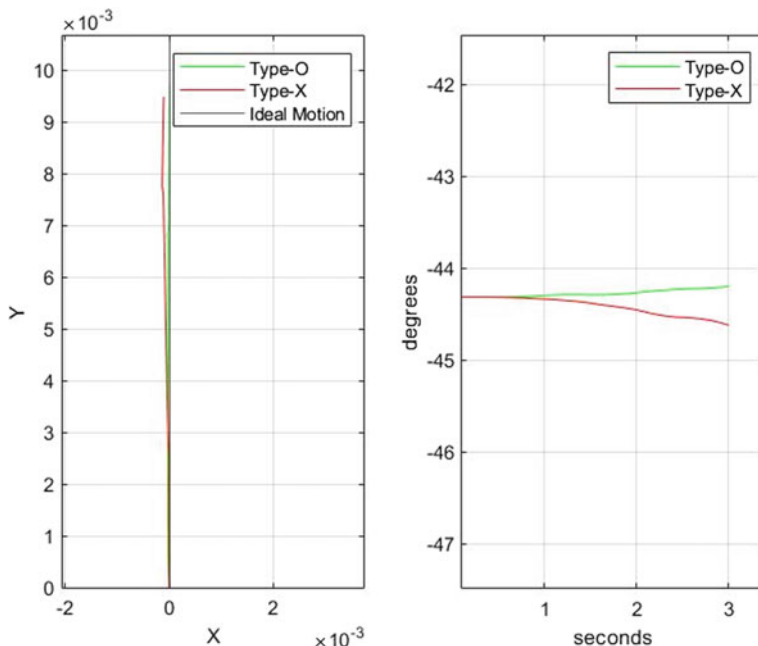


Fig. 6 Forward motion for Type-X and Type-O robots

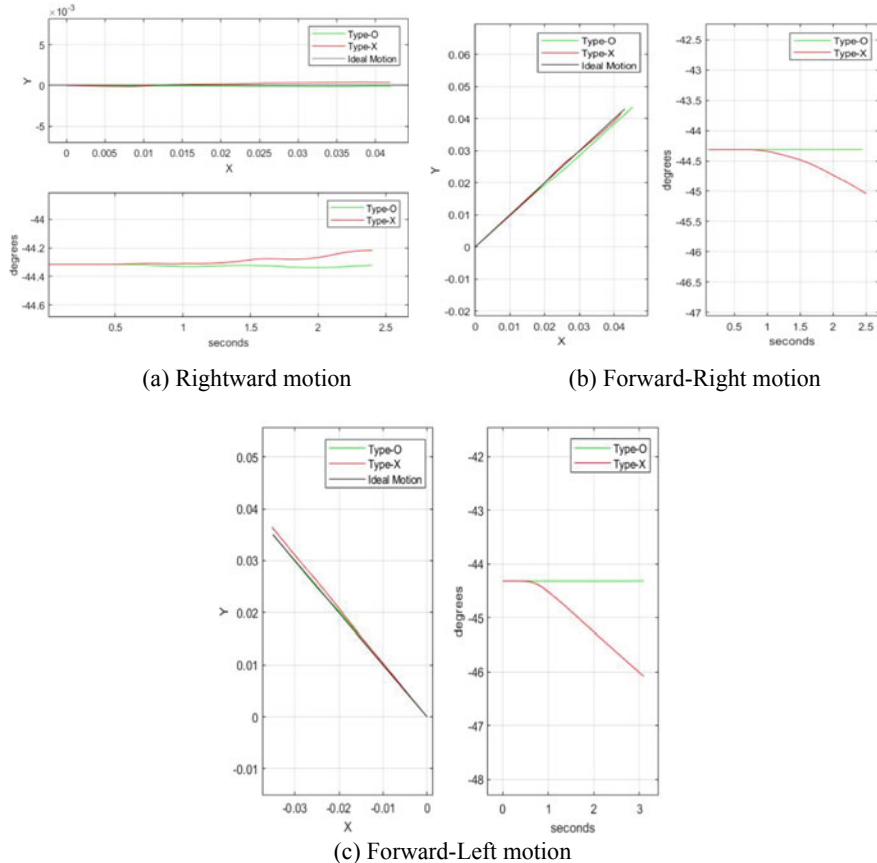


Fig. 7 Plots for the simulation in V-REP for various motion

Type-O is the preferred choice for achieving 2-DOF motion as proposed by the authors. There is a slight deviation in the Type-O from the ideal or desired trajectory, which could be due to approximation in an ‘stl’ file, which was used for wheels.

6 Physical Prototype

The prototype for Type-X was developed by the authors as shown in Fig. 8a. For the platform, plywood was used and four omni-wheels from Nex Robotics (online portal that sells robotics components) were mounted on the platform. When looked from top, the right and the front wheels were considered as active wheels and were coupled to DC motors, which, in turn, were powered by a 12-V battery. The other two wheels are free to rotate about their axes and hence are passive and provide



Fig. 8 Physical prototypes of the proposed 2-DOF translating mobile robots

only support and take the load. Motor driver (L298N) was used to power the motors and the control of the motors was commanded from an Arduino microcontroller. For easier control of the prototype, Bluetooth module (HC-05) was used to command the motor rotation. Further details about the specifications of the motors, driver circuits, etc., are given in [5], a related work by the authors of this paper, on the development of a 3 omni-wheel robot platform.

Type-X prototype was tested for translation in all directions. The sideways and front-back motion had a slight rotation of the yaw angle, hence the platform rotated about its vertical axis. However, for two diagonal motion (equivalent to Right-Front and Left-Back in Fig. 2), the platform translated with negligible yaw rotation. For the other diagonal motions, considerable yaw rotation was observed in the prototype's motion, thus validating the formulation and simulation results.

Similarly, Type-O prototype was developed as shown in Fig. 8b. Again, the right and the front wheels were considered as the active ones and the other two as the passive ones. The components used in Type-X were used in the same way in this prototype as well. The motion mentioned in Fig. 3 for the Type-O was given as input and the motion of the platform was observed. There was a pure translation with negligible yaw rotation in all the possible scenarios. The undesired yaw rotation could be attributed to imperfections in the assembly of the robot. Thus, the authors propose that Type-O based layout can be used for 2-DOF translating robots that require strict translation. Care should be taking in the fabrication and assembly of the components such that the forces on the platform pass through the centroid of the platform.

7 Conclusion

The authors carried out an extensive literature review on mobile robots and Mecanum wheels to finally choose to work with omni-wheels to achieve 2-DOF translatory motion, without any rotation about its vertical axis. The proposed configurations namely Type-X and Type-O were formulated to have only two active wheels, supported by two more passive wheels. Both of these configurations were simulated in V-REP in order to understand the motion of the centroid of the robotic platform

over a time interval. The simulations also provided evidence that Type-O configuration achieved 2-DOF translatory motion only as suggested by the authors, whereas Type-X had yaw rotation in simulation. Physical prototypes were made and the simulation results were found to match in a real-world scenario. In the future, the authors plan to work on the prototype to perform various tests on the platform to check for the payload capacity and durability. The authors also want to use the robotic platforms for various applications such as integration with other robotic arms for pick and place operations. The authors hope that the proposed designs will be of great help in making future robotic platform applications cheaper and more efficient.

References

1. Muir, P.F., Neuman, C.P.: Kinematic modeling of wheeled mobile robots. *J. Robot. Syst.* **4**(2), 281–340 (1987)
2. He, C., Wu, D., Chen, K., Liu, F., Fan, N.: Analysis of the Mecanum wheel arrangement of an omnidirectional vehicle. *Proc. Inst. Mech. Eng. Part C: J. Mech. Eng. Sci.* **233**(15), 5329–5340 (2019)
3. Li, Y., Dai, S., Zhao, L., Yan, X., Shi, Y.: Topological design methods for Mecanum wheel configurations of an omnidirectional mobile robot. *Symmetry* **11**(10), (2019)
4. Pin, F.G., Killough, S.M.: A new family of omnidirectional and holonomic wheeled platforms for mobile robots. *IEEE Trans. Robot. Autom.**IEEE Trans. Robot. Autom.* **10**(4), 480–489 (1994)
5. Pasupuleti, D., Dannana, D., Maddi, R., Manne, U., Chittawadigi, R.G.: Intuitive control of 3 omni-wheel based mobile platform using leap motion. In: Congress on Intelligent Systems Proceedings, Virtual Conference (2020)
6. Shen, J., Hong, D.: OmBURo: a novel unicycle robot with active omnidirectional wheel (2020). [arXiv:2001.07856](https://arxiv.org/abs/2001.07856)

Kinematic Error Modeling of a Parallelogram Arm of the Delta Robot and Its Dimensional Optimization



Venkata Sai Prathyush Idumudi and Arshad Javed

1 Introduction

Parallel manipulators have been highly advantageous to their serial counterparts owing to factors like large workspace, high flexibility, high stiffness, better accuracy. As the demand for sophisticated industrial tasks increased the need to have a higher accuracy seemed very desirable, hence the need for research in the areas of error analysis and motion accuracy grew. Previous studies include the study of variation of positional error with respect to structural parameters, joint clearances, driver errors [1], variation in orientation error based on parallelogram configuration of the passive legs out of its plane [2], the study showing the influence of the pose error of the joints to be much higher than the dimensional error [3], influence of parallelism error on the motion accuracy [4], pose error analysis in parallel mechanisms due to joint clearance [5]. However, the influence of both the structural errors and joint clearance haven't been considered simultaneously. This paper shows the influence of both joint clearances and structural errors on the orientation error.

V. S. P. Idumudi (✉) · A. Javed

Department of Mechanical Engineering, Birla Institute of Technology and Science Pilani,
Hyderabad Campus, Hyderabad, India

e-mail: f20171320@hyderabad.bits-pilani.ac.in

A. Javed

e-mail: arshad@hyderabad.bits-pilani.ac.in

2 Kinematic Analysis

A manipulator is a kinematic chain of links with joints connecting the links. The chain is bound between the base at one end and an end effector at the other. The combination of the motion of each link is what results in the motion of the whole structure. Hence there is a need to provide the position and orientation of the end effector in order to manipulate an object in space. Mathematical equations are used in describing such motions of the delta robot and this area belongs to the family of forward and inverse kinematics.

2.1 Inverse Kinematics

To calculate inverse kinematics effectively and efficiently, the frame of reference was taken from the center of the base platform. This can be perceived as an equilateral triangle with side length ' p '.' For easier calculation, one of the three arm links was placed on the YZ plane. This implied that the X component does not need to be considered, thereby reducing a variable and hence the complexity of the calculation.

The joint B_1C_1 as seen Fig. 1 can rotate only in the YZ plane and can therefore form a circle in it. Unlike B_1 , a fixed joint, D_1C_1 can rotate freely relative to D_1 . This forms a sphere with the center at point D_1 with radius ' r_e '.

The intersection of the YZ plane and the sphere resulted in the formation of a circle with center point D'_1 , which is the projection of point D_1 on the YZ plane, and radius D'_1C_1 .

Point C_1 can now be perceived as the intersection of the two formed circles with known centres and radii. So if the position of C_1 in the coordinate system is known, the angle ϕ_1 can be found with simple geometry.

The delta robot's symmetry was taken to advantage in the calculation of the other two angles ϕ_2 and ϕ_3 . The process of calculation of ϕ_1 was repeated with a shift in

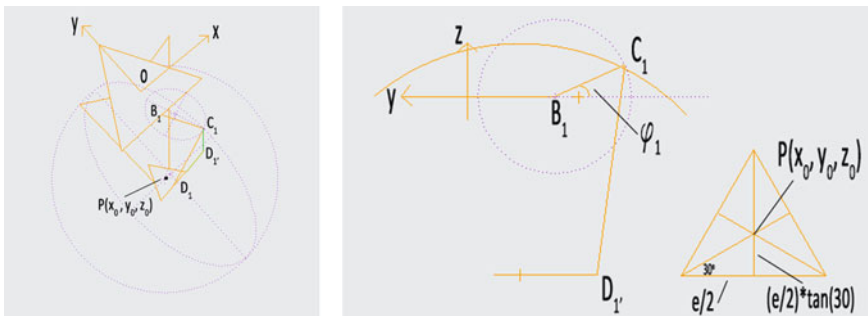


Fig. 1 Figures show the intersection of the sphere and the YZ plane (left) and dimensions of the mobile platform (right)

the {o} frame by +120 and -120 degrees, respectively. Below are the corresponding Eq. [6]:

$DD_1 = e/2\sqrt{3}$, where e represents the side length of the mobile platform triangle,

$$D_1 \rightarrow (0, y_0 - e/2\sqrt{3}, z_0) \quad (\text{Since } x_0 = 0)$$

$$D_1 D'_1 = x_0 = D'_1 C_1 = \sqrt{(r_e^2 - x_0^2)}$$

$$F_1 \rightarrow (0, -p/2\sqrt{3}, 0)$$

$$(y_{C1} + p/2\sqrt{3})^2 + z_{Cl}^2 = r_p^2 \quad (1a)$$

$$(y_{C1} - y_0 + e/2\sqrt{3})^2 + (z_{C1} - z_0)^2 = r_e^2 - x_0^2 \quad (1b)$$

$$\phi_1 = \arctan(z_{Cl}/(y_{B1} - y_{Cl})) \quad (1c)$$

2.2 Forward Kinematics

The motor encoders give the angular position of the motors from which the position of the end effector can be calculated. A mathematical way to find the end effector position is by calculating the intersection of three sphere equations, where the origin point of the spheres is determined by the dimensions of the upper arms and the angular position of motors.

The forward kinematics can provide the end effector triangle center for the given three angles. This is then formulated in a set of three coupled quadratic equations that must be solved simultaneously.

Now the three joint angles ϕ_1 , ϕ_2 , and ϕ_3 are known, and the coordinates (x_0, y_0, z_0) of end effector point P need to be found out. Since ϕ_1 , ϕ_2 and ϕ_3 are known, the coordinates of points C_1 , C_2 and C_3 can be calculated easily.

Joints $C_1 D_1$, $C_2 D_2$ and $C_3 D_3$ rotate freely around points C_1 , C_2 and C_3 , respectively, forming three spheres with radius r_e .

Next, the centers of the spheres were moved from points C_1 , C_2 and C_3 to the points C'_1 , C'_2 and C'_3 using transition vectors $D_1 P$, $D_2 P$ and $D_3 P$, respectively. After this transition, all three spheres intersect at a single point: P, as shown in Fig. 2.

The coordinates of points C_1 , C_2 and C_3 are taken as (x_1, y_1, z_1) , (x_2, y_2, z_2) and (x_3, y_3, z_3) . Note that $x_0 = 0$.

$$C'1 \rightarrow (0, -(p - e)/2\sqrt{3} - r_p \cos(\phi_1), -r_p \sin(\phi_1))$$

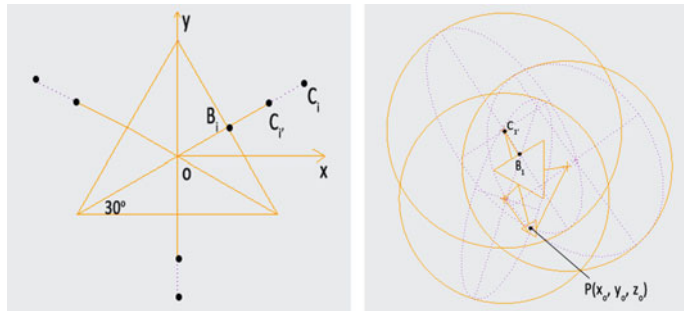


Fig. 2 Illustrations show the displacements of point C_i (left) and the intersection of the 3 spheres (right)

$$\begin{aligned} C'2 &\rightarrow \left(\left((p - e)/2\sqrt{3} + r_p \cos(\phi_2) \right) \cos(30), \left((p - e)/2\sqrt{3} + r_p \cos(\phi_2) \right) \sin(30), -r_p \sin(\phi_2) \right) \\ C'3 &\rightarrow \left(\left((p - e)/2\sqrt{3} + r_p \cos(\phi_3) \right) \cos(30), \left((p - e)/2\sqrt{3} + r_p \cos(\phi_3) \right) \sin(30), -r_p \sin(\phi_3) \right) \end{aligned}$$

The equations are as follows [6]:

$$x^2 + y^2 + z^2 - 2y_1y - 2z_1z = r_e^2 - y_1^2 - z_1^2 \quad (2a)$$

$$x^2 + y^2 + z^2 - 2x_2x - 2y_2y - 2z_2z = r_e^2 - x_2^2 - y_2^2 - z_2^2 \quad (2b)$$

$$x^2 + y^2 + z^2 - 2x_3x - 2y_3y - 2z_3z = r_e^2 - x_3^2 - y_3^2 - z_3^2 \quad (2c)$$

Now let $w_i = x_i^2 + y_i^2 + z_i^2$

$$x_2x + (y_1 - y_2)y + (z_1 - z_2)z = (w_1 - w_2)/2 \quad (3a)$$

$$x_3x + (y_1 - y_3)y + (z_1 - z_3)z = (w_1 - w_3)/2 \quad (3b)$$

$$(x_2 - x_3)x + (y_2 - y_3)y + (z_2 - z_3)z = (w_2 - w_3)/2 \quad (3c)$$

Here $(3a) = (2a) - (2b)$, $(3a) = (2a) - (2c)$ and $(3c) = (2b) - (2c)$. Subtracting Eq. (3b) from (3a) results in

$$x = m_1z + n_1; y = m_2z + n_2 \quad (4)$$

where

$$m_1 = (1/d)[(z_2 - z_1)(y_3 - y_1) - (z_3 - z_1)(y_2 - y_1)]$$

$$m_2 = (1/d)[(z_2 - z_1)x_3 - (z_3 - z_1)x_2]$$

$$n_1 = (1/d)[(w_2 - w_1)(y_3 - y_1) - (w_3 - w_1)(y_2 - y_1)]$$

$$n_2 = (1/d)[(w_2 - w_1)x_3 - (w_3 - w_1)x_2]$$

$$d = (y_2 - y_1)x_3 - (y_3 - y_1)x_2$$

Substituting (4) in (2a)

$$(m_1^2 + m_2^2 + 1)z^2 + 2(m_1 + m_2(n_2 - y_1) - z_1)z + (n_1^2 + (n_2 - y_1)^2 + z_1^2 - r_e^2) = 0 \quad (5)$$

Upon solving Eq. (5), the z coordinate is obtained. To find out x & y, z was substituted in Eq. (4). Finally, the point (x, y, z) was achieved.

2.3 Dimensional Optimization

Dimensional optimization and synthesis is an important aspect that needs to be considered while designing any manipulator. It is because the efficiency of such robots is highly sensitive toward their geometry. Among the kinematic model parameters taken into consideration, the robot workspace is one of the most important indices in the design of such robots.

So, to achieve a good workspace model, the robot's design parameters must be considered, especially those that can influence the geometry of the design. Such parameters must be optimized according to a certain goal, which in our case is maximizing the workspace volume. But maximizing the workspace alone does not necessarily optimize the design. This is due to the various undesirable kinematic/dynamic performance within the workspace. Hence, a better optimization includes stiffness analysis, kinematic and dynamic parameters like Jacobian matrix homogenization, singularity analysis, index of kinematic entropy and index of dynamic entropy, as performed in [7]. These parameters haven't been here considered due to time constraints.

Further, the maximum workspace of the robot can be defined as the region that can be reached by the center point of the movable platform within the maximum and minimum values of all the joint angles. The plot of such a workspace would resemble a parabolic cone with irregular surfaces as shown in Fig. 3.

Practical operations using such robots require a more regularly shaped workspace like cuboid, cube or cylinder. So, while optimizing, the regularly shaped workspace



DIMENSIONAL OPTIMIZATION ALGORITHM
 Step1: Solve equations (2), (3), (4) & (5),
 Step2: Proceed to find the value of z_i ,
 Step3: Define $R = \sqrt{(m_1 z + n_1)^2 + (m_2 z + n_2)^2}$,
 Step4: Using *paretosearch* minimize the value of R with respect to the desired ranges (upper and lower limit) of the geometric link lengths and iterating 200 times

Fig. 3 Shape of the workspace volume (left) and optimization procedure (right)

Table 1 Results of optimization

	Base triangle radius (m)	Moving platform radius (m)	Driver arm length (m)	Connecting arm length (m)
Before optimization	0.64	0.1	0.4	0.8
After optimization	0.5	0.15	0.334	0.6

is maximized rather than the irregularly shaped ones. It is possible to obtain a regular form of the workspace. Considering a cylinder, it can be achieved by forming a circle equation $x^2 + y^2 = R^2$ perpendicular to z (Vol. Of cylinder = $\pi R^2 z$). Inside this cylinder, a parallelopiped (when robot is used for machining applications) of volume $2R^2 z$ can be prescribed. The goal of the optimization is maximizing 'r', which in turn means maximizing the workspace volume.

Also, the optimization included a set of constraints on the link lengths and the angles included in the model. These constraints basically set the maximum permissible values of the above-mentioned parameters. The optimized values of these geometric parameters were found out among those satisfying the constraints and also returning larger values of workspace volume simultaneously. The optimization was carried out in MATLAB using the *paretosearch* function owing to its ability to optimize multi-objective functions (Table 1).

3 Error Modeling

Error modeling refers to the method of establishing a relation between the pose errors in the end effector and the geometric errors present within the mechanism to provide kinematic calibration to help improve the accuracy of the design.

3.1 Differential Vector Method

This method is used in studies related to the sensitivity of the pose of the manipulator to geometric and design variations especially those occurring in the parallelogram

arm. An interesting advantage of this method is the ability to separate the parameters causing the orientation error of the end effector from the ones responsible for the positional error.

In Fig. 4a, $\{O\}$ is placed as the reference frame. $\{B_i\}$ represents the frame attached to the driver unit, where b_i is the nominal position, δb_i is the error vector and θ_{Bi} is the attitude error of the $\{B_i\}$ relative to $\{O\}$. Similarly, $\{C_i\}$ is placed at the knee of the manipulator and on the horizontal axis connecting the two joints of the parallelogram arm. The distance between $\{B_i\}$ and $\{C_i\}$ is given by L_1 and unit vector u_i with the error vector being $\delta(L_1 u_i)$. The shorter link of the parallelogram has a length t and an error δc_i which is shared equally on either side of $\{C_i\}$. The orientation error of $\{C_i\}$ relative to $\{B_i\}$ is denoted by θ_{Ci} . The longer side of the parallelogram has a length L_2 and an error vector $\delta(L_2 w_i)$, where w_i is the direction vector. Next $\{D_i\}$ is placed on the movable platform, but is also placed in a manner similar to $\{C_i\}$. It is also located at the midpoint of the shorter side of the parallelogram with an error vector δd_i and an attitude error θ_{Di} relative to $\{P\}$. Now $\{P\}$ is located at the center of the movable platform and has a nominal position r_0 with respect to $\{O\}$ and has an orientation error θ which could be simply written as $\delta\theta_z$ since the degrees of freedom restricts rotation in x and y direction.

Apart from geometric errors, another major source that can affect the pose of the end effector is joint clearance. The error motions that arise due to the joint clearance mainly influence the end effector pose. A revolute pair with joint clearance has 6-DoFs and hence has 6 twists associated with it. Among these 6 twists, only one causes the desired motion while the other 5 result in error motions. The five error motions comprise of $\Delta_1, \Delta_2, \Delta_3$ that represent infinitesimal error translations in x, y, z directions and ϕ_1, ϕ_2 represent the infinitesimal rotational error about x, y axes considering the desired rotation to be about the z-axis. The set of constraints for calculating the bounding values error motions is given in Eq. (2) of [5].

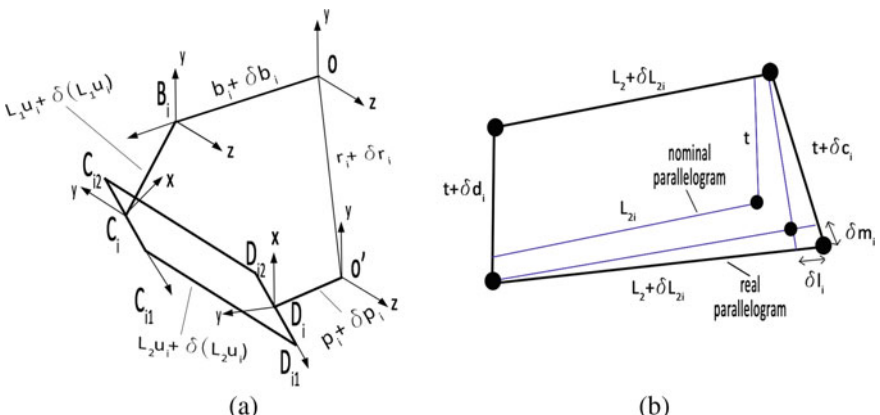


Fig. 4 a Represents the geometric model for a single leg, b parallelism error

In this article Δ_{Ci} , Δ_{Di} and Δ_{ij1} , Δ_{ij2} represent the translation error motion of joints at the joints C_i , D_i and C_{ij} , D_{ij} , respectively, and hence are 3×1 vectors that contain error motions in x , y , z directions. ϕ represents the rotational error motions of the joints about x , y axes and since these values are infinitesimally small they can be directly added to the attitude error at the joint position.

3.2 Error Mapping Function

To formulate the error mapping function, a closed-loop chain of a single leg is considered [8]. This kinematic chain consists of various design parameters in their vectorial form. The chain is $O-B_i-C_i-C_{ij}-D_{ij}-D_i-P$. The points O , B_i , C_i , C_{ij} , D_{ij} , D_i , P are represented by the coordinates \mathbf{o} , \mathbf{b}_i , \mathbf{c}_i , \mathbf{c}_{ij} , \mathbf{d}_{ij} , \mathbf{d}_i , \mathbf{p} .

In the below loop closure Eq. (6), \mathbf{R}_i is the rotational transformation matrix from R_{Bi} to R_o frame with angle = 0° , 120° , 240° for $i = 1, 2, 3$, respectively.

$$\begin{aligned} \mathbf{r}_i + \delta\mathbf{r}_i &= R_i(b_i + \delta b_i) + R_i R(\theta_{Bi})\{(L_{1i}u_i + \delta L_{1i}u_i + L_{1i}\delta u_i) + \Delta_{Ci} + E(j)R(\theta_{Ci})(t/ \\ &\quad 2 + \delta c_i/2 + \Delta_{ij1})e1\} + \mathbf{R}(\phi_i)(\mathbf{L}_{2i}v_i + \delta \mathbf{L}_{2i}v_i + \mathbf{L}_{2i}\delta v_i) - \\ &\quad \mathbf{R}_i \mathbf{R}(\theta)(\mathbf{p} + \delta \mathbf{p}) + \Delta_{Di} + \\ &\quad E(j)\mathbf{R}(\theta_{Di})(t/2 + \delta d_i/2 + \Delta_{ij2})e1 \} \end{aligned} \quad (6)$$

Here, $\mathbf{R}(\theta_{Bi}) = [I_3 + \delta\theta_{Bi} \times]$ where I_3 is the 3×3 unit matrix and $\delta\theta_{Bi} = [\delta\theta_{Bxi}, \delta\theta_{Byi}, \delta\theta_{Bzi}]^T$ represent the attitude error matrix. Also, $\mathbf{R}(\theta^*) = [I_3 + (\delta\theta^*_i + \delta\phi^*_i) \times]$ is also an attitude error matrix but additionally include the rotational joint error motions.

$$(\theta^* = \theta_{Ci}, \theta_{Di}, \delta\phi_i^* = [\delta\phi_{xi}^*, \delta\phi_{yi}^*, 0]^T)$$

Further, $E(j) = (-1)^j$ where $j = 1, 2$ and $e1 = [0, 0, 1]^T$.

Next, the variables associated with the nominal Eq. (7), which is represented by

$$\mathbf{r}_i = \mathbf{R}_i(\mathbf{b}_i + \mathbf{L}_{1i}u_i + \mathbf{p}) + \mathbf{L}_{2i}v_i \quad (7)$$

are removed from the loop closure equation with errors. This results in an Eq. (8) consisting of small perturbations given below:

$$\begin{aligned} \delta\mathbf{r}_i &= \mathbf{R}_i\delta\mathbf{b}_i + \mathbf{R}_i\delta\mathbf{L}_{1i}u_i + \mathbf{R}_i\mathbf{L}_{1i}\delta u_i + \delta\mathbf{L}_{2i}v_i + \mathbf{L}_{2i}\delta v_i + \mathbf{R}_i\mathbf{L}_{1i}[\delta\theta_{Bi} \times u_i] + \\ &\quad \mathbf{R}_i\mathbf{E}(j)(t/2)[\delta\theta_{Bi} \times e1] + \mathbf{R}_i\mathbf{E}(j)(t/2 + \delta c_i/2 + \Delta_{ij1})e1 + \mathbf{R}_i\mathbf{E}(j)(t/2) \\ &\quad [\delta\theta_{Ci} \times e1] + \mathbf{R}_i\mathbf{E}(j)(t/2)[\delta\phi_{Ci} \times e1] + \mathbf{L}_{2i}[\delta\phi_i \times v_i] - \mathbf{R}_i\delta\mathbf{p} \\ &\quad - \mathbf{R}_i\mathbf{E}(j)(t/2 + \delta d_i/2 + \Delta_{ij2})e1 - \mathbf{R}_i\mathbf{E}(j)(t/2)[\delta\theta_{Di} \times e1] - \mathbf{R}_i\mathbf{E}(j)(t/2) \\ &\quad [\delta\phi_{Di} \times e1] - \mathbf{R}_i\delta\theta_z\mathbf{p} - \mathbf{R}_i\mathbf{E}(j)(t/2)[\delta\theta_z \times e1] + \mathbf{R}_i\delta\theta_{Bi}\Delta_{Ci} - \mathbf{R}_i\delta\theta_z\Delta_{Di} \end{aligned} \quad (8)$$

The above equation is then multiplied by v_i^T on both sides and making use of the circularity of hybrid product gives us Eq. (9):

$$\begin{aligned}
 v_i^T \delta \mathbf{r}_i = & \mathbf{R}_i v_i^T \delta \mathbf{b}_i + \mathbf{R}_i v_i^T \delta \mathbf{L}_{1i} u_i + v_i^T \mathbf{R}_i \mathbf{L}_{1i} \delta u_i + \delta \mathbf{L}_{2ij} + \mathbf{L}_{1i} [\mathbf{R}_i u_i \times v_i]^T \delta \theta_{Bi} + \\
 & \mathbf{E}(j)(t/2) [\mathbf{R}_i e_1 \times v_i]^T \delta \theta_{Bi} + v_i^T \mathbf{R}_i \mathbf{E}(j)(t/2 + \delta c_i/2 + \Delta_{ij1}) e_1 + \\
 & \mathbf{E}(j)(t/2) [\mathbf{R}_i e_1 \times v_i]^T \delta \theta_{Ci} + \mathbf{E}(j)(t/2) [\mathbf{R}_i e_1 \times v_i]^T \delta \phi_{Ci} + \mathbf{L}_{2i} \delta \phi_i - \\
 & v_i^T \mathbf{R}_i \delta \mathbf{p} - v_i^T \mathbf{R}_i \mathbf{E}(j)(t/2 + \delta d_i/2 + \Delta_{ij2}) e_1 - \mathbf{E}(j)(t/2) [\mathbf{R}_i e_1 \times \\
 & v_i]^T \delta \theta_{Di} - \mathbf{E}(j)(t/2) [\mathbf{R}_i e_1 \times v_i]^T \delta \phi_{Di} - v_i^T \mathbf{R}_i \delta \theta_z \mathbf{p} - \mathbf{E}(j)(t/2) [\mathbf{R}_i e_1 \times v_i]^T \delta \theta_z \\
 & + v_i^T \mathbf{R}_i \delta \theta_{Bi} \Delta_{Ci} - v_i^T \mathbf{R}_i \delta \theta_z \Delta_{Dj}
 \end{aligned} \tag{9}$$

Using which we can proceed with error separation and move into the orientation error mapping function.

3.3 Orientation Error Mapping Function

To obtain the previous equation in terms of orientation error, the term $\delta \mathbf{r}_i$ must be eliminated. This can be performed by subtracting the two equations that result from substituting the value of $j = 1, 2$ in Eq. (9). The reason this action can be performed is because between $\{\mathbf{C}_i\}$ and $\{\mathbf{D}_i\}$ the length error is equally shared on both sides.

$$t(\mathbf{R}_i e_1 \times v_i)^T \delta \theta_z = t(\mathbf{R}_i e_1 \times v_i)^T (\delta \theta_{Bi} + \delta \Psi_i + \delta \Gamma_i) + (\delta m_i + \Delta_i) v_i^T \mathbf{R}_i e_1 + \delta l_i \tag{10}$$

where, $\delta m_i = \delta c_i - \delta d_i$, $\delta \Psi_i = \delta \theta_{Ci} - \delta \theta_{Di}$, $\delta \Gamma_i = \delta \phi_{Ci} - \delta \phi_{Di}$, $\delta l_i = \delta \mathbf{L}_{2i1} - \delta \mathbf{L}_{2i2}$.
and

$$\Delta_i = \Delta_{il} - \Delta_{i2} = (\Delta_{i11} + \Delta_{i21}) - (\Delta_{i12} + \Delta_{i22}).$$

Hence, the above Eq. (10) can be converted into matrix form:

$$\begin{aligned}
 \Delta \theta &= \mathbf{J}_{\theta\theta} \boldsymbol{\varepsilon}_\theta, \text{ with} \\
 \boldsymbol{\varepsilon}_\theta &= (\boldsymbol{\varepsilon}_{\theta 1}^T, \boldsymbol{\varepsilon}_{\theta 2}^T, \boldsymbol{\varepsilon}_{\theta 3}^T)^T
 \end{aligned}$$

where $\boldsymbol{\varepsilon}_{\theta i} = (\delta l_i \quad (\delta m_i + \Delta_i) \quad (\delta \theta_{Bi} + \delta \Psi_i + \delta \Gamma_i))^T$

$$\mathbf{J}_{\theta\theta} = \mathbf{A}^{-1} \mathbf{B}$$

$$\mathbf{B} = \text{diag}[\mathbf{B}_i]$$

$$\mathbf{B}_i = [1 \ v_i^T \mathbf{R}_i e_1 \ t(\mathbf{R}_i e_1 \times v_i)^T]$$

$$\mathbf{A} = \begin{bmatrix} t(\mathbf{R}_1 e_1 \times \mathbf{V}_1)_T \\ t(\mathbf{R}_2 e_1 \times \mathbf{V}_2)_T \\ t(\mathbf{R}_3 e_1 \times \mathbf{V}_3)_T \end{bmatrix}$$

In the above equations, the relative length errors of the parallelogram are δl_i , $(\delta m_i + \Delta_i)$ (δl_i and δm_i are the parallelism errors) and the relative orientation error of {P} relative to {O} is $(\delta\theta_{Bi} + \delta\Psi_i + \delta\Gamma_i)$. It also has to be noted that the z-components of $(\delta\theta_{Bi} + \delta\Psi_i + \delta\Gamma_i)$ onto $(\mathbf{R}_i e_1 \times v_i)$ is zero since $(\mathbf{R}_i e_1 \times v_i) \perp \mathbf{R}_i e_1$. This implies that these z direction components of $(\delta\theta_{Bi} + \delta\Psi_i + \delta\Gamma_i)$ do not have any impact on the orientation error and hence can be removed. Thus, after eliminating the unnecessary parameters, the remaining thirty components are: δl_i , δm_i , Δ_{i1} , Δ_{i2} , $(\delta\theta_{Bi}, \delta\Psi_i, \delta\Gamma_i)_x$, $(\delta\theta_{Bi}, \delta\Psi_i, \delta\Gamma_i)_y$ for $i = 1-3$.

4 Conclusion

In this paper, the kinematics of a Delta Robot has been studied and the workspace volume has been optimized constrained to the dimensional parameters. Following which, the Differential Vector method was implemented to formulate the error mapping function, accomodating joint clearances as well. Using this the parameters affecting the orientation error were found in an analytical manner. The presented work will be helpful to design and simulate an accurate mechanism for the Delta robot.

References

1. Li, Y., Shang, D., Fan, X., Liu, Y.: Motion reliability analysis of the delta parallel robot considering mechanism errors. *Math. Probl. Eng.* (2019)
2. Chouaibi, Y., Chebbi, A.H., Affi, Z., Romdhane, L.: Analytical modeling and analysis of the clearance induced orientation error of the RAF translational parallel manipulator. *Robotica* **34**(8), 1898–1921 (2016)
3. Xu, D.T.: Kinematic reliability and sensitivity analysis of the modified delta parallel mechanism. *Int. J. Adv. Robot. Syst.* **15**(1), 1–8 (2018)
4. Li Y., Shang, D., Liu, Y.: Kinematic modeling and error analysis of Delta robot considering parallelism error. *Int. J. Adv. Robot. Syst.* **16**(5) (2019)
5. Meng, J., et al.: Accuracy analysis of general parallel manipulators with joint clearance. In: *Proceedings 2007 IEEE International Conference on Robotics and Automation*, pp. 889–894. Roma (2007). (10–14 Avril)
6. <https://filipposanfilippo.inspitivity.com/reports/sanfilippo-parrallel-delta-robot-iphone-accelerometer.pdf>
7. Kelaiaria, R., Company, O., Zaatri, A.: Multiobjective optimization of a linear delta parallel robot. *Mech. Mach. Theorem* **50**, 159–178 (2012)

8. Caro, S., Wenger, P., Bennis, F., Chablat, D.: Sensitivity analysis of the orthoglide: a three-DOF translational parallel kinematic machine. ASME. J. Mech. Des. **128**(2):392–402 (2006). <https://doi.org/10.1115/1.2166852>

Design and Control of Mobile Robots with Two and Four Independent Rotatable Power Wheels



Divyansh Khare, Kausadikar Varad Prashant, and Santhakumar Mohan

1 Introduction

The use of Automated guided Vehicles (AGVs) and Autonomous Mobile Robots (AMRs) has increased tremendously in recent years due to the upsurge of Industry 4.0. There is a need for robots that can intelligently act and cooperate with the human staff while being in the workplace. A great majority of these robots are needed for warehouse automation and shop-floor assistance tasks. These robots are expected to be capable of manoeuvering through the warehouse, picking and placing the packages and should be intelligent enough to be able to avoid any obstacles which may come in their path while they perform the operations. Though various such robots have been developed and deployed by companies like Amazon.Inc and others, the need for general purpose robots that can be deployed in almost all kinds of warehouse environments still remains unaddressed.

In this paper, we have tried to come up with a generalised design of a mobile robot that can be used either as an AGV or an AMR. A basic functional design has been created that is easy to manufacture and can be scaled as per use. The design has been equipped with independently rotatable power wheels, meaning the wheels have one steering axis and one power axis. The conventional AGVs and AMRs either rely on differential wheel drive for steering or are equipped with a synchro drive mechanism. Although the differential wheel drive does provide the steering, it

The work has been supported by ‘Ministry of Electronics and Information Technology, Government of India’.

D. Khare (✉) · K. V. Prashant · S. Mohan
Indian Institute of Technology, Palakkad 678557, Kerala, India
e-mail: divyanshkhare.99@gmail.com

K. V. Prashant
e-mail: varadk.2020@gmail.com

S. Mohan
e-mail: santhakumar@iitpkd.ac.in
URL: <https://iitpkd.ac.in/people/santhakumar>

requires the vehicle to turn about an axis which might not be possible in congested environments. Synchro-drive solves this problem, but as the wheels are steered by a single actuator, there are greater chances of failure. The independently rotatable power wheel drive utilises two motion inputs (steering + power) for each wheel, thus reducing the chances of failure. This is because, if one of the steering/power inputs fails, the inputs of other wheels can be adjusted such that the robot follows the required path. A scissors mechanism was also employed on the robot for adding payload lifting capabilities, which is very much required in warehouse operations. For the purpose of controlling a simple kinematic feed forward and feedback control scheme was used.

The paper starts from discussing the mechanical design of the robot in Sect. 2, where a few design iterations were made to obtain an optimum design moving to Sect. 3, discussing the system description and to Sects. 4 and 5 for looking at the inverse kinematics/feed forward control and the Kinematic control/Feedback control and the concluding remarks are made in Sect. 6.

2 Mechanical Model

2.1 *Mechanical Structure*

Two kinds of designs were analysed. The first design is a six wheeled robot with two independently rotatable power wheels (one power axis + one steering axis), while the rest four wheels were for stability and acted as the castor wheels maintaining a six point contact with the ground. The second design consisted of four independently rotatable power wheels, with no requirement of additional castor wheels as the structure forms a statically stable four point contact. A scissors mechanism was also added to both the designs so as to equip the robots with payload lifting capabilities. The design process was primarily split into two parts: chassis construction and wheel drive design.

2.2 *Major Design Considerations*

1. Dimensions: 500 mm × 300 mm × 200 mm
2. Payload capacity: 50 kg
3. Vehicle self weight: 25 kg
4. Ground clearance: Approximately 20 cm.

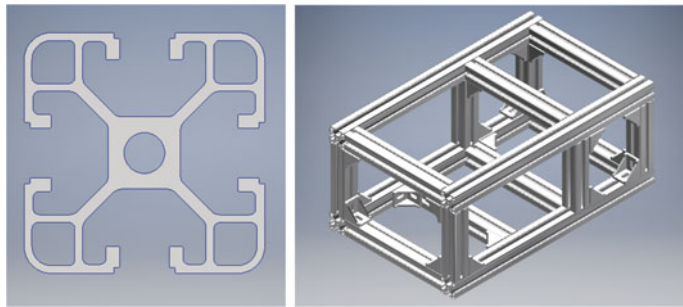


Fig. 1 Aluminium 4040 extrusion cross-section and the chassis

2.3 Chassis Construction

From the manufacturing perspective, it was decided that the chassis will be made using Aluminium 4040 extrusions (refer Fig. 1). This extrusion, as in the figure shown below, allows for construction by using T-nuts and bolts which can be slid into the openings in the extrusion. The chassis was designed in a manner that it leaves space for the internal mechanisms and the electronic components to be placed inside.

2.4 Wheel Drive Design

The wheel drive consists of powering and steering mechanisms for the wheel. To satisfy the design requirements, the robot should have a powered cum rotatable wheel drive mechanism. For this purpose, three design iterations were made to arrive at the final design, which is explained below.

Design iterations-Please refer Fig. 2.

1. Bevel gear design

- The wheel power was achieved by using a gear-train of spur gears with an effective gear ratio of 1. The gear-train consists of two gears with 24 teeth and one idler gear with 48 teeth. The steering action is performed by a set of bevel gears having 23 teeth each aligned at right angles with each other.
- The design is functional but is incapable of absorbing any shocks or vibrations that may arise due to the robot's motion. Also, all the shocks or vibrations will be transferred to the actuating elements, in this case, the motors and thus damaging them.
- It is also incapable of providing gear reduction for steering as the steering is usually done at low speeds considering the vehicle's stability.



Fig. 2 (From left to right) Bevel gear design, Spur gear design, Timing pulley-belt design

- Moreover, the bevel gears experience an axial force which tends to separate the two meshed gears and also makes the assembly more difficult.

2. Spur gear design

- This design replaces the bevel gear steering mechanism with a set of spur gears having a gear ratio of 3. This design mitigates the low-speed steering problem, as it provides a gear reduction and the axial separation problem of the previous design, but still is incapable of absorbing any shocks or vibrations.

3. Timing pulley-belt design

- In this design, both powering and steering action of the wheel is achieved by the means of timing belts and pulleys.
- This design mitigates both the problems faced in the earlier designs. It provides flexibility over the steering speed as a great range of speeds can be obtained by changing the pulley diameter. Also, it is capable of absorbing shocks or vibrations as the flexible belts help in absorbing them.

From these observations, it can be concluded that the timing pulley-belt design is the best suited for the wheel drive construction as it provides a scope for high-speed reduction and the flexible belt helps in absorbing the vibrations and thus preventing the actuators from any possible damage.

Power and Castor wheels A 100 mm diameter plastic wheels were used as the power wheels in the wheel drive for both, two and four independently rotatable power wheel robots, whereas, for the two independently rotatable power wheel robot, 125 mm diameter castor wheels were also used for supporting the overall structure forming a six point contact. Rectangular extrusions were made to align the castor wheels with the driving wheels and maintain the required ground clearance. These were made by using sheet metal bending.

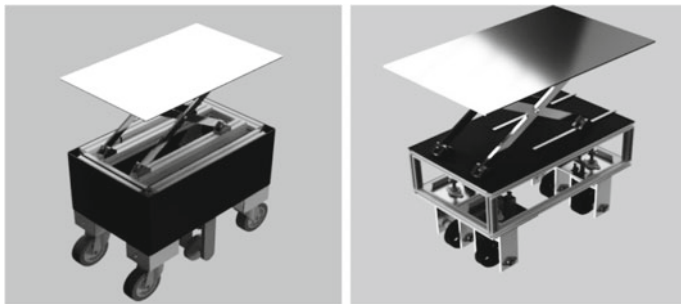


Fig. 3 Assembled two and four independently rotatable power wheel robot designs with scissors mechanism

2.5 *Lifting Mechanism*

For the purpose of equipping the robot with payload lifting capabilities, a scissors mechanism was designed and implemented on both the robots (refer Fig. 3). The mechanism utilises two adjacent sliders on the base and two adjacent sliders on the top panel placed directly over the base sliders so as to facilitate the motion. The mechanism is controlled by a linear actuator attached to the base of the machine or at the robot top.

2.6 *Final Design*

The final mechanical design of the mobile robot consists of the chassis, wheel drive arrangement and the lifting (scissors) mechanism. The robot model was covered with plastic/aluminium panels to protect the internal mechanisms and the electronics that will be placed. The end result provides two different kinds of robot models. One with two independently rotatable power wheels and the other with four independently rotatable power wheels both equipped with a scissors mechanism for lifting payloads. Following are the major components of the mechanical designs of both the robot models.

1. Aluminum 4040 extrusion sections
2. 125 mm diameter Castor wheels
3. Timing belts and pulleys
4. 100 mm diameter robot wheels
5. Corner brackets
6. Wheel drive frame
7. Plastic casing panels
8. Ball bearings (housed and angled)
9. Aluminium sheet cut-outs.

For the two independently rotatable power wheel design, the number of motion inputs required is less than that of the four independently rotatable power wheel design. The four independently rotatable power wheel design makes the robot less prone to failure as the number of controllable inputs is more. For example, if some of the inputs (steering/power) fail, the speeds and steering angles of the rest of the wheels can be adjusted to make the robot follow the required path. This safety against failure reduces in the two independently rotatable power wheel designs. Also, the two independently rotatable power wheel design requires additional four castor wheels for static stability. Also, the designs do require simple suspensions in the form of springs so as to maintain proper contact. The development of a sophisticated suspension system will be required in the case of rough grounds. The development of dedicated suspensions has been kept as a part of the future work.

3 System Description

The geometric description of Mobile robots with two and four independently rotatable power wheels is depicted as shown in the following figure (refer Fig. 4). Here an even terrain workspace is under consideration, thus at low acceleration (less than 5 m/s^2) the Degree of Freedom (DoF) is 3. The number of controllable inputs in the case of Two wheel mobile robot is 4 (two power + two steering input) similarly, in case of Four wheel mobile robot it's 8. Thus, in both the configurations, as the number of control inputs is greater than the Degree of Freedom, they are Holonomic/Omnidirectional system. Such a system is preferred as it provides the robot with the ability to move and follow the required path in case of one or more actuators failing. For example, in case of the two wheel mobile robot, even if the two steering inputs fail, the velocities of the wheels can still be adjusted allowing the robot to move in a differential wheel drive fashion. Similarly, in case of the four wheel robot with eight controllable inputs, even if two wheels fail (power and steering failure) the other two wheels can still provide control over the robot as the number of controllable inputs becomes four, keeping the system holonomic.

4 Inverse Kinematic Model/Feed Forward Control

In this section, Inverse kinematic model of the mobile robot system is discussed. Let a particular wheel of the Mobile robot be denoted by ‘ i ’ with wheel angular velocity denoted by ω_i , steering angle by θ_i and wheel radius by ‘ a_i ’. For two wheel mobile robot $i=1, 2$ and for Four wheel mobile robot it’s $i = 1, 2, 3, 4$. Where the velocities of each of the wheels can be expressed as

$$v_{ix} = a_i \omega_i \cos(\theta_i) \quad v_{iy} = a_i \omega_i \sin(\theta_i) \quad (1)$$

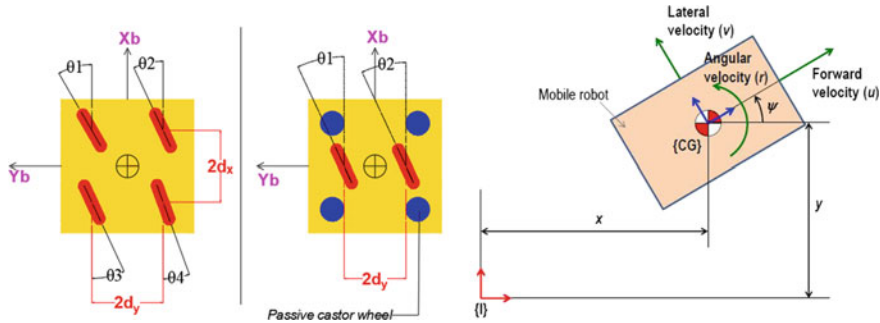


Fig. 4 (from left to right) Mobile robot configurations for Four wheel and Two wheel, and Kinematic model

Here, v_{ix} and v_{iy} are the components of i th wheel velocities in the forward and lateral directions respectively w.r.t the body/robot frame; u , v and r are the forward, lateral and angular velocities of the robot w.r.t the body/robot frame; x , y and ψ denote the Cartesian and angular positions of the robot respectively w.r.t ground frame and, d_x and d_y are the robot configuration parameters in X_b and Y_b direction in the body-fixed co-ordinate system.

Now referring to Mishra et al. [1] paper's equation no. 2, the following Inverse Kinematics relations are obtained which are used to map v_{ix} and v_{iy} with u , v , r and subsequently with \dot{x} , \dot{y} , $\dot{\psi}$ using the general relation between body fixed and ground fixed velocities.

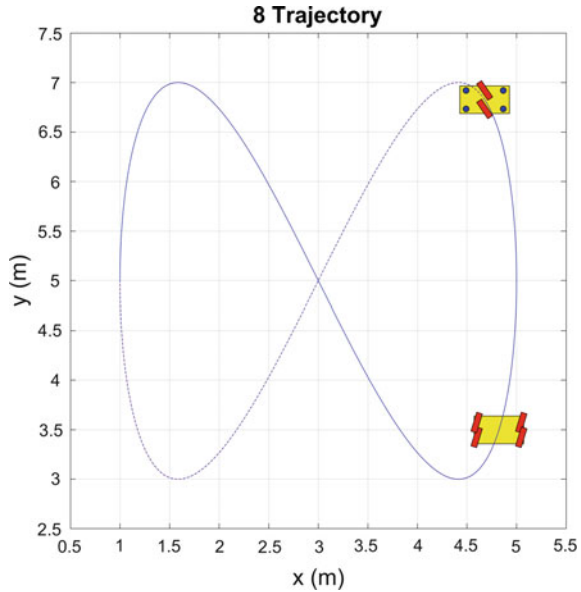
Inverse Kinematics Model for Four wheel Mobile Robot

$$\begin{pmatrix} v_{1x} \\ v_{1y} \\ v_{2x} \\ v_{2y} \\ v_{3x} \\ v_{3y} \\ v_{4x} \\ v_{4y} \end{pmatrix} = \begin{bmatrix} 1 & 0 & -d_y \\ 0 & 1 & d_x \\ 1 & 0 & -d_y \\ 0 & 1 & -d_x \\ 1 & 0 & d_y \\ 0 & 1 & -d_x \\ 1 & 0 & d_y \\ 0 & 1 & d_x \end{bmatrix} \begin{pmatrix} u \\ v \\ r \end{pmatrix} = \begin{bmatrix} 1 & 0 & -d_y \\ 0 & 1 & d_x \\ 1 & 0 & -d_y \\ 0 & 1 & -d_x \\ 1 & 0 & d_y \\ 0 & 1 & -d_x \\ 1 & 0 & d_y \\ 0 & 1 & d_x \end{bmatrix} \begin{pmatrix} \cos \psi & \sin \psi & 0 \\ -\sin \psi & \cos \psi & 0 \\ 0 & 0 & 1 \end{pmatrix} \begin{pmatrix} \dot{x} \\ \dot{y} \\ \dot{\psi} \end{pmatrix} \quad (2)$$

Inverse Kinematics Model for Two wheel Mobile Robot

$$\begin{pmatrix} v_{1x} \\ v_{1y} \\ v_{2x} \\ v_{2y} \end{pmatrix} = \begin{bmatrix} 1 & 0 & -d_y \\ 0 & 1 & 0 \\ 1 & 0 & d_y \\ 0 & 1 & 0 \end{bmatrix} \begin{pmatrix} u \\ v \\ r \end{pmatrix} = \begin{bmatrix} 1 & 0 & -d_y \\ 0 & 1 & 0 \\ 1 & 0 & d_y \\ 0 & 1 & 0 \end{bmatrix} \begin{pmatrix} \cos \psi & \sin \psi & 0 \\ -\sin \psi & \cos \psi & 0 \\ 0 & 0 & 1 \end{pmatrix} \begin{pmatrix} \dot{x} \\ \dot{y} \\ \dot{\psi} \end{pmatrix} \quad (3)$$

Fig. 5 The given eight-shaped desired trajectory (followed by the both robot)



5 Kinematic Control Design/Feedback Control

In this paper a simple Proportional control feedback system is employed which is explained as follows. As per the basic Inverse Kinematic relations:

$$\zeta = \mathbf{J}^{-1}(\boldsymbol{\eta})\dot{\boldsymbol{\eta}}_d \quad (4)$$

where, ζ are the control inputs or command velocities (u , v and r), $\boldsymbol{\eta}$ is the vector of actual position variables (x , y and ψ), $\dot{\boldsymbol{\eta}}_d$ is the vector of desired position variables and $\mathbf{J}(\boldsymbol{\eta})$ is the Jacobian or kinematic transformation matrix. For simple proportional feedback control (closed-loop control) we have:

$$\boldsymbol{\eta}_d(t) - \boldsymbol{\eta}(t) = e^{-\lambda t} \quad \Rightarrow \tilde{\boldsymbol{\eta}} = e^{-\lambda t} \quad \text{Here as: } t \rightarrow \infty \Rightarrow \tilde{\boldsymbol{\eta}} \rightarrow 0 \quad (5)$$

$$\text{Differentiating w.r.t time : } \dot{\boldsymbol{\eta}}(t) = \dot{\boldsymbol{\eta}}_d(t) + \lambda \tilde{\boldsymbol{\eta}}(t) \quad (6)$$

$$\Rightarrow \zeta = \mathbf{J}^{-1}(\boldsymbol{\eta})[\dot{\boldsymbol{\eta}}_d(t) + \lambda \tilde{\boldsymbol{\eta}}(t)] \quad (7)$$

Here, λ is the controller gain. For the purposes of simulation, the gain value or λ was set at 5. This is a combination of feedback and feed forward control and is called as ‘Computed velocity control’. Following is a profile in the shape of an ‘8’ (refer Fig. 5) which was used to simulate the performances of both the robots for a time

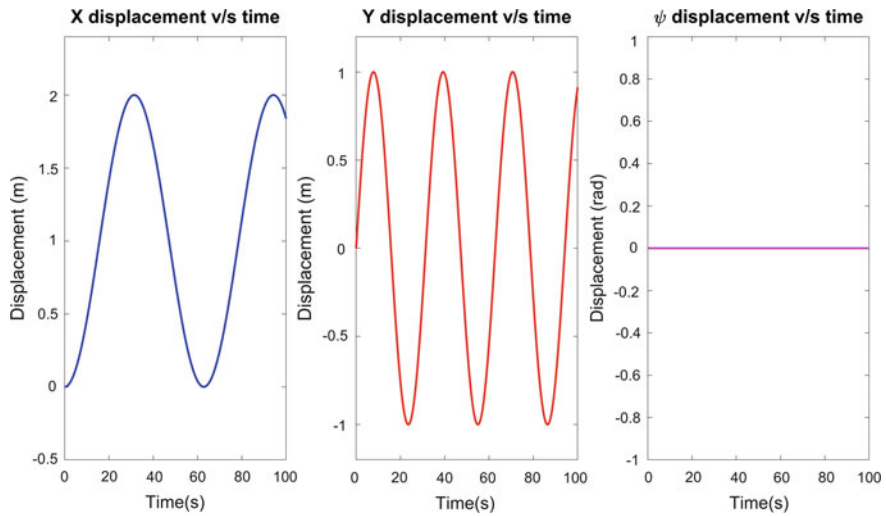


Fig. 6 Time trajectories of the generalised coordinates for the given eight-shaped trajectory

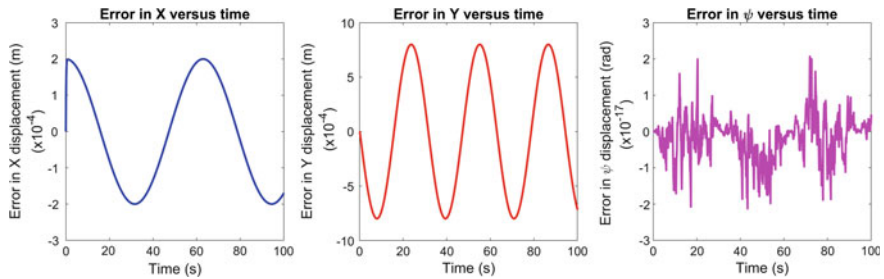


Fig. 7 Position error plots for the two independently rotatable power wheel design

period of 100s. The position, errors in the position and orientation were studied on the basis of the kinematic design (refer Figs. 6, 7 and 8) and the variations of the

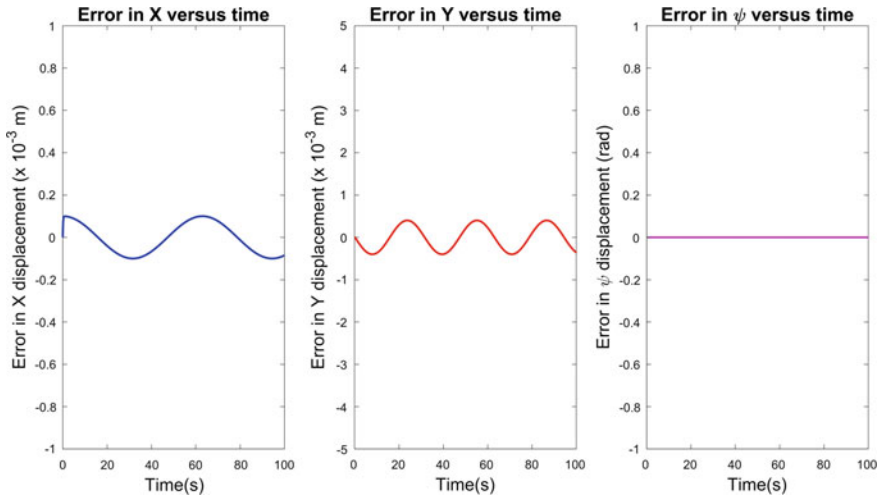


Fig. 8 Position error plots for the four independently rotatable power wheel design

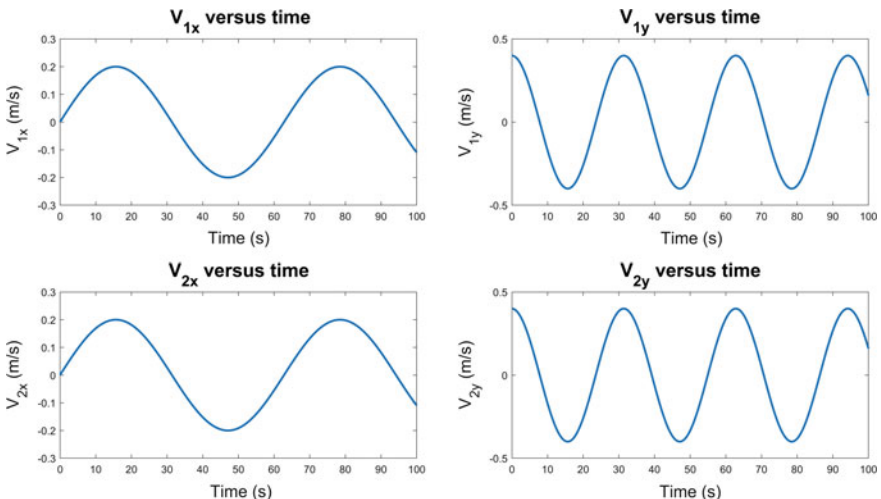


Fig. 9 Variation of wheel velocity components with time for the two independently rotatable power wheel design

velocity components with time were analysed (refer Figs. 9 and 10). The maximum angular velocities of the wheels in the two and four independently rotatable power wheel designs were 85.44 rpm and 42.72 rpm, respectively. It is important to note that the maximum wheel angular velocity in four wheel design is nearly half of that in the two wheel design, which can be justified by considering the number of power wheels in both the design.

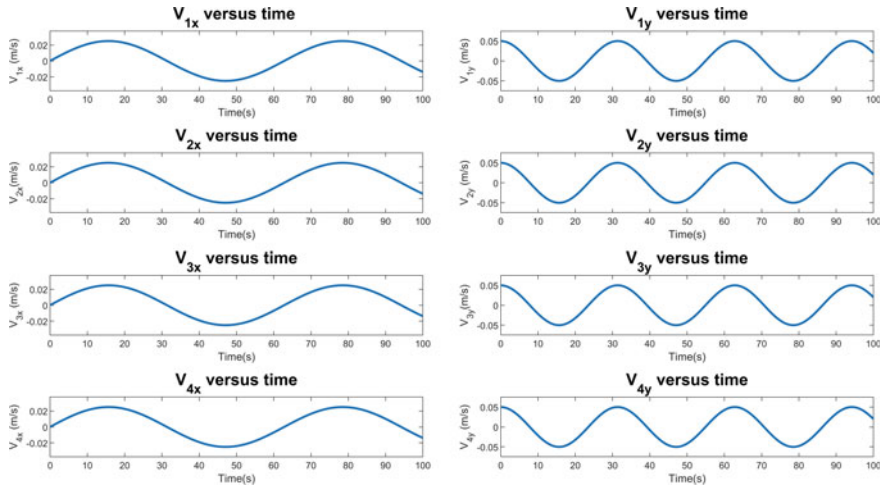


Fig. 10 Variation of wheel velocity components with time for the four independently rotatable power wheel design

6 Concluding Remarks

From the perspective of design for manufacturing and vibration absorption, the wheel drive with timing pulley-belt design was chosen along with Aluminium 4040 chassis and the castor wheels. The scissors mechanism was also added to both the robot designs. The final designs offer the user a higher degree of safety against failures. The above results show that the error in the position and orientation is small for the two independently rotatable power wheel design, but it is even less for the four independently rotatable power wheel design. Hence, the four independently rotatable power wheel design offers better control over position and orientation. It also provides a greater degree of control for the robot with the same control scheme. Moreover, the four independently rotatable power wheeled robot offers a higher safety against failure as compared to the two independently rotatable power wheeled design and provides the required stability to the robot by creating a four point contact but is more complex to analyse and implement, and thus mostly preferred for the outdoor environment. The two independently rotatable power wheeled design utilises four castor wheels to achieve the required stability and is simpler to analyse and implement and is best suited for the indoor environment.

This paper doesn't account for the transient behaviour of the system which comes into play because of the sluggish response from the mechanical drive train and the threshold value of actuator's angular speed and is left for future work along with the development of a sophisticated controller, fabrication of the robot and testing.

Reference

1. Mishra, S., Sharma, M., Mohan, S.: Behavioural fault-tolerant-control of an omni-directional mobile robot with four-mecanum wheels. Defence Sci. J. **69**(4), 353–360 (2019). <https://doi.org/10.14429/dsj.69.13607>

Analysis of a 4-DOF 3T1R Parallel Robot for Machining Applications: A Stiffness Study



Paulo Rossi, Roberto Simoni, and Andrea Piga Carboni

1 Introduction

Robots are increasingly present in industrial machining applications that require relatively low cutting forces. Activities such as trimming, drilling, and polishing on composite parts, likewise deburring, grinding, and milling on metal parts, belong to the tasks performed by such a robot. Similar to machine tools, machining robots can carry out multiple machining works, costing less than machine tools with the same workspace (WS) [11]. Further, a particular machine in this sector, referred to as parallel kinematic machine (PKM), has drawn academia and industry attention.

Traditional numerical control machines (CNCs) have serial topology structures. These topologies carry all the driving joints connected in a sequence, with the first joint lifting the one above it. This feature culminates in the accumulation of errors along with the joints and bounds of the whole machine's stiffness and dynamic performance [12]. The PKM counterpart has the fixed base connected toward the end-effector by several serial chains called legs, in a closed-loop arrangement.

Five-axis machines provide a complete solution for highly complicated and sophisticated surface machining, mainly due to its spindle (end-effector) orientation. However, they are costly, and the maintenance is also complex. According to some authors (see [3, 8, 9]), the end-effector orientation of most employed PKMs in machining applications, ranges from a limited bound. Some of them, e.g., Okuma PM600, vary it from -30° to 30° , while other ones, like Deckel Maho DMT100, ranges from -60° to 60° .

PKMs have notable advantages over their serial counterparts, related to the high load/weight ratio, stiffness, low inertia, high velocities, accelerations, and accuracy. Despite these improvements, PKMs have limited WS and complex kinematics [3].

P. Rossi (✉)

Universidade Federal de Santa Catarina, Florianópolis, SC 88040-900, Brazil
e-mail: paulo.rossi@posgrad.ufsc.br

R. Simoni · A. P. Carboni

Universidade Federal de Santa Catarina, Joinville, SC 89219-600, Brazil

More elementary PKMs for industrial applications are desirable. The 3T1R or Schönflies motion parallel mechanism is one of them; it usually has a cleaner topology and uncomplicated kinematics. These characteristics aid in overcoming those mentioned PKMs' shortcomings.

It is of outstanding importance to calculate and measure the production machines' parameters required to determine their quality. Generally, the structural stiffness of industrial robot manipulators is considerably smaller compared to the CNC machine tools. It can cause considerable deflection on its end-effector during the machining process, influencing its performance. Therefore, stiffness is one of the main properties to be considered, especially when dealing with a robotic machining system [5].

Encouraged by recent PKM for machining applications developments [6, 10, 12], this manuscript presents a comparative analysis between the traditional 3-axis parallel CNCs, and a novel 4-DOF 3T1R PKM, synthesized by Gogu [1]. The aim is to provide a new PKMs perspective for machining applications, comparing these different equipment types. Such a study can wider the state-of-art in terms of machining apparatus possibilities, improving this study field. The mentioned analysis concentrates on both PKMs theoretical stiffness, one of the main requirements for manufacturing procedures. The stiffness analysis was conducted considering the Global Stiffness Index (GSI) [7].

2 Methodology

This section will discuss the adopted methods to solve both PKMs kinematics and stiffness, scrutinizing the background reasonings and theories.

The kinematic analysis investigates the relationships between the actuators' inputs in the joint space and the end-effector output in the operation space. In differential kinematics, it is desirable to obtain a mapping between the joint velocities and moving platform velocities. This mapping is known as the Jacobian matrix (J) [4]. When studying PKMs, J can be obtained by differentiating the position kinematics equations.

By the kinematic and static duality principle, forces and moments applied on the moving platform at static conditions are equivalent to the forces and moments applied in the actuators to maintain the equilibrium. This relationship can be obtained through J transpose as depicted below

$$f = J^T \cdot \tau, \quad \text{where} \quad J = J_p^{-1} \cdot J_s, \quad (1)$$

where τ is the vector of actuator forces or torques, and f is a generalized vector of Cartesian forces and torques at the moving platform. J_p and J_s are inverse and direct Jacobian matrices, respectively. Each of them multiply the primary and secondary variables, in such a manner: $J_s \cdot \dot{q}_s = J_p \cdot \dot{q}_p$.

Furthermore, considering all links as perfectly rigid, and only the actuators' mechanical transmissions are compliance, it can be stated the following equation:

$$\tau = \chi \cdot \dot{q}_p, \quad (2)$$

χ means a diagonal matrix that represents the actuators' elastic coefficients. Substituting \dot{q}_p into Eq. 2, then applying on Eq. 1

$$f = K \cdot \dot{q}_s \Rightarrow K = J^T \cdot \chi \cdot J, \quad (3)$$

if all actuated joints have the same elastic coefficient, then $\chi = k$. Since k is a scalar, it might be adopted $k = 1$, resulting in the stiffness matrix

$$K = k(J^T \cdot J) \Rightarrow K = J^T \cdot J. \quad (4)$$

K value can depend on the moving platform's both position and orientation. In the investigated topologies, only the orientation will influence K , regard the decoupled motion characteristic, as discussed in Sect. 4.

Performance indices are used to find a scalar that represents some kinematic or dynamic "overall" behavior. The matrix condition number (CN) can be described as the error generated in the solution space of a linear system of equations by the error on the data [7]. In other words, the matrix CN highlights the matrix sensibility, indicating how well is the matrix behavior, when its inputs fluctuate.

Usually, the CN is applied to J . This parameter can be regarded as a J invertibility measure. The CN for inversion can be defined as a function of the J , as exposed below

$$\zeta = \|J\| \|J^{-1}\|, \quad (5)$$

where the $\|*\|$ norm can be addressed as different types, e.g., 2-norm, Frobenius, infinity, among others. Lower ζ values mean a better-conditioned matrix [2].

The CN depends on the J , likewise the K . Consequently, it varies along with the WS. Hence, to obtain a kind of overall scalar, which represents global architecture behavior, one can proceed as follows:

$$\eta = \frac{A}{B}, \text{ where } A = \int_W \left(\frac{1}{\zeta} \right) dW, \text{ and } B = \int_W dW, \quad (6)$$

η is referred to as the global condition index (GCI), ζ is the CN in a particular WS point, while B is the WS volume.

The ζ reciprocal is used, intending to limit the range, as depicted below

$$0 \leq \left(\frac{1}{\zeta} \right) \leq 1 \Rightarrow 0 < \eta < 1, \quad (7)$$

in that case, the closer η value is than unity better is the architecture behavior.

Furthermore, as detailed by Gosselin [2], the CN and GCI concepts could also be used with another argument than the CN. Therefore, the global optimization of

either kinematic or dynamic parameters is also possible, by directly replacing $\left(\frac{1}{\zeta}\right)$ in Eq. 6 by the requested local index.

This paper will analyze the stiffness index to evaluate the K instead of the J . Thus, Eqs. 5 and 6, turns into

$$\zeta_K = \|K\| \|K^{-1}\|, \text{ and } \eta_K = \frac{A_K}{B}, \quad (8)$$

ζ_K is the local stiffness index (LSI), and η_K is named global stiffness index (GSI).

3 Architectures Analysis

Two distinct parallel architectures will be analyzed in this section. The traditional 3-DOF 3T machining architecture and the 4-DOF 3T1R fully parallel topology. Functional representations were developed on SOLIDWORKS® software are exposed in Fig. 1, including their WS volume.

Most of the machining processes, including the milling, are performed with three translations along the Cartesian axes. These motions are enough to manufacture the more significant part of the workpieces. This type of movement is the most common in machining centers, lathes, milling machines, among others.

The traditional 3-DOF machining architecture, known here as “traditional architecture,” performs three translations along the X , Y , and Z Cartesian axes. The architecture’s topology is $3\bar{P}PP$, where overline represents the actuated joint. It has

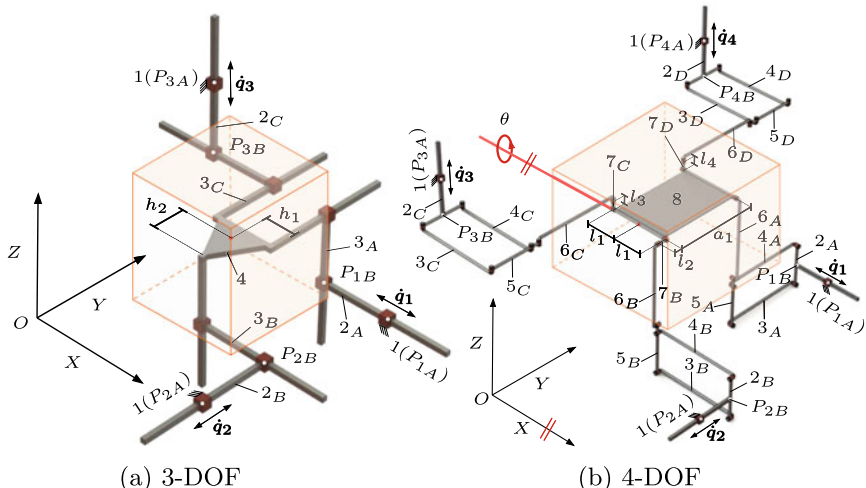


Fig. 1 Both architectures functional representation with WS

three identical limbs that consist of three translational joints; each leg connects the fixed platform (1) toward the moving platform (4). The topology comprises 8 links, 9 joints, 2 closed independent circuits, and 3 degrees of mobility. Each limb has an actuator. The suffixes A, B, C, D , that can be observed in Fig. 1, symbolize the alphabetical ordering from the first limb (A) to the last one (D).

Specifically, the limb topology can be represented as $\overline{P} \perp P \perp P$. Thus, each limbs' translational joints have their axes as orthogonal to each other. Translational motions depend on only one actuated joint velocity $V_i = V_i(\dot{q}_i)$, $i = 1, 2, 3$. Consequently, the J is diagonal, and the architecture has uncoupled motions. The WS has a parallelepiped shape and does not alter its morphology regardless of the kinematic configuration. The WS volume size depends only on the prismatic joints' translational magnitude. If all joints have the same configuration, the WS is a perfect cube.

Points P_{iA} , $i = 1, 2$, and 3 are located in the fixed links (fixed platform). While the points P_{iB} are representing 2_j , $j = A, B$, and C links distal points in the actuator action line, near to the 3_j link. The \dot{q}_i vectors represents 2_j links input velocities, also h_1 and h_2 are moving platform dimensional parameters. The highlighted red dot is named "action point," i.e., the selected reference point to analyze the whole kinematics.

Considering the foregoing, one can state the following equations:

$$P_{1B} = P_{1A} + q_1 \begin{bmatrix} -1 \\ 0 \\ 0 \end{bmatrix}, \quad P_{2B} = P_{2A} + q_2 \begin{bmatrix} 0 \\ 1 \\ 0 \end{bmatrix}, \quad P_{3B} = P_{3A} + q_3 \begin{bmatrix} 0 \\ 0 \\ -1 \end{bmatrix}, \quad (9)$$

since the points P_{iA} are located on the fixed links, their coordinates are fixed too, depending only on the traditional architecture dimensions. Furthermore, points P_{iB} coordinates differ only on one axis regarding the P_{iA} points, which relies on the translational actuator joint direction. That is, the distance between both points leans on the translation magnitude of the 2_j input link.

Examining the presented equations and taking into account the set of geometric parameters, it can be written the following:

$$\begin{bmatrix} P_x \\ P_y \\ P_z \end{bmatrix} = \begin{bmatrix} P_{1A_x} - q_1 - h_1 \\ P_{2A_y} + q_2 + h_2 \\ P_{3A_z} - q_3 \end{bmatrix}, \quad \begin{bmatrix} q_1 \\ q_2 \\ q_3 \end{bmatrix} = \begin{bmatrix} P_{1A_x} - h_1 - P_x \\ P_y - P_{2A_y} - h_2 \\ P_{3A_z} - P_z \end{bmatrix}, \quad (10)$$

in which the right side equation describes the direct kinematics, where the moving platform position and orientation are determined through the actuators' inputs. Furthermore, the left side equation exposes the inverse kinematics, where the actuators' inputs are achieved using the moving platform position.

As mentioned in Sect. 2, differentiating the kinematic equations in Eq. 10, explicitly considering the direct kinematic equations, yields:

$$J_s \cdot \dot{q}_s = J_p \cdot \dot{q}_p \Rightarrow \begin{bmatrix} 1 & 0 & 0 \\ 0 & 1 & 0 \\ 0 & 0 & 1 \end{bmatrix} \cdot \begin{bmatrix} V_x \\ V_y \\ V_z \end{bmatrix} = \begin{bmatrix} -1 & 0 & 0 \\ 0 & 1 & 0 \\ 0 & 0 & -1 \end{bmatrix} \cdot \begin{bmatrix} \dot{q}_1 \\ \dot{q}_2 \\ \dot{q}_3 \end{bmatrix}. \quad (11)$$

By means of Eq. 1 one can reach J . Regarding traditional architecture J and calculating K as exposed in Eq. 4, it is possible to achieve the following matrices:

$$J = \begin{bmatrix} -1 & 0 & 0 \\ 0 & 1 & 0 \\ 0 & 0 & -1 \end{bmatrix} \quad \text{and} \quad K = \begin{bmatrix} 1 & 0 & 0 \\ 0 & 1 & 0 \\ 0 & 0 & 1 \end{bmatrix}. \quad (12)$$

The studied 4-DOF topology, henceforth known as “decoupled architecture,” belongs to the “Fully-Parallel Topologies with Decoupled Schönflies Motions” family. Gogu [1] synthesized this PKM family, using a unified approach for type synthesis, providing novel solutions for PKMs topologies.

Decoupled architecture has 4-DOF 3T1R motion, also known as Schönflies motion. This kind of movement consists of three translations along the X , Y , and Z Cartesian axes, added with one rotation along some specific axis, in that case, the X axis. The topology has four limbs, three of them are identical, and one is slightly different. The limbs have four or five joints and connect the fixed platform (1) to the moving one (8). All limbs have a translational joint actuator. The topology contains 25 links, 31 joints, 3 independent closed circuits, and 4 degrees of mobility.

Figure 1b limb’s topology can be expressed as $\overline{P} \parallel P_a \parallel R \parallel R$ and $\overline{P} \parallel P_a \parallel R \parallel R \perp R$. R , and P_a represent the revolute and parallelogram joints. Thus, each limb’s joints have their axes all parallel each other, except for the one with three consecutive revolute joints, where the last revolute joint is perpendicular to the previous one. The limbs combine one planar parallelogram loop (P_a) each one. Translational motions depend on one actuated joint velocity $V_i = V_i(\dot{q}_i)$, $i = 1, 2, 3$ and the rotational velocity on two actuated joints velocities $\theta = \theta(\dot{q}_3, \dot{q}_4)$. Therefore, J is triangular, and the manipulator has decoupled motions. That is, the motions depend on only one or at least two joints velocities.

As well as in traditional architecture, the WS volume has the same parallelepiped shape. However, in the decoupled architecture, the WS volume can vary according to the kinematic configuration. Depending on the moving platform orientation angle, the WS volume can decrease or increase. The closer the θ is to zero, the greater the WS volume. This fact can be proven by observing the Eq. 14, that is, to maintain a specific θ angle along with the WS, should exist a geometric discrepancy between the P_{3B} and P_{4B} . The mentioned discrepancy, namely the a_2 parameter in Fig. 2, will lead to a smaller translation capacity along the Z Cartesian axis, then reducing the WS volume.

A functional representation of all limbs, including the adopted geometric features, is depicted in Fig. 2. In which the first limb is at the left corner. The selected coordinate perspective follows the Fig. 1b pattern, where the first limb representation is on the XZ plane perspective, while the other ones are on the YZ plane. Additionally, points P_{iA} , $i = 1, 2, 3, 4$ represent the fixed links (fixed platform). While the points P_{iB} are

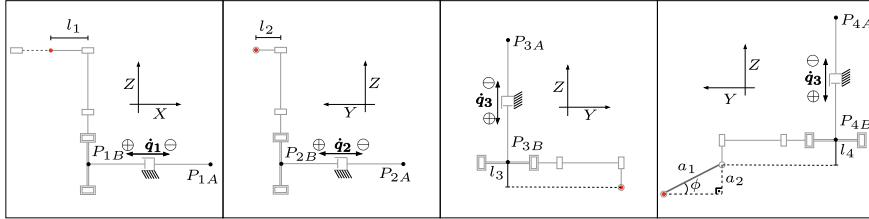


Fig. 2 Functional representation of all decoupled architecture limbs

representing 2_j , $j = A, B, C, D$ links distal points in the actuator action line, near to the P_a joints.

The P_a joints are illustrated as doubled lines with rectangles; the revolute joints are either rectangles or circles, depending on their axes' direction. Vectors \dot{q}_i are the 2_j links input velocities. l_1 is a generic geometric parameter, which represents the moving platform half-length along with the X axis, l_2 , l_3 , and l_4 are representing the 2_j links length. Finally, a_1 is the moving platform length concerning the Y axis. Also, a_2 is a geometric variable that depends on the X axis's moving platform angle, namely θ .

Observing Fig. 2 and considering the actuation of the inputs, it can be written

$$\begin{cases} P_{1B} = P_{1A} + q_1 \begin{bmatrix} -1 \\ 0 \\ 0 \\ 0 \end{bmatrix}, \\ P_{2B} = P_{2A} + q_2 \begin{bmatrix} 1 \\ 0 \\ 0 \\ 0 \end{bmatrix}, \end{cases} \quad \begin{cases} P_{3B} = P_{3A} + q_3 \begin{bmatrix} 0 \\ 0 \\ -1 \\ 0 \end{bmatrix}, \\ P_{4B} = P_{4A} + q_4 \begin{bmatrix} 0 \\ 0 \\ -1 \\ -1 \end{bmatrix}, \end{cases} \quad (13)$$

since the P_{iA} points coordinates are fixed, points P_{iB} differ their coordinates only on one axis regarding the P_{iA} points.

Using the θ sine relation, where $a_2 = (P_{4B_z} - l_4) - P_z$, where P_z is the last P vector coordinate, one can achieve the direct kinematics equations

$$P = \begin{bmatrix} P_x \\ P_y \\ P_z \end{bmatrix} = \begin{bmatrix} P_{1A_x} - q_1 - l_1 \\ P_{2A_y} + q_2 + l_2 \\ P_{3A_z} - q_3 - l_3 \end{bmatrix}, \quad \theta = \sin^{-1} \left(\frac{(P_{4A_z} - q_4 - l_4) - P_z}{a_1} \right). \quad (14)$$

Likewise done earlier in the traditional architecture, differentiating the direct kinematics equations exposed in Eq. 14, yields

$$\begin{bmatrix} 1 & 0 & 0 & 0 \\ 0 & 1 & 0 & 0 \\ 0 & 0 & 1 & 0 \\ 0 & 0 & 0 & a_1 \cos(\theta) \end{bmatrix} \cdot \begin{bmatrix} V_x \\ V_y \\ V_z \\ \dot{\theta} \end{bmatrix} = \begin{bmatrix} -1 & 0 & 0 & 0 \\ 0 & 1 & 0 & 0 \\ 0 & 0 & -1 & 0 \\ 0 & 0 & 1 & -1 \end{bmatrix} \cdot \begin{bmatrix} \dot{q}_1 \\ \dot{q}_2 \\ \dot{q}_3 \\ \dot{q}_4 \end{bmatrix}. \quad (15)$$

Then applying the Eqs. 1 and 4, J and K are achieved

$$J = \begin{bmatrix} -1 & 0 & 0 & 0 \\ 0 & 1 & 0 & 0 \\ 0 & 0 & -1 & 0 \\ 0 & 0 & -1 & -a_3 \cos(\theta) \end{bmatrix}, \quad K = \begin{bmatrix} 1 & 0 & 0 & 0 \\ 0 & 1 & 0 & 0 \\ 0 & 0 & 2 & a_1 \cos(\theta) \\ 0 & 0 & a_1 \cos(\theta) & a_1^2 \cos^2(\theta) \end{bmatrix}. \quad (16)$$

4 Stiffness Analysis and Comparison

Examining Eq. 12 and applying in Eq. 8, one can achieve both the LSI and GSI of the traditional architecture. The norm used to calculate it is the Frobenius norm. Thus, this norm will lead to an LSI measured as the square root of the sum of the absolute K elements squares. This procedure produces some crucial data, facilitating the visualization of the well-conditioned regions. Since K is an identity matrix, the local stiffness index value is $\zeta_K = 3$, along with the whole WS, and also, $GSI = \frac{1}{3}$. It can be concluded that traditional architecture is an isotropic topology; that is, it has unity and constant values for the whole WS in terms of LSI and GSI.

To achieve the decoupled architecture LSI, the same norm as used in the traditional architecture was employed. Examining Eq. 16, the LSI will be calculated numerically, i.e., adopting some generic a_1 and θ values. The curves in Fig. 3a are plotted against θ , varying the a_1 value. This figure shows the LSI behavior according to these parameters variation, including the maximum reachable LSI value respecting a_1 . Figure 3a shows that the optimum GSI value may be attained when the a_1 value is around 1,4, especially because of the LSI straight shape behavior, rather than maximum reachable value, since the GSI measures the overall behavior.

Computing the GSI as shows in Eq. 8, it is necessary to analytically calculate the LSI through the Frobenius norm, which results in an eighth order polynomial. Then, an algorithm was used to compute the A_k parameter as follows:

$$A_k = \int_{\theta} \int_Z \int_Y \int_X \left(\frac{1}{\zeta_K} \right) d_x d_y d_z d_{\theta}. \quad (17)$$

These integrals limits represent the operation space, X , Y , and Z are the magnitude of the translation, θ is the moving platform orientation range. To solve the above exposed integral was used the global adaptative quadrature method.

It possible to note that WS volume B changes according to the θ angle variation, resulting in a non-vanishing WS volume for every θ angle. To compute the B parameter,¹ then calculate the GSI, one should integrate the decoupled architecture WS volume equation in relation to θ , in such a way

¹The WS parallelepiped shape, as depicted in Sect. 3, can be naturally calculated similar to a cube volume. However, the $a_2 = a_1 \sin \theta$ parameter should be subtracted by the Z translation magnitude, since there is a non-vanishing WS.

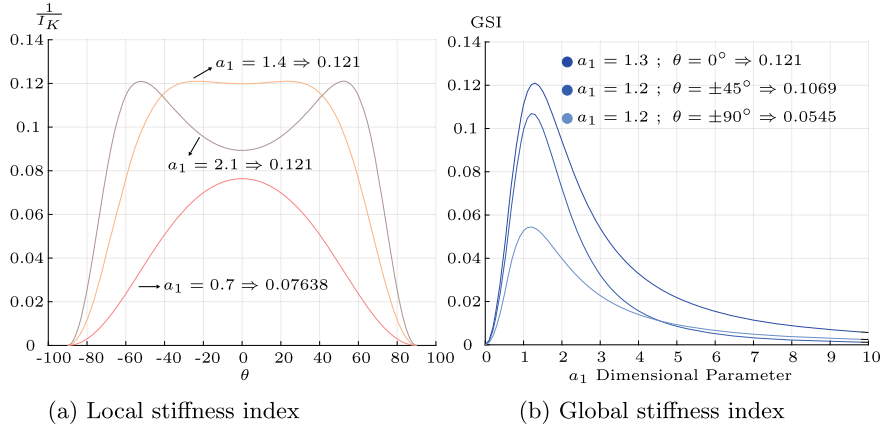


Fig. 3 Decoupled architecture performance indices

$$B = \int_{\theta} XY \|Z - a_1 \sin \theta\| d\theta. \quad (18)$$

Equation 18 calculates the global WS volume, that is, the volume for every orientation of the moving platform. Translations along Cartesian axes magnitude do not interfere with the GSI values. Increasing the translation magnitude in A parameter integral limits will lead to a proportional increase in the B parameter, resulting in the same GSI values. Only the θ variation will influence this index because there is a non-vanishing WS volume. The curves plotted in Fig. 3b shows the achieved GSI results for two distinct θ integral limits (-45° to 45° , and -90° to 90°), and for $\theta = 0^\circ$, including the maximum reachable GSI value.

As expected, the optimum GSI value are given when $a_1 = 1.3$, $\theta = 0^\circ$ and it is $GSI = 0.121$. It is important to say these GSI values are inversely proportional to θ limits. A lower spindle range capacity results in greater GSI values. This fact is in line with the foregoing since the LSI value decreases with higher absolute θ values. This data indicates the decoupled architecture better-suited dimensional parameters regarding its theoretical structural stiffness. Also, it gives an insight regarding the spindle angle range effects in the stiffness conditioning.

Decoupled architecture has smaller theoretical stiffness values when compared to the traditional architecture. However, it gains an additional DOF, contributing to machine more complex surfaces than the traditional CNC. Moreover, if the demanded task requires 5-DOF, it might be possible to achieve them by adding a rotary table in the work-frame, allowing the extra rotational DOF.

5 Conclusions

3-DOF Cartesian PKMs maybe not sufficient to operate in some cases, for example, in the machining of high complex surfaces workpieces. 5-DOF 3T2R PKMs usually possess high coupled and complex kinematics, leading to arduous design, modeling, and control strategies. 4-DOF 3T1R PKMs, like the decoupled architecture, may represent a practical compromise among them. Decoupled architecture presents a straightforward kinematic analysis, decoupled motions, and well-conditioned performance indices; these properties are desirable for machining applications. Similar to traditional architecture, decoupled architecture has its workspace in a parallelepiped shape, which is another attractive characteristic.

The traditional architecture has better stiffness indices since it owns uncoupled motions. Its K is an identity matrix and $GSI = \frac{1}{3}$. Decoupled architecture, in turn, realizes its best results when the dimensional parameter $a_1 = 1.3$, in which $GSI = 0.121$. It is worth saying that the made stiffness analysis does not consider the decoupled architecture's full potential. In other words, there are more detailed analyses, such as an analytical approach based on the structural matrix, the numerical method using finite element software, among others. A more detailed analysis will probably feature the decoupled architecture rigidity, mainly due to the existing P_a joints, as other researches indicate.

Acknowledgements The authors would like to thank CAPES. Moreover, Paulo Rossi is thankful to CAPES Foundation for financial support: Bolsista da CAPES - Proc. n 88887.357849/2019-00.

References

1. Gogu, G.: Structural synthesis of Parallel robots. In: Part 5: Basic Overconstrained Topologies with Schönhflies Motions, vol. 206. Springer Science & Business Media (2013)
2. Gosselin, C., Angeles, J.: A global performance index for the kinematic optimization of robotic manipulators (1991)
3. Hernández, A., Urízar, M., Macho, E., Petuya, V.: Parallel manipulators: practical applications and kinematic design criteria. Towards the modular reconfigurable robots. In: International Workshop on Computational Kinematics, pp. 131–140. Springer (2017)
4. Jamwal, P.K., Kapsalyamov, A., Hussain, S., Ghayesh, M.H.: Performance based design optimization of an intrinsically compliant 6-dof parallel robot. Mech. Based Des. Struct. Mach. 1–16 (2020)
5. Ji, W., Wang, L.: Industrial robotic machining: a review. Int. J. Adv. Manuf. Technol. **103**(1–4), 1239–1255 (2019)
6. Lian, B., Sun, T., Song, Y., Jin, Y., Price, M.: Stiffness analysis and experiment of a novel 5-DoF parallel kinematic machine considering gravitational effects. Int. J. Mach. Tools Manuf. **95**, 82–96 (2015)
7. Liu, X.J., Jin, Z.L., Gao, F.: Optimum design of 3-DOF spherical parallel manipulators with respect to the conditioning and stiffness indices. Mech. Mach. Theory **35**(9), 1257–1267 (2000)
8. Pandilov, Z., Dukovski, V.: Parallel kinematics machine tools: overview-from history to the future. Ann. Fac. Eng. Hunedoara **10**(2), 111 (2012)
9. Serje-Martínez, D.A., Pacheco-Bolívar, J.A.: Parallel kinematics machine tools: research, development and future trends. Dyna **84**(201), 17–26 (2017)

10. Song, Y., Lian, B., Sun, T., Dong, G., Qi, Y., Gao, H.: A novel five-degree-of-freedom parallel manipulator and its kinematic optimization. *J. Mech. Robot.* **6**(4), (2014)
11. Verl, A., Valente, A., Melkote, S., Brecher, C., Ozturk, E., Tunc, L.T.: Robots in machining. *CIRP Ann.* **68**(2), 799–822 (2019)
12. Xu, P., Cheung, C.F., Li, B., Wang, C., Ho, L.T.: Design, development, and analysis of a hybrid serial-parallel machine for precision polishing. *Precis. Mach.* 171–205 (2020)

Modelling and Simulation of Industrial Robot Using SolidWorks



Chinmaya Sabnis, N. Anjana, Amit Talli , and Arunkumar C. Giriyapur

1 Introduction

Manipulators are used in various fields such as industrial, medical and social applications. They are used in modern industrial factories such as production lines of cars, ships, and rockets. They can finish the given task in a much shorter time as compared to humans. The manipulators or industrial robots have three or more degrees of freedom to perform various tasks. Industrial robots are classified as an open chain or serially connected chain of rigid links [1]. The open-chain or industrial robot kinematics is based on Denavit–Hartenberg (DH) parameters to describe the end-effector's position and orientation [2]. The main problem associated with the industrial robot is the lack of visualisation of task planning faced by the technicians, increased training period and accidents [3]. Hence, a systematic approach is required to overcome the lack of visualisation of task planning.

The commercial and open-source software are specifically available for robot visualisation such as V-REP, Gazebo and RoboAnalyzer [4]. The computer-aided design (CAD) software such as SolidWorks, CATIA, Solid Edge, OPEN CASCADE and Autodesk fusion are also used for the simulation [5]. The CAD software's have become sophisticated and are equipped with more advanced libraries [6]. Many CAD software tools support Parasolid, STEP files for seamless data exchange without losing information. The robot manufacturer provides a CAD data file to understand the robot's structure and specifications in various formats. The file containing the information regarding the robot arm can be imported directly into any CAD software. The simulation can be performed in the assembly module of any CAD tool for

C. Sabnis · N. Anjana · A. Talli (· A. C. Giriyapur
Automation and Robotics, KLE Technological University, Hubli 580031, India
e-mail: amit@kletech.ac.in

A. C. Giriyapur
e-mail: aaron@kletech.ac.in

task planning. Virtual reality is the newest technology used to visualise the robot programming in offline mode [7, 8].

In this paper, SolidWorks, a CAD tool from Dassault Systemes, is used to simulate an industrial robotic arm. It has the capabilities to perform simulation by applying constraints in motion analysis. The output, such as linear displacement, velocity, acceleration can be plotted in the form of graphical format or excel sheet for data analysis and optimisation. Most of the industries use the most popular CAD tool for the design and require no extra training or investment to visualise the task planning of the robotic arm. This paper focuses on simulating an industrial robot's task using the event-based module of the SolidWorks software. The event-based module is useful for the robot technician's working in an industry, and it can be used effectively to reduce the training times to improve work efficiency in those industries. This paper is divided into, modules on 'Problem Statement', 'Workflow', 'Denavit-Hartenberg Parameters', 'Methodology', 'Results', and 'Conclusion' are presented.

2 Problem Statement

There is much speculation that by 2030 as per reports estimate, there will be a shortage of 85.2 million talented workforces and will cause immense loss to various companies. The untrained workforce also leads to less working hours and more unfinished work to complete due to which many companies are now dependent on robotics for a solution. Though robots do not replace human force, they are beneficial in challenging times for companies to rely on them.

Major disasters are due to human enforcement because humans get tired quickly and cannot work continuously as the robots are more reliable [2] and are unharmed even during any disaster. One more area where the human workforce might fail is the accomplishments of intricate designs as they may get complicated for a human to solve. Technicians may feel challenging to visualise the kinematics of industrial robotics and systematic planning of robotics tasks. Figure 1 shows the various components of any typical industrial robotics system. The technicians should be trained in proprietary software provided by the manufacturer to program the industrial robot.

3 Workflow

The workflow for the visualisation of path planning or task planning is shown in Fig. 2. The first step starts with the part modelling module. The industrial robot parts are designed as per the dimensions recommended by the manufacturer catalogue or the Parasolid file, or a STEP file of the industrial robot can be imported directly into the CAD platform. The second step is assembling the parts of the industrial robot. In this step, the individual part is checked, and constraints are applied between the rigid links for providing the relative motion between the links. After applying all

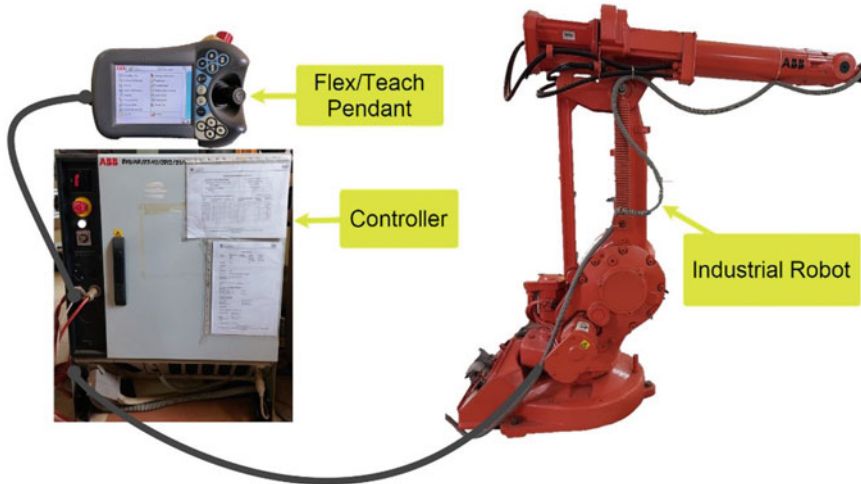


Fig. 1 Industrial robotic system

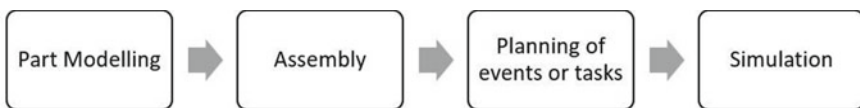


Fig. 2 Workflow

the constraints to the industrial robot, the motion analysis module of SolidWorks is activated for the planning of events or tasks. Finally, the simulation is performed for visualisation and interpreting the results.

The interface of the SolidWorks with event-based motion analysis is shown in Fig. 3. The event-based motion analysis consists of planned tasks that can be triggered by motors or actuator's action. The results such as linear displacement, linear velocity, linear acceleration, path tracing, can be plotted for interpretation.

4 Denavit–Hartenberg Parameters

Denavit–Hartenberg (DH) parameter is the standard method developed for the serial robot manipulators [1]. For illustration purpose, the KUKA KR6 robot is used for understanding DH-parameters. The DH-parameter process applies to all serial robots. The DH-parameters act as a guideline for constructing the kinematic architecture of the robotic manipulator. Figure 4 shows the CAD model of the KUKA KR6 robot [2, 9].

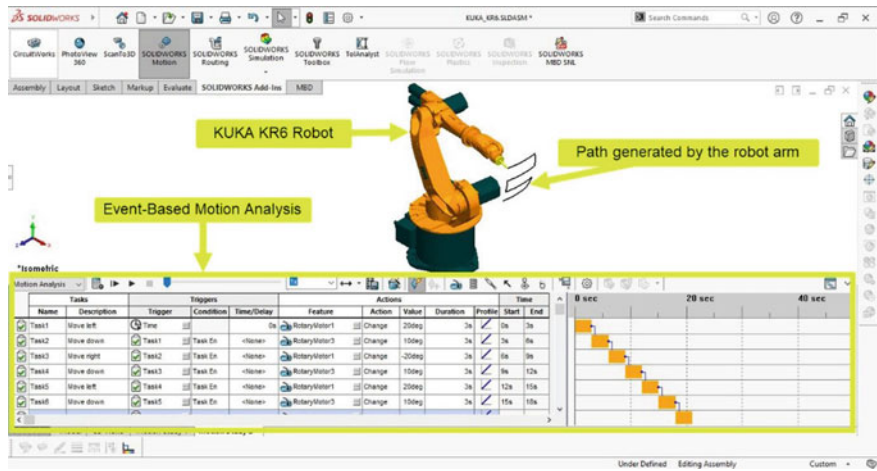


Fig. 3 SolidWorks interface

Fig. 4 KUKA KR6

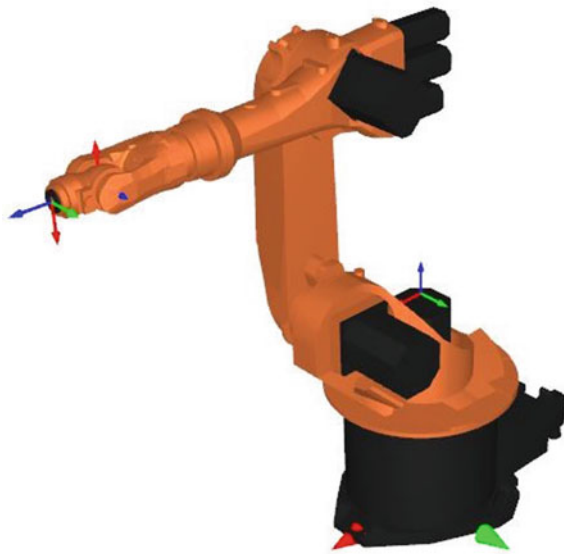


Table 1 shows the DH-parameters of KUKA KR6 [3] robot with six-degrees of freedom. Each row in the table represents the joint with a limited range of motion. The joint angle (θ) and joint offset (d) are for the prismatic or pin joint. The link parameters give link length, and the twist angle, represented as (a) and (α), respectively. The axis of rotation and joint offset is considered about the z-axis. The link parameter such as length and twist angle are taken along and about the x-axis as per the DH-parameters conventions. The last column of Table 1 represents the limited motion

Table 1 DH-parameters for the KUKA KR6 robot [3, 10]

Joint	θ	d	a	α	Robot motion range
1	θ_1	d_1	a_1	$-\pi/2$	$\pm 185^\circ$
2	θ_2	0	a_2	0	$+35^\circ - 155^\circ$
3	θ_3	0	a_3	$\pi/2$	$+154^\circ - 130^\circ$
4	θ_4	d_4	0	$-\pi/2$	$\pm 350^\circ$
5	θ_5	0	0	$\pi/2$	$\pm 130^\circ$
6	θ_6	d_6	0	π	$\pm 350^\circ$

range in terms of degrees. Different robot models have a limited operating range and working space or envelope.

The end-effector or tool such as welding gun or spray-painting tool is attached at the joint 6. To describe the position and orientation of the joint 6 or the tool is determined by using the Homogeneous Transformation Matrices (HTM). The homogeneous transformation matrix consists of four rows and four columns (4×4). The last column of the homogeneous transformation matrix represents the end-effector position and orientation in the spatial workspace. The remaining elements of the homogeneous transformation matrix represent the orientation in X, Y, and Z-axis. The homogeneous transformation matrix is obtained by multiplying each row of Table 1 in the following format:

$$T = T_{\text{rot}}(\theta, z)^* T_{\text{trans}}(d, z)^* T_{\text{trans}}(a, x)^* T_{\text{rot}}(\alpha, x) \quad (1)$$

The homogeneous transformation matrix is given below:

$$T = \begin{bmatrix} \cos(\theta) & -\sin(\theta)\cos(\alpha) & \sin(\theta)\cos(\alpha) & \cos(\theta) \\ \sin(\theta) & \cos(\theta)\cos(\alpha) & -\cos(\theta)\cos(\alpha) & \sin(\theta) \\ 0 & \sin(\alpha) & \cos(\alpha) & d \\ 0 & 0 & 0 & 1 \end{bmatrix} \quad (2)$$

The information about the KUKA KR6 robot is used to build the kinematics model. The forward kinematics equations are developed by using the homogeneous transformation matrix. After performing the matrix multiplication as per Eq. (1) of the homogeneous transformation, the matrix yields 4×4 homogenous transformation.

The position of the KUKA KR6 in the spatial workspace is given by

$$\begin{aligned} X = & a1 * c1 - d6 * (s5 * (s1 * s4 - c4 * (c1 * c2 * c3 - c1 * s2 * s3)) - c5 * (c1 * c2 * s3 + c1 * c3 * s2)) \\ & + a3 * (c1 * c2 * c3 - c1 * s2 * s3) + d4 * (c1 * c2 * s3 + c1 * c3 * s2) + a2 * c1 * c2 \end{aligned} \quad (3)$$

$$\begin{aligned} Y = & d4 * (c2 * s1 * s3 + c3 * s1 * s2) - a3 * (s1 * s2 * s3 - c2 * c3 * s1) + a1 * s1 \\ & + d6 * (s5 * (c1 * s4 - c4 * (s1 * s2 * s3 - c2 * c3 * s1)) + c5 * (c2 * s1 * s3 + c3 * s1 * s2)) \\ & + a2 * c2 * s1 \end{aligned} \quad (4)$$

Table 2 Robot Specifications [3, 10]

Parameters:	Value
Axes	6
Payload	6.00 kg
H-reach	1570.00 mm
Repeatability	± 0.0500 mm
Robot mass	235.00 kg
Structure	Articulated

$$\begin{aligned}
 Z = & d1 - a3 * (c2 * s3 + c3 * s2) + d4 * (c2 * c3 - s2 * s3) \\
 & + d6 * (c5 * (c2 * c3 - s2 * s3) - c4 * s5 * (c2 * s3 + c3 * s2)) - a2 * s2
 \end{aligned} \tag{5}$$

where $c1 = \cos(\theta_1)$, and $s1 = \sin(\theta_1)$. To simplify and to create a compact equation, the trigonometric identities are written in short form.

5 Methodology

5.1 Development of Industrial Robot in SolidWorks

The KUKA KR6 robot has seven links connected with six joints to provide relative motion between the links robot. The KUKA KR6 is used to show the process followed to visualise task planning in SolidWorks [4]. This process or method applies to all serial or open-chain industrial robotic arms. Table 2 shows the specifications of the KUKA KR6. The Parasolid or STEP file of KUKA KR6 can be directly imported into SolidWorks. The KUKA KR6 is a six-axis robot with a payload of 6 kg. The payload of the robot is defined as the load-carrying capacity of the industrial robot. The horizontal reach of the robot is around 1570 mm when the arm is fully extended. The repeatability of the robot is given in terms of tolerance values of ± 0.0500 mm. The ability to reproduce the same value within the allowable tolerance is known as repeatability. The total mass of the KUKA KR6 is 235 kg, and the base of the robot is attached to the ground.

5.2 Event-Based Motion Analysis

The tool's initial position or end-effector of KUKA KR6 robot with respect to the base in the Y-axis is found to be 1310.58 mm. Figure 5 shows the initial position

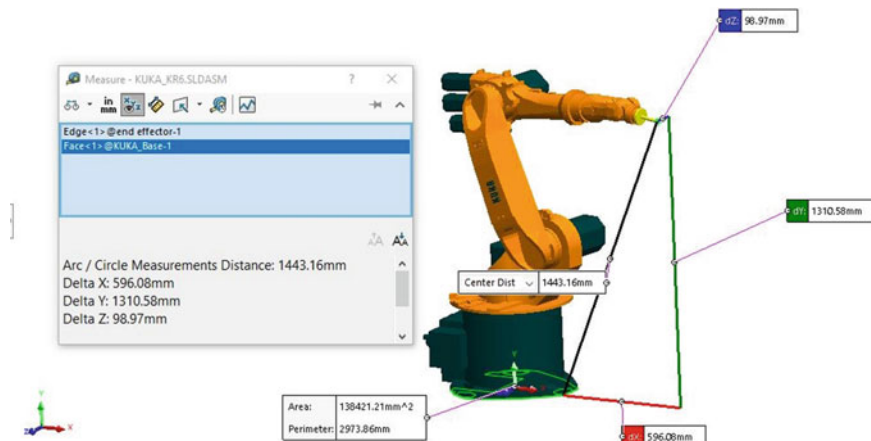


Fig. 5 Initial position of KUKA KR6

of the end-effector or tool. The initial position of the robot can be considered as the home position of the robot.

The six-degrees of freedom robots are widely used in arc welding, spot welding, and spray-painting operation. The CAD tool does not require any programming languages such as python, java, and VAL to plan the robot's task. The event-based motion analysis is based on the set of tasks arranged logically. Figure 6 shows an example of a path traced by the robot in SolidWorks. The path appears to be zig-zag manner, which depicts the motion of arc welding or spray painting.

Motion Analysis is an add-in module available in SolidWorks for performing the motion study. These modules are also available in other CAD software such as CATIA, and Solid Edge as motion simulation. The motion analysis includes force,

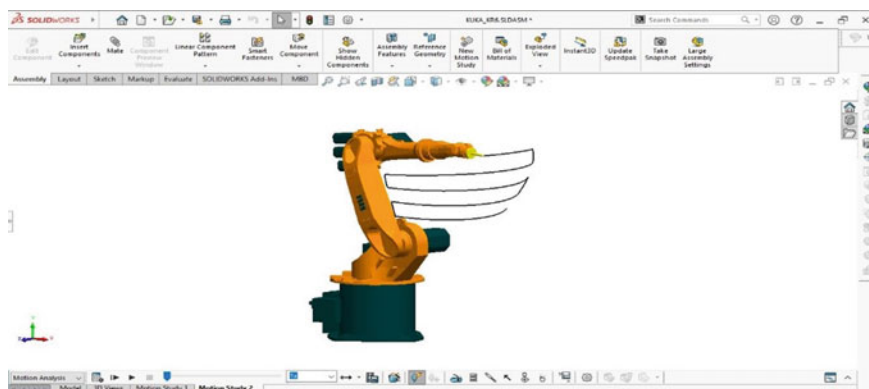


Fig. 6 Trace path of KUKA KR6

Tasks		Triggers			Actions					Time	
Name	Description	Trigger	Condition	Time/Delay	Feature	Action	Value	Duration	Profile	Start	End
Task1	MOVE LEFT	Time		0s	RotaryMotor1	Change	40.00deg	3s	✓	0s	3s
Task2	MOVE DOWN	Task1	Task En	<None>	RotaryMotor3	Change	-10.00deg	3s	✓	3s	6s
Task3	MOVE RIGHT	Task2	Task En	<None>	RotaryMotor1	Change	-80.00deg	3s	✓	6s	9s
Task4	MOVE DOWN	Task3	Task En	<None>	RotaryMotor3	Change	-10.00deg	3s	✓	9s	12s
Task5	MOVE LEFT	Task4	Task En	<None>	RotaryMotor1	Change	80.00deg	3s	✓	12s	15s
Task6	MOVE DOWN	Task5	Task En	<None>	RotaryMotor3	Change	-10.00deg	3s	✓	15s	18s
Task7	MOVE RIGHT	Task6	Task En	<None>	RotaryMotor1	Change	-80.00deg	3s	✓	18s	21s
Task8	MOVE DOWN	Task7	Task En	<None>	RotaryMotor3	Change	-10.00deg	3s	✓	21s	24s
Task9	MOVE LEFT	Task8	Task En	<None>	RotaryMotor1	Change	80.00deg	3s	✓	24s	27s

Fig. 7 Event-Based motion analysis interface

gravity, spring, damper, solid contact, and other playback options. The motion analysis can be applied, when all the constraints are satisfied in SolidWorks. The error or over-constrained warnings must be cleared to conduct error-free analysis.

Figure 7 shows the interface of event-based motion with tasks. The ‘Tasks’ column consists of name and description such as Task 1, Task 2 Task n and description column consist of a description of a particular task. The next column consists of a trigger, condition, and Time/Delay. The trigger activates the task and the condition specifies whether the task should start after the previous task or start simultaneously. The Time/Delay is used to mentions the delay in starting any task as per the requirements. Actions column consists of features, action, value, duration, and profile. The last option under actions is profile. There are four types of motion profiles: linear, constant acceleration, harmonic, cycloidal, and cubic. The motion profile is selected depending upon the requirements. For our study, the linear motion profile is used to perform the simulation. The last column in event-based motion analysis represents the start and end time of the task.

6 Results

Figure 8 shows the linear displacement of the tool in the y-direction. The tool’s initial position was at 1350 mm in the y-direction, as shown in Fig. 5. After tracing the path, as shown in Fig. 8, the tool’s final linear displacement is at 893 mm approximately in the y-direction. The total time taken to complete the operation was around 27 s, as shown in the event-based motion analysis. The other parameters such as linear velocity, acceleration, torque, motor power consumption can be plotted for further analysis.

Figure 9 shows a circular and rectangular path traced by the KUKA KR6. The path could be designed by using path mate available in the SolidWorks for planning complex paths. The path mate can be incorporated in the event-based motion analysis.

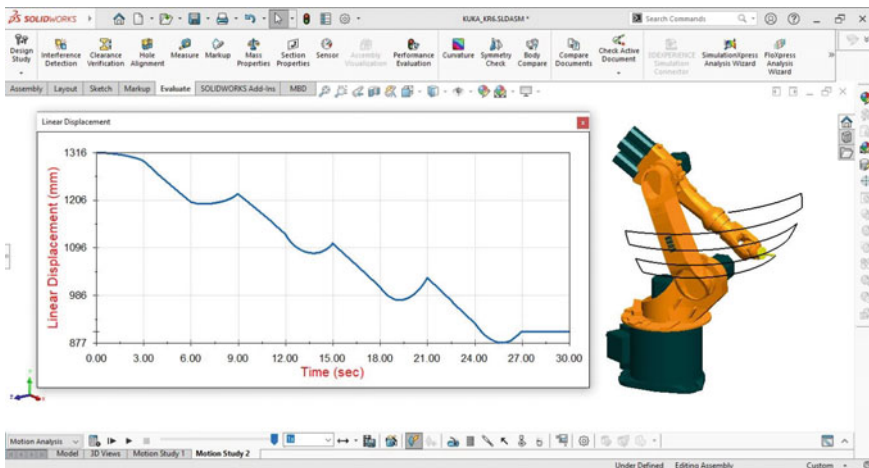


Fig. 8 The linear displacement of KUKA KR6

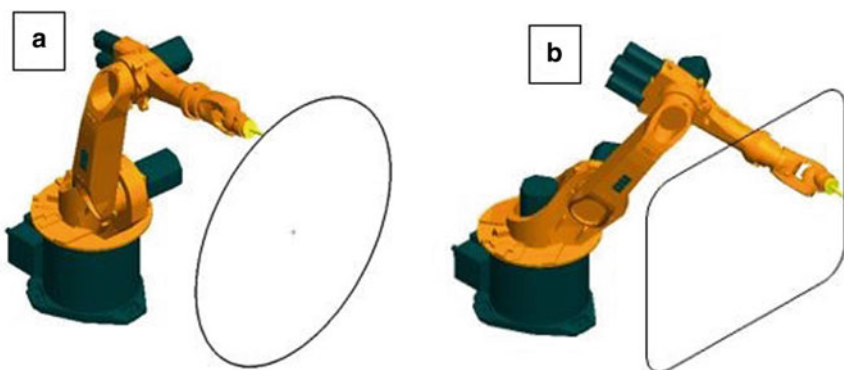


Fig. 9 Circular (a) and rectangular path (b)

7 Conclusion

The event-based motion analysis of SolidWorks can be used to visualise the path planning of industrial robots. In this paper, an overview of how SolidWorks motion analysis software can be used to enhance the understanding and abilities of robot technicians was discussed. The standard method of defining the industrial robot's architecture based on Denavit–Harteneberg parameters are discussed. The robotic system consists of a controller, flex pendant, and robotic arm, which becomes difficult to visualise the robot's kinematics. In that case, there is a high probability of not analysing or predicting the wrong trajectories or even wrong entries in a program which may lead to accidents, or unwanted maintenance issues, by this, we can eliminate the

losses or damages caused by the operation as well as training time by enhancing the visualisation by using the offline programming presented in this paper. Since there are many difficulties in programming a robot or manipulator, which increases the error or lack of efficiency, it is always good to program it offline or simulate it in a virtual environment. In summary, event-based motion analysis in SolidWorks can help robot technicians understand the robot's kinematics, making them more prolific.

References

1. Ma, F., Jia, R.-Q.: Virtual realisation and geometric discriminant algorithm of the industrial robot end-effector's position and orientation. *J. Discret. Math. Sci. Cryptogr.* **21**, 471–477 (2018). <https://doi.org/10.1080/09720529.2018.1449328>
2. Raza, K., Khan, T.A., Abbas, N.: Kinematic analysis and geometrical improvement of an industrial robotic arm. *J. King Saud Univ. Eng. Sci.* **30**, 218–223 (2018). <https://doi.org/10.1016/j.jksues.2018.03.005>.
3. Gupta, V., Chittawadigi, R.G., Saha, S.K.: Robo analyser: robot visualisation software for robot technicians. In: ACM International Conference Proceedings Series Part F1320, pp. 1–5. <https://doi.org/10.1145/3132446.3134890> (2017)
4. Othayoth, R.S., Chittawadigi, R.G., Joshi, R.P., Saha, S.K.: Robot kinematics made easy using RoboAnalyzer software. *Comput. Appl. Eng. Educ.* **25**, 669–680 (2017). <https://doi.org/10.1002/cae.21828>
5. Imamovic, M., Hadžikadunić, F., Talić-Čikmiš, A., Bošnjak, A.: Examples of kinematic analysis of complex mechanism using modern software applications. In: IOP Conference Series: Materials Science and Engineering, vol. 659. <https://doi.org/10.1088/1757-899X/659/1/012019> (2019)
6. Bedaka, A.K., Lin, C.Y.: CAD-based robot path planning and simulation using OPEN CASCADE. *Procedia Comput. Sci.* **133**, 779–785 (2018). <https://doi.org/10.1016/j.procs.2018.07.119>
7. Holubek, R., Ružarovský, R., Delgado Sobrino, D.R.: Using Virtual Reality as a Support Tool for the Offline Robot Programming. *Res. Pap. Fac. Mater. Sci. Technol. Slovak Univ. Technol.* **26**, 85–91 (2018). <https://doi.org/10.2478/rput-2018-0010>
8. Flanders, M., Kavanagh, R.C.: Build-A-Robot: using virtual reality to visualise the Denavit–Hartenberg parameters. *Comput. Appl. Eng. Educ.* **23**, 846–853 (2015). <https://doi.org/10.1002/cae.21656>
9. Ramish, Hussain, S.B., Kanwal, F.: Hussain, S.B.R., Kanwal, F.: Design of a 3 DoF robotic arm. In: 2016 Sixth International Conference on Innovative Computing Technology (INTECH), pp. 145–149. <https://doi.org/10.1109/INTECH.2016.7845007> (2017)
10. RobotWorx—KUKA KR 6. <https://www.robots.com/robots/kuka-kr-6>. Last accessed 03 Sept 2020

Machinery Associated with Manufacturing

Long-Range Drilling System with Constrained Tool Path Based on Scissor-Like Elements



Juan G. Grijalva, Edson R. De Pieri, and Daniel Martins

1 Introduction

In the manufacturing of large products, such as cars, airplanes and ships, a typical challenge is the long-range machining [7]. Traditional industrial robots cannot fit on the large products conveyor line [1] as they have to access manufacturing sites within large parts. Another requirement in the manufacturing of these products is industrial safety and high quality standards [1]. Overshoot in the tool path can cause inaccurate machining on products [5] leading to a low quality manufacture. By constraining the path of the tool, accidents can be avoided; thus, improving industrial safety.

A solution, for manipulating workpieces in aircraft assembly, is presented in [7]. This solution consists of a parallel robot made up of three pairs of SLEs and six prismatic actuators, giving a total of six degrees of freedom (DoF). The novelty of this solution is the integration of SLEs in the Gough-Stewart hexapod platform [8, 14]. The main advantage of this parallel robot, compared with the Gough-Stewart platform, is the significant larger workspace. The dynamic equation of SLEs assemblies can be obtained by identification systems theory [9]. With the dynamic model, it is possible to apply a MPC. MPC is an optimal control strategy able to deal with unstable and nonminimum phase plants, which employs a dynamic equation to obtain an optimal control sequence by minimizing an objective or cost function [2]. At each sampling interval, the dynamic equation is used to predict the output of the system over a prediction horizon. General predictive control (GPC) is one of the most pop-

J. G. Grijalva (✉)

Federal University of Santa Catarina, Control and Automation Laboratory (LCA-DAS),
Florianópolis, SC 88040-900, Brazil

E. R. De Pieri · D. Martins

Raul Guenther Robotics Laboratory (LRRG-EMC), Florianópolis, SC, Brazil
e-mail: edson.pieri@ufsc.br

D. Martins

e-mail: daniel.martins@ufsc.br

ular MPC algorithms due to the effectiveness in the industrial process showing good performance and a certain degree of robustness [12].

Thus, in this paper, we present a long-range drilling system, regulated by a GPC, which, in addition to stabilization, is responsible for constraining both the overshoot and the tool path. Aiming to obtain a large workspace, the displacement mechanism of this system is made up of simple SLEs [10]. This document is organized as follows: in Sect. 2, the geometric design analysis of the system is presented. Also, the main components of the system are detailed. In Sect. 3, we introduce the MPC as well as the approach to constraint the tool path and the overshoot. In addition, the results of the simulation are shown in Sect. 3. Finally, the conclusions of this work are presented in Sect. 4.

2 Geometric Design Analysis

The novelty of this research is to integrate a SLE structure in a conventional drilling machine and regulate the advance of the tool with a constrained GPC (GPCC). Therefore, the parts of the drilling system and the geometric design of the SLE assembly are detailed in this section.

2.1 Parts of the Drilling System

The drilling system, based on Fig. 1, is made up of the next parts:

1. *Tool*: In this case a drill bit, which is a cutting tool used to remove material to create holes, almost always of circular cross-section.
2. *Chuck and torque generator*: The chuck is in charge to secure the drill bit. The torque generator, which can be a motor impelled by pneumatic or electrical energy, is responsible to transmit the power to the tool.
3. *Prismatic actuator*: This actuator regulates the deployment of the SLE structure, at the same time the advance of the tool by the chuck.
4. *SLE assembly*: This deployable structure gives the characteristic of reaching a long-range to the tool. In the next subsection, we discuss about its geometric design.

2.2 Design of the SLE Structure

SLE based assemblies give the possibility to design folding structures. A SLE consists of a pair of links joined by a pivot, a revolute joint, to allow free rotation of one link

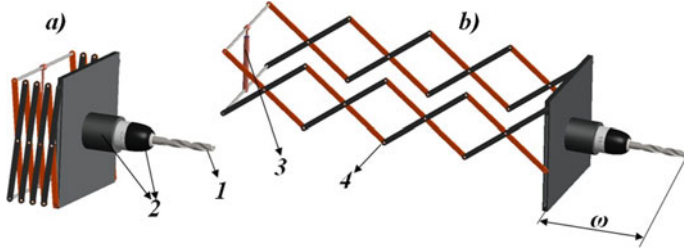


Fig. 1 Drilling system composed by 4 SLEs: **a** folding state **b** deploying state

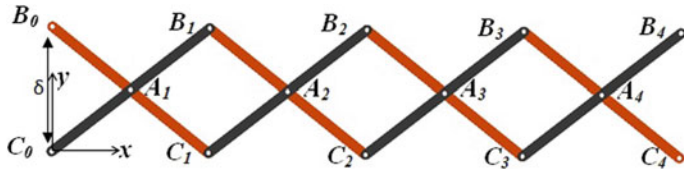


Fig. 2 SLE structure: geometry

relative to the other around the pivot axis [15]. In Fig. 2, the SLE structure employed in the drilling system shown in Fig. 1 is depicted, which is made up of four SLEs; nevertheless, it is possible to design uncountable configurations of SLE assemblies by using the geometrical relations described below

$$\overline{B_0 B_1} = \overline{C_0 C_1} = \sqrt{4a^2 - \delta^2}, \quad (1)$$

$$\overline{B_0 B_4} = \overline{C_0 C_4} = N \overline{C_0 C_1}, \quad (2)$$

where $a = \overline{B_0 A_1} = \overline{C_0 A_1} = \overline{A_1 C_1} = \overline{A_1 B_1}$, $\delta = \overline{B_0 C_0}$ is the input overture of the SLEs, and N is the number of SLEs. In the drilling system presented in Fig. 1, we can compute the maximum deployment as follows: the length of the links in the SLE is $a = 15$ cm with an input overture $\delta = 10$ cm. By using (1), it is possible to calculate $\overline{C_0 C_1} = 28.28$ cm. Then, by using (2), the total length of the deployment of the SLE structure can be calculated, in this case $\overline{B_0 B_4} = 113.13$ cm. The total deployment of the system, in this case, can be computed by summing the length of the SLE structure plus the length of the tool, the chuck, and the motor $\omega = 27$ cm (see Fig. 1); so, we have a total path of 140.13 cm. In the next section, we present an approach to control and constraint the path of the drilling system.

3 Model Predictive Control for the Drilling System

In this section, we first present an approach to derive the dynamic model of the system using identification systems theory. Then, we introduce the adapted version of GPC for the drilling system. Finally, we detail the optimal conditions to define the constraints on the performance of the system.

3.1 Dynamic Equation

The dynamic equation is obtained by using the approach based on the theory of identification systems presented in Grijalva et al. [9]. The model, used in the identification process, is an auto-regressive with exogenous input (ARX) given by

$$y_k + a_1 y_{k-1} + a_2 y_{k-n_a} = b_0 u_{k-n_k}. \quad (3)$$

The simulation, to control and identify the parameters, of the drilling systems was developed by using Simscape-Simulink. Unlike other Simulink blocks, which represent mathematical operations or operate on signals, Simscape blocks represent physical components or relationships directly being possible to configure mass, inertia, friction, among other dynamic forces. The values identified from the drilling system are $a_1 = -1.95$, $a_2 = 0.93$, and $b_0 = 0.0015$. For convenience, we write the identified parameters as polynomials in Z -domain as follows

$$B(z^{-1}) = b_0, \quad A(z^{-1}) = 1 + a_1 z^{-1} + a_2 z^{-2}. \quad (4)$$

We choose a sampling time $T s = 0.1$ s for the drilling system under the fact that the desired settling time is about 2 s. In the next subsection, the Eq. 4 is used to develop the predictive control algorithm.

3.2 Generalized Predictive Control

This algorithm was introduced in [6] being a successful and popular method in industry as well as in academia [13]. Six years later, a paper [4] presenting a constrained approach of GPC was published. Because of safety, high quality (in manufactured products), sensor limitations, among other reasons, considering constraints in control systems is important. The omission of constraints can lead into a poor performance or instability [11]. Based on the dynamic equation, in discrete time, obtained by identification procedure in Sect. 3.1, we can define a controller auto-regressive with integrated moving-average (CARIMA), without delays, to apply the GPC as follows:

$$A(z^{-1})y_k = B(z^{-1})u_{k-1} + C(z^{-1})\frac{e_k}{\Delta}, \quad (5)$$

where u_k and y_k are the input and output, respectively, of the drilling system at each sample k , e_k is a zero mean white noise characterized by a C polynomial, and $\Delta = 1 - z^{-1}$ is a discrete time integrator. For convenience, the C polynomial is chosen to be 1. Since GPC uses predictions in the future, we define a prediction of the output advanced j steps ahead in the future as y_{k+j} . To compute the future outputs, we consider the Diophantine equation

$$1 = E_j(z^{-1})\bar{A}(z^{-1}) + z^{-j}F_j(z^{-1}). \quad (6)$$

In (6), the polynomial $\bar{A} = \Delta A(z^{-1})$, E_j can be obtained by dividing 1 by $\bar{A}(z^{-1})$ being $z^{-j}F_j(z^{-1})$ the remainder of the division. The Eq. 5 can be expressed in future predictions by multiplying it by $z^jE_j(z^{-1})$ as follows:

$$E_j(z^{-1})\bar{A}(z^{-1})y_{k+j} = E_j(z^{-1})B(z^{-1})\Delta u_{k+j-1} + E_j(z^{-1})e_{k+j}. \quad (7)$$

As the terms of the white noise in the future have zero mean and by replacing (6) in (7), we can rewrite (7) as

$$y_{k+j} = G_j(z^{-1})\Delta u_{k+j-1} + F_j(z^{-1})y_k, \quad (8)$$

in Eq. 8 the polynomial $G_j(z^{-1}) = E_j(z^{-1})B(z^{-1})$. The GPC technique consists of applying a control sequence that minimizes a cost function of the form

$$J = \sum_{j=N_1}^{N_P} \beta \varepsilon_j^2 + \sum_{j=1}^{N_U} \lambda \Delta u_{j-1}^2, \quad (9)$$

where N_U and N_P are the control and prediction horizons, respectively, the predicted error is $\varepsilon = y_{k+j} - r_{k+j}$ being r_{k+j} the desired reference, and β and λ are the weights of the cost function. Since we did not consider delays in our plant, the value of the starting prediction horizon N_1 can be equal to 1. By using Eq. (8), and for simplicity Eq. 9 can be rewritten in the following matrix form [3]

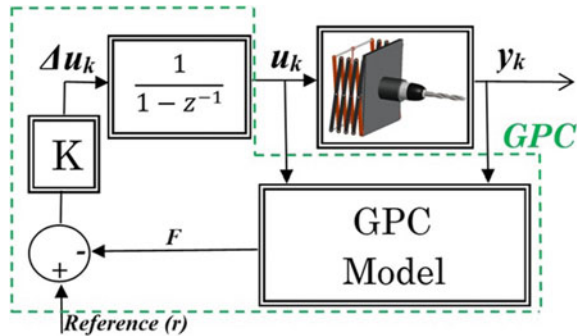
$$J = (\mathbf{Gu} + \mathbf{F} - \mathbf{r})^T \beta (\mathbf{Gu} + \mathbf{F} - \mathbf{r}) + \mathbf{u}^T \lambda \mathbf{u}. \quad (10)$$

By minimizing the cost function J , in (10) over \mathbf{u} , we can derive the control law as follows

$$\Delta u = \underbrace{(\mathbf{G}^T \beta \mathbf{G} + \lambda)^{-1} \mathbf{G}^T \beta (\mathbf{r} - \mathbf{F})}_K. \quad (11)$$

Based on (11), the discrete time controller can be represented by the scheme depicted in Fig. 3. Note that in Fig. 3, the input u_k corresponds to the force supplied by the prismatic actuator to the SLE structure, and the output y_k represents the drilling path. In the next subsection, we describe the optimal condition to constraint the tool path.

Fig. 3 GPC scheme for the drilling system



3.3 Constraints on the Tool Path

To adapt the drilling system constraints, when minimizing J from equation (10) the condition in (12) [3] must be considered where H and b are matrices with the corresponding dimensions.

$$H \Delta u \leq b. \quad (12)$$

This procedure is detailed in the following subsection.

3.3.1 Restriction on the Advance of the Tool

Because of industrial safety, the availability of space, among other reasons, it is possible to have the need to restrict the path of the tool. In the case of the drilling system, it was defined a constraint of $y_{Max} = 1$ m in the output of the system. This restriction can be represented by the following inequality:

$$y \leq y_{Max}. \quad (13)$$

By replacing (8) in (13), we have

$$G \Delta u + F \leq y_{Max}, \quad (14)$$

the Eq. 14 can be rewritten in the form of (12), see below

$$[G_{N_P \times N_U}] \Delta u \leq [1_{N_P \times 1} y_{Max} - F_{N_P \times 1}]. \quad (15)$$

In Fig. 4, we can see a simulation of a drilling process where the tool has to reach a distance of 1.4 m to make a hole. Then the tool moves back to a reference of 0.3 m, and finally the tool has to reach a distance of 1.2 m to make a second hole. In red line on Fig. 4, the performance of the plant by using the GPC is shown. The performance of the GPCC, in which condition (15) applies, is represented by a blue line. Also, it

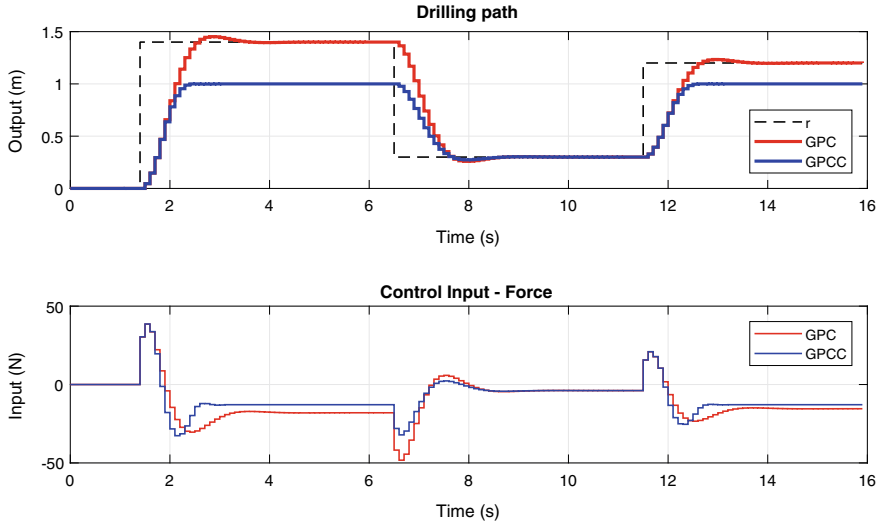


Fig. 4 Constraint on the tool path of the drilling system

is possible to see that even though output reference is greater than y_{Max} , the tool path does not exceed the constraint of $y_{Max} = 1$ m. The force supplied by the prismatic actuator to the mechanism can be seen in Fig. 4 too. We can conclude that an actuator with a maximum force equal or greater than 50 N is necessary. The controller was tuned as follows: $N_P = 40$, $N_U = 8$, $\lambda = 0.001$, and $\beta = 1$. More information about the tuning of GPC can be found in Camacho et al. [3].

3.3.2 Constraint on the Overshoot

The overshoot of the tool path can cause poor quality in the manufacturing of many products. The condition to avoid overshoot can be defined as

$$\begin{aligned} y &\leq r, \quad \text{if } r > y, \\ y &\geq r, \quad \text{if } r < y, \end{aligned} \quad (16)$$

where r is the reference or set point. By replacing (8) in (16), we have

$$G\Delta u + F \leq r \quad \wedge \quad G\Delta u + F \geq r. \quad (17)$$

The inequalities in (17) can be rewritten in the form of (12) as follows:

$$\begin{bmatrix} G_{N_P \times N_U} \\ -G_{N_P \times N_U} \end{bmatrix} \Delta u \leq \begin{bmatrix} 1_{N_P \times 1} r - F_{N_P \times 1} \\ -1_{N_P \times 1} r + F_{N_P \times 1} \end{bmatrix}. \quad (18)$$

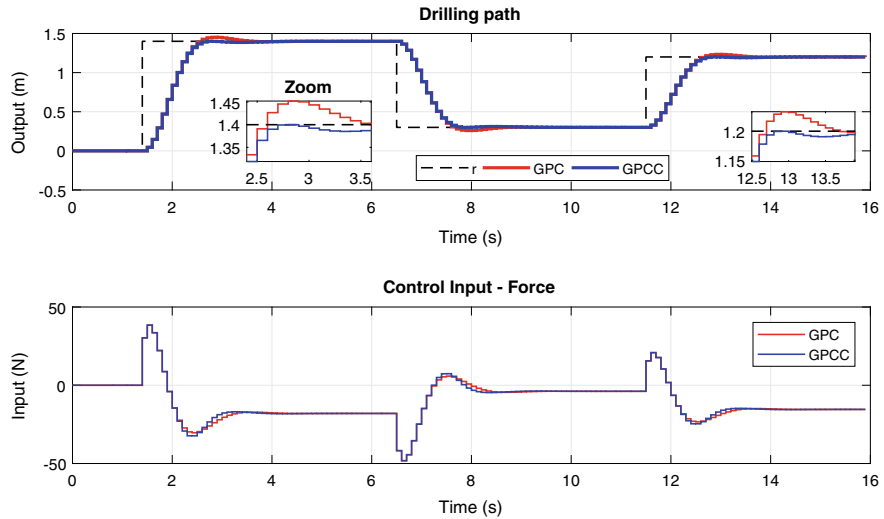


Fig. 5 Constraint on the overshoot of the drilling path

In Fig. 5, we can see a comparison of GPC and GPCC of the drilling path performance. In blue line, the effectiveness of the GPCC using the condition in (18) is depicted. The overshoot of about 5 cm in the process can cause poor quality in the manufacture or even worse a collision. The force supplied by the actuator is almost similar in both cases, being necessary for an actuator able to supply at least 50 N.

4 Conclusion

The drilling system presented in this paper offers the possibility of reaching long distances, thanks to the integration of SLEs. Besides stabilization, due to the GPCC, it is possible to avoid the overshoot, improving machining quality. By using GPCC, it is possible to constraint the tool path as it is a software-based solution in industrial safety.

Acknowledgements We would like to gratefully acknowledge the financial support of the Brazilian Coordination for the Improvement of Higher Education Personnel (CAPES) during this research.

References

1. Atkinson, J., Hartmann, J., Jones, S., Gleeson, P.: Robotic drilling system for 737 aileron (No. 2007-01-3821). SAE Technical Paper (2007)
2. Bemporad, A., de la Peña, D.M.: Multiobjective model predictive control. Automatica **45**(12), 2823–2830 (2009)

3. Camacho, E.F., Alba, C.B.: Model Predictive Control. Springer Science and Business Media (2013)
4. Camacho, E.F.: Constrained generalized predictive control. *IEEE Trans. Autom. Control* **38**(2), 327–332 (1993)
5. Chen, S.-Y., Zhang, T., Zou, Y.-B.: Fuzzy-sliding mode force control research on robotic machining. *J. Robot.* (2017)
6. Clarke, D.W., Mohtadi, C., Tuffs, P.S.: Generalized predictive control—Part I. The basic algorithm. *Automatica* **23**(2), 137–148 (1987)
7. Gonzalez, D.J., Asada, H.H.: Design and analysis of 6-dof triple scissor extender robots with applications in aircraft assembly. *IEEE Robot. Autom. Lett.* **2**(3), 1420–1427 (2017)
8. Gough, V.E.: Contribution to discussion of papers on research in automobile stability, control and tyre performance. *Proc. Auto Div. Inst. Mech. Eng.* **171**, 392–395 (1957)
9. Grijalva, J.G., De Pieri, E.R., Martins, D.: Robust control of scissor-like elements based systems. *Mech. Mach. Theory* **150**, 103849 (2020)
10. Grijalva, J.G., De Pieri, E.R., Martins, D.: Dual-quaternion on simple scissor-like elements. In: *IFTOMM World Congress on Mechanism and Machine Science*. Springer, Cham (2019)
11. Grijalva, J.G., Klug, M., Castelan, E.: Control of a quadrotor under sensors sampling limitations using TS fuzzy modeling: a discrete time approach. In: *Simpósio Brasileiro de Automacão Inteligente*, SBIAI, pp. 351–357 (2017)
12. Kerrigan, E.C., Maciejowski, J.M.: Robust feasibility in model predictive control: necessary and sufficient conditions. In: *Proceedings of the 40th IEEE Conference on Decision and Control* (Cat. No. 01CH37228), vol. 1. IEEE (2001)
13. Marruedo, D.L., Alamo, T., Camacho, E.F.: Input-to-state stable MPC for constrained discrete-time nonlinear systems with bounded additive uncertainties. In: *Proceedings of the 41st IEEE Conference on Decision and Control*, vol. 4. IEEE (2002)
14. Stewart, D.: A platform with six degrees of freedom. *Proc. Inst. Mech. Eng.* **180**(1), 371–386 (1965)
15. You, Z., Chen, Y.: Motion Structures: Deployable Structural Assemblies of Mechanisms. CRC Press (2011)

Development of an Automatic Thread Tension Adjusting Device for Single Needle Lock Stitch Machine



Bhaskar Guin and Rohan Roy

1 Introduction

Textile products have worldwide demand, with the largest global manufacturer and exporter being China followed by Europe and India [1]. The textile industry serves as the backbone of small and micro-scale industries in major 3rd world countries. It is a labour-intensive industry, and not much of technological development have been implemented after the late nineteenth century. The industry retains its indigenous practices like hand-crafting and the use of primitive machinery. The major drawback of traditional manufacturing is its incapability to regulate quality control during production. Hence, the percentage of defective products is generally higher, which is a huge setback for the industry. During commercial garments manufacturing, several defects may be observed like broken/skipped/unbalanced stitches, puckering, wavy seams, etc. Identification of the root cause of these problems could be useful for developing quality control measures [2, 3]. The single needle lockstitch (SNLS) machine is one of the most common sewing machines used in the industry for stitching garments. The mechanics of stitch formation, material properties of thread, and process details have been vividly described in [4]. The common industrial practice to obtain balanced stitches is by adjusting the thread tension based on the fabric and thread material, using a trial and error method [5]. A balanced stitch is formed when tensions in the needle thread and bobbin thread are correct for a given pair of fabric and thread materials. During one complete stitch cycle, 4 tension peaks are obtained for needle thread and 2 peaks for bobbin thread [6]. The highest peak is obtained during the interlacing of needle and bobbin thread being pulled into the fabric, this has been validated through simulations [7] and experiments [8].

B. Guin

Department of Mechanical Engineering, Jadavpur University, Kolkata, India

R. Roy

National Institute of Fashion Technology, Kolkata, India

Thread tension is influenced by several factors like stitch length, feed rate, check spring tension [9], stitch velocity, properties of sewing thread [10], type of lubrication used [11]. The stitch balance can be effectively controlled by adjusting the peak tension [12]. For the needle thread, peak tension is regulated using the tension regulator [13] which induces a pretension. The bobbin tension is adjustable by loosening or tightening the screw of the bobbin case. For tension measurement, the thread is allowed to pass through a cantilever, deflecting it and the proportional load is calculated using strain-gauges [8]. This technique has been used to develop automatic machines capable of real-time monitoring of sewing parameters [14]. Advanced models used neural and fuzzy-based control systems [15] producing better results. However, for an industry to implement such a technology overnight, can be challenging. Hence, this paper is aimed at developing a cost-effective and ergonomically designed machine that could be easily retrofitted. Such a device could reduce idle time, changeover time, production flaws while ensuring high return on investment (ROI).

2 Problem Investigation

Stitch balance is a crucial quality control parameter in the garments industry. The conventional industrial practices need to be reviewed to develop an automation-based solution. For balanced stitching, the needle and the bobbin thread tension setting of the SNLS machine need to be adjusted for a given pair of fabric and thread material. The needle thread tension is adjusted by rotating the spring-loaded tension knob, which induces a pretension on the thread. The bobbin thread tension is adjusted, by rotating the screw on the bobbin case. Stitches are checked by rough sewing and suitably adjusting the tension using a trial and error method. The same process is then repeated for all the machines in the production line. Hence, the time for changeovers is enormous [16]. Moreover, machines are subjected to continuous vibration due to rotating and reciprocating parts, which, in turn, alters the tension setting gradually over time. Maintenance workers are employed to retune the machines periodically during a batch production to reduce defects due to unbalanced stitches. Hence, there occurs a significant loss in production time.

The solution to this problem would be to develop a device that can monitor and adjust the thread tension in real-time. It should also be able to self-calibrate the system if the ideal needle and bobbin thread tensions are known for a given pair of fabric and thread material. This will result in a drastic reduction of changeover time, idle time, and eliminate unbalanced stitching defects. Garment industries have numerous sewing machines employed for a particular batch/style of production. Developing a completely new machine would be uneconomical, as it would imply discarding existing machinery to install the new ones and therefore a huge capital investment. The alternative solution would be retrofitting. The design should be ergonomic with switchable manual control mode to allow the machine to be operated manually in case the automatic system fails.

3 Planning and Design

The device has to be designed in two modules—one for thread tension and the other for bobbin tension, as shown in Fig. 1a. Both modules must have a force-sensing unit to detect the existing tension and an actuation unit for automatic tension adjustment. There must also be an electronic control unit that can coordinate the operation. The controller will receive a reference signal (required tension values) from a database and compare it with the current tension value, if it exceeds the acceptable limits, then a proportionate adjustment will be made. The overall layout and industrial implementation have been shown graphically in Fig. 1b. A single dedicated master system can be used to measure the ideal tension values for the given fabric and thread pair and upload the data into a common database. This database will be accessible to the slave systems (machines in the production line) using an ethernet network. The device is designed for single needle lockstitch (SNLS) machines since they are widely used for general stitching purposes.

3.1 Needle Thread Tension Adjustment Module

Design: The needle thread tension is conventionally adjusted by applying a pretension through a spring-loaded pair of discs, as shown in Fig. 2a. This system is automated by adding a pressure sensor and a custom motorized lead screw actuator, as shown in Fig. 2b. A force-sensitive resistor (FSR) is used to detect the amount of pretension, and the motorized lead screw slides along the mounting shaft adjusting the applied pretension. The FSR is sandwiched between two eccentric washers, mounted behind the discs, as shown in Fig. 2c. To provide adequate workspace, the motor is placed in the rear end of the machine, and the rotational motion is converted to translational motion using a lead screw. The mounting shaft is modified by increasing its length

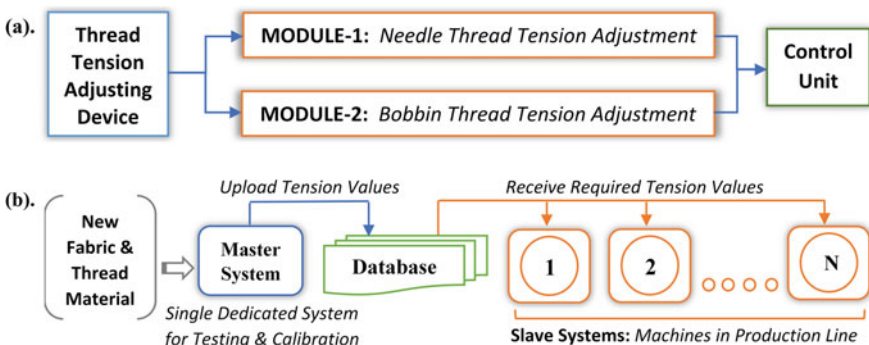


Fig. 1 Schematic layout of the proposed thread tension adjustment device, **a** parts of the device, **b** method of implementation in industry

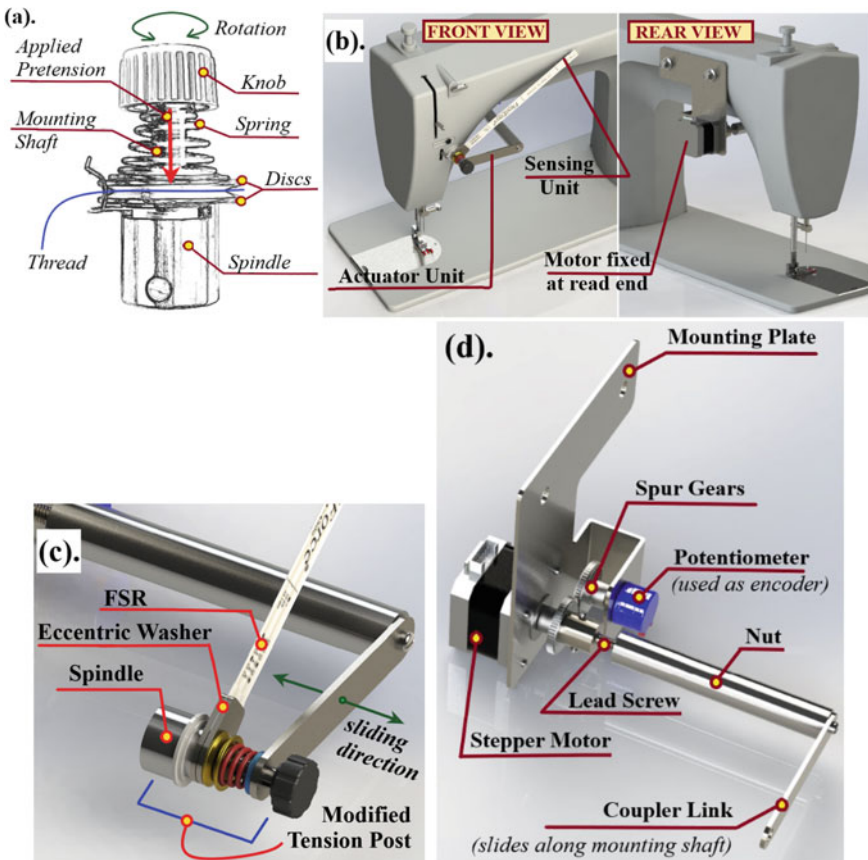


Fig. 2 a Manual thread tension correction unit, b designed module comprising of sensors and actuators, c modified thread tension unit showing the position of FSR and coupler link, d parts of the thread tension actuator (assembled view)

and removing the thread, to accommodate the new components and allow the coupler link to slide freely. Stepper motor is used for the purpose, as it can generate very small actuation which, in turn, improves the accuracy and precision of the system. An encoder is required to obtain feedback of the motor, this is done by coupling a potentiometer using a spur gear arrangement, as shown in Fig. 2d.

Working Principle: The current pretension is measured using the FSR, which produces a voltage proportional to the applied force. The controller obtains the ideal thread tension from the database and compares it with the current value. $\pm 5\%$ tolerance is allowed to prevent hunting. If the FSR reading is beyond acceptable limits, then the stepper motor rotates, which, in turn, causes the coupler link to slide on the mounting shaft. This motion compresses or releases the spring altering the pretension applied.

Modification: During experimentation, it was observed that the FSR suffers from repeatability when used for continuous long durations. So, the readings of the FSR and encoder were correlated using data from multiple trials. The FSR was then removed. The feedback is now provided by the encoder, which is correlated to the applied tension. The controller is programmed to monitor and adjust the tension after every 5 min of production. The new system is reliable, having high accuracy and repeatability for use in the continuous production process.

3.2 Bobbin Thread Tension Adjustment Module

Design: The thread storing capacity of bobbins is significantly smaller than the needle thread spool. Generally, bobbin rewinding is done after the production of every 20–25 garments. Therefore, continuous tension monitoring is not necessary, instead, the bobbin tension can be checked and adjusted after each rewinding. The bobbin tension gauges available in the market are manually operated. However, the designed device should work autonomously. The complete setup is shown in Fig. 3a. The system comprises a sensor and an actuator. The sensor is a load cell which has a hook attached to it. The thread from the bobbin passes through the load hook to the thread pickup spindle. This spindle is rotated by a dc motor. The actuator, in this case, is a stepper motor with a screwdriver head attached to its shaft. The bobbin is allowed to slide using a spring-loaded plunger to engage or disengage with the motorized screwdriver. The plunger has a pin which allows it to lock it in place when pulled back to disengage the actuator and bobbin case.

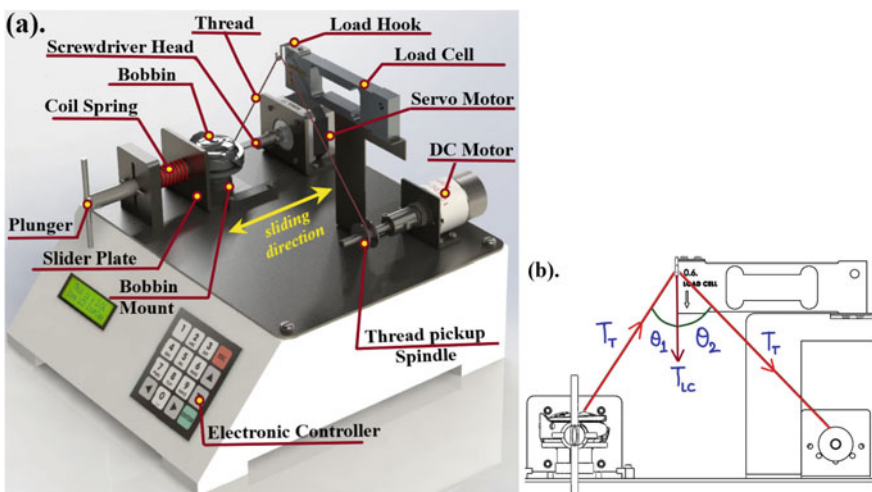


Fig. 3 **a** The designed bobbin tension adjustment module showing different parts of the system, **b** free body diagram showing the relation between load-cell reading (T_{LC}) and Thread tension (T_T)

Working: The bobbin case after refilling is placed on the bobbin mount. The plunger is released, the spring forces the slider plate to slide towards the actuator engaging it. The thread is wrapped around the pickup spindle passing through the load hook. The thread is pulled by the DC motor rotating at 60 rpm to obtain a thread speed of 30 mm/s. The load cell is now able to detect the normal force acting on the load hook (T_{LC}). The actual thread tension (T_T) can be found by resolving the forces as shown in Fig. 3b. The included angles θ_1 and θ_2 are constant depending on the mechanical construction of the device. The electronic controller obtains the signal T_{LC} , converts it to T_T and rotates the stepper motor to adjust the thread tension. After this, the plunger is pulled back and locked in position. The bobbin case can now be lifted and reinstalled in the SNLS machine. It takes just a few seconds to adjust the tension, making it faster, accurate, and reliable for use in large-scale production purposes.

3.3 Control System

To operate the needle and bobbin thread tension adjusting modules, an electronic controller is required. ArduinoTM based ATmegaTM 2560 microcontroller is used for each module. Arduino microcontroller is selected as it supports a wide range of add-on modules like ethernet shield, real-time clock, motor drivers, LCD line displays, and matrix keypads which can be connected as per requirement. The controller is programmed to take inputs, for selecting the material (thread/fabric). Accordingly, the ideal tension values are retrieved from the database. The actuation signal to drive the actuators is obtained by comparing the sensor reading and the ideal tension. For the master system, the controller has special provisions to add new tension values, edit, or delete existing data from the database. Visual feedback is provided using an LCD. A 12 V 10A dc power supply powers the controllers, sensors, and actuators. The electronic components are enclosed in a PVC box. The controller for the needle thread is screwed to the rear end of the SNLS machine, and the controller for the bobbin thread is placed inside the base of the bobbin tension adjustment module, as shown in Fig. 4.

4 Prototype Fabrication

A working prototype was developed to test the success of the design. It was installed on an SNLS machine manufactured by BrotherTM. The microcontroller was programmed using the Arduino IDE. All testing and calibration were performed at the Garments Construction Laboratory, National Institute of Fashion Technology (NIFT), Kolkata, India. The photographs of the device installed on the SNLS machine are shown in Fig. 5. For the prototype, the ethernet-based database access was discarded to avoid complexity. Instead, the ideal thread tension for a few fabric and thread materials was recorded and saved in the microcontroller memory. Sewing

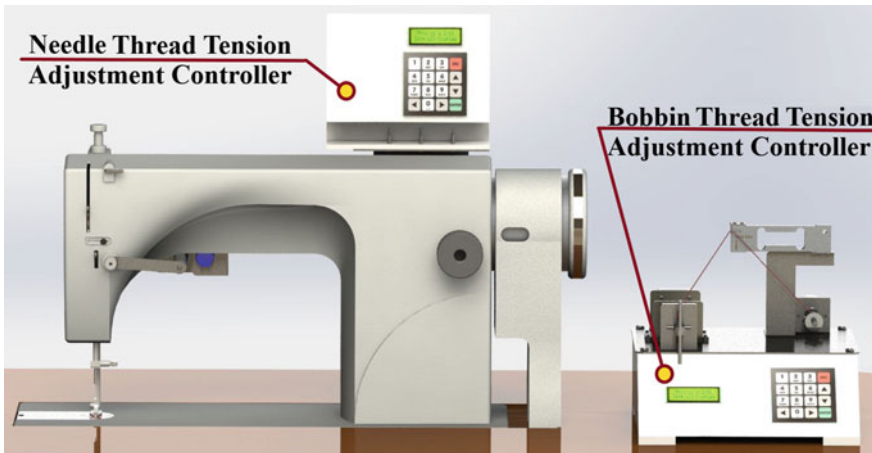


Fig. 4 Electronic controllers for the needle and bobbin thread tension adjustment modules



Fig. 5 Prototype of the thread tension adjustment device installed on an SLNS machine, at the garments construction laboratory, NIFT, Kolkata, India

with the new setup produced controlled and balanced stitch tensions, drastically reducing machine idle and style change over time. The total cost for purchasing the raw materials and manufacturing the device was approx. US \$130 (INR. 10,000) as of July 2017.

5 Results and Discussion

The device was tested for two types of fabric—Cambric cotton and Canvas with Polyester sewing thread. The needle and bobbin thread tension for a balanced stitch was experimentally determined. These values were stored in the controller, and the auto-calibration time for the device was recorded when changing from one fabric to another. The experimental data obtained are enlisted in Table 1. A tolerance of ± 1 g was allowed on both needle and bobbin thread tensions. The results show, that automation was fairly successful and outweighs the conventional calibration process practiced in the industry. Installing this device on existing machines in a production line will drastically improve productivity.

The production leverage obtainable by garments, industries can be illustrated using a sample calculation. Considering a garment manufacturing company has an order of 12,000 t-shirts.

The conventional industrial scenario:

Order Quantity: 12,000 T-Shirts.

Working days per week: 6 days.

Time for changeover and maintenance: 10 h after every 5 days of production.

Daily working hours: 10 h (600 min).

No of sewing machines in the production line: 50.

Standard Minutes Value (SMV) for a t-shirt: 30 min including 5% idle time.

Estimated daily production: 1,000 t-shirts/day.

. . . The time required to complete the work order: **14 working days**.

(12 days for manufacturing + 2 days for changeover and maintenance).

Table 1 Experimental data obtained during testing of thread tension adjusting device

Material		Balanced thread tension (g)		Maximum calibration time during fabric/thread change (s)	
Fabric	Thread	Needle	Bobbin	Needle device	Bobbin device
Cambric	Polyester	33	31	10	5
		70	58		

Retrofitting with Automatic Thread Tension Adjusting Device:

Approx. reduction of daily production idle time from 5 to 3%.

Approx. reduction of changeovers and maintenance by 60% i.e. 240 min instead of 1 day.

New SMV for a t-shirt: 29.43 min incl. 3% idle time.

Estimated daily production: 1019 t-shirts/day.

. . . The time required to complete the work order: **12 working days.¹**

One-time investment on Retrofitting: **US \$ 3,300** (approx.)

(Needle Thread Module @ US \$ 50/unit to be installed for all 50 machines, and Bobbin Thread Module @ US \$ 80/unit shareable by 5 machines).

Hence, using this machine can save 2 full working days. Besides, there are fewer production defects due to unbalanced stitches. The initial cost of retrofitting can be easily recovered from the additional productivity obtained.

6 Conclusion

The concept of an automatic thread tension adjusting device has been successfully designed. The device is capable of producing perfectly balanced stitches by sensing the current tension and adjusting it to match the ideal tension value. Based on the design, a working prototype was developed and tested in the laboratory. The performance of the prototype was satisfactory, monitoring and adjusting the thread tension took just a few seconds. The device has enormous potential in improving productivity by reducing the idle and change over time, reducing the manpower required for frequent maintenance. Moreover, the production defects due to unbalanced stitches can be eliminated. There is scope for further improvement by implementing a design and process optimization and using industrial trials to further assess its performance. A similar device could also be developed for other types of sewing machines. The simplistic and yet ergonomic design of this device makes retrofitting convenient, economical, and profitable for the garments industries.

Acknowledgements The authors would like to acknowledge Prof. Bibekananda Banerjee, National Institute of Fashion Technology (NIFT), Kolkata, for his guidance. Mr. N. C. Dutta, Sun Enterprises, for fabricating the mechanical machine parts following the given design. Special thanks to Satyam garments for providing an opportunity to study the garments industry scenario, which helped in understanding the need and the ergonomics of the design better.

Funding The project was carried out with 75% financial assistance from the Design Clinic Scheme (Ref No: SDP-17-1004) supported by the Ministry of Micro, Small and Medium Enterprises, in

¹The calculation presented above is an estimation provided for illustration only, it has not been industrially verified.

coordination with the National Institute of Design, Ahmedabad (Nodal Agency), and 25% financial assistance from the Satyam Garments, an MSME garments manufacturing unit in Kolkata, India.

References

1. O'Connell, L.: Value of the leading 10 textile exporters worldwide in 2018, by country. <https://www.statista.com/statistics/236397/value-of-the-leading-global-textile-exporters-by-country/>. Last Accessed 04 Aug 2020
2. Hashi, M.R.: Different types of defects identification and controlling method. Qual. Prod. Improv. **3**, 2348–31–81 (2016). <https://doi.org/10.9790/019X-03020118>
3. Thilagavathi, G., Viju, S.: Process control in apparel manufacturing. Woodhead Publishing Limited (2012). <https://doi.org/10.1533/9780857095633.3.428>
4. Ukpomwan, J.O., Mukhopadhyay, A.: Sewing threads. Text. Prog. **30**, 1–91 (2000). <https://doi.org/10.1080/00405160008688888>
5. Baker, M.M.: Adjusting sewing machine tension (2006)
6. Ferreira, F.B.N., Harlock, S.C., Grosbera, P.: A study of thread tensions on a lockstitch sewing machine (Part I). Int. J. Cloth. Sci. Technol. **6**, 39–42 (1994). <https://doi.org/10.1108/09556229410074592>
7. Žunič-Lojen, D., Gotlih, K.: Computer simulation of needle and take-up lever mechanism using the ADAMS software package. Fibres Text. East. Eur. **11**, 39–44 (2003)
8. Žunič-Lojen, D., Geršak, J.: Thread loadings in different measuring positions on the sewing machine. Text. Res. J. **75**, 498–506 (2005). <https://doi.org/10.1177/0040517505053870>
9. Rengasamy, R.S., Wesley, D.S.: Study on dynamic needle thread tensions in a single needle lock stitch (SNLS) sewing machine. I. Effect of stitch length, check spring tension, fabric feed timing and needle thread in-take length. Fibers Polym. **15**, 1766–1772 (2014). <https://doi.org/10.1007/s12221-014-1766-7>.
10. Rengasamy, R.S., Samuel Wesley, W.: Effect of thread structure on tension peaks during lock stitch sewing. Autex Res. J. **11**, 1–5 (2011)
11. Koncer, P., Gürarda, A., Kaplangiray, B., Kanik, M.: The effects of sewing thread properties on the needle thread tension in an industrial sewing machine. Tekst. Ve Konfeksiyon **24**, 118–123 (2014)
12. Ferreira, F.B.N., Harlock, S.C., Grosbera, P.: A study of thread tensions on a lockstitch sewing machine (Part II). Int. J. Cloth. Sci. Technol. **6**, 39–42 (1994). <https://doi.org/10.1108/09556229410074592>
13. Žunič-Lojen, D., Geršak, J.: Study of the tensile force of thread in relation to its pre-tension. Int. J. Cloth. Sci. Technol. **13**, 240–250 (2001). <https://doi.org/10.1108/09556220110396812>
14. Rocha, A.M., Lima, M.F., Ferreira, F.N., Araújo, M.D.: Developments in automatic control of sewing parameters. Text. Res. J. **66**, 251–256 (1996). <https://doi.org/10.1177/004051759606600411>
15. Stylios, G.K.: Intelligent sewing systems for garment automation and robotics. Woodhead Publishing Limited (2013). <https://doi.org/10.1533/9780857093967.1.208>
16. Karim, R.: Impact of changeover time on productivity: a case study. Int. J. Eng. Technol. IJET-IJENS **13**, 46–52 (2013)

Bearing Fault Diagnosis in Induction Motor Using Modified AlexNet Algorithm



Swapnil K. Gundewar and Prasad V. Kane

1 Introduction

In the era of twenty-first century, the internal combustion engines were dominating the personal transport sector. It seems that the EV is on the verge of rapid growth in both developing and developed vehicle market. Lower fuel cost, environmental stewardship, and energy independence are the key reasons to go for an EV. The All-Electric type of EV is dependent on the motor for its propulsion. The EV uses different types of motors such as DC Series Motor, Brushless DC Motor (BLDC), Permanent Magnet Synchronous Motor (PMSM), Three Phase Induction Motor (IM), and Switched Reluctance Motor (SRM) [1]. The selection of a particular type of motor is dependent upon performance requirements, Operating conditions, and the cost associated with the vehicle [2]. In two-wheeler applications, the power required is less and also the cost is low, hence BLDC hub motor is used. However, in the performance-oriented high power applications like cars, buses, trucks the ideal choice would be PMSM or IM [3].

IM is the preferred choice in the performance-oriented EV due to its cheap cost, robust constructions, and ability to withstand rugged environmental conditions. The IM can be designed up to the efficiency of 90–95% [4]. The major automotive manufacturers like Tata, Mahindra, and Tesla used IM in the EV for its propulsion [5]. In an EV, the vehicle is subjected to variations in the loading, speed, and torque. The continuous variation causes various types of stresses on the motor like thermal stress, Shear stress, and Environmental stress. These types of stresses can lead to defects in IM such as bearing defect, Rotor defect, Eccentricity, and Unbalance, etc. The bearing defect is responsible for 40–45% of the failure of IM [6]. Thus, the predictive maintenance of the IM is necessary to avoid any catastrophic failure.

S. K. Gundewar · P. V. Kane

Department of Mechanical Engineering, VNIT, Nagpur 440010, Maharashtra, India

In the bearing fault diagnosis, the conventional methods such as Vibration-based monitoring [7–10], Acoustic analysis [11, 12], Motor Current Signature Analysis (MCSA) [13–15], and Stray flux analysis [16, 17] are proposed by the researcher. Advanced signal processing techniques are also effectively applied by the researcher to improve the conventional fault diagnosis methods performance [18, 19]. In this decade, fault diagnosis is adapted from conventional methods to AI techniques [20]. These AI techniques include Artificial Neural Network (ANN) [21, 22], Support Vector Machine (SVM) [23–25], Fuzzy [26], and Adaptive Neuro-Fuzzy Inference System (ANFIS) [10], etc. The classification accuracy for these Machine Learning (ML) techniques is dependent on the selection of feature input [27, 28]. The importance and selection of features are based on the experimental setup used in the analysis. It also needs expert domain knowledge for the selection of effective features. This limitation of feature selection can be avoided using deep learning techniques.

In this paper, bearing fault diagnosis of an IM using modified AlexNet algorithm is proposed. The next section shows the bearing and the fault diagnosis techniques. Section 3 outlines the deep learning techniques along with the architecture of the modified AlexNet algorithm. Section 4 highlights the proposed methodology. Section 5 shows the experimental setup used for validation of the proposed methodology and results for the training and testing of proposed methodology with and without noise addition. Finally, conclusions are reached.

2 Bearing Defects and Fault Diagnosis Techniques

2.1 Bearing Defects and Characteristic Frequencies

The bearing plays an important role in the induction motor. The bearings used in the induction motor can be a rolling element bearing or ball-bearing. Continuous operation leads to various types of defects on the bearing. These defects are broadly classified into two major types: Localized defects and Distributed defects. Localized defects are further classified into four types based on the location of the fault and these are Outer Race Defect (ORD), Inner Race Defect (IRD), Ball Defect (BD), and Cage Defect (CD). All these defects appear as the characteristic defective frequency in the vibration spectrum or current spectrum. The characteristic defective frequency is dependent on the speed of rotation and the bearing specification [29]. The localized defects in the bearing are shown in Fig. 1.

Every rotating machine component represents the characteristic vibration, which uniquely differentiates it, known as vibration signature. In the bearing fault diagnosis, each defect represents the particular type of vibration signature for healthy and defective bearing as shown in Fig. 2. The defects in the bearing cause impulse at a particular frequency known as characteristic frequency which is dependent on the speed of rotation and bearing specifications. The impulses at a bearing defective frequency can damage the other connected component in the system. Hence,

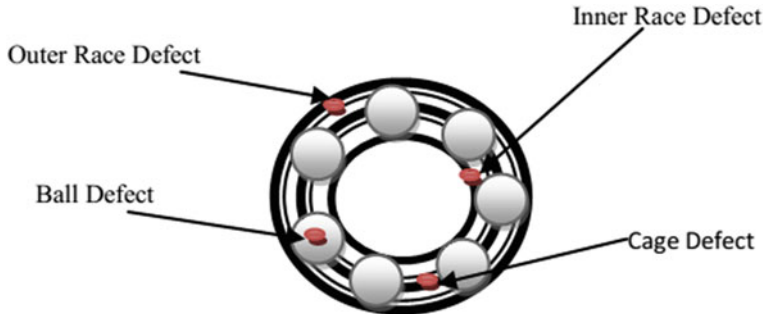


Fig. 1 Localized bearing defects

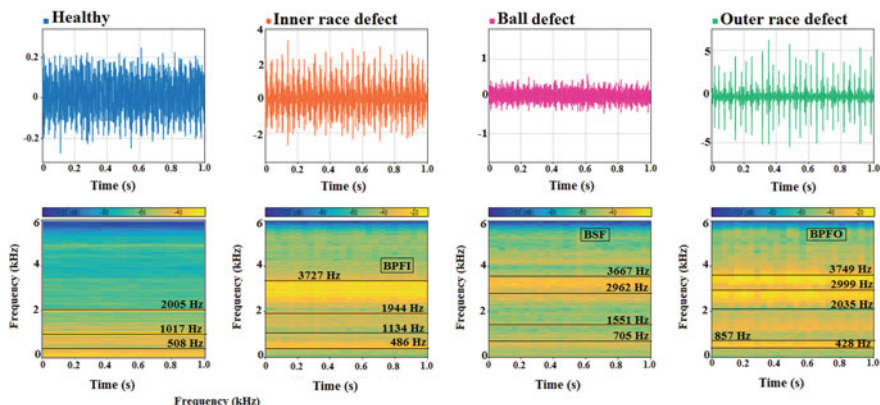


Fig. 2 Vibration signature and spectrogram for healthy and defective bearing

it is essential to diagnose the bearing fault at an incipient level. Table 1 indicates the formulas for the characteristic defective frequency and the critical values along with their harmonics. The critical values for characteristic frequencies and their harmonics are calculated from publically available CRWU bearing dataset. Some of the harmonics of the characteristic frequencies are indicated in Fig. 2 (Table 1).

2.2 Bearing Fault Diagnosis Techniques

Bearing fault diagnosis is presented by researchers using various condition monitoring techniques such as Vibration-based monitoring, MCSA, Acoustic based analysis, etc. [8–11, 15]. However, Vibration-based monitoring is a preferred choice for a bearing fault diagnosis. The bearing fault diagnosis is implemented by the researchers under three major sections: Time-domain analysis, Frequency-domain analysis, and Time–Frequency analysis followed by ML techniques [20].

Table 1 Bearing defect frequencies and their harmonics

Sr. no.	Type of Characteristic frequency	Formula	Characteristic frequency (Hz) and its harmonics
1	Ball pass frequency inner (BPFI)	$\frac{N_b}{2} S \left(1 + \frac{B_d}{P_d} \cos \theta \right)$	162.07, 324.14, 486.21, 648.28, 810.35, 972.42, 1134.49, 1296.56, 1458.63, 1620.7, 1782.77, 1944.84
2	Ball spin frequency (BSF)	$\frac{P_d}{2B_d} S \left(1 - \left(\frac{B_d}{P_d} \right)^2 \cos \theta^2 \right)$	141.07, 141.07, 282.14, 423.21, 564.28, 705.35, 846.42, 987.49, 1128.56, 1269.63, 1410.7, 1551.77, 1692.84
3	Ball pass frequency outer (BPFO)	$\frac{N_b}{2} S \left(1 - \frac{B_d}{P_d} \cos \theta \right)$	107.14, 214.28, 321.42, 428.56, 535.7, 642.84, 749.98, 857.12, 964.26, 1071.4, 1178.54, 1285.68, 1392.82, 1499.96, 1607.1

Where N_b is the number of rollers, B_d is the ball or roller diameter, P_d is the pitch diameter, θ is the contact angle, and S is the revolutions per second

Table 2 Types of spectrogram datasets used in experimental validation

Load Condition	Fault types	Fault severity (inch)	Total number of spectrogram dataset
No-load	Inner race defect,	0.007, 0.014, 0.021	30 types of Spectrogram datasets
1HP Load	Outer race defect,		
2HP load	Ball defect		

In the time-domain analysis, the variation of physical parameters such as vibration signal, acoustic signal, or current signal is mapped against time. The statistical features are extracted from the acquired signal and applied as input to ML classifiers. These statistical features can be RMS, Kurtosis, Variance, Standard Deviation, Shape factor, and Crest Factor, etc. [29]. However, to reduce the dimensionality and processing time, most effective statistical features are selected by using various feature selection methods such as GA, PCA, Wrapper Method [30]. The frequency-domain analysis indicates the quantity of the signal existing in a given frequency band concerning a range of frequencies. In the frequency-domain analysis, the characteristic frequencies are used as a fault indicator. Each defect produces an impulse at the desired frequency known as characteristic defect frequency. The characteristic defect frequency can be seen in the vibration or current spectrum [31]. The Time-Frequency (T-F) analysis indicates the variation of amplitude against time and frequency both. The T-F analysis is widely used for the characterizing the transient signals. T-F analysis can effectively diagnose the bearing fault in an IM [32]. In the T-F analysis, various T-F plots are employed such as Spectrogram, Kurtogram, Synchro-squeezed transform, Wavelet transforms, etc. [33, 34].

In all these domains of analysis, whether it may be time-domain, frequency-domain or time-frequency-domain analysis, the selection of features plays an important role in the classification accuracy. The selection of the most effective features can reduce the processing time and may improve fault diagnosis accuracy [35].

2.3 Spectrogram

The spectrogram is a visual representation of STFT where the X-axis and Y-axis represent the time and frequency and the colour scale represents the amplitude of the frequency. The STFT is a series of sinusoidal. Spectrograms are widely used in different fields such as music, linguistics, sonar, radar, and signal processing.

The spectrogram is one of the well-known time-frequency representations defined as the squared magnitude of the Short-Time Fourier Transform.

$$S(t, \omega) = |X(t, \omega)|^2 \quad (1)$$

The STFT is defined as a complex function of continuous-time t and radian frequency ω given by,

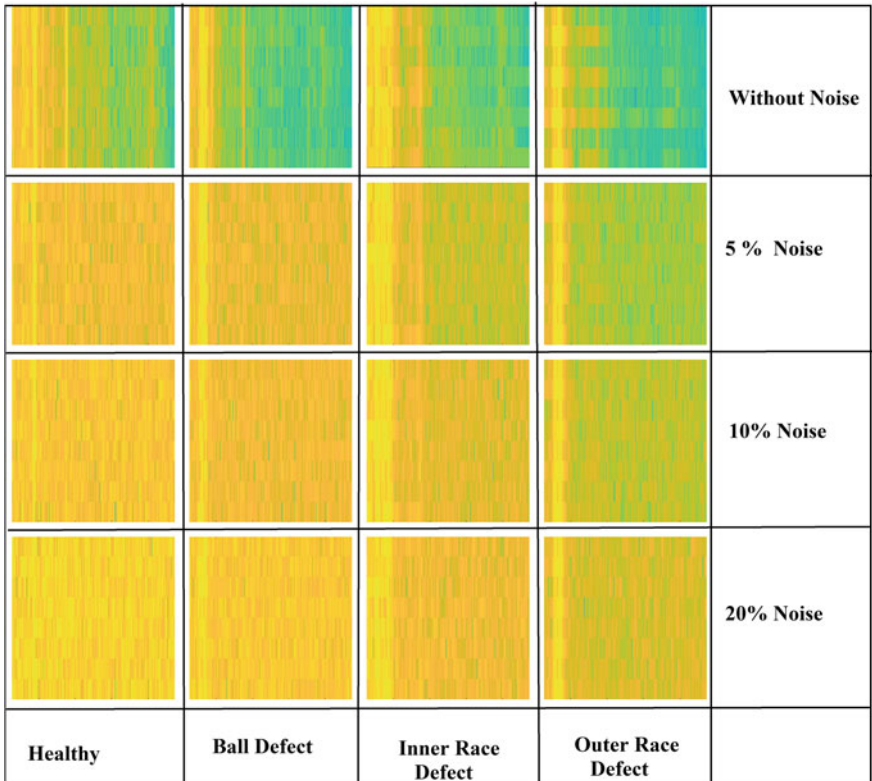


Fig. 3 Spectrogram plots with desired noise percentage for four classes of bearing at the no-load condition and 0.007-inch defect severity using bearing dataset provided by Case Reserve Western University

$$X(t, \omega) = M(t, \omega)e^{j\varphi(t, \omega)} \quad (2)$$

where, $M(t, \omega)$ is the magnitude of STFT and $\varphi(t, \omega)$ is its phase. The spectrogram plots for raw vibration signals with noise addition and without noise are shown in Fig. 3.

3 Deep Learning Techniques

Traditional ML techniques have been applied widely in the last decade for the fault diagnosis of rolling element bearing. However, several drawbacks are associated with ML techniques. The ML technique classification accuracy is dependent on the selection of features. The shallow structure of the ML classifier limits the capability of the classifier to learn from a complex nonlinear relationship in fault diagnosis.

Recently Deep Learning (DL) techniques emerged as a trend in fault diagnosis. The DL techniques overcome the machine learning techniques in terms of feature extraction. Deep learning techniques automatically extract the features from the provided input signal. The bearing fault diagnosis is presented by the researchers using various network models in DL techniques such as Recurrent Neural Network (RNN) [36], Convolution Neural Network (CNN) [36–38], Deep Belief Network (DBN) [39], Deep Boltzmann Machine [40], etc. However, CNN is widely used in the bearing fault diagnosis. CNN consists of different types of pre-trained networks and networks from scratch. The pre-trained networks are AlexNet, GoogLeNet, ResNet 50, etc.

3.1 Modified AlexNet Algorithm

The AlexNet is a pre-trained deep neural network designed by Alex Krizhevsky [41]. The AlexNet algorithm is trained by 1.2 million high-quality images in the ImageNet contest LSVRC-2010 [42]. The pre-trained AlexNet consists of 60 million parameters and 65000 neurons in it. It is capable to classify the given set of inputs into 1000 different classes. The AlexNet architecture consists of five convolution layer and three fully connected layers. The Relu activation function is used in the AlexNet algorithm which is faster than other activation functions like tanh and sigmoid.

The architecture for the AlexNet algorithm is shown in Fig. 4. In the first layer of the AlexNet algorithm, the convolution window size is 11×11 . Considering the image input size of the AlexNet algorithm, the first window is kept of large size to capture the entire object. In the second convolution layer, the window size reduced to 5×5 , followed by 3×3 . In this AlexNet algorithm after the first, second, and fifth convolution layers, the maximum pooling layer is kept with the window size of 3×3 and stride 2. In this AlexNet algorithm after the convolution layer, there are two fully connected layers with 4096 outputs. The last three layers in the AlexNet algorithm are capable to configure 1000 different classes. In the proposed AlexNet algorithm, the last three layers are replaced with the fully connected layer, softmax layer, and

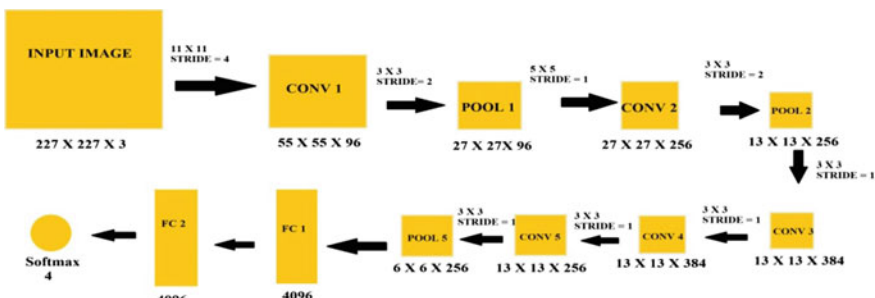


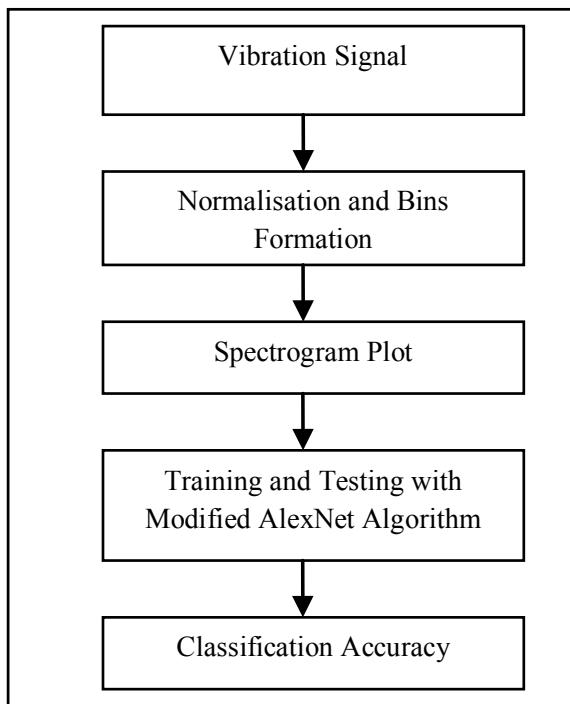
Fig. 4 Modified AlexNet algorithm

classification output layer. In this last fully connected layer, the output class is kept as four which can classify the bearing fault in four different categories.

4 Proposed Methodology

The acquired vibration signals are normalized by dividing with maximum value in a vector. After the normalization, the vibration signals are converted into bins where each bin carries 2048 data points. After the formation of bins, the spectrogram is generated from each bin. These spectrograms are the RGB image with a size of $227 \times 227 \times 3$. The size of the image input is kept 227×227 since the image input requirement of AlexNet is 227×227 . These spectrograms are applied as input to the modified AlexNet algorithm. In the modified AlexNet algorithm 70% image dataset is used for training and the remaining 30% for the testing. Finally, accuracy is compared. The process flow for the proposed methodology is shown in Fig. 5.

Fig. 5 Proposed methodology



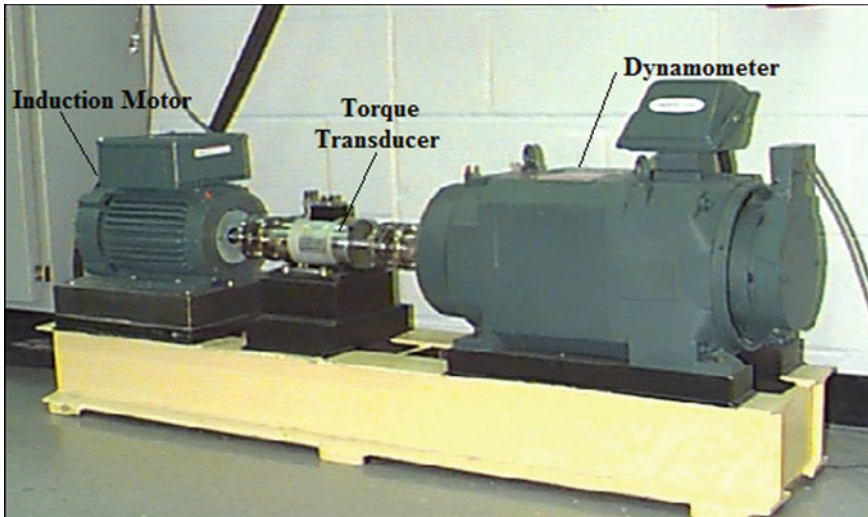


Fig. 6 Experimental setup by CRWU

5 Experimental Validation

5.1 Experimental Setup

The Case Reserve Western University [43] has made the rolling element bearing datasets available in the open forum. This dataset is used in this paper. The experimental setup is shown in Fig. 6. The experimental setup consists of a 2HP three-phase induction motor, a dynamometer, and a torque transducer. The vibration signals are acquired by the piezoelectric sensor at a sampling frequency of 12 kHz. In the experimental setup, vibration readings are acquired for three different types of fault: Outer race defect, Inner race defect, and Ball defect. These defects are induced in the rolling element bearing using electric discharge machining. The fault severities used for the bearing defects are 0.007 inches, 0.014 inches, and 0.021 inch. The readings are acquired for three types of load conditions: no-load, 1HP load, and 2HP load. In the experimental validation, three different types of faults, four load conditions, and three different fault sizes along with healthy condition dataset constitute 30 types of the image dataset (Figs. 7 and 8).

5.2 Training of the Modified AlexNet Algorithm

The spectrogram plots are used as input for the modified AlexNet algorithm. The spectrogram plots of size $227 \times 227 \times 3$ are used for the training and testing of

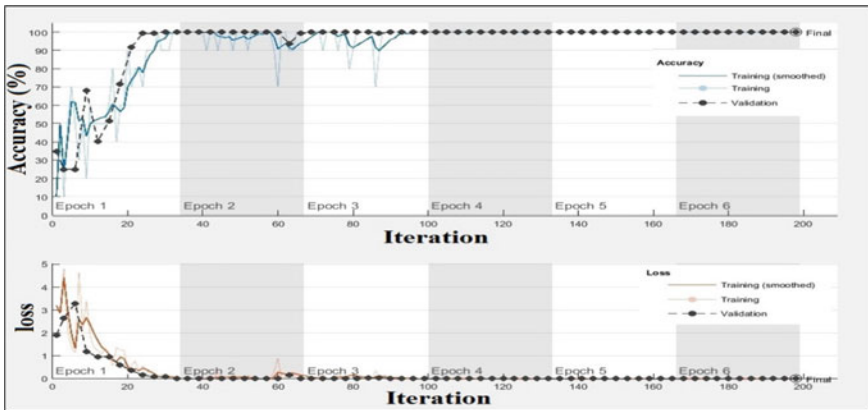


Fig. 7 Training and Validation plot for the bearing fault diagnosis at the no-load condition and 0.007-inch defect severity

Fig. 8 Confusion Matrix plot for the bearing fault diagnosis at the no-load condition and 0.007-inch defect severity

		Output class				
		BD	Healthy	IRD	ORD	
Target class	BD	36 25%	0 0.0%	0 0.0%	0 0.0%	100% 0.0%
	Healthy	0 0.0%	36 25%	0 0.0%	0 0.0%	100% 0.0%
IRD	IRD	0 0.0%	0 0.0%	36 25%	0 0.0%	100% 0.0%
	ORD	0 0.0%	0 0.0%	0 0.0%	36 25%	100% 0.0%
		100% 0.0%	100% 0.0%	100% 0.0%	100% 0.0%	100% 0.0%

the modified AlexNet algorithm. For each type of image dataset, 70% spectrogram images are used for training and the remaining 30% images are used for the validation. In the training of the modified AlexNet algorithm, the momentum learning rule is used with the learning rate of 0.0001. The other parameters are stated as follows in Table 3.

The Training and validation results of the modified AlexNet algorithm for three different types of load conditions are stated in Table 4.

Table 4 indicates that the testing classification accuracy at the no-load condition for each of the defect severity (0.007, 0.014, and 0.021 inch) is 100% which reduces

Table 3 Modified AlexNet algorithm parameters

Parameter	Value
Momentum rate	0.0001
Maximum number of epoch	6
Validation frequency	3
Number of events considered at a time	10

Table 4 Training and Validation classification accuracy of the modified AlexNet algorithm

Load	Defect severity (inches)	Training accuracy (%)	Testing accuracy (%)
No load	0.007	100	100
	0.014	99	100
	0.021	100	100
1HP load	0.007	100	100
	0.014	99.60	99.60
	0.021	100	100
2HP load	0.007	100	100
	0.014	100	98.29
	0.021	100	96.53

slightly at 1HP and 2HP load conditions. The presence of the other frequency components at loading conditions can affect the spectrogram plots. Thus, the classification accuracy in the loading condition is slightly affected.

5.3 Noise Addition

The working condition can never be ideal for the IM. In real life, the surrounding vibration near the IM can affect fault diagnosis accuracy. Hence, to simulate the real-life condition, noise is added externally in the acquired vibration signal to check the performance. The white Gaussian noise is added in the acquired vibration signal using MATLAB. The noise is added in terms of the percentage of the original signal. After the noise addition, the performance is analyzed at each load and defect severity condition. The training and testing accuracy of the classification after the addition of desired percentage of noise is stated in Table 5.

Table 5 indicates the average classification accuracy of 98.14% with a 5% noise addition. The classification accuracy is reduced to 96.84% for 10% noise addition. Further noise addition, i.e., 20% noise addition reduces the accuracy to 88.24%. The proposed method can efficiently diagnose the bearing fault at no load condition up to 10% noise, while the performance gets affected with the further addition of load and 20% noise. The loading condition may produce a wide range of load-related frequencies which reduces the fault diagnosis performance in loading conditions. The

Table 5 Training and validation classification accuracy after noise addition

Load	Defect severity	5% noise		10% noise		20% noise	
		Training accuracy (%)	Testing accuracy (%)	Training accuracy (%)	Testing accuracy (%)	Training accuracy (%)	Testing accuracy (%)
No load	0.007	100	100	100	100	98.33	98.33
	0.014	100	100	99.17	99.17	90	95
	0.021	100	100	100	96.67	80	85.83
1HP load	0.007	100	100	98	100	100	96.67
	0.014	90	97.83	90	94.44	90	94.17
	0.021	80	98.33	90	98.33	80	85.83
2HP load	0.007	100	100	100	98.33	90	97.50
	0.014	70	87.12	80	90.48	60	73.33
	0.021	100	100	80	94.17	100	67.50

application of advanced noise cancellation techniques may improve the diagnosis performance even at a high level of noise.

6 Conclusions

In this paper, a modified AlexNet algorithm using a spectrogram plot is proposed for the bearing fault diagnosis in an IM. The proposed method effectively diagnoses the bearing fault in an IM even at noisy conditions up to 10% of white Gaussian noise. However, the performance decreases with a 20% noise addition. The classification is performed for four different classes by using the data provided by CRWU bearing dataset. The proposed technique achieved the classification accuracy of 100% without the addition of any external noise at no-load condition. However, the average classification accuracy at 5%, 10%, and 20% noise addition are 98.14%, 96.84%, and 88.24%, respectively. The application of proposed techniques in an EV can diagnose the fault at an incipient level. The application of advanced noise reduction techniques may help to improve diagnosis performance. In near future, the proposed technique can be applied for the fault diagnosis of other faults in an IM.

References

1. Xue, X., Cheng, K., Cheung, N.: Selection of electric motor drives for electric vehicles. In: 2008 Australasian Universities Power Engineering Conference, pp. 1–6. IEEE (2008)
2. Karthik, S.H.: Types of motors used in electric vehicles (2019). <https://circuitdigest.com/article/different-types-of-motors-used-in-electric-vehicles-ev>

3. Băltățanu, A., Florea, L.M.: Comparison of electric motors used for electric vehicles propulsion. In: Proceeding of International Conference of Scientific Paper AFASES (2013)
4. DOE U.: Improving motor and drive system performance: a sourcebook for industry. US Department of Energy (2008)
5. Singh, K.V., Bansal, H.O., Singh, D.: A comprehensive review on hybrid electric vehicles: architectures and components. *J. Modern Transport.* **27**, 77–107 (2019)
6. Nandi, S., Toliyat, H.A., Li, X.: Condition monitoring and fault diagnosis of electrical motors—A review. *IEEE Trans. Energy Convers.* **20**, 719–729 (2005)
7. Konar, P., Chattopadhyay, P.: Bearing fault detection of induction motor using wavelet and support vector machines (SVMs). *Appl. Soft Comput.* **11**, 4203–4211 (2011)
8. Li, B., Chow, M.-Y., Tipsuwan, Y., Hung, J.C.: Neural-network-based motor rolling bearing fault diagnosis. *IEEE Trans. Industr. Electron.* **47**, 1060–1069 (2000)
9. Adjallah, K.H., Han, T., Yang, B.S., Yin, Z.J.: Feature-based fault diagnosis system of induction motors using vibration signal. *J. Qual. Maint. Eng.* (2007)
10. Zhang, L., Xiong, G., Liu, H., Zou, H., Guo, W.: Bearing fault diagnosis using multi-scale entropy and adaptive neuro-fuzzy inference. *Expert Syst. Appl.* **37**, 6077–6085 (2010)
11. Glowacz, A., Glowacz, W., Glowacz, Z., Kozik, J.: Early fault diagnosis of bearing and stator faults of the single-phase induction motor using acoustic signals. *Measurement* **113**, 1–9 (2018)
12. Hasan, M.J., Islam, M.M., Kim, J.-M.: Acoustic spectral imaging and transfer learning for reliable bearing fault diagnosis under variable speed conditions. *Measurement* **138**, 620–631 (2019)
13. Singh, S., Kumar, A., Kumar, N.: Motor current signature analysis for bearing fault detection in mechanical systems. *Procedia Mater. Sci.* **6**, 171–177 (2014)
14. Lau, E.C., Ngan, H.: Detection of motor bearing outer raceway defect by wavelet packet transformed motor current signature analysis. *IEEE Trans. Instrum. Meas.* **59**, 2683–2690 (2010)
15. Alwodai, A., Wang, T., Chen, Z., Gu, F., Cattley, R., Ball, A.: A study of motor bearing fault diagnosis using modulation signal bispectrum analysis of motor current signals. *J. Signal Inf. Process.* **4**, 72 (2013)
16. Vitek, O., Janda, M., Hajek, V., Bauer, P.: Detection of eccentricity and bearings fault using stray flux monitoring. In: 8th IEEE Symposium on Diagnostics for Electrical Machines, Power Electronics & Drives, pp. 456–461. IEEE (2011)
17. Frosini, L., Harlışça, C., Szabó, L.: Induction machine bearing fault detection by means of statistical processing of the stray flux measurement. *IEEE Trans. Industr. Electron.* **62**, 1846–1854 (2014)
18. Xu, L., Chatterton, S., Pennacchi, P.: Rolling element bearing diagnosis based on singular value decomposition and composite squared envelope spectrum. *Mech. Syst. Signal Process.* **148**, (2020)
19. Amarouyache, I.I.E., Saadi, M.N., Guersi, N., Boutasseta, N.: Bearing fault diagnostics using EEMD processing and convolutional neural network methods. *Int. J. Adv. Manuf. Technol.* **107**, 4077–4095 (2020)
20. Gangsar, P., Tiwari, R.: Signal based condition monitoring techniques for fault detection and diagnosis of induction motors: a state-of-the-art review. *Mech. Syst. Signal Process.* **144**, (2020)
21. Yu, Y., Junsheng, C.: A roller bearing fault diagnosis method based on EMD energy entropy and ANN. *J. Sound Vib.* **294**, 269–277 (2006)
22. Dubey, R., Agrawal, D.: Bearing fault classification using ANN-based Hilbert footprint analysis. *IET Sci. Meas. Technol.* **9**, 1016–1022 (2015)
23. Fernández-Francos, D., Martínez-Rego, D., Fontenla-Romero, O., Alonso-Betanzos, A.: Automatic bearing fault diagnosis based on one-class v-SVM. *Comput. Ind. Eng.* **64**, 357–365 (2013)
24. Abbasion, S., Rafsanjani, A., Farshidianfar, A., Irani, N.: Rolling element bearings multi-fault classification based on the wavelet denoising and support vector machine. *Mech. Syst. Signal Process.* **21**, 2933–2945 (2007)

25. Zhi-qiang, J., Hang-guang, F., Ling-jun, L.: Support vector machine for mechanical faults classification. *J. Zhejiang Univ.-Sci. A* **6**, 433–439 (2005)
26. Berredjem, T., Benidir, M.: Bearing faults diagnosis using fuzzy expert system relying on an improved range overlaps and similarity method. *Expert Syst. Appl.* **108**, 134–142 (2018)
27. Khodja, A.Y., Guersi, N., Saadi, M.N., Boutasseta, N.: Rolling element bearing fault diagnosis for rotating machinery using vibration spectrum imaging and convolutional neural networks. *Int. J. Adv. Manuf. Technol.* **106**, 1737–1751 (2020)
28. Wei-dong, J., Shi-xi, Y., Zhao-tong, W.: Extracting invariable fault features of rotating machines with multi-ICA networks. *J. Zhejiang Univ.-Sci. A* **4**, 595–601 (2003)
29. Kankar, P.K., Sharma, S.C., Harsha, S.P.: Fault diagnosis of ball bearings using machine learning methods. *Expert Syst. Appl.* **38**, 1876–1886 (2011)
30. Li, B., Zhang, P.-l., Tian, H., Mi, S.-S., Liu, D.-S., Ren, G.-Q.: A new feature extraction and selection scheme for hybrid fault diagnosis of gearbox. *Expert Syst. Appl.* **38**, 10000–10009 (2011)
31. Rai, A., Upadhyay, S.: A review on signal processing techniques utilized in the fault diagnosis of rolling element bearings. *Tribol. Int.* **96**, 289–306 (2016)
32. Chen, Z., Cen, J., Xiong, J.: Rolling bearing fault diagnosis using time-frequency analysis and deep transfer convolutional neural network. *IEEE Access* **8**, 150248–150261 (2020)
33. Wang, J., Mo, Z., Zhang, H., Miao, Q.: A deep learning method for bearing fault diagnosis based on time-frequency image. *IEEE Access* **7**, 42373–42383 (2019)
34. Jin, Y., Hao, Z-Y., Zheng, X.: Comparison of different techniques for time-frequency analysis of internal combustion engine vibration signals. *J. Zhejiang Univ.-Sci. A* **12**, 519–531 (2011)
35. Lei, Y., He, Z., Zi, Y.: Application of an intelligent classification method to mechanical fault diagnosis. *Expert Syst. Appl.* **36**, 9941–9948 (2009)
36. Yang, Y., Zheng, H., Li, Y., Xu, M., Chen, Y.: A fault diagnosis scheme for rotating machinery using hierarchical symbolic analysis and convolutional neural network. *ISA Trans.* **91**, 235–252 (2019)
37. Tra, V., Kim, J., Khan, S.A., Kim, J.-M.: Bearing fault diagnosis under variable speed using convolutional neural networks and the stochastic diagonal levenberg-marquardt algorithm. *Sensors* **17**, 2834 (2017)
38. Ye, C-M., Liu, X., Xu, H., Ren, S-C., Li, Y., Li, J.: Classification of hyperspectral images based on a convolutional neural network and spectral sensitivity. *J. Zhejiang Univ.-Sci. A* **21**, 240–248 (2020)
39. AlThobiani, F., Ball, A.: An approach to fault diagnosis of reciprocating compressor valves using Teager-Kaiser energy operator and deep belief networks. *Expert Syst. Appl.* **41**, 4113–4122 (2014)
40. He, X.-H., Wang, D., Li, Y.-F., Zhou, C.-H.: A novel bearing fault diagnosis method based on gaussian restricted boltzmann machine. *Math. Probl. Eng.* (2016)
41. Nawaz, W., Ahmed, S., Tahir, A., Khan, H.A.: Classification of breast cancer histology images using alexnet. In: International Conference Image Analysis and Recognition, pp. 869–876. Springer (2018)
42. Shi, X., Cheng, Y., Zhang, B., Zhang, H.: Intelligent fault diagnosis of bearings based on feature model and Alexnet neural network. In: 2020 IEEE International Conference on Prognostics and Health Management (ICPHM), pp. 1–6. IEEE
43. Case Western Reserve University bearing data center website. <http://csegroups.case.edu/bearingdatacenter/home>

Improved Design and Development of Crop Conveying Mechanism in Reaper Machine



Anand Kumar Jangir, Narendra Achera, Saurav Khandelwal,
Chirag Gupta, Himanshu Chaudhary, and N. R. N. V. Gowripathi Rao

1 Introduction

Reaping is the process of removing the stalk from the ground. Before automation, reaping process was done by hand with sickle and scythe. Sickle has curved blades on wooden handle. Mechanical reapers use cutter bars to cut the crops. Most modern mechanical reapers cut the grass; and gather it, either by windrowing it or picking it up.

1.1 Need of Reaper [1]

A. Farm workforce, which was accessible in abundance a while ago, was becoming scarce and expensive due to transfers within the nation to other nations and urban industrial areas.

B. Wheat production increased significantly due to the use of high yielding varieties and other inputs such as irrigation water, organic fertilizers, and pesticides.

C. Wheat reaping was one of the harvesting operations that was most boring, time-consuming and tiring, so farmers started looking for relaxed alternatives.

D. The harvest season is lower and crop loss is expected with bad weather. In such a situation, a fast way of harvesting and harvesting is needed.

A. K. Jangir · N. Achera · S. Khandelwal · C. Gupta · H. Chaudhary
Malaviya National Institute of Technology Jaipur, Rajasthan 302017, India

N. R. N. V. G. Rao (✉)
Aditya Engineering College, Surampalem, Andhra Pradesh 533437, India

2 Literature Review

Chavan et al. used an already existing manually operated reaper, i.e., there was no motor tractor used. It was meant for small scale farmers. The mechanism was having single slider crank mechanism for cutting mechanism. He found optimum angle (22°) for crop divider. The position of crop divider in already existing crop divider was not accurate so author found correct position of crop divider. He found optimum angle and speed for star wheel. [2].

Wahane used an already existing self-propelled vertical conveying reaper and found a major problem of conveying the crop in reaper. So she provided an arrangement on crop divider to keep crop erect. She used two star wheels in a single crop divider instead of just one. She used a compression spring with crop divider for better contact with conveyor belt. She also increased the size of conveying lugs. She designed a conveying box so that crop can go aside easily. After iterative optimization, the size of conveying box was increased. She made a modification in the reaper so that height of cut of crop can be varied. The author calculated optimum forward speed of tractor so that energy consumption is minimum. The experiment was carried out on crops of wheat and chickpea [3].

Kunpeng Tian et al. did his research on moving blades. Bionic is referred to a shape which is having arc type shapes and protrusions at the end of arc which gives the blade high strength. Compared to ordinary blade bionic blade has variable rake angle. Due to variable rake angle, crop cutting is flat and smooth, whereas in ordinary blade rough cutting takes place. For bionic blade, cutting force and energy was lesser than that of ordinary one [4].

2.1 Conclusion from the Reviews

From literature review, some key finds were such as in most of the reapers slider crank mechanism is used as cutting mechanism. For proper dividing of crop, crop divider should be at optimum angle, which is 22° . For proper conveying of crop, star wheel should also be aligned at 22° and crop should be straight throughout. For proper cutting of crop, modification in cutting blade can be done to reduce force.

2.2 Research Gap

While doing the literature review, some problems were identified such that improper crop conveying, jamming of crop in cutting blade and if crop is fallen due to rain or windstorm (crop is slant) available reaper are unable to cut. There has been a little research work in the fields of improper conveying of crop and jamming of crop but we did not find any research work in the area of slant crop. There is no option to

cut slant crop by reaper. Combined harvester is an option but for slant crop losses are very high. So only option to cut slant crop is manual cutting. That's why we chosen to work in the field to cut slant crop.

3 Mechanism Selection

3.1 Four Bar Mechanism

In this mechanism, four bar crank rocker mechanism is used. This is a single degree of freedom mechanism. In this type of mechanism, a point on coupler is traced as a straight line, and this point is connected to moving blade of reaper.

Merits

1. Power requirement will be less.
2. Mechanism can be balanced completely.

3.2 Slider Crank Mechanism

In this mechanism, first inversion of slider crank mechanism is used which is a single degree of mechanism. Here, moving blade acts as the slider of mechanism and fixed blade is the link (cylinder) in which moving blade reciprocates.

Merits

1. Stroke will be exact straight line in this mechanism.
2. Stroke length can be varied easily by just changing crank length.

Demerits

1. Power requirement will be more.
2. Complete balancing of the mechanism is not possible since reciprocating parts are there.

4 Power

4.1 Power Transmission in Reaper

The reaper we selected is a tractor powered reaper. Power is taken by power take off (PTO) through a shaft which is finally connected to gear box. Gear box has two purposes, viz., increase the speed at which shaft rotates and divides the power between

crank and conveying mechanism. For this purpose, a gear box using three bevel gears is used. For conveying mechanism, belt pulley system is used and conveying belt has lugs. Cutting mechanism is single slider crank mechanism that is used. For proper cutting and crop conveying gear ratio is calculated. To bear the exerted load, different gear parameters are calculated.

4.2 Gear Ratio Calculation

Tractor Speed = 9 km/h = 2.5 m/s (Assumption)

Average Slider Speed (v_{avg}) = $2.5 * 1.3 = 3.25$ m/s [5].

$v_{avg} = 2LN/60$ & $L = 2r = 0.11$ m

Now

$N_{pinion} = 812.5$ rpm

$N_{gear} = 540$ rpm

Gear Ratio = $N_{pinion}/N_{gear} = 1.50$

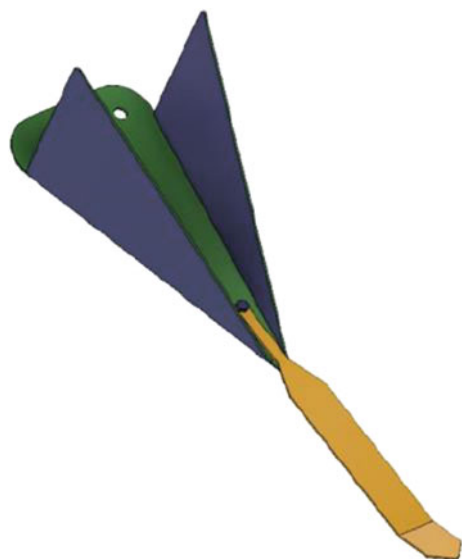
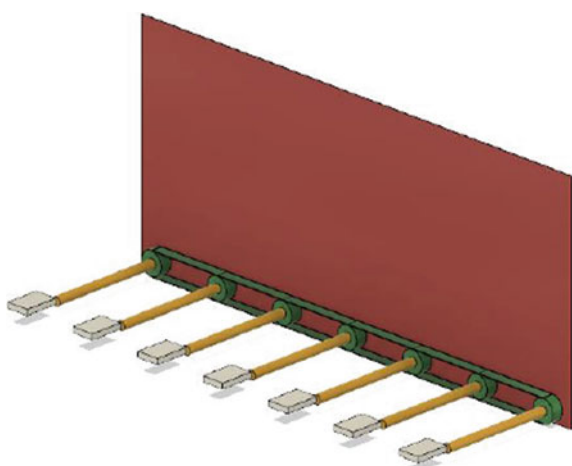
5 Concept Generation

5.1 Modified Crop Divider

In this concept, a deflector plate is attached at front end of crop divider. Crop will slide over the deflector plate and get some elevation. After this, side way of crop divider are in taper form so that crop can be gradually straightened. Clearance of deflector from ground is 50 mm. In this mechanism, the deflector plate can be removed if not in use (Fig. 1).

5.2 Mechanized Deflector Plate

In this concept, crank rocker mechanism is used. The output link of crank rocker mechanism is connected to a pulley. This pulley drives belt pulley system, and there is pulley for each of crop divider. From these pulleys, a shaft is taken to drive deflector plates. Rocker motion is such that for a rotation of crank output link rotates for 900 and comes back (Fig. 2).

Fig. 1 Modified crop divider**Fig. 2** Mechanized deflector plate

5.3 *Mechanical Fingers*

This concept uses both hydraulic and mechanical movement. There is a hydraulic operated sliding joint used for straight motion of fingers. By this motion, fingers go underneath the crop and there is a revolute joint which moves fingers upward and crop gets straightened (Fig. 3).

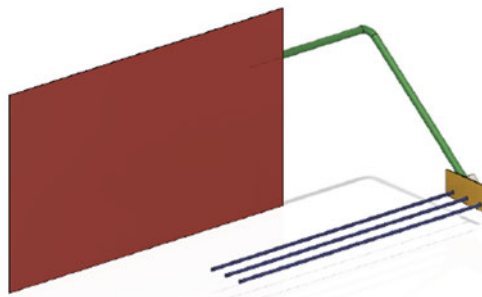


Fig. 3 Mechanical fingers

6 Final Model

See Figs. 4 and 5.

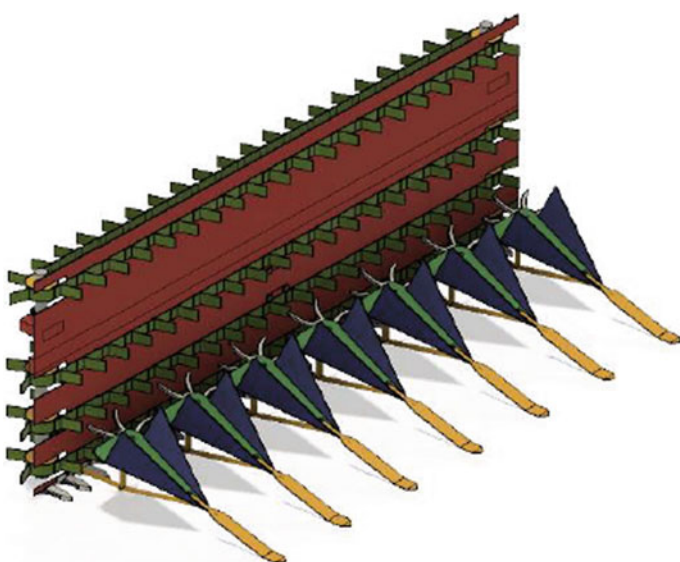


Fig. 4 Reaper model (Front end)

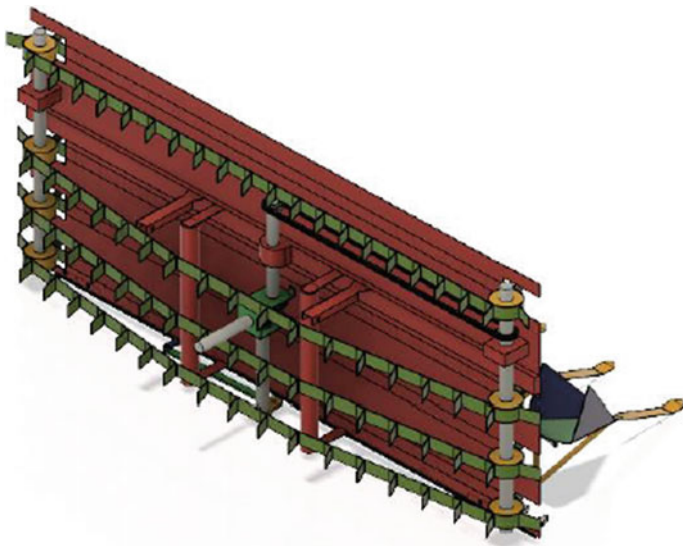


Fig. 5 Reaper model (Back end)

7 Kinematic Analysis

Kinematic analysis involves displacement, velocity and acceleration analysis of the mechanism without considering any forces and mass on the body. Code of Kinematic analysis was written in MATLAB. The results were generated by using data of reaper obtained in field survey which are as following (Fig. 6).

8 Prototyping

Prototyping of the model is done to verify the design of the product. Fabricating of the prototype was challenging because of small and intricate parts. So it was chosen that a scaled prototype would be manufactured by 3D printing. Major components were 3D printed while some parts like gear casing and lugs were cut from aluminum sheet and belts were cut from thick cotton taping (Table 1) (Fig. 7).

9 Conclusion

This modified reaper machine will be great helpful to cut slant crops. The additional mechanism which is used to lift the slant crop is removable, so if the crop is not slanted, the attachment can be removed.

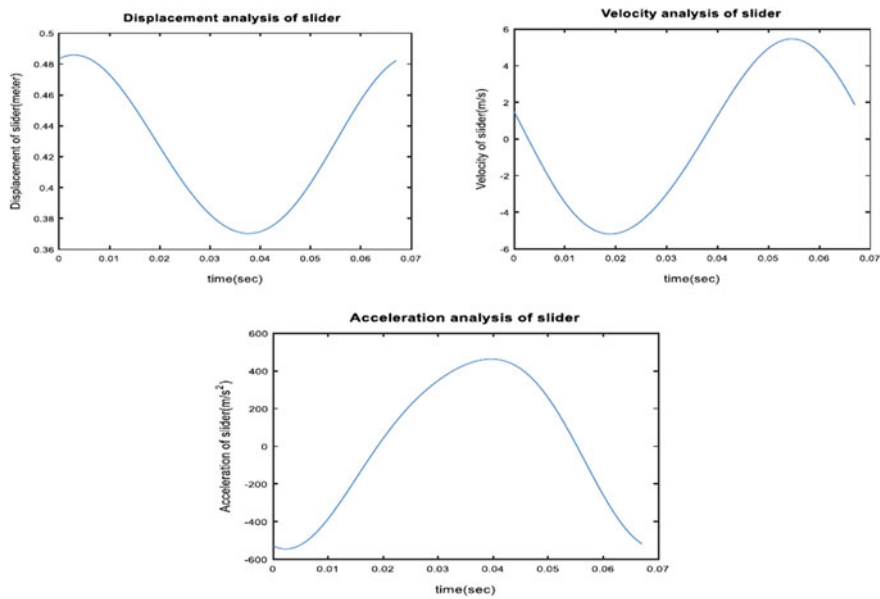


Fig. 6 Kinematic analysis results

Table 1 Changes made in design

Serial no.	Designed model	Prototype (with reason for change)
1	Gear ratio for power transmission from PTO to crank and conveyor belt is 1.5	Gear ratio is kept 1, since gears are 3D printed. But due to complexity gears are removed and shafts are directly connected. (Gear ratio = 1)
2	For power transmission from gear box to conveyor belts chain sprocket is used	Since chain sprocket takes more space and it is difficult to find small chain sprocket, so belt pulley is used for power transmission
3	Deflector plate is removable, so it is temporarily fastened by nut and bolt	Since in prototype deflector plate need not to be removable, so it is permanently joined
4	Four conveyor belt is used	Due to less power available, only two conveyor belts are used

The major parts of prototype were manufactured by 3D printing. Gear box casing and lugs were made of aluminum. Assembly of parts was done manually. Due to manufacturing and power requirement limitations, some modifications were done. Finally, since model had some delicate parts so motor was not used, instead of that rotation to shaft was given manually. After complete assembly rotation was given and all parts were moving and as a conclusion it can be said that prototype is working successfully.



Fig. 7 Prototype images

10 Future Work

There is not much research being done in the field of agriculture in India, and attention needs to be paid to this field. Crop cutting is a time-consuming process, and it is more rigorous when the crop is slanted. The model we made can cut the crop which is slanted in a particular direction. But if the crop is slanted in an uneven manner then the solution provided is not successful. Jamming of the crop in blades, star wheel, and conveyor belt is still an issue which needs to be resolved. If the crop length is more, flow of crop by conveyor belt is not efficient, so the problem needed to be addressed. The cost of present reaper available in the market is high, and this needs to be optimized so that it is readily available for small scale farmers.

References

1. Kulshreshtha, A., Chaudhary, H.: Kinematic and dynamic analysis of reaper machine, Malaviya National Institute of Technology Jaipur (Unpublished M.Tech Thesis) (2016)
2. Chavan, P.B., Patil, K., Dhondge, S.: Design and development of manually operated reaper. IOSR J. Mech. Civil Eng. **12**(3), 15–22 (2015)
3. Wahane, T.B.: Modification and performance evaluation of self-propelled reaper windrower for harvesting chickpea and wheat, Department of Farm Power and Machinery, Dr. Panjabrao Deshmukh Krishi Vidyapeeth, Akola, 94 (Unpublished M.Tech thesis) (2017)
4. Tian, K., Li, X., Zhang, B., Chen, Q., Shen, C., Huang, J.: Design and test research on cutting blade of corn harvester based on bionic principle. Appl. Bionics Biomech. 1–8 (2017)
5. Datt, P., Kumar, A., Gayakwad, H.R.: Design Data Book

Ergonomic Workstation Design for Welding Operation—A Case Study



T. A. Madankar, P. V. Kane, D. Agrawal, and S. V. Kedar

1 Introduction

This work is carried out in one of the small-scale industries involved in the manufacturing of Tractor Trolleys and Tractor Driven Agricultural Equipment which is located in the rural area of Central India. These industries have also become aware of the productivity improvement techniques through work-study and ergonomic design of the workstation. The comprehensive ergonomic audit of the industry was carried out, and the most critical posture involved in the welding process has been selected for detailed analysis. As the work involved is highly repetitive and has the potential for ergonomic design which has been assessed by tools like RULA. The manufacturing process involved in the manufacturing of the turntable required for the trailer of the tractor is discussed in the following section.

2 Fabrication of Turntable

This study focuses on the welding operation of manufacturing process of turntable of tractor trailer. The following operation sequence is observed during this process. The welding of the turntable is done on the fixture which has been made with mild steel. The fixture is used to fix the free channels within it as shown in Fig. 1. The

T. A. Madankar (✉) · S. V. Kedar

Department of Industrial Engineering, RCOEM, Nagpur, India

e-mail: madankarta@rk nec.edu

P. V. Kane

Department of Mechanical Engineering, VNIT, Nagpur, India

D. Agrawal

Mechanical Engineering Department, DMCOE, New Mumbai, India



Fig. 1 Channels and fixtures

free channels are fixed in the fixture one by one as shown in Fig. 2. The channels are fixed by hand or with the help of the little hammering which is shown in Fig. 3. The process is further moved for welding. The welding is done on every corner and every joint of the turntable. The channels are also welded as a basic structure of a round disc. Figure 4 shows the welding of the round disc. After completion of the much possible welding of the turntable lied on the fixture, it is taking off the fixture



Fig. 2 Channel



Fig. 3 Channel placement



Fig. 4 Locating turntable

manually, for the welding the other side as shown in Fig. 5. The welding of the other side is done along with fitting of leaf spring as shown in Fig. 6.



Fig. 5 Tilting of table



Fig. 6 Tilted turntable

3 Problem Identification

The problem in the industry related to the welding process are identified such as (i) Posture of worker (ii) Job positioning (iii) Job clamping methods (iv) Manual material handling.

Worker's posture while performing the work is an important factor that determines the performance and effectiveness. The need to have a scientific design for workers

sitting, job table, job holding devices place of tools, the position of tools while carrying welding operations was found. Jobs are lying on the ground, and they were welded on the ground as shown in Figs. 7 and 8.

Job positioning means the orientation of a job during the work that is performed resulted in the effective outcome of any operation, process, and method. The positioning of the job is done manually with the trial and error method as shown in Figs. 9 and 10. Many times, they adopted body posture according to the position of the job.

The clamping of the job at the workplace while operating is an important factor that is responsible for determining the worker's fatigue level. The clamping should be simple, provide rigid positioning, easy to place and remove the job with minimum input efforts and should not create an obstacle to the workman during the operation.



Fig. 7 Job positioning



Fig. 8 Welding operation



Fig. 9 Job positioning



Fig. 10 Job positioning



Fig. 11 Job positioning



Fig. 12 Job positioning

It is observed that mostly material handling is done manually and without following the ergonomic norms. To carry out the welding of the structure of tractor trolley, there is a need to turn the position of it. This turning is also done manually which decreases the material handling efficiency and also causes fatigue.

4 Review of Literature and Methodology

Ergonomic-related injuries and illnesses such as eye strain, headaches, musculoskeletal ailment like chronic backache, neck and shoulder pain are always the matter of investigation for many researchers even in small scale industries [1]. Roland Kadefors et al. reported ergonomic intervention for welding operation where they also advocated the need to overcome occupational injuries [2]. Kumru and Kilicogullari [3] reported the issue of occupational injuries during the welding operation and presented means to overcome it by designing the ergonomic workstation. Researchers like Orawan Kaewboonchoo et al. [4], Alzuheri et al. [5], Ghosh et al. [6], Lorusso et al. [7], Choobineh et al. [8] reported similar studies of work-related musculoskeletal disorders in different occupations and applications of various ergonomic tools such as RULA and REBA for ergonomic assessment [8]. Based on the review of literature, a methodology is followed in this work is as follows. (1) Identification of various postures involved in the above-mentioned manufacturing process (2) Application of ergonomic risk analysis tool such as RULA for assessing the need for ergonomic intervention (3) Identifying the exact need of the workstation for the process (4) Proposing the modified design of a workstation keeping in mind the ergonomic need of that process.

The findings of the application of ergonomic assessment are discussed in the following section.

5 Ergonomic Risk Analysis

For the ergonomic assessment of any workplace, the tools such as RULA and REBA are used. RULA means Rapid Upper Limb Assessment and REBA means Rapid Entire Body Assessment. Rapid Upper Limb Assessment (RULA) was developed to evaluate the exposure of individual workers to ergonomic. Risk factors associated with upper extremity MSD. This tool considers biomechanical and postural load requirements of job tasks/demands. It focuses on the neck, trunk, and upper limbs, and is ideal for sedentary workers. RULA scores indicate the level of intervention required to reduce MSD risks. The ergonomic assessment worksheet is obtained, and the score was found to be 8 indicating the need of the investigation and changes in the workstation immediately. The sample of ergonomic assessment of RULA score for one of the operations out of many operations mentioned above is demonstrated in Figs. 13, 14, and 15.

The comprehensive RULA worksheets are obtained for the complete process as per the image analysis and RULA software. Based on the finding of assessment, the grand score was found to be 8 which indicates the need for immediate intervention. Hence, the special welding fixture design for this operation is proposed which is discussed in the following section.

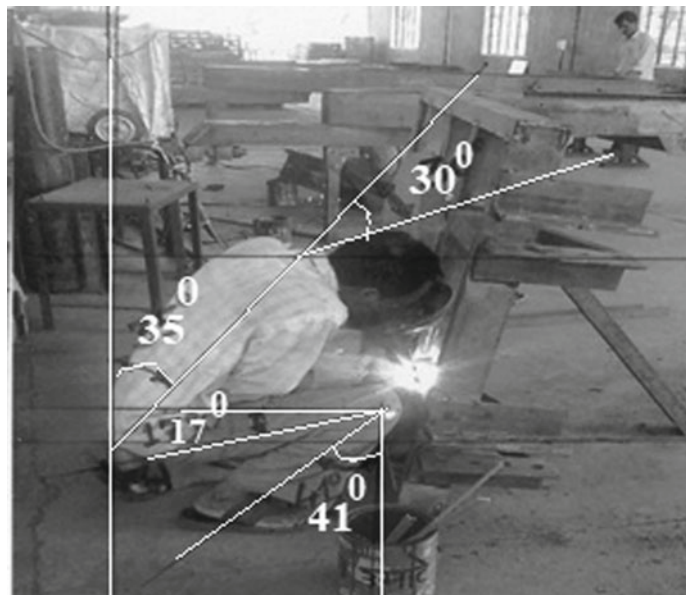


Fig. 13 Image analysis to identify angle

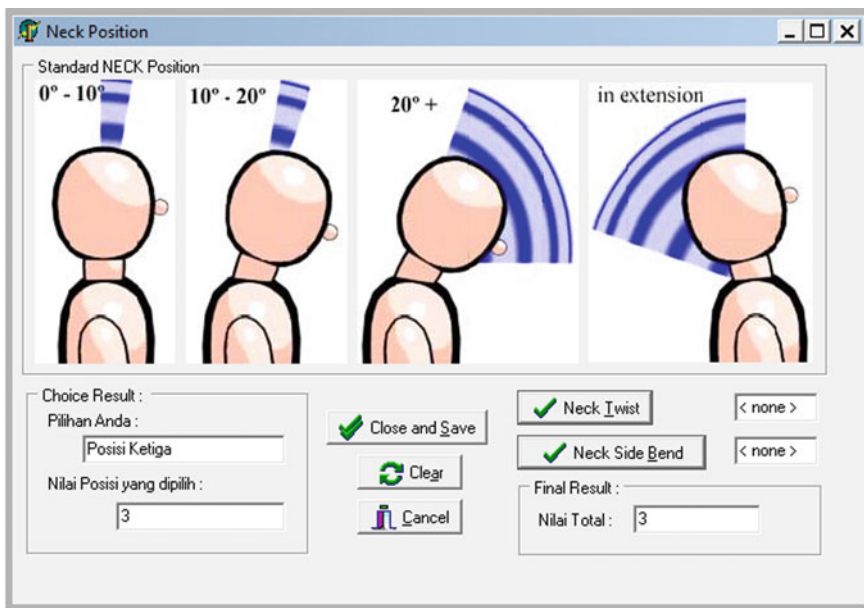


Fig. 14 Rula score for neck position

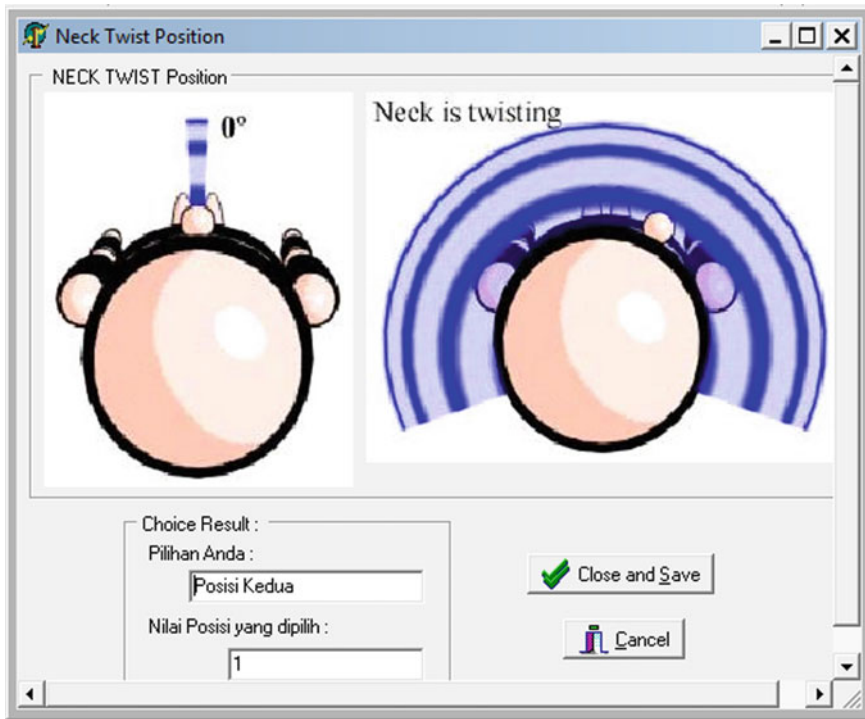


Fig. 15 Rula score for neck twist position

6 Design of Turntable Welding Fixture

Based on the ergonomic assessment, the most critical activity was found to be the welding operation. Hence, efforts made to design the new fixture by overcoming the limitation of the existing fixture are used for the welding of the turntable.

The existing fixture that is used for welding is shown in Fig. 16. It has to be placed on the ground and the workers need to work in kneeling and bending postures with it. There is no proper positioning of the job in the workpiece, and the job has to weld at an inclined position. Due to these limitations of the fixture, the *postures of worker* becomes unergonomic leading to fatigue and causing MSD to workers when used over a longer period. Hence, with all ergonomic considerations, the new design of the fixture is proposed. The solid model of the fixture with all modifications is shown in Fig. 17.

The new modified fixture has been designed at the height of 900 mm which is considering the anthropometry height of standing posture. The fixture is so designed that it can be tilted to any angle by the difference of 10 degrees which will eliminate the unnecessary kneeling angles and would improve neck position.

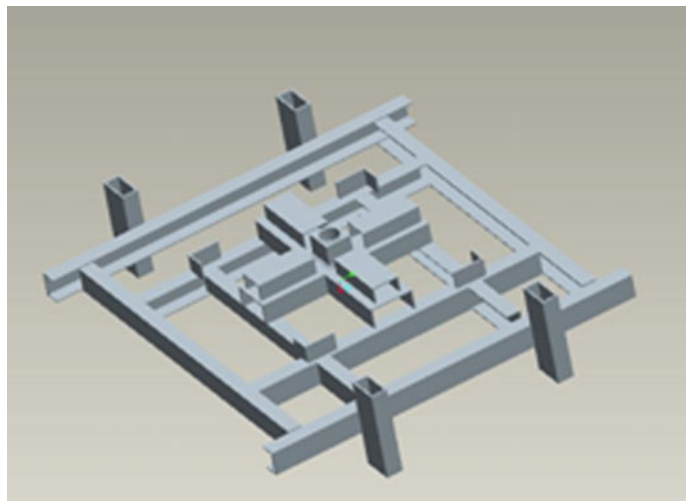


Fig. 16 Solid model of existing fixture

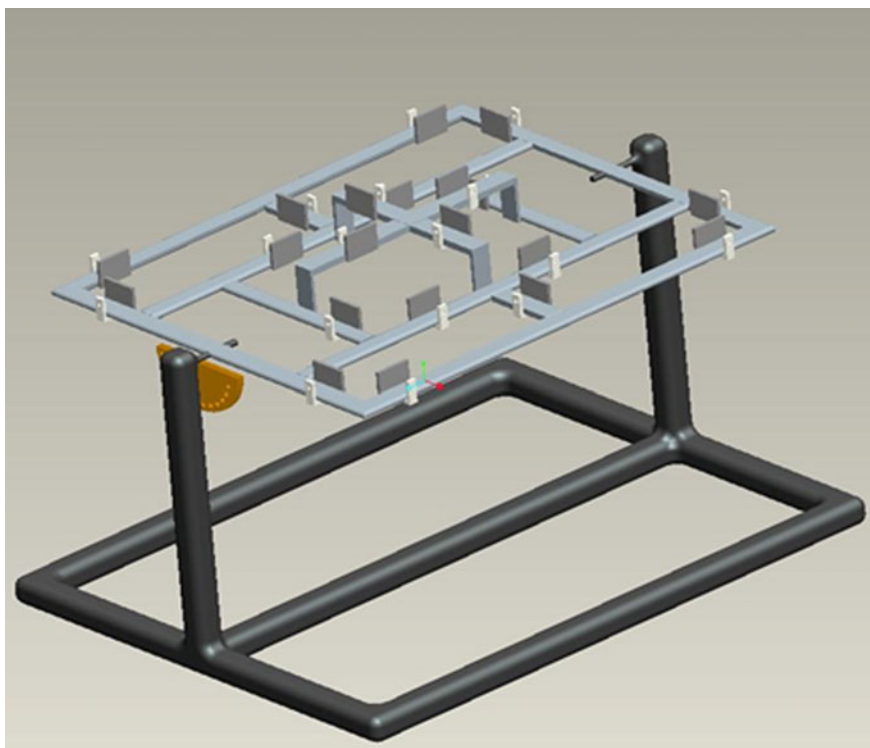


Fig. 17 Solid model of modified design of fixture

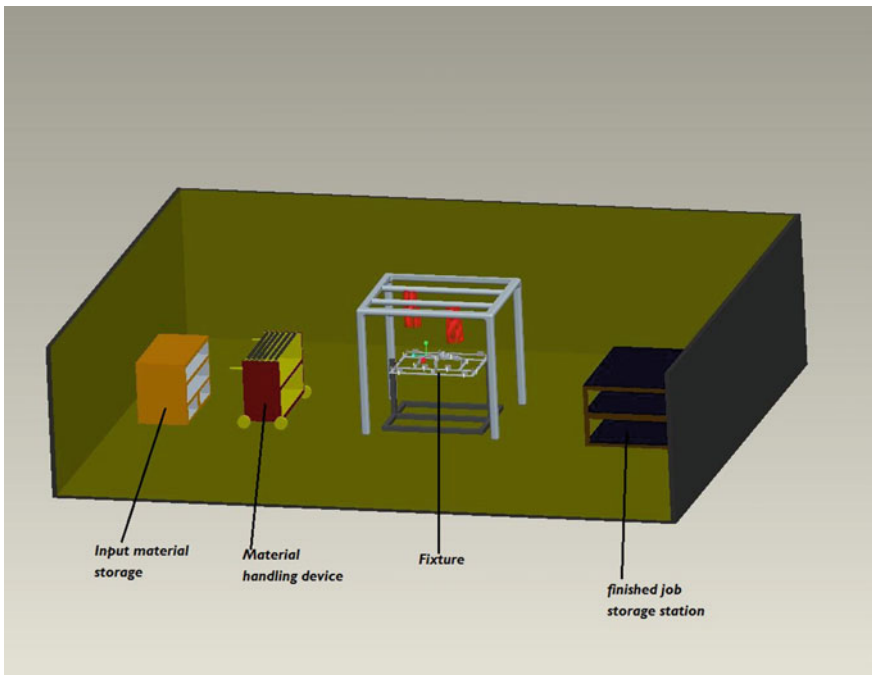


Fig. 18 Proposed layout

Figure 18 shows the proposed design of the layout of the welding workstation of turntable which consists of material storage, material handling devices, the position of the fixture, and the position of the finished job storage station. Overhead fixtures with rollers are proposed in the modified design to hold and convey the welding torch with exhaust gases hood for ventilation. This can be provided which would improve the working condition of the workers.

7 Conclusion and Future Scope

All the industries are now concerned about the performance improvement of the shop floor operations through macro and micro modifications in their processes. Efforts are made in this work to propose the modified fixture which would improve the ergonomic score of the welding process which was assessed by applying the RULA tool. The score obtained for the complete process indicated an immediate need to improve the process to avoid the MSD issues among workers. The image analysis was carried out in this process.

The limitation of the existing fixtures is assessed, and the modifications are proposed in the fixtures considering the anthropometric need of the workstation. The

proposed workstation with all the necessary supporting material handling devices and fixture are also suggested. These changes would lead to reduced RULA score and improve the morale of the workers and the productivity of the manufacturing unit.

References

1. Rongo, L.M.B., Barten, F.J.M.H., Msamanga, G.I., Heederik, D., Dolmans, W.M.V.: Occupational exposure and health problems in small-scale industry workers in Dar es Salaam, Tanzania: a situation analysis. *Occup. Med.* **54**(1), 42–46 (2004)
2. Kedefors, R., Areskoug, A., Dahlman, S., Kilbom, Å., Sperling, L., Wikström, L., Öster, J.: An approach to ergonomics evaluation of hand tools. *Appl. Ergon.* **24**(3), 203–211 (1993)
3. Kumru, M., Kılıçogulları, P.: Process improvement through ergonomic design in welding shop of an automotive factory. In: 10th QMOD Conference. Quality Management and Organizational Development. Our Dreams of Excellence, no. 026. Linköping University Electronic Press, Helsingborg, Sweden (2008)
4. Kaewboonchoo, O., Yamamoto, H., Miyai, N., Mirbod, S.M., Morioka, I., Miyashita, K.: The standardized nordic questionnaire applied to workers exposed to handarm vibration. *J. Occup. Health* **40**(3), 218–222 (1998)
5. Alzuheri, A., Luong, L., Xing, K.: Ergonomics design measures in manual assembly work. In: 2010 Second International Conference on Engineering System Management and Applications, pp. 1–6. IEEE (2010)
6. Ghosh, T., Das, B., Gangopadhyay, S.: A comparative ergonomic study of work-related upper extremity musculo skeletal disorder among the unskilled and skilled surgical blacksmiths in West Bengal, India. *Indian J. Occup. Environ. Med.* **15**(3), 127 (2011)
7. Antonio, L., Bruno, S., L'abbate, N.: A review of low back pain and musculoskeletal disorders among Italian nursing personnel. *Ind. Health* **45**(5), 637–644 (2007)
8. Choobineh, A., Lahmi, M., Shahnavaz, H., Khani Jazani, K., Hosseini, M.: Musculoskeletal symptoms as related to ergonomic factors in Iranian hand-woven carpet industry and general guidelines for workstation design. *Int. J. Occup. Saf. Ergon.* **10**(2), 157–168 (2004)

Prediction of Torque and Cutting Speed of Pedal Operated Chopper for Silage Making



Pravin B. Khope and Sagar D. Shelare

1 Introduction

In livestock production, proper feedstuff is a very important aspect as it is a limiting factor in the rearing of animals to meet the increasing demand for milk and other dairy products. It is a common practice, in India and other countries to allow the cattle to graze freely in the pasture or fields, in most of the cases after harvest [1]. In some cases, farmers collect the crop residues to home and feed the cattle directly or after chopping it into 2–3 pieces using axes or sharp knives. But this traditional method of chopping is tedious, time-consuming, and quite dangerous to the operator [2]. Also, it has low output and a lack of uniformity. If the fodder and other grasses are properly collected and chopped into fine and uniform pieces of 25–35 mm long, it is easy for consumption by the animals and will ensure optimum utilization. Thus there will no wastage of fodder.

The fodder choppers available are electric-powered and hand-operated. But, India is facing problems of power shortage due to rapid industrialization coupled with limitations on additional power generation and non-availability of power in the rural/tribal area. In this context, the sources of energy are human power-operated systems which are considered to be one of the forms of non-conventional energy sources. Thus there is a need for alternate power sources. Also, there is a scarcity of availability of electricity especially in the rural and tribal regions, it is necessary to adopt sustainable alternative energy sources for low-cost mechanization of a chopper [3, 4]. The arm muscles are well known to be poorer than the leg muscles. In comparison with arm cranking, the individual can produce four times more power. Because the thigh or quadriceps is the human body's largest and most potent muscles. Making use of thigh or leg muscles to generate as much energy from the human body as it does

P. B. Khope (✉) · S. D. Shelare

Department of Mechanical Engineering, Priyadarshini College of Engineering, Hingna Road, Nagpur 440019, Maharashtra, India

makes sense. The current paper provides the prediction of torque and cutting speed of pedal operated chopper for silage making operation. This would be helpful for the optimized performance of the pedal-operated chopper for silage making.

2 Materials and Methods

By pedaling an individual will produce four times additional energy (1/4 horsepower (hp)) rather than arm-cranking. Consistent pedaling can also be achieved at a pace of 1/4 hp for just brief intervals, about 10 min. Pedaling at halves such power (1/8 hp) however, can be managed for approximately 60 min [5]. Pedal systems allow a human to operate machines at the same speed as manual cranks, with much less energy and exhaustion. Over the centuries, the treadle was the most popular way of transmitting power through the legs. In the low power, range treadles are still popular, particularly for sewing machines [6].

2.1 Human Powered Flywheel Motor

The concept is whenever the horsepower requirement of processing is far over the continuous capacity of a human being; a flywheel can be used to store human energy (analogous to a capacitor in an electric circuit). After enough energy is stored in the flywheel, then it can be made accessible to a processing unit by appropriate torque and clutch amplification gears [7]. Through this concept higher demand for power for some processes can meet. It has one drawback; the process unit shaft is always in a transient state of operation (initial sudden speed increase followed by a continuous decline in speed until it becomes zero). The processes which are intensive to machine speed variation as far as product quality is concerned can adopt this concept e.g. fodder cutting, oil expelling, etc. The human-powered flywheel motor (HPFM) consisting of three sub-systems namely an energy supply unit, an appropriate clutch, and transmission and a processing unit [8–10].

The total system consisted of a mechanism of bicycles, a suitable clutch and transmission system, and a processing unit that may be any processing system involving power about 1–5 h. Referring to Fig. 1, when the clutch is in a detached position the operator sits upon this seat and pedals the bicycle mechanism. Therefore the pressure on the rider's legs is just the flywheel's inertial pressure. A Flywheel is propelled by a young age group rider of 20–25 physically fit of around 165 cm to a maximum of 800 rpm in minutes. The rim diameter of the Flywheel is 95 cm, the rim width is 10 cm, and the rim thickness 2 cm. When energized to a speed of 600 rpm, such a Flywheel stores energy to a maximum of 3200 kgf m. The peddling is stopped after achieving target speed by flywheel, and the clutch is engaged. Via the clutch, the energy contained in the flywheel is transmitted to the process machine. Evidently, due to rapid momentum transfer, the clutch is subject to extreme shock.

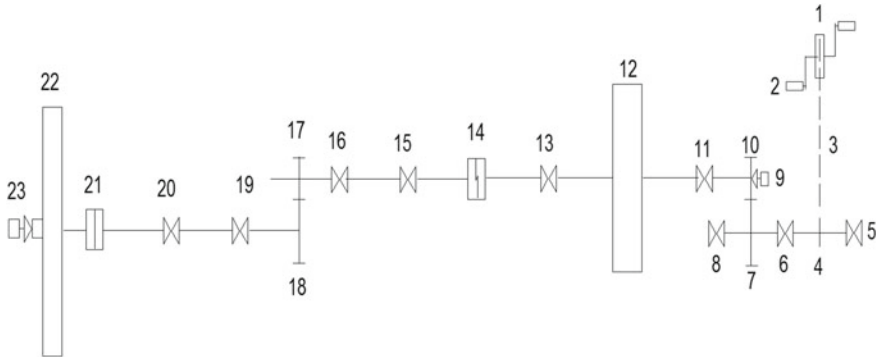


Fig. 1 Schematic of human powered flywheel motor. Note 1: Chain Sprocket, 2: Pedal, 3: Chain, 4: Freewheel, 5–6: Bearings for bicycle side, 7: Gear-I, 8: Bearing, 9: Speed sensor for flywheel shaft, 10: Pinion-I, 11: Bearing for flywheel shaft, 12: Flywheel, 13: Bearing for flywheel, 14: Double jaw spiral clutch, 15& 16: Bearing of the intermediate shaft, 17: Pinion II, 18: Gear II, 19 & 20: Bearing for process unit shaft, 21: Coupling, 22: Chaff Cutter blade, 23: Speed sensor for chaff Cutter shaft

This is so the Flywheel is subject to a process load as the clutches engaged, and the processing unit consumes the flywheel's energy. The stored energy of the flywheel is exhausted in 15–20 s after application [11, 12], after the clutch engagement. This type of system has a capacity of range 1–5 hp. It also confirmed the practical viability and financial feasibility of the system [13]. Schematic arrangement of the complete unit.

2.2 Experimental Design

This research aims to design a safe and easy to operate a human-powered energy unit for fodder cutting. The power unit and its operating parts, chopping unit, and its parts were fabricated and constructed at Priyadarshini College of Engineering, Nagpur. The actual fabricated model is shown in Fig. 2.

The process of fodder cutting energised by HPFM is a complex phenomenon. In this method, there is the automatic momentum transition from clutch towards a processing unit after the clutch contact, such that the processing unit is unexpectedly granted extreme acceleration. Based on the resistance of the device, the input shaft, and the control unit undergo deceleration. A process resistance concerning the application form is any incremental speed feature thereby consigning the flywheel, clutch, and control unit to the extreme state of the transient phases of the dynamics of this novel machine device operation.

It is also extremely difficult to devise logical models able to simulate different processes of energy transfer including the transfer of energy phenomena i.e. energy escape by the individual into the flywheel (requires 60 s) but energy escapes phenomenon b a highly nonlinear individual [5]. On clutch engagement instantaneous

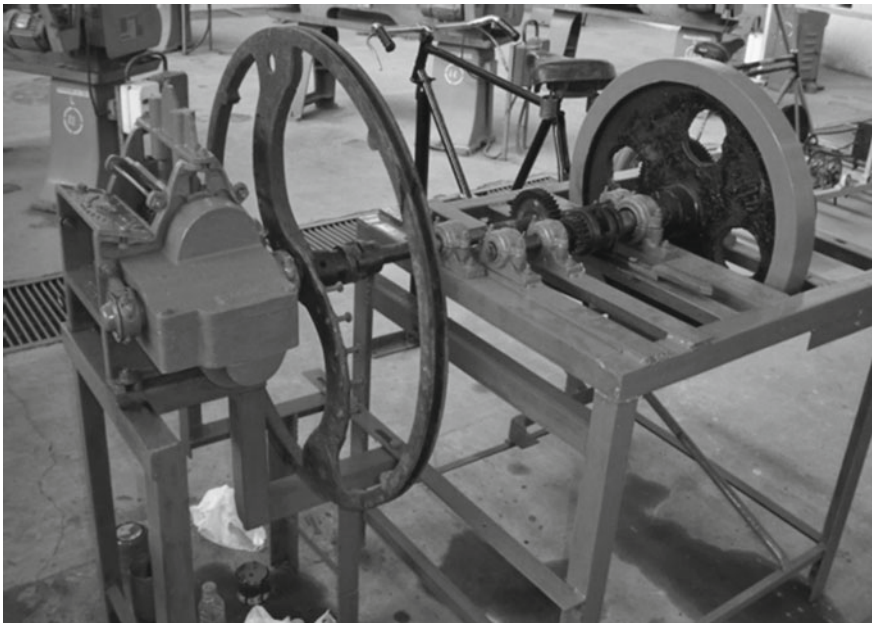


Fig. 2 The fabricated model of human-powered fodder cutter

(0–10 ms) strong exchange of momentum by two jaw spiral clutch into processing unit running upon the load, causing extreme arbitrary motions into a clutch and movement of flywheel energy by clutch, torque amplification gear-pair, and processing unit [14]. A gear ratio in a shaft of the flywheel and shaft of the processing unit is controlled. In this experiment, a gear ratio was attempted in the ratio of 1:2, 3, 4. Consider every gear ratio like a test point [15]. The number of blades varied was 2 and 3; the flywheel terminal speed is changed in between 300 and 600 rpm, with 100 rpm phase. At a first gear ratio of 1:2, a processing unit speed is greater than 1:4 but the torque increases with an increase in gear ratios. Which reflects the torque is minimal at 1:2 while maximum at 1:4 gear ratio but speed is comparatively lower. The cutting blades are positioned at the head wheel of the cutter and are mounted on a shaft of the process machine. The cutter head is utilized to mount the two and three cutting blades respectively, with two and three blades being attempted with different flywheel speeds for each gear ratio.

The bicycle system speeds the flywheel. The energy contained into a flywheel is then utilized for cutting off fodder. The speed of the flywheel increases, the energy reserve inside the flywheel increases. Varying the speed of the flywheel from 300 to 600 rpm is determined.

The speed could be increased up to 700–800 rpm but unnecessary movements could impact sensors utilized to calculate various parameters. The test sequence is from min to max speed, which means between 300 and 600 rpm and gear ratio between 2:1 and 4:1.

3 Results and Discussion

The HPFM cutter findings indicate that when the gear ratio is 1:2, dried sorghum is sliced around a rate of 0.017 kg/s with a flywheel at a speed of 300 rpm. The avg sliced material yield was observed to be between 20 and 25 mm. The cutting performance was found out to be 81 percent. With the rise in flywheel rpm, the chopping rate is increased gradually. The chopping rate at 1:2 gear ratio and 600 rpm of the flywheel was 0.032 kg/s. The chopping rate was found to be 0.25 kg/s at a 1:4 gear ratio and 300 rpm of a flywheel. At 600 rpm the chopping rate having the same gear ratio was 0.045 kg/s. Compared to the hand-operated cutter, the developed cutter energized by HPFM is identified to become less tedious, quicker, and easier. It is possible to adjust the length of the chops by changing the clearance of the shear plate and blade by the amount of flywheel rpm or blade.

After paddling for one minute, the flywheel shaft is attached to the cutter shaft, the cutter speed decreases significantly due to the resistance provided by the material to be sliced and eventually stops the cutter. Because of this, it is important to create an effective mechanical transmission system that smoothes a constantly changing flywheel speed and retains an essentially constant cutter speed over an expected deviation period in the speed of the flywheel. Even the cutting rate of the cutter (C_r) can be improved when the cutter shaft's uniform velocity is preserved.

In the experimentation, we tried gear ratios i.e. 1:2, 1:3, and 1:4. The Pinion flywheel shaft has 20 teeth and the 40, 60 80 teeth cutter shaft gear is varied. Figure 3 shows the effect of gear ratio on the torque being produced. Is attached to the cutter shaft by torque amplification gear pair 1:2 the torque produced is 13.44 Nm, i.e. at 400 rpm of the flywheel. As the gear ratio increased the torque grows, the torque produced is 24.29 Nm at a 1:4 gear ratio.

The flywheel is accelerated to 400 rpm then paddling is stopped and the cutter shaft connected to the flywheel shaft at a gear ratio of 1:3 whereas the number of blades is two, the angular velocity of the cutter is gradual decreases as energy stored in the flywheel consumed for cutting fodder material thereby decreasing the number of cuts. Figure 4 gives the effect of angular velocity on a number of cuts.

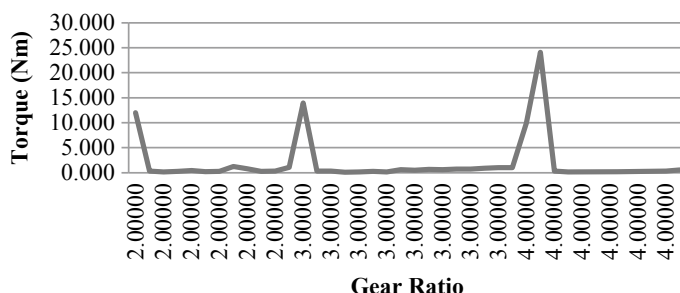


Fig. 3 Effect of gear ratio on developed torque

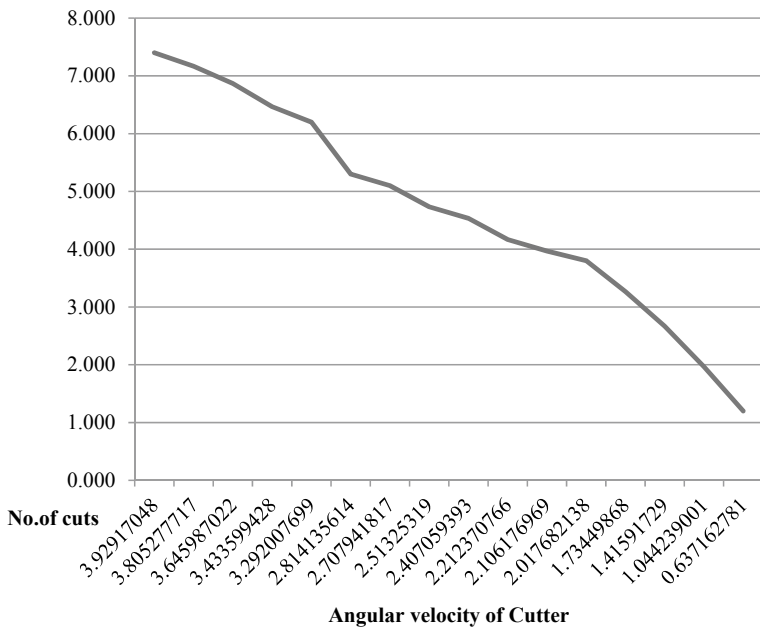


Fig. 4 Effect of angular velocity on number of cuts

4 Conclusion

The established cutter energized by HPFM is described as less stressful, smoother, and simpler compared to the hand-operated cutter. By adjusting the clearance of the shear plate and blade by the amount of flywheel rpm or blade, it is possible to adjust the length of the chops. The lack of available electrical power is a significant issue and it affects the daily life of those people lives in remote parts of India. The human-powered energy unit is a reliable source of energy that could provide solutions to critical problems. The human-powered energy unit for the fodder cutter is the most suitable for the marginal farmer. The established cutter energised by HPFM is described as less stressful, smoother, and simpler compared to the hand-operated cutter. By adjusting the clearance of the shear plate and blade by the amount of flywheel rpm or blade, it is possible to adjust the length of the chops. The result indicates the drastic development upon hand-worked chopper, as the size of chopped has become consistent. Human-powered fodder cutting would find significance to dairy farmers especially into remote rural and tribal areas wherever the stability of electricity is very limited. The parameters examined are gear ratio, number of cuttings, and rpm of the flywheel.

Acknowledgements Rajiv Gandhi Science & Technology Committee, Government of Maharashtra (India), offered financial assistance for research published in this paper.

References

1. Jawalekar, S.B., Shelare, S.D.: Development and performance analysis of low cost combined harvester for rabicrops. *Agric Eng Int.: CIGR J.* **22**(1), 197–201 (2020)
2. Khope, P.B., Modak, J.P.: Design of experimental set-up for establishing empirical relationship for chaff cutter energized by human powered flywheel motor. *Int. J. Agric. Technol.* **9**(4), 779–791 (2013)
3. Shelare, S.D., Kumar, R., Khope, P.B.: Formulation of a mathematical model for quantity of Deshelled Nut in Charoli Nut Deshelling machine. In: Prakash, C., Krolczyk, G., Singh, S., Pramanik, A. (eds.) *Advances in Metrology and Measurement of Engineering Surfaces*. Lecture Notes in Mechanical Engineering, pp 89–97. Springer, Singapore (2021)
4. Waghmare, S.N., Sakhale, C.N., Tembhurkar, C.K., Shelare, S.D.: Assessment of average resistive torque for human-powered stirrup making process. In: Iyer, B., Deshpande, P., Sharma, S., Shiurkar, U. (eds.) *Computing in Engineering and Technology. Advances in Intelligent Systems and Computing*, vol. 1025, pp. 845–853. Springer, Singapore (2020)
5. Wilson, D.G.: *VITA Volunteer: understanding the Pedal Power* (1986)
6. Ghatole, S., Yashpal, Bundele, M., Modak, J.P.: Development of mathematical model for reduction of process time for peddle-driven sewing machine. In: Vasudevan, H., Kottur, V., Raina, A. (eds.) *Proceedings of International Conference on Intelligent Manufacturing and Automation*. Lecture Notes in Mechanical Engineering. pp. 513–521, Springer, Singapore (2020)
7. Waghmare, S.N., Shelare, S.D., Tembhurkar, C.K., Jawalekar, S.B.: Development of a model for the number of bends during stirrup making process. In: Prakash, C., Krolczyk, G., Singh, S., Pramanik, A. (eds.) *Advances in Metrology and Measurement of Engineering Surfaces*. Lecture Notes in Mechanical Engineering, pp. 69–78. Springer, Singapore (2021)
8. Dhale, A.D., Modak, J.P.: Formulation of experimental data based model for oil press using human powered flywheel motor as energy source. *Agric. Eng. Int.: CIGR J.* **14**(3), 218–229 (2012)
9. Undirwade, S.K., Singh, M.P., Sakhale, C.N.: Experimental investigation of processing time, number of slivers and resistive torque required for human powered bamboo sliver cutting operation. *J. Bamboo Rattan* **14**(1–4), 33–51 (2015)
10. Undirwade, S.K., Singh, M.P., Sakhale, C.N.: Formulation of mathematical model for processing time required for bamboo sliver cutting using HPFM. *Mater. Today: Proc.* **4**(9), 10174–10178 (2017)
11. Khope, P.B., Modak, J.P.: Development and performance evaluation of a human powered flywheel motor operated forge cutter. *Int. J. Sci. Technol. Res.* **2**(3), 146–149 (2013)
12. Dhande, H.K., Shelare, S.D., Khope, P.B.: Developing a mixed solar drier for improved postharvest handling of food grains. *Agric. Eng. Int.: CIGR J.* **22**(4), 166–173 (2020)
13. Deshpande, S.B., Modak, J.P., Tarnekar, S.B.: Confirming application of human powered flywheel motor as an energy source for rural generation of electrical energy for rural applications, and computer aided analysis of battery charging process. *Hum. Power USA Int. Hum. Power Veh. Assoc.* **58**, 10–16 (2009)
14. Dhale, A., Modak, J.P.: Formulation of the approximate generalized data based model for oilseed presser using human powered flywheel motor as an energy source. *Int. J. Agric. Eng.* **3**(2), 354–384 (2010)
15. Schenk Jr., H.: *Test sequence and experimental plans, theories of engineering experimentation*. McGraw Hill Book Co., New York (1961)

Finite Element Modeling and Parametric Investigation of Friction Stir Welding (FSW)



K. S. Mehra, S. Kaushik, G. Pant, S. Kandwal, and A. K. Singh

1 Introduction

Aluminum alloy parts of high strength are extensively used in aerospace, defence, sports, and other safety-critical applications [1, 2]. Due to the damages resulting from corrosion, impact or wear, need of component replacement arises which is time taking, expensive and inefficient [3]. Friction stir enabled additive manufacturing proved to be a solution to repair aluminium alloys used for aerospace and defence industries [4]. They used additive friction stir deposition for the volume damage repair of AA7075 alloy. Friction Stir Welding is a comparatively new welding process that provides important benefits to aluminium alloys and other materials that had been difficult to weld in the past using more traditional fusion techniques [5–7]. The FSW process uses low energy input and requires no outside (filler) material, no shielding gases, when compared to other welding processes. Heat generation analytical model in friction stir welding, with contact conditions like sticking, sliding was introduced by [14]. A heat transfer model (3-D) for FSW was examined [15]. In this work, the heat generated by the tool pin and shoulder were measured, and were assumed to be frictional heat. Numerical and experimental analysis is carried out for the

K. S. Mehra (✉)

Birla Institute of Applied Sciences, Bhimtal 263136, India

S. Kaushik

Shivalik College of Engineering, Dehradun 248001, India

G. Pant

GLA University, Mathura 281406, India

e-mail: gauravpant.me@gla.ac.in

S. Kandwal

Institute of Technology Gopeshwar, Chamoli Gopeshwar 246401, India

A. K. Singh

Graphic Era Hill University, Dehradun 248001, India

heat transfer characteristics of the FSW process (in normal and cold weld) [16]. FSW process thermal history, distribution of stresses and forces by a 3-D model based on finite element analysis method presented in [17]. A FSW thermal model is proposed with a welding seam(straight) in which a full sliding type contact was applied [8]. Material characteristics are introduced into a Finite Element model [9]. Welding seam considered for this study was flat, and the numerical analysis was performed in two phase. In first phase, friction modeling is done and in second case thermo-mechanical simulation performed to study the thermal behavior of the specimen. The study concluded that temperature distribution depends on factors like geometry of tool, workpiece properties, and contact state [10] established the three-dimensional models using HyperXtrude and ANSYS numerical tool. ANSYS Parametric Design Language (APDL) codes are developed to model heat source and vary boundary conditions. The study [11] carried out to predict the defect pattern and thermal behaviour [12] performed a thermo-mechanical model simulation with flat seam. This study compared two 3D models (linear) and concluded that both analysis direct to similar results [19] presented a 3-D model simulation to investigate the thermo-mechanical behavior. Numerical simulation are conducted to find residual stresses and maximum temperatures with a non-moving shoulder (straight weld seam) during the welding process [20]. A more consistent and narrower pattern was observed compared to conventional form of Friction stir welding, because the rotating pin effects the material flow. It is concluded that the tool geometry affects mechanical and thermal behavior. It is indicated by [21] that the heat generation in friction stir welding can be divided into two parts, frictional heat generation by tool and heat generation by the deformation of material.

The above mentioned literature study reveals that FE package used by the researchers for solving problems are in common use to everyone. However, present work explores a comparatively new FE package having enormous potential in the domain of friction stir welding process yet to be revealed. There are rare studies which used this new FE package module “Altair Hyperweld” and reported the process parameter influence on the FSW.

In the present study, simulation of friction stir welded joint of aluminum alloy AA6061 is done using Altair Hyper-Weld software. Altair Hyperweld friction stir welding module (FEM based) in Altair’s HyperWorks is a suitable package to perform virtual experiments of friction stir welding process to predict useful results prior to conduct actual experiment or production. Arbitrary Eulerian Lagrangian (ALE) approach is used for the computational system to avoid large distortions in mesh around the tool. The results from the developed model are validated with experimental study. Compared to other FE packages the present solver solve the numerical model in less time with 25 number of non linear iterations. Furthermore, parametric investigation is performed to find the influence of process parameters(Translation and rotational spindle speed) on the FSW.

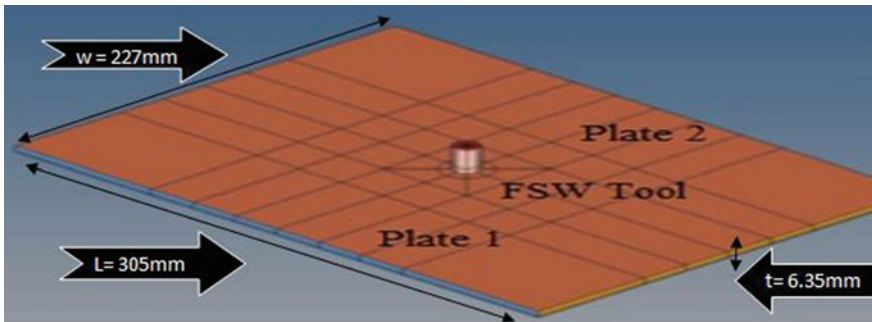


Fig. 1 Prepared butt joint geometric model

2 Model Description

Figure 1 shows the geometric model prepared using Altair's Hyper-Weld Friction Stir Welding (FSW) tool 17.0. Material selected for the welding is aluminum AA6061 alloy which is difficult to be welded by conventional welding techniques and extensively used in defence and aerospace industries. Properties of material defined in material library of the software tool is selected for AA6061 aluminium alloy. Material dimension are 6.35 mm of thickness(t), 305 mm of length(L) and 227 mm of width(w).

Friction Stir welding tool made of H-13 (hot-die) steel material is considered. It has circular profile type shoulder of diameter 19 mm. Pin profile is also selected circular of length 4 mm and diameter 6 mm for the analysis.

3 Numerical Analysis

Three dimensional model is selected for the computational analysis. Material is considered to be isotropic and continuous. The governing equations considered for the numerical analysis are:

- (1) Fourier law of Heat conduction: Three dimensional equation in Cartesian coordinates

$$\rho C_p \frac{\partial T}{\partial t} = \frac{\partial}{\partial x} \left(k_x \frac{\partial T}{\partial x} \right) + \frac{\partial}{\partial y} \left(k_y \frac{\partial T}{\partial y} \right) + \frac{\partial}{\partial z} \left(k_z \frac{\partial T}{\partial z} \right) \quad (1)$$

where, T represents temperature, C_p (heat capacity), ρ (density) and k (thermal conductivity of material).

- (2) Convection equation: Newton's Law of cooling

$$q_{\text{conv}} = h_{\text{conv}}(T - T_{\infty}) \quad (2)$$

where q_{conv} is heat transfer per unit area due to convection, T_∞ is ambient temperature and h is convection coefficient.

- (3) Torque equation: Torque required to rotate the welding tool under axial load

$$\int_0^{T_R} dT = \int_0^R \mu P(r) 2\pi r^2 dr = \frac{2}{3} \mu \pi P R^3 \quad (3)$$

where, T is interfacial torque, μ (friction coefficient), R is surface radius, and $P(r)$ (pressure distribution across the interface).

- (4) Frictional heat generated equation: Heat generated in material due to the tool rotation

$$Q_g = \int_0^{T_R} \omega dT = \int_0^R \omega \mu P(r) 2\pi r^2 dr \quad (4)$$

where, Q_g is the rate of heat generated and ω is the angular velocity.

4 Boundary Condition

Convection coefficient of $30 \text{ W/m}^2 \text{ K}$ at ambient temperature of 298 K is applied as a boundary condition at the top and side surfaces. Bench convection coefficient of $350 \text{ W/m}^2 \text{ K}$ is applied on the bottom surface [13]. Conductive heat loss from the bottom surface of the weld plate is assumed to be of very high value of heat transfer coefficient [13, 16]. Arbitrary Eulerian Lagrangian(ALE) approach is used for the computational system to avoid large distortions in mesh around the tool. Three-dimensional nonlinear thermal numerical simulations are performed using Altair Hyper Weld Friction Stir Welding (FSW) tool for AA6061 (aluminium alloy) material plates.

5 Computational Solver Model and Validation

Model geometry is meshed by the meshing mode of Altair Hyperweld. Discretization of material domain into elements is done through meshing. Altair hyperweld uses Hyperextrude analysis solver for the computational outcomes. Solution is done by employing 25 non linear iterations with non linear iteration tolerance of 0.001. Validation of the Virtual experiment tool is done by comparing it with experimental study [18]. Figure 2 shows the 3-D simulation of FSW for AA6061 material using Altair Hyperweld tool with reference to the experimental work under the same boundary conditions. Temperature distribution at the middle plane is considered as function of

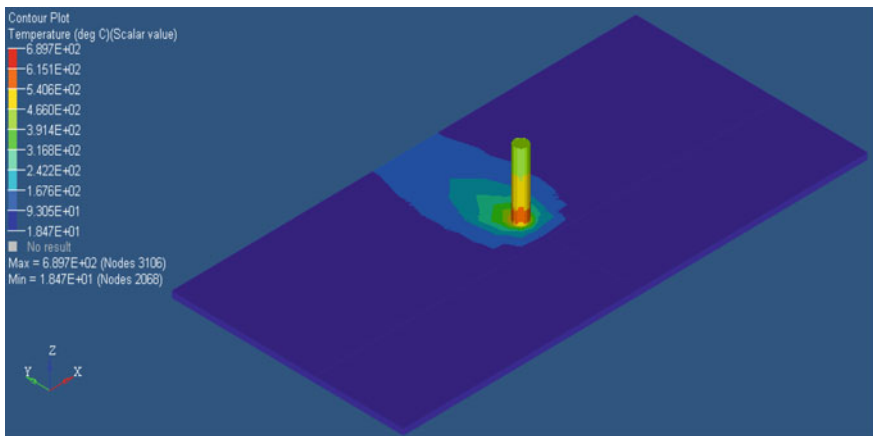


Fig. 2 Simulation of FSW joint using Altair hyperweld software 17.0

distance from weld centerline. The simulated results shows deviation of 3.74–5.90% for the temperature at different location. Therefore, our numerical tool said to be reliable and promising for further investigations. Comparison of Present study with the experimental work for the validation purpose is shown in Fig. 3.

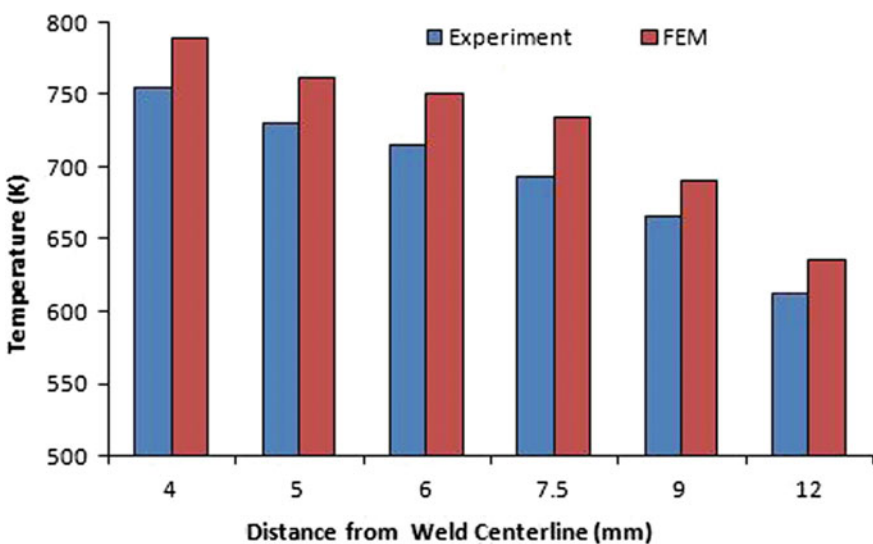


Fig. 3 Validation of present work with Feng et al. [18]

6 Results and Discussion

Influence of input process parameter variation (Translation and rotational spindle speed) on heat generation of friction stir weld material is considered in the present study. The peak temperature (T_p) generated by parametric variation is used to study the effect of process parameter on heat generation. Numerical simulation of Friction stir weld of AA6061 material are performed using Altair Hyper-weld software.

6.1 Effect of Tool Rotational Speed

Computational analysis is performed at five different Rotational speed (i.e., 600, 1000, 1400, 1600 and 1800 rpm) of the tool and peak temperature is investigated. Figure 4 shows Maximum Temperature of the material at five different speeds. It is observed that Tool rotational speed significantly affects the Heat generation in material during FSW process. Increase in rotational speed rises the Peak temperature of the weld [22, 23]. The observed value of peak temperature is below the melting point (923 K) of the material at all rotational speeds and it is about in a range of 65–95% of solidus temperature (855 K). Peak Temperature is observed at weld zone and temperature decreases as we move further away from it. It is also noticed for all speeds Temperature in the is symmetrically distributed along the welding line.

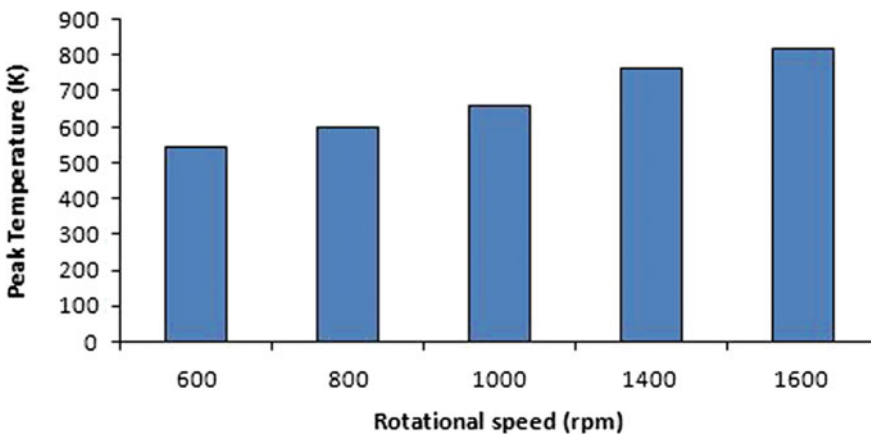


Fig. 4 Peak temperature at five different rotational speed of tool

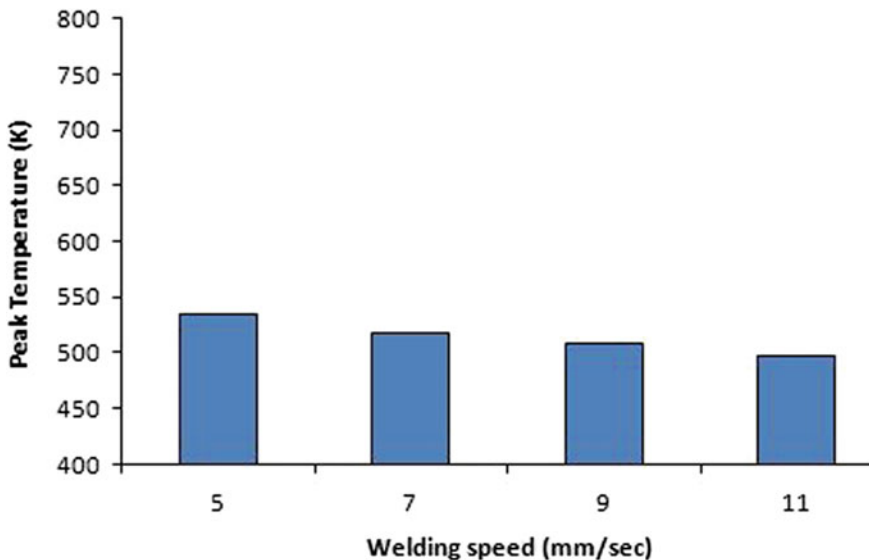


Fig. 5 Peak temperature at four different welding speed

6.2 Effect of Weld Speed (Translation Speed)

Fig. shows the variation of Peak temperature at different weld speed. Four values of weld speed (5, 7, 9 and 11 mm/s) with step of two are considered for the simulation. Heat generation is indicated by the peak temperature which is investigated at four different weld speed. It is observed from the Fig. 5 that there is a slight decrease in the Peak temperature with the rise in welding speed. Temperature is seen to be symmetrically distributed along weld line for all weld speed. Peak temperature at all speeds is under melting point (923 K) of the material. Temperature at weld zone is observed to be maximum and decreases as we move further away from it. No significant effect on peak temperature is noticed in the case of variation of weld speed [22].

7 Comparison with Previous Work

Present work results are compared with some of the previous similar experimental and numerical studies and shown in Table 1. It is observed from the table that the findings of present work are in good agreement with the results of [22, 23]. Moreover, present research covers broader analysis which is absent in case of [22, 23]. Present analysis also details the slight decrease in peak temperature when welding speed is increased whereas [22] reported no significant effect. Hence, Altair hyperweld software proved

Table 1 Comparison of present results with the previous experimental work [22, 23]

Process parameter	Present work (T_{peak})	[22] (T_{peak})	[23] (T_{peak})
Increase in tool rotation speed	Increase	Increase	Increase
Increase in welding speed	Slightly decrease	No significant effect	Not reported

to be a powerful tool and explores a new way in the field of numerical simulations of friction stir welding process.

8 Conclusion

Present article proposes a comparatively new numerical tool for simulating Friction stir welding process. Influence of tool rotation speed and welding speed on Heat generation is investigated using Altair Hyperweld 17.0. Friction stir additive manufacturing is a new explored field which is gaining importance nowadays. Following conclusions are drawn out from the present numerical study:

- Validation of simulation results with experimental work represents the effectiveness of the Altair Hyperweld tool.
- Symmetric distribution of temperature is observed along the welding line and it is independent of spindle rotation and welding speed variation. Temperature at weld zone is observed to be maximum and decreases as we move further away from it.
- With the increase in Tool rotation speed, Heat generation (Peak Temperature) is increased.
- Slight decrease in Peak Temperature observed when welding speed is increased.
- Comparative study with previous work indicates good agreement of the results and elaborated findings.
- Friction Stir welding use in additive manufacturing has broader perspective and the current study can be utilized for the same.

References

1. Kumar, P.V., Reddy, G.M., Rao, K.S.: Microstructure, mechanical and corrosion behavior of high strength AA7075 aluminium alloy friction stir welds, effect of post weld heat treatment. *Def. Technol.* **11**, 362–369 (2015)

2. Veeravalli, R.R., Nallu, R., Mohiuddin, S.M.M.: Mechanical and tribological properties of AA7075-TiC metal matrix composites under heat treated (T6) and cast conditions. *J. Mater. Res. Technol.* **5**, 377–383 (2016)
3. Liu, Y., Mol, J.M.C., Janssen, G.C.A.M.: Combined Corrosion and Wear of Aluminium Alloy 7075-T6. *J. Bio Tribos Corros.* **2**, 9 (2016)
4. Griffiths, R.J., Dylan, T.P., David, G., Hang, Z.Y.: Additive friction stir-enabled solid-state additive manufacturing for the repair of 7075 aluminum alloy (2019)
5. Thomas, W.M.: Int. Patent Appl. No PCT/GB92 Patent Application No. 9125978.8 (1991)
6. Dawes, C.J., Thomas, W.M.: Weld. J. **75**(3), 41–45 (1996)
7. Kallee, S., Nicholas, D.: SAE Technical Paper No 982362 (1998)
8. Hamilton, C., Sommers, A., Dymek, S.: A thermal model of friction stir welding applied to sc -modified Al-Zn-Mg-Cu alloy extrusions. *Int. J. Mach. Tools Manuf.* **49**, 230–238 (2009)
9. Riahi, M., Nazari, H.: Analysis of transient temperature and residual thermal stresses in friction stir welding of aluminum alloy 6061-T6 via numerical simulation. *Int. J. Adv. Manuf. Technol.* **55**, 143–152 (2011)
10. Binmur, G.K., Mustafa, T., Tarik, S.: Finite element modeling of friction stir welding in aluminum alloys joint. *Math. Comput. Appl.* **18**(2), 122–131 (2013)
11. Al-Badour, F., Merah, N., Shuaib, A., Bazoune, A.: Coupled eulerian lagrangian finite element modeling of friction stir welding processes. *J. Mater. Process. Technol.* **213**, 1433–1439 (2013)
12. Busetta, P., Feulvarch, E., Tongne, A., Boman, R., Bergheau, J.-M., Ponthot, J.-P.: Two 3D thermomechanical numerical models of friction stir welding processes with a trigonal pin. *Numer. Heat Transf. Part A: Appl.* **70**, 995–1008 (2016)
13. Zhu, X.K., Chao, Y.J.: *J. Mater. Process. Technol.* **146**, 263–272 (2004)
14. Schmidt, H., Hattel, J., Wert, J.: *Model. Simul. Mater. Sci. Eng.* **12**, 143–157 (2004)
15. Song, M., Kovacevic, R.: *Int. J. Mach. Tools Manuf.* **43**, 605–615 (2003)
16. Chao, Y.J., Qi, X., Tang, W.: *J. Manuf. Sci. Eng.* **125**, 138–145 (2003)
17. Chen, C., Kovacevic, R.: *Proc. Inst. Mech. Eng.* **218**, 17–33 (2004)
18. Feng, Z., Wang, X.L., David, S.A., Sklad, P.: 5th International Friction Stir Welding Symposium. Metz, France (2004)
19. Jain, R., Pal, S.K., Singh, S.B.: Finite element simulation of temperature and strain distribution during friction stir welding of AA2024 aluminum alloy. *J. Inst. Eng. (India): Ser. C* 1–7 (2016)
20. Sun, T., Roy, M., Strong, D., Withers, P.J., Prangnell, P.B.: Comparison of residual stress distributions in conventional and stationary shoulder high-strength aluminum alloy friction stir welds. *J. Mater. Process. Technol.* **242**, 92–100 (2017)
21. Kumar, S., Wu, C., Zhen, S., Ding, W.: Effect of ultrasonic vibration on welding load, macrostructure, and mechanical properties of Al/Mg alloy joints fabricated by friction stir lap welding. *Int. J. Adv. Manuf. Technol.* **100**, 1787–1799 (2019)
22. Anand, R.S., Prakash, P., Jha, S.K., Singh, A.K.: Numerical investigations of effect of input process parameters on heat generation in friction stir welding. *Mater. Today: Proc.* (2020)
23. Andradea, D.G., Leitão, C., Rodriguesa, D.M.: Influence of base material characteristics and process parameters on frictional heat generation during Friction Stir Spot Welding of steels. *J. Manuf. Process.* **43**(2019), 98–104 (2019)

Wear Analysis of Polytetrafluoroethylene (PTFE) Reinforced with Carbon and Bronze



Prasun Kumar Pandey, S. Thirumalini, R. Padmanaban,
and G. Jayashankar

1 Introduction

1.1 Motivation

Conventional oil-lubricated compressor requires frequent monitoring and maintenance of oil quality, oil filters and valves. This adds to the operational & service cost and raises the environmental concern for oil disposal and downstream contamination. On the other hand, oil-free compressor is the more favourable technology due to its inherent advantages over oil-lubricated compressor like pure compressed air, low downstream contamination and lesser maintenance. Elimination of oil from the system is made possible by the recent advancement in dry lubricant technology, specially, PTFE composites. However, due to lower durability of these composite materials, the oil-free technology is restricted only to critical applications like pharmaceutical and food processing.

On the other hand, the composition & manufacturing process of these composites are kept as a closely guarded secret by manufacturers. Due to proprietary technology and limited information in public domain, any attempt to improve the properties must follow elementary study of “know how” & “know why” of the technology. The objective of this work is to study different PTFE composites suitable for compressor application, establish a method to improve their tribological properties,

P. K. Pandey · S. Thirumalini (✉) · R. Padmanaban

Department of Mechanical Engineering, Amrita School of Engineering, Amrita Vishwa Vidyapeetham, Coimbatore 641112, India
e-mail: st_malini@cb.amrita.edu

R. Padmanaban
e-mail: dr_padmanaban@cb.amrita.edu

G. Jayashankar
GM - Technology, ELGi Equipments Ltd, Coimbatore, India

formulate a wear model based on test parameter and utilize this learning to solve real application problem.

1.2 PTFE-Based Piston Rings

A compressor has a wide range of operating parameters like temperature, load, sliding distance and velocity which influence the choice of materials. The piston ring needs to have good sealability, life, thermal conductivity and lower thermal expansion. In addition, oil-free compressor requires a ring material which can function in dry condition for longer duration. Carbon graphite was used for many years as a piston ring material in oil-free compressors. It combines strength, hardness and wear resistance of carbon with the lubricity and machinability of graphite. It also has a lower thermal expansion. However, due to inherited in-flexibility, carbon graphite ring was manufactured into two pieces and needed a metal expander ring to seal against the cylinder wall. Other limitations of this material included high micro-finish of mating surfaces, manufacturing with precise tolerance, heavy dust formation during operation and low useful life. Use of filled PTFE as a solid lubricant between piston and cylinder surface overcomes most disadvantages of the carbon-graphite ring. PTFE is a partially crystalline substance obtained from the monomer tetrafluoroethylene (TFE) by polymerization (Fig. 1).

It has a linear chain of carbon and fluorine where fluorine atoms completely shield the chain. Due to weak intermolecular force, it exhibits a very low coefficient of friction but also has low wear resistance. Also, strong C-F bonds provide high chemical and thermal resistance. To reduce the wear rate, PTFE is reinforced with hard phases like carbon, glass, bronze, organic fillers, etc. But, in turn, the reinforcement compromises with its natural property of low friction and causes high frictional power loss in compressor. Despite much technological advancement, the useful life of PTFE piston ring is only half of the metallic piston rings used in oil-lubricated compressors. It requires frequent replacement which if not done, may lead to loss of performance or a catastrophic failure due to destructive rubbing of components. These limitations combined with high material cost have limited the competitiveness of oil-free compressors technology.



Fig. 1 Molecular chain of PTFE

1.3 Literature Review

The literature review is focused on the properties of PTFE and PTFE composites, manufacturing process, methods to enhance tribological properties and various analysis techniques.

Meece et al. [1] have described past and present technology of oil-less air compressors and vacuum pumps. Khedkar et al. [2] have investigated wear behaviour of pure PTFE & six other PTFE composites on pin-on-disc type tribometer under a fixed load and sliding velocity. He used analysis techniques like SEM to study wear mechanism and DSC to study thermal stability. Kowandy et al. [3] have found out the co-relation between the characteristics of the wear particles, the coefficients of friction and the wear rates. The surface morphology of generated wear particles is studied to determine wear mechanisms. On the similar line, Conte et al. [4] have investigated the effects of fillers on PTFE Tribology in relation with wear-specific energy (ratio of friction work to mass loss) and composites crystallinity. Wang et al. [5] have made the study on tribological behaviour of transfer films formed between different PTFE composites containing 15 vol.% of fillers MoS₂, graphite, aluminium and bronze, respectively, and AISI-1045 steel bar. Morphology of transfer film, worn surface and wear debris of the composites are studied under SEM and EDS. Conte et al. [6] have studied the link between crystallinity and wear mechanism using considerations of frictional heating on different PTFE composites. Kapsiz et al. [7] have investigated the effect of sliding velocity, applied load and oil type on tribological characteristics of cylinder liner and piston ring pair under lubrication. The result indicated that weight loss of piston ring & cylinder is greatly affected by sliding velocity and load, whereas coefficient of friction is mainly affected by the sliding velocity.

The literature study gave information on PTFE & PTFE composite properties, method to enhance the properties, various analysis tools & techniques and current research and industry trends. Since most of the researches are done with an aim to understand the wear and frictional phenomenon, the results or conclusion cannot be directly used for air compressor application. However, the same methodology can be performed on favourable materials under relatable application conditions. In this research work, the learning from these literatures is incorporated to obtain conclusive results.

1.4 Methodology

The study of polymer tribology is limited mainly to experimental investigation. Performing the wear tests in a compressor for various materials is tedious and hence laboratory tests are preferred for the preliminary analysis. Since the research is focused only on finding the most suitable material composition for piston ring and establish the method to enhance its tribological properties, different PTFE composites are manufactured by incrementally varying the filler content and are tested on a

pin-on-disc tribometer. The wear rate and coefficient of friction are recorded under different spectrums of load and sliding velocity. The load range is established by trial & error method to have significant wear in short duration of the test (~15 min), whereas the sliding velocity is derived from the design guideline on mean piston velocity [8]. Morphological study is done on the worn out surfaces under Scanning Electron Microscope. Further, design of experiment is carried out on two samples (with lowest wear rate) to investigate the effect of load and sliding velocity on tribological properties.

Though, tribology is a system property which not only depends on the material but also on interacting surface & operating variables, these laboratory tests will certainly yield different values than the real application. However, the tests will help to understand the material properties, rank various materials and understand the wear pattern.

2 Experiment

2.1 Material

Out of various fillers available for PTFE, three fillers (i) Carbon (ii) Bronze (iii) MoS₂ are selected for study because of high thermal conductivity, low thermal expansion and low abrasiveness to mating surface, as required for piston ring application. For obvious reasons, PTFE filled with glass or ceramics is not investigated. Molybdenum disulfide (MoS₂) also adds to lubricity and hence is used in combination with carbon and bronze. The list of materials manufactured is tabulated in Table 1.

The PTFE particle sizes of 0.25 µm are produced by polymerization of tetrafluoroethylene (CF₂ = CF₂) carried out by aqueous suspension and emulsion methods. The PTFE particles are then blended mechanically with filler materials based on composition by weight. The average sizes of carbon particles and graphite flakes are of 20–50 µm, MoS₂ of 10–15 µm and bronze particles of 10–30 µm. The mixtures are compression moulded and sintered at 370–380 °C for 5 h. and cooled inside the furnace. Finally, the moulded samples are machined in form of cylindrical rods of

Table 1 PTFE material composition

Sample No	Composition
1	PTFE + 25% Carbon
2	PTFE + 20% Carbon + 5% Graphite
3	PTFE + 35% Carbon
4	PTFE + 35% Carbon + 5% MoS ₂
5	PTFE + 40% Bronze
6	PTFE + 55% Bronze + 5% MoS ₂
7	PTFE + 60% Bronze

Table 2 Wear disc properties

Disc No	Material	Garde	Hardness	Surface finish (μm)
1	Alloy steel	EN 31	653–746 HV	Ra: 0.45
2	Aluminium	LM 25	300–450 HV (After anodizing)	Ra: 1.46
3	Cast iron	FG 200	190–230 HV	Ra: 0.2

ϕ 12 mm and length 50 mm. The end of rod which slides against the wear discs is machined in form of hemisphere to have uniform point loading.

Three different wear discs are fabricated with alloy steel, Aluminium and Cast iron with surface properties as listed in Table 2. These properties are maintained the same as that of cylinders used in oil-free reciprocating air compressor. The PTFE composite rods are used as Pin and wear discs are disc of pin-on-disc tribometer.

2.2 Tribometer Test

The samples are tested for tribological properties in TR-20LE-PHM 200 pin-on-disc tribometer (manufactured by Ducom Instruments, USA). A schematic diagram of tribometer is shown in Fig. 2.

Load on the pin is applied using dead weights through a lever arm loading system, whereas a load cell measures the frictional force acting between pin and disc. The tribometer gives a continuous plot of wear and frictional force with respect to time, whereas the coefficient of friction at any point can be calculated as the ratio of frictional force to load applied. The weight loss of sample due to wear is recorded by finding the difference of initial and final weight using an analytic balance with sensitivity of 0.1 mg.

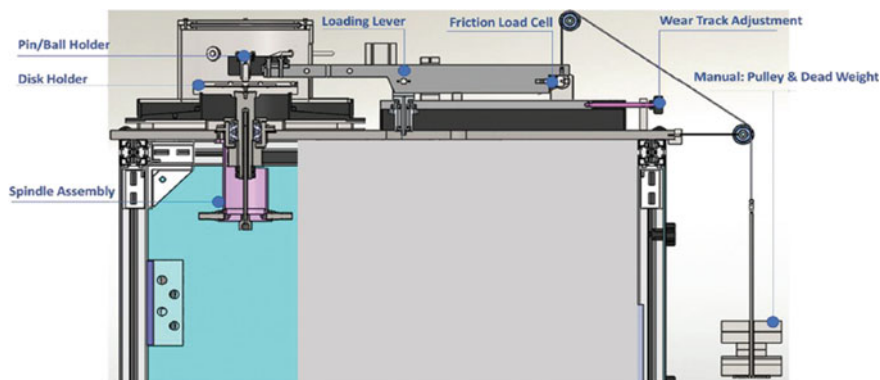


Fig. 2 Pin-on-disc tribometer set-up. Courtesy: Ducom Instruments, USA

Table 3 Level of tribometer test parameter

Sl. no	Coded value	Linguistic term	Real value—load (kg)	Real value—speed (m/s)
1	-1	Low	8	3.35
2	0	Medium	10	3.85
3	1	High	12	4.24

2.3 Design of Experiment

DOE is performed during tribometer test on one sample PTFE + 35% C + 5% MoS₂ to determine individual and interactive effect of load and sliding velocity on factors wear rate and friction coefficient of the specimens. The load and speed are varied at three levels and experimental trials are conducted as per full factorial design. The travel distance is kept constant by varying the test duration. The sliding speed is varied by changing wear track diameter and disc rotation speed (Table 3).

3 Result and Discussion

3.1 Tribometer Test

Wear rate.

The weight loss observed during the tribometer test is shown in Fig. 3. Carbon-filled PTFE exhibited high wear rate as compared to bronze-filled PTFE. The wear rate with Aluminium disc is relatively higher than alloy steel and cast iron. The wear rates are comparable among 20% C + 5% Gr and 35% C filled PTFE. The addition of MoS₂ in 35% C filled PTFE degraded the wear resistance, however, the addition of same quantity in bronze-filled PTFE provided much reinforcement.

Coefficient of friction.

The coefficient of friction noticed during the tribometer test is shown in Fig. 4. In this, all four-carbon filled PTFE exhibited low coefficient of friction as compared to bronze filled PTFE. 25–35% C-filled PTFE exhibited the lower value but is significantly affected by the disc. The addition of MoS₂ in 35% C filled PTFE has resulted in increase in friction coefficient but in bronze filled, the reduction in friction is appreciable. In general, the COF is found to be the lowest against Aluminium disc.

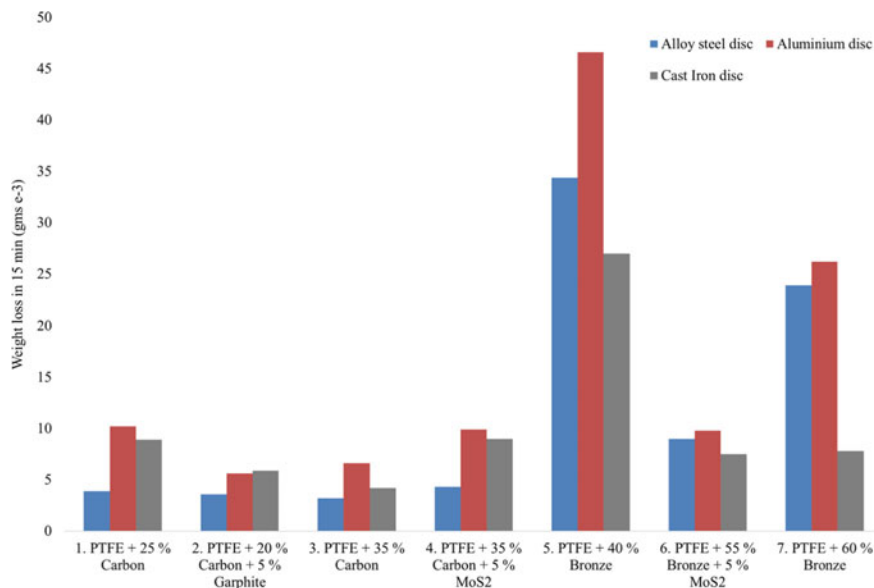


Fig. 3 Weight loss of various samples due to tribometer test

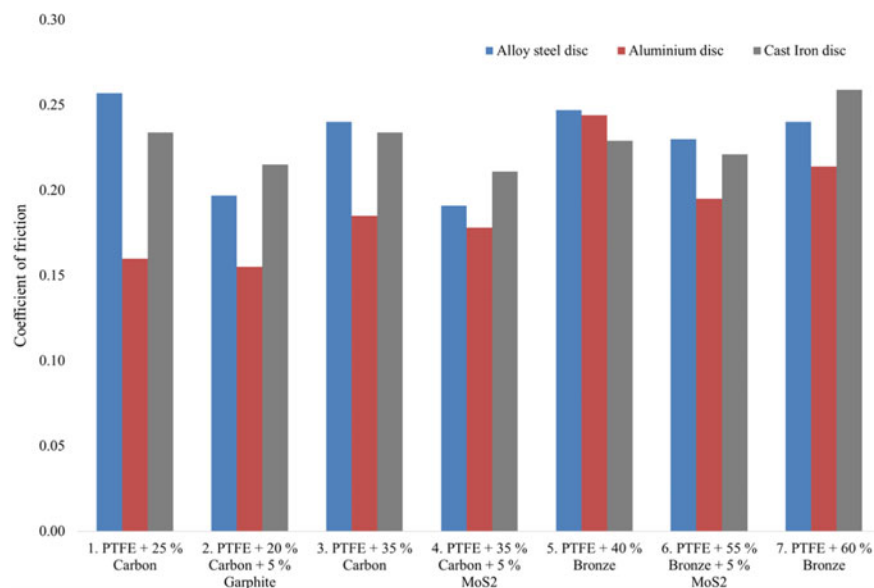


Fig. 4 Coefficient of friction observed in tribometer test

3.2 Morphological Study of Worn Out Surfaces

The below series of figures shows the magnified image of worn out surfaces obtained under Scanning Electron Microscope (SEM). Figure 5 presents the comparative study of carbon-filled PTFE. In 35% C filled PTFE, as the carbon is blended with PTFE in granular form, the filler is completely merged with bulk material. The low coefficient of friction can be attributed to its smooth surface texture. However, the addition of MoS₂ resulted in rough texture which resulted in high friction coefficient. The image also shows small voids appearing between filler and base material which would have crossed easy removal of particles.

Figure 6 presents the comparative study of bronze-filled PTFE. Elemental mapping is done for these composites to differentiate the filler elements using Electron Dispersive X-ray (EDX) as shown in Fig. 7. In 40% Bronze-filled PTFE, the surface shows the crack around the filler which resulted in wear. The wear can be noticed in both bronze and PTFE. Due to high concentration of bronze in the matrix, its resultant interaction with mating surface lead to high coefficient of friction.

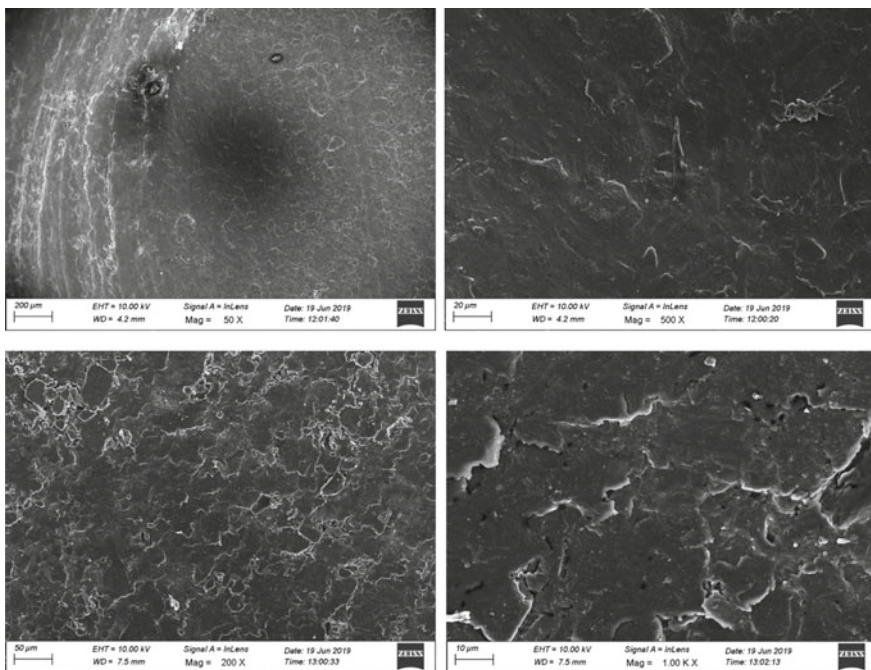


Fig. 5 Worn out surface after test. **a** PTFE + 35% C. **b** PTFE + 35% C + 5% MoS₂

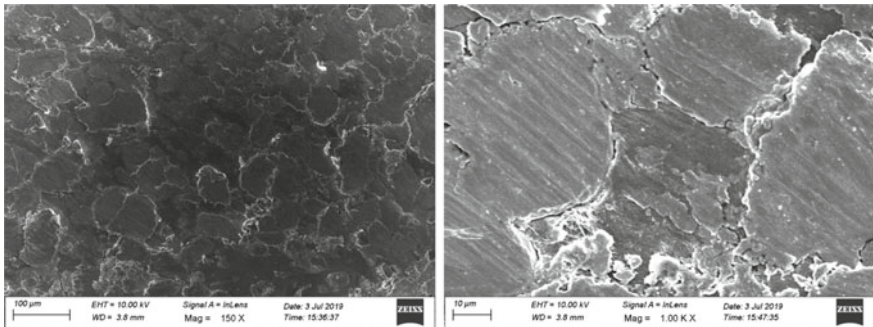


Fig. 6 Worn out surface after test. **a** PTFE + 40%Br. **b** PTFE + 55%Br + 5%MoS₂

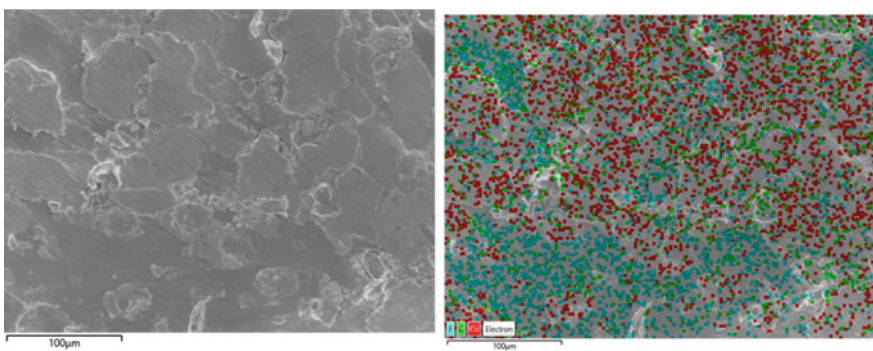


Fig. 7 EDX element mapping. **a** SEM image. **b** Element mapping

3.3 Design of Experiment

The wear rate during the test and friction coefficient observed are presented in Table 4.

Mathematical models based on Radial Basis Function (RBF) have been generated to predict the weight loss due to wear and coefficient of friction. RBF is a real-valued function whose value depends only on the distance from centre point. Mathematically, the function can be represented as Eq. (1) follows:

$$\phi(x, c) = \phi(\|x - c\|) \quad (1)$$

To analyse the results, multi-quadratic type RBF is chosen whose mathematical equation for the variables each related with diverse centres is given by Eq. (2).

$$\phi(\|x - x_i\|) = \sqrt{1 + [\varepsilon(\|x - x_i\|)]^2} \quad (2)$$

Table 4 Design of experiment results

Sl. no	Load (kgs)	Speed (rpm)	Wear track dia. (mm)	Test duration (min)	Velocity (m/s)	Distance travelled (km)	Weight loss (mg)	Coefficient of friction
1	8	800	80	19.0	3.35	3.82	0.0125	0.183
2	10	800	80	19.0	3.35	3.82	0.0176	0.19
3	12	800	80	19.0	3.35	3.82	0.0313	0.183
4	8	700	105	16.5	3.85	3.82	0.0226	0.192
5	10	700	105	16.5	3.85	3.82	0.0187	0.173
6	12	700	105	16.5	3.85	3.82	0.0239	0.196
7	8	900	90	15.0	4.24	3.82	0.0199	0.193
8	10	900	90	15.0	4.24	3.82	0.0221	0.208
9	12	900	90	15.0	4.24	3.82	0.0212	0.169

The polynomial RBF model for predicting the wear and friction coefficient is given below in Eqs. (3) and (4), with parameters of RBF models listed in Table 5.

$$\begin{aligned} \text{Weightloss} = & 0.036002 + 0.098381L - 0.090726V - 0.0059789L^2 \\ & - 0.0081516V^2 + \text{RBF}_1 \end{aligned} \quad (3)$$

$$\begin{aligned} \text{COF} = & 0.14371 + 0.077191L - 0.088629V - 0.044174L^2 \\ & - 0.039383V^2 + \text{RBF}_2 \end{aligned} \quad (4)$$

The values of R^2 , adjusted R^2 and RMSE are presented in Table 6. Low Root Mean Squared Error (RMSE) values indicate the high precision accuracy of the model and value of R^2 close to unity indicates good model fitness. Also, the nearness of R^2 and adjusted R^2 values indicated high prediction effectiveness of the models.

Table 5 RBF network parameters for the generated model

Sl. No	Radial basis function	No. of centres	Global width	Regularization parameter
1	RBF_1	3	1.0794	0.0001
2	RBF_2	3	0.00011911	0.0001

Table 6 RBF model statistical summary

Sl. No	Output parameter in RBF model	R^2	Adjusted R^2	RMSE
1	Wear rate	0.992	0.999	0.0001467
2	Coefficient of friction	0.992	0.947	0.002744

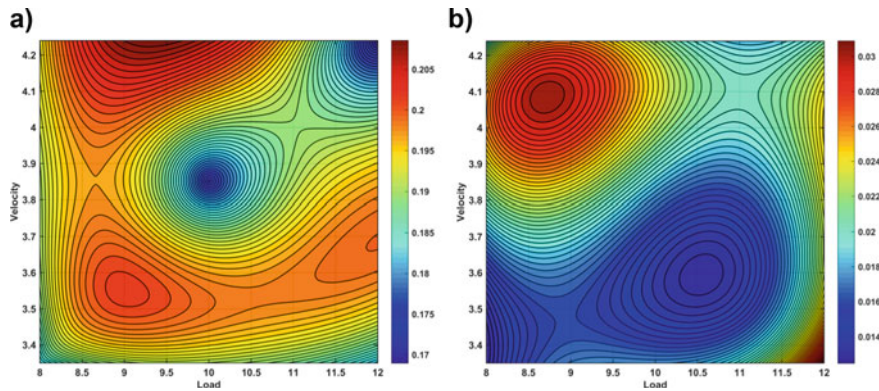


Fig. 8 Contour plot for interaction of load and velocity on. **a** Weight loss. **b** Coefficient of friction

The optimization plot of weight loss due to wear and friction coefficient is shown in Fig. 8. From Fig. 8a, the wear is maximum in the velocity range of 3.9–4.2 m/s and load of 8–9.5 kg. It indicates low wear rate for wide range of loads if the velocity is maintained below 3.5 m/s. Figure 8b shows that the coefficient of friction is lowest only for a small region in velocity range of 3.75–3.95 m/s and load of 9.5–10.5 kg. Very low variation is found in coefficient of friction for wide range of input variables.

4 Conclusion

The following conclusions can be drawn from the study:

- Carbon-filled PTFE exhibits better wear resistance as compared to bronze-filled PTFE. Carbon and carbo-graphite reinforcement are self-sufficient to carry the load and provide lubrication at the interface
- Addition of other solid lubricants like MoS₂ doesn't necessarily enhance the tribological properties. Due care must be taken for its composition, distribution, and bonding with base material
- Carbon-filled PTFE bears the load uniformly and wear is multi-phase. However, in bronze filled PTFE, bronze particles bear the load and wear occurs due to separation of these particles from the matrix
- Coefficient of friction to be low when the sliding velocity is lower than 3.8 m/s. No direct relationship could be established for tribological properties and test parameters as the properties are distinctive for each tribo-system.

References

1. Meece, W., Blank, O., Ickes, C.W.: Design of oil-less Compressors and Pumps. In: Purdue University, Purdue e-Pubs (1974)
2. Khedkar, J., Negulescu, I., Meletis, E.I.: Sliding wear behavior of PTFE composites. Wear **252**, 361–369 (2002)
3. Kowandy, C., Richard, C., Chen, Y.M.: Characterization of wear particles for comprehension of wear mechanisms case of PTFE against cast iron. Wear **265**, 1714–1719 (2008)
4. Conte, M., Igartua, A.: Study of PTFE composites tribological behavior. Wear **296**, 568–574 (2012)
5. Wang, Y., Yan, F.: Tribological properties of transfer films of PTFE-based composites. Wear **261**, 1359–1366 (2006)
6. Conte, M., Pinedo, B., Igartua, A.: Role of crystallinity on wear behavior of PTFE composites. Wear **307**, 81–86 (2013)
7. Kapsiz, M., Durat, M., Ficici, F.: Friction and wear studied between cylinder liner and piston ring pair using Taguchi design method. Adv. Eng. Softw. **42**, 595–603 (2011)
8. O'Neill, P.A.: Industrial Compressor Theory and experiments (1993)

Modelling of a Porous Functionally Graded Rotor-Bearing System Using Finite Element Method



Aneesh Batchu, Bharath Obalareddy, and Prabhakar Sathujoda

1 Introduction

When traditional composites are subjected to high-temperature conditions, interlaminar stresses develop in between the layers due to which delamination of layers takes place. Thus, for improving structural performance, a new class of composites, FGMs, are developed to mitigate the problems of debonding, delamination, and residual stresses in fibre reinforced composites at high temperatures while making use of the advantages of the material properties of both ceramic and metal. An FGM is a heterogeneous micromechanical composite, generally made from using different phases of ceramic and metal. Material gradation laws such as exponential, sigmoid and power law are used for smooth and continuous variation of volume fractions of constituent materials from one layer to another along the desired direction. FGMs were first discovered by a group of Japanese scientists in the mid-1980s. There is a wide range of FGM fabricating techniques based on material applications; a few of them are physical vapour deposition, chemical vapour deposition, tape casting, slurry dipping, sintering and powder metallurgy. Miyamoto et al. [1] and Mortensen and Suresh [2] discussed a few of the fabricating techniques mentioned above. Typically, FGMs are made for the aerospace industry as the temperature of the aerospace structures is enormous, hence the material used must withstand the high temperatures. Owing to a wide range of applications in industries like automotive, biomedical, construction, defence, electronics and marine, functionally graded materials have

A. Batchu · B. Obalareddy · P. Sathujoda (✉)
Bennett University, Greater Noida 201310, UP, India
e-mail: prabhakar.sathujoda@bennett.edu.in

A. Batchu
e-mail: ba8527@bennett.edu.in

B. Obalareddy
e-mail: bo2559@bennett.edu.in

become a topic of interest for many scientists. FG structures are investigated by many researchers and excellent review papers are reported in the literature [3, 4].

FG rotor-bearing systems also play a major role in the mechanical industries; many investigations were performed on rotor-bearing systems. By considering the effects of translational kinetic energy and elastic bending energy, Ruhl and Booker [5] have developed an FE model for the turbo rotor bearing. Nelson [6], by considering the effects of translatory inertia, rotatory inertia, gyroscopic moments, and transverse shear deformations, developed a finite shaft element using Timoshenko beam theory. However, porosity is the most prominent imperfection to consider for assigning material properties as well as the modelling of an FG rotor-bearing system, since, during the fabrication process, the formation of porosities is unavoidable. Ebrahimi and Jafari [7] have analyzed the thermo-mechanical performance of porous FG beams under various thermal loadings. Wattanasakulpong and Ungbhakorn [8] investigated linear and nonlinear vibration problems of porous FG beams. Few researchers have been studying the effects of cracks on FG rotor-bearing systems. Gayen et al. [9] have formulated a finite FG beam element with a surface crack and extended their work to formulate an FG beam element with a transverse crack [10]. Recently, Bose and Sathujoda [11] investigated the natural frequencies of a porous FG rotor-bearing system using ANSYS. However, the works on dynamic analysis of FG rotor-bearing systems are limited despite their importance in the research community.

To the best of the Authors knowledge, the dynamic analysis of porous FG rotor systems is rarely found in the literature. Since porosity affects the dynamic characteristics of FG rotor-bearing systems, it is important to investigate the natural frequencies of an FG rotor system using proper finite element modelling. The primary task of the present work is to model a two-nodded finite porous FG shaft element based on Timoshenko beam theory by including the effects of translational inertia, rotary inertia and transverse shear deformations.

2 Material Modelling of Circular FG Shaft

Material properties such as Young's modulus, modulus of rigidity, density, thermal conductivity and Poisson's ratio are varied along the gradation direction in the case of FGMs. The radial direction is considered as the gradation direction in the case of circular FG shafts. Aboudi et al. [12] categorized the microstructure of material gradation into the continuously graded microstructure, discretely graded microstructure and multi-phase graded microstructure. FGMs are classified into metal-ceramic, ceramic-ceramic, metal-metal and many other combinations but the most used FGM is metal-ceramic. As the accurate details of the graded microstructure are uncharted, volume fractions of different phases are used for material gradation. The continuously graded microstructure of metal-ceramic FGM is represented in Fig. 1. The material properties' dependence on position is attained by the Voigt model [13], which is a simple rule for the mixture of composites in which the material properties of a specific layer P_i are obtained by using Eq. 1.

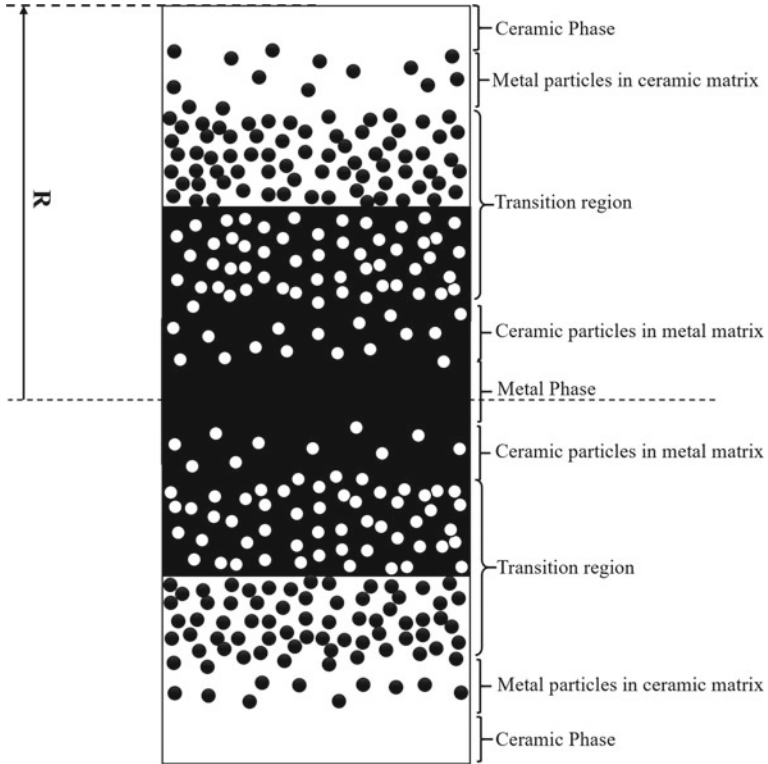


Fig. 1 The continuously graded microstructure of metal-ceramic FGM

$$P_i = P_m V_m + P_c V_c \quad (1)$$

where P_m and P_c are material properties and V_m and V_c are volume fractions of metal and ceramic of the respective layer. The temperature dependency of material properties is attained by Eq. 2 [14].

$$P(T) = P_0(P_{-1}T^{-1} + 1 + P_1T + P_2T^2 + P_3T^3) \quad (2)$$

P_{-1} , P_0 , P_1 , P_2 and P_3 are the coefficients of material and are temperature dependent. Reddy and Chin [15] listed these coefficients, which are in Table 1. T is the temperature in Kelvin. However, in the present work, the porous FG rotor-bearing system is considered to be at room temperature.

Table 1 Coefficients of the temperature of the constituent materials

Material Properties		P ₀	P ₋₁	P ₁	P ₂	P ₃
Steel	E	201.04e9	0	3.08e-4	- 6.534e-7	0
	K	15.379	0	- 1.26e-3	2.09e-6	- 3.7e-10
	v	0.326	0	- 2e-4	3.797e-7	0
ZrO ₂	E	244.27e9	0	- 1.37e-3	1.21e-6	- 3.7e-10
	K	1.7	0	1.276e-4	6.648e-8	0
	v	0.2882	0	1.133e-4	0	0

2.1 Power Law Gradation of FG Shafts

Since it is difficult to attain the position dependency by the distribution of volume fractions of porosity, various laws such as exponential law, power law and sigmoidal law are used to attain the position-dependent material gradation. Amid all the material gradation laws, power law is most used. Power law for a circular FG shaft is

$$P(r, T) = P_m + (P_c - P_m) \left[\frac{r - R_i}{R_o - R_i} \right]^k \quad (3)$$

k is the power law index; it can range from 0 to ∞ . $P(r, T)$ represents the material properties of an FGM. r is the radial coordinate of the shaft. R_i is the inner radius and R_o is the outer radius of the shaft.

2.2 Material Gradation of Porous Circular FG Shafts

The porosity distribution modelling in functionally graded beams with rectangular cross section has been carried out by [7, 8]. However, material gradation of porous circular FG shafts using Timoshenko beam theory is unexplored. An FG shaft whose inner metal core is composed of stainless steel (SS) and the outer ceramic layer is made of Zirconium Oxide/Zirconia (ZrO₂) with evenly distributed porosities is considered in the present work. The material properties are modified as Eq. 4 due to the porosities present in the FG shaft.

$$P_l = P_m \left(V_m - \frac{\alpha}{2} \right) + P_c \left(V_c - \frac{\alpha}{2} \right) \quad (4)$$

Since the material properties depend on the volume fraction of porosity consequently, power law can be modified as

$$P(r, T, \alpha) = P_m + (P_c - P_m) \left[\frac{r - R_i}{R_o - R_i} \right]^k - (P_c + P_m) \frac{\alpha}{2} \quad (5)$$

where α is the volume fraction of porosity, $\alpha \ll 1$ for the FG shafts with porosity and $\alpha = 0$ for the FG shafts without porosity. A python code is developed to calculate and assign the material properties to a circular FG shaft graded based on the power law.

3 Finite Element Modelling of A Porous FG Rotor-Bearing System

An FG Jeffcott rotor system, consisting of a uniform steel disc, an FG shaft and linear isotropic bearings, shown in Fig. 2, is considered in this work. A novel two-nodded porous FG shaft element with four degrees of freedom (two translational and two rotational degrees of freedom) at each node have been developed using the finite element method based on Timoshenko beam theory. The effects of elastic bending energy, translational kinetic energy, rotatory inertia and transverse shear deformations are considered while modelling the shaft element. Porous FG shaft elemental stiffness and mass matrices are derived in the present paper, which is currently not available in the literature. The equation of motion of all the components of Jeffcott rotor system is discussed in the following sections.

3.1 Porous Circular FG Shaft Element

The porous circular FG shaft is discretized into two-nodded finite beam elements. A novel two-noded shaft element with four degrees of freedom on each node is represented in Fig. 3. Where v and w are translational degrees of freedom and β and τ are the rotational degree of freedom. Nelson and McVaugh [16] derived the

Fig. 2 FG Jeffcott rotor system

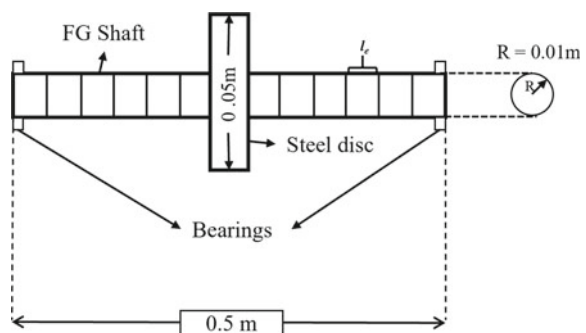
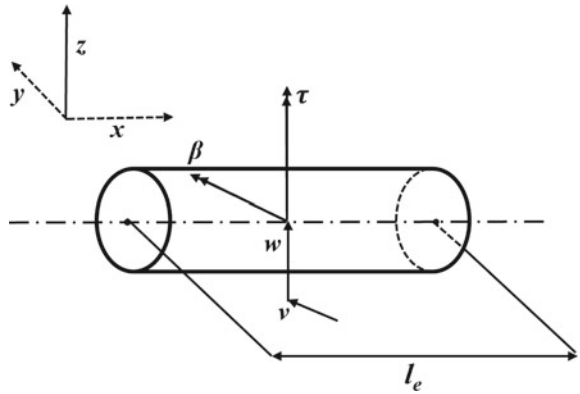


Fig. 3 A two-nodded porous FG shaft element



equation of motion of a uniform shaft element. However, in the case of the porous FG shaft, the material properties depend on position, temperature and porosity index. The corresponding elemental translatory, rotatory mass and stiffness matrices depend on the volume fraction of porosity, unlike the uniform elemental matrices. The equation of motion, Eq. 6, of the porous FG shaft element can be developed by the application of Hamilton's extended principle, equation of energy and work functions as discussed in Nelson [6].

$$([M^e] + [N^e])\{\ddot{q}\} - \Omega[G^e]\{\dot{q}\} + [K^e]\{q\} = \{Q_s^e\} \quad (6)$$

$$[K^e] = C_1 \left(\int_0^{l_e} E(r, T, \alpha) I(r) [\psi'']^T [\psi''] ds + \int_0^{l_e} \kappa(r, T, \alpha) G(r, T, \alpha) A(r) [\psi']^T [\psi'] ds \right) \quad (7a)$$

$$[M^e] = C_2 \int_0^{l_e} m[\psi]^T [\psi] ds \quad (7b)$$

$$[N^e] = C_3 \int_0^{l_e} I_D[\varphi]^T [\varphi] ds \quad (7c)$$

$$[G^e] = [H^e] - [H^e]^T \text{ where } [H^e] = C_4 \int_0^{l_e} I_P[\varphi_w]^T [\varphi_v] ds \quad (7d)$$

$[M^e]$ is the elemental translational mass matrix, $[N^e]$ is elemental rotatory matrix and $[G^e]$ is the elemental gyroscopic matrix, $[K^e]$ is elemental stiffness matrix, $\{q\}$ is the nodal displacement vector, $\{Q_s^e\}$ is the external loading vector. $[K^e]$, $[M^e]$, $[N^e]$ are symmetric matrices, whereas $[G^e]$ is a skew-symmetric matrix. Ω is the spin speed of the shaft in rad/sec. $E(r, T, \alpha)$ is Young's modulus, $\kappa(r, T, \alpha)$ is the transverse shear form factor, $G(r, T, \alpha)$ is the modulus of rigidity of the shaft element, $I(r)$ is the moment of inertia, $A(r)$ is the area of a thin layer of the shaft whose inner radius is r and the outer radius is $r + dr$, l_e is the length of the element. C_1 , C_2 , C_3 and C_4 are the coefficients of the elemental stiffness matrix, translatory

mass matrix, rotatory mass matrix and gyroscopic matrix, respectively

$$C_1 = \frac{1}{l_e^3(1 + \Phi_R)} \int_0^R E(r, T, \alpha) I(r) dr \quad (8a)$$

$$C_2 = \frac{l_e}{420(1 + \Phi_R)^2} \int_0^R \rho(r, T, \alpha) A(r) dr \quad (8b)$$

$$C_3 = \frac{1}{120 l_e (1 + \Phi_R)^2} \int_0^R \rho(r, T, \alpha) A(r) r^2 dr \quad (8c)$$

$$C_4 = \frac{1}{60 l_e (1 + \Phi_R)^2} \int_0^R \rho(r, T, \alpha) A(r) r^2 dr \quad (8d)$$

Φ_R is the transverse shear effect and is shown in Eq. 9.

$$\Phi_R = \int_0^R \Phi(r, T, \alpha) dr = \int_0^R \frac{12E(r, T, \alpha)I(r)dr}{\kappa(r, T, \alpha)A(r)G(r, T, \alpha)el^2} \quad (9)$$

3.2 Equation of Motion of the Complete System and Solution Procedure

A uniform steel disc located at the mid-span of the FG rotor-bearing system is considered. Bearings used for the modelling are linear isotropic. The equations of motion of the uniform steel disc and linear bearings are taken from the lines of Nelson [6]. The global equation of motion of the porous FG rotor-bearing system is expressed in Eq. 10.

$$[M_f]\{\ddot{q}\} - \mathcal{Q}[G_f]\{\dot{q}\} + [K_f]\{q\} = \{Q\} \quad (10)$$

$[K_f]$ is the global stiffness matrix which includes the stiffness matrices of the porous FG shaft and linear bearings. $[M_f]$ is the global mass matrix which incorporates the translatory and rotatory matrices of the porous FG shaft and uniform disc. $[G_f]$ is the global gyroscopic matrix which includes the gyroscopic matrices of the porous FG shaft and disc. $\{Q\}$ is the external force vector. \mathcal{Q} is the spin speed. Equation 10 can be converted into an eigenvalue problem and can be expressed as Eq. 11.

$$Ah + Bh = 0 \quad (11)$$

$$A = \begin{bmatrix} 0 & [M_f] \\ [M_f] & -\mathcal{Q}[G_f] \end{bmatrix}, B = \begin{bmatrix} -[M_f] & 0 \\ 0 & [K_f] \end{bmatrix}, h = \begin{Bmatrix} \dot{q} \\ q \end{Bmatrix}$$

On solving, the eigenvalues obtained are of the form

$$\lambda_n(\Omega) = \xi_n(\Omega) \pm i\omega_n(\Omega) \quad (12)$$

ξ is damping constant, and ω is the natural frequency in rad/s when spin speed is zero.

4 Results and Validations

Finite element formulations have been developed in Python, and the validation has been carried out to check the correctness of the code. A step-by-step code validation has been carried out and presented in the following subsection. Rotor-bearing data used in the work are tabulated in Table 2.

4.1 Validation—Natural Frequencies of A Simply Supported Porous FG Square Beam

To validate the porosity formulation, non-dimensional natural frequencies $\bar{\omega}$ ($\bar{\omega}^4 = \omega^2 L^4 \rho_{ss}/E_{ss}h^2$) of a simply supported FG square beam have been calculated using Python code. Slenderness ratio of the beam is considered as 20, materials used in the porous FG beam are Si_3N_4 and SUS304. Material properties are tabulated in Table 2. The computed non-dimensional natural frequencies using Python code, given in

Table 2 Rotor-bearing data

<i>Shaft</i>		
Length (L)		0.5 m
Diameter (D)		0.02 m
<i>Disc</i>		
Location		Mid-span
Mass (m)		2 kg
Polar moment of inertia (I_p)		0.0024 kg m ²
Diametral moment of inertia (I_d)		0.0012 kg
Bearing Stiffness		10 ⁵ N/m
Material Properties	Stainless Steel (SS)	Zirconia (ZrO_2)
Young's Modulus (GPa)	207.8	168
Density (kg/m ³)	8166	5700
Poisson's ratio	0.3	0.24

Table 3 Non-dimensional natural frequencies of simply supported porous FG square beam

α	k = 0.5			k = 1		
	Present	[7]	error%	Present	[7]	error%
0	4.5283	4.5158	0.28	3.9695	3.9583	0.28
0.1	4.5947	4.5821	0.27	3.9621	3.9509	0.28
0.2	4.6806	4.6678	0.27	3.9516	3.9406	0.28
α	k = 2			k = 5		
	Present	[7]	error%	Present	[7]	error%
0	3.5659	3.5553	0.3	3.2436	3.2332	0.32
0.1	3.5188	3.5082	0.3	3.1736	3.1634	0.33
0.2	3.4599	3.4495	0.3	3.0888	3.0787	0.33

Table 3, are in good accord with the values in the literature [7] with a percentage error of less than 0.4.

4.2 Results—Non-dimensional Natural Frequencies of Porous FG Rotor-Bearing System

Non-dimensional natural frequencies $\bar{\omega}$ (NDNFs) $\bar{\omega}^4 = \rho_{ss} AL\omega^2 / E_{ss} I$ of the porous FG rotor-bearing system for different values of power-law index and volume fractions of porosity are calculated and tabulated in Table 4. Due to the presence of porosities in the FG shaft, the material properties of the shaft reduce, and hence the NDNFs of the rotor system decreases with increase in the volume fraction of porosity. Similarly, with the increase in power law index, NDNFs decrease due to the reduction of stiffness in the FG rotor-bearing system.

Table 4 NDNFs of porous FG rotor-bearing system

α	k = 0.3	k=0.5	k = 1	k = 3	k = 5	k = 8	k = 10
0	1.5029	1.5008	1.4969	1.4900	1.4875	1.4859	1.4853
0.1	1.5041	1.5022	1.4986	1.4925	1.4904	1.4891	1.4886
0.2	1.5027	1.5010	1.4979	1.4930	1.4915	1.4906	1.4903
0.3	1.4974	1.4960	1.4938	1.4906	1.4899	1.4898	1.4898
0.4	1.4861	1.4854	1.4844	1.4840	1.4846	1.4855	1.4859
0.5	1.4654	1.4658	1.4668	1.4709	1.4736	1.4760	1.4770
0.6	1.4290	1.4312	1.4359	1.4475	1.4535	1.4585	1.4605

5 Conclusion

Non-dimensional natural frequencies of a porous FG rotor-bearing system have been calculated. The inner core of the shaft is composed of stainless steel, whereas the outer layer of the shaft is made of zirconia.

- A two-noded porous FG shaft element with four degrees of freedom (two translational and two rotational) on each node has been developed using Timoshenko beam theory.
- A python FE code is developed to compute the natural frequencies of a porous FG rotor system; the computed natural frequencies are validated with the published results.
- NDNFs decrease with increase in the volume fraction of porosity due to the reduction in material properties of the shaft.
- NDNFs decrease with increase in power-law index due to the reduction of stiffness of the FG shaft.

References

1. Miyamoto, Y., Kaysser, W., Rabin, B., et al.: Functionally Graded Materials. Springer, New York (2013)
2. Suresh, S., Mortensen, A.: Fundamentals of Functionally Graded Materials. IOM Communications Ltd, London (1998)
3. Swaminathan, K., Naveenkumar, D., Zenkour, A., Carrera, E.: Stress vibration and buckling analyses of FGM plates—A state-of-the-art review. Compos. Struct. **120**, 10–31 (2015)
4. Dai, H., Rao, Y., Dai, T.: A review of recent researches on FGM cylindrical structures under coupled physical interactions, 2000–2015. Compos. Struct. **152**, 199–225 (2016)
5. Ruhl, R., Booker, J.: A finite element model for distributed parameter turborotor systems. J. Eng. for Ind. **94**(1), 126–132 (1972)
6. Nelson, H.: A finite rotating shaft element using Timoshenko beam theory. J. Mech. Des. **102**(4), 793–803 (1980)
7. Ebrahimi, F., Jafari, A.: A higher-order thermomechanical vibration analysis of temperature-dependent FGM beams with porosities. J. Eng. **2016**, 1–20 (2016)
8. Wattanasakulpong, N., Ungbhakorn, V.: Linear and nonlinear vibration analysis of elastically restrained ends FGM beams with porosities. Aerosp. Sci. Technol. **32**(1), 111–120 (2014)
9. Gayen, D., Chakraborty, D., Tiwari, R.: Whirl frequencies and critical speeds of a rotor-bearing system with a cracked functionally graded shaft—Finite element analysis. Europ. J. Mech. A/Solids **61**, 47–58 (2017)
10. Gayen, D., Chakraborty, D., Tiwari, R.: Free vibration analysis of functionally graded shaft system with a surface crack. J. Vib. Eng. Technol. **6**(6), 483–494 (2018)
11. Bose, A., Sathujoda, P.: Natural frequency analysis of a porous functionally graded shaft system. Int. J. Aerosp. Mech. Eng. **14**(3), 123–131 (2020)
12. Aboudi, J., Pindera, M., Arnold, S.: Higher-order theory for functionally graded materials. Compos. Part B: Eng. **30**(8), 777–832 (1999)
13. Shen, H.: Functionally Graded Materials. [S.I.], CRC press (2009)
14. Touloukian, Y.: Thermophysical Properties of High Temperature Solid Materials. Macmillan, New York (1967)

15. Reddy, J., Chin, N.: Thermomechanical analysis of functionally graded cylinders and plates. *J. Therm. Stress.* **21**, 593–626 (1998)
16. Nelson, H., McVaugh, J.: The dynamics of rotor-bearing systems using finite elements. *J. Eng. Ind.* **98**(2), 593–600 (1976)

Influence of Workpiece Mating Gap on Friction Stir Welding of 316L for Fixture Design on a Machine



B. Raghu Prem, Kundan K. Singh, and Ravi Shanker Vidyarthi

1 Introduction

Welding is one of the most important operations in metal joining and is used widely in Automobile, Aerospace and Defence Industries. Joining metals usually requires High Heat or High Pressure or both for a good bond. The quality of the weld is the most important aspect, as it determines the integrity of the structure of the object fabricated and its life. It is estimated that the welding operations account for a lion's share of major operations in the process industry or manufacturing industry. Friction Stir Welding is relatively a new type of Solid State welding, which was invented by The Welding Institute (TWI), Cambridge, U.K in 1991 [6], where in two metals are joined by using a high rotating tool, which has a pin and a shoulder and moves along the weld joint, wherein the pin is plunged into the metal and the shoulder is plunged to a certain depth so that the friction between the shoulder and the metal workpieces to be joined generates high amount of heat in the metal. This high heat generation causes plastic deformation, i.e. softening of metal at localized zone, due to which the mixing of metals will be formed and this mixing will ultimately result in formation of joining of two metals. In this type of welding process, the base metal does not reach its melting point, hence reducing the amount of energy needed to perform the weld. Moreover, there is no use of gas or flux during the process, hence making it environment friendly. The recent investigations show that a wide range

B. R. Prem · K. K. Singh · R. S. Vidyarthi (✉)

Department of Mechanical Engineering, Birla Institute of Technology and Science Hyderabad Campus, Hyderabad, Telangana 500078, India

e-mail: ravi.vidyarthymfe@hyderabad.bits-pilani.ac.in

B. R. Prem

e-mail: h20191060518@hyderabad.bits-pilani.ac.in

K. K. Singh

e-mail: ksingh@hyderabad.bits-pilani.ac.in

of metals and alloys can be joined using FSW. However, process parameters play a very important role to achieve the defect-free sound weld with required mechanical and metallurgical properties. The workpiece mismatch and workpiece mating gap are inherent process variation because of welding process setup. The workpiece mating gap has a significant influence on the weldment strength. The understanding of workpiece mating gap on the temperature and stress distribution in weldment can help in achieving the desired strength. This understanding of gap is very critical for designing of a fixture for a friction welding machine. The design for fixture must have high rigidity to avoid the large variation in workpiece mating gap during the friction welding process.

Mathematical approach is found as one of the best-suited practices to study the influence of different process parameters on the weld quality. Colegrave, P. [7] presented a method to determine the heat generation using CFD approach and researchers [12, 14] have followed the similar methodology to predict different parameters and material flows during the FSW process. Zhang et.al [8] used the eule-
rian approach to simulate the FSW of Al Alloy to determine the heat transfer, plastic strain, temperature distribution and microhardness. Ahmad et al. [1] have studied the temperature distribution and strain by Coupled Eulerian–Lagrangian approach during the FSW process on steel. The results of the model were compared with the previously available experimental results of the same grade. It was stated that no flaws were detected in both models, which demonstrates that the process is durable for diverse process parameters. Camilleri et al. [2] have evaluated the effect of the heat source characteristics by assuming FSW tool as moving heat source for DH36 workpiece. Various researchers [3–5] studied the influence of process parameters on the weld quality through finite element approach.

From the literature, it is observed that there is significant work available on the studies of various FSW process parameters such as tool rotational speed, tool shoulder characteristics, pin geometry, tool linear movement speed and plunge depth for weld quality. However, the influence of gap between the plates to be welded (mating gap) is not being investigated in significant number. The mating gap is an important factor for designing the fixture and consequently for the quality of the weld. Therefore, in the current work, efforts have been made to study the effect of workpiece mating gap on temperature and stress distribution in welding zone by carrying out the modelling of friction welding process.

2 Materials and Method

2.1 *Electrodes Used and General Characterization of Wire/Wire-Rods*

In the current work, 316 L austenitic stainless steel is taken as base metal for FSW. The thickness and the width of the plate were kept 2 mm and 16 mm, respectively.

The physical properties of the base metal such as thermal conductivity, co-efficient of expansion and specific heat are given in Table 1. Titanium carbide was selected as tool material for friction stir welding of 316 L austenitic stainless steel. The shoulder diameter and pin diameter were kept 6 mm and 4 mm, respectively. Geometry of the FSW tool selected is given in Fig. 2. Physical properties of the tool material used are given in Table 2. The alignment of the plate and the FSW tool in both conditions, i.e. without any gap and with gap is shown in Fig. 1 (a and b). The welding speed was 30 mm/s, rotational speed of the tool 200 rad/s and plunging velocity of 25 mm/s (Table 3).

In this work, Johnson–Cook Material model is considered as it best describes the material under high-strain-rate deformation, and can be used with most metals. Johnson–Cook hardening is a particular type of isotropic hardening where the static yield stress, σ_0 , is assumed to be of the form:

$$\sigma_0 = \left[A + B(\epsilon^{pl})^n \right] \left(1 - \hat{\theta}_m \right) \quad (1)$$

where ϵ^{pl} is the equivalent plastic strain and A, B, n and m are material parameters measured at or below the transition temperature, $\theta_{transition}$. θ^* is the nondimensional temperature defined as

$$\hat{\theta} = \begin{cases} 0 & \text{for } \theta < \theta_{transition} \\ (\theta - \theta_{transition}) / (\theta_{melt} - \theta_{transition}) & \text{for } \theta_{transition} \leq \theta \leq \theta_{melt} \\ 1 & \text{for } \theta > \theta_{melt} \end{cases} \quad (2)$$

where θ is the current temperature, θ_{melt} is the melting temperature and $\theta_{transition}$ is the transition temperature defined as the one at or below in which there is no temperature dependence of the yield stress. The material parameters must be measured at or below the transition temperature.

To determine the temperatures, use Fourier's Law of Heat Conduction as the heat generated in the FSW is primarily due to frictional contact.

$$\rho c \frac{dT}{dt} = \operatorname{div}(k \cdot \operatorname{grad} T) + q_{in} \Omega \quad (3)$$

The heat generated at any point r on the tool is given by the formula.

$$d\dot{q} = 2\pi\omega \cdot r^2 \mu(T) p(T) dr \quad (4)$$

and the heat generation over the contact area is given by

$$\dot{q} = \int_{r_0}^{R_0} 2\pi\omega \cdot r^2 \mu(T) p(T) dr = \frac{2}{3}\pi\omega\mu(T)p(T)(R_0^3 - r_0^3) \quad (5)$$

Table 1 Properties of 316 L alloy

Temperature (K)	Density (kg/m ³)	Young's modulus (GPa)	Poisson's ratio	Thermal conductivity (W/m k)	Sp. heat (kJ/Kg K)	Yield strength (MPa)	α -coefficient of thermal expansion (10^{-6}) (K ⁻¹)
300	8238	194.18	0.27	13.4	468	206.85	15.156
400		188.49		15.2	504	167.49	160.51
500		182.02		16.75	527	143.38	16.933
600		174.29		18.30	550	128.64	17.511
700		166.17		19.8	563	121.36	17.946
800		157.96		21.3	573	117.62	18.297
900		148.63		22.75	589	112.52	18.592
1000		136.5		24.2	602	102.99	18.847

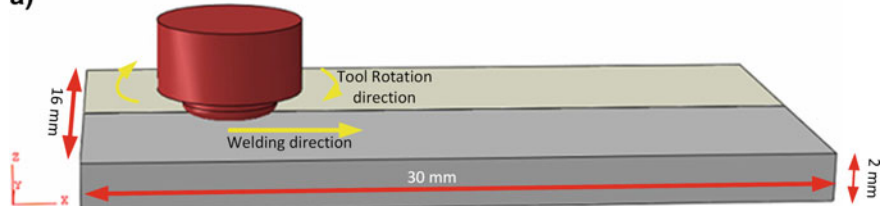
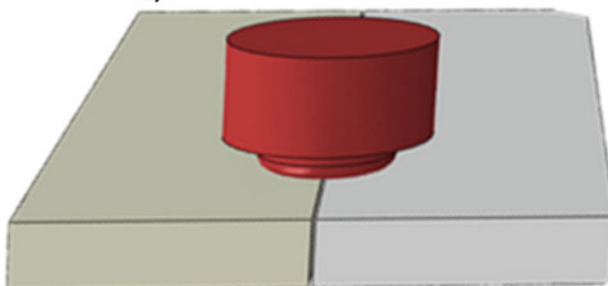
Table 2 Properties of tungsten carbide tool

Density (Kg/m ³)	Young's modulus (GPa)	Poisson's ratio	Thermal conductivity (W/m k)	Sp. heat (KJ/Kg K)	α -coefficient of thermal expansion (10^{-6}) (K ⁻¹)
11,900	534	0.22	50	400	45

Table 3 Johnson Cook parameters of 316 L

Johnson Cook Parameters of Al 6061 – T6

A(MPa)	B(MPa)	N	m	Melting temp (K)	Transition temp (K)	C	$\dot{\varepsilon}$
305	1161	0.61	0.517	1673	300	0.01	1

a)**b)****Fig. 1** **a** Welding setup with no gap. **b** Welding setup with gap

The equations used to determine strain are

$$\epsilon_{\phi,\psi} = \frac{d_{\phi,\psi} - d_0}{d_0} = \frac{1 + \nu}{E} S_\phi \sin^2 \psi - \frac{\gamma}{E} (S_{xx} + S_{zz}) \quad (6)$$

where E is Young's modulus, γ stands for Poisson's ratio and d_0 represents the lattice spacing in the unstressed state. The stresses in the ϕ direction can be determined from the equation below.

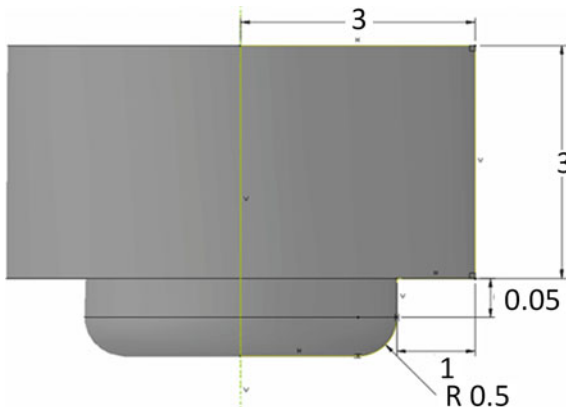


Fig. 2 FSW tool dimensions

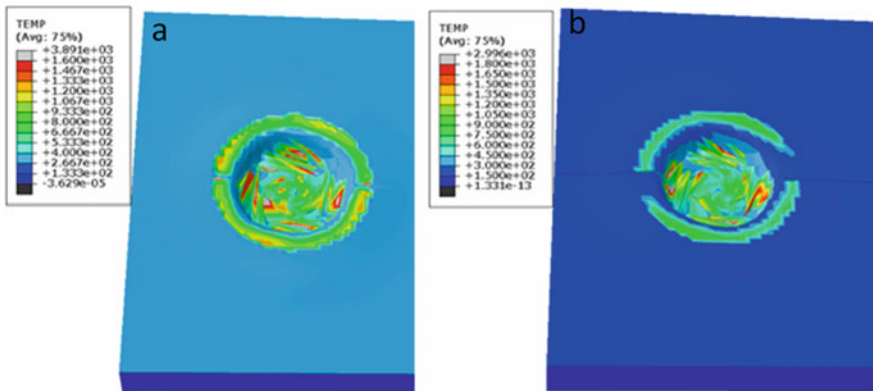


Fig. 3 Temperature variation during the tool plunging, **a** no gap; **b** gap of 100 μm

$$S_\phi = S_{xx} \cos^2 \phi + S_{xz} \sin(2\phi) + S_{zz} \sin^2 \phi \quad (7)$$

The biaxial surface stresses are calculated using the Eqs. (6) and (7) and determined directly from the slope of least-squares of d versus $\sin^2(\psi)$ [13].

3 Results and Discussions

3.1 Thermal Analysis

Figure 3 a, b shows the simulation results for temperature distribution while plunging the FSW tool in the base material. The rotational direction of the tool while plunging and the linear movement was clockwise. The temperature profile shown in the figure is at time 0.032 s after the tool plunging start. It is clear from the figure that the maximum temperature was more in case of no gap condition as compared to the case when plates were 100 μ apart from each other. It could also be noted that the temperature profile on the base plates due to the shoulder contact is forming circular ring. The ring is almost complete in no gap condition (Fig. 3a). However, in case of gap, both sides of the ring are broken and disappear before the plate end. The amplitude of temperature was also found less in 2nd case. The temperature profile suggests that the width of the heat-affected zone may narrow with gap as compared to no gap condition.

Figure 5 shows the temperature variation at a distance 2.3 mm from the weld centreline with time during plunging and the linear movement of the tool after plunging. The plunging time for both the cases was 0.032 s. It is evident from the temperature profile that increase of temperature with time during plunging was almost same in no gap condition and with gap condition. After plunging, when tool starts linear movement, a steep increase of temperature takes place. This steep increase in temperature starts early in no gap condition as compared to the gap condition. Maximum temperature at this point was also found more in no gap condition.

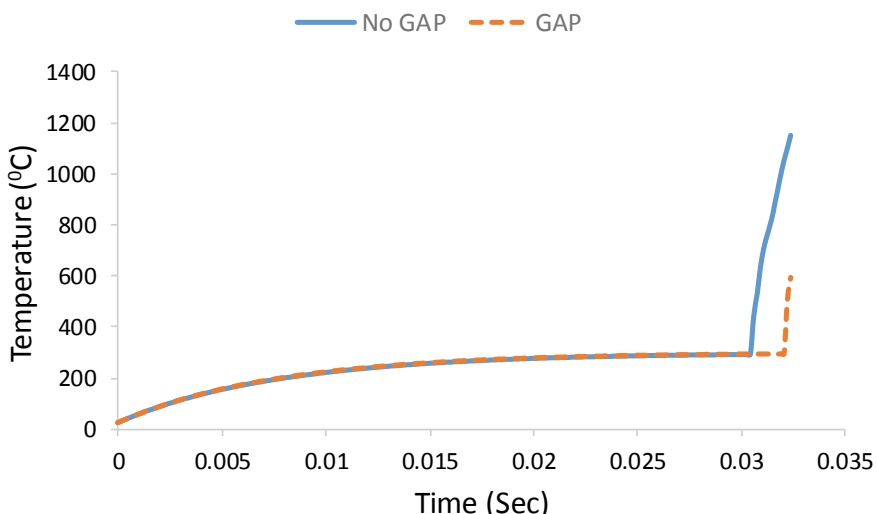


Fig. 4 Variation of temperature at shoulder for plate 1

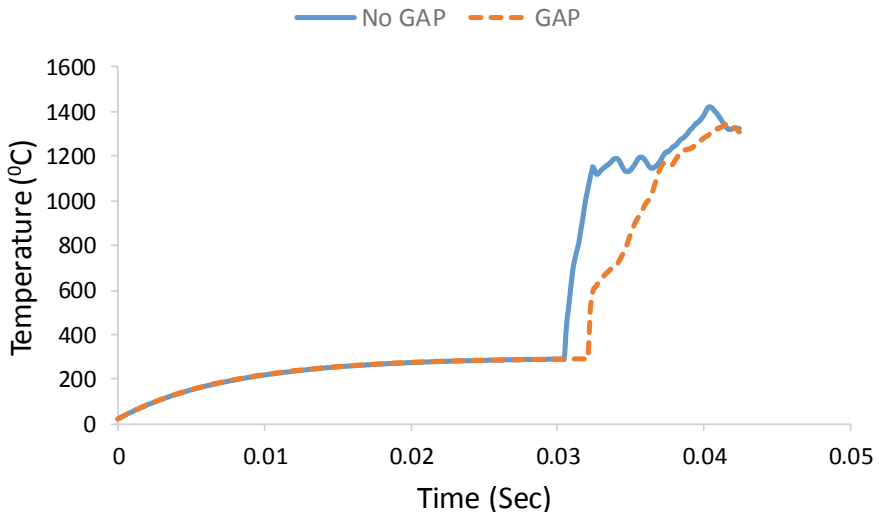


Fig. 5 Temperature variation during plunging and welding on shoulder at distance 2.3 mm from centre of tool

3.2 Stress Analysis

Figure 6a, b shows the stress distribution on the surface for both the conditions. It is evident that more stress was developed in the plate where gap was zero as compared to the plate with 100- μ gap. The pattern of the stress near centre was found similar in both cases. Figure 6a also suggests that the almost continuous stress circle is formed in outer contact peripheral of the tool shoulder and the workpiece. However, fine gap (discontinuity) can be clearly observed in the plate having 100- μ gap. This may be due to the free end of the base material in the gap. From Fig. 6b, we can infer that the stress seems continuous after significant mixing of the material from both plates (shown by white arrow).

Figure 7 shows the change in stress at a point 2.3 mm from the weld centreline. Gradual increase in stress during purging was observed. The stress profile for both the cases was found similar during plunging. However, the stress intensity was slightly more in case of no gap. Once the tool shoulder came into the contact with the workpiece, a sudden increase in stress is observed. Fluctuation in stress intensity was also found significantly more after shoulder touched the workpiece surface. Even after shoulder contact, the stress level of the workpiece with 100- μ was found less as compared to that of the no gap condition. The stress profile of the 100-micron gap workpiece was found slightly smoother than that of the no gap workpiece. Smoother stress profile may be attributed to the gap available for absorbing the deformation and compensating the stress level (Fig. 8).

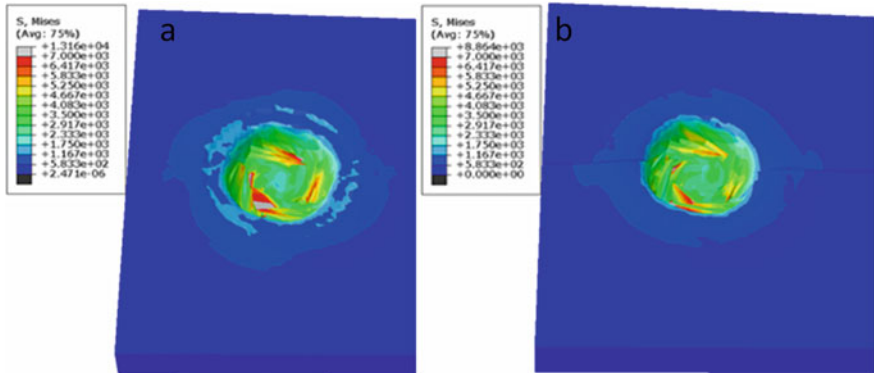


Fig. 6 Stress distribution on the work surface during the tool plunging. **a** no gap; **b** gap of 100 μm

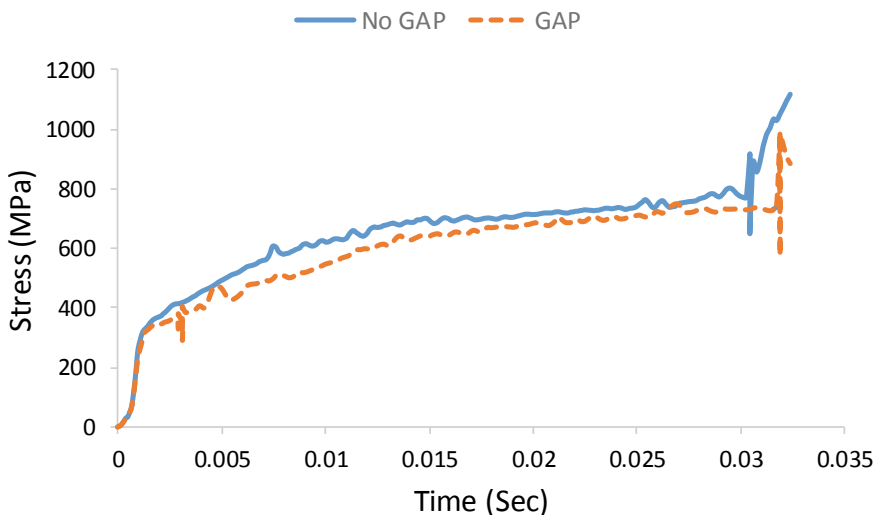


Fig. 7 Variation of stress at shoulder for plate 1

4 Conclusions

The simulations are performed for the plates with and without gap and the observations are as follows. In the no gap scenario, there is a continuity in the temperature ring at the edges, which is missing in the gap situation, the same which is exhibited by the stresses. However, providing a gap paved a way for a smooth stress profile which would reduce the post-weld stress at the local region. This implies that having a small amount of gap is beneficial in reducing the stresses and temperature effects as well.

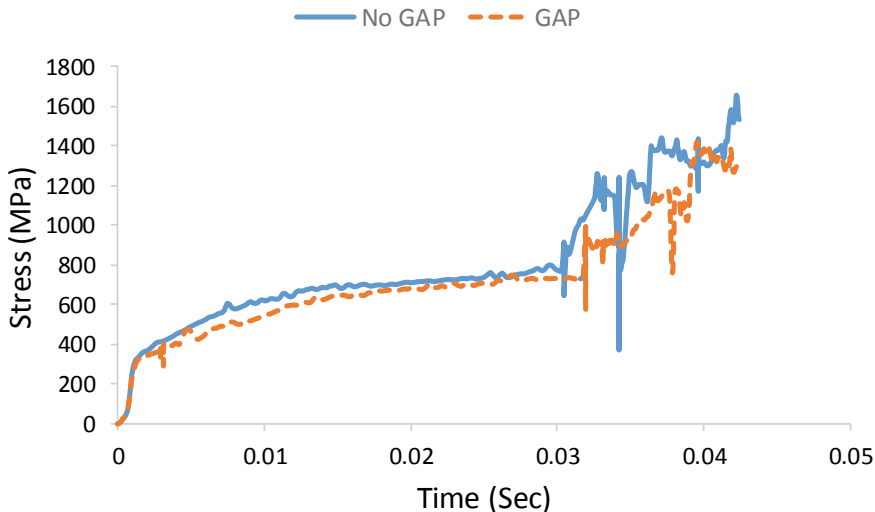


Fig. 8 Stress variation during plunging and welding on shoulder at distance 2.3 mm from centre of tool

References

- Ahmad, B., Galloway, A., Toumpis, A.: Advanced numerical modelling of friction stir welded low alloy steel. *J. Manuf. Process.* **34**, 625–36 (2018). <https://doi.org/10.1016/j.jmapro.2018.07.003>
- Camilleri, D., Micallef, D., Mollicone, P.: Thermal stresses and distortion developed in mild steel DH36 friction stir-welded plates: an experimental and numerical assessment. *J. Therm. Stress.* **38**, 485–508 (2015). <https://doi.org/10.1080/01495739.2015.1015856>
- Dialami, N., Chiumenti, M., Cervera, M., Segatori, A., Osikowicz, W.: Enhanced friction model for Friction Stir Welding (FSW) analysis: simulation and experimental validation. *Int. J. Mech. Sci.* **133**, 555–67 (2017). <https://doi.org/10.1016/j.ijmecsci.2017.09.022>
- Dialami, N., Cervera, M., Chiumenti, M., Agelet de Saracibar, C.: A fast and accurate two-stage strategy to evaluate the effect of the pin tool profile on metal flow, torque and forces in friction stir welding. *Int. J. Mech. Sci.* **122**, 215–27 2017. <https://doi.org/10.1016/j.ijmecsci.2016.12.016>
- Gülerüç, G.: Relationship between FSW parameters and hardness of the ferritic steel joints: modeling and optimization. *Vacuum* **178**, 109449 (2020). <https://doi.org/10.1016/j.vacuum.2020.109449>
- Thomas, W.M., et al., *Friction Stir Butt Welding*. The Welding Institute, Cambridge, UK (1991)
- Colegrove, P.: Three dimensional flow and thermal modelling of the friction stir welding process (Doctoral dissertation) (2001)
- Zhang, Z., Zhang, H.W.: A fully coupled thermo-mechanical model of friction stir welding. *Int. J. Adv. Manuf. Technol.* **37**(3–4), 279–293 (2008)
- Durdanović, M.B., Mijajlović, M.M., Milčić, D.S., Stamenković, D.S.: Heat generation during friction stir welding process. *Tribol. Ind.* **31**(1–2), 8–14 (2009)
- Riahi, M., Nazari, H.: Analysis of transient temperature and residual thermal stresses in friction stir welding of aluminum alloy 6061-T6 via numerical simulation. *Int. J. Adv. Manuf. Technol.* **55**(1–4), 143–152 (2011)
- Neto, D.M., Neto, P.: Numerical modeling of friction stir welding process: a literature review. *Int. J. Adv. Manuf. Technol.* **65**(1–4), 115–126 (2013)

12. Padmanaban, R.V.R.K., Kishore, V.R., Balusamy, V.: Numerical simulation of temperature distribution and material flow during friction stir welding of dissimilar aluminum alloys. *Procedia Eng.* **97**, 854–863 (2014)
13. Chen, C.M., Kovacevic, R.: Finite element modeling of friction stir welding—thermal and thermomechanical analysis. *Int. J. Mach. Tools Manuf.* **43**(13), 1319–1326 (2003)
14. Colegrove, P.A., Shercliff, H.R.: CFD modelling of friction stir welding of thick plate 7449 aluminium alloy. *Sci. Technol. Weld. Join.* **11**(4), 429–441 (2006)

Integration of IoT and Industry 4.0 in Mechanism and Machines

Physics-Driven Process Digital Twins to Aid Pharma and Specialty Material Manufacturing



Jenil P. Dedhia and Ravichandra Palaparthi

1 Introduction

Specialty industry (comprising pharma, materials, etc.) relies on providing a technologically advanced quality product serving niche areas. Typically the characteristics of the industry include low throughputs of products (~0.1–100 kg annually) with strict quality control specifications; high cost of raw materials (for example, APIs in the case of pharma); need to maintain multiple product lines each customized to a market/customer segment; ability to manufacture a given product in different plant settings that do not necessarily have the same specification of equipment; and quick turnaround times to launch the right product meeting customer needs via R&D and scaling up to manufacturing. The method of manufacture of the product at any scale consists of a series of unit operations as shown in Fig. 1. Leveraging the full benefits of the automation of the various practices and operations in this industry involves not only on how well one identifies, captures the relevant process data, and implements appropriate controls in the manufacturing scale, but also on how one can expedite product/process development by designing the customized formulation and process steps at the lab scale and effectively translating them to the manufacturing scale with minimum trials and errors.

The latter part demands adequate understanding of the underlying process physics of each of these unit operations and appropriate implementation of the engineering principles of scale-up. This is typically done through physics-based digital twins for

J. P. Dedhia · R. Palaparthi (✉)
Anagha Consultants, Bhagyanagar 500050, India
e-mail: rpalaparthi@anagha.consulting

J. P. Dedhia
e-mail: jedhia@anagha.consulting

R. Palaparthi
Anagha Consultants LLC, Hockessin, DE 19707, USA

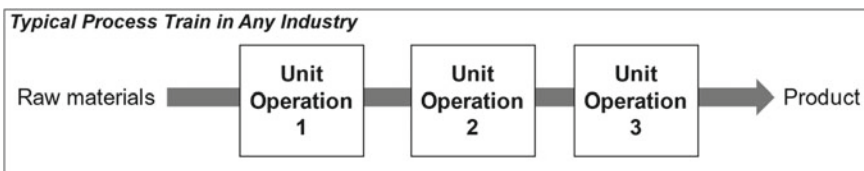


Fig. 1 Process train of unit operations

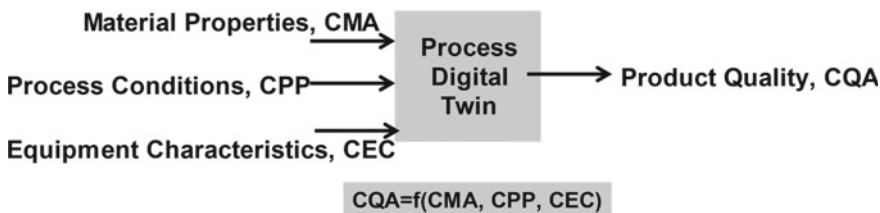


Fig. 2 Process digital twins linking product quality to input material, process, and equipment characteristics

individual operations (see Fig. 2) that offer the end-user quantitative guidance in their development/scale-up efforts by capturing relevant level of process physics to link the inputs (both incoming material properties, equipment characteristics, and process conditions) to the outputs (the quality characteristics of the intermediate product).

Given the interaction of the equipment characteristics with the product quality, the digital twins need to appropriately integrate details of both the machine and the material with the process. The level of process physics that needs to be taken care of can range from simple calculations to detailed computational simulations taking long times. In cases where adequate physics-based understanding does not exist to link inputs and final outputs completely, the following approaches can be leveraged within the limitations: data or machine learning (ML) type of models [1], and fit for purpose models (either physics or ML based) that address the need in parts [2]. Given the multi-disciplinary technical nature of the problem, and the fact that the end-user is not expected to be conversant in the physics or ML aspects, successful deployment of such capabilities relies on how best to distill these details and make the offering friendly for routine use by the end-user in a fail-safe way. The complexity of such a scenario demands efficient integration of the needs of R&D, and manufacturing operations within the elements of the Industry 4.0 vision for the specialty industry.

This work presents a framework through an example case study showing how such needs within the context of a pharma industry can be addressed through a combination of approaches. Depending on the dosage form to be manufactured, the pharma processes involve the use of different unit operations and the associated equipment [3]. These include compounding vessels for Newtonian or non-Newtonian fluids, solid powder blenders, wet and dry granulators, various types of dryers (like fluidized bed driers and lyophilizers), size reduction equipment, tablet compactors, coaters, etc. This article focuses on how elements of automation in expediting processes and

product development at the R&D through tech transfer to the manufacturing scale can be implemented using pharmaceutical liquid mixing, and solid powder blending unit operations as examples. The generality of the approach presented facilitates extension to the needs of any other industry. Given the proprietary nature of the efforts involved and the need to provide an educational experience to the audience, this article strikes an appropriate balance in revealing the relevant details, algorithms, etc.

2 Materials and Methods

2.1 Example Process and Unit Operation

Figure 3 shows a set of example processes and the associated series of unit operation steps in the pharma space [4]. The unit operations can vary with the drug dosage form to be manufactured. The quality attributes of the finished product are dependent on the material properties of the incoming raw materials (the API and the excipients), equipment characteristics, and the process conditions of the various relevant unit operations. Hence, a good understanding of the underlying interactions within and across each of the unit operations in this process train enables us to achieve and control the quality attributes of the final product.

Specifics of the automation features considered are presented using mixing and blending unit operation as examples (highlighted in the dotted boxes in Fig. 3). The mixing step shown in Fig. 4a can consist of two different phases getting mixed in a tank where one liquid (Phase B, say a surfactant) is introduced into the mixing vessel originally consisting of a suspension (Phase A) of particles of certain size distribution (PSD) phase dispersed in a continuous phase. As Phase B is added, items of interest can be on the lines of how best to disperse the particles further

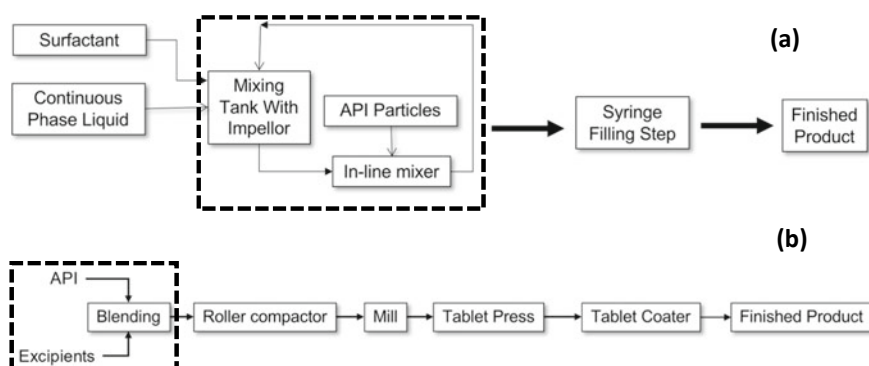


Fig. 3 Typical pharma manufacturing process steps: **a** Injectable; **b** Oral solid tablet forms

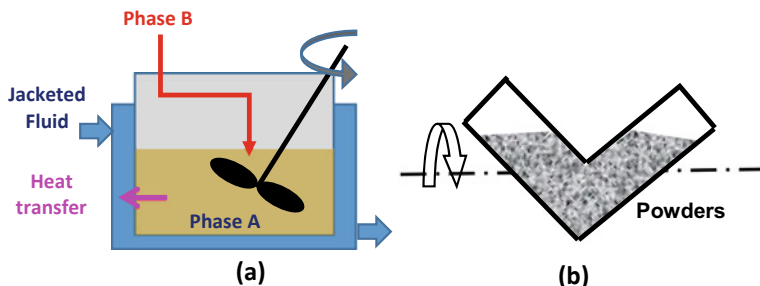


Fig. 4 Example pharma unit operations: **a** Liquid mixing; **b** Powder blending in V-Blender

accounting for continuous phase rheology and thermal stability to achieve the right PSD by controlling the

- Rate, and location of addition of Phase B,
- RPM of the impellor,
- Heat transfer and viscosity characteristics, and
- Total time of mixing.

In the powder blending step, the powders of API and a set of other ingredients (like glidant, lubricant, etc.) including the excipients can be added in a certain order and blended using either a diffusive or convective mechanisms using tumbling action (V, double-cone or bin blenders) or shear action (paddle blenders); for example, see [5] to achieve a uniformly blended powder of the right flow characteristics. Figure 4b shows a typical V-blender where ingredients blend by tumbling mechanisms. The items of interest can be expected to be on the lines of how to achieve the required (a) blend uniformity, (b) the right surface properties (say hydrophobicity) of the blend right after blender or after the downstream steps, and (c) the finished tablet properties. The control variables can be

- the order of addition of ingredients,
- the blender RPM, and
- blending time.

Figure 5a, b shows the various material, equipment, and process inputs that are expected to be accounted for by the digital twins of the mixing tank and the blender to link to the quality characteristics of the output product.

2.2 Process Digital Twins

The process outputs of each of the mixing and blending processes listed in Fig. 5 can be linked to the inputs either directly or indirectly through intermediate parameters. In addition, the level of physics needed for these linkages can be different based

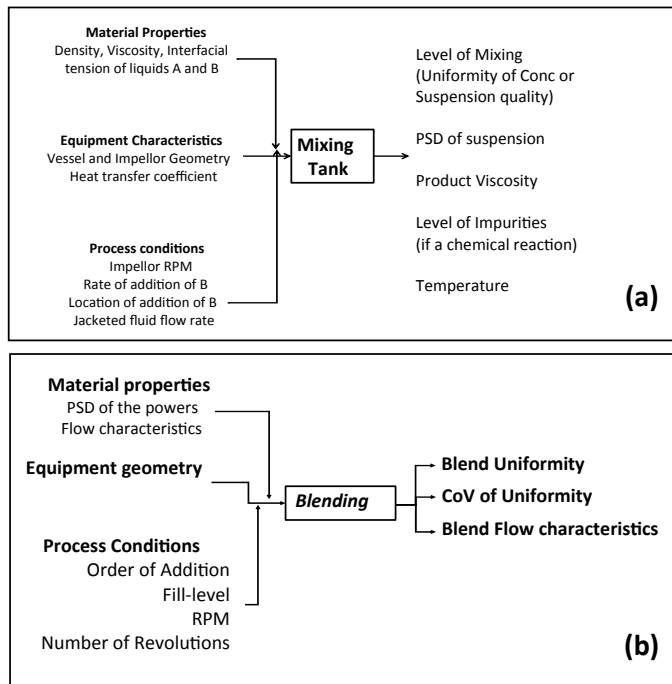


Fig. 5 Inputs and outputs in **a** liquid/liquid or liquid/suspension mixing process, **b** a powder blending process

on the details involved. Accordingly, a combination of different types of twins is employed as part of the implementation of MixingTwin and BlendingTwin (which are proprietary products of Anagha).

Simple twins. These twins capture process models where simple calculations link the outputs directly or indirectly to the inputs. These are useful in scenarios when a process needs to be translated from one scale to another by maintaining a non-dimensional process parameter.

Computational twins. These link the outputs to inputs through detailed numerical computations like discrete element modeling (DEM) as is or in conjunction with computational fluid dynamic (CFD) simulations. They provide visibilities into the details and are employed when one wants to identify concentration hot spots or flow dead zones during blending/mixing. Thus, they help with needs in troubleshooting at one scale and guiding in scale-up. Commercial or open-source computational software [6, 7] and cloud computing resources are leveraged with custom-designed software to obtain the required simulation outputs within the acceptable time frames to help with end-user needs.

For employing CFD or DEM approaches, experimental characterizations of ingredient properties (like physical properties of the liquids, and powders; their shear

or stress sensitivities, etc.) are essential. These properties are either used as is or processed further and fed to the computational purposes. For example, with DEM approaches due to computational issues the material parameters of the particles in the mixture are obtained and scaled up using standard procedures captured in the literature [8] leveraging the appropriate experimental characterizations. This ensures that the output measures of interest are based on appropriate physics and obtained using reasonable computational resources.

ML twins. These are employed to care for the following example needs: (a) when detailed physics-based understanding does not exist to link the process outputs to the inputs; (b) when process outputs need to be predicted at certain process conditions in real time via interpolation by leveraging results from detailed computations run over a range of conditions as training data. For needs in case (a), the twins are designed to take experimental (training) data from the end-user over a custom-defined range of process conditions. A variety of standard ML techniques [9, 10] are employed to predict the required outputs at the sought-out conditions leveraging the training data. Customized software interfaces designed per end-user requirements facilitated access and leveraging of these capabilities.

3 Results and Discussion

3.1 Process Measures and Digital Twins

Extensive literature exists in the fields of liquid mixing (for example, see some case studies in [6, 11–13]), powder blending (for example, [5, 8, 14]) that tries to decode the underlying physics, and mechanisms involved in achieving the right homogeneity of the suspension or the blend quality.

In the case of liquid + suspension mixing, the literature points at the influence of the following on the quality of the suspension (PSD and its uniformity, viscosity, and rheology) : mixing tank/impeller geometrical designs; heat transfer characteristics; location of addition of phase B; impellor RPM; material properties like wettability of the particles, and shear and temperature sensitivity of the continuous phase.

In the case of powder blending, the current understanding points at the influence of the following on the rate and uniformity of mixing: blender geometry and the symmetry; rotation and vibrating action of the blender; and properties of the blend ingredients, like size distributions of the various ingredient particles and flow/material properties like particle–particle, particle–wall frictions, and cohesive and adhesive strengths.

While these are active areas of research, the current understanding points out certain measures/dynamics of liquid mixing and blending that can be linked either directly or indirectly to the suspension/blend quality of the output discharged from the mixing tank/blender. Given the influence of the material properties, some of these linkages can have qualifiers, and need to be handled accordingly. For example,

- a. For dispersion of particles in the suspension, a critical shear rate and temperature should not be crossed, and hence to be accounted for in determining the RPM and heat transfer characteristics;
- b. For free-flowing powders, the blend uniformity is found to be dependent on the total number of revolutions of the blender without dependency on blender RPM whereas, the RPM is found to have significant influence on cohesive powders [15].

In addition, depending on the complexity involved, these measures may need the use of appropriate algorithms (like simple calculations or detailed computations like CFD, DEM, etc.). Tables 1 and 2, respectively, capture some of these details for relevant measures and their expected linkages to the liquid/suspension mixing and powder blend behavior. The complex twins leverage CFD/DEM computations of the relevant materials to predict the dynamics of (liquid + suspension) mixing/powder blending.

Table 1 Various measures in mixing operation, their linkages to process performance, and the relevant twins

Measure	Description and relevance	Expected link to mixing product quality	Type of twins
Power, and Reynolds numbers	Level of overall mixing, flow field in the vessel, and power imparted to the liquid phase	Indirect to level of dispersion of suspension (PSD) Direct to average temperature rise	Simple
Tip speed, geometry based shear rate	Shear history, particle dispersibility and degradation	Indirect to PSD, and final rheology	Simple
Distributions of velocity, shear rate, Conc(B), and temperture	Detailed measure of flow field presence of dead zones, fluid mixing times, shear history, meso mixing of B in A, and effectiveness of heat dissipation	Indirect to <ul style="list-style-type: none"> – extent of suspension non-uniformity, – PSD (via and particle breaking/ collisions) and – final rheology – Time needed for dispersing the suspension Direct to <ul style="list-style-type: none"> – Max. temperatures experienced – Location of hot spots and maximum shear rates – Recommendations on design changes 	Complex

Table 2 Various measures in blending operation, their linkages to process performance, and the relevant twins

Measure	Description and relevance	Expected link to blend behavior	Type of twins
Froude number	Similarity of tumbling behavior for free flow powders	Indirect to level of blend uniformity	Simple
Particle velocities on the surface	Similarity of particle level dynamics for free flow powders	Indirect to level of blend uniformity and final PSD	Simple
Stokes number of breakage	Similarity of particle/ aggregate level dynamics for non-free flowing powders	Indirect to level of blend uniformity and final PSD	Simple
Conc standard deviation (RSD)	Measure of relative level of blending	Direct to level of blending	Complex
Powder mixing rate	Measure of relative comparison of blending time	Indirect to blending time	Complex
Particle travel distance	Exposure time of a particle with other ingredients (indirect)	Indirect to surface properties of the powder post blending	Complex
Particle collision frequency	Aggregation of powders, and final PSD	Indirect to final PSD, and level of blend uniformity	Complex

3.2 Typical Workflow in the Usage of the Process Digital Twins

Figure 6 shows the typical architecture and workflow expected of the working of the digital twins for each of the mixing and blending processes. Depending on what the end-users ask for, different elements of the twins are leveraged to provide the necessary and actionable insights. These insights enable end-users to take appropriate decisions toward formulation or process development and optimization.

3.3 Process Digital Twins and Process Control

The quality of the product resulting from either the mixing tank or the blender is expected to depend on the process conditions employed. For example, along the lines of earlier literature [15], one can expect dependencies of the blend output quality parameters (like RSD vs. time) on V-blender equipment characteristics like the RPM, rocking frequency, powder fill-level, geometry, symmetry, and size of the blender. Figure 7 shows schematics of typically expected behavior depending on powder characteristics. Such behaviors indicate an opportunity to efficiently control

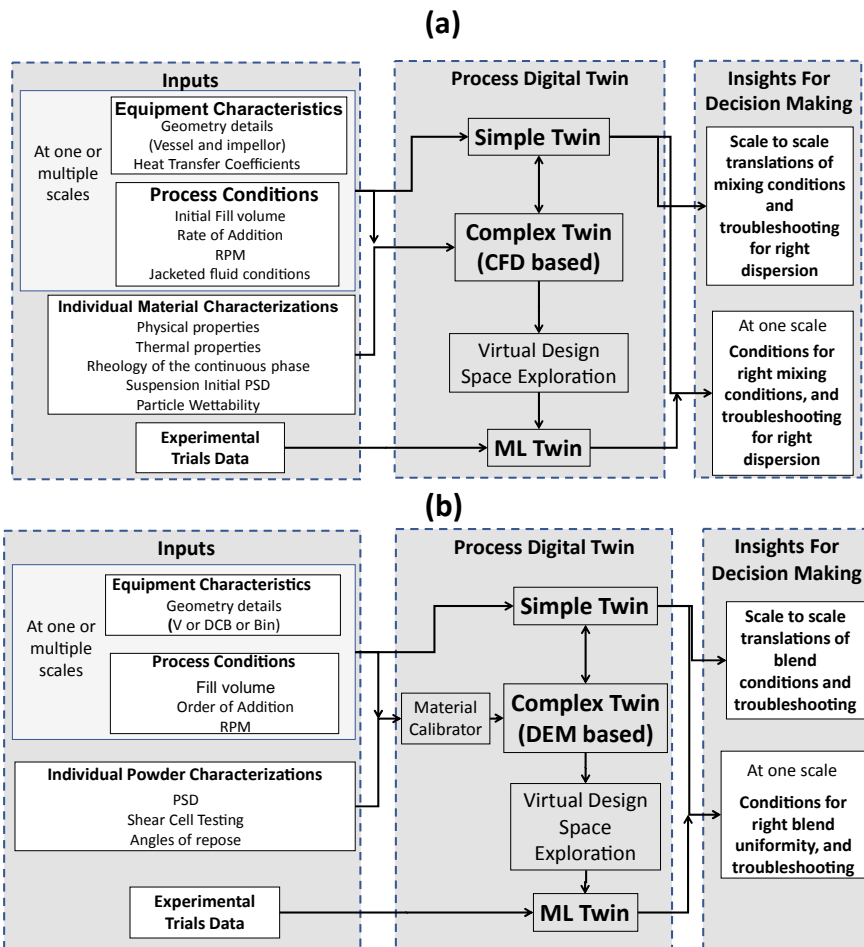
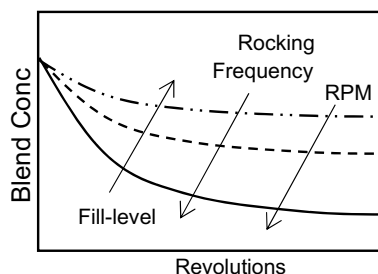


Fig. 6 Workflow and architecture in leveraging digital twins for needs in **a** liquid mixing and **b** powder blending

Fig. 7 Blend output quality with process conditions



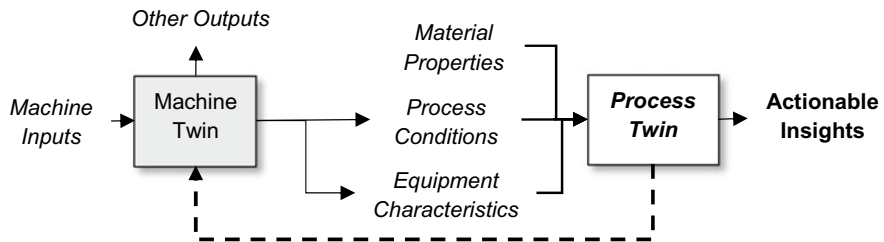


Fig. 8 Interaction of the Machine and Process Twins in the overall automation

the process output via a feedback mechanism that adjusts the blender operation in real time based on the output measures of the digital twins (Fig. 8). While not implemented yet in this effort, such a capability can help in realizing the full benefits of the Industrial IoT in the pharma space.

4 Conclusions

Effective leveraging of automation in the industry relies on how effectively the machines (equipment) talk to the processes (unit operations) that they are used for. This demands a good integration of the elements of process physics into the automation aspects of the machines. In any given unit operation, process digital twins capturing different levels of physics link process outputs to inputs (material properties, process conditions, and equipment characteristics). Hence, appropriate design and implementation of process digital twins are critical to realizing the Industry 4.0 vision for any industry.

This article focuses on an example case study of process digital twins for the pharma industry using test cases of a (liquid + suspension) mixing and powder blending unit operations. Given the complexity of the processes, digital twins for each of the mixing and blending steps is expected to be a composite of Simple, Complex, and ML-based twins to handle the different levels of understanding of the underlying physics in each scenario of the end-user need. A wide range of standard and proprietary approaches and algorithms need to be leveraged in developing such a process twin. The outputs from such twins are expected to be a combination of measures that are either directly or indirectly linked to the output (liquid suspension or blend quality), which can provide actionable insights to the end-user in either formulation or process development.

Given the dependence of these measures on the equipment characteristics like the RPM or rocking behavior, the eventual integration of such a process twin to the equipment's digital twin is essential to achieving the paradigm of Industry 4.0. While this article focuses on a pharma case study, the learnings are general and translatable to any industry.

References

1. Landin, M.: Artificial Intelligence Tools for Scaling Up of High Shear Wet Granulation Process. *J. Pharm. Sci.* **106**, 273–277 (2017)
2. Sen, M., et al.: A multi-scale hybrid CFD-DEM-PBM description of a fluid-bed granulation process. *Processes* **2**, 89–111 (2014)
3. Pandey, P., Bharadwaj, R.: Predictive modeling of pharmaceutical unit operations, 1st edn. Woodhead Publishing Series in Biomedicine: Number 87, Amsterdam (2016)
4. Ierapetritou, M., AIChE Webinar Series, Computing and Systems Technology Division, <https://www.youtube.com/watch?v=7n8bPPkWiOk>, last accessed 2020/09/06.
5. Lemieux, M., et al.: Comparative study of the mixing of free-flowing particles in a V-blender and a bin blender. *Chem. Eng. Sci.* **62**, 1783–1802 (2007)
6. ANSYS Homepage, www.ansys.com
7. OpenFoam Homepage www.openfoam.org
8. Sen, M., et al.: Analyzing the Mixing Dynamics of an Industrial Batch Bin Blender via Discrete Element Modeling Method. *Processes* **5**, 22 (2017)
9. Millen, N., et al.: Machine learning modeling of wet granulation scale-up using particle size distribution characterization parameters. *J. Pharmaceutical Innovat.* (2019)
10. Gams, M., et al.: Integrating artificial and human intelligence into tablet production process. *AAPS PharmSciTech* **15**(6), 1447–1453 (2014)
11. COMSOL Homepage www.comsol.com
12. Zhu, W., et al.: Preferential adsorption of polysorbate 20 molecular species in aqueous paliperidone palmitate suspensions. *Colloids Surf., A* **384**, 691–697 (2011)
13. Vallés, C., Young, R.J., Lomax, D.J., et al.: The rheological behavior of concentrated dispersions of graphene oxide. *J. Mater. Sci.* **49**, 6311–6320 (2014)
14. Horibe, M., et al.: Scale-up of lubricant mixing process by using V-type blender based on discrete element method. *Chem. Pharm. Bull.* **66**, 548–553 (2018)
15. Muzzio, F.J., Alexander, A.W.: Scale up of powder blending operations. *Pharmaceutical Technol.* **1**, s37-s44 (2005)

EEG-Based Hand Movement Recognition: Feature Domain and Level of Decomposition



Nabasmita Phukan, Nayan M. Kakoty, Nipun Gupta, and Neelanjana Baruah

1 Introduction

With advances in technology, brain computer interface (BCI) is established as a promising concept in the area of rehabilitation robotics. Recognition of brain signals, i.e. electroencephalogram (EEG), is one of the key steps in BCI and its performance is dominantly determined by the type of features used for recognition [1]. Sepulveda [2] has reported specific frequency bands of EEG as features for the recognition of right- and left-hand imaginary movements. Independent component analysis and time-frequency techniques were used in the interpretation of neural information for five types of hand movements [3]. Recognition rates of 65% and 71% were achieved using Mahalanobis distance and neural networks, respectively. The energy of EEG components derived using the Welch method achieved an accuracy of 70% in recognizing imaginary left- and right-hand movements [4]. Features like autoregressive coefficients [5], event-related desynchronization of spatial patterns [6], amplitude of EEG [7], movement-related cortical potentials, mean, power, and energy of EEG [8] have been explored in BCI systems for recognition of left/right hands and foot movements. Deep learning technique has been explored for motor imagery classification using EEG and EEG-fNIRS [9, 10]. Although numerous features have been explored and experimented with for the recognition of EEG-based upper and lower limb movements, a methodology for identifying EEG feature set for the recognition

N. Phukan (✉) · N. Baruah
Jorhat Engineering College, Jorhat, India

N. M. Kakoty
Embedded Systems and Robotics Laboratory, Tezpur University, Tezpur, India
e-mail: nkakoty@tezu.ernet.in

N. Gupta
Madhav Institute of Technology and Science, Gwalior, India
e-mail: nipun.gupta2212@mitsgwalior.in

of specific tasks holds promise in BCI applications. The presented work establishes a methodology based on the cross correlation of features with EEG for the selection of a feature set to maximize recognition results.

2 Proposed Methodology

Figure 1 shows the proposed methodology for the selection of feature domain and level of decomposition for the recognition of hand movements using EEG. A 21-channel EEG was pre-processed passing through a bandpass filter of pass band 8–40 Hz. Four time domain, four frequency domain, and time-frequency domain features [11] were extracted from the pre-processed EEG. Following this, the features were fed into a radial basis function (RBF) support vector machine (SVM) [12]. Having obtained maximum recognition rate with time-frequency domain features, this has been explored at four levels of decomposition. Further, the correlation of DWT features at each level of decomposition has been established with the pre-processed EEG.

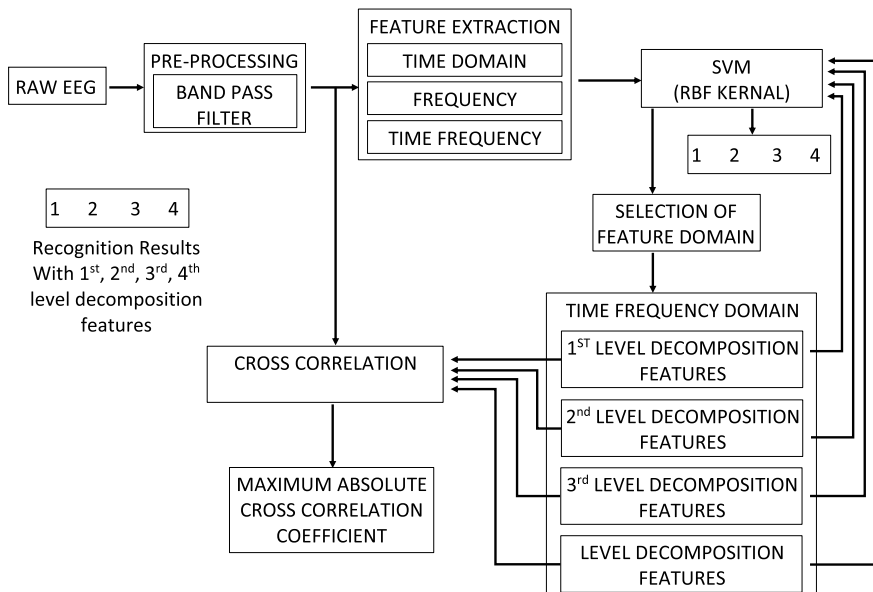


Fig. 1 Proposed methodology for EEG-based hand movement recognition

2.1 Experimental Protocol

EEG from PhysioNet of the BCI2000 Instrumentation system has been used for the experiment. The original raw EEG was acquired using 64 electrodes following 10–20 electrode placement systems [13]. This was excluding electrodes Nz, F(9-10), F_T(9-10), A(1-2), TP(9-10), and P9. Out of the 64 channels, EEG signal obtained from C3, C4, and C_Z correlates to the neural activity associated with the left- and right-hand movements [3]. Moreover, EEG channels FC3, FC_Z, FC4, C3, C1, C_Z, C2, and C4 are commonly used for the purpose of motor cortex activity [3]. Following this and the EEG acquisition presented in [8], this work considered 21 EEG electrodes, viz., FC5, FC3, FC_Z, FC2, FC4, FC6, C5, C3, C1, C_Z, C2, C4, C6, CP5, CP3, CP1, CP_Z, CP2, CP4, and CP6 for the experiment.

The experiment considered data for seven subjects. Each subject performed 14 trials: two one-minute initial trials (one with eyes open, one with eyes closed), and three two-minute trials of each of the four following tasks (Task 3–Task 6). The rest state is denoted as event T0, and the onset of motion (real or imagined) is denoted by either T1 or T2 depending on the task performed. During the task 3 and 4, event T1 denotes motion involving the left fist and T2 denotes motion involving the right fist. The tasks performed are enumerated as follows:

1. Task 1: One-minute initial task (rest state) with eyes open, (event T0).
2. Task 2: One-minute initial task (rest state) with eyes closed, (event T0).
3. Task 3: Two-minute performance of opening-closing left or right fist, according to a location of a target object presented on the computer screen and relaxation, (event T1 and event T2, respectively).
4. Task 4: Two-minute performance of imagining opening-closing left or right fist, according to a location of a target object presented on the computer screen and relaxation, (event T1 and event T2, respectively).
5. Task 5: Two-minute performance of opening and closing fists or moving both feet, accordingly to a location of a target object presented on the top or on the bottom of the computer screen and then resting, (event T1 and event T2, respectively).
6. Task 6: As above, but imaginary motion was performed, (event T1 and event T2, respectively).

Tasks 3, 4, 5, and 6 were repeated three times during the experiment which results in a total of 14 trials ($2+4\times 3$).

2.2 EEG Dataset

There were fifteen (15) segments of T0, eight (8) segments of T1, and seven (7) segments of T2. For a single person, who performed three trials of the same task, there are 45 (15×3) T0 epochs, 24 (8×3) T1 epochs, and 21 (7×3) T2 epochs. This resulted in 630 ($15 \times 21 + 8 \times 21 + 7 \times 21$) 21-channel EEG for a single trial. From

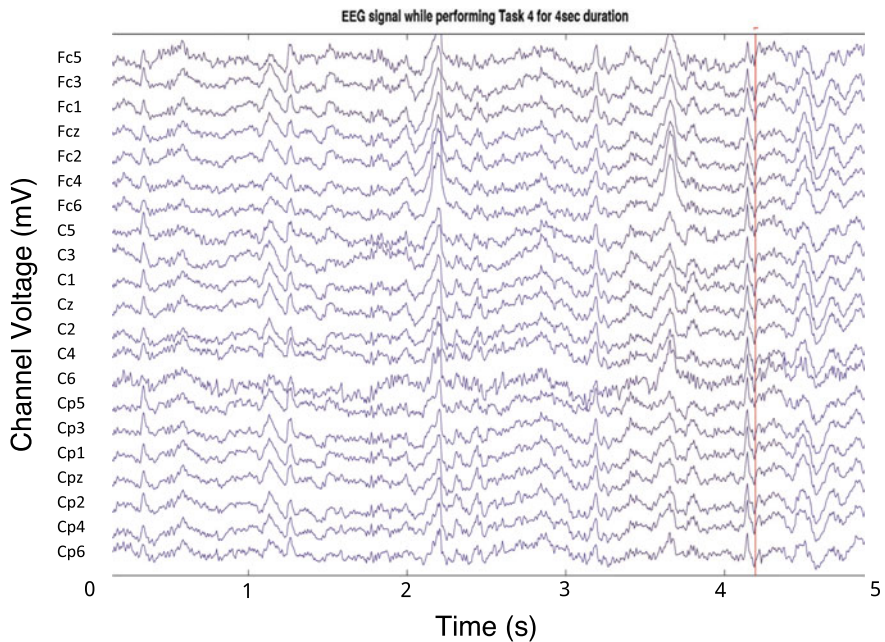


Fig. 2 EEG signal obtained from a subject for Task4

the seven subjects, the dataset of the size of (7 subjects \times 3 trials \times 630 EEG) 13230 EEG was used in the experiment. Figure 2 shows the EEG signal for 4.2 s (S) while performing Task 4 using 21 electrodes. The X-axis represents time in seconds and the Y-axis represents voltage in millivolt (mV). The red line in the figure marks the end of Task 4.

2.3 Feature Extraction

Features in time, frequency, and time-frequency domains were extracted for the recognition of the right- and left-hand fist movements. Time domain features: integrated EEG (IEEG), mean absolute value (MAV), root mean square (RMS), and simple square integral (SSI); frequency domain features: mean frequency (MNF), peak frequency (PF), modified mean frequency (MMF), mean power (MNP); time-frequency domain features: approximate coefficients of DWT using 2 Daubechies mother wavelets were used in the experiment.

2.3.1 Time Domain Feature

- IEEG: This feature was used based upon the assumption that the amplitude of EEG shifts from its baseline value during a task. This shift is different for the left fist as compared to the right fist [14]. It is estimated as

$$IEEG = \sum_{i=1}^N |x_i| \quad (1)$$

- MAV: It is related to the statistical distribution of EEG. It is assumed that statistical distribution of EEG are different during two tasks [14]. It is estimated as

$$MAV = \frac{1}{N} \sum_{i=1}^N |x_i| \quad (2)$$

- RMS: This feature is relevant to amplitude measurements. It is the square root of the average power and is estimated as

$$RMS = \sqrt{\frac{1}{N} \sum_{i=1}^N |(x_i)^2|} \quad (3)$$

- SSI: It is the summation of absolute squared value of each sample in the signal. It represents temporal characteristics of EEG, which are different for right- and left-hand fist movements [14]. It is estimated as

$$SSI = \sum_{i=1}^N |x_i|^2 \quad (4)$$

where x_i represents ith sample value of the EEG with N as the total number of EEG samples.

2.3.2 Frequency Domain Feature

- MNF: This feature gives the mean of the frequency distribution using the normalized power spectrum density. It is estimated as

$$MNF = \frac{\sum_{i=1}^M f_i P_i}{\sum_{i=1}^M P_i} \quad (5)$$

where f_i is frequency of the spectrum at frequency bin i, P_i is the EMG power spectrum at frequency bin i, and M is the length of the frequency ratio.

- PF: This feature is also called dominant frequency. As peak frequencies of different tasks are located differently [14], they can be used to differentiate EEG for right- and left-hand fist movements. It is estimated as

$$PKF = \max(P_i); i = 1, 2 \dots M \quad (6)$$

- MMF: It indicates information about the mean of the EEG spectrum. It is estimated as

$$MMF = \frac{1}{2} \sum_{i=1}^M A_i \quad (7)$$

where A_i is the EEG amplitude spectrum at frequency bin i and M is the length of the frequency bin i .

- Mean Power: This feature is used to represent the total power partition at each frequency. It is estimated as

$$MNP = \frac{\sum_{i=1}^M P_i}{M} \quad (8)$$

where P_i is the EEG power spectrum at frequency bin i , and M is the length of the frequency bin i .

2.3.3 Time-Frequency Domain Feature

DWT includes successive high- and low-pass filtering of a time series with a down-sampling rate of 2. The ability of DWT to extract features from the signal is dependent on the mother wavelet function; as such it should exhibit good localization properties in both the frequency and time domains [15]. Following [16], Daubechies mother wavelet of order 2 was used in this experiment.

DWT of a signal $x[n]$ is calculated by passing it through a series of filters [17]. The samples are passed through a low-pass filter and a high-pass filter with impulse response $g[n]$ and $h[n]$, respectively, resulting in a convolution of two as in Eq. 9 and 10.

$$y_{low}[n] = \sum_{i=-\infty}^{\infty} x[n] * g[2n - k] = cA \quad (9)$$

$$y_{high}[n] = \sum_{i=-\infty}^{\infty} x[n] * h[2n - k] = cD \quad (10)$$

The output of the high-pass filter gives the detail coefficients, (cD_i), and the output of the low-pass filter gives approximation coefficients, (cA_i). The value of i

corresponds to the level of decomposition. cA_1 is the approximate coefficients in level 1. These coefficients (cA_1) are further decomposed to obtain the next levels of coefficients.

3 Results and Discussion

3.1 Recognition of Left-Right Hand Fists

The features from each domain, i.e. time, frequency, and time-frequency domains have been experimented independently for the recognition of left and right hand fist movements. The features from each domain have been input to an RBF kernel SVM [12] following tenfold cross-validation [1]. The entire dataset is divided into 10 equal sub-sets. Of the 10 sub-sets, a single sub-set has been used for testing in SVM and the remaining 9 sub-sets have been used as training data. The cross-validation process is then repeated ten times, with each of the 10 sub-sets used once as testing data. The recognition rate (A) was estimated following Eq. 11.

$$A = \frac{\text{Total number of correctly classified movements}}{\text{Total number of movements}} \times 100 \quad (11)$$

Figure 3a–c shows the confusion matrix obtained from the RBF kernel SVM classifier using time, frequency, and time-frequency domain features averaged across seven subjects. It has been found that an average recognition rate of 90%, 92%, and 97.5% was achieved using time, frequency, and time-frequency domain features. Time-frequency domain features, having resulted in the highest recognition rates, were explored at four decomposition levels. Table 1 shows recognition rates using time-frequency domain features at four decomposition levels for each subject. It has been found that the highest recognition rate of 98.6%, averaged across seven subjects, was achieved with the time-frequency domain features at decomposition level 2. Figure 4a–c shows the recognized feature plots for time, frequency, and time-frequency domain at the output of RBF kernel SVM, respectively, for one subject.

		Actual Class		
Predicted Class		Left	Right	A (%)
	Left	3.7	0.3	92.5
	Right	0.5	3.5	87.5
Average Accuracy (%)		90		

		Actual Class		
Predicted Class		Left	Right	A (%)
	Left	3.75	0.25	93.75
	Right	0.4	3.6	90
Average Accuracy (%)		92		

		Actual Class		
Predicted Class		Left	Right	A (%)
	Left	3.8	0.2	95
	Right	0	4	100
Average Accuracy (%)		97.5		

(a) Time Domain

(b) Frequency Domain

(c) Time-Frequency Domain

Fig. 3 Confusion matrix of recognition results with (a) time, (b) frequency, and (c) time-frequency domain features

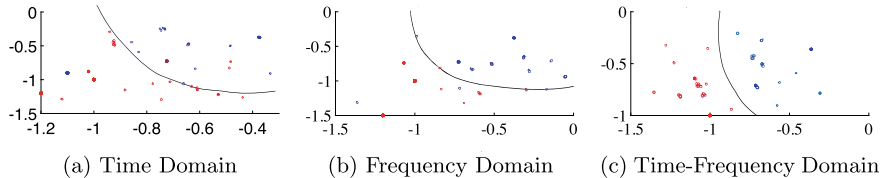


Fig. 4 Recognized feature with (a) time, (b) frequency, and (c) time-frequency domain features at the output of RBF kernel SVM

Table 1 Recognition rates at four decomposition levels

Subjects	Level 1	Level 2	Level 3	Level 4
Subject 1	98	98.2	97	96
Subject 2	98.2	99	97.6	96
Subject 3	97.8	98.4	97	96
Subject 4	96.2	98.6	96	95.2
Subject 5	94.8	98	94	93
Subject 6	94	99	92	89.2
Subject 7	94.4	99	92.8	92
Average	96.2 ± 1.8	98.6 ± 0.6	95.2 ± 3.2	94.2 ± 4

Both the X-axis and Y-axis denote the feature domain. The red coloured and blue coloured unfilled circles denote the two classes in the recognition of left and right hand movements.

3.2 Cross Correlation

The cross correlation [12] was used as a measure for evaluating similarity between feature set and corresponding EEG. Given two signals $x[m]$ and $y[m]$, the factor of similarity has been estimated as

$$r_{max} = \frac{\max(r_{xy}[n])}{\sqrt{E_x E_y}} \quad (12)$$

where n was the time shift expressed in terms of number of samples of $y[m]$ with reference $x[m]$; E_x and E_y are energies of the two signals under consideration, and

$$\max(r_{xy}[n]) = \sum_{m=-\infty}^{\infty} x^*[m]y[m+n] \text{ at maximum absolute value.} \quad (13)$$

Table 2 Cross correlation factors of time-frequency domain features and EEG

Decomposition Level	r_{max}
Level 1	$6.00 \times 10^5 \pm 0.20 \times 10^5$
Level 2	$6.42 \times 10^5 \pm 0.20 \times 10^5$
Level 3	$2.82 \times 10^5 \pm 0.40 \times 10^5$
Level 4	$2.26 \times 10^5 \pm 0.12 \times 10^5$

Table 2 shows the cross-correlation factor averaged across seven subjects for the four decomposition levels of time-frequency domain features. Time-frequency domain features at decomposition level 2 show the highest correlation with corresponding EEG. This substantiates the fact that cross correlation varies with recognition rates obtained using time-frequency domain features at four decomposition levels.

4 Conclusions

This manuscript focuses on EEG-based recognition of left and right fist movements. A methodology was proposed to identify the feature domain and level of decomposition in order to improve the recognition rate. Time, frequency, and time-frequency domain features have been used in RBF kernel SVM resulting in recognition rates 90%, 92%, and 97.5%, respectively. Time-frequency domain features, having the highest recognition rate, were further analysed at four decomposition levels. It has been found that the decomposition level 2 of time-frequency domain features shows the highest recognition rate of $98.6 \pm 0.6\%$ averaged across all the subjects and establishes the maximum correlation with the respective EEG. These experimental results suggest that the cross correlation of time-frequency domain features with EEG can be used as a benchmark for identifying the feature set for higher recognition rates.

Acknowledgements Support under project No. 1-5728870614-NPIU (TEQIP III) Collaborative Research Scheme CRS, project No. CRD/2018/000049-ASEAN-India R&D Scheme, SERB-DST, and project No. NECBH/2019-20/144 NECBH-DBT, Government of India, is acknowledged.

References

1. Phukan, N., Kakoty, N.M., Shivam, P., Gan, J.Q.: Finger Movements Recognition using Minimally Redundant Features of Wavelet Denoised EMG. *Health and Technology* **9**(4), 579–593 (2019)
2. F. Sepulveda. *Advances in Robot Navigation*, chapter Brain-actuated Control of Robot Navigation. InTech, Europe, 2011

3. A-K. Mohamed. Towards Improved EEG Interpretation in a Sensorimotor BCI for the Control of a Prosthetic or Orthotic Hand. Technical report, University of Witwatersrand, Johannesburg, 2011
4. Machado, J., Balbinot, A.: Executed Movement using EEG Signals through a Naive Bayes Classifier. *Micromachine* **5**(4), 1082–1105 (2014)
5. P. P. M. Shanir, Y. U. Khan, and E. Khan. Classification of EEG Signal for Left and Right Wrist Movements using AR Modelling. In *Proceedings of Conference on Modern Trends in Electronics and Communication Systems*, pages 65–69, Aligarh, 2008
6. Y. Wang, B. Hong, X. Gao, , and S. Gao. Implementation of a Brain- Computer Interface Based on Three States of Motor Imagery. In *IEEE International Conference on Engineering in Medicine and Biology Society*, pages 5059–5062, France, 2007
7. C. Guger, W. Harkam, C. Hertnaes, and G. Pfurtscheller. Prosthetic Control by an EEG-based Brain-Computer Interface (BCI). In *5th European Conference for the Advancement of Assistive Technology*, pages 1–6, Germany, 1999
8. M. H. Alomari, A. Samaha, and K. Al. Kamha. Automated Classification of L/R Hand Movement EEG Signals using Advanced Feature Extraction and Machine Learning. *Advanced Computer Science and Applications*, 4(6):207–212, 2013
9. Syed UmarAmin, Mansour Alsulaiman, Ghulam Muhammadand Mohamed AmineMekhtiche, and M.Shamim Hossain. Deep Learning for EEG motor imagery classification based on multi-layer CNNs feature fusion. *Future Generation Computer Systems*, 101, 2019
10. Antonio Maria Chiarelli, Pierpaolo Croce, Arcangelo Merla1, and Filippo Zappasodi. Deep learning for hybrid EEG-fNIRS brain-computer interface: application to motor imagery classification. *Journal of Neural Engineering*, 15(3):1–24, 2018
11. Kakoty, N.M., Hazarika, S.M., Gan, J.Q.: EMG Feature Set Selection Through Linear Relationship for Grasp Recognition. *Journal on Medical and Biological Engineering* **36**(6), 883–890 (2016)
12. S. W. Hilt and Sam Merat. SVM Clustering. *BMC Bioinformatics*, 8(7), 2007
13. Schalk, G., McFarland, D.J., Hinterberger, T., Birbaumer, N., Wolpaw, J.R.: BCI2000: A General-Purpose Brain-Computer Interface (BCI) System. *IEEE Transactions on Biomedical Engineering* **51**(6), 1034–1043 (2004)
14. P. Geethanjali, Y.K. Mohan, and J. Sen. Time domain Feature extraction and classification of EEG data for Brain Computer Interface . In *9th International Conference on Fuzzy Systems and Knowledge Discovery*, pages ii36–1139, Sichuan, China, 2012. IEEE
15. Lemarie, P.G., Meyer, Y.: Ondelettes et Bases Hilbertiennes. *Revista Matematica Iberoamericana* **2**(1), 1–19 (1986)
16. P. Jahankhani, V. Kodogiannis, and K. Revett. EEG Signal Classification Using Wavelet Feature Extraction and Neural Networks. In *Proceedings IEEE John Vincent Atanasoff 2006 International Symposium on Modern Computing*, 2006
17. N. M Kakoty and S. M. Hazarika. Recognition of Grasp Types Through Principal Components of DWT based EMG Features. In *IEEE International Conference on Rehabilitation Robotics*, pages 1–6, Switzerland, 2011

Burr Registration Using Image Processing



Anup Pillai , Shital Chidderwar , M. R. Rahul , and Mohsin Dalvi

1 Introduction

Machine vision, with still its vast possibilities, together with image processing, finds diverse application in the quality control, inspection, and measurement domain. Such systems can provide inline quality control. This is very important in the lean context, as inspection, though being non-value-adding from a customer's perspective, is very much essential and adds value to the organization. Manual inspection, if avoided, can give benefits in time, costs, and accuracy; also, not all products can be inspected manually. There have been studies related to the industrial applications of machine vision, particularly in the automotive, manufacturing, and pharmaceutical industries. Some applications are optical gauging, barcode reading, optical character recognition (OCR), object detection, measurement of part dimensions, sorting, checking the presence or absence of tablets in a blister pack, detecting bottle caps, and obtaining fluid levels in vials and bottles [1]. Machine vision is often considered a perfect non-contact inspection method for measuring the roundness errors on cylindrical machined parts [2].

A burr is a raised edge, a sharp protrusion, or a firmly adhered or loosely hanging projection that remains attached to a workpiece after a modification process. Burrs are most commonly created by machining operations, such as turning, grinding, drilling, milling, engraving, reaming, and by press working operations. A deburring tool is often used to remove these undesirable pieces of material by a process known as 'deburring'. Deburring is critical to quality in parts where a high level of quality is desired. Although deburring is a non-value-adding process, it is impossible to eliminate burr completely in a process and produce burr-free parts. A study estimated that the economic impact of burrs to be around 9% of the manufacturing costs due to increased manpower, extended cycle times, rejection rate, and machine breakdown

A. Pillai · S. Chidderwar · M. R. Rahul · M. Dalvi
Visvesvaraya National Institute of Technology, Nagpur 440010, India

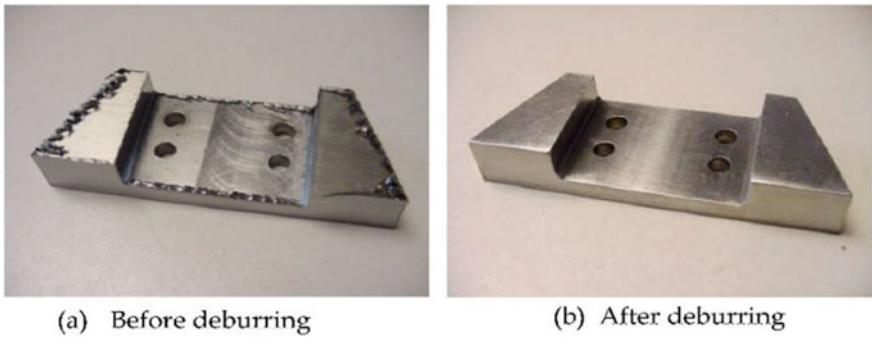


Fig. 1 A metallic component before and after deburring

[3] (Fig. 1). Machine vision systems have been developed for automatic burr and peripheral defect detection in castings [4]. For automatic deburring operations, burred images are segmented, edges are identified, coordinate data of the workpiece edges are extracted from the image, and comparison with standard part coordinates is done to obtain the burr geometry [5].

In the placement of vision sensors, view-cone, i.e. a generalized cone that bounds the directions from a viewpoint along which there is an unobstructed view of the face, plays a major role as it defines the visibility of a given object face. The locus of such potential viewpoints forms the viewsphere, of which the optimal number of viewpoints are selected to adequately image the region of interest in the object [6]. A thermographic method based on infrared image rectification has been used to characterize crack geometry in weldments [10]. Infrared Thermography (IRT) has been widely used for detecting defects in concrete structures [11]. Photogrammetric techniques have been used to monitor cracks in infrastructure using reflective targets [12]. CCD and CMOS camera-based setups are often used to detect internal surface defects caused due to wear, rust, erosion, and corrosive pitting in gun barrels and the inspection of machine surfaces of critical components for their finishing [7, 8]. On burr registration, a trajectory can be generated for robotic deburring [9].

2 Vision System Design

The basic design of the image acquisition setup is similar to a baggage scanner system where a box frame isolates the image acquisition environment from its surroundings. A semi-circular slotted spinning ring is connected via a shaft connector and a rigid coupling to a stepper motor. Two CMOS cameras are held in position inside the spinning ring slot with the help of adjustable camera mounts. The cameras and the motor are connected to the Arduino microcontroller board using appropriate accessories. LEDs mounted on the inside of the spinning ring provide adequate

illumination for imaging. The system can also be easily connected in-line with a belt conveyor and object detecting sensor.

Figure 2 explains the simple working of the image acquisition setup. The spinning ring rotates a complete 360° in pre-defined angular intervals and takes images of the object from all sides using both cameras. The position of the cameras along the slot as well as the number of intervals can be altered accordingly.

The spinning ring is polygonized for ease of manufacturing and assembly. The parts are laser-cut from medium-density fibreboard (MDF) sheets and are then glued together using strong adhesives. The adjustable camera mounts are also fabricated similarly. The box frame is made from $3/8''$ steel pipes. All the components are put together and the image acquisition setup is assembled as in Fig. 3.

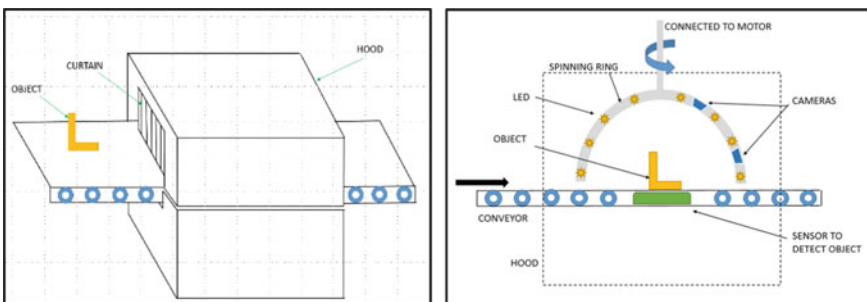


Fig. 2 Basic design of image acquisition setup



Fig. 3 Image acquisition setup

3 Image Acquisition

The key to efficient image acquisition using this developed setup lies in expeditiously controlling the cameras during image capture and the stepper motor. The Arduino forms the anchor of the system, reading inputs and controlling outputs using its extensible and easy-to-use programming interface, known as Arduino Integrated Development Environment (IDE).

Figure 4 vividly depicts the interrelation between the electronic components using USB cables and jumper wires. The connections between the components are first individually established and verified, and later synchronously operated.

Low-cost OV7670 CMOS cameras are utilized for image acquisition. The data and clock lines of the I2C communication bus and the external clock line are appropriately applied pull-up resistances. The pin mapping table of the Arduino MEGA 2560 was used in determining suitable pins for connection to both the OV7670 cameras. Special JAVA files are run from the command-line interface and used to read the data received at the port of the system from the Arduino and save the images from the cameras alternatively in BMP format. For synchronous operation, an I2C multiplexer is used to overcome the I2C address conflict of the cameras.

A bipolar stepper motor with a 1.8° step angle is interfaced with the L298N motor driver and the Arduino to control both the speed and spinning direction. An external 12 V supply runs the motor, while the internal 5 V logic of the L298N is powered by the Arduino. The camera position is set at 30° and 60° , focusing on the spinning ring center to capture images.

The Arduino is connected to a computer system, which powers it and runs commands on the command-line interface to start acquisition and storing of images. The acquired images are then saved in separate folders for further processing.

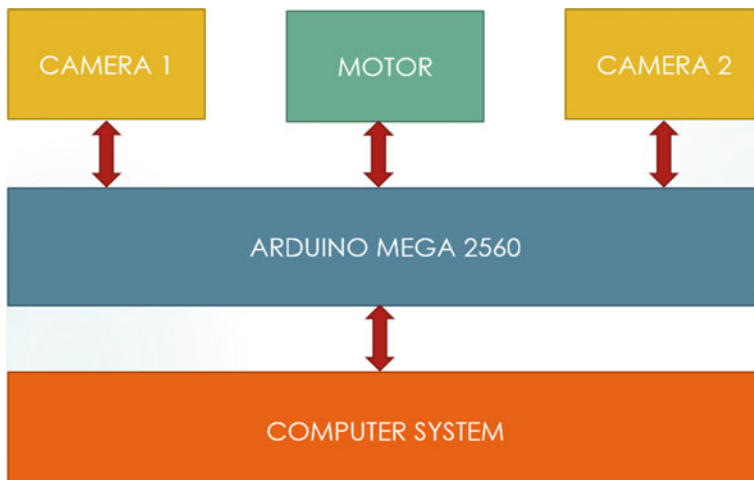


Fig. 4 Basic electronic setup

4 Photogrammetry

In simple terms, photogrammetry is the technique of measuring or interpreting objects from photographs. Though there are many categories for classification, photogrammetry is broadly classified into metric photogrammetry and interpretative photogrammetry. The former deals with obtaining metric data from photos or other similar sources to gauge the relative locations of points in the object whereas the latter deals primarily in evaluating and assessing objects, and judging their relevance through careful and systematic analysis such as in remote sensing applications. Another important classification based on camera orientation is aerial photogrammetry with images taken from satellites, aircraft or drones and terrestrial or close-range photogrammetry with images taken from cameras. Close-range photogrammetry using multiple photographs, also known as stereophotogrammetry, along with sensor parameters can yield 3D measurements. Photogrammetry is widely used in the areas of archeological documentation, 3D face construction, crime scene recreation, surveying technique in the fields of geomorphology, oceanography, hydrology and water resources, military intelligence, and other inspection-based industrial applications [13].

5 Burr Identification Process

The photogrammetry-based burr detection approach involves taking multiple images of the object using the already built image acquisition setup. The setup enables the images to be taken at intervals with proper lighting conditions. These images are then loaded in a photogrammetric software that enables point cloud generation, generating mesh and 3D reconstruction along with many other pre-processing and post-processing tools. The 3D reconstruction phase starts with the images acquired from the setup imported into the software. The software has a specially designed auto-calibration feature to perform calibration from the loaded images; manual calibration of images is also possible. An auto-accuracy evaluation feature then shows the images that may have to be excluded for reconstruction purpose based on mean reprojection error and the number of points whose position has been detected. These are then used to generate a sparse point cloud reconstruction from the images using optical triangulation techniques such as bundle adjustment [14]. Based on this as an input, a dense point cloud is then created. The bounding box feature defines a control volume that enables to remove any outliers and restrict the reconstruction to specifically the object, eliminating the background with the help of a smart reset tool. This is then followed by generating a watertight mesh using a photoconsistency-based optimization technique. A multi-textured mesh is then created, which can be saved as a .obj file.

To identify the burrs, this is then compared to the CAD model of the master burr-free part in an inspection software that can perform 3D inspection and mesh

processing for dimensional analysis of 3D point clouds. This is achieved by first importing these files in the software. An auto-alignment procedure then aligns them together; manual alignment is also possible. The surface comparison feature helps in displaying burrs along with size visually in the form of a color scale.

6 Results

A sample object with different types of burr [15], viz., corner burrs (A), tear burr (B), small edge burrs [(C) and (D)], long edge burr (E), and rollover burr (F) is prepared as in Fig. 5.

The images acquired from the setup are then loaded into the photogrammetric software and processed further.

The result of sparse reconstruction is shown in Fig. 6a. This is then followed by the dense reconstruction point cloud as in Fig. 6b. The bounding box is then defined and the background subtraction is done using the smart reset tool in the bounding box feature. Mesh is then generated for the newly defined control volume as shown in Fig. 6c. Further, an enhanced multi-textured mesh is created using photoconsistency-based optimization as in Fig. 6d. This mesh is then exported and saved as a .obj file and is used as an input to the inspection software.

The inspection is based on a surface comparison of the mesh against the CAD model. Both the obj file and the CAD model are loaded in the inspection software. An auto-alignment feature helps to align the two entities that need comparison as in

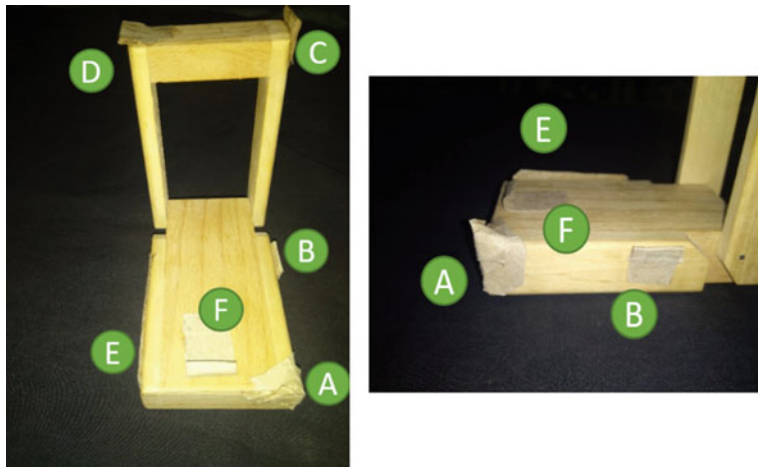


Fig. 5 Sample burr part

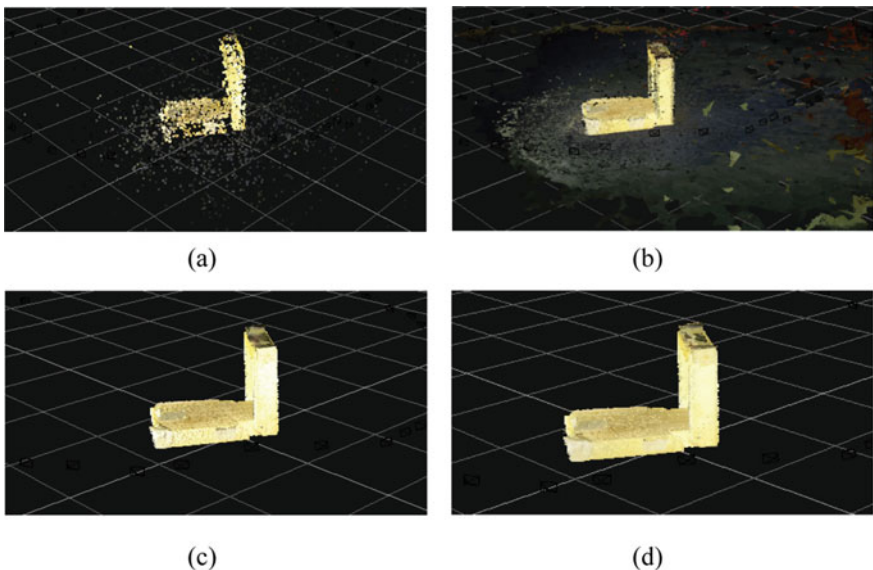


Fig. 6 Mesh generation from images

Fig. 7b. A surface comparison is then done which shows the burrs and their sizes as in Fig. 8. Also, deviation labels can be used to display the burr sizes at specific points.

As evident from the results obtained, the burrs have been identified and their sizes measured. Additionally, to account for small errors in mesh extraction and geometrical deviations or errors in the CAD model, the measurement scale is redefined by

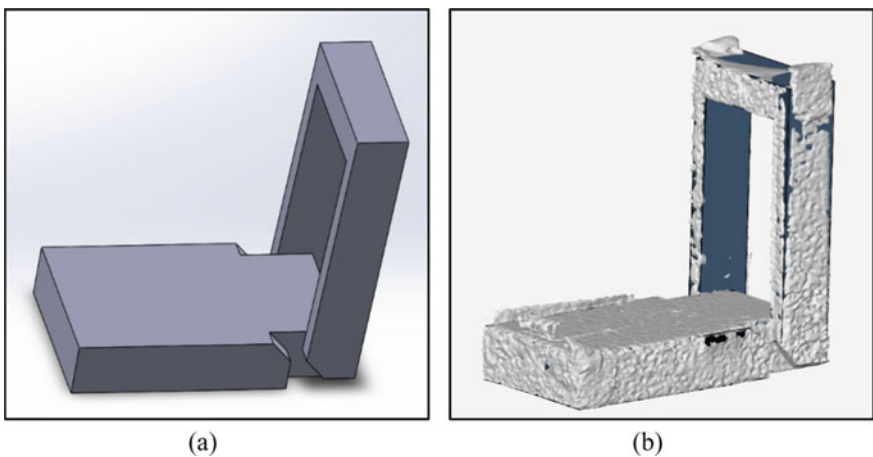


Fig. 7 CAD model and its alignment with the generated mesh

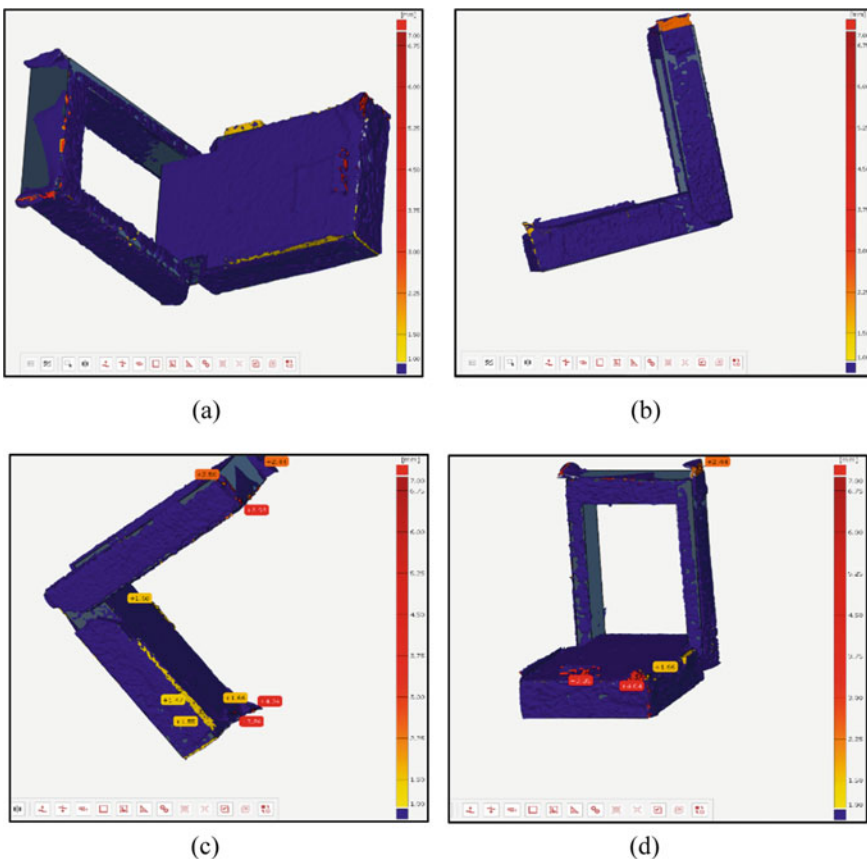


Fig. 8 Results of surface comparison

setting a minimum value of 1 mm. Thus, burr larger than 1 mm can be accurately identified. The acceptable tolerance levels can also be accounted for, by defining them in the software before comparison. Maximum burr size can be determined by using maximum deviation labels feature as in Fig. 9.

These maximum values obtained from the software are compared with actual sizes of burrs. The results of this accuracy analysis are shown in Table 1.

7 Conclusion

This paper presents a novel method of image acquisition and processing system, to identify burrs with a high degree of accuracy and without the use of highly sophisticated data processing and vision sensing techniques. The use of CMOS cameras attached to a spinning ring enables the capturing of maximum edges of an object to

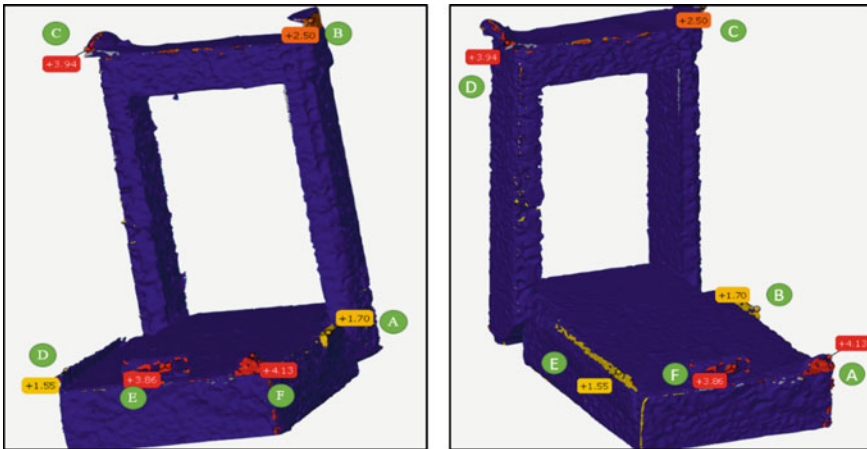


Fig. 9 Maximum deviation

Table 1 Accuracy analysis

	Maximum burr size (in mm)					
	A	B	C	D	E	F
Inspection software	4.13	1.70	3.86	1.55	3.94	2.50
Actually measured	4.25	1.75	4.00	1.75	4.00	2.75
Percentage accuracy	97.18	97.14	96.50	88.57	98.50	90.91

identify the burrs present in them through photogrammetry-based image processing techniques. Besides, the setup is capable of processing any irregular geometry of a size range as compared to a fixed size object that is usually done with the help of a turntable. The number of images that needs to be captured for an object can be altered by changing the number of steps that the motor rotates between image capture. The camera angles can also be modified accordingly to an object. Thus, the system is ideal in dealing with batch production lines wherein such changes are not that frequent but just enough for such a system to exist that meets this purpose. Also, the system can be used in line with the already existing production systems by proper line balancing. A major limitation of the system is the high computation power required for processing. The quality and speed of output from photogrammetry is dependent on the computation abilities of the system.

The research work can be extended in the following ways:

- Based on the burr data, close curve fitting can be done and a trajectory can be generated for a deburring tool to perform vision-assisted robotic deburring.
- The system also doubles as an optical gauging system for measurement and inspection purposes.

- The system with appropriate modifications can be tuned as an Automatic Quality Inspection System to identify and remove any form of defects from production lines. In addition, the performance of the manufacturing process can be evaluated by statistical analysis of multiple such parts produced.
- This system is not restricted to inspection but can be applied to any process that requires identification through images, such as barcode reading and OCR in assembly lines to select correct components.

References

1. Sathiyamoorthy, S.: Industrial application of machine vision. *Int. J. Res. Eng. Technol.* **3**(7), 678–682 (2014)
2. Ayub, M.A., Mohamed, A.B., Esa, A.H.: In-line inspection of roundness using machine vision. *Procedia Technol.* **15**, 807–816 (2014)
3. Aurich, J.C., Dornfeld, D., Arrazola, P.J., Franke, V., Leitz, L., Min, S.: Burrs-analysis, control and removal. *CIRP Ann.-Manuf. Technol.* **58**(2), 519–542 (2009)
4. Tsai, D.M.: Use machine vision to detect burrs and defects of castings. *Machine Vision Lab* (1991)
5. Leo Princely, F., Selvaraj, T.: Vision assisted robotic deburring of edge burrs in cast parts. *Procedia Eng.* **97**, 1906–1914 (2014)
6. Roberts, D.R., Marshall, A.D.: Viewpoint selection for complete surface coverage of three dimensional objects. In: *British Machine Vision Conference*, pp. 74.1–74.11 (2013)
7. Shanmugamani, R., Sadique, M., Ramamoorthy, B.: Detection and classification of surface defects of gun barrels using computer vision and machine learning. *Measurement: J. Int. Meas. Confed.* **60**, 222–230 (2015)
8. Manish, R., Venkatesh, A., Denis Ashok, S.: Machine vision based image processing techniques for surface finish and defect inspection in a grinding process. *Mater. Today: Proc.* **5**(5), 12792–12802 (2018)
9. Rahul, M.R., Bhute, R.Y., Chiddarwar, S.S., Dalvi, M., Sahoo, S.R.: Burr registration and trajectory planning of 3D workpiece using computer vision. In: *Advances in Mechanical Engineering. Lecture Notes in Mechanical Engineering*. Springer, Singapore (2021)
10. Rodríguez-Martín, M., Lagüela, S., González-Aguilera, D., Martínez, J.: Thermographic test for the geometric characterization of cracks in welding using IR image rectification. *Autom. Constr.* **61**, 58–65 (2016)
11. Sirca, G., Adeli, H.: Infrared thermography for detecting defects in concrete structures. *J. Civ. Eng. Manag.* **24**, 508–515 (2018)
12. Nishiyama, S., Minakata, N., Kikuchi, T., Yano, T.: Improved digital photogrammetry technique for crack monitoring. *Adv. Eng. Inform.* **29**(4), 851–858 (2015)
13. Wolf, P.R., DeWitt, B.A., Wilkinsion, B.E.: *Elements of Photogrammetry with Applications in GIS*, 4th edn. McGraw-Hill Higher Education, New Delhi (2000)
14. 3DF Zephyr tutorials, <https://www.3dflow.net/technology/documents/3df-zephyr-tutorials>. Accessed 31 May 2020
15. Gillespie, L.K.: *Deburring and Edge Finishing Handbook*. Society of Manufacturing Engineers, USA (1999)

LoRa-Based Infrastructure for Medical IoT System



P. Muthu Subramanian and A. Rajeswari

1 Introduction

The development of fitness and electronic health services is robustly connected to the concept of Internet of Things, so as to say the interconnection of countless devices, sharing heterogeneous information on the surroundings or the substance with which you are involved in an intelligent way. The IoT paradigm aims to link billions of heterogeneous devices with various features and potential troubles in the Internet and applications [1, 2]. The progress of interconnecting sources [3] is very demanding and has to address the questions of interoperability: devices and other services, the design of the communication that convenes energy-efficiency requirements [4], security, integrity and coverage of data.

In the stipulations of interoperability, the development of services and applications can be accelerated by means of middleware to support the integration of various user equipment and various computing and communication devices [3]. At anytime and anywhere, unattended communication must be possible between the huge number of devices and connected services [1, 3]. In terms of power consumption, the communications technologies adopted will be highly efficient, especially in places where the equipment is not simply reachable or where the power resources are restricted. The Internet of Things space includes wireless communication units, which are also significantly limited by low energy consumption, due to the need for a multi-year lifetime of the devices [5]. In order to work independently, IoT and medical IoT platforms generally and in particular should have intelligence; that is to say, they should understand and be aware; they should learn, plan, decide and take action. All of the current health IoT solutions are related to Wi-Fi, VSAT or cellular devices [6], which, with respect to energy consumption or range, are not efficient. In the

P. M. Subramanian (✉) · A. Rajeswari

Department of Electronics and Communication Engineering, Coimbatore Institute of Technology, Coimbatore, India

majority of cases, the computing job is also performed lying on the back-end servers and therefore the system latency, which has to function in serious and non-critical applications. Another important issue is the coverage of the existing networks that cannot be reached in difficult areas.

In this paper, we propose a health IoT solution to deal with the hospital scenario. Thus, the network layer is connected with LoRa, and the analysis and processing information is referred to as Edge Computing Paradigm in classifying to remove surplus or inappropriate data as close as possible. The paper also highlights the problems in connectivity in current medical applications and, finally, proposes a communication solution for medical IoT which enhances medical and eHealth sectors.

2 Medical Internet of Things (MIoT)

Medical IoT is the link between the IoT and health applications and a key element of eHealth and eCare. It enables medical devices and sensors to be connected to hospital servers with increased data rates. In addition, it can transmit and exchange medical data worldwide. Now in hospitals or ambulatory services, a paper contains a medical history, and every clinician who reviews the patient has to absolute it according to the outcome of the trial. This paper is a multi-specialist investigational requirement (e.g. cardiology examination and neurological tests). After the investigation, the doctor will receive the document and add the medical data. Furthermore, health devices are somewhat or not linked to a home network, and there is no exchange of medical results between doctors. The present medical platforms are also limited to the level of the hospital. In addition, the networks are dependent and no alternative solution is available. But MIoT must continue reliable patient monitoring based on a scalable platform for the collection, transmission, analysis and processing of a multi-layer system. Medical IoT not only refers to emergencies, however. System, alerts the ambulance and other services as well as to rehabilitation, routine monitoring, prevention and faster diagnosis and treatment (especially for severe conditions). MIoT can also boost patient motivation and comfort and reduce hospital time. There are currently several described IoT medical architectures. In [6], the MIoT architecture includes RTU gates which transmit the medical data via the VSAT communications, the WLAN connectivity or GSM/GPRS to a large data framework. Unfortunately, even if this is not indicated, these technologies consume many resources. Big Data Analytics offers data display and reporting and a better monitoring center, predictive models and the basis of rule engines.

3 LoRa in Medical Internet of Things

LoRa Alliance was mainly intended to develop a technology for smart city and other related applications, but the LoRa and LoRaWAN protocol features disclose far above the ground possible for other processes, including telemedicine or surveillance of the disabled [7]. LoRa and LoRaWAN technology are able to provide physicians, pharmacists, nurses and other stakeholders with very important information. The LoRa and LoRaWAN practice and devices can therefore hold up supervisory, diagnostic systems and additional medical fundamentals. In addition to the aforesaid costs, the entire cost of a health IoT system would be considerably lower compared to other technologies. Other advantages may be the option of interconnections with further smart uses, time savings for medical procedures, self-sufficiency for chronic patients requiring regular physician visits, etc.

4 Proposed Architecture

Figure 1, describes the existing hospital infrastructure, respectively. The example in Fig. 1, as we stated previously, is currently the best existing architecture. Many

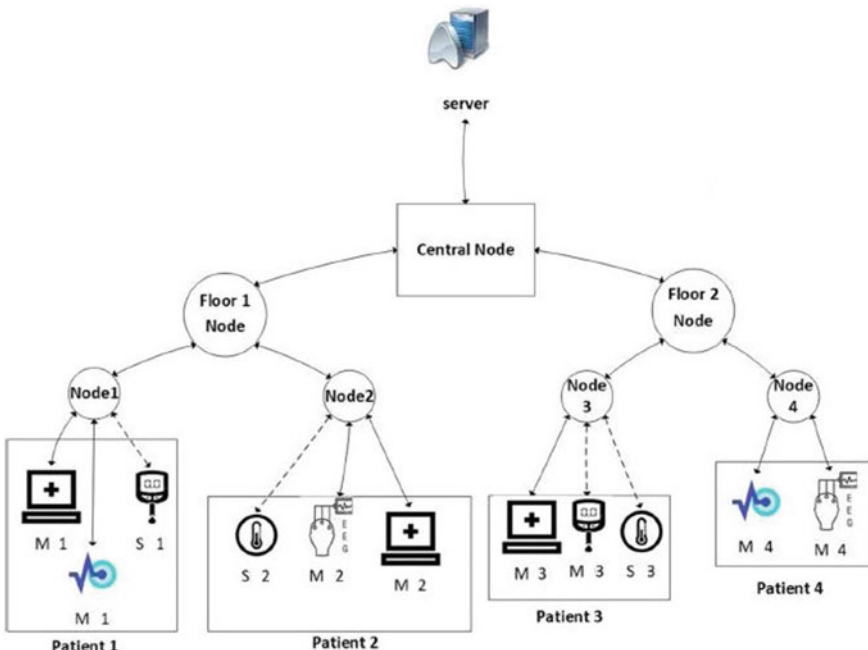


Fig. 1 Wi-Fi based infrastructure

hospitals don't include health devices or applications connected to each other. Health devices are often not wirelessly linked but are wired. Wireless points for the transmission of information from sensors or devices to a server are also not used. A monitoring node is built up for each patient. The patients are attached to the nodes of the same floor, and other nodes are subordinated to each other to a node which is a central unit. The information collected from the central sensor node is forwarded to the server. As it is observed, there is no transitional diagnosis of data.

5 Proposed Architecture of Medical IoT

For medical use cases, a related architecture may be suggested (Fig. 2). The same LoRa node can be accessed to more patients, and the porch or portals used have to cover up the whole region of a hospital. If the LoRa gateway is optimally placed, the units of LoRa gates will be significantly brought down.

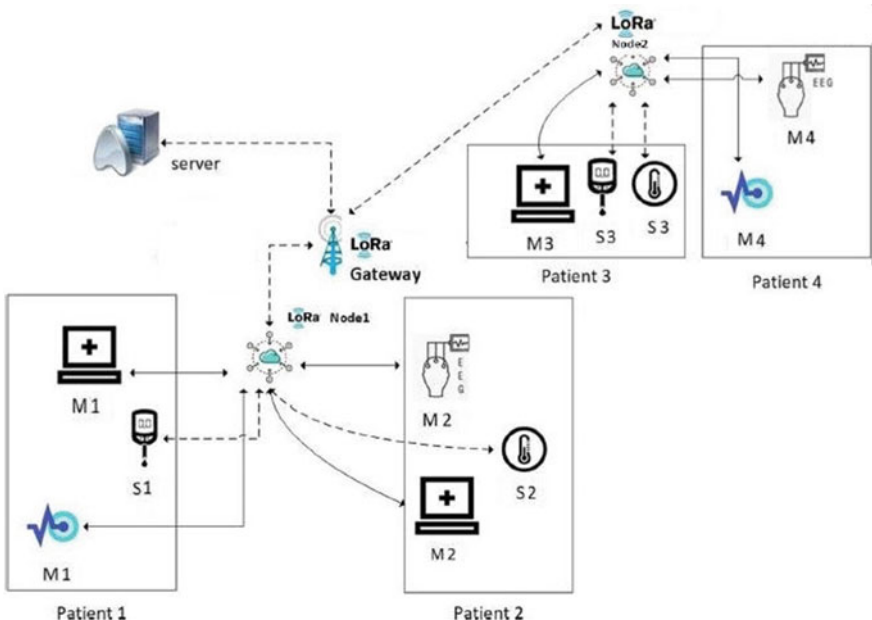


Fig. 2 LoRa-based infrastructure

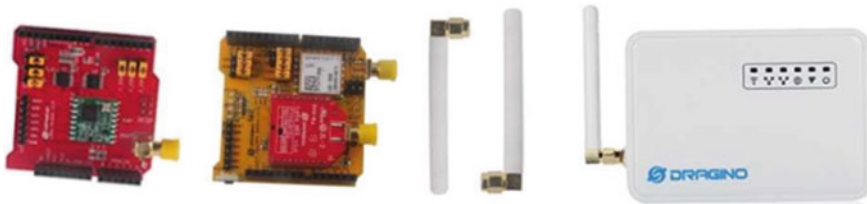


Fig. 3 Hardware—LoRa shield with antenna

6 Hardware Units of the Proposed System

- Dragino LoRa gateway—868 MHz (Fig. 3)
- LoRa Shield + UNO
- LoRa/GPS Shield + UNO Board
- Sensors

7 Proposed Architecture of Medical IoT

Figures 4 and 5 show the experimental setup with a 4.7 cm antenna at the frequency 868 MHz which was used for the hospital installation. The Spread Factor selected was 12, but normally it would be best for a lower distance and higher data rate to be achieved. The communication range of the hospital base and the terminal equipment found at Coimbatore Institute of Technology shall be described in conjunction with the temperature sensor values returned. The distance from the hospital to Coimbatore Institute of Technology is 217 m, and the configuration proposed is



Fig. 4 Real-time infrastructure

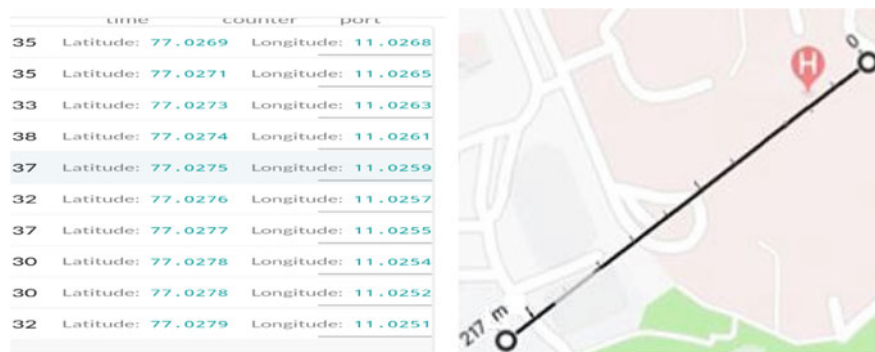


Fig. 5 Temperature sensor and Geo test results

successfully covered. The value was also validated for temperature. The proposed system is focused on observing the data in the THINGS NETWORK; once the data is received, it can be converted into the required mobile app or web service front ends. The proposed technology is mainly to say how LoRa is efficient in transferring data than using general IoT solutions like Bluetooth and Wi-Fi, also the system doesn't concentrate much about the sensor readings.

8 Conclusion

In the course of this paper, we suggested a solution to the Internet communications of medical systems consisting of hospital architectures. Architecture is based on LoRa technology. It would be very expensive and cumbersome to substitute for the modern health devices that broadcast via Bluetooth, Wi-Fi, etc. The present work therefore proposes the use of both earlier technologies and LoRa.

Reference

1. Hussain, F.: Internet of everything. *Internet of Things. Briefs in Electrical and Computer Engineering*, Springer, Cham (2017)
2. Marais, J.M., Malekian, R., Abu-Mahfouz A.M.: LoRa and LoRaWAN Testbeds: A Review, vol. 8, pp. 1496–1501. IEEE, AFRICON, Cape Town (2017)
3. Rghioui, A. et al.: Internet of things for measuring human activities in ambient assisted living and e-health. *Netw. Protoc. Alg. J.* 15–28 (2016)
4. Mahmoud, M., Mohamad, A.: A study of efficient power consumption wireless communication techniques/modules for internet of things (IoT) applications. *Advances in Internet of Things*, vol. 6, pp. 19–29 (2016)
5. Mekki, K., Bajic, E., Chaxel, F., Meyer F.: Overview of cellular LPWAN technologies for IoT deployment: Sigfox, LoRaWAN, and NB-IoT. In: *IEEE International Conference on Pervasive Computing and Communications Workshops (PerCom Workshops)*, pp. 197–202, Athens (2018)

6. Khanna, A., Misra, P.: Internet of things-success stories. In: Cousin, P. (ed.) (2019). https://www.smartaction.eu/fileadmin/smartaction/publications/IoT_Success_Stories_2. Retrieved 07 May 2019
7. Wang, Y.-E. et al.: A primer on 3GPP narrowband internet of things. *IEEE Commun. Mag.* **55**(3), 117–123 (2017)

A Robust Image Analysis Method for Cutting Tool Wear Monitoring in High-Speed Micromilling Process



Aman Sharma, Vaibhav Rathore, Brajesh Panigrahi, and Kundan K. Singh

1 Introduction

The micro-machining process allows the manufacturing of miniaturized parts, and functional surfaces can be machined with high precision [1]. All across the industries like aerospace, automobile, pharmaceutical, electrical, military, and microelectronic packaging sectors, demand for miniaturized products with high aspect ratio and superior surfaces has been growing rapidly [2]. The major advantage of this process is its ability to create complex shapes, while simultaneously ensuring better surface finish and high material removal rate. The primary requirement for high-speed micromachining is doing the machining in a stable zone to prevent chatter [3]. However, it has some disadvantages also, like the limited stiffness of cutting tools and gradual deflection in them, leading to rise in tool wear and their catastrophic failure. Tool wear of cutting tool is often used as the measure of tool life because it determines the diametric accuracy of the machining, its stability, and durability [4]. Hence, it becomes crucial to measure tool wear for predicting a cutting tool's life. The prediction of tool wear can be useful in monitoring and researching the effects on the efficiency of the machined workpieces and the manufacturing process's economy. Presently, many studies measure tool wear with the signals coming from various types of sensors such as machined workpiece's surface texture, acoustics, vibration, feeding forces, and current consumption [5, 6]. The prediction model of tool wear is then prepared based on the magnitude of the collected signals. The tool wear parameters have a substantial impact on the development of quality workpiece surface and also provide

A. Sharma · V. Rathore · B. Panigrahi · K. K. Singh (✉)

Department of Mechanical Engineering, Birla Institute of Technology and Science-Pilani,
Hyderabad Campus, Hyderabad 500078, Telangana, India

e-mail: ksingh@hyderabad.bits-pilani.ac.in

B. Panigrahi

e-mail: brajesh@hyderabad.bits-pilani.ac.in

an economic advantage[5, 6]. The image processing technique has been discussed in this study. It has diverse applications in the field of Machine/Computer Vision, remote sensing, image sharpening and blurring, and pattern recognition. In a machine vision system, digital image processing algorithms and light source arrangement are very important factors for high precision tool wear analysis [7]. Detailed analysis after the monitoring of tool condition shows that this a machine vision system can be beneficial for direct measurement of various forms of tool wear in real time. Some statistical approaches are also useful for predicting the wear of devices in competition with the machine vision system and can be used to verify the accuracy of the result of the machine vision system. The cutting tool images can be taken at different instances and the surface tool wear may be identified based upon the spectral analysis of images using the computer vision technique [8]. The analysis may be done in the frequency domain. To get the magnitude of spectrum for an image, transformations such as Fast Fourier transformation have to be used for obtaining the centered spectrum. Similarly, the Inverse Fourier transformation can be used to decentralize an image. A technique of contour mapping has been employed in the present work to monitor the cutting edge wear. When the image processing algorithm and pixel calibration of the image get completed, this superimposed image generates a contour map of the given input image to the contour map of the new cutting tool's image. As the new cutting tool's image provides the base value for original tool dimensions, this superimposed image can then be utilized to measure the change in tool wear parameters such as tool wear area, wear perimeter, and average wear width. Finally, some thresholds can be set on tool wear parameters, such as defining the amount of tool wear area which the tool can sustain, which in turn can help in predicting the time a tool has before it breaks off (tool life).

2 Literature Review

The lighting condition affects the edge detection for accurately identifying the cutting insert edge. Lim and Ratnam [9] used the flatbed scanned with internal lighting to identify the cutting insert edge and proposed an algorithm to detect the edge of the insert and finally detected the nose radius of the insert. The digital image processing has been carried out to identify the wear for the broaching tool [10]. An approach like image cropping was used to measure broaching tool wear volume to measure the progress of wear. The critical cutting tool wear has been identified based on the flank wear, and hence Castejon et al. [11] carried out the image analysis of cutting insert to identify the flank wear. The Fowlkes–Mallowsn index was used to identify the different wear levels. The cutting tool surface texture analysis can also be a good indicator for cutting tool wear as analyzed by Dutta et al. [12]. The flank wear was identified based on the cutting tool texture feature in the milling process. The micro-end mill used in micromilling has a low diameter and hence is more susceptible to wear and breakage [13]. The micro-end mill wear analysis requires the more accurate identification of cutting tool edge. The monitoring of the edge radius of the micro-end

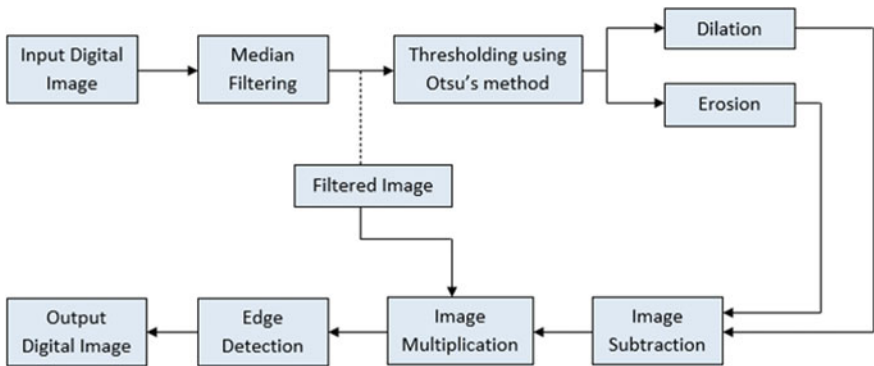


Fig. 1 Edge detection steps used in the present work

mill is of utmost importance to identify the wear progress. Dai and Zhu [7] proposed an automated machine vision system to identify the cutting tool wear during the micromilling process. The use of three-dimensional motion platform enables the synchronization of the vision system with the cutting tool for in-situ cutting tool monitoring. The flank wear measurement was measured by performing the image analysis on the captured image.

3 Methodology

The cutting tool image has been captured using a microscope after machining. The captured image has been analyzed. Edge detection is an important step to identify the edge radius of the micro-end mill. The edge radius for the micro-end mill lies in the micron range, and the steps outlined in Fig. 1 have been used for edge detection. The first step is to convert the image in RGV format and filtering was carried out to remove the shadow in the image. After filtering, thresholding was done using the Otsu method to highlight the cutting edge portion, and the process was followed by dilation and erosion. Finally, the edge was detected by multiplying the filtered image with the image subtracted by output from the dilation and erosion of the image obtained by thresholding.

4 Experiment

The experiment has been carried out on the developed high-speed micromachining center at IITB. The high-speed micromachining center has a high-speed spindle with a maximum rpm of 140000 and maximum allowable torque 4.3 N-cm.

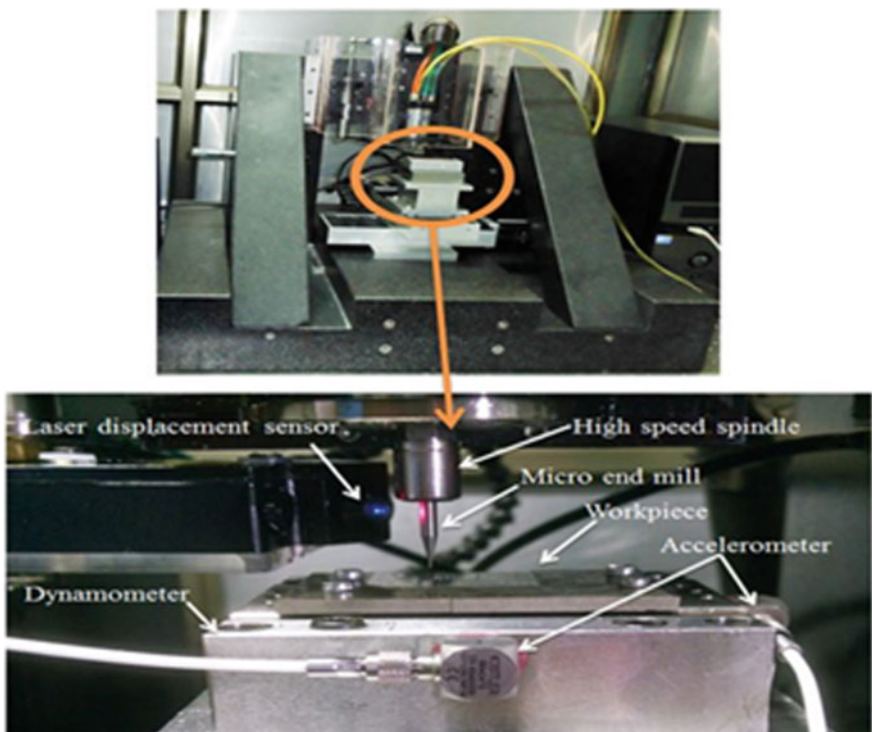
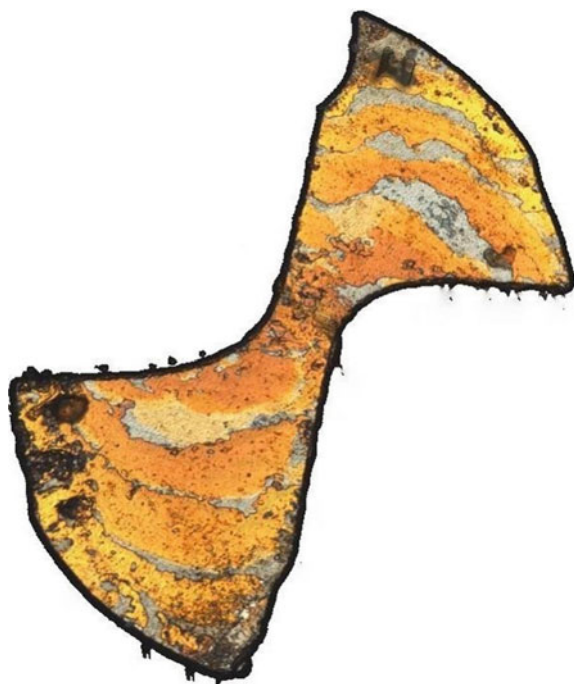


Fig. 2 Experimental setup

The Z-axis has the pneumatically controlled counterbalance stages. The micromachining center has X- and Y-stages with a ball screw driven by a DC brushless motor. The Z-axis has a positioning resolution of 5 nm. There is a positioning resolution of $0.5 \mu\text{m}$ and accuracy of $\pm 1 \mu\text{m}$, respectively, for X- and Y-stages. All the stages are fixed on granite structures and the developed micromachining center is placed on the vibration isolation table. The experimental setup is shown in Fig. 2. The experiment has been carried out on Ti6Al4V. The machining has been carried out with two fluted micro-end mills of diameter $400 \mu\text{m}$. The experiments were conducted for two different micro-end mills; one micro-end mill is coated with TiAlN and the second micro-end mill is coated with TiAlNSiN. The experiments were carried out at a speed of 50000 rpm, $50 \mu\text{m}$, and $4 \mu\text{m}/\text{flute feed}$.

Fig. 3 Captured image after machining



5 Results and Discussion

The image has been captured after the machining and is shown in Fig. 3 for a micro-end mill coated with TiAlN. The captured image has been analyzed to observe all the intensities present against each pixel. The image obtained after performing the thresholding using otsu's method for the filtered image is shown in Fig. 4a.

The boundary of the micro-end mill image has been identified for edge detection of the micro-end mill. The identified edge of the micro-end mill is shown in Fig. 4b. The micro-end mill wear has been identified by analyzing the edge radius of both micro-end mills of different coatings. The edge identification requires the micro-end edge boundary to be detected accurately. The edge detection of the micro-end mill has been done by separating the edge of the micro-end mill (Fig. 5).

The edge radius of the micro-end mill has been obtained by fitting a circle on the detected edge (Fig. 5). The change in shape and the edge in the micro-end mill are identified for the micro-end mill of two different coatings. The micro-end mill with a coating of TiAlSiN has an edge radius of $4.7 \mu\text{m}$ compared to an edge radius of $3.13 \mu\text{m}$ with a coating of TiAlN (Fig. 6). The increase in wear of the micro-end mill with coating TiAlSiN shows the coating TiAlSiN is able to decrease the temperature during the machining. However, the micro-end mill with a coating of TiAlN is able to dissipate more heat compared to the coating of TiAlSiN and hence the micro-end mill with a coating of TiAlN is less susceptible to wear during the machining.

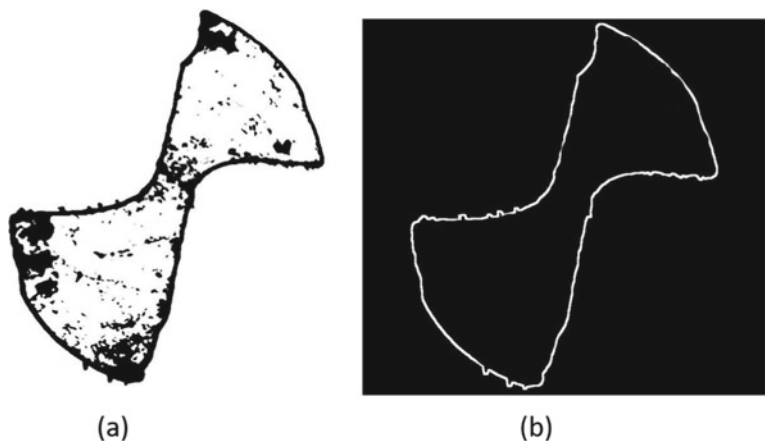
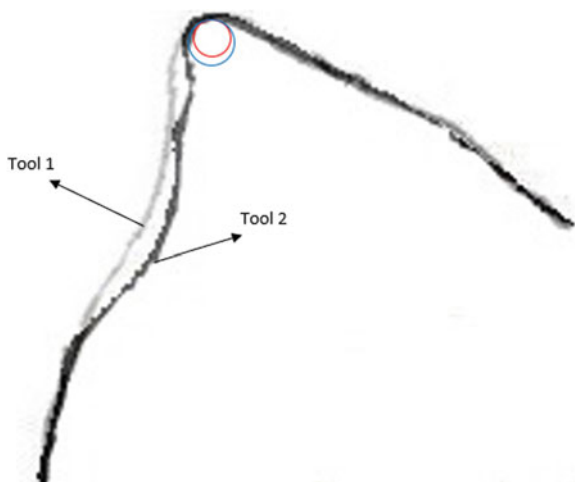


Fig. 4 Edge detection **a** Image after thresholding; **b** detected edge

Fig. 5 Fitted circle for edge radius



6 Conclusions

The present research work analyzes the image processing method to identify the cutting tool wear for the high-speed micromachining process. The different steps for the accurate identification of the edge of the micro-end mill have been identified for accurate detection of micro-end mill wear. The following conclusions can be made from the present work:

- The filtering followed by thresholding is required to identify the edge of the micro-end mill.

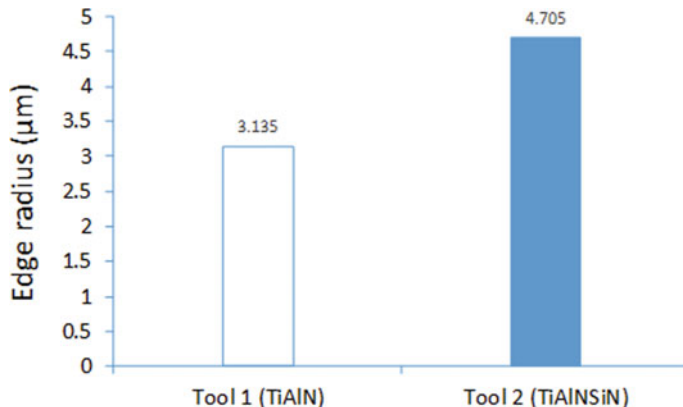


Fig. 6 Measured micro-end mill edge radius

- The change in the shape of the micro-end mill with different coatings has been identified.
- The edge radius of the micro-end mill was observed to be increased by 51% when machining with micro-end mill coated with TiAlNSiN compared to TiAlN coated micro-end mill.
- The micro-end mill coated with TiAlN has more life compared to the micro-end mill coated with TiAlNSiN.
- The image processing steps discussed in the present work can be used for monitoring the in-situ cutting tool wear.

References

1. Ardila, L.K., Ramos, L.W., Del Conte, E.G., Abackerli, A.J., Picarelli, T.C., Perroni, F.A., Uhlmann, E.: Micro-milling process for manufacturing of microfluidic moulds. In: Proceedings of the 23rd ABCM International Congress of Mechanical Engineering (2015)
2. Özel, T., Liu, X., Dhanorker, A.: Modelling and simulation of micro-milling process. In: 4th International Conference and Exhibition on Design and Production of Machines and Dies/Molds, pp. 21–23 (2007)
3. Singh, K.K., Singh, R.: Process mechanics based uncertainty modeling for cutting force prediction in high speed micromilling of Ti6Al4V. Procedia Manuf. **1**(48), 273–82 (2020)
4. Astakhov, V.P.: The assessment of cutting tool wear. Int. J. Mach. Tools Manuf. **44**(6), 637–47 (2004). <https://doi.org/10.1109/HPDC.2001.945188>
5. Bourne, K.A., Jun, M.B., Kapoor, S.G., DeVor, R.E.: An acoustic emission-based method for determining contact between a tool and workpiece at the microscale. J. Manuf. Sci. Eng. **130**(3) (2008)
6. Sodemann, A., Mayor, J.R.: Parametric investigation of precision in tool-workpiece conductivity touch-off method in micromilling. In: 37th Annual North American Manufacturing Research Conference, NAMRC 37, pp. 565–572 (2009)

7. Dai, Y., Zhu, K.: A machine vision system for micro-milling tool condition monitoring. *Precision engineering*. **1**(52), 183–91 (2018)
8. Yamashina, H., Okumura, S.: A machine vision system for measuring wear and chipping of drilling tools. *J. Intell. Manuf.* **7**(4), 319–27 (1996)
9. Lim, T.Y., Ratnam, M.M.: Edge detection and measurement of nose radii of cutting tool inserts from scanned 2-D images. *Opt. Lasers Eng.* **50**(11), 1628–42 (2012)
10. Loizou, J., Tian, W., Robertson, J., Camelio, J.: Automated wear characterization for broaching tools based on machine vision systems. *J. Manuf. Syst.* **1**(37), 558–63 (2015)
11. Castejón, M., Alegre, E., Barreiro, J., Hernández, L.K.: On-line tool wear monitoring using geometric descriptors from digital images. *Int. J. Mach. Tools Manuf.* **47**(12–13), 1847–53 (2007)
12. Dutta, S., Kanwat, A., Pal, S.K., Sen, R.: Correlation study of tool flank wear with machined surface texture in end milling. *Measurement* **46**(10), 4249–60 (2013)
13. Malekian, M., Park, S.S., Jun, M.B.: Tool wear monitoring of micro-milling operations. *J. Mater. Process. Technol.* **209**(10), 4903–14 (2009)

Space Applications and Modern Structures

Behavior Study of Tape Springs for Space Deployment Applications



Rutvik Dangarwala , Hemant Arora , Shashikant Joshi ,
and Sudipto Mukherjee

1 Introduction

Many space equipment need to be packed in small volumes during launching and deployed in space when required. The most common mechanisms for this purpose are composed of kinematic joints such as rigid hinges [1] and have to be combined with a motor, electrical winding, power source, lubrication system, a latch and a spring. On the other hand, tape springs, commonly used for measurements, being continuous and having completely passive, self-actuating, self-locking properties, provide lightweight cost-effective systems and thus offer overall robustness to the deployment system.

Theoretical Background of Tape Springs. Tape springs have very small thickness as compared to the in-plane dimensions. This makes their study, as in general for any thin plate, as a three-dimensional solid using theory of elasticity, rather complicated and unnecessary. Hence the fold is to be analyzed using “Thin Plate Theory” [2]. Moreover, to analyze regions other than the fold area having thin as well as curved geometry, another theory called “Theory of Shell Structures” [3] is to be used.

R. Dangarwala · S. Joshi

Institute of Technology, Nirma University, Ahmedabad, India

e-mail: 16bme064@nirmauni.ac.in

S. Joshi

e-mail: s.j.joshi@nirmauni.ac.in

H. Arora

Space Applications Centre, ISRO, Ahmedabad, India

e-mail: hemant_arora@sac.isro.gov.in

S. Mukherjee

Department of Mechanical Engineering, IIT Delhi, New Delhi, India

e-mail: sudipto@mech.iitd.ac.in

The differences in behaviors shown by Tape Springs depending upon the sense of load are categorized as “Equal” and “Opposite”. The sense is defined based on whether the change of transverse curvature is in the opposite or the same direction of the initial transverse curvature. When tape spring is subjected to pure moments or end forces and end couples within the plane of its longitudinal axis, it deforms with three distinct deformation zones (see Fig. 1), where the fold region has no transverse curvature and the straight region has no longitudinal curvature.

Wüst [4], Rimrott [5] and Mansfield [6] determined the relation between the bending moment and corresponding change in longitudinal curvature using different methodologies to understand the Moment-Rotation characteristics. The M- θ plots give an overview of the non-linearity in the behavior and the hysteresis (Fig. 2).

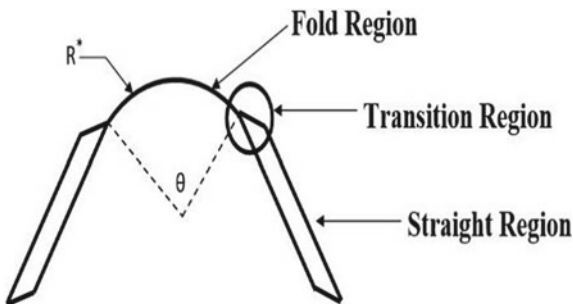


Fig. 1 Deformation zones of tape spring

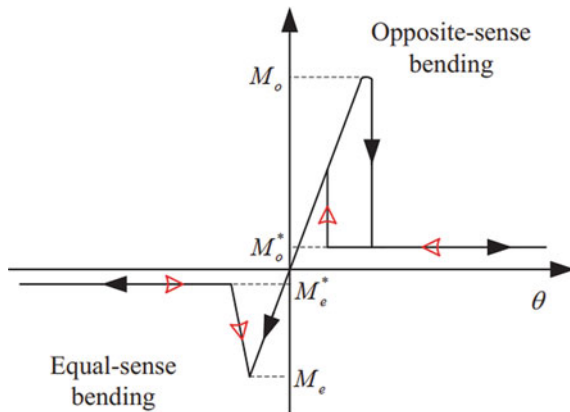


Fig. 2 Moment versus bending angle [7]

2 Problem Definition

In the most direct application of tape spring as hinges, they are to be fixed at one end to a fixed body while the other end is to be displaced for stowing purpose and released for deployment when required. For example, they can be used to deploy a Reflector [1] at a particular orientation around a Solar panel and also to deploy large size Space Antenna Reflectors [8].

Tape springs show highly varying and non-linear mechanical behavior depending upon the sense of loading. So the behavioral understanding when folded in different senses under cantilever configuration is necessary. Also, the potential problem that may arise is of hard folding as when stowed, the fold formation and its interaction with the fixed support may expose the fold area to stress concentration. Any hard folding, therefore, may hinder the desired deployment. Hence, the strain analysis of the fold becomes critical.

The Analytical estimation of stresses and strains using the shell theory requires the estimation of changes in longitudinal curvature which is difficult to be determined experimentally with sufficient accuracy due to the highly transient behavior, unless relied upon expensive digital measurements. Therefore, an analytical method is to be tested to obtain stress and strain from the displacements of the free end which are easier to measure, which is then required to be validated using experimental strain measurements and reproduced using FEA.

3 Strain Evaluation at Tape Spring Fold

3.1 Analytical Method Using Displacements of Free End

The Geometric parameters and Material properties of the tape spring used are noted in Tables 1 and 2. The Experiments are performed for the tape spring kept in horizontal cantilever configuration and loaded by vertical transverse end loads (Figs. 3 and 4). Weights of 4 gm (15 qty.) and 10 gm (15 qty.) are used and the displacements of the free end are measured.

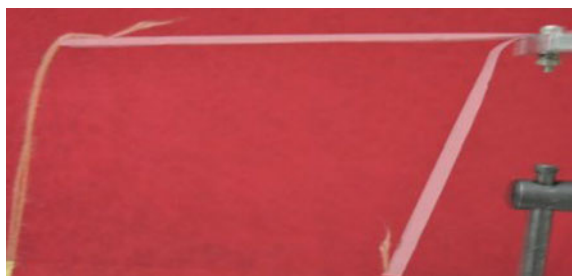
From the theory of shell structures [3], the generalized Hooke's law for a shell element is as follows:

Table 1 Geometric properties

L (mm)	t (mm)	α ($^{\circ}$)	R (mm)
110	0.12 mm	59.73	14.9425

Table 2 Material properties of tape spring

E (GPa)	v	ρ (kg/m 3)	σ_{yt} (MPa)
200	0.33	7850	1300

Fig. 3 Opposite sense**Fig. 4** Equal sense

$$\begin{bmatrix} M_x \\ M_y \\ M_{xy} \end{bmatrix} = \begin{bmatrix} D & vD & 0 \\ vD & D & 0 \\ 0 & 0 & D(1-v) \end{bmatrix} \begin{bmatrix} k_x \\ k_y \\ k_{xy} \end{bmatrix} \quad (1)$$

where

$$D = \frac{Et^3}{12(1-v^2)}$$

D Flexural rigidity of plate element

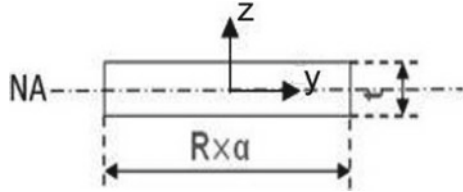
v Poisson's ratio

E Modulus of Elasticity

M_j Bending Moment per unit length on a cut-plane with normal in j direction [3]

k_j Change in curvature in j direction.

It is important to note that the moments shown in Eq. (1) are per unit length of application. So, to obtain the total moment acting on a particular cut-plane with its normal in j direction, it is to be multiplied by the length upon which it acts. It is known that the cross-section at the fold flattens upon loading (see Fig. 5). The moment M applied about the y axis will cause the change in longitudinal curvature of tape spring (k_x). Let r and R be the final longitudinal curvature and initial transverse curvatures,

Fig. 5 Cross-section at fold

respectively. β and α are the fold angle and initial angle subtended by the cross-section, respectively. The length of application of moment is ($R\alpha$) at the fold. At the fold,

$$\text{Change in longitudinal curvature: } k_x = \frac{1}{r} - 0 = \frac{1}{r}$$

$$\text{Change in transverse curvature: } k_y = 0 - (\pm \frac{1}{R}) = \mp \frac{1}{R}$$

where $+\frac{1}{R}$ change in transverse curvature that occurs for equal sense loading and the $-\frac{1}{R}$ corresponds to opposite sense loading. From the generalized Hooke's law for shell element applied at the fold, we get

$$M_x = Dk_x + vDk_y \quad (2)$$

And using the relation, Total applied moment $M = M_x * (R\alpha)$ and further simplification gives

$$M = D(R\alpha)(k_x + vk_y) \quad (3)$$

Substituting the values of changes in curvature and flexural rigidity yields

$$M = (R\alpha) \frac{(Et^3)}{12(1-v^2)} \left(\frac{1}{r} \mp v \frac{1}{R} \right) \quad (4)$$

where - sign corresponds to "Equal sense" and + sign corresponds to "Opposite sense". From Eq. (4), the Moment at fold M is found, and then the maximum tensile bending stress (at the farthest layer i.e. $z = t/2$) is found using the bending equation within the elastic limits as follows:

$$\sigma = \frac{M \times z}{I} \quad (5)$$

For the elastic region, as the tape spring has linear elastic material, the maximum longitudinal normal strain is obtained from the above calculated stress using Hooke's law. As can be seen that for evaluating the strain at the fold, the only unknown is the

radius of longitudinal curvature r . It is seen from the experiments that once the fold is generated near the fix end, the longitudinal distance of the fold remains majorly the same though the radius of longitudinal curvature and the fold angle keep changing with the load applied. The straight portion of the tape spring is observed to simply rotate with pivot point at the end of the fold. (see Figs. 6, 7).

The longitudinal distance of the fold as marked in Figs. 6 and 7 is measured as 7 and 5 mm for equal and opposite sense loading, respectively, which is, in general, a function of material properties, the initial cross-section, length and also the sense of loading. The schematic diagram (see Fig. 8) shows the free end displacements Δx and Δy . The straight portion of tape spring which is forming an angle β with

Fig. 6 Rotation about fold—equal sense

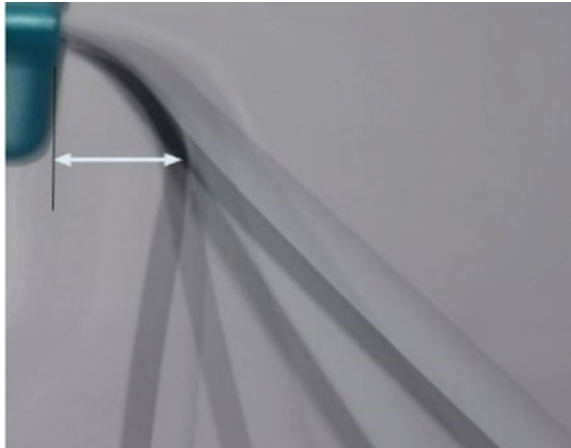
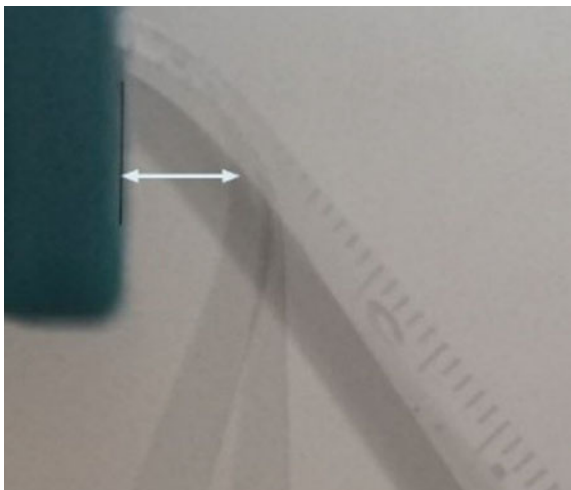


Fig. 7 Rotation about fold—opposite sense



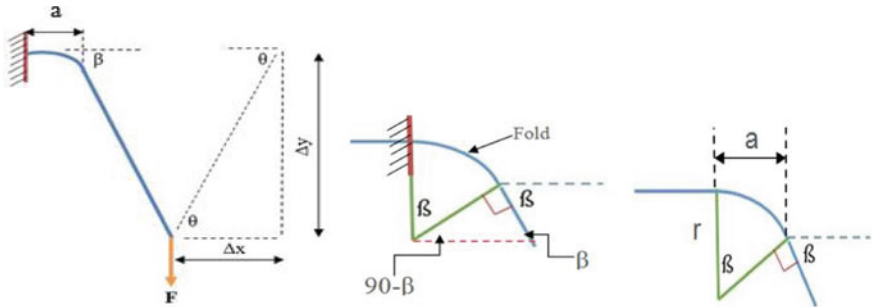


Fig. 8 Deformed tape spring and fold angle schematic

horizontal has length L . Applying the sine rule, in the approximated triangle having angles β and θ , we have

$$\frac{\sin(\beta)}{[\Delta x^2 + \Delta y^2]^{\frac{1}{2}}} = \frac{\sin(\theta)}{L} \quad (6)$$

Using Eq. (6), knowing the displacements of free end and the length of the straight portion, the angle β is obtained. The calculated angle β is the fold angle as shown in Fig. 8. The radius of longitudinal curvature r is obtained from the fold angle β and measured distance “ a ” (7 mm for equal sense and 5 mm for opposite sense) as below

$$r \times \sin\beta = a. \quad (7)$$

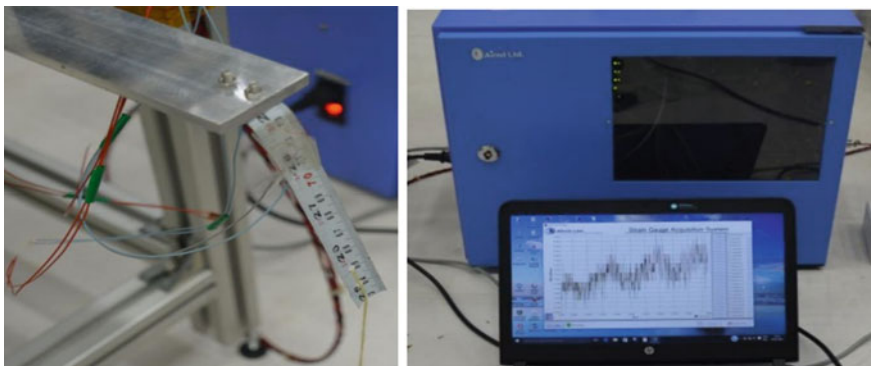
As the radius and the fold angle β vary with loading, the length of the straight portion of the tape spring is also observed to change. For equal sense loading, it is measured to be 103 mm (up to 20 gm load), 102 mm (30–60 gm load) and 101 mm (70–150 gm load) and for opposite sense loading, it is measured to be 105 mm (up to 100 gm load) and 104 mm (110–150 gm load). The calculated moment, stress and strain results are shown in Table 3.

3.2 Strain Measurements Using Strain Gauge

Electrical strain gauge in quarter bridge configuration is used to measure strain at the fold. Strain gauge is attached at the fold location such that it measures the normal longitudinal strain. Adequate importance is given to the procedure of bonding the strain gauge with the tape spring surface. The strain gauge is connected to the strain measurement setup consisting of the data-acquisition system and the strain measurement software (Fig. 9). The frequency of the measurement setup was set to 10 Hz. (Measured values are shown in Table 4).

Table 3 Calculated results

Load (gm)	Equal sense			Opposite sense		
	Moment (Nmm)	Stress (MPa)	Analytical microstrain	Moment (Nmm)	Stress (MPa)	Analytical microstrain
10	0	0	0	0	0	0
20	22.949	613.78	3069	12.09	323.43	1617
30	38.794	1037.55	5188	13.05	349.08	1745
40	49.373	1320.48	6602	15.93	426.04	2130
50	51.489	1377.07	6885	39.91	1067.37	5337
60	52.194	1395.93	6980	39.91	1067.37	5337
70	53.528	1431.6	7158	49.5	1323.91	6620
80	54.952	1469.7	7349	68.68	1836.97	9185
90	54.952	1469.7	7349	68.68	1836.97	9185
100	57.089	1526.85	7634	78.28	2093.5	10,468
110	57.089	1526.85	7634	88.6	2369.77	11,849
120	57.089	1526.85	7634	88.6	2369.77	11,849
130	57.089	1526.85	7634	98.29	2628.77	13,144
140	57.801	1545.9	7729	98.29	2628.77	13,144
150	57.801	1545.9	7729	98.29	2628.77	13,144

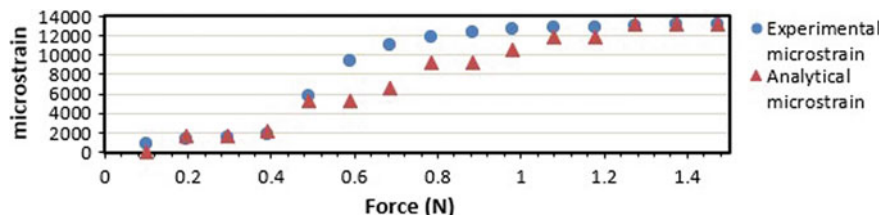
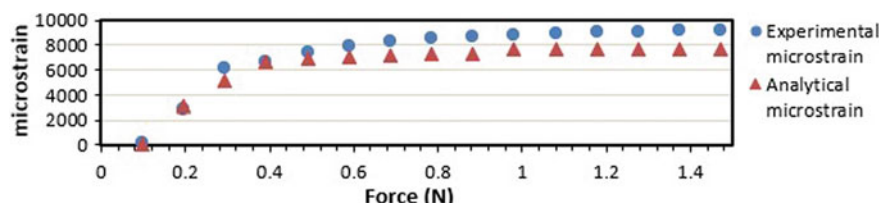
**Fig. 9** Strain gauge experiment setup

3.3 Comparison of Analytical Strains with Strain Gauge Measurements

The important points to note are as follows (Figs. 10 and 11):

Table 4 Experimentally measured data

Load (gm)	Equal sense			Opposite sense		
	X Displacement (mm)	Y Displacement (mm)	Experimental microstrain	X Displacement (mm)	Y Displacement (mm)	Experimental microstrain
10	0	32.5	140	0	0	904
20	10	48	2800	2	1	1400
30	65	70	6200	3	2	1489
40	65	85	6635	8	5	1869
50	70	88	7400	45	30	5750
60	70	89	7950	60	30	9350
70	70	90	8300	65	40	11,100
80	80	92	8500	70	60	11,900
90	80	92	8700	70	60	12,400
100	90	95	8850	73	70	12,640
110	90	95	8950	73	80	12,780
120	90	95	9020	73	80	12,920
130	90	95	9100	73	90	13,031
140	100	96	9150	73	90	13,110
150	100	96	9175	73	90	13,180

**Fig. 10** Strain comparison graph—opposite sense**Fig. 11** Strain comparison graph—equal sense

- Although the snap is seen during the experiment at 0.49 N load for the opposite sense loading, at the load of 0.59 N, the experimental strain is observed to rise significantly while no significant deformation is observed. A similar observation is made in the equal sense case at 0.2943 N. This is attributed to the effect of stress concentration at the fold as due to the snap, the fold is generated and any further increase in the load causes stress to be concentrated at the fold, thus giving additional rise to strains which are not predicted from displacements.
- The Analytical method predicts the experimental strains with significant accuracy up to a certain load. The reason for deviation at higher loads is the stress at the fold crossing the yield strength and thus violating the “within elastic limit” assumption of the analytical method. Therefore, the mean absolute error when calculated for readings within the elastic limit is found to be 9% and 19% for equal and opposite sense, respectively.
- Another important point to note from the stress consideration is that before the snap, the opposite sense loading shows lesser stress and strain while after the snap, a sudden rise causes higher stress and strain than the equal sense, for the same applied load.

4 Finite Element Analysis of Tape Spring

4.1 Analysis Settings

As the loading of a tape spring involves sudden and large non-linear deformation behavior and a sudden change in internal energy due to snap, Explicit dynamic analysis is performed using the FEA tool ANSYS. The material used in the analysis is a linear isotropic structural steel with modified yield tensile strength of 1300 MPa. An edge at a distance of 7 mm from the fixed end is used to measure strain at the fold using a strain probe tool.

The tape spring is meshed with “Linear shell elements” with Non-linear mechanical physical preference. As the tape spring has a thickness of 0.12 mm, which is very less than other in-plane dimensions, fine meshing with uniform sizing of 2 mm is used to avoid the possibility of element distortion (see Fig. 12).

The analysis is performed for a time of 0.05 s to limit the computational time. The force increasing linearly with time from 0 to 2 N and 3 N is applied for equal and opposite sense loading, respectively, to ensure the propagation of the fold to the fixed end in the given analysis duration. The other edge is applied the fixed boundary condition (see Fig. 13).

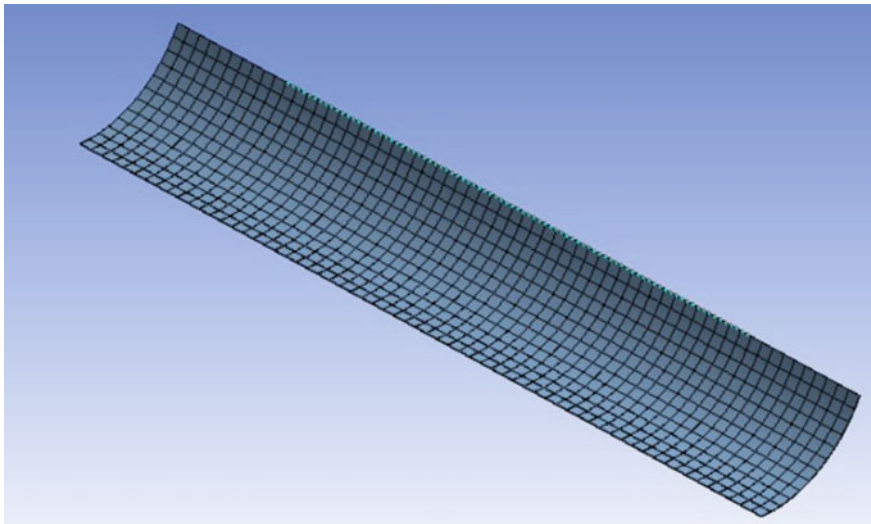


Fig. 12 Meshing

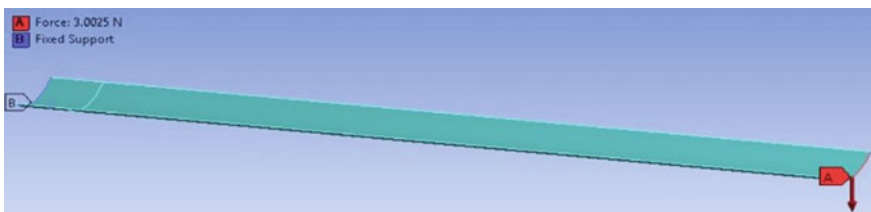


Fig. 13 Boundary conditions

4.2 Analysis Results

The equivalent stress and strain results at the fold, for the equal and opposite sense, are shown in Figs. 14, 15, 16 and 17. The sudden snap phenomenon is observed in the opposite sense. The deformation in equal sense loading is followed by torsional effects which is also observed during the experiments.

4.3 Validation of FEA Results

The maximum stress and strain at the fold along with maximum free end displacement, obtained from FEA, are validated as shown in Table 5. After the snap, although experimentally and analytically the strain at the fold is noted to be increasing, it is not seen in the FEA (see Figs. 16, 17). The reason behind this is the excessive and

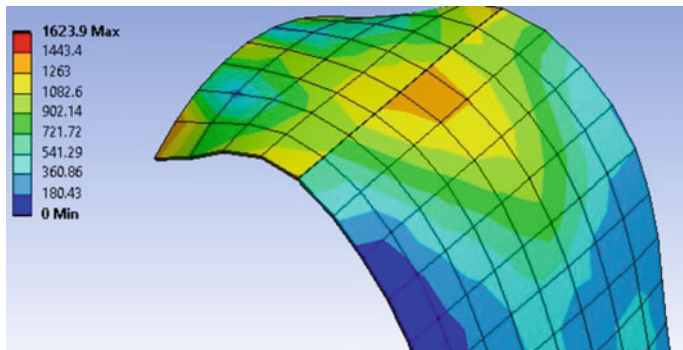


Fig. 14 Equivalent stress—equal sense

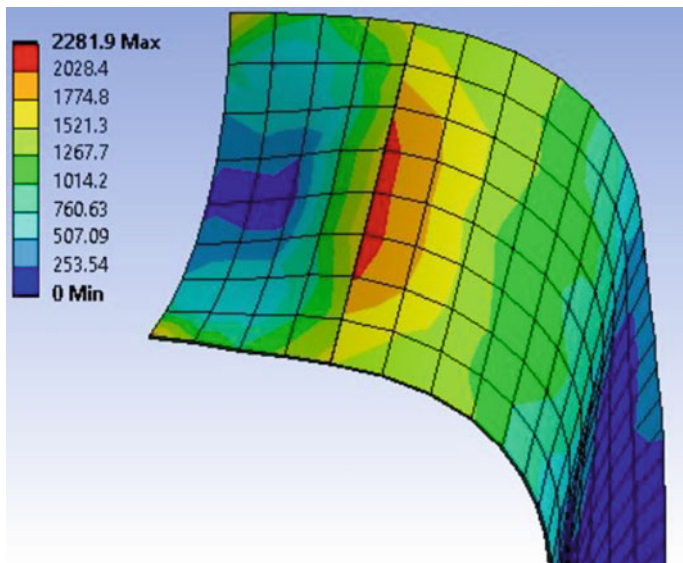


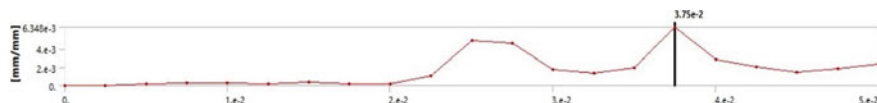
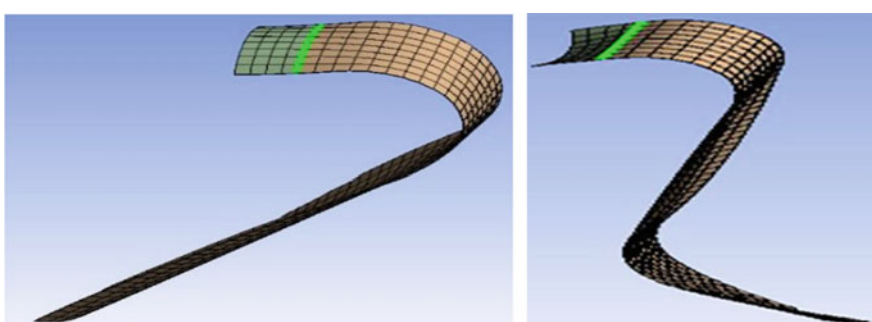
Fig. 15 Equivalent stress—opposite sense

unrealistic X deformation due to the momentum gained after the snap, which shifts the fold away from the fixed end (see Fig. 18). This shows the need for additional constraints to capture the post-snap behavior accurately.

Table 5 Validation of FEA results

Result	Equal sense			Opposite sense		
	Experiment result	FEA result	% Error**	Experiment result	FEA result	% Error**
Equivalent stress [MPa]	1545.90*	1443.4	6.6	2628.77*	2281.9	13.2
Strain at snap [microstrain]	6200	6348	-2.3	9350	8967.5	4.1
X deformation [mm]	100	94.546	5.4	73	72.361	0.8
Y deformation [mm]	96	102.25	-6.5	90	97.643	-8.5

* Stress is compared with the Analytical stress values; ** Error is w.r.t. Experimental results

**Fig. 16** Strain probe results—equal sense**Fig. 17** Strain probe results—opposite sense**Fig. 18** Excessive X deformation after snap

5 Conclusion

- Before the snap has occurred in the opposite sense loading, for the same amount of applied load, lower stresses and strains at the fold are noted. Also, the load at which the snap and fold formation occurs is higher in the opposite sense. Thus, opposite sense loading results in higher deployed stiffness and lesser deformations at the same loads (prior to the snap), reducing the effects of disturbances in the deployed state.
- After the snap, the effect of stress concentration is higher in the opposite sense which is evident by a higher rate of increase and a higher magnitude of stress and strain. Thus, when stowed, if loaded beyond a certain load, opposite sense loading is more prone to hard folding. This shows the need for trade-offs while selecting between equal and opposite sense configurations for higher deployed stiffness and resistance to hard folding.
- The analytical strains when validated against the experimental measurements show 9 and 19% Mean absolute error within the elastic limit, for equal and opposite sense, respectively. The results are reproduced using FEA with significant accuracy. Nonetheless, to capture the post-snap behavior accurately, additional constraints are required.

References

1. Dewalque, F., Collette, J., Brüls, O.: Mechanical behaviour of tape springs used in the deployment of reflectors around a solar panel. *Acta Astronaut.* (2016)
2. Bhaskar, K., Varadan, T.K.: *Plates: Theories and Applications*. Wiley (2014)
3. Calladine, C.: *Theory of Shell Structures*. Cambridge University Press (1983)
4. Wüst, W.: Some applications of the theory of the cylinder shell. *Z. Angew. Math. Mech.* **34**, 444–454 (1954)
5. Rimrott, F.P.J.: Cross-sectional deformation in torsion of open profiles. *Z. Angew. Math. Mech.* **50**, 775–778 (1970)
6. Mansfield, E.: Large-deflexion torsion and flexure of initially curved strips. *Proc. R. Soc. Lond. A* **334**, 1125–1132 (1973)
7. Hui, Y., Ruipeng, Z., Zhanwen, F., Yan, W., Rongqiang, L.: Deploying dynamics experiment of tape-spring hinges for deployable mechanism, pp. 106–110. <https://doi.org/10.1109/YAC.2017.7967387>. (2017).
8. Arora, H., Munjal, B.S., Mukherjee, S.: Design and validation of flexure based hinges for space deployable antenna reflector. In: 4th International and 19th National conference of Machine and Mechanisms (iNacoMM 2019). IIT Mandi, India (2019)

Parametric Optimization of Joints and Links of Space Deployable Antenna Truss Structure



Hemant Arora , Vrushang Patel , B. S. Munjal ,
and Sudipto Mukherjee

1 Introduction

Large diameter reflectors (LDR) are designed with foldable configuration widely known as ‘*Unfurlable*’ or ‘*Deployable*’ which consists of many joints and linkages explored by many researchers for space applications [1]. Joints and Linkages of these deployable configurations are designed based on the understanding of kinematics and dynamics [2] simulations considering deployment parameters of a truss structure. These joints are required to be optimized for making the truss configuration highly compact in a fully folding or stowed position. Critical parameters of each joint are considered for the optimization study presented in this paper. The parametric optimization technique [3] is deliberated to optimize specific values of a set of parameters that gives the best performance of the system in given circumstances. These parameters are termed as design variables, and circumstances of the system are described by design constraints. An objective function is formulated on the criteria of minimizing the stowed volume of the deployable truss structure. Constraints that represent a limitation on performance are called functional constraints which are defined with reference to the geometry of joints and linkages.

H. Arora · S. Mukherjee
Department of Mechanical Engineering, IIT Delhi, New Delhi, India
e-mail: contact2hemantarora@gmail.com

S. Mukherjee
e-mail: sudipto@mech.iitd.ac.in

V. Patel
Institute of Technology, Nirma University, Ahmedabad, India
e-mail: vru1992@gmail.com

B. S. Munjal
Space Applications Centre-ISRO, Ahmedabad, India
e-mail: bsmamsd@sac.isro.gov.in

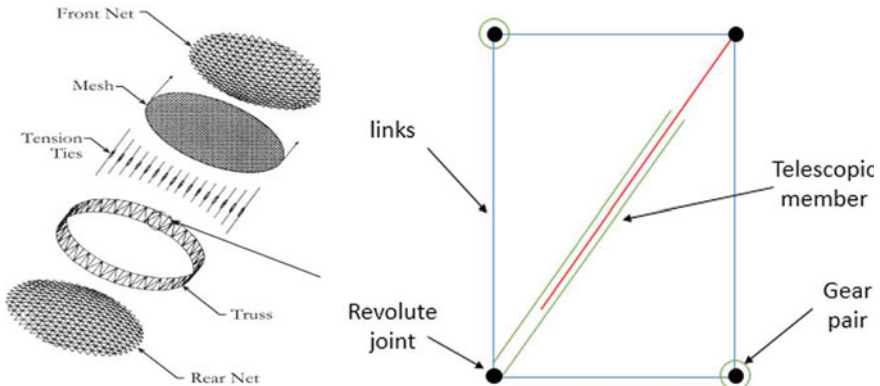


Fig. 1 Exploded view of deployable mesh reflector with a description of single bay

2 Design Configuration of Deployable Mesh Reflector

The simplest type of ring structure used for Mesh Antenna is known as *AstroMesh* [4] configuration in which a four-bar mechanism is used as a basic entity with one diagonal telescopic member. A cable is passing through the diagonal telescopic member, and pulling this cable helps in the deployment of *AstroMesh* configuration. This configuration consists of a number of bays, and each bay is an inversion of the four-bar mechanism. Four links of individual bays are connected with two 5J joints and two 3J joints. 5J joints are diagonally connected with a telescopic member, and 3J joints are configured with a gear pair for synchronized motion between adjacent bays (see Fig. 1). These bays are interconnected at joints to form a ring truss which supports RF reflective mesh. After deployment, it forms an antenna reflector and after folding, it forms a cylindrical compact structure accommodated with mesh and joint elements. The present paper focuses on optimizing the joint and link parameters to make it a compact stowed configuration which should be easily integrated with the satellite during launching and later deployed to a full configuration in space.

3 Optimization Methodology

The objective is to minimize the size of the mechanism [5] in a stowed configuration which mainly depends on the diameter and height of the antenna. The height of the antenna depends on the number of bays, ratio of focal length and diameter (F/D) of parabolic surface, and offset distance of the parabolic surface. The height of the stowed configuration is also limited to the space available in launch vehicle payload fairing space. Therefore, the height of the stowed configuration is optimized based on these parameters. The diameter of stowed configuration is taken as a design

parameter which is required to be optimized for accommodation in limited fairing space. Mainly, the joint parameters decide the diameter of stowed configuration which should incorporate folded RF mesh along with support net [6]. Therefore, a relative location of various hinge points is considered as dimensional characteristics of the joints which are taken as design parameters.

3.1 Design Variables

Deployment of AstroMesh configuration happens with the motorized winding of a cable passing through the telescopic diagonal members. The motor is positioned on one vertical member which is rigidly fixed with the structure. Coordinate of this fixed member is considered as a reference frame. The coordinate of different points on 5J joint, 3J joint and slider members are obtained from fixed reference frame [7], and equations of constraints are also formulated with reference to the fixed frame (see Fig. 2).

The reference frame is marked on fixed vertical members in which X-axis is marked as the direction of motion, Y-axis is along the longitudinal axis of vertical fixed member and Z-axis is along the rotational axis of hinges on the fixed member. Various critical points are identified on moving joints. Coordinates of these points are defined with reference to the fixed frame which are considered as design parameters. *Point_1* is pointed at the end of the slider member revolute joint at the fixed vertical member. *Point_2* is pointed at the end of slider member revolute joint at moving vertical member on the same bay. *Point_3* is the end of circumferential

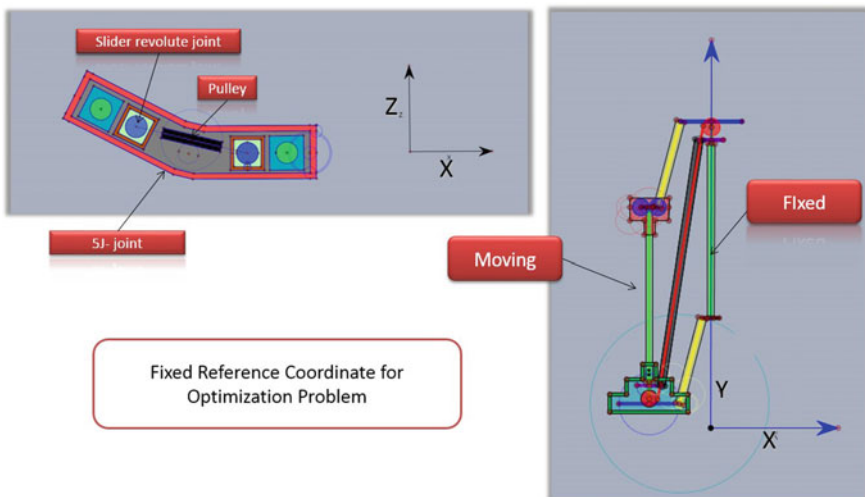


Fig. 2 Fixed reference frame shown on a single bay for optimization problem formulation

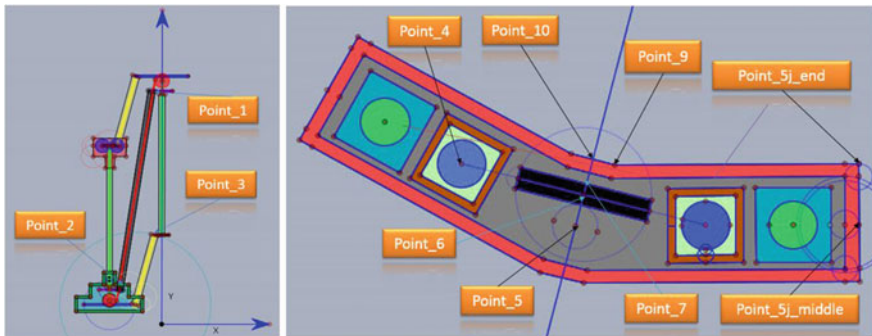


Fig. 3 Description of various critical points

member revolute joint at 3J joint with the fixed member. *Point_4* is marked at the end of a diagonal member on the axis of the revolute joint of the moving 5J joint. *Point_5j_middle* and *Point_5j_end* are middle and end points of the 5J joint subsequently at the extreme side edge of 5J joint. *Point_5* is the intersection of the X-axis and the center axis of the pulley. *Point_6* is the center of the pulley in the top view, *Point_7* is end point of the pulley, *Point_9* and *Point_10* are points at the inner wall of the 5J joint body (see Fig. 3).

3.2 Design Parameters

Co-ordinates of various critical points are required to describe the dimensional characteristics which are further described as design parameters. These design parameters are a function of independent design parameters which describe the geometry of the component in the assembly [5] (see Fig. 4).

- P_1 is the distance between point_5j_center and point_2 in the x-direction.
- P_2 is the distance between origin and point_3 in the x-direction.
- P_3 is the distance between the end of the circumferential member at the 5J joint and the axis of the vertical rod of the moving member in the x-direction.

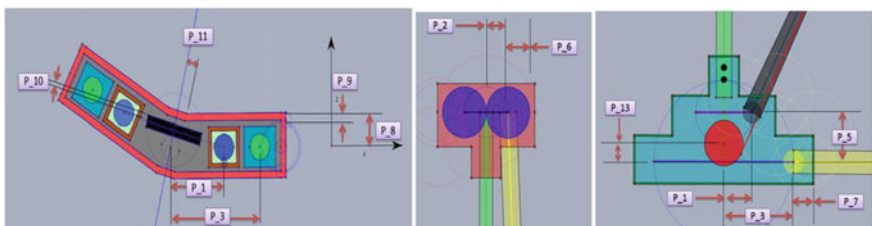


Fig. 4 Description of design parameters

- P_8 is the depth of the 5J joint body in the z-direction with reference to the origin.
- P_9 is the thickness of the 5J joint body from the fixed coordinate system in the z-direction.
- P_10 is the half-thickness of the pulley along the rotational axis.
- P_6 is the distance between the horizontal member hinge axis and the extreme edge of the 3J joint body along the x-direction.
- P_13 is the distance between the center of the pulley to the circumferential/horizontal member hinge axis at the 5J joint along the y-direction.
- P_7 is the distance between circumferential member hinge axis and extreme edge of the 5J joint body along the x-direction.
- P_5 is the distance between diagonal member revolute hinge joint to circumferential member revolute joint at the 5J joint along the y-direction.
- P_11 is the design variable defined for the width of the 5J joint body.

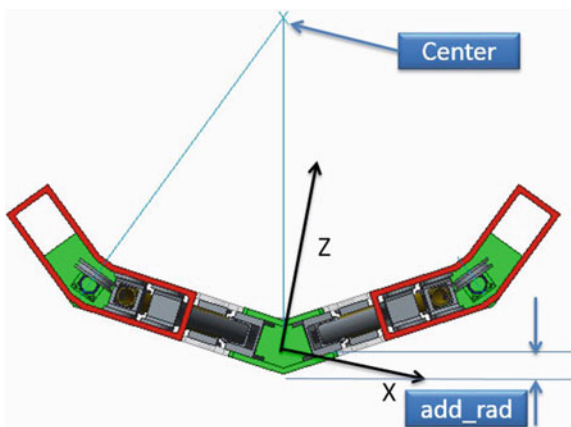
3.3 Objective Function

An objective function is formulated for minimizing the radius of the stowed configuration of the deployable antenna mechanism. The stowed radius of the mechanism can find out with the help of the 5J center point of the moving member.

Radius in the stowed configuration is represented by the distance between the center of the inscribed circle which is made by the tangent to the inner edge of the 5J joint body and the center point of the 5J joint (see Fig. 5). To describe the length of this radius mathematically, the equation of a straight line is formulated based on the defining center point of the circle and the geometrically defined center point of the 5J joint considered as the origin. The centre point of the circle is described by the intersection of the center axis of two joints.

Therefore, the final radius of the antenna in the stowed configuration is the distance between the origin to point (x_r, z_r) which is defined as

Fig. 5 Description of center point and radius of stowed configuration



$$\text{radius} = \text{dis_bet_two_points}(x_r, z_r, 0, 0) \quad (1)$$

In addition, it is also required to optimize the extreme radius of configuration which can be defined by adding an additional component which is half of the width of the 5J joint body which is defined by variable *add_rad* (see Fig. 5).

$$\text{Therefore, } \text{Total_radius} = \text{radius} + \text{add_rad} \quad (2)$$

The radius of the stowed configuration also depends upon the width of the 5J joint. *P_11* is a variable parameter defined for optimizing the width of the joint body. Therefore, this parameter is required to be included in Eq. (2) to get the appropriate behavior of the objective function.

Therefore, the objective function is defined as

$$\text{Objective function} = \min\{\text{Total_radius} + (p_{11})\} \quad (3)$$

3.4 Formulation of Constraints

Constraints for mechanism configuration are defined on the basis of interference of different members. There are many geometric constraints formulated based on the deployable configuration and a few are presented here for understanding.

Required clearance between the diagonal member and the 3J joint body (see Fig. 6) is defined as an optimization constraint. Clearance is denoted as clearance const_1 which is a constant parameter and taken as 1 mm. The constraint is defined as

$$\text{clearance_const_1} + (\text{var_mdia}/2) - \text{var_3j_p12} < 0 \quad (4)$$



Fig. 6 CAD view of Interference of 3J joint body with diagonal member and 5J joints interfering with each other

where variable *var_mdia* is the major diameter of diagonal member and variable *var_3J_p12* is the perpendicular distance between point 1 and point 2 on the 3J joint.

To formulate the constraint of interference between 5J joints, an intersection path is marked with orange color (see Fig. 7). Point 1 is the final interference point and point 2 is marked on the intersection with the line joining the 5J body end. The condition of avoiding interference is only possible when the distance between these two points is greater than zero which is defined by clearance parameter *clearance_end_5j*.

$$\text{clearance_end_5j} - \text{var_5j_end} < 0 \quad (5)$$

where variable *var_5j_end* defines the distance between the end points of two adjacent 5J joint bodies.

Interference between the rope and inner wall of the diagonal telescopic sliding member is a cause of continuous rubbing of the rope during deployment and energy lost due to friction (see Fig. 8). Therefore, this interference should be necessarily

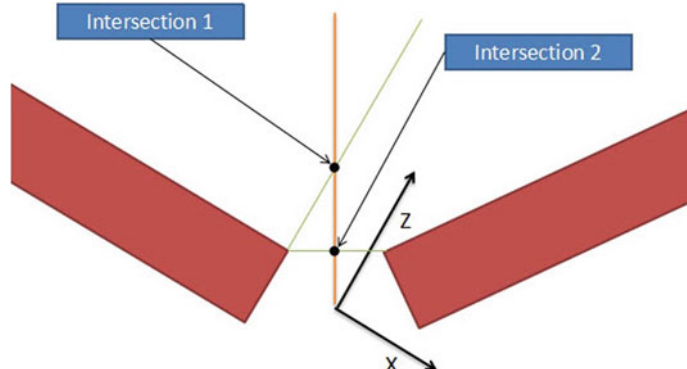


Fig. 7 Interference of 5J joint bodies

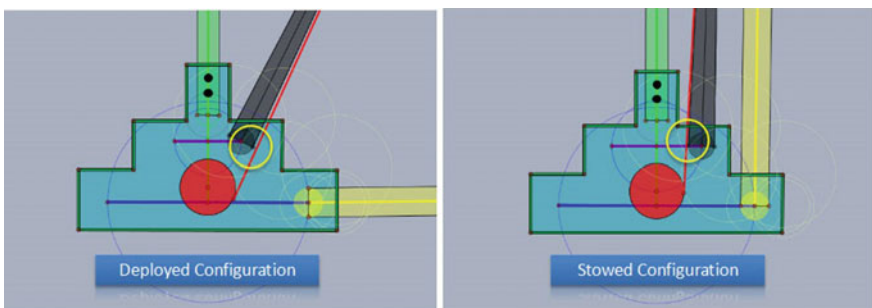


Fig. 8 Interference of rope with slider inner surface

eliminated. For elimination of this interference, center line of the rope passing through the diagonal member should coincide with the tangent of the pulley.

Clearance between rope and slider = (Inner diameter of diagonal member—diameter of rope)/2.

Therefore, the constraint equation is formulated as

$$\text{Per_slider} - \text{clearance_bet_rope_inner_wall} > 0 \quad (6)$$

where *Per_slider* is the perpendicular distance between the rope axis and the diagonal member central axis.

4 Optimization Problem Formulation with MATLAB

The optimization process needs an initial design point to start with [3, 5]. Optimization solver fmincon is selected as a derivative method which checks all local minima and converges to a global minimum value. As this is a problem of multiple design variables and multiple constraints with a single objective function, the function ‘fmincon’ is used to solve parametric optimization which makes necessary changes in design variables meeting with the objective function.

4.1 Initial Design Input Parameters

Initial parameters from the design configuration are considered as input parameters for solving this problem. The initial input parameters are described as follows:

- Diameter of fully deployed configuration = 3000 mm
- Height of fully deployed ring structure = 400 mm
- Number of bays = 14
- Length of vertical members = 400 mm
- Radius of pulley = 6.5 mm
- Pulley thickness = 6 mm
- Diameter of rope = 1.5 mm
- Inner diameter of diagonal member = 9 mm
- Wall thickness of diagonal member = 0.75 mm
- Wall thickness of end connection = 1 mm
- Outer diameter of circumferential member = 10 mm.

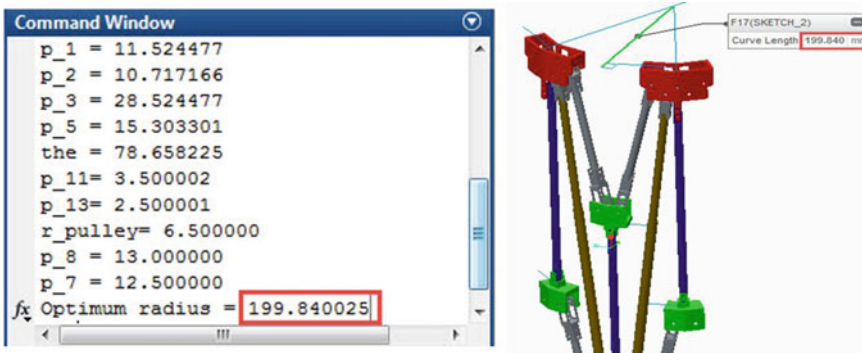


Fig. 9 Screenshot of MATLAB result and CAD model

4.2 Solution of Optimization Problem

The solution of the optimization function is obtained using MATLAB optimization tools with consideration of design constraint, value of objective function and value of design variables. A screenshot of these parameters and results for optimum stowed radius are captured from the MATLAB simulation environment. The same parameters are modeled using CAD software ‘Autodesk Inventor’ and the result for stowed radius obtained is validated (see Fig. 9). The optimized radius of stowed configuration comes out to be 199.84 mm for the present set of input parameters.

4.3 Extrapolating the Design Parameters for 12 m Deployable Truss

The optimized parameters obtained for the 3 m diameter configuration are extrapolated and optimized for designing a 12 m deployable truss. The optimization is further carried out with a variation of the number of bays. As the number of bays increases, stowed radius also increases. It is also required to optimize the number of bays to avoid complexity and to maintain the circularity of the reflector with mesh holding points located circumferentially on the joints of bays. An increase in the number of joints or bays would also make the system more complex with reference to alignment, integration and testing. Therefore, the optimum number of bays are predicted between 14 and 18 for 12 m diameter configuration (see Fig. 10). The optimum values of various design variables are predicted for the 12 m deployed diameter configuration. These are specified as

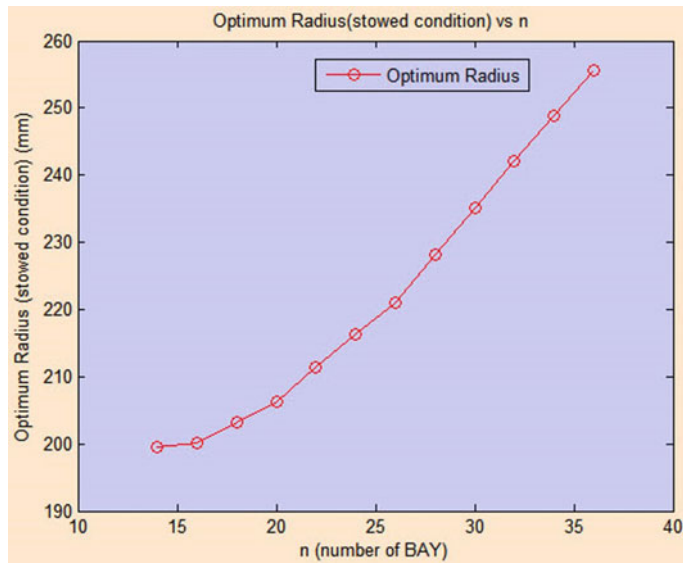


Fig. 10 Plot of optimum stowed radius versus number of bays

$p_1 = 10.46 \text{ mm}$, $p_2 = 10.16 \text{ mm}$, $p_3 = 30.21 \text{ mm}$, $p_5 = 30.0 \text{ mm}$
 $\theta = 89.41^\circ$, $p_11 = 3.5 \text{ mm}$, $p_13 = 16.11 \text{ mm}$, $r_pulley = 4.05 \text{ mm}$
 $p_8 = 15.25 \text{ mm}$, $p_7 = 12.50 \text{ mm}$
Optimum stowed radius = 206.260 mm

4.4 Volumetric Efficiency

The volumetric efficiency of a deployed space system depends upon the ratio of stowed volume to fully Deployed Volume. Volumetric efficiency also varies with various sizes of configuration. Variation of volumetric efficiency with the number of bays is predicted for the 12 m diameter reflector configuration. It is clearly observed that the optimum number of bays is 20 at which the maximum value of volumetric efficiency (99.77%) is obtained. Beyond this point, it starts to reduce further (see Fig. 11).

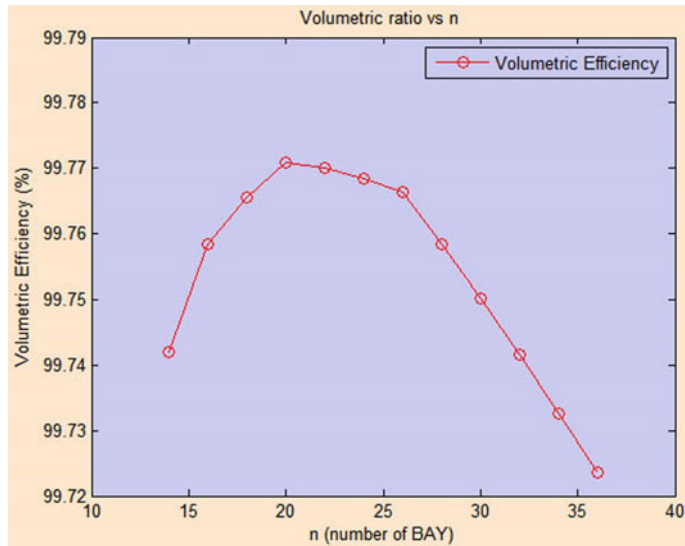


Fig. 11 Plot of volumetric efficiency versus number of bays

5 Conclusion

This paper describes the detail of parametric optimization of joint configuration of the AstroMesh deployable antenna reflector. Focus is made on reducing the size of joint hinges, hinges separation distances and other parameters which would have a direct impact on the overall size of the stowed configuration. Design constraints and objective function are formulated with geometric equations of truss linkages. Optimization results of the stowed radius is predicted as 199.8 mm which is validated with CAD modeling of the same design configuration. Design variables are also extrapolated and optimized for the 12 m diameter configuration. Volumetric efficiency of 99.77% is predicted with optimized design parameters and the number of bays for 12 m diameter configuration. The present exercise in this paper has given the confidence to move further, as this optimized deployable antenna design has potential applications in the satellites for futuristic Indian space missions in Geo Stationary Orbits.

Reference

1. Arora, H., Patel, V., Munjal, B.S., Mukherjee, S., Joshi, S.: Review of various concepts of deployable ring structure for space deployable antenna. In: 10th National Symposium and Exhibition on Aerospace Related Mechanisms (ARMS 2016), Kerala, India (2016)
2. Patel, V., Arora, H., Munjal, B.S., Joshi, S.: Kinematic and dynamic simulation of 12m space deployable antenna. In: International Conference on Automation in Industries (ICAI-2016),

- OEC Junagadh, India (2016)
- 3. Still, G.: Lectures on Parametric Optimization: An Introduction. University of Twente, The Netherlands (2018)
 - 4. Thomson, M.W.: The astromesh deployable reflector. *IEEE Antenna Prop. Soc.* 1516–1519 (1999)
 - 5. Qi, X., Deng, Z., Li, B., Liu, R., Guo, H.: Design and optimization of large deployable mechanism constructed by Myard Linkages. *CEAS Space J.* **2**(13), 5:147–155
 - 6. Sheth, D., Arora, H., Joshi, S., Munjal B.S., Shah, D.: Investigation on design methods for cable mesh configuration of deployable space antenna reflector. *Int. J. Space Struct.* SPS-18-0020.R2 (2019)
 - 7. Arora, H., Munjal, B.S., Mukherjee, S.: Design and validation of flexure based hinges for space deployable antenna reflector. In: 4th International and 19th National conference on Machines and Mechanisms (iNaCoMM 2019), IIT Mandi, India (2019)

Response of a Vibratory System Under Impact Using Contact Force Models



Deepak Maslekar, Anirban Guha, and Sripriya Ramamoorthy

1 Introduction

The classical problem of the vibratory response of a system under impact is still an open issue in engineering application. The classical approach of obtaining response of a spring mass system under impact involves the transformation of impact into initial velocity. This approach treats the impacting bodies as rigid and neglects geometry characteristics of contact surfaces and material properties of impacting bodies during impact [1, 2].

The contribution and merit of the present work deal with the quantification of dynamic response of spring mass systems composed of a deformable body under the impact of a deformable body, in which geometry characteristics of contact surfaces, impact velocities, material properties, etc. are included.

2 Contact Force Models

Many contact impact force models have been used by researchers. The contact force models described in this paper express contact force as a continuous function of penetration between contacting bodies. Lankarani and Nikravesh [3] and Flores et

D. Maslekar (✉) · A. Guha · S. Ramamoorthy

Department of Mechanical Engineering, Indian Institute of Technology Bombay, Mumbai 400076, India

e-mail: deepakmaslekar@iitb.ac.in

A. Guha

e-mail: anirbanguha@iitb.ac.in

S. Ramamoorthy

e-mail: ramamoor@iitb.ac.in

al. [4] suggest the contact force model. These contact force models are based on Hertz elastic contact law, wherein the hysteresis damping function is incorporated to represent the energy dissipated during the impact.

2.1 Lankarani–Nikravesh Contact Force Model

Lankarani and Nikravesh suggested a contact force model by separating normal contact force into elastic and dissipative components as

$$F_N = K\delta^n + D\dot{\delta} \quad (1)$$

where K is generalized stiffness constant and δ is the relative normal indentation between the bodies as shown in Fig. 1. For parabolic distribution of contact stresses, the exponent n is taken as 1.5, as in the original work by Hertz [5]. For metallic materials, the expressions for contact force based on experimental or numerical work use $n = 1.5$. The generalized parameter K is dependent on material properties and the shape of contacting surfaces. For the frictionless Hertzian contact between two spheres i and j , the stiffness parameter K is given by

$$K = \frac{4}{3(\sigma_i + \sigma_j)} \left[\frac{R_i R_j}{R_i + R_j} \right]^{\frac{1}{2}} \quad (2)$$

where R_i and R_j are radii of spheres and the material parameters σ_i and σ_j are given by

$$\sigma_k = \frac{1 - \nu_k^2}{E_k}, \quad (k = i, j) \quad (3)$$

and the quantities ν_k and E_k are Poisson's ratio and Young's modulus associated with each sphere, respectively.

In Eq. (1), the quantity $\dot{\delta}$ is the relative normal impact velocity and D is the hysteresis coefficient. The hysteresis coefficient is expressed as a function of penetration as

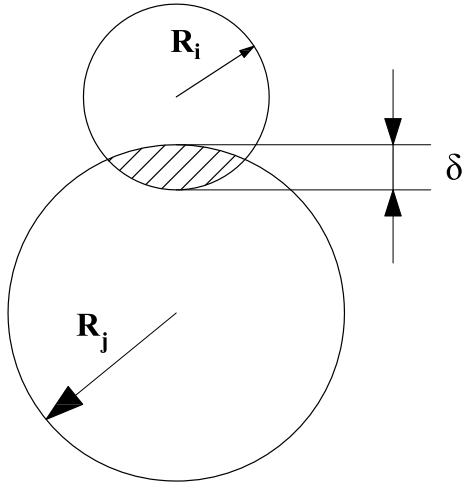
$$D = \chi\delta^n \quad (4)$$

where the hysteresis factor χ is given as

$$\chi = \frac{3K(1 - c_e^2)}{4\dot{\delta}^{(-)}} \quad (5)$$

where $\dot{\delta}^{(-)}$ is initial impact velocity and c_e is coefficient of restitution. By substituting (4) and (5) into Eq. (1), the normal contact force can be expressed as

Fig. 1 Relative penetration depth during the impact between two spheres



$$F_N = K \delta^n \left[1 + \frac{3(1 - c_e^2)}{4} \frac{\dot{\delta}}{\dot{\delta}^{(-)}} \right] \quad (6)$$

A major drawback of this model is the dependency of the hysteretic damping factor χ on the impact velocity $\dot{\delta}^{(-)}$. It can be shown that this model underestimates the amount of dissipated energy, which results in a higher velocity after impact.

2.2 Flores Contact Force Model

Based on the work of Lankarani and Nikravesh, Flores proposed a contact force model to capture the contact force induced due to impact between two spherical bodies of isotropic material. As discussed in Sect. 2.1, the Lankarani–Nikravesh contact force model is well suited when the coefficient of restitution is closer to one, i.e. impact is almost elastic. Flores developed a contact force model, which is well suited for soft materials than for wide range of values of coefficient of restitution. According to Flores, the contact force is given as

$$F_N = K \delta^n + \chi \dot{\delta} \quad (7)$$

where the hysteresis factor χ is given as

$$\chi = \frac{8K(1 - c_e)}{5c_e \dot{\delta}^{(-)}} \quad (8)$$

By substituting Eq. (8) into Eq. (7), the normal contact force can be expressed as

$$F_N = K \delta^n \left[1 + \frac{8(1 - c_e)}{5 c_e} \frac{\dot{\delta}}{\dot{\delta}^{(-)}} \right] \quad (9)$$

where the generalized parameter K can be evaluated by Eqs. (2) and (3), c_e is the restitution coefficient, $\dot{\delta}$ is the relative penetration velocity and $\dot{\delta}^{(-)}$ is the initial impact velocity.

2.3 Illustrative Example

In this section, impact between two spheres is analyzed [6] by using the abovementioned contact force models. A sphere with radius $R_i = 9.5$ mm and mass $m = 0.145$ kg collides on a fixed concave surface of radius $R_j = -10$ mm with an initial velocity $\dot{\delta}^{(-)} = 5$ m/s. The materials in contact have the properties of steel with Young's modulus $E = 206$ GPa, Poisson's ratio $\nu = 0.3$ and coefficient of restitution $c_e = 0.95$. Figure 2 shows the influence of coefficient of restitution on the contact force between two impacting spheres, which shows that magnitude of contact force decreases and contact duration increases with decrease in the value of coefficient of restitution. Figure 3 shows the influence of the same on contact force-indentation, which shows more loss in energy associated with smaller values of coefficient of restitution for a typical impact.

3 Vibratory Response of System with Linear Spring and Damper by Classical Approach

In this section, a spring mass and damper under impact are used as an illustrative example to demonstrate how to obtain response of a spring mass damper system by the classical approach. Figure 4 shows a block of mass M resting on the floor with

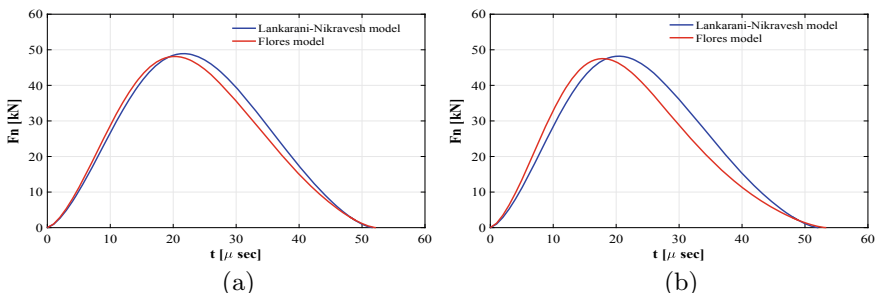


Fig. 2 Influence of the coefficient of restitution on the contact force between two spheres for **a** $c_e = 0.8$; **b** $c_e = 0.7$

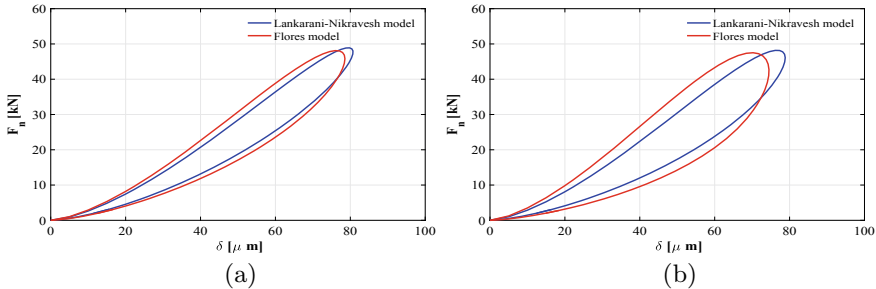


Fig. 3 Influence of the coefficient of restitution on hysteresis loop (contact force versus indentation) for **a** $c_e = 0.8$; **b** $c_e = 0.7$

a buffer spring of stiffness k and damper of damping coefficient c connected to a wall. A sphere of mass m is thrown on vertical face of the mass with velocity u . The coefficient of restitution of the impact is c_e . The first part of the phenomenon is a direct central impact between block and the sphere. If V and v are velocities of M and m immediately after the impact, then

$$mu = MV + mv \quad (10)$$

$$\text{and} \quad V - v = c_e u \quad (11)$$

Solving Eqs. (10) and (11),

$$V = \frac{(1 + c_e) mu}{M + m}, \quad v = \frac{(m - c_e M) u}{M + m} \quad (12)$$

Equation of motion of the system shown in Fig. 4 is

$$M\ddot{x} + c\dot{x} + kx = 0 \quad (13)$$

Equation (13) is solved using the adaptive step size Runge–Kutta fourth order method with zero and V as the initial condition.

4 Vibratory Response of System with Linear Spring and Damper Using Contact Force Models

In this section, response of the system shown in Fig. 4 is obtained by using contact force models, as described in Eqs. (6) and (9). The corresponding equation of motion of the system is

$$M\ddot{x} + c\dot{x} + kx = F_N \quad (14)$$

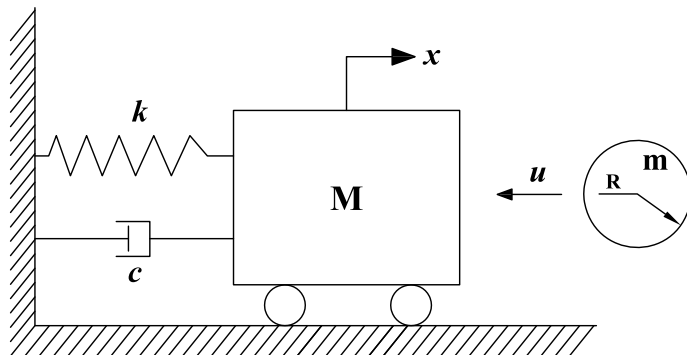


Fig. 4 Spring mass and damper system with linear spring and damper under impact

Table 1 Parameters used in the dynamic simulation of a system with linear spring and damper under impact

Parameter		Value
M	Mass of block (kg)	10
m	Mass of impacting sphere (kg)	1
R	Radius of impacting sphere (m)	0.05
u	Velocity of sphere just before impact (m/s)	10
k	Spring coefficient (N/m)	6.4×10^5
c	Damping coefficient (Ns/m)	100
E	Young's modulus (GPa)	207
ν	Poisson's ratio	0.3
K	Contact stiffness ($N/m^{1.5}$)	3.39×10^{10}

where F_N is the contact force as described by Eqs. (6) and (9). Figures 5 and 6 show response of the system under impact obtained by the Lankarani–Nikravesh model and the Flores model, respectively, for different values of coefficient of restitution. Dimensions and inertia properties of each body are listed in Table 1.

5 Vibratory Response of a System with Nonlinear Spring and Damper Using Contact Force Models

In Fig. 7, the block of mass M is attached by nonlinear spring and damper [7], where $f_k(x)$ and $f_c(x, \dot{x})$ are nonlinear spring force and damping force, respectively.

The forces can be written as follows:

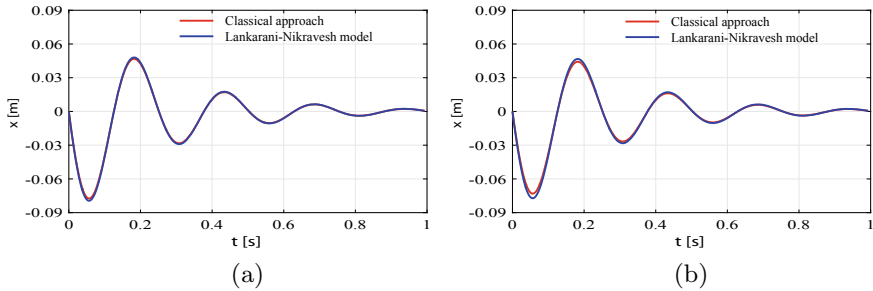


Fig. 5 Response (displacement versus time) of spring mass and damper system under impact using the Lankarani–Nikravesh model for **a** $c_e = 0.8$; **b** $c_e = 0.7$

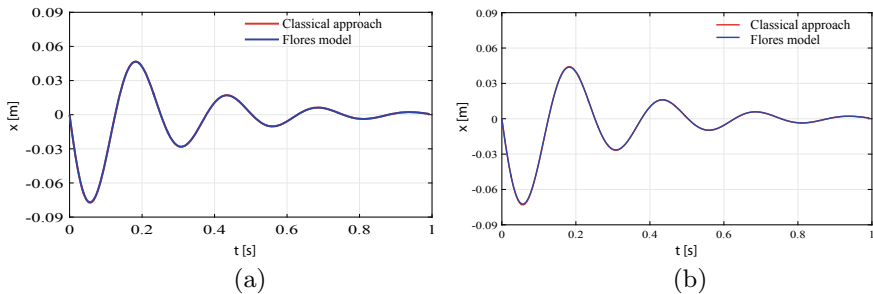
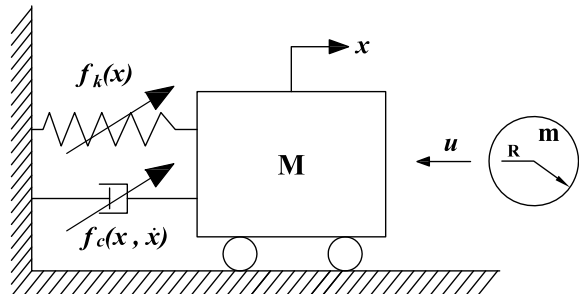


Fig. 6 Response (displacement versus time) of spring mass and damper system under impact using the Flores model for **a** $c_e = 0.8$; **b** $c_e = 0.7$

Fig. 7 Spring mass and damper system with linear spring and damper



$$f_k(x) = k_1x + k_2x^2 + k_3x^3 \quad (15)$$

$$f_c(x, \dot{x}) = c_1\dot{x} + c_2x\dot{x} + c_3x^2\dot{x} \quad (16)$$

where k_1 and c_1 represent linear stiffness and linear damping, k_i and c_i ($i = 2, 3$) are nonlinear stiffness and damping coefficient, respectively. Applying Newton's second law of motion to the model in Fig. 7, the differential equation of vibration of the system can be written as

Table 2 Parameters used in the dynamic simulation of the system with nonlinear spring and damper under impact

Parameter		Value
M	Mass of block (kg)	250
m	Mass of impacting sphere (kg)	10
R	Radius of impacting sphere (m)	0.1
u	Velocity of sphere just before impact (m/s)	15
$k_1/k_2/k_3$	Spring coefficient (N/m)/(N/m ²)/(N/m ³)	$1.2 \times 10^5/30 \times 10^4/2.0 \times 10^5$
$c_1/c_2/c_3$	Damping coefficient (Ns/m)/(Ns/m ²)/(Ns/m ³)	200/180/50
E	Young's modulus (GPa)	207
v	Poisson's ratio	0.3
K	Contact stiffness (N/m ^{1.5})	4.8×10^{10}

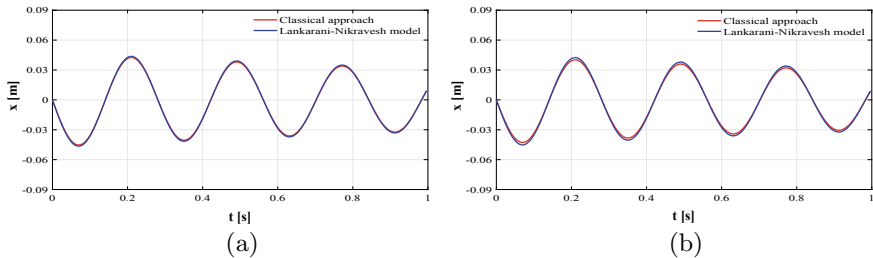


Fig. 8 Response (displacement versus time) of the system with nonlinear spring and damper under impact using the Lankarani–Nikravesh model for **a** $c_e = 0.8$; **b** $c_e = 0.7$

$$M\ddot{x} + f_k(x) + f_c(x, \dot{x}) = F_N \quad (17)$$

Submitting Eqs. (15) and (16) into Eq. (17), the equation of motion can be rewritten as

$$M\ddot{x} + k_1x + k_2x^2 + k_3x^3 + c_1\dot{x} + c_2x\dot{x} + c_3x^2\dot{x} = F_N \quad (18)$$

where F_N is the contact force as described by Eqs. (6) and (9). Dimensions and inertia properties of each body are listed in Table 2.

Response of the system shown in Fig. 7 is obtained by the classical approach as well as by using contact force models and plotted in Figs. 8 and 9.

In order to better understand the dynamic effect of the contact force model in the response of vibratory system, two dimensionless amplitude amplification parameters (AAP) are defined for displacement and for velocity of the block [8]. The amplification parameter for the displacement is expressed by

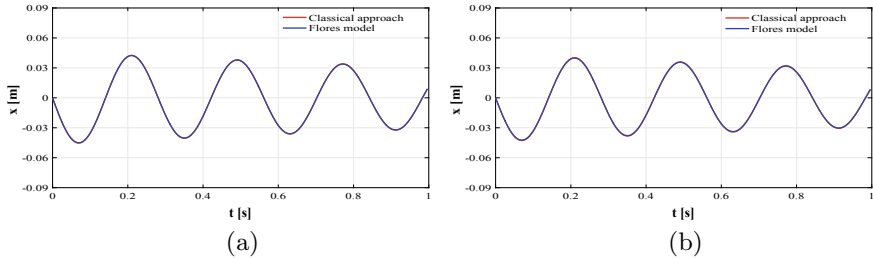


Fig. 9 Response (displacement versus time) of the system with nonlinear spring and damper under impact using the Flores model for **a** $c_e = 0.8$; **b** $c_e = 0.7$

Table 3 Amplitude amplification parameters for different values of coefficient of restitution

c_e	Lankarani–Nikravesh model				Flores model			
	Linear		Nonlinear		Linear		Nonlinear	
	AAP (x)	AAP (v)	AAP (x)	AAP (v)	AAP (x)	AAP (v)	AAP (x)	AAP (v)
1.0	-0.001	0.04	$-4.43e-05$	0.0103	-0.0019	0.04	-0.07	-0.06
0.9	-0.69	-0.64	-0.69	-0.68	0.31	0.36	0.25	0.26
0.8	-2.61	-2.56	-2.62	-2.60	0.63	0.68	0.58	0.59
0.7	-5.64	-5.59	-5.65	-5.63	0.98	1.04	0.94	0.96
0.6	-9.76	-9.70	-9.78	-9.74	1.41	1.47	1.39	1.40
0.5	-15.01	-14.95	-15.05	-15.00	1.96	2.03	1.95	1.95

$$\text{AAP} (x) = \frac{x_c - x_f}{x_c} \times 100 \quad (19)$$

where x_c and x_f are maximum displacement of the block obtained by the classical approach and using the contact force model, respectively. Similarly, the amplification factor for velocity can be written as

$$\text{AAP} (v) = \frac{v_c - v_f}{v_c} \times 100 \quad (20)$$

where v_c and v_f are maximum velocity of the block obtained by the classical approach and using the contact force model. Amplitude amplification parameters are estimated by using the data from Figs. 5, 6, 8 and 9. Table 3 shows amplitude amplification parameters obtained for a system with linear as well as nonlinear spring and damper using the Lankarani–Nikravesh and the Flores model.

6 Results and Discussion

Data from Table 3 reveals that when compared with the response obtained by the classical approach, the Lankarani–Nikravesh model overestimates the response. As the coefficient of restitution varies from 1 to 0.5, the variation in response goes on increasing up to 15 percent. This is obvious due to the fact that the said model underestimates the amount of dissipated energy, which results in a higher velocity after impact.

In comparison with the response obtained by the classical approach, the Flores model underestimates the response of the vibratory system. For coefficient of restitution values used in this work, the percent variation in the response goes on increasing when the coefficient of restitution varies from 1 to 0.5. The response obtained by using the Flores model is much closer to that obtained by the classical approach. This is expected because the contact stiffness (K) between impacting bodies is sufficiently large.

7 Summary

The application of the existing approach for modeling impact is presented and discussed in this paper. In particular, the influence of coefficient of restitution on dynamic response of spring mass and damper system under impact using contact force models is studied. Further investigation is being carried out to formulate design guidelines on the use of a relevant contact force model to design a mechanical system involving impact.

References

1. Rao, S.S.: *Mechanical Vibrations*, 2004. Pearson Education (1990)
2. Ghosh, A.: *Introduction to Dynamics*. Springer, Singapore (2018)
3. Lankarani, H.M., Nikravesh, P.E.: A contact force model with hysteresis damping for impact analysis of multibody systems (1990)
4. Flores, P., Machado, M., Silva, M.T., Martins, J.M.: On the continuous contact force models for soft materials in multibody dynamics. *Multibody Sys. Dyn.* **25**(3), 357–375 (2011)
5. Hertz, H.: On the contact of solids—on the contact of rigid elastic solids and on hardness. *Misc. Pap.* 146–183 (1896)
6. Schwab, A., Meijaard, J., Meijers, P.: A comparison of revolute joint clearance models in the dynamic analysis of rigid and elastic mechanical systems. *Mech. Mach. Theory* **37**(9), 895–913 (2002)
7. Zhou, S., Song, G., Sun, M., Ren, Z.: Nonlinear dynamic analysis of a quarter vehicle system with external periodic excitation. *Int. J. Non-Linear Mech.* **84**, 82–93 (2016)
8. Flores, P., Ambrósio, J., Claro, J.P., Lankarani, H.: Dynamic behaviour of planar rigid multi-body systems including revolute joints with clearance. *Proc. Inst. Mech. Eng., Part K: J. Multi-Body Dyn.* **221**(2), 161–174 (2007)

Failure Behaviour of a Thin Domed Steel Disc with and without Scores Under a Pressure Impulse



K. Gopinath, V. Narayananamurthy, and Y. V. D. Rao

1 Introduction

Clamped circular flat metallic plates subjected to lateral loads were extensively studied in literature to understand the failure phenomenon during quasi-static and impulsive loads. A comprehensive review by Nurick and Martin [1] compares the theoretical and experimental results of fully clamped flat circular plates subjected to impulsive loads. They observed and reported failure of the plates in three different modes, viz., (1) failure mode-1 where disc exhibits large plastic deformation under low impulse levels; (2) failure mode-2 when impulse increases to a threshold limit and accompanied by the observation of tensile failure at the boundary or central area depending on the impulse threshold; and (3) failure mode-3, upon further increase in impulsive load where transverse shear occurs at the boundary of the disc. Petalling can only be observed under localized impulsive loads [1–4].

The metallic discs in the form of thin circular plates, subjected to fluid pressure at quasi-static or at varying loading rates, are used in safety pressure relief systems. They are designed to fail at the exceedance of a pre-determined pressure. These discs are called as rupture discs [5]. The maximum pressure at which a rupture disc operates is called as a limit pressure. Gao et al. [6] proposed a theoretical formulation based on the strength coefficient of material to obtain the limit pressure of rupture disc. The rupture discs which are domed such that the fluid pressure is acting on

K. Gopinath · V. Narayananamurthy (✉)
Research Centre Imarat, Hyderabad 500069, India
e-mail: v.narayananamurthy@rcilab.in

K. Gopinath
e-mail: gopinath.k@rcilab.com

K. Gopinath · Y. V. D. Rao
BITS Pilani, Hyderabad 500078, India
e-mail: yvdrao@hyderabad.bits-pilani.ac.in

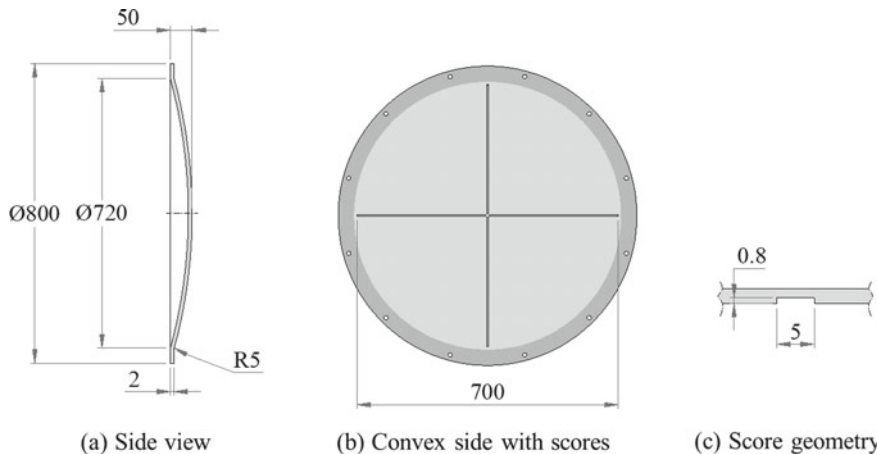


Fig. 1 Geometry of the domed disc with score details (all dimensions in mm)

the concave side of the disc are called as forward domed rupture discs. This enables them to make out of comparatively thin sheets for a given burst pressure or failure pressure. Commonly, they are featured with well-defined scores in a particular pattern to concentrate the fracture energy and initiate the failure along the pre-determined direction [7].

Colombo et al. [8], Jeong et al. [9] and Gong et al. [10] have studied the effect of these scores or grooves pattern on the failure of the rupture disc. Coincidentally, all existing research on failure of rupture discs assumed the four-petal pattern without stating any specific reason. This paper attempts to numerically simulate the deformation and failure behaviour of forward domed rupture disc, with rectangular scores at a high impulse loading rate of 500 MPa/s, adopting a visco-plastic, and Johnson–Cook (J-C) constitutive and damage models. This paper helps to understand the effect of score pattern on the failure of the rupture disc in underlying selection of a four-petal pattern.

2 Geometry, FE Model, Material and Damage Models

The details of geometry, FE model with loads and boundary conditions, material and damage models employed in numerical simulations are discussed in this section.

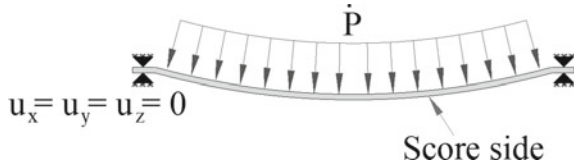


Fig. 2 Loads and boundary conditions

2.1 Geometry

The domed thin metallic disc considered in the present study is shown in Fig. 1. The disc is made of S235 JR structural steel having 2 mm uniform thickness. Rectangular scores or grooves of dimensions 5 mm wide and 0.8 mm depth are provided on the convex side of the disc. The impulsive pressure load is applied on its concave side as shown in Fig. 1. The dome height is 50 mm, its outer diameter is 800 mm and the pressure acts within the diameter of 720 mm. The flat annular portion with a radial distance of 40 mm from the outer diameter is constrained in all degrees of freedoms as shown in Fig. 2, as it will be attached to the pressure chamber using bolted joint with a sealing gasket.

2.2 FE Model

The geometry considered for FEA consist of a full model of domed disc. It is discretized using C3D8R-hexahedral elements having 8 node with single point integration, in ABAQUS Explicit [11] FEA code using a Lagrangean approach. A total number of 1,301,878 elements are used. The model for FEA is shown in Fig. 3. A minimum element size of 0.5 mm is adopted based on mesh convergence studies. All nodal degrees of freedom are constrained at the extremely flat annular portion having outer 40 mm radial distance. A pressure impulse at the rate of 500 MPa/s is applied for a duration of 1 s.

2.3 Material and Damage Models

The constitutive behaviour accounting large strain, large variation in strain rates and thermal softening in the material are captured through a visco-plastic based Johnson–Cook (J-C) material model [12, 13]. The yield stress is given by the following expression:

$$\sigma_y = [A + B\bar{\varepsilon}_p^n][1 + C\ln(\dot{\varepsilon}^*)][1 - (T^*)^m] \quad (1)$$

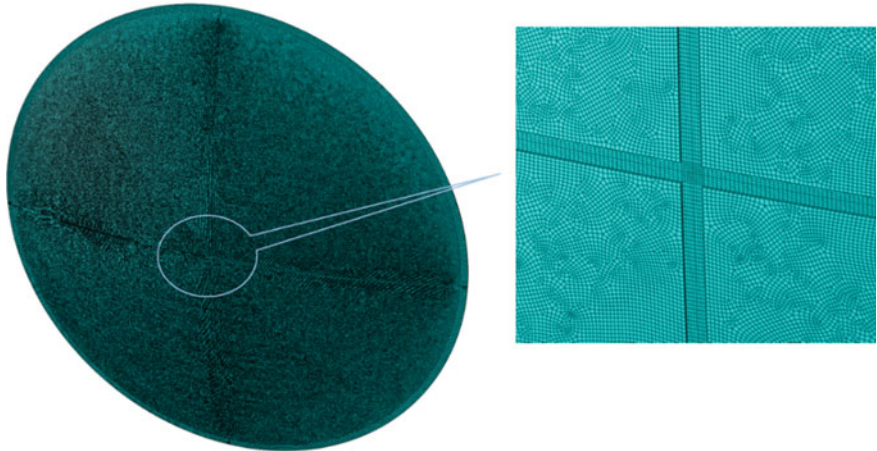


Fig. 3 FE model of domed disc with 4 scores

where

$$\dot{\varepsilon}^* = \frac{\dot{\varepsilon}_p}{\dot{\varepsilon}_0}; \text{ and } T^* = \frac{T - T_r}{T_m - T_r} \quad (2)$$

in which A is the initial yield stress, B is the strain hardening coefficient and n is the strain hardening exponent, $\bar{\varepsilon}_p$ is the effective plastic strain, $\dot{\varepsilon}_p$ is the effective plastic strain rate, $\dot{\varepsilon}_0$ is the user defined reference strain rate (taken as 0.0001 s^{-1}) and C is the strain rate coefficient. This equation shows that the yield model is valid from room temperature T_r to the melting temperature T_m . The thermal softening exponent is given by m .

$$\varepsilon_f = [D_1 + D_2 \exp(D_3 \sigma^*)][1 + D_4 \ln(\dot{\varepsilon}^*)][1 + D_5 T^*] \quad (3)$$

Here, ε_f = equivalent plastic strain at fracture; σ^* = stress tri-axiality; $\dot{\varepsilon}^*$ = ratio of effective plastic strain rate to reference strain rate; and D_1, \dots, D_5 are empirical material parameters which have to be calibrated for each material. An element is supposed to fail if the damage parameter D reaches the value of 1 where D is the ratio of the effective plastic strain to the equivalent failure strain.

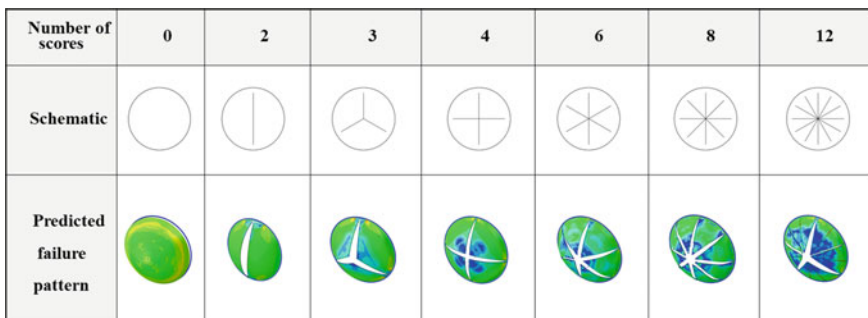
The material and damage parameters provided in Eqs. (1) and (3), used in simulations are provided in Table 1 and are taken, respectively, from [8] and [14] for the selected steel material. Here, E = elastic modulus; μ = Poisson's ratio and ρ = material's density. The material and damage constants taken from the literature are slightly fine-tuned during simulation trials to match with standard experimental results.

Table 1 Elastic and material constants in J-C material and damage models

Elastic parameters	E (MPa)	μ	ρ (kg/m ³)		
	210,000	0.3	7850		
				C	m
J-C material model	A (MPa)	B (MPa)	n		
	252	520	0.638	0.046	1.0
J-C damage model	D_1	D_2	D_3	D_4	D_5
	0.05	0.8	-0.44	-0.042	0

3 Numerical Simulation of Failure Behaviour of Domed Metallic Disc

A series of numerical simulations are carried out on the domed steel disc using the FE model and material and damage models provided in Sect. 2. The simulations are performed in ABAQUS Explicit [11] FEA code with varying number of scores to study the failure behaviour of domed disc with and without any score. The failure pattern of disc with different number of scores is studied as shown in Fig. 4. When there are no scores, the disc failure is observed near clamped boundary. This failure near boundary is due to the increased magnitude of stress near boundary. When scores are implemented, the first failure is observed at the centre of the disc which has minimum thickness due to score. Then this failure is propagated through the score till the end of score geometry.

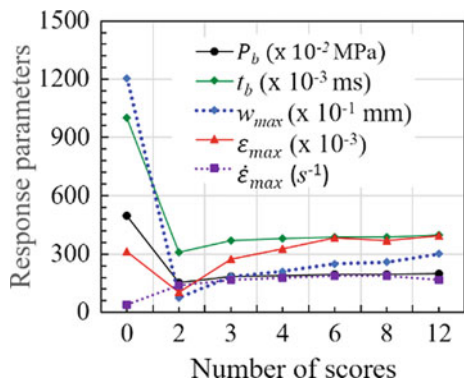
**Fig. 4** Predicted failure pattern without and with number of scores in the disc

4 Results and Discussion

A number of burst parameters such as burst pressure P_b , time of burst t_b , maximum central deflection w_{max} , strain ε and strain rate $\dot{\varepsilon}$, with increase in number of scores, i.e. number of preformed petals are studied from the results of several numerical simulations. These parameters as a function of number of scores are presented in Fig. 5.

It can be observed that when no scores are there in the disc, the values of all the burst parameters are relative high except strain rate as compared to the disc with a given number of scores. The disc fails as a whole dome dish near the circumferential fixid region. The burst pressure is about 5 MPa, the burst time is 0.01 s, the maximum central deflection before burst is 120 mm, the failure strain is 0.3 and the strain rate at failure is 40 s^{-1} . These values reduce drastically when two numbers of radial scores along the diameter are introduced. As number of scores is increased from 2 to 4, the values of burst time, burst pressure and the strain rate increase slowly up to 4 scores and thereafter they remain almost same irrespective of increase in number of scores. This indicates that the minimum number of scores to achieve a stabilized value in most of the burst parameters is 4. The failure strain increases from 0.1 to 0.4 when number of scores is increased from 2 to 6 and thereafter it remains almost at 0.4 strain only even when the number of scores is increased to 8, 10 or 12. Exception is the central deflection alone which increases steadily from 5 to 30 mm as number of scores is increased from 2 to 12. This study reveals that a number of scores either 2, 3 or 4 may be preferred as far as the low burst parameters are concerned but the selection of a particular number of scores between 2 and 4 depends on the choice of a designer in consideration with other parameters not mentioned so far, such as the minimum obstruction to the instantaneously released pressure, minimum geometry of the opened or busted disc in the form of petals, and machining easiness.

Fig. 5 Variation of different burst parameters with increase in number of scores



5 Conclusion

The failure behaviour of domed steel thin disc with number of scores ranging from 0 to 12, provided along radius of the disc has been studied using series of non-linear explicit FEA simulations adopting J-C material and damage models. Different burst response parameters such as burst pressure, burst time, strain at burst, strain rate at failure, and central deflection up to burst have been analysed with increase in number of scores, keeping the score geometry and disc geometry as constant. All the burst parameters are consistent for scores above 3 numbers. Also, higher number of scores doesn't always guarantee the failure of disc along all grooves. Minimum of 4 scores generates 4 petals during burst and gives consistent failure pattern with minimum machining requirement in formation of scores.

References

1. Nurick, G.N., Martin, J.B.: Deformation of thin plates subjected to impulsive loading—a review: part I: theoretical considerations. *Int. J. Impact Eng.* **8**(2), 159–170 (1989)
2. Nurick, G.N., Martin, J.B.: Deformation of thin plates subjected to impulsive loading—a review part II: experimental studies. *Int. J. Impact Eng.* **8**(2), 171–186 (1989)
3. Teeing-Smith, R.G., Nurick, G.N.: The deformation and tearing of thin circular plates subjected to impulsive loads. *Int. J. Impact Eng.* **11**(1), 77–91 (1991)
4. Yuen, S.C.K., Nurick, G.N., Langdon, G.S., Iyer, Y.: Deformation of thin plates subjected to impulsive load: part III—an update 25 years on. *Int. J. Impact Eng.* **107**, 108–117 (2017)
5. Somayajulu, D., Narayananamurthy, V.: Analysis of rupture disc. In: Proceedings of Indian Conference on Applied Mechanics (INCAM 2017). MNNIT Allahabad, pp. 1–7 (2017)
6. Gao, G., Wang, G., Ding, X., Chen, J.: Limit pressure of rupture discs found on tensile instability condition. *Adv. Mater. Res.* **97–101**, 296–300 (2010)
7. Smith, P., Zappe, R.W.: Valve Selection Handbook, 5th edn. Gulf Professional Publishing, UK (2004)
8. Colombo, M., Martinelli, P., di Prisco, M.: Validation of a computational approach to predict bursting pressure of scored steel plates. *Exp. Mech.* **54**(9), 1555–1573 (2014)
9. Jeong, J.Y., Jo, W., Kim, H., Baek, S.H., Lee, S.B.: Structural analysis on the superficial grooving stainless-steel thin-plate rupture discs. *Int. J. Precis. Eng. Manuf.* **15**(6), 1035–1040 (2014)
10. Gong, L., Duan, Q., Liu, J., Li, M., Jin, K., Sun, J.: Effect of burst disk parameters on the release of high-pressure hydrogen. *Fuel* **235**, 485–494 (2019)
11. Dassault System's Simulia Corp: ABAQUS 2018 User's Manual. Providence, RI, USA (2018)
12. Johnson, G.R., Cook W.H.: A constitutive model and data from metals subjected to large strains, high strain rates and high temperatures. In: Proceedings of 7th International Symposium on Ballistics. The Hague Netherlands, pp. 541–547 (1983)
13. Johnson, G.R., Cook, W.H.: Fracture characteristics of three metals subjected to various strains, strain rates, temperatures and pressures. *Eng. Fract. Mech.* **21**(1), 31–48 (1985)
14. Banerjee, A., Dhar, S., Acharyya, S., Datta D., Nayak, N.: Determination of Johnson cook material and failure model constants and numerical modelling of Charpy impact test of armour steel. *Mater. Sci. Eng. A* (640), 200–209 (2015)

Development of Shape Memory Alloy (SMA) Based Hold-Down and Release Mechanism for Space Applications



Harshkumar Patel , Hemant Arora , Shashikant Joshi , and Sudipto Mukherjee

1 Introduction

After satellites are launched by launch vehicles, several appendages, certain antennas, and solar arrays are required to be separated successfully from the main body of the satellite in orbit for intended functions. The separation device has both functions to secure the payload against the launch loads and to release the payload on-orbit at an appropriate time while minimizing shock. Most existing release devices such as pyrotechnics device which possesses minimum weight, instantaneous operation, and requires little input energy. However, these systems induce a high level of shock which is not desirable for electronic and optical subsystems positioned nearby and these types of devices use an explosive to initiate combustion to generate release force which can be used for one time only [1]. Therefore, better holding and release devices have become an important research topic in the field of spacecraft.

Shape Memory Alloy (SMA) works on the principle of shape memory effect (SME). In SME previously deformed alloy can be made to recover its original shape simply by heating. Material is brought to the austenite phase at high temperature by heating and in the martensite phase at low temperatures by cooling. The maximum deformation generated by SME is limited to 8%. When the alloy is stressed and it returns to the original shape without heating then it is called Super Elasticity (SE). [2]. Fan et al. developed a release mechanism using SMA. The preload capacity of the designed mechanism was limited to 800 N which requires a high amount of current to generate shape memory effect [3]. Tuszyński et al. (2002) developed

H. Patel · S. Joshi

Institute of Technology, Nirma University, Ahmedabad, India

H. Arora

EMDD, Space Applications Centre, ISRO, Ahmedabad, India

S. Mukherjee

Department of Mechanical Engineering, IIT Delhi, New Delhi, India

the release mechanism using NiTinol, but having a high response time [4]. These devices can provide a low-shock and no-contamination having good response time and high load capacity [5–7]. Therefore, efforts are made in the realization of a release mechanism for space application with advantages of fast release time, simple mechanism configuration, lightweight, produces a low level of shocks, reusable to confirm operational reliability during ground testing, and easy to reset.

2 SMA-Based Hold-Down and Release Mechanism (HDRM)

2.1 Design Configuration

The proposed mechanism of a non-explosive release mechanism is based on a contraction of SMA wire by heating which produces sufficient force to eject the nut. The configuration of the proposed device is shown in Fig. 1. It consists of various parts as ball stopper, base, core, latch 1, latch 2, mounting plate, nut segment, ball, compression spring, bias spring, Teflon bush 1, Teflon Bush 2, U-Clamp. The material of most of the components is considered as Al 6061 alloy except balls, ejector nut which is made of Stainless Steel, and springs are made of spring steel. Also, bushes of Teflon material are used to electrically insulate the SMA wire from the HDRM body.

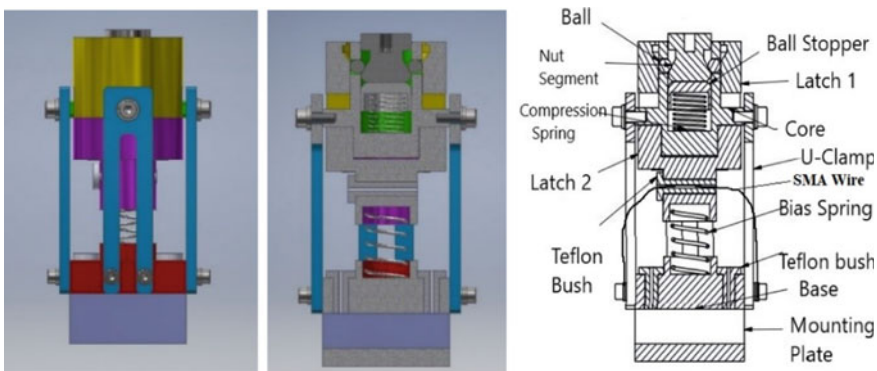


Fig. 1 CAD Schematic of the HDRM assembly

2.2 Working Principle

The working principle of the release mechanism is based on the shape memory effect of the SMA wire used for the ejector release mechanism. The trigger operation for the bolt release is performed by heating of SMA wire to austenitic temperature. Heat is generated by an electric charge using a DC power source. The SMA wire shrinks to its original shape by heating it to more than 60 °C (the austenite finish temperature) using a DC power source. The ends of the SMA wire are fixed to the base and connected to terminals of the power supply.

When SMA wire shrinks, it pulls the latch assembly downwards and the bias spring compresses. As the latch assembly moves downwards, the compression spring which is already in a compressed condition, will expand and pushes the ball stopper and nut segment. The ball moves inwards and the nut segment is released. When the SMA wire is cooled down it regains its normal shape. Therefore, the bias spring expands, and latch assembly comes back to the initial position. The mechanism can be reset by just pressing the nut segment from the top. The process of resetting is happened with the compression of the bias spring by a push force of the nut and adjusting the balls in the arresting place available on the nut which generates the holding force.

3 Design Calculations

3.1 Free Body Diagram (FBD) of Various Components

Free body diagrams are generated for each component for a better understanding of forces due to friction, spring stiffness, and pull a load. FBD of the Nut segment, ball, and the latch is shown in Fig. 2. Equations formulated with the static equilibrium of forces as shown by Eqs. (1), (2), (3), and (4).

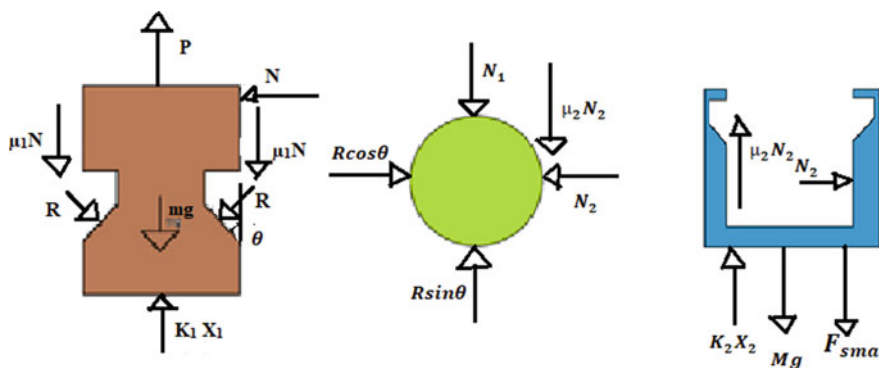


Fig. 2 Free body diagrams

Horizontal Equations:

$$R \cos \theta = N_2 \quad (1)$$

Vertical Equations:

Here,

$\mu_1 = \text{Negligible}$, so $\mu_1 N = 0$, the weight of the ball is negligible.

$$K_1 X_1 = mg + 2 \times R \sin \theta - P \quad (2)$$

$$R \sin \theta = N_1 + \mu_2 N_2 \quad (3)$$

$$F_{\text{sma}} = K_2 X_2 + \mu_2 N_2 - Mg \quad (4)$$

Nomenclature

m	Mass of Nut segment.
g	Acceleration due to gravity.
μ_1	Co-efficient of friction between Nut segment and Core.
N	Reaction by Core.
K_1	Stiffness of compression spring.
N_2	Normal reaction between ball and Latch Assembly.
μ_2	Co-efficient force between ball and Latch Assembly.
K_2	Stiffness of bias spring.
X_1	Initial Compression length of compression spring.
R	Reaction by ball.
θ	Taper angle of the Nut Segment notch.
N_1	Normal reaction between ball and core.
X_2	Final compression length of bias spring.
M	Mass of Latch Assembly.
F_{SMA}	Force exerted by SMA.

3.2 Design of Helical Springs

There are two springs used in this configuration as shown by Fig. 1. Helical Springs are chosen and designed based on the deflection requirement.

As we know, Deflection of Helical Spring,

$$\delta = \frac{8 \times W \times D^3 \times n}{G \times d^4} \quad (5)$$

Table 1 Spring parameters

Sr. no.	Parameters	Compressed spring	Bias spring
1	Material	Spring steel	Spring steel
2	Mean coil diameter (mm)	10	11
3	Spring wire diameter (mm)	1	1
4	Spring free length (mm)	20.7	20
5	Deflection (mm)	9.7	4.3
6	No. of turns	7	7
7	Modulus of rigidity (GPa)	79.3	79.3
8	Spring stiffness (N/mm)	1.416	1.064

Nomenclature

- δ Deflection.
- w Load.
- D Mean Diameter of Spring.
- n Number of turns.
- G Modulus of rigidity.
- d Wire diameter of Spring.

Design parameters of compression spring and bias spring are mentioned in Table 1.

4 Modal Analysis

Modal analysis is carried out to compute the natural modes of HDRM to meet with Space environmental test level specifications which define the targeted natural frequency of any space-based payload subsystem to be at least 100 Hz to keep away the design from satellite resonant modes. Modal analysis has been carried out using Autodesk Inventor professional 2018. Boundary conditions are formulated by locking the interface points. Predicted modes with natural frequencies of the system are shown in Fig. 3. The first fundamental mode is predicted at 159 Hz which proves its worthiness for application of space-based payload subsystem (Table 2).

Fig. 3 Simulated Mode Shape

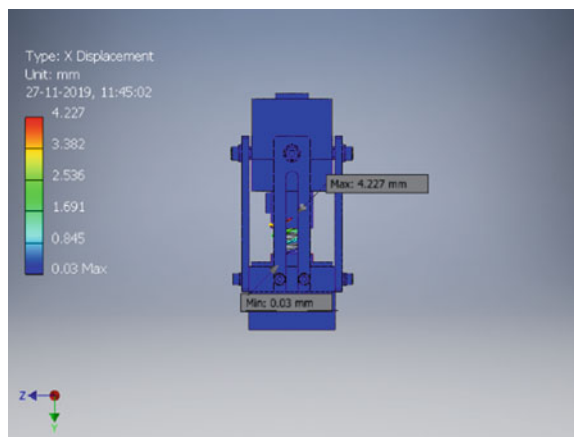


Table 2 Modal analysis result

Mode number	Frequency (Hz)
1	159.09
2	159.35
3	187.99
4	213.35
5	269.48

5 Design Configuration of SMA Wire

5.1 SMA Wire Selection

NiTinol wire (Ni–Ti alloy) [8] is considered to be used for HDRM. Basic requirement is to generate a counterforce to compress a bias spring which is requires nearly 20 N force in present configuration to deflect by 5 mm. For characterization, three-wire diameters (0.5, 1, and 2 mm) are taken of equal length of 100 mm as required in HDRM configuration. One end of the wire is kept fixed and a weight of 2 kg is mounted on other ends. A constant electrical energy of 2 W is supplied by connecting the two ends of wire to a DC power supply and measured the final contraction and response time of contraction are tabulated in Table 3 for all three-wire samples.

Table 3 Performance parameters of SMA NiTinol wire

Sr. no.	Wire size (mm)	Contraction (mm)	Response time (s)
1	0.5	5	4
2	1	3	130
3	2	0	–

It is clearly observed that no contraction made by 2 mm wire at the input energy. It requires more energy to show a quantitative deflection. 0.5 mm wire shows contraction of 5 mm at a quick response time of 4 s as compared to 1 mm wire. Therefore, meeting with the design requirement of quick operation, a 0.5 mm diameter wire is selected for the development of the release mechanism.

5.2 Actuation Force Measurement

NiTinol wire, when heated with an electrical charge by connecting to a DC power source, a contraction force is generated which is used as an actuation force to pull the latch component against the spring force. To compute this actuated force, an experiment is carried out by fixing one end of the wire and on the other end, variable masses are mounted. Current is kept constant. Contraction and response time parameters are observed with an increment of masses in steps of 500 g. It is clearly observed from the Table 4 that the wire is contracting by same amount of 5 mm at constant response time of 4 s even at higher load of 3000 g. As this wire is required to be used in ‘U’ shape loop, the actuation force generation by SMA wire will be double. For generating 5 mm contraction, the wire will produce nearly 60 N force which is almost three times the force required to compress bias spring by 5 mm (Table 5).

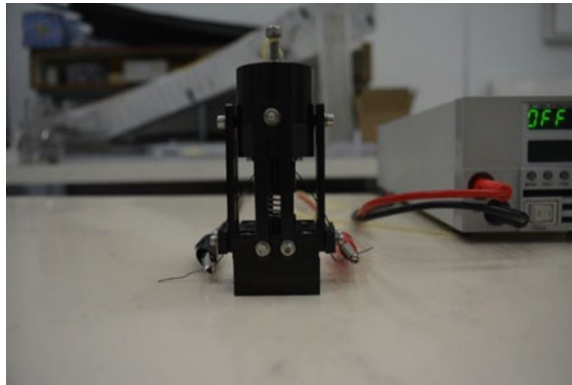
Table 4 SMA wire force calculation

Sr. no.	Mass (g)	Current (A)	Contraction (mm)	Response time (s)
1	500	2	5	4
2	1000	2	5	4
3	1500	2	5	4
4	2000	2	5	4
5	2500	2	5	4
6	3000	2	5	4

Table 5 Measured data of current versus release time

Sr. no.	Current (A)	Release time (s)
1	2.4	4
2	2.5	3
3	3.0	2
4	3.2	2
5	3.5	1

Fig. 4 Experimental setup of HDRM assembly



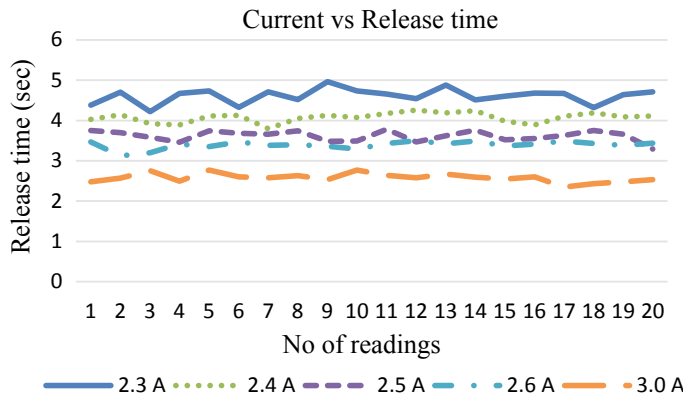
6 Test and Evaluation

6.1 Functional Test

All manufactured components are assembled as shown in Fig. 4. SMA wire is also stretched, routed and both ends are fixed to respective terminals. A DC power supply is connected with both terminals. An experiment conducted with a supply of variable current values and measured the response time for the release of ejector nut at no-load condition. It is observed that for quick operation, higher energy is required but operational reliability needs to be ensured for the usage of multiple numbers of cycles.

6.2 Operation Repeatability Test

An operational repeatability test is carried out to check the performance of HDRM for the number of operation cycles. For a particular current value, 20 number of measurements are taken. A total of 100 operation cycles are performed with 20 cycles at each current value. As this mechanism is targeted for operation in space for one time only but for evaluating the reliability of the mechanism, it is required to test several times on the ground before applying for space application. It is observed that the release time remains almost constant for a particular set of readings as shown in Fig. 5. This HDRM working perfectly for 100 cycles with less than 1% error in release time. This operation repeatability test confirms the adequate reliability of the mechanical system.

**Fig. 5** Repeatability test**Table 6** Preload test

Sr. no.	Mass (g)	Current (A)	Release time (s)
1	500	2.3	5
2	1000	2.3	4
3	1500	2.3	3
4	2000	2.3	3
5	2200	2.3	2
6	2500	2.3	1
7	3000	2.3	1

6.3 Functional Performance at Various Loads

In this testing, the current is kept constant and tensile load is applied by hanging masses to the ejector with a pulley arrangement. It is observed that as the preload increases, the response time of release decreases as shown in Table 6. The test results are useful in defining the tension load capacity of HDRM and its release time.

6.4 Tensile Load Test

The tensile load test is carried out to check the load-bearing capacity of the mechanism which will indicate the margin of safety with the requirement of hold-down force. The tensile test is carried out at a Universal testing machine (UTM) by fixing the base of HDRM and pull force applied at release nut as shown in Fig. 6. Tensile load

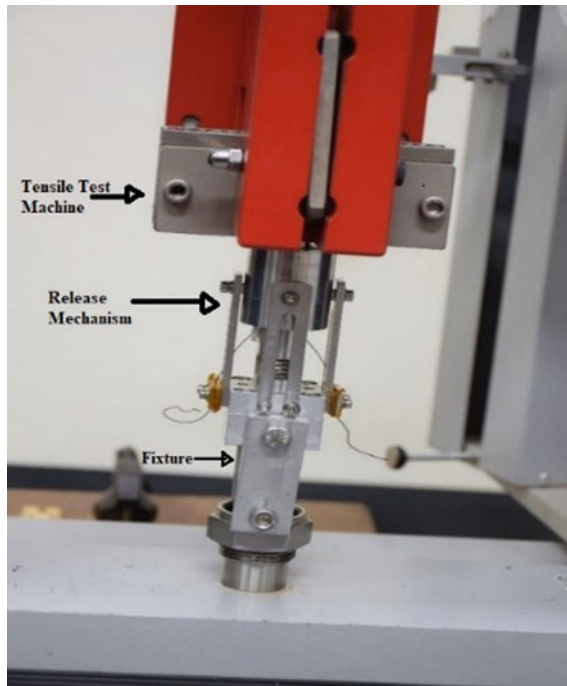


Fig. 6 Tensile test setup

is applied gradually by UTM and plotted the result till releasing of Nut. The tensile test result is as shown in Fig. 7. The release of the Nut was observed at a load of 1509.0 N which shows the ultimate load capacity of HDRM.

7 Conclusion

A non-explosive release mechanism based on shape memory alloy-based actuation methodology is designed, manufactured, assembled, and tested. The First Natural frequency of mechanism assembly is predicted at 159 Hz which is more than the targeted frequency of 100 Hz to avoid any resonant condition. Characterization of SMA wire is carried out for a selection of suitable diameter, current parameters, and various loads to ensure its suitability for the release mechanism. 0.5 mm diameter with a 100 mm length of SMA wire is selected and implemented in HDRM. Adequate reliability is ensured with multiple numbers of operation cycles at various loads. Load-bearing capacity is also checked for deciding the safe tension load to be applied to the ejector. Breaking Load bearing is observed at 1509 N which is almost 10 times more than the required tension is kept in hold-down mechanisms. The performance test shows the release time is 1 s at 3.5 A current. The performance of the mechanism

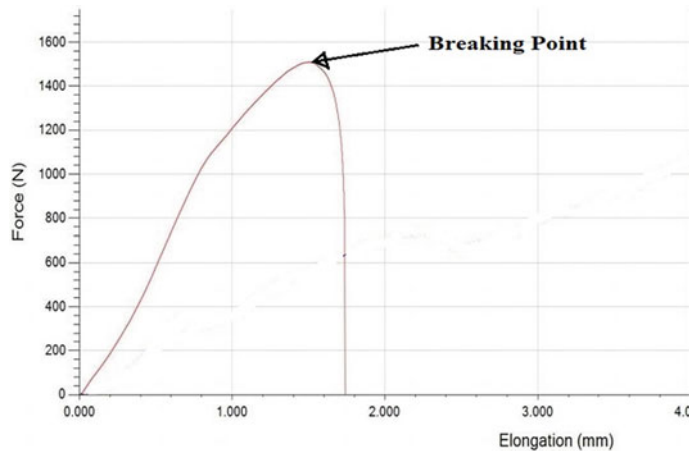


Fig. 7 Tensile test result

is found the same in various current settings. A total of 100 test operations are carried out with no degradation of parameters which confirm its operational reliability for space use. The other advantages of this mechanism are also formulated in terms of its simple, compact, and lightweight design which is easy to reset, quick response, and reusable. Therefore, SMA-based HDRM is demonstrated to be a prominent option for space application.

References

1. Fosness, E.R., Steven, S.J., Gammill, W.F.: AIAA Paper No. 2001-4601 (2001)
2. Bellouard, Y.: Mater. Sci. Eng. A **582**, 481–482, (2008)
3. Fan, L., Huang, H., Li, B.: Design of a locking-release device using shape memory alloy. In: Proceedings of the 2018 IEEE International Conference on Cyborg and Bionic Systems Shenzhen, China, October 25–27 (2018)
4. Tuszyński, A.: Alternatives to pyrotechnics—nitinol release mechanisms. In: Proceedings of the 36th Aerospace Mechanisms Symposium, Glenn Research Center, May 15–17, NASA/CP—2002-211506, pp. 137–140 (2002)
5. Vazquez, J., Bueno, J.: Non explosive low shock reusable 20 kN hold-down release actuator. In: Proceedings of the 9th European Space Mechanisms and Tribology Symposium, 19–21 September 2001, Liege, Belgium, Compiled by R.A. Harris, ESA SP-480, Noordwijk, Netherlands, ESA Publications Division, pp. 131–136 (2001)
6. Christiansen, S., Tibbitts, S., Dowen, D.: Fast acting non- pyrotechnic 10 kN separation nut. In: Space Mechanisms and Tribology, Proceedings of the 8th European Symposium, 29 September–1 October, 1999 in Toulouse, France, edited by D. Danesy, European Space Agency, ESA-SP, vol. 438, pp. 323–328 (1999)
7. Zhang, X., Yan, X., Yang, Q.: Design and experimental validation of compact, quick-response shape memory alloy separation device. J. Mech. Des. ASME Dig. Collection **136**, 011009 (2014)
8. SMA wires India, Nitinol Wire Shape Memory Alloys, Actuation finish temperature: - 55°C, Strain Recovery: 8 to 9%

Applicability of Low-Cost Duct-Shaped Wind Turbine for Domestic Purpose and Low Wind Speed



S. V. S. K. Prasad Raju, M. Govindaraju, and T. Satish Kumar

1 Introduction

Renewable energies are obtained from natural sources that renew themselves in a short amount of time compared to conventional energy sources which take millions of years to replenish. Renewable energies are most important to safeguard the environment from pollution and disasters like oil spills and for conserving natural resources and also to produce reliable sources of energy, as we are running short of coal and fuels. “Worldwide around 1.1 trillion tons of coal reserves are available, which would only last around another 150 years based on current consumption. And the oil and gas reserves are going to stay for 50 to 60 years based on current consumption rate” as quoted by the world coal association [1].

Types of renewable energies include solar, wind, hydro, and geothermal energy among them wind power is a very fast-growing and evolving energy currently. Throughout the world. Globally a 75% increase in wind power generation in the past two decades, this includes both onshore and offshore, increasing from 7.5 gigawatts (GW) in 1997 to 564 GW by 2018, based on IRENA’s data [2]. The kinetic energy from the wind is converted into electrical energy using the support of wind turbines. Wind energy rotates the turbine blades and thereby rotating the turbine connected to it. The useful power that can be extracted from the wind depends on the size and length of the turbine blades. Theoretically, when the speed of wind doubles, wind power potential increases by a factor of eight. The domestic wind turbines also help in reducing the large power plant setups that are used for storing and transporting the energy in the case of commercial large-scale wind mills [3].

S. V. S. K. P. Raju (✉) · M. Govindaraju · T. S. Kumar

Department of Mechanical Engineering, Amrita School of Engineering, Amrita Vishwa Vidyapeetham, Coimbatore, India

2 Literature Survey

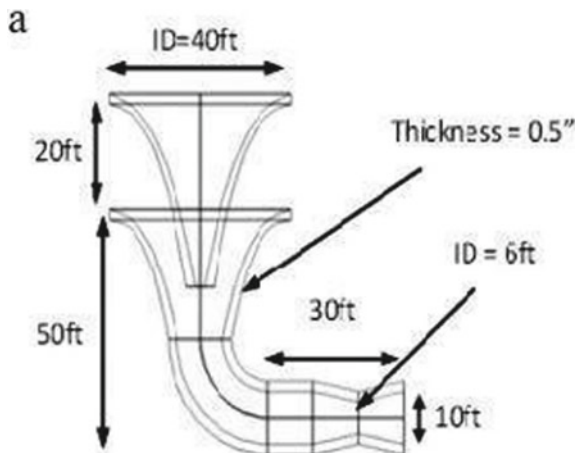
In the year 2015, a total of 422 GW wind power generation was installed worldwide, with an increase of 60 GW in 2015 and it is aimed to reach 760 GW in 2020 [4]. India is in the fifth position in the harvesting of wind energy with an installed capacity of around 25 GW [5]. A. D. Sahin proposed a solution toward the usage of renewable energy, after the oil crisis in European countries that occurred in 1973. A lot of studies have been carried out on wind-energy history, wind turbine innovations and technologies, wind-energy potential all over the globe [6]. Kaoshan Dai and R. Saidur proposed on the environmental issues which occur due to large-scale commercial wind energy and wind farms conversion, provided highly technical aspects in the various environmental aspects, and concluded on the less impact toward the environment. Various energy policies that are already used and the necessary policies for future implementation are thoroughly studied since energy policies play a major role in changing the energy harvesting methods [7, 8]. National Research Council in Advancing the Science of Climate Change declared that excessive consumption of conventional sources like coal, petroleum, and natural gases for energy production and the emission of carbon dioxide is increasing drastically. It is predicted to increase up to 36 billion metric tons globally in the year 2020 and with a drastic impact on climate changes [9]. Allaei, Daryoush Andreopoulos, Yiannis proposed an innovative duct shape for increasing the velocity of the wind thereby producing more power from the available wind speed. This was proposed to prove that an industrial-scale model of 18.288 m height can increase the velocity of the wind by 1.5 times [10]. Dong Xiang Jiang, Qian Huang, Liangyou Hong studied the mechanical problems that occur in the wind turbines in their working cycle like unbalance in rotation based on the number of blades. A special rig is developed for testing these faults by taking the vibration values while the turbine is rotating [11]. Most of the research in wind turbines is going on large-scale wind turbines of 2 to 3 MW rated turbines like onshore and offshore turbines. These large-scale plants need a very huge investment and supporting systems to connect them to the grid [12]. In this perspective, domestic wind turbines provide a very good solution to tackle the financial problems, transportation, and connection problems as they are very cheap and can be installed very easily because of the portability and can be connected to the particular house very easily.

The ducted wind turbine is a very innovative idea which has a huge potential for domestic scale power production, its potential lies in its simplicity.

$$\text{Power} = 0.5 * \text{Efficiency} * \text{Density} * \text{Swept area} * \text{Velocity}^3$$

It is very obvious from the equation that the power is directly proportional to the cube power of the wind velocity. This implies, a small increase in the wind causes a significant amount of power to rise. Taking this as an advantage a duct shape is introduced in front of the turbine in order to increase the velocity of the wind striking the turbine blades. This duct shape is highly advantageous in areas where there are

Fig. 1 Industrial-scale duct-shaped wind turbine [10]



irregular winds and low wind speeds. This also nullifies the directional changes of wind since it works with the wind coming from any direction.

3 Experimental Methodology

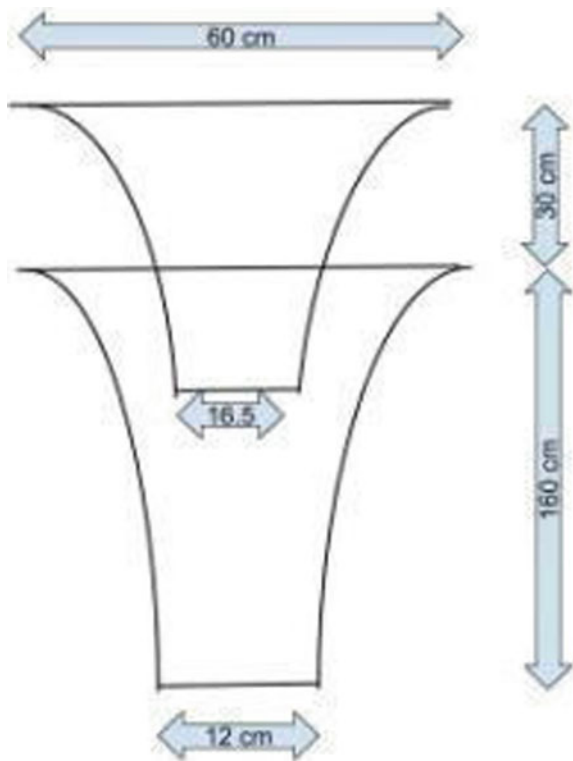
3.1 Industrial Model

The ducted turbine made by the INVELOX [10] is initially validated on a small scale. This is carried out by making a prototype of the duct shape using steel rods and tarpaulin, then it is covered from all the sides by covering tarpaulin and conducting experiments on it as shown in Fig. 1. The validation is done to see the applicability of the INVELOX turbine for domestic purposes.

3.2 Full-scale Model

The full-scale model developed by the INVELOX for commercial purposes is shown in Fig. 1. This model is scaled down for checking the applicability on a domestic scale.

Fig. 2 Scaled model of INVELOX duct



3.3 Scaled Model

Figure 2 represents the scaled model of the industrial prototype which is reduced by a factor of 0.05, this was done to ease the prototype making with available materials. The fabrication of the prototype is made by welding the bent rods around the ring to obtain the duct shape [13, 14]. The tests are conducted on this prototype to check the validity of the model on a domestic scale as shown in Fig. 3. Tests are conducted on this prototype by placing the ducts in an open area and measuring the wind velocity at the inlet and at the outlet 3 times a day and for 3 days.

3.4 Experimental Results

The experiment is conducted by placing the prototype in an open space and measurements are taken three times a day for three consecutive days. The wind velocity is measured by a portable wind anemometer of velocity measuring a range of 0–30 m/s



Fig. 3 Prototype of the scaled model

and the least count of 0.1 m/s. The wind velocity is measured once at the inlet of the duct and other at the exit of the duct.

The measured reading of the experiment is presented in Tables 1, 2 and 3.

The wind velocity is increased by a factor of 1.25 on an average based on the experimental results conducted on the prototype.

Table 1 Test reports on prototype wind turbine on day 1

S.No	Time	Inlet Velocity (km/h)	Outlet Velocity (km/h)
1	9:00	8.7	11.2
2	13:00	11.1	12.9
3	18:00	12.5	15.6

Table 2 Test reports on prototype wind turbine on day 2

S.No	Time	Inlet Velocity (km/h)	Outlet Velocity (km/h)
1	9:00	9.2	11.5
2	13:00	10.8	13.5
3	18:00	12.3	15.4

Table 3 Test reports on prototype wind turbine on day 3

S.No	Time	Inlet Velocity (km/h)	Outlet Velocity (km/h)
1	9:00	8.4	10.5
2	13:00	11	13.75
3	18:00	12.1	15.2

Table 4 Results obtained from industrial model [10]

S.No	Inlet Velocity (km/h)	Outlet Velocity (km/h)
1	6.71	10.6

3.5 Industrial Results

In the commercial model of the INVELOX [10], the velocity of the wind outside the duct with the help of cup anemometer and the velocity of wind at the wind turbine with help of a venturi are measured. 1.5 times the increase in the velocity from the entrance of the tower to the wind turbine is observed from the data collected. The average of the data collected from the wind turbine is presented in the Table 4.

4 Results and Discussions

4.1 Power Produced

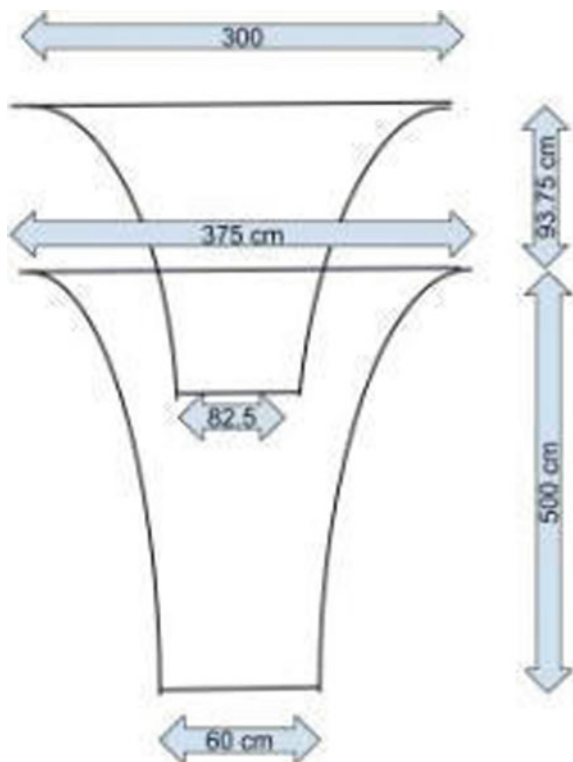
The power produced from the kinetic energy of the wind is

$$\text{Power} = 0.5 * \text{Efficiency} * \text{Density} * \text{Swept area} * \text{Velocity}^3 \quad (3)$$

The density of air	= 1.2 kg m-3.
The diameter of the turbine, d	= 12 cm.
Wind velocit	= 15.6 km/h.
Efficiency = betz limit* transmission efficiency	= 58
Betz limit	= 59.3%
Transmission efficiency	= 99%.

The swept area of a wind turbine is the total area swept by the turbine wings while rotating, and the power increases proportionally to it. Betz limit indicates the practical limitation of the wind turbines with respect to the efficiency with which the energy from the wind's kinetic energy is utilized, because if the complete kinetic energy of wind is utilized then the wind at the turbine will have zero velocity blocking further wind coming onto it.

Fig. 4 Designed model to produce 0.5 units of power daily



4.2 Targeting for 0.5 Unit of Power Daily

For producing power of half unit, the diameter of the turbine can be increased to 60 cm and placed in a wind velocity of 6 m/s as shown in Fig. 4, which increases the swept area of the turbine. By producing the ducted shape with a very smooth surface, i.e., with smooth plastic, the velocity increasing factor can be further increased to make it work in much more low wind speed regions.

4.3 Simulation Validation

Figure 5 is the simulated model in the CFD FLUENT which increased the velocity of the air by a factor of 1.4 and is similar to the result as predicted in both prototype and predicted model. Free stream velocity of air = 6 m/s (given as input in the FLUENT simulation) the exit velocity from the model = 8.6 m/s as seen from the above-predicted model.

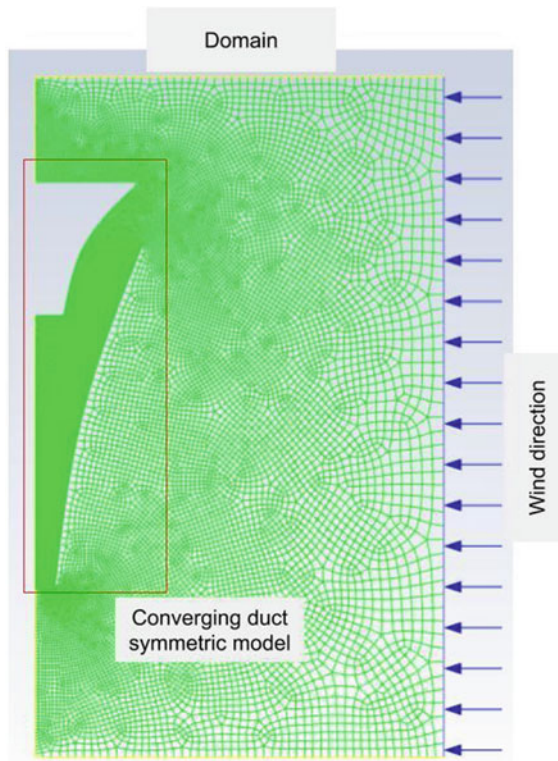


Fig. 5 Symmetric turbine model with meshing and boundary conditions

Figure 6 is the simulation results showing velocity contours of the wind flowing into the duct and coming out from it with increased velocity.

In the above symmetric model as shown in Fig. 5, air is made to flow parallel to the ground.

$$\begin{aligned}
 Power &= 0.5 * EfficiencyDensity * Swept\ area * Velocity^3 \\
 &= 0.5 * 0.593 * 0.99 * 1.2 * ((\pi/4) * 0.6^2) * 6^3 \\
 &= 21.253\text{Watts}
 \end{aligned}$$

$$\text{Units} = (21.253/1000) * 24 = 0.5.$$

To produce 0.5 units of power 6 m/s wind speed is required at the turbine, but because of the duct based on the above calculations, the turbine can produce this at a wind speed of 4.2 m/s, which will be the average wind speed in most of the regions in India.

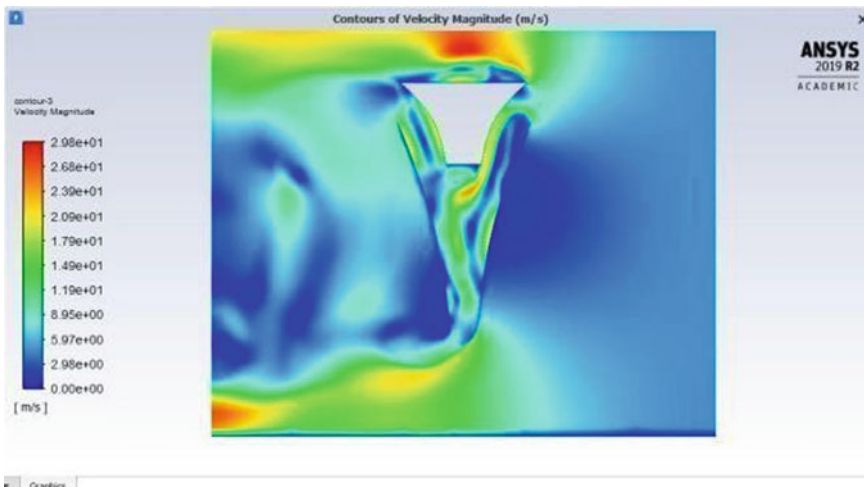


Fig. 6 Simulation of the proposed model in FLUENT

5 Conclusions

This study performed on the innovative wind harvesting methods for low and irregular wind speeds showed that the duct-shaped wind turbine has huge potential in low wind speed regions. Test results have proved that the wind speed can be increased up to 1.25 times from the prototype that was made, which can be further improved by refining the shape and material furthermore. In addition, proposed a design that is capable of producing half a unit daily and validated with simulation in CFD FLUENT.

References

1. <https://www.worldcoal.org/coal/where-coal-found>
2. <https://www.irena.org/wind>
3. Mahalakshmi, R., Sindhu Thampatty, B.C., Grid connected multilevel inverter for renewable energy applications, *Procedia Technology* 21:636–642 (2015)
4. Global wind energy council, Global wind report-2016-Annual market update (IMSNA), Toronto, pp 567–570
5. Global wind energy council, India wind energy outlook (2012)
6. Sahin, A.D.: Progress and recent trends in wind energy. *Prog Energy Combust Sci* **30**(5), 501–543 (2004)
7. Dai, K., Bergot, A., Liang, C., Xiang, W.N., Huang, Z.: Environmental issues associated with wind energy—A review. *Renewable Energy* **75**:911–921 (2015)
8. Saidur, R., Islam, M.R., Rahim, N.A., Solangi, K.H.: A review on global wind energy policy. *Renew Sustain Energ Rev* **14**(7), 1744–1762 (2010)
9. National Research Council: Advancing the science of climate change. The National Academies Press, Washington, DC, USA (2010)

10. Daryoush Allaei, A., Yiannis, A.: INVELOX: Description of a new concept in wind power and its performance evaluation, *Energy* 69 (2014) 336e344.
11. Jiang, D., Huang, Q., Hong, L.: Theoretical and experimental study on wind wheel unbalance for a wind turbine
12. Sreelekshmi, R.S., Prasad, A., Nair, M.G.: Control and operation of microgrid connected Hybrid Energy Storage System, *Int Conf Energ Effi Technol Sustain*
13. Shalini, S., Satis Kumar T., Prasannac S., Balasundaraprabhu R.: Optik. *Int J Light Electron Opt* 212 164672 (2020). <https://doi.org/10.1016/j.ijleo.2020.164672>
14. Vignesh, P., Krishna Kumar, R., Ramu, M., Lakshminarayanan, A., Idapalapati, S., Vasudevan, M.: Advances in materials and metallurgy. *Lect Notes Mech. Eng* pp 415–425 (2019)

**Bio-medical Devices and Bio-mechanisms,
Devices for Aerospace, Automobile
and Railways**

Novel CAM Mechanism-Based Life-Support Ventilators in Animal Healthcare



Prem Dakshin and Shashank Khurana

1 Introduction

Animal health care is being developed by almost all the countries in the world. The main idea is to protect the health of various animals and also prevent the extinction of endangered species. A serious outbreak of animal related diseases can harm the entire environmental ecosystem as sectors like farming [1], dairy, and many more are depended on animals. Also many diseases which originated and communicated from animals have had a significant impact in the humans' life. Various policies and guidelines are created and followed by many leading nations alongside international organizations to keep a track on Global animal health care [1].

1.1 Animal Healthcare Ventilation

Animal healthcare ventilation is the process for artificially inducing the process of respiration, when the animal is unable to breathe on its own. It is considered to be one of the most challenging processes in animal healthcare as it requires a great level of precision and accuracy [2]. The process of artificial mechanical ventilation is need under many conditions and unpredicted circumstances [2–5]. The respiratory process depends on the lung size of the animal, age, body weight, and other health factors like respiratory infections like pneumonia [1, 5] and many more. Other conditions including Hypoxemia and Hypercapnia [3] are caused due to changes in the levels

P. Dakshin (✉)
BITS Pilani Dubai Campus, Dubai 345055, UAE

S. Khurana
Department of Mechanical Engineering, BITS Pilani Dubai Campus, Dubai 345055, UAE
e-mail: skhurana@dubai.bits-pilani.ac.in



Fig. 1 Ventilation in different animals [4]

of different gases during the respiratory process. Apart from the basic requirements, the health condition of the patient should be evaluated and the required tidal volume must be calculated before initiating the artificial respiration process. The required rate of respiration and the tidal volume are greatly influenced by the above-mentioned health factors and a wrong value of tidal volume could be fatal. For this reason the ventilators must be able to provide different modes of ventilation [5].

The tidal volume is the amount of air that's entering and leaving a patient's lungs for one complete breath (Fig. 1). It is defined by the size of the patient's lungs and hence the same value cannot be used for different animals. The tidal volume is calculated based on the body weight of the animal, however, the final values are also influenced by other health conditions of the animal-like respiratory illness, pulmonary diseases, and many more [6, 7]. The respiration rate is defined as the number of breaths required in one minute, it also depends upon the animal and the condition under which it is ventilated. Considering all the circumstances, a vast range of tidal volume and rate of respiration is needed for different animals under different conditions. The tidal volume requirement of different animals based on weight is shown in Table 1 [8]. The table categorizes animals based on their body weight. Smaller animals' category has animals with a weight range of 0.5–120 kg and larger animals category has animals with weight range of 50–300 kg. A small overlap exists between the weight range 50–120 kg, where animals are placed based on other health and body conditions [8].

Table 1 Estimated tidal volume requirements [8]

S.No	Kilogram	Pounds	Large animal (11 ml/kg) (in milliliters)	Small animal (14.3 ml/kg) (in milliliters)
1	0.5	1.1	—	7
2	1	2.2	—	14
3	2	4.4	—	29
4	3	6.6	—	43
5	4	8.8	—	57
6	50	110	550	715
7	60	132	660	858
8	70	154	770	1001
9	80	176	880	1144
10	90	198	990	1287

1.2 The Existing Challenges

The health conditions of animals in forests are closely monitored and treated if necessary, especially if the species are endangered. If an animal is critically wounded or ill, it may require a detailed health recovery or even a surgery [9]. The health care of animals in zoo is also challenging as a wide range of animals are housed [4, 10]. In addition to the above-mentioned applications, many other places require a ventilator for animals with a wide range of tidal volumes to treat different animals. There are a number of ventilators available for different animals [2, 10] but are not accessible everywhere due to output limitations, cost, and size. This research work aims to develop a single system that can provide a wide range of tidal volume output, yet being cost-efficient using the Frustum CAM (FC) Mechanism.

2 The Frustum CAM (FC) Mechanism

The Frustum CAM mechanism is an improved version of a circular eccentric cam mechanism. Unlike a lobed cam, a circular eccentric cam has a circular cross-sectional area with the camshaft machined at a required eccentric distance from the center and it provides a follower lift at a constant speed. Dakshin and Khurana [11] proposed the novel Frustum CAM Mechanism. The mechanism uses the concept of variable valve lift to control the lift length of the controlling valves and by that controlling the flow rate of air. The Frustum CAM is a modified circular eccentric cam with a tapered body (Part 1 in Fig. 2). The dimensions are based on the range of valve lift required. The system has other supporting mechanisms (Part 3 in Fig. 2) which help the movable camshaft (Part 2 in Fig. 2) along with the frustum CAM to

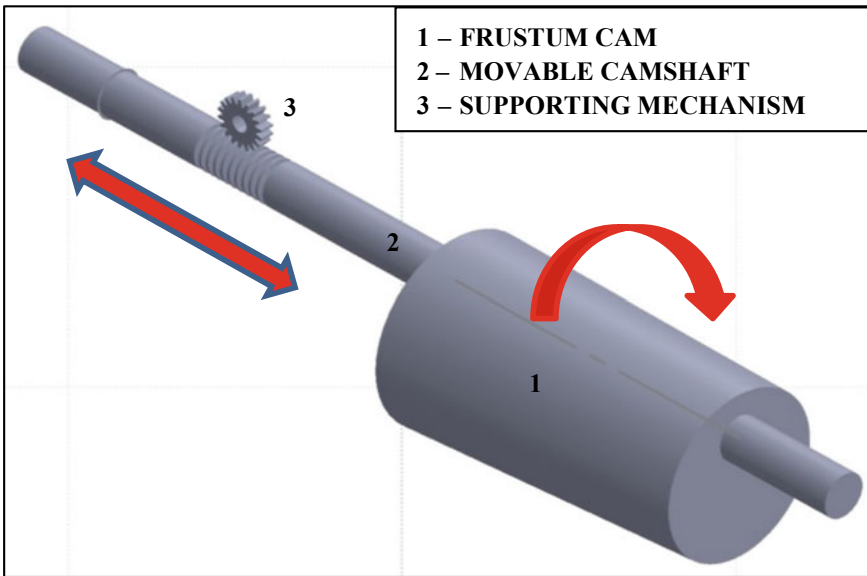


Fig. 2 Frustum CAM Mechanism

experience two types of motion at the same time, linear, and rotational. The valves are positioned over the body of the Frustum CAM at the exact required point by effectively rotating and moving the camshaft. The valves experience different lift values at different contact positions.

2.1 Supporting Mechanisms

The required flow rate for air can be achieved only by effectively positioning the valve over the surface of the Frustum CAM. The main objective of using supportive mechanism (Part 3 in Fig. 2) is to assist the camshaft with two degrees of motion to position the valves. Any possible combination of existing systems can be used for this purpose. A modified rack and pinion mechanism is a possible mechanism [11]. The supporting mechanism is subjective to alterations or improvisations based on requirements. Specialized bearings are used to support the camshaft at both the ends as it will experience two degrees of motion simultaneously.

2.2 Working of FC Mechanism

The Frustum CAM is manufactured with dimensions based on the range of valve lift requirements. The linear moment of the camshaft is achieved using servo motors. The motors are controlled using an Arduino controlling system. Based on the input given, the control system calculates and moves the camshaft at the required point of contact with the valves using the motors as shown in Fig. 3. The valves are positioned using spring action in such a way that the valves completely close and open as per the rotation of the camshaft [11].

Position 1 in Fig. 3 shows the valve positioned at the smallest end, at this position the valve will experience the most minimum lift for one complete rotation. Position 2 and 4 in Fig. 3 shows the valve positioned at the center of the cam, where the valve will experience a central lift value in the range. Position 3 in Fig. 3 shows the valve positioned at the big end, at this point the valve will experience the greatest lift for one complete rotation of the camshaft.

The rate of flow of air is defined based on how much the valve opens and closes. The flow rate will be very high in a given period of time if the valves have greater lift (Position 3 in Fig. 3) and vice versa. In this case, the lift range of the valve is defined based on the diameter of the CAM. By effectively moving and positioning the Frustum CAM at the exact point with the valve, the required valve lift can be achieved, which in turn achieves the required rate of flow. The follower experiences wear due to the rubbing over the CAM surface over a period of time. The wear is minimal as the speed of rotation and liner movement is very slow. This can be reduced by replacing a roller type follower or a ball point follower. The wear can also be reduced by proper lubrication. The waveform of flow is controlled by the rotation speed of the camshaft.

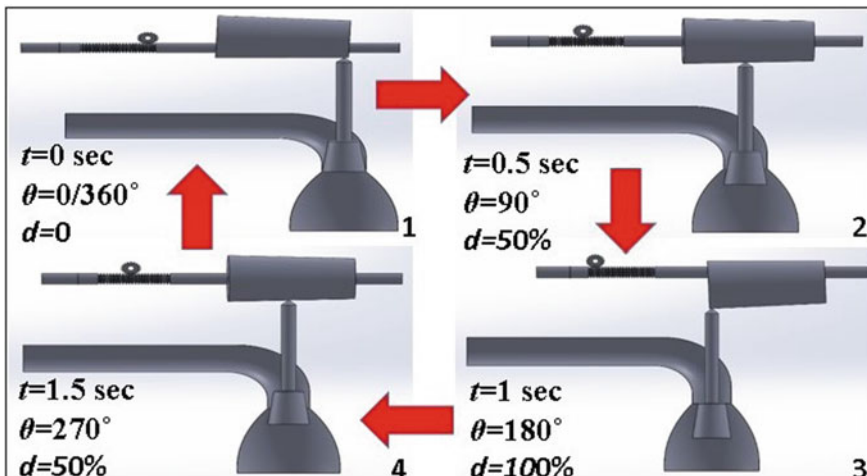


Fig. 3 Working cycle of Frustum CAM Mechanism with follower

The variables t , θ , and d correspond to time, angle of rotation, and the displacement of follower in percentage, respectively. The time t keeps increasing the corresponding stages to show the complete rotation of the camshaft. However, the time can vary based on the rotating speed of the camshaft, which defines the rate of respiration. The displacement of the valve d achieves 50% at opposite angles 90° and 270° and the maximum valve lift height is achieved at $\theta = 180^\circ$.

3 FC Mechanism in a Ventilator

The existing ventilators have two valves to control the respiratory process—The inspiratory valve to control the flow of air to the patient and the expiratory valve to control the expiratory gases from the patient. These are controlled using a number of various actuation mechanisms and in this system the FC mechanism is replaced as the actuation mechanism.

3.1 Ventilator Layout

The FC mechanism can be integrated or developed as a ventilator, as shown in Fig. 4, which will have pressurized gas as the input and the patient on the operational end, the conditions for ventilation is fed using electronic system and the mechanism is positioned and controlled using mechatronics or any other controlling system. Ventilators use 2 valves—inspiratory and expiratory valves to achieve the breathing cycle. In this system, both the valves are actuated by two Frustum CAM's, machined on a single camshaft as shown in Figs. 5 and 6. The identical faces of the CAM's face in opposite directions. One complete rotation of the camshaft completes one cycle of operation and is divided into two stages—inspiration stage and expiration stage.

Inspiration Stage. The process of inhaling is achieved in this stage. The FC Mechanism is positioned as shown in Fig. 5. In his stage, the pressurized air flows

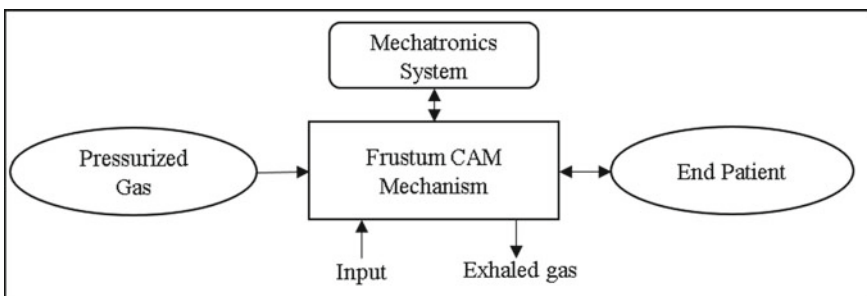


Fig. 4 FC Mechanism in Ventilator

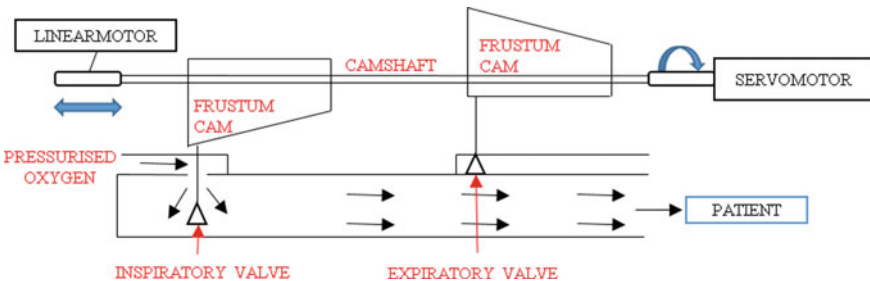


Fig. 5 Inspiration stage **b** Expiration cycle

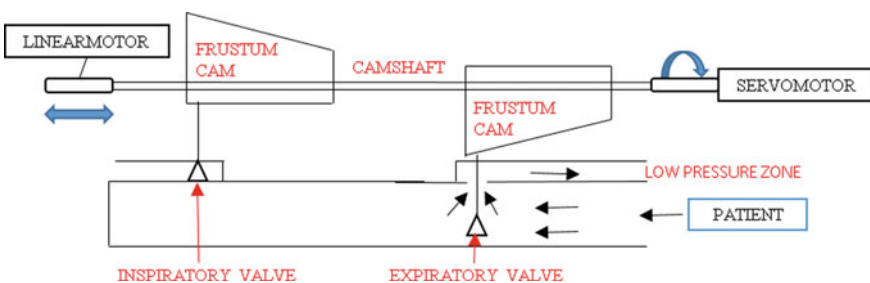


Fig. 6 Expiration cycle

into the patient's lungs through the inspiratory valve. The expiratory valve remains closed.

Expiration Stage. The process of exhaling is achieved in this stage. The FC Mechanism is positioned as shown in Fig. 6. In this stage, the exhaled air from the patient's lungs flows out into a low-pressure zone through the expiratory valve. The inspiratory valve remains closed at this point.

The inspiration stage occurs during the first half of rotation of the CAM (first 180°), followed by the expiration stage on the second half of the rotation. Both the valves remain open for some time during this process, during this time the fresh pressurize air from the inspiratory valve flushes out the remaining residual air from the patient through the expiratory valve.

4 Tidal Volume Calculation

The required tidal volume for a patient is calculated based on the body weight using the equations [4, 12, 13]

$$\text{Tidal Volume} = (\text{Weight in KG} * 10)/1000L \quad (1)$$

Table 2 Tidal volume calculation

Weight	20 kg
Required tidal volume	200 ml/0.2L {From Eq. (1)}
ET diameter	10 mm [14]
Cross-sectional area	78.54 mm ² {From Eq. (2)}
Velocity of air at orifice	2.547 m/s
Volume of flow	200,041.38 mm ³ {From Eq. (3)}
Output volume achieved	200.041 ml

$$\text{Cross-sectional area} = (\pi d^2)/4 \quad (2)$$

$$\text{Volume of Flow} = \text{Cross-sectional area} * \text{Velocity of Flow} \quad (3)$$

The standard weight chart categorizes all the animals based on their weight into two categories, small and big [8]. The tidal volume requirements are calculated using the above equation and summarized in Table 2. The standard Endotracheal or the ET tube to be used for animals based on weight is summarized by Kristen Hunyady [14]. The calculations are done for a healthy dog weighing 20 kg. The required ET diameter is identified [14] and the velocity of air at the orifice is set to 2.547 m/s. The required tidal volume, cross-sectional area, and the volume of flow are calculated using Eqs. (1), (2) and (3). The achieved tidal volume is 200.041 ml, and the required tidal volume for a 20 kg healthy dog is 200 ml [8]. By making fine adjustments to input velocity of air and the valve position, the accuracy can be improvised.

The calculated tidal volume can be achieved by effectively positioning the valve over the body of the Frustum CAM and the input pressure and velocity of air. An Arduino-powered mechatronic control system can effectively be used to achieve the above with a great precision. A single system can be built to achieve the complete required range of tidal volume [8], this can be done by modeling and manufacturing the Frustum CAM with dimensions required to achieve the needed levels of valve lift with an accurate supporting mechanisms and controlling unit.

5 Conclusion

In this research, it is demonstrated that the presented novel cam mechanism can be used to develop a single ventilator for different animals. The dimensions of the frustum CAM can be altered to achieve a wide range of required output flow and tidal volume. By integrating a mechatronic control unit, a single system can be used to treat a wide range of patients by giving in the required inputs with an effective and simple user interface. This ventilator will be of great use in zoos, wildlife parks, drug development testing on animals, and many other related places where a single

system can be used to treat all the different animals rather than having individual ventilators for different species.

References

1. Vaarst, M., Padel, S., Younie, D., Hovi, M., Sundrum, A., Rymer, C.: Animal health challenges and veterinary aspects of organic livestock farming identified through a 3 year EU network project. The open Veterinary Science Journal—Research Gate (2008)
2. Perth Vet Emergency, <https://pve.net.au/38-pet-ventilator/>. Accessed 05 Sep 2020
3. Hopper, K., Lisa, L., Powell.: Basics of mechanical ventilation for Dogs and Cats. Elsevier Inc (2013)
4. Vetronic online documents, Ventilation in zoo Animals, https://www.vetronic.co.uk/images/documents/Ventilation_in_Zoo_Animals_October_2014.pdf. Accessed 15 July 2020
5. Luna, C.M., Sibila, O., Agusti, C., Torres, A.: Animal models of ventilator-associated pneumonia. Eur Respir J (2009)
6. Drorbaugh, J.E.: Pulmonary function in different animals. Am Psychol Soc (2018)
7. Clare, M., Hopper, K.: Mechanical ventilation: Indications, goals, and prognosis. Compendium (2005)
8. Muir, W., Hubbell, J.: Handbook of Veterinary Anesthesia, 5th edn. Elsevier (2012)
9. Fantoni, D.T., Alvarenga, J.D., SILVA, L.C.L.C.D., Cortopassi, S.R.G., Mirandola, R.M.S.: Controlled mechanical ventilation in horses under vecuronium blockage. São Paulo, 35(4), p 182–187 (1997)
10. Conduct Science 2020, <https://conductscience.com/animal-lab/animal-ventilation/>. Accessed 03 Sep 2020
11. Dakshin, P., Khurana, S.: Frustum CAM (FC) mechanism: Achieving differentiating feed in continuous production machines of non-similar parts. In: 2nd International Conference on Recent Advances in Materials & Manufacturing Technologies (IMMT 2019), Elsevier, Materials Today: Proceedings. Dubai, UAE (2019)
12. Donati, P.A., Plotnikow, G., Benavides, G., Belerenian, G., Jensen, M., Londoño, L.: Tidal volume in mechanically ventilated dogs: can human strategies be extrapolated to veterinary patients?. J Vet Sci (2019)
13. Wiley Online Library Appendix 2: Tidal volume calculations, <https://onlinelibrary.wiley.com/doi/pdf/https://doi.org/10.1002/9780470690376.app2>. Accessed 25 Aug 2020
14. Anesthesia Cheat Sheet - Vetmed Science, <https://www.vetmed.wisc.edu/wp-content/uploads/2019/07/Anesthesia-1.pdf> Accessed 15 July 2020

Multi-body Topology Optimization of Connecting Rod Using Equivalent Static Load Method



G. Lakshmi Srinivas and Arshad Javed

1 Introduction

The IC engine is a prime mover for the automobile industry applications [1]. In IC engine, connecting rod plays an important role between crank and piston for motion transmission. When the connecting rod operates in a working cycle, it is subjected to high dynamic loads with high-stress values. To improve the dynamic performance and reduce the weight of the system, topology optimization techniques are implemented. Topology optimization is the well-established approach to distribute the material in the design space [2].

As per the available literature review, the connecting rod of IC engine was optimized using topology optimization considering linear static analysis [3]. The mass of the connecting rod was reduced by 11.7%, and stress is also minimized compared to the initial design. The topology optimization is conducted using MSC-NASTRAN software. However, the design space is not considered properly because the same optimization loop removed the material from big end of the crank. Du and Tao were conducted numerical simulations of topology optimization on IC engine piston [4]. The topology optimization analysis was conducted using HyperWorks software, and the piston mass was minimized by 30%. Similarly, the four-wheeler connecting rod is optimized using topology optimization using ANSYS software [5]. The final model is 10.38% lighter compared to the optimized model. The stress analysis was compared among different materials such as forged steel, aluminum, and titanium. A two-stroke engine connecting rod was optimized topologically using finite element

G. L. Srinivas () · A. Javed

Department of Mechanical Engineering, Birla Institute of Technology and Science, Hyderabad, Telangana, India 500 078

e-mail: p20170411@hyderabad.bits-pilani.ac.in

A. Javed

e-mail: arshad@hyderabad.bits-pilani.ac.in

analysis [6]. Most of the researchers are focused on the optimization of IC engine components, considering static loading conditions. However, when the engine operated at high speed, its components are subjected to dynamic loads. The equivalent static load (ESL) method is adopted to conduct a dynamic analysis of the connecting rod for topology optimization [7]. The ESL method computes the dynamic values based on the varying static loads with time step [8, 9].

In the present work, connecting rod is optimized topologically, considering dynamic loading conditions. The multi-body of the IC engine components is modeled using SOLIDWORKS software. The boundary conditions of the connecting rod, such as force and torque values, are analyzed dynamically using Altair INSPIRE software. The topology optimization study is conducted based on ESL method using Altair Inspire software. The numerical simulations are performed for various volume fractions ranging from 0.3 to 0.9. The obtained final topology is again analyzed to capture the performance values such as deflection and Von-Mises stress. The proposed method is useful to obtain light-weight components in automobile industries to improve the performance of the engine.

1.1 Equivalent Static Load Method

Equivalent static loads are set of static loads, which generate the same displacement effect as static analysis at each time step for non-linear dynamic analysis [10, 11]. In ESL process, multiple loads are calculated with respect to the time, as shown in Eq. 1.

$$\mathbf{M}(z)\ddot{\mathbf{D}}_N(t) + \mathbf{K}_N(z, D_N(t))D_N(t) = F(t) \quad (1)$$

where ‘ $\mathbf{M}(z)$ ’ is the mass matrix of design variable, ‘ $F(t)$ ’ is the force at each time step value. ‘ \mathbf{K}_N ’ is the stiffness matrix for non-linear analysis, and ‘ z ’ is the design variable. The displacements from non-linear analysis (D_N) are multiplied by stiffness matrix of linear study (\mathbf{K}_L) to capture the ESL at time step, as shown in Eq. 2.

$$F_{ESL}(t_a) = \mathbf{K}_L D_N(t_a) \quad (2)$$

where ‘ F_{ESL} ’ is the load or force at the given instance (t_a). The several loading conditions are successfully handled by structural optimization without much computational time. The optimization is conducted using ESL will update the design variables based on non-linear analysis.

1.2 Topology Optimization Approach

Topology optimization is the subcategory of structural optimization, which is a promising method to distribute the needful material in design area [12, 13]. The objective function is chosen as maximizing the stiffness or minimization of compliance (C), which is subjected to constraints such as force vector (\mathbf{F}_{ESL}), volume fraction (f), and density variable (z), as shown in Eq. 3.

$$\left. \begin{array}{l} \min_z : C(z) = \mathbf{D}_L^T \mathbf{K}_L \mathbf{D}_L \\ s.t : \frac{v(z)}{v_0} = f \\ \mathbf{F}_{\text{ESL}} = \mathbf{K}_L \mathbf{D}_L \\ 0 < z_{\min} \leq z_e \leq 1 \end{array} \right\} \quad (3)$$

where ‘ $v(z)$ ’ is the final design space after topology optimization and ‘ v_0 ’ is the initial design space. ‘ z_{\min} ’ and ‘ z_e ’ are the minimum and element design variable. The ESL method updates the design variable until it converges.

2 Modeling and Dynamic Analysis of the IC Engine

IC engines are playing a significant role in the automobile industry. When the engine operates at high speed, the machine components are subjected to huge unbalanced forces and high stress [14]. To improve the dynamic performance of the IC engine block, a topology optimization study is conducted. In this section, modeling and dynamic analysis of the IC engine is detailed.

2.1 Modeling of the IC Engine

Initially, to analyze the dynamic nature of components, the IC engine block is modeled using SOLIDWORKS 2019 software. The assembly components mainly consist of a piston, connecting rod, crank, and Plummer block, as shown in Fig. 1. The connecting rod is the crucial component in the IC engine, connecting the piston and crank in the IC engine. It converts the reciprocating motion of the piston into rotary motion at the crank. To simplify the study connecting rod is selected for topology optimization process. When the connecting rod is in motion, it is subjected to the varying loading conditions at the joints. These boundary conditions, such as forces and torques, are captured using the ESL method with Altair INSPIRE-2019 software at each joint.

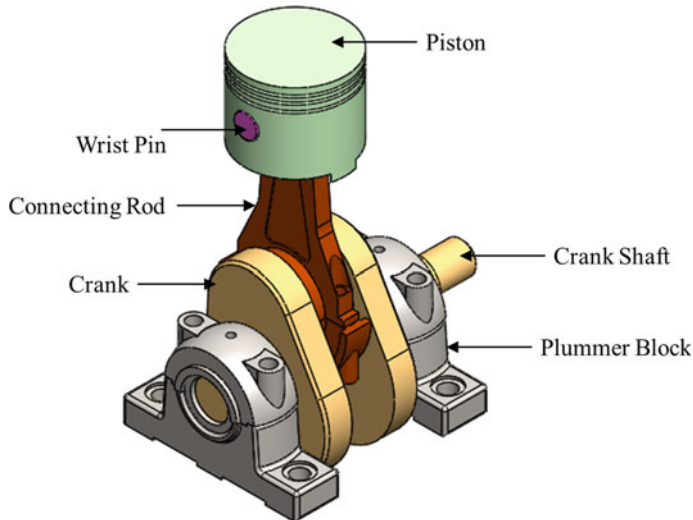


Fig. 1 Schematic diagram of the IC engine block and its components

2.2 Dynamic Analysis of Connecting Rod

The model of the IC engine block is imported into Altair Inspire software for dynamic analysis. Initially, the joints are defined relative to the mechanical components such as fixed joint between Plummer block and ground; hinge joint between crankshaft and Plummer block; pin joint between connecting rod and crankshaft; hinge joint between piston and connecting rod; finally, a planar joint between piston and grounded cylinder. Various materials are assigned to the IC engine components, as shown in Table 1.

The connecting rod is operated for a full range of motion at a speed of 600 rpm of the crank using servo motor in Altair INSPIRE software. The input velocities are predefined as per the acceleration and deceleration phase of motor, known as trapezoidal profile. The simulations are performed in motion study option, which calculates the force and torque values using ESL technique. The post-processing results of force and torque at connecting rod big end small end with respect to the time is shown in Fig. 2. The obtained boundary conditions using proposed method

Table 1 Assigned material for various components of the IC engine

Component name	Material
Plummer block	Cast iron
Crank and crankshaft	Micro-alloyed steel
Connecting rod	Carbon steel
Wrist pin	Nodular cast iron
Piston	Al-Si-Cu-Mg alloy

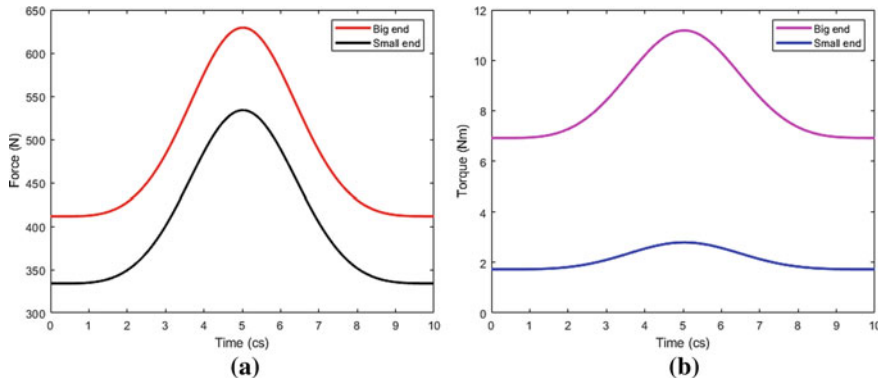


Fig. 2 **a** Force and **b** torque readings at the big and small end of the connecting rod

are used for topology optimization load cell. The process of obtaining topology optimization of connecting rod is detailed in the next section.

3 Topology Optimization of the Connecting Rod

The application of dynamic loading is very important in topology optimization method when the engine components are in motion [15]. The obtained results of dynamic analysis of the connecting rod are used as boundary conditions for topology optimization. The connecting rod of IC engine is isolated and imported into Altair INSPIRE software, as shown in Fig. 3.

The connecting rod space is divided into two parts, such as design space and non-design region (NDR). The big end and small end of the connecting rod are included in NDR, which means in topology optimization study, these regions are not included. The remaining area is considered a design space; the topology optimization loop

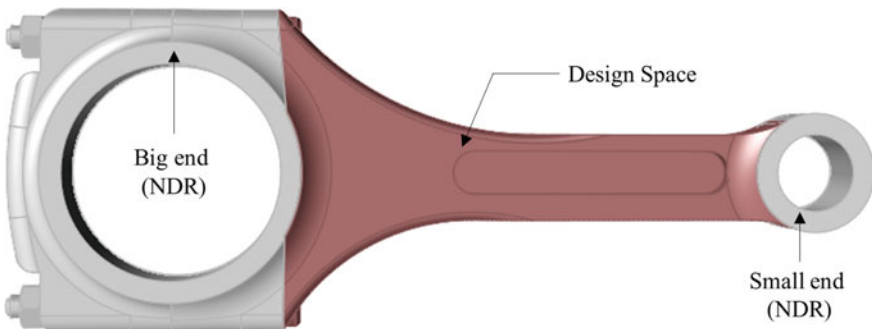
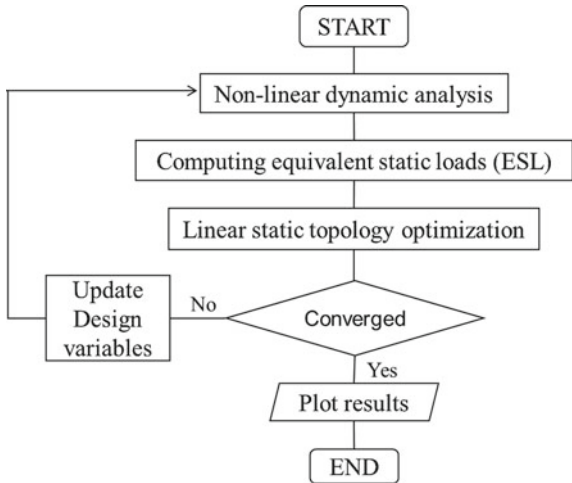


Fig. 3 Initial design space of the connecting rod

Fig. 4 Flow chart of obtaining topology optimization of the connecting rod



removes the needless material from this region. The process of obtaining topology optimization for connecting rod using ESL method is shown in Fig. 4. Initially, the design variables are considered as very small to avoid the singularity of stress. The non-linear dynamic analysis was conducted to obtain the linear stiffness and non-linear displacement vector. The obtained ESL results in motion study are used for topology optimization of connecting rod using Altair INSPIRE software. If the obtained results are converged, the loop terminates and plot the results, or else the design variables update and continue from the beginning.

4 Results and Discussions

The results obtained from the Altair INSPIRE software are presented here. The topology optimization method is conducted to find the optimized connecting rod with various volume fractions ranging from 0.3 to 0.9. After the topology optimization, the obtained structure is again analyzed to find performance values such as deflection and Von-Mises stress. The failure criteria for minimum volume fraction are also analyzed in this theoretical study.

4.1 Before Topology Optimizations

The connecting rod is analyzed dynamically before applying the topology optimization method. The results of the deflection and stress for a solid link are shown in Fig. 5. The maximum deflection and stress are recorded as 0.1632 mm and 72.14 MPa, respectively. The obtained performance values are in safe limits, the region which

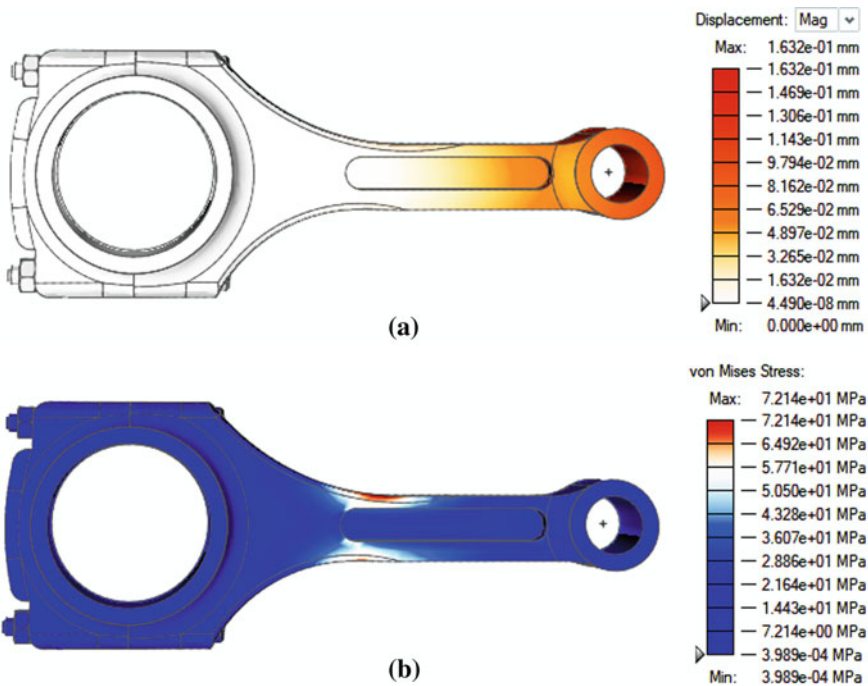
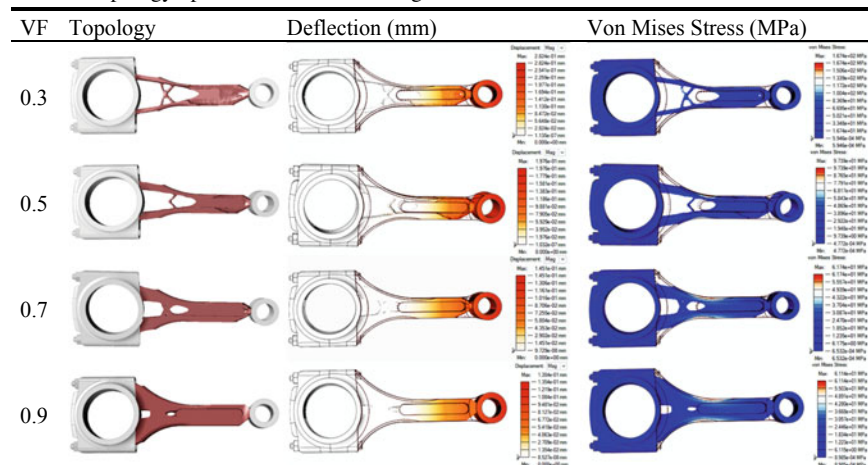


Fig. 5 a Deflection and b stress of connecting rod before topology optimization

are in safe limits can be removed using topology optimization method because these elements are not bearing any load, which is known as stress-free zone. The topology optimization method is implemented for various volume fractions with performance values that are detailed in the next section.

After Topology Optimization. As detailed earlier, the needless material is eliminated using topology optimization method considering ESL technique. In this approach, objective function is chosen as maximization of stiffness or minimization of compliance. The volume fraction is selected from 0.3 to 0.9, with a step value of 0.2. The ESLs captured in the motion study are used as boundary conditions for topology optimization method. To obtain better manufacturability of the topology, different shape controls are implemented to the design space, such as symmetry and split draw. The obtained topologies for various volume fractions with performance values are shown in Table 2.

From Table 2, it is evident that the deflection and stress values are increasing when volume fraction decreases. For volume fraction 0.7, the performance values of deflection (0.145 mm) and Von-Mises stress (61.74 MPa) are reduced by 11.09% and 14.42%, respectively, when compared to the solid connecting rod. This is because of reduction in mass of the connecting rod [3]. Since it significantly contributes to the dynamic loading, the reduction in mass by 30% brings better performance values. The volume fraction less than 0.7; the performance values increases compared

Table 2 Topology optimization of connecting rod at a various volume fraction

to the connecting rod before topology but which are in safe limits. However, at volume fraction 0.3, the deflection and stress values are calculated as 0.2824 mm and 167.4 MPa, respectively, as expected. These values are very high when compared to the initial conditions and not under the safe limits.

5 Conclusions

This paper mainly focused on the multi-body topology optimization of the IC engine connecting rod using ESL method. The connecting rod was a crucial component in the IC engine to improve dynamic performance because it was subjected to more unbalanced forces. Thus the weight reduction of connecting rod was attempted using a topology optimization technique. The complete model of IC engine block was modeled using SOLIDWORKS software and imported into Altair INSPIRE to conduct the dynamic analysis. The boundary conditions were captured using ESL method, which will be used for topology optimization study. The topology optimization study was conducted for connecting rod at various volume fractions ranging from 0.3 to 0.9. After topology optimization, again, dynamic analysis was conducted to capture the performance values such as deflection and stress. It is noticed that, at volume fraction 0.7, the performance values of deflection (0.145 mm) and Von-Mises stress (61.74 MPa) are reduced by 11.09% and 14.42%, respectively, when compared to the solid connecting rod. The failure condition of connecting rod for volume fraction is also noticed at 0.3. The volume fraction can be selected based on the factor of safety of the engine components. The proposed method is useful to obtain the light-weight components of the IC engine parts. This method is also applicable for other mechanical members which subjected to dynamic loading conditions.

Acknowledgements The effort presented in this work is funded by the “Department of Science and Technology (DST)—Science and Engineering research board (SERB), India” (File Number: ECR/2017/000799).

References

1. Cardenas, Y.D., Valencia, G.E., Acevedo, C.H.: Bibliometric study of state observer research applied to internal combustion engine. *J. Phys. Conf. Ser.* 1126, (2018). <https://doi.org/10.1088/1742-6596/1126/1/012028>
2. Besndsoe, M.P., Sigmund, O.: *Topology optimization theory, methods and applications*. Springer Singapore (2003)
3. Shaari, M.S., Rahman, M.M., Noor, M.M., Kadirgama, K., Amiruddin, A.K.: Design of connecting rod of internal combustion engine: a topology optimization approach. *Fac. Mech. Eng.* 3–4 (2010)
4. Du, F., Tao, Z.: Study on light-weight of the engine piston based on topology optimization. *Adv. Mater. Res.* **201–203**, 1308–1311 (2011). <https://doi.org/10.4028/www.scientific.net/AMR.201-203.1308>
5. Gopinath, D., Sushma, C.V.: Design and optimization of Four wheeler connecting rod using finite element analysis. *Mater. Today Proc.* **2**, 2291–2299 (2015). <https://doi.org/10.1016/j.matpr.2015.07.267>
6. Valero-Páez, L.B., Chacón-Velasco, J.L., González-Estrada, O.A.: Optimization of the connecting rod of a two-stroke engine using finite element analysis. *J. Phys. Conf. Ser.* 1386, (2019). <https://doi.org/10.1088/1742-6596/1386/1/012114>
7. Jeong, S.B., Yoon, S., Xu, S., Park, G.J.: Non-linear dynamic response structural optimization of an automobile frontal structure using equivalent static loads. *Proc. Inst. Mech. Eng. Part D J. Automob. Eng.* 224, 489–501 (2010). <https://doi.org/10.1243/09544070JAUTO1262>
8. Tromme, E., Sonneville, V., Guest, J.K., Brüls, O.: System-wise equivalent static loads for the design of flexible mechanisms. *Comput. Methods Appl. Mech. Eng.* **329**, 312–331 (2018). <https://doi.org/10.1016/j.cma.2017.10.003>
9. Lee, Y., Ahn, J.-S., Park, G.-J.: Crash optimization of an automobile frontal structure using equivalent static loads. *Trans. Korean Soc. Automot. Eng.* **23**, 583–590 (2015). <https://doi.org/10.7467/ksae.2015.23.6.583>
10. Dong, H., Leiva, J.P., Adduri, P., Miki, T., Fukuoka, T.: Large scale structural optimization using GENESIS®, ANSYS® and the equivalent static load method
11. Kang, B.S., Park, G.J.: Optimization of flexible multi-body systems Using the equivalent static load method. *CISM Int. Cent. Mech. Sci. Courses Lect.* 511, 375–426 (2009). https://doi.org/10.1007/978-3-211-99461-0_18
12. Sigmund, O., Maute, K.: Topology optimization approaches: A comparative review. *Struct. Multidiscip. Optim.* **48**, 1031–1055 (2013). <https://doi.org/10.1007/s00158-013-0978-6>
13. Lakshmi Srinivas, G., Javed, A.: Topology optimization of rigid-links for industrial manipulator considering dynamic loading conditions. *Mech. Mach. Theory* **153**, 103979 (2020). <https://doi.org/10.1016/j.mechmachtheory.2020.103979>
14. Kirk, R.G., Gunter, E.J.: Stability analysis of a high-speed automotive turbocharger. *Tribol. Trans.* **50**, 427–434 (2007). <https://doi.org/10.1080/10402000701476908>
15. Srinivas, G.L., Javed, A.: Topology optimization of industrial manipulator-link considering dynamic loading. *Mater. Today Proc.* **18**, 3717–3725 (2019). <https://doi.org/10.1016/j.matpr.2019.07.306>

Challenges in the Design of a Laparoscopic Surgical Forceps



Md. Abdul Raheem Junaidi , Harsha Sista , Y. V. Daseswara Rao,
and K. Ram Chandra Murthy

1 Introduction

Laparoscopy is a minimally invasive surgical process for performing operations on the abdominal region since it contains more organs and is relatively easier to access. Small incisions are made to pass instruments and a camera, showing the operating region on a monitor. The complexity of the operation is minimized in laparoscopy, reducing the mortality rate to 0.1% [1]. However, surgeons experience discomfort (fatigue) in performing laparoscopic procedures due to instrument exchange and extending all movements to the site through their hands [2]. Besides running the risk of trauma, exchanging instruments disrupts the flow of the procedure and increases the operating time [3, 4]. Around 40–60% of surgeons complain about the discomfort related to the laparoscopic approach, instrument design, and repetitive usage of instruments [5]. Challenges faced by surgeons include stress caused by improper placement of monitor, minimal access to the operating area, restricted degrees of freedom, lack of direct visualization in the operating area, and ergonomic limitations due to poor instrument design. These challenges, along with reusability and multi-functionality of instruments and avoiding their re-insertion are addressed in this article while prioritizing the patient's safety.

Md. A. R. Junaidi · H. Sista · Y. V. D. Rao · K. R. C. Murthy
Mechanical Engineering Department, BITS Pilani, Hyderabad Campus, Hyderabad, Telangana,
India

Y. V. D. Rao
e-mail: yvdrao@hyderabad.bits-pilani.ac.in

K. R. C. Murthy
e-mail: rcmurthy@hyderabad.bits-pilani.ac.in



Fig. 1 Currently used Maryland forceps (*Source* <https://www.teleflexsurgicalcatalog.com/pilling/product/728014-maryland-dissector-forceps-rotating-monopolar>)

2 Overview of the Laparoscopic Procedure

Three slits are made for laparoscopic surgery: one for introducing forceps meant for grasping or cutting, another for a camera to view the operating area on a monitor, and a third for a Suction-Irrigation (S-I) device. The forceps employed in laparoscopic procedures have long shafts and are introduced into the abdominal region through trocars. The handle mechanism actuates the jaws at the end of the long rod, enabling the surgeon to perform activities such as grasping and cutting. The cable at the end in Fig. 1 is used for bipolar power supply to cauterize the infected tissue, while the knob is used to orient the jaws according to the requirements of the surgeon.

The S-I device is used to clean and disinfect the operating region by removing blood and other bodily fluids through the suction feature and irrigating a disinfectant such as saline water through the irrigation feature. A typical S-I apparatus is shown in Fig. 2.

Carbon dioxide (CO_2) is insufflated into the abdomen before the procedure to maintain stable pressure and give more operating room for the surgeon, increasing his field of view as well. Multiple insertions and removals of instruments result in this pressure going down, due to which CO_2 has to be pumped into the abdomen again.

3 Basic Components of the Proposed Instrument

Our proposed instrument combines the functionality of the forceps, the S-I device, and the CO_2 insufflator into a single instrument, which can be sterilized and re-used with ease. This instrument does not require multiple re-insertions, leading to a stable CO_2 pressure in the abdomen. Each component has its specific purpose and contributes to the overall functionality of the instrument. The characteristics, features, functions, and materials of every component are explained briefly in this section. The details of this instrument are described in the patents [6, 7]. The fits and tolerances of each of the components described below should be such that the entire mechanism operates smoothly without play.

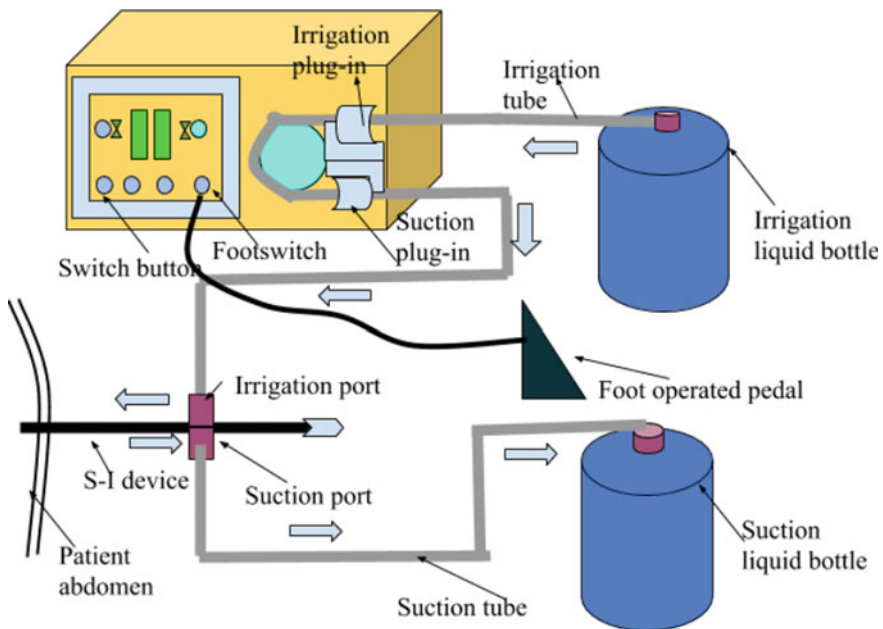


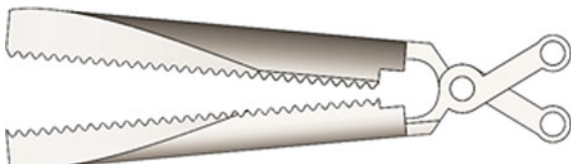
Fig. 2 Suction-irrigation apparatus

1. Jaws

Jaws are one of the essential components of the instrument as they directly operate on the tissue. The jaws, as shown in Fig. 3, are used to grasp, manipulate, cauterize, and seal the tissue. They are replaceable with other suitable forceps heads for other laparoscopic procedures. Stainless steel of the martensitic 420 series is a preferred material for the jaws. The required features of the jaws are as follows:

- outer edges and corners of the jaws have to be smooth and rounded to avoid injury to tissues.
- withstand sterilization and surgical procedures, as they are subjected to thermal, chemical, and mechanical stresses.
- a high surface finish, strength, and toughness.

Fig. 3 Pair of jaws



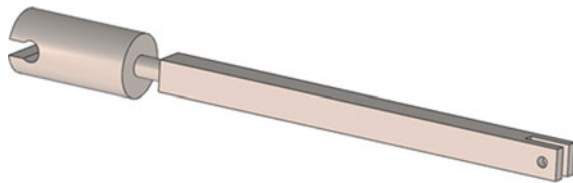


Fig. 4 Actuating connector

2. End Effector Assembly

The end effector comprises the jaws, four-bar mechanism, and the head, as seen in Fig. 4. The head encases the four-bar linkage and is used to open and close the jaws. Two of the four bars are connected to the jaws while the other two bars are hinged to the head. The end effector continuously comes in contact with different fluids; hence it is made of 304 series stainless steel. The required features of this end effector assembly are as follows:

- should be sleek and strong enough to bear the stresses exerted during the operation.
- links should be compact to fit inside the head and should have better machinability.
- head, jaws, and four-bar linkage are subjected to a high-frequency current supply and are constantly in touch with body fluids. So, the material should be non-corrosive and be able to withstand damage over multiple sterilization cycles.

3. Inner Rod and Outer Tube

The inner rod and the outer tube are major components of laparoscopic forceps. The inner rod is 2.5 mm in diameter and transmits the motion of the handle to the four-bar mechanism near the jaws. A metallic outer tube of 3.5 mm outer diameter encloses the inner rod, as shown in Fig. 5. It is covered with an insulating material like PEEK to prevent leakage of electric current. The inner rod and outer tube are made of austenitic stainless steel of 316 series due to material requirements like corrosion resistance, toughness, rigidity, hardness, and mechanical strength. The required features of the inner rod and outer tube are as follows:

- should incorporate threading and small drill holes for dimensional accuracy.
- the inner rod should be able to transmit the motion of the handle to the jaws.
- the outer tube should be biocompatible to prevent inflammation or allergic reactions as it comes in contact with the tissue.
- both of them should be easily sterilizable.



Fig. 5 Outer sleeve enclosing the inner rod

4. Outer Sleeve

The outer sleeve is important because it acts as a suction-irrigation channel to either irrigate disinfecting saline or suck the body fluids from the patient's abdominal cavity, as shown in Fig. 5. It is restricted in two extreme positions over the connector to serve multiple purposes. At the extreme left end position of the sleeve, the suction or irrigation process is carried out. While, at the extreme right end of the sleeve, the jaws are exposed and grasping, dissection or cauterization is performed. The recommended material is 304 series stainless steel. The required features of the outer sleeve are as follows:

- must ensure the fluid is sucked or irrigated within the channel only, and leakage should be avoided.
- ease of assembling, disassembling, and effective sterilization.
- the distal end near the jaws should be rounded without sharp edges to avoid injury while inserting it inside the abdominal cavity.

5. Actuating Connector

The actuating connector is a link which connects the inner rod and the handle, as shown in Fig. 4. A small ball and socket joint is used to connect the inner rod to the actuating connector. Stainless steel of 304 series is a recommended material. The required features of the actuating connector are as follows:

- should be rigid, tough, and strong enough to bear the loads.
- it should impart rotary motion of the knob to the jaws using a ball and socket joint.

6. Handle

The handle is a primary component that is held by the surgeon and provides access to the instrument functions. The end at which the handle is located is known as the 'proximal end.' It comprises the fixed handle and movable handle. The fixed handle is used to rest the surgeon's fingers while the movable handle is used to transmit the motion to a four-bar mechanism near the jaws. The conventional instrument handle uses different grades of stainless steel and PEEK (Polyetheretherketone) material. The desirable material properties of a handle are chemical resistance, toughness, rigidity, hardness, and mechanical strength. The required features of the handle are (Fig. 6) as follows:

- provision to accommodate the high-frequency electrical power cable for electrocauterization operation.
- ergonomically designed to enable surgeons to hold it longer durations without causing strain or injury.
- it should be properly insulated against electrical shock to both surgeon and patient during electrocauterization.



Fig. 6 Design of handle

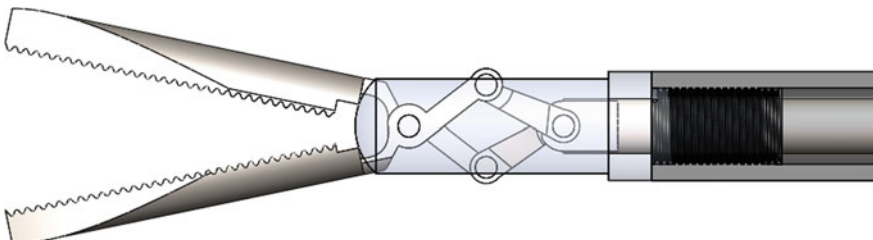


Fig. 7 Inner rod and outer tube front view

7. Knob

Its purpose, as shown in Fig. 8, is to facilitate the surgeon to orient the jaws in the desired direction. It is connected over the outer tube and imparts 360° rotation to the jaws. PEEK material is recommended for the knob, whose required features are as follows:

- should have a firm grip over the outer tube such that the rotation of the knob rotates the outer tube and, eventually, the jaws.
- the spacing between the protrusions should be ergonomically suitable for the surgeon to operate using fingers.

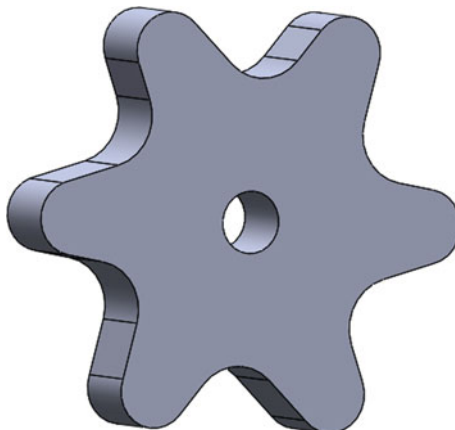


Fig. 8 Knob

8. Connector

Its function is to restrict fluid flow in one direction and to hold the outer sleeve in two extreme positions. The outer sleeve slides over the rubber washers, which prevent the leakage of fluids. The connector is provided with a groove on the collars for the locking pin to slide into, which restricts the axial motion of the outer sleeve, as shown in Fig. 9. The recommended material for the connector and collars is 304 series stainless steel, which has good corrosion resistance. Biocompatible rubber is recommended for the two washers close to the right end. The required features of the connector are as follows:

- must prevent fluid from oozing out of the device during surgery.
- rubber washers must facilitate the easy movement of the outer sleeve.

9. Link

The purpose of the link, as shown in Fig. 10, is to convert the angular motion of the handle to the translatory motion of the actuating connector such that it imparts



Fig. 9 Connector

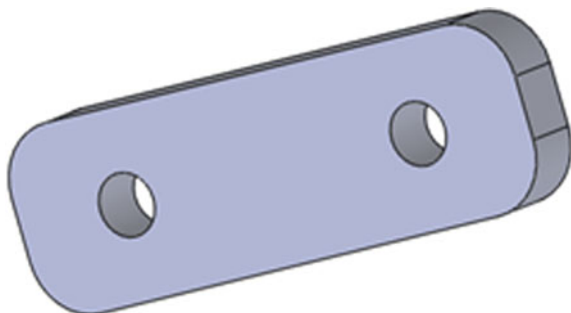


Fig. 10 Link

movement to the end effector assembly. The preferred material is 304 series stainless steel.

10. Outer Cap

The outer cap, as shown in Fig. 11, is threaded to hold the inner rod and the handle assembly together. The preferred material is 304 series stainless steel.

11. Locking Pin and Pins

The locking pin, as shown in Fig. 12a, is used to fix the outer sleeve at two extreme positions by sliding into the grooves on the collars of the connector. Pins, like those

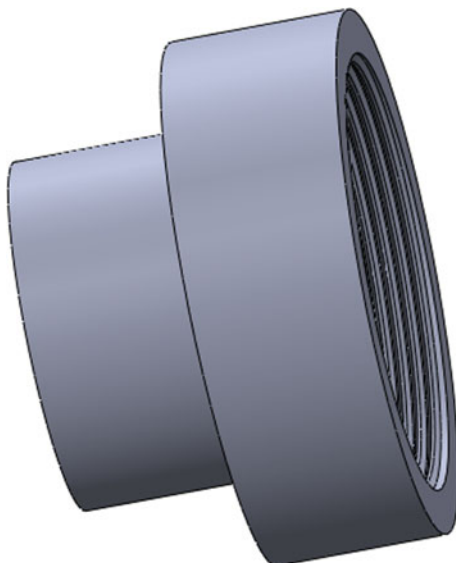


Fig. 11 Outer cap

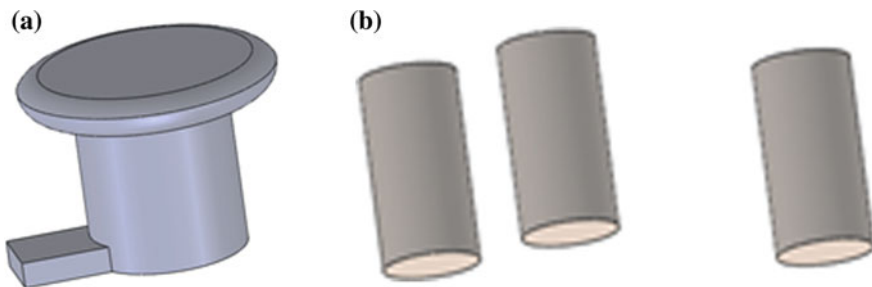


Fig. 12 **a** Locking pin. **b** Pins

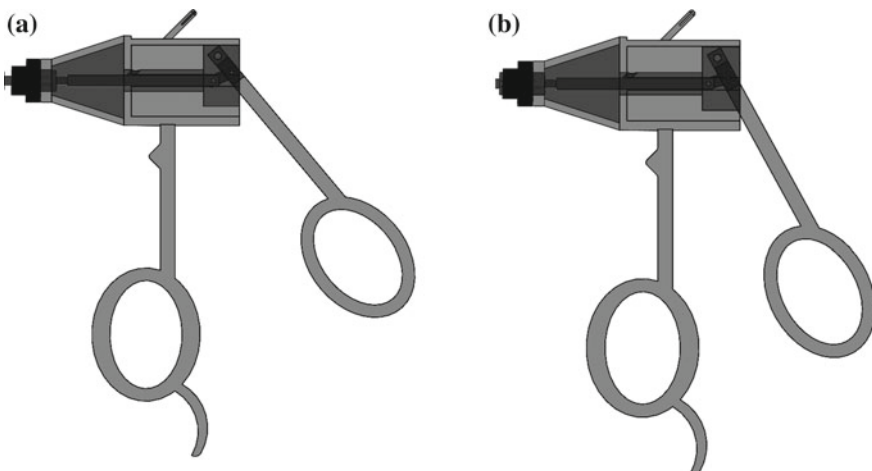


Fig. 13 **a** Handle in default position. **b** Handle position when actuated

in Fig. 12b, are used to join the four bars of the end effector assembly at the two ends of the link and the pivot of the handle. The preferred material for locking pin and pins is 304 series stainless steel. The pins should withstand forces experienced during the actuation of the handle and the jaws.

4 Mechanisms

The previous section describes the various components and their working. In this section, the different mechanisms connecting the components are described. The basic mechanisms in our current design of forceps include a four-bar mechanism, a sliding mechanism for an outer sleeve, the outer sleeve locking mechanism, a knob to change the orientation of the jaws, and the handle mechanism with suitable linkages.

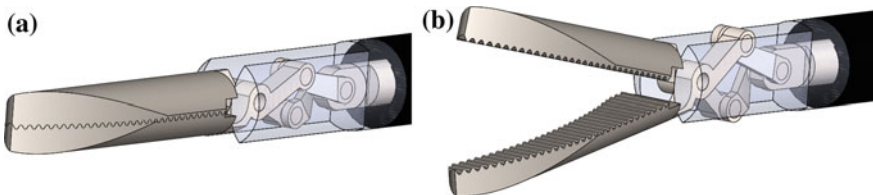


Fig. 14 **a** Closed configuration of jaws. **b** Open configuration of jaws

1. Handle Mechanism

It comprises three distinct parts, namely, the fixed hub, the movable handle, and the link. The movable handle is pivoted to the fixed hub so that it can rotate around that point within the constraints of the geometry of the hub when moved by the surgeon. The link joins the movable handle to the connector, transforming the angular motion of the movable handle into the translatory motion of the connector. The default position of the handle is shown in Fig. 13a. Therefore, when the handle is moved toward the fixed handle, the link transmits the motion to the connector, which is affixed to the inner rod, making it move toward the jaws. This movement activates the four-bar mechanism encased in the head, which is explained below.

2. Four-Bar Mechanism

The head encloses a four-bar mechanism that connects the two jaws to the end of the inner rod. The main function of this mechanism is to open and close the jaws. The bars extending from the two jaws are held together at their center using a pin, which is one end of the four-bar mechanism. The other end of this mechanism is attached to the inner rod, as shown in Fig. 14a. When the surgeon actuates the handle, the inner rod moves to the left, resulting in the jaws being opened, as shown in Fig. 14b.

3. Outer Sleeve and Locking Pin Mechanism

The outer sleeve is capable of sliding over the outer tube of the forceps. It has two extreme positions, which are defined by the grooves in the connector, as shown in Fig. 8. The locking pin fixes the outer sleeve into either of these grooves, ensuring that the outer sleeve cannot move during operation. When the outer sleeve completely covers the jaws, it is in the S-I mode, as shown in Fig. 15a. When the sleeve is retracted to the other extreme position, and the jaws are uncovered, the device is in the Forces mode, as shown in Fig. 15b.

The locking pin depicted in Fig. 12a is inserted within the groove in the outer sleeve and the connector. Then the pin is rotated to lock the outer sleeve in either of the positions described above. This arrangement ensures that the outer sleeve does not move and disrupt the surgery.

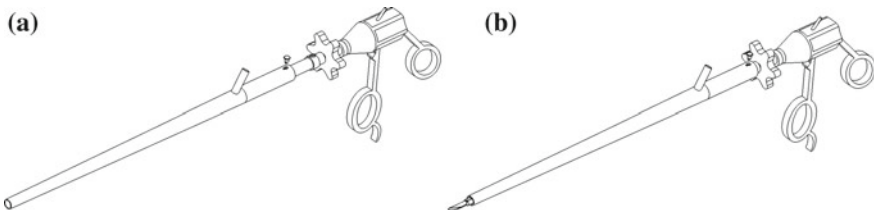


Fig. 15 **a** Device in S-I mode. **b** Device in forceps mode

4. Knob

The surgeon can change the orientation of the jaws as and when required by rotating the knob clockwise or anticlockwise, as shown in Fig. 7.

5 Challenges and Possible Solutions

1. Four-bar jaws mechanism

This is an intricate mechanism and could result in:

- accumulation of tissue particles during the surgery when the instrument is operating in the forceps mode.
- higher pressure drop during the S-I process when it operates in the S-I mode.

2. Sliding mechanism for the outer sleeve

The current mechanism constraints the outer sleeve in the radial direction only at one end. This might lead to the end covering the jaws of the forceps to yaw in the radial direction. This might affect the ergonomics and S-I capabilities of the device since the concentric arrangement of the outer tube and the outer sleeve will be disturbed.

3. Locking mechanism

The proposed locking pin is lightweight, compact, requires minimal effort in terms of locking torque, is directly mounted on the connector, and provides ease in actuation. However, there is a chance of the pin slipping during the surgical process. In addition, the surgeon has to physically remove the pin and reinsert it to switch between modes of the instrument. Therefore, the following designs are suggested as improvements to the existing mechanism and address the above issues:

- Switch with spring: It would be more ergonomically suitable to have a mechanical switch with a spring, which, when pressed, releases the outer sleeve to move between the two modes of operation. However, this is more complicated than the proposed locking pin mechanism.

- Electrically operated toggle switch: It could be another improvement to overcome the aforementioned difficulties.
4. Valve mechanism

As mentioned in Sect. 2, the CO₂ insufflation and S-I processes require separate instruments and exchange of multiple devices. This compromises the patient's safety in addition to causing fatigue to the surgeon and prolonging the duration of surgery. These challenges can be addressed by having the outer sleeve act as the CO₂ insufflation pathway in the currently proposed design. This is incorporated using a three-way valve to allow the S-I fluids and CO₂ to flow through the same pathway.

6 Suggested Improvements

1. The proposed design has a long, inflexible shaft, which makes some regions inside the abdomen inaccessible and restricts the grasper head in an axial orientation. Adding shaft flexibility will allow an additional degree of freedom to the head [8].
2. The proposed design can further be universalized by standardizing laparoscopic and endoscopic devices so that the outer sleeve can be slid over them to enhance their individual capabilities with the S-I feature.
3. In the current design, the jaws, the four-bar mechanism, and the inner rod constitute a single assembly. To change the laparoscopic functionality with a different set of jaws, the entire assembly must be replaced. This design can be improved by ensuring that the jaws can be easily detached from the four-bar mechanism.
4. A specially designed miniature 3-axis distal force sensor can be added to perform tissue palpation and measure tissue interaction forces at the tip of a surgical instrument [9]. This feature will lead to the widespread adaption of the proposed design in robot-assisted laparoscopic surgery.

7 Conclusion

The dissector forceps with long tubes are introduced into the abdominal region through trocars in laparoscopic procedures. The suction feature of the S-I device removes blood and other bodily fluids and irrigation feature sprays disinfectant like saline water. This paper intends to bring about a change in laparoscopic surgical procedure by combining dissector forceps with the S-I instrument, making it faster and easier for the surgeon to operate. The new design, therefore, eliminates the need of multiple insertion and removal of instruments which results in less trauma to the patient. Further, since the operating time is reduced, there will be minimal fatigue to the surgeon. Detailed description of individual components and their functionality in the proposed design is given. The challenges and improvements in design are

discussed, and suitable materials for the components are suggested. The proposed instrument is potentially advantageous over other forceps and is recommended for both educational and surgical purposes.

Acknowledgements We would like to thank the Mechanical Engineering Department, BITS Pilani, Hyderabad Campus for the infrastructural support and resources provided.

References

1. Faraz, A., Payandeh, S.: Engineering approaches to mechanical and robotic design for minimally invasive surgery. In: The Springer International Series in Engineering and Computer Science, 1st edn. Springer, US (2000)
2. Rosen, J.E., Size, A., Yang, Y., Sharon, A., Sauer-Budge, A.: Artificial hand for minimally invasive surgery: design and testing of initial prototype. *Surg. Endosc.* **29**(1), 61–67 (2015)
3. Den Boer, K.T., Straatsburg, I.H., Schellinger, L.T., De Wit, L.T., Dankleman, J., Gouma, D.J.: Quantitative analysis of the functionality and efficiency of three surgical dissection techniques: a time motion analysis. *J. Laparoendosc. Adv. Surg. Tech. A* **9**, 389–395 (1999)
4. Sjoerdsma, W., Meijer, D.W., Jansen, A., Den Boer, K.T., Grimbergen, C.A.: Comparison of efficiencies of three techniques for colon surgery. *J. Laparoendosc. Adv. Surg. Tech. A* **10**, 47–53 (2000)
5. Park, A., Lee, G., Seagull, F.J., Meenaghan, N., Dexter, D.: Patients benefit while surgeons suffer: an impending epidemic. *J. Am. Coll. Surg.* **210**(3), 306–313 (2010)
6. Junaidi, M.A.D., Sista, H., Kalluri, R.C.M., Rao, Y.V.D.: Laparoscopic Surgical Device, IN 202011034072. Birla Institute of Technology and Science (2020)
7. Junaidi, M.A.D., Sista, H., Kalluri, R.C.M., Rao, Y.V.D.: Laparoscopic Surgical Device, Design patent IN 334185–001. Birla Institute of Technology and Science (2020)
8. Amat, J., Casals, A., Bergés, E., Avilés, A.: Challenges in the design of laparoscopic tools. In: Robot 2015. Second Iberian Robotics Conference, pp. 463–475 (2015)
9. Puangmali, P., Liu, H., Seneviratne, L.D., Dasgupta, P., Althoefer, K.: Miniature 3-axis distal force sensor for minimally invasive surgical palpation. *IEEE/ASME Trans. Mechatron.* **17**(4), 646–656 (2012)

Improvement in Wear and Friction Properties of Heat-Treated Steel Using Micro-grooved Patterns



Nikhil More and S. S. Lakade

1 Introduction

In recent year, various efforts are being made in surface treatment industry for modification of surface properties of metals. As there are certain issues related to sheet metal industries, where forming dies are used for production of sheet metal components subject to less productivity, increase in cost per component, and high machinery maintenance.

Dies surface wear out is the leading cause for surface damage. Such problem occurs due to inaccurate clearance between die and punch while setting up dies and punches on the fixtures. This causes severe damage to the die and punch surface reducing average working life affects productivity and cost of production ultimately affecting dimensional accuracy and poor-quality sheet metal component which in turn increases possibility of rejection in quality check.

The present work has been carried out to get rid of this problem. Improvement in surface properties such as surface hardness, surface roughness along with tribological properties such as wear and friction coefficient. It will help to enhance the productivity and will provide cost-effective solution. This needs to go with some modern surface modification techniques such as heat treatment, solid lubrication, and micro-grooving.

The most common material used in forming dies is AISI D2 steel. It is also called as high carbon high chromium steel noted as HCHCr. High carbon content provides surface hardness and high chromium provided corrosion resistance. Hence work is focused on surface modification of AISI D2 steel. There three different modern techniques which were used are micro-grooving, heat treatment, and solid

N. More (✉) · S. S. Lakade

Pimpri-Chinchwad College of Engineering, Pune University, Pune, India

S. S. Lakade

e-mail: sanjay.lakade@pccoeplive.org

lubrication. Treatments to be done at micron level. Hence nowadays, these three techniques are viable options and cost effective.

Micro-grooving is carried out using surface texturing. Available techniques for micro-grooving are grinding and honing, electron-ion etching, chemical etching, electric discharge machining, and laser beam machining. Among these, laser beam machining is more appropriate method because it is environmentally friendly, time saving. As same tool can be used a number of times hence it is cost effective. Trial and error experimentation is possible. This method is used in the process of surface texturing for micro-grooving; therefore, it is also called as laser surface texturing (LST) [14].

Heat treatments are applied to the material to improve surface hardness, surface roughness, and micro-roughness. In the present work, plasma ion nitriding is used for surface hardening. This is a closed chamber process. It is environmentally friendly, no oxide formation, controlled temperature process (operating temperature less than 570 °C) hence no heat exposure to the atmosphere, minor distortion in dimensions of processed component. It is pure diffusion process hence no addition to the thickness. Only nitrides of chromium and ferrous are formed during the process. Control over process parameters such as voltage, current, frequency, gas ratio are possible, hence required hardness and depth of hardness is possible to obtain. The improvement in surface properties provides control over wear and friction coefficient properties. Change in wear and friction can be determined by Experimentation and Testing. In the current scenario, to improve above properties, Plasma ion nitriding is used [11].

Experimentation and testing are carried out in dry lubrication condition. Graphite is used as a solid dry lubricant hence process is also called as Solid lubrication, has large advantages over liquid lubrication. Graphite, MoS₂ are common solid lubricants used in the market but graphite has comparable high load-bearing capacity, high working life, and good working reliability in humid and dry environment. Also, micro-grooves act as a storage spaces for lubricant which ensures necessary supply during operation increases service life of lubricant [8, 13].

2 Material Processing, Experimentation, and Testing

2.1 Sample Preparation

Disc samples to be prepared for Experimentation. AISI D2 steel (*wt. %: 1.46 C, 0.22 Mn, 0.17 Si, 11.10 Cr, 0.48 Mo, 0.23 V, 0.014 P, and 0.012 S*). having hardness of 56 HRC, 165 × 8 mm in dimensions followed with grinding and polished [12, 13]. The Pin sample was Alumina (Al_2O_3 , 99% *pure*) with hardness 80 HRC [4].

Micro-grooved samples were prepared using fiber laser surface texturing. Five samples grooved with Dimple, Asterisk, Rhombus, Concentric Circles, Cross Groove, respectively, are prepared. Micro-level texturing is carried out with fiber laser machine equipped with 0.2% accuracy at 50KW power, 1064 nm wavelength,

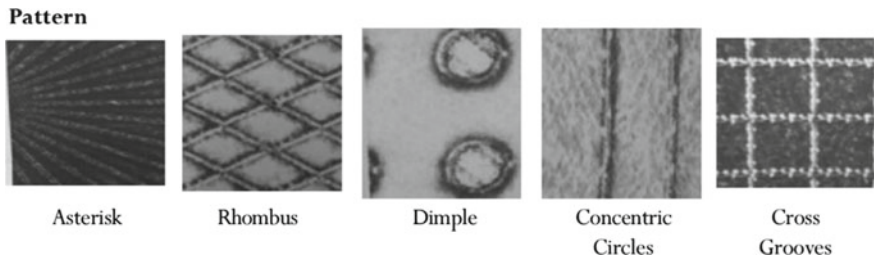


Fig. 1 Micro-grooves with various textures (Images by high resolution, magnification 75x)

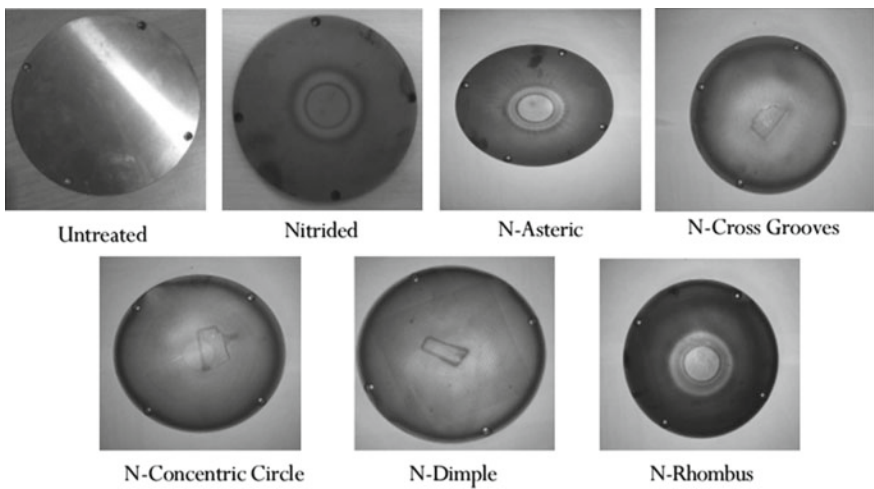


Fig. 2 Disc samples

and pulse frequency of 10KHz of laser beam. Grabowski et al. [1, 7] the high-resolution images are captured with 75 \times magnification using vision measurement system are shown in Fig. 1.

Samples are processed for plasma ion nitriding in complete vacuum at 450–500 °C for 8 to 10 h. Hence total seven samples prepared includes plane D2 steel disc, Plasma nitrided Disc, and five textured nitrided discs. Tang et al. [10] the processed samples with and without laser micro-grooving and plasma nitriding are shown in Fig. 2.

3 Experimentation and Testing

Tribological properties of samples are determined using Pin-on-Disc Tribometer (Fig. 3) as per ASTM wear test standard G-99 with sliding distance of 1000 m, sliding speed of 2.5 m/s [2].

Fig. 3 Pin-on-disc tribometer



Tests were conducted at three different loads 39.24 N, 88.29 N, 127.53 N. Rajpoot [3, 13] as D2 steel is subjected to higher friction loads, It is required to test the specimen at higher test load values. Alumina pin, disc specimens are cleaned with acetone before each test.

Graphite powder is burnished on textured samples for dry lubrication. After testing the disc samples, reports are generated for friction coefficient. Reports for wear Depths created due to testing are obtained on vision measurement system having accuracy of 4μ . The tested samples are shown in Fig. 4.

4 Results and Discussion

According to Archard's law, "wear rate is proportional to the applied test load". But the linear increase in wear with respect to applied loads is not observed. The solid lubricant using micro-grooved patterns as a storage spaces found to be effective at higher loads, i.e., 88.29 N, 127.53 N, etc. The graphite used as a solid lubricant could enhance its ability to reduce wear and friction coefficient significantly for all micro-grooved textures. Type of wear is adhesive. Hardness of Alumina is 80HRC

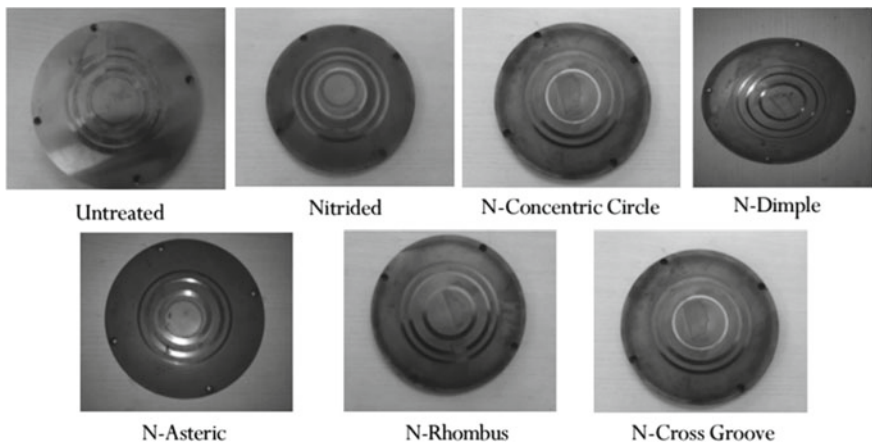


Fig. 4 Tested samples

which is much higher than D2 steel having hardness of 61 ± 1 HRC. Hence D2 steel tested against the Alumina Pin. The wear of Alumina pin observed is found to be negligible and wear loss is 0.000036 g. The material wear delamination was observed at higher load of 127.53 N for all samples.

The laser textured micro-grooves storing graphite are getting supplied only when required contact between pin and disc takes place. Hence life of graphite is increased. Unlike liquid lubricants, Graphite has high load-bearing capacity and anti-sticking properties. Hence durability of Graphite is much higher than liquid lubricants.

Figure 5, graph of ‘Wear vs load’, shows that compared to untreated D2 steel, significant reduction in wear and friction coefficient values occurred for dimple and rhombus pattern up to 95%. Similarly, in Fig. 6, dimple and rhombus pattern could show the reduction in friction coefficient up to 80%.

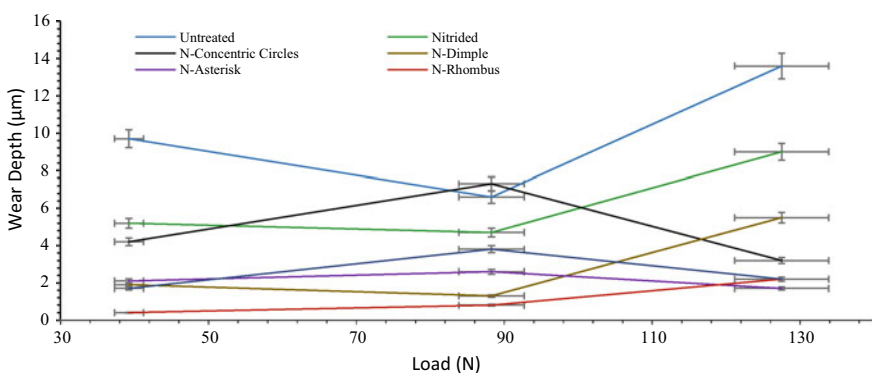


Fig. 5 Graph of wear depth (μm) versus Load (N)

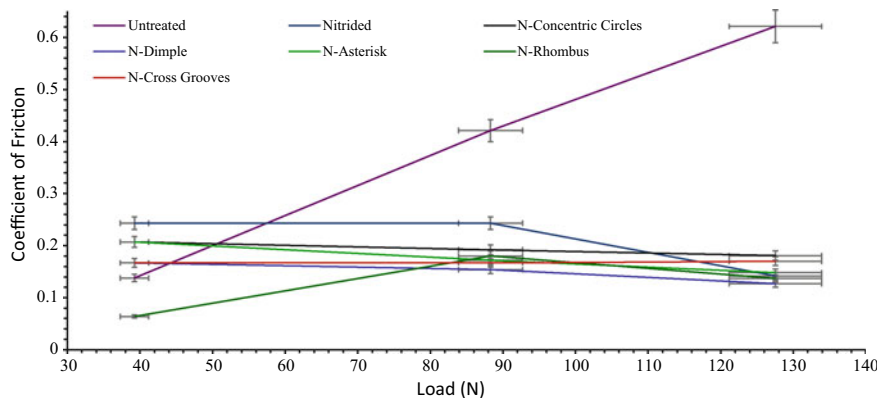


Fig. 6 Graph of coefficient of friction versus Load (N)

5 Conclusion

The wear and friction have significant control up to 95% and 80%, respectively, observed in case of dimple and rhombus pattern when results are compared with untreated D2 specimen because of the better adaptability with graphite supply during testing at both low and high friction condition.

The implementation of micro-grooved laser textured patterns for the contacting surfaces (Die and Punch) where wear and friction are required to control, the dimple pattern is more feasible for any type of critical geometry of the surfaces as compared to rhombus pattern.

Hence, for adhesive wear mechanism, dimple and rhombus pattern produced effective results in presence of graphite for D2 steels.

References

1. Grabowski, A., Sozański, M., Adamiak, M. et al.: Laser surface texturing of Ti6Al4V alloy, stainless steel and aluminum silicon alloy, (2018). www.elsevier.com/locate/apsusc
2. ASTM: Standard test method for wear testing with a Pin-On-Disk apparatus, Designation G 99–95a (2000)
3. Rajpoot, B.S.: Study of wear characteristics of AISI D2 steel, IJFRCSC (2017). <https://www.ijfrcsc.org>
4. Bourithis, L., Papadimitriou, G.D., Sideris, J.: Comparison of wear properties of tool steels AISI D2 and O1 with the same hardness. Tribol. Int. **39**, 479–489 (2006). <https://doi.org/10.1016/j.triboint.2005.03.005>
5. Zheng, D., Cai, Z.B., Shen, M.X. et al.: Investigation of the tribology behavior of the graphene nanosheets as oil additives on textured alloy cast iron surface, Appl. Surf. Sci. (2016). <https://doi.org/10.1016/j.apsusc.2016.06.080>
6. Tobola, D., Brostow, W., Czechowski, K., Rusek, P.: Improvement of wear resistance of some cold working tool steels. Wear (2017). <https://doi.org/10.1016/j.wear.2017.03.023>

7. Demir, A.G., Maressa, P., Previtali, B.: Fibre laser texturing for surface functionalization. Physics Procedia **41**, 759–768 (2013). <https://doi.org/10.1016/j.phpro.2013.03.145>
8. Li, J., Liu, S., Aibing, Yu., Xiang, S.: Effect of laser surface texture on CuSn6 bronze sliding against PTFE material under dry friction. Tribol. Int. **118**, 37–45 (2018). <https://doi.org/10.1016/j.triboint.2017.09.007>
9. Jones, K., Schmid, S.R.: Experimental investigation of laser texturing and its effect on friction and lubrication. Procedia Manuf. **5**, 568–577 (2016). <https://doi.org/10.1016/j.promfg.2016.08.047>
10. Tang, L., Gao, C., Huang, J., et al.: Dry sliding friction and wear behavior of hardened AISI D2 tool steel with different hardness levels. Tribol. Int. **66**, 165–173 (2013). <https://doi.org/10.1016/j.triboint.2013.05.006>
11. Poursafar, A., Sabet, M., Pesteei, S.M., Zarifkar, B.: Influence of plasma nitriding on wear behavior of AISI D2 tool steel. Proceeding of AMPT 2006, Las Vegas, USA (2006)
12. Zhang, R.L., Rahman, M.L., Liu, M., Liu, W.: Surface roughness effect on the friction and wear of bulk metallic glasses. Wear **332–333**, 1231–1237 (2015). <https://doi.org/10.1016/j.wear.2014.11.030>
13. Rapoport, L., Moshkovich, A., Perfiliev, V., et al.: Friction and wear of MoS₂ films on laser textured steel surfaces. Surf. Coat. Technol. **202**, 3332–3340 (2008). <https://doi.org/10.1016/j.surcoat.2007.12.009>
14. Voevodin, A.A., Zabinski, J.S.: Laser surface texturing for adaptive solid lubrication. Wear **261**, 1285–1292 (2006). <https://doi.org/10.1016/j.wear.2006.03.013>

Force Optimization for an Active Suspension System in a Quarter Car Model Using MPC



Jayesh Narayan, Saman Asghari Gorji, and Mehran Motamed Ektesabi

1 Introduction

In recent years, passenger safety and comfort have emerged as critical areas of research in automotive design and development. Vehicle manufacturers are striving to enhance the comfort level of passengers as well as the drivability experience. Suspension system has a vital role in the overall vehicle stability, drivability, and passenger comfort. Over the years, the suspension system has undergone a lot of improvements from an elementary spring-damper system to the more recent hydraulic and pneumatic systems. An active electromagnetic suspension was demonstrated in [1]. It has been demonstrated in many studies that active suspension system provides superior ride control and vehicle handling capabilities [2–7]. Due to their high weight, energy demand, and cost, the active suspension has not been extensively used in mainstream commercial vehicles. The study conducted in [3] has demonstrated the dynamics and the regenerative capability of electromagnetic suspension. An in-depth study on the electromagnetic dampers was conducted in [8]. Gysen et al. [1] has demonstrated a significant improvement in passenger comfort, road handling, and power consumption using LQR control. Gysen et al. [1, 9–12] have all used LQR control for the control of semi-active or active suspension systems. Numerous studies have been

J. Narayan (✉) · M. M. Ektesabi

School of Software and Electrical Engineering, Swinburne University of Technology,
Melbourne, Australia

e-mail: jnarayan@swin.edu.au

M. M. Ektesabi

e-mail: mektesabi@swin.edu.au

S. A. Gorji

Science and Engineering Faculty, Institute for Future Environments, Queensland University of
Technology, Brisbane, Australia

e-mail: saman.asgharigorji@qut.edu.au

conducted on the control of the suspension system using LQR [1, 9, 10, 12–15]. This control method has been used extensively in the control of active suspensions. The LQR is an optimal control problem and solution of these types of control problems involves the minimization or the maximization of the cost function. The LQR is an offline optimization method. Vehicle suspension-related parameters like tire stiffness and spring damping offer high sensitivity in a car model [16]. These physical parameters accumulate tolerance with temperature cycles and mechanical wear.

Model predictive control provides a more elegant solution to this problem. More recently, automotive manufacturers have introduced active suspension systems which use the vehicle's vision system and Light Detection and Ranging (LIDARs) to scan and preview the road [17]. MPC has the option of reference tracking along with preview information option. Furthermore, MPC is a finite horizon optimization problem. Using these options in conjunction with online optimization, the MPC can provide a much better control scheme for the suspension system.

In this paper section, the control schemes for the LQR and MPC have been discussed. The cost function using the state, output, and input variable has been presented and the effect of varying the weights on the cost function has been analyzed.

A. System model for Quarter Car

A Quanser quarter car model as shown in Fig. 1 has been used to describe the dynamics of the active suspension. Dynamics of the quarter car model has been defined in state-space format [18] in the equation below.

$$\begin{aligned}\dot{x} &= Ax + Bu \\ y &= Cx + Du\end{aligned}\quad (1)$$

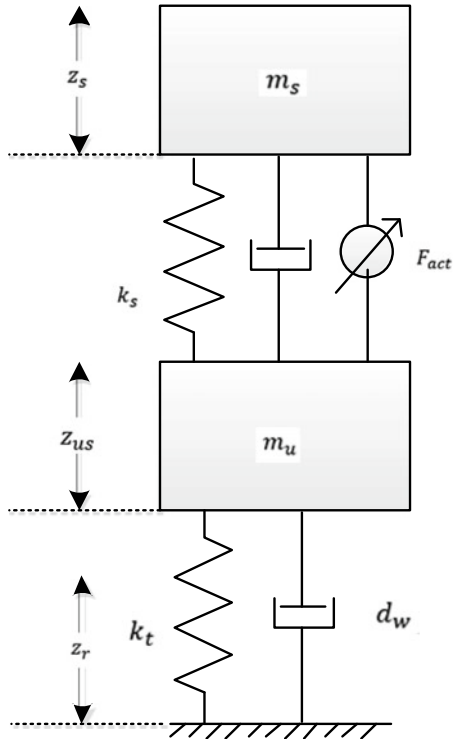
A transient road excitation has been considered as perturbation to the system. The parameters used for the road perturbation have been defined in Table 1.

The state variables and the control input vector were defined by Eq. (2). The state vectors represent the suspension deflection, sprung mass velocity, road handling, and the tire velocity. The input variable represents the actuator force. The output vector was defined as Eq. (3)

$$\begin{aligned}x &= [z_s - z_{us} \ z_s \ z_{us} - z_r \ z_{us}]^T \\ u &= [f_{act}]^T\end{aligned}\quad (2)$$

Table 1 Parameters for the transient road input

Parameter	Value	Unit
Amplitude	0.02	m
Period	3	sec
Pulse width	50	%
Phase delay	0.1	sec

Fig. 1 Quarter car model

$$y = [z_s - z_{us} \ z_s^{\ddot{}}]^T \quad (3)$$

which represents the suspension deflection and vertical acceleration of the sprung mass. The state vectors, input, output, and the feedforward matrices were defined as

$$A = \begin{bmatrix} 0 & 1 & 0 & -1 \\ \frac{-k_s}{m_s} & \frac{-d_s}{m_s} & 0 & \frac{d_s}{m_s} \\ 0 & 0 & 0 & 1 \\ \frac{k_s}{m_{us}} & \frac{d_s}{m_{us}} & \frac{-(k_s+k_t)}{m_{us}} & \frac{(-d_s+d_{us})}{m_{us}} \end{bmatrix} \quad (4)$$

$$B = [0 \ 1/m_s \ 0 \ -1/m_s]^T$$

$$\mathbf{C} = \begin{bmatrix} 1 & 0 & 0 & 0 \\ \frac{-k_s}{m_s} & \frac{-d_s}{m_s} & 0 & \frac{d_s}{m_s} \end{bmatrix} \mathbf{D} = \begin{bmatrix} 0 \\ \frac{1}{m_s} \end{bmatrix} \quad (5)$$

Table 2 Parameters for system simulation of active suspension

Parameter	Description	Value	Unit
m_s	Sprung mass	2.45	Kg
m_u	Unsprung mass	1	Kg
k_s	Spring constant for sprung mass	900	N/m
k_t	Spring constant for tire	1250	N/m
d_s	Damping force of actuator	7.5	N/m/s
d_w	Damping force of tire	5	N/m/s

2 Control Design

Stability of the Model:

The dynamic model for the suspension system has been defined in the state-space format by Eq. (4).

Taking the Laplace transform on both sides Eq. (4) can be written as

$$\begin{aligned} sX(s) - X(0) &= AX(s) + BU(s)X(s) = (sI - A)^{-1}X(0) + (sI - A)^{-1}BU(s) \\ Y(s) &= CX(s) + DU(s) \\ Y(s) &= C((sI - A)^{-1}X(0) + (sI - A)^{-1}BU(s)) + DU(s) \end{aligned} \quad (6)$$

An initial condition of $X(0) = 0$ has been assumed.

$$\begin{aligned} Y(s) &= G(s)U(s) \\ G(s) &= C(sI - A)^{-1}B + D \end{aligned} \quad (7)$$

where $G(s)$ is the transfer function and the characteristic equation of the suspension system model has been defined by

$$G(s) = \begin{bmatrix} G(s) \frac{z_s - z_{us}}{z_r} & G(s) \frac{z_s - z_{us}}{F_{act}} \\ G(s) \frac{z_s}{z_r} & G(s) \frac{z_s}{F_{act}} \end{bmatrix} \quad (8)$$

The stability of the above transfer function is evaluated in MATLAB using the pole-zero plot. The plot obtained in Fig. 2 shows the poles of the transfer function $G(s)$ in the left-hand side of the complex plane, which from the Nyquist stability criterion is a sufficient condition for the convergence of a transfer function. The poles and zeros location below are represented by 'x' and zeros by 'o'.

Controllability and Observability

The controllability of the continuous time-invariant system defined by Eqs. (4), (5) can be depicted using the controllability matrix P and defined using the equation below [19].

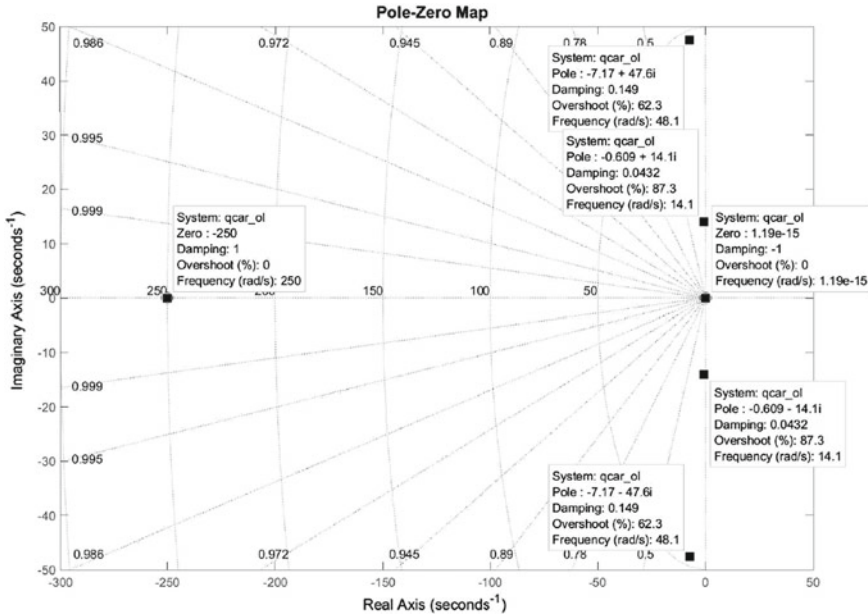


Fig. 2 Pole Zero plot for the active suspension model

$$P = [BABA^2B \dots A^{n-1}B] \quad (9)$$

where A is a square matrix with n x n dimension. The system is deemed controllable if the rank of the controllability matrix P equals n, defined by the dimension. The controllability matrix has been calculated in MATLAB using the “ctrb” command and subtracted from the length of the A matrix. From the calculation, it was found that the system is controllable as well.

LQR Design

Cost function for the LQR control has been defined as a quadratic function which includes state variables and the control input and has been defined by Eq. (2). The states have been used as the part of the cost function due to the dynamics of the model.

$$J(u) = \sum_{i=1}^{\infty} x^T Q_x x + u^T R_u u \quad (10)$$

In the above equation, where Q_x and R_u penalizes the state vector x and control variable u . The control vector u can be denoted as

$$u = -kx \quad (11)$$

and the gain matrix can be expressed as

$$k = -R_u^{-1} B^T P x \quad (12)$$

where P is the solution of Riccati equation given by

$$PA + A^T P - PBR_u^{-1}B^T P + Q_x = 0 \quad (13)$$

Using the system model defined by Eq. (1)–(5) the system was simulated in MATLAB-SIMULINK.

Transient Response

In this section, a simulation of transient response for the active suspension model is presented. For the road input, a pulse input with an amplitude of 0.02 m has been used to provide the perturbation to the system. The amplitude of the road profile is guided by the road deflection motor in the Quanser active suspension setup [18]. The parameters for the road and the quarter car model have been listed in Table 1 and Table 2.

The simulation is set up as defined in Fig. 3. The weights for states Q_x have been defined as a diagonal matrix so that the weights have direct effect on the corresponding state variable.

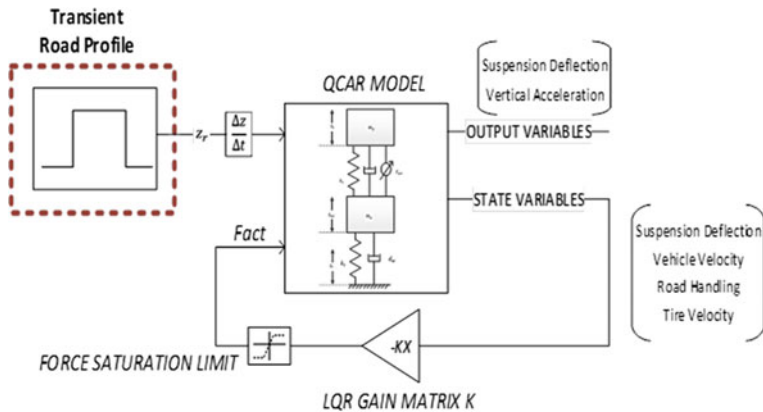


Fig. 3 Transient setup for the LQR control

$$Q_x = \begin{bmatrix} 0.9 & 0 & 0 & 0 \\ 0 & 10 & 0 & 0 \\ 0 & 0 & 100 & 0 \\ 0 & 0 & 0 & 0.01 \end{bmatrix}$$

The simulation was conducted to investigate the effect of the input weight R_u . The input weight R_u was varied from 0.001 to 0.5 and the response of the suspension deflection based on the overshoot and settling time was observed. The peak values for the actuator force and the suspension deflection have been extracted. Furthermore, the settling time, defined by the time taken for the signal to converge, has been plotted for the suspension deflection.

MPC Design

In this section, the linear MPC has been defined and the transient response and the variation of the input and the output weight of the active suspension have been investigated. The cost function for the MPC has been defined by Eqs. (14)–(16) and (18).

$$J_{mpc}(z_k) = J_y(z_k) + J_u(z_k) + J_{\Delta u}(z_k) \quad (14)$$

$$J_u(z_k) = \sum_{j=1}^{n_y} \sum_{i=1}^p (u_j(k+i|k) R_{mpc} u_j(k+i|k))^T \quad (15)$$

$$J_{\Delta u}(z_k) = \sum_{j=1}^{n_y} \sum_{i=1}^p \Delta u(k+i|k) W_{mpc} \Delta u(k+i|k)^T \quad (16)$$

where $J_{mpc}(z_k)$ is the cost function defined by the output variables, input, and rate of change of input variables.

$J_y(z_k)$ defined in Eq. (18) represents the cost function associated with the output. Here, n_y represents the number of output variables, p signifies the prediction horizon, and k represents the current control horizon. $r_j(k+i|k)$ is the reference signal. $J_u(z_k)$ denotes the cost function for the input. u_j represents the input to the system. $J_{\Delta u}(z_k)$ corresponds to the cost function for the rate of change of the input and Q_{mpc}, R_{mpc} , and W_{mpc} represent the weight for $J_y(z_k)$, $J_u(z_k)$ and $J_{\Delta u}(z_k)$.

Transient Response

Since it has already been established that the active suspension model is both controllable and observable, this step has been omitted for the MPC section. In this section, the prediction output, and its relation to the state variables have been defined. The prediction output \hat{y}_p for the system model defined using suspension model can be written as

Table 3 Conditions for I/O weights

Input weight (Actuator force)	Output weight (Suspension deflection)	Output weight (Vertical acceleration)
0.001	0.1	1.1
0.01	0.2	1.2
0.1	0.3	1.3
1	0.4	1.4
10	0.5	1.5

$$\hat{y}_p = \begin{bmatrix} CA \\ CA^2 \\ \vdots \\ CA^p \end{bmatrix}_{px1} x_k + \begin{bmatrix} CB \\ CAB \\ \vdots \\ CA^{p-1}B \end{bmatrix}_{px1} u_k + \begin{bmatrix} D & 0 & 0 & 0 \\ CB & \ddots & 0 & 0 \\ \vdots & \ddots & \ddots & 0 \\ CA^{p-2}B & \ddots & CB & D \end{bmatrix} \begin{bmatrix} u_{k+1} \\ \vdots \\ u_{k+n} \end{bmatrix}_{px1}$$

$$\hat{y}_p = \begin{bmatrix} y_{k+1} \\ y_{k+2} \\ \vdots \\ y_{k+p} \end{bmatrix}_{px1} \quad (17)$$

The input weight has been varied from 0.001 to 1 in the first scenario. In the second and third scenarios, the output vectors weights, suspension deflection, and vertical acceleration, which affect the cost function J_y have been varied. Table 3 outlines the weights that have been used for transient response analysis.

3 Results

The simulation for LQR has been swept for different values of R_u and the corresponding suspension deflection has been plotted (Fig. 4). The plot shows maximum suspension deflection for $R_u = 0.001$ and the signal converges to zero. With the increase in the value of R_u , the suspension deflection decreases but the oscillatory nature of the signal is observed, which prevents the signal from converging. Oscillations in the suspension deflection (Fig. 4) lead to the transfer of higher frequency content signal to the vertical acceleration (Fig. 5), which subsequently deteriorates the passenger comfort. This is evident from Fig. 5, which depicts the output response of the vertical acceleration. An increase in the input weight R_u exhibits an increase in the vertical acceleration as well as the ringing behavior of the output.

From the combined analysis of these plots (Figs. 4, 5 and 6), it can be concluded that with cheap control, i.e., low input weight, $R_u = 0.001$, the maximum suspension deflection occurs, and the settling time is minimum. With the increase in weight, both the actuator force and the suspension deflection decrease, however, the setting time of the suspension deflection increases, which is evident from Fig. 7. These oscillations have a direct impact on the vertical acceleration of the sprung mass, that leads to a reduction of passenger comfort.

From the simulation performed for MPC, it can be concluded that input weight variation from 0.001 to 0.01 does not affect the actuator transient response (Fig. 8). One of the primary observations from both the plots (Figs. 8 and 9) is the convergence of the actuator force and the suspension deflection, which explains the minimization of the cost function. This is evident from Fig. 9 where the transient plots for 0.001 and 0.01 have the same trajectory and can be supported by the output response variation plot Fig. 8, which clearly shows no change in suspension deflection and the vertical acceleration. It can also be deduced from Fig. 9 that with an increase in the input weight outside the 0.001 and 0.01 window causes the magnitude of the actuator force to decrease and finally become zero at input weight, $R_u = 10$. This can also be regarded as a condition where the suspension is passive with zero actuator force. This is again evident and consistent from the oscillation observed in the suspension deflection transient response and vertical acceleration response, which depicts a steady increase in the oscillations with an increase in the input weight.

In Fig. 10 the output weight for the suspension deflection has been swept from 0.1 to 0.5 in steps of 0.1. It can be concluded from the first plot in Fig. 10 that the suspension deflection converges with an increase in the suspension deflection weight. The magnitude of the response does not change irrespective of the weight. It can also be noted that the suspension deflection settling time is inversely affected by the suspension deflection weight. The second plot in Fig. 10 also depicts that the output response of the vertical acceleration does not change with the weight of the suspension deflection.

In the final part of this transient response analysis, the output weight for the vertical acceleration is varied and is depicted in Fig. 11. The output weight swept from 1.1 to 1.5. The acceleration response plot shows a difference of $\sim 0.5 \text{ m/s}^2$ between the maximum and the minimum overshoot. The maximum magnitude of the vertical acceleration is $\sim 2.5 \text{ m/s}^2$.

$$J_y(z_k) = \sum_{j=1}^{n_y} \sum_{i=1}^p \left\{ [r_j(k+i|k) - y_j(k+i|k)] Q_{mpc} [r_j(k+i|k) - y_j(k+i|k)]^T \right\} \quad (18)$$

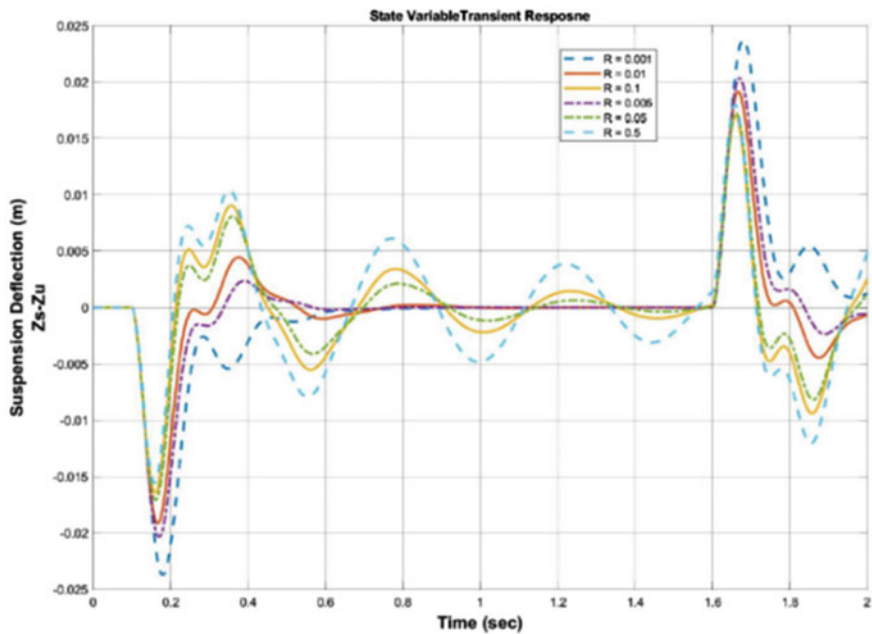


Fig. 4 Variation of actuator force with input weight using LQR

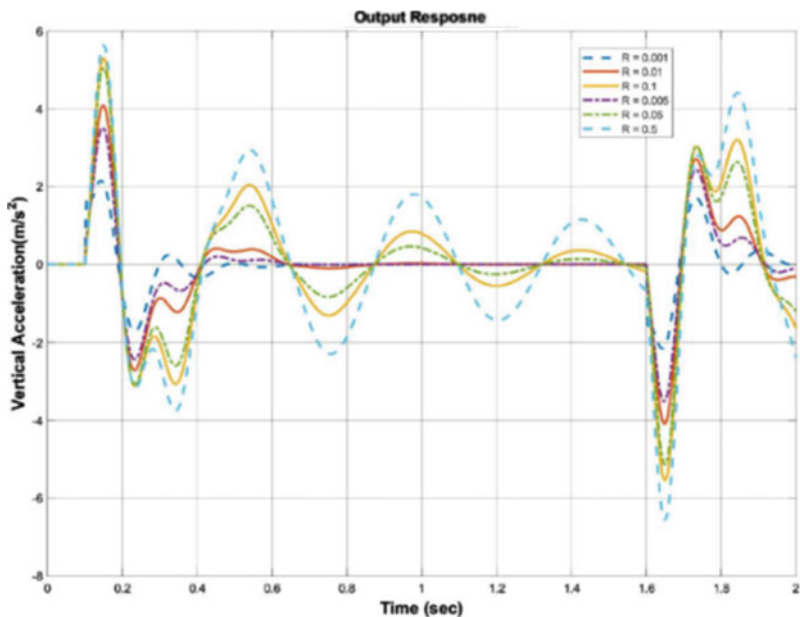


Fig. 5 Variation of vertical acceleration with input weight for LQR

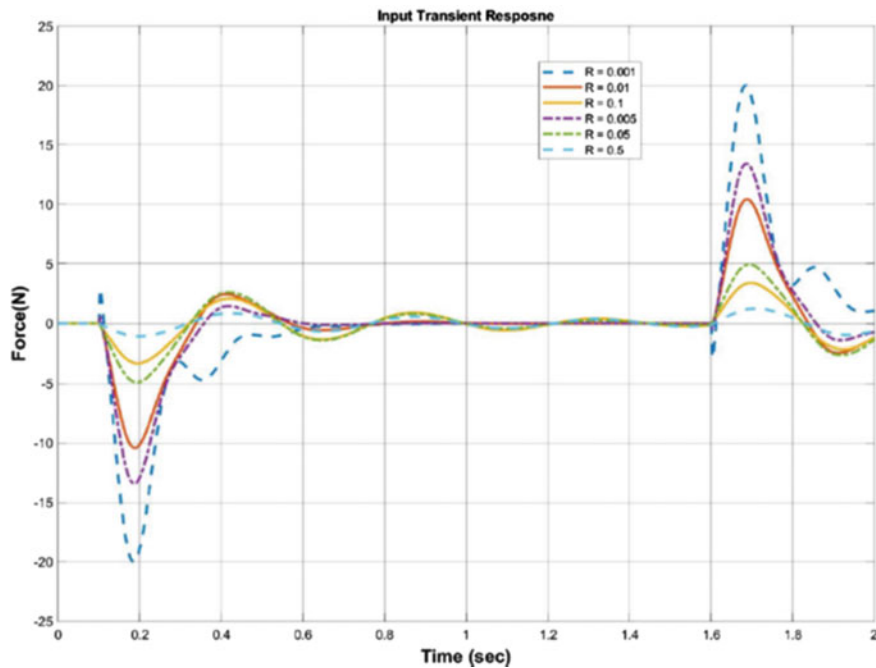


Fig. 6 Variation of vertical acceleration with input weight for LQR

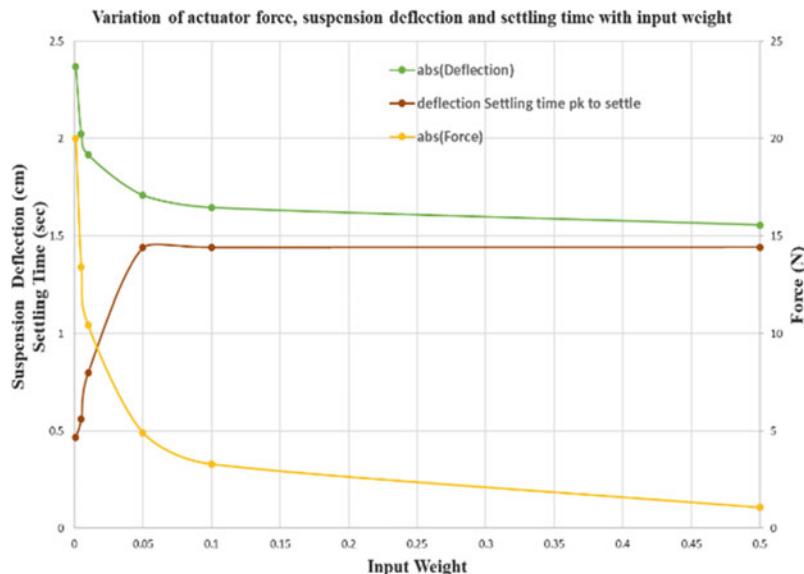


Fig. 7 Comparison of the suspension deflection, settling time, and actuator force with input weight for LQR

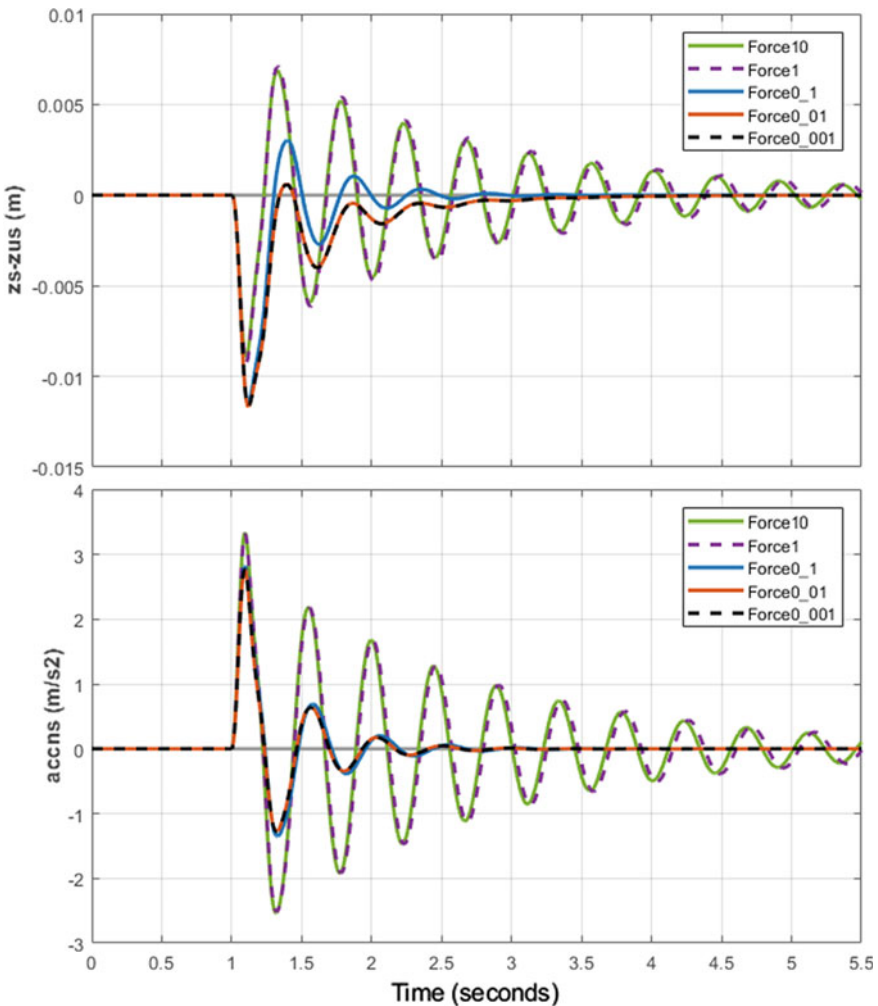


Fig. 8 Variation of vertical acceleration and suspension deflection with input weight for MPC

4 Conclusion

The transient analysis of the MPC control and variation of the input and output weights was carried out. Same road profile as the one in the LQR transient analysis was used. The transient response indicated that with a cheap control and an input weight of 0.001, the maximum actuator force of 6.2 N is required to attain a suspension deflection of 1.25 cm and a vertical acceleration of 2.75 m/s^2 . It can be stated that the MPC control requires approximately 69% less actuator force to attain a 48% reduction in suspension deflection. The vertical acceleration in the MPC control case increased by 12%. Since the MPC in comparison to the LQR control performs better

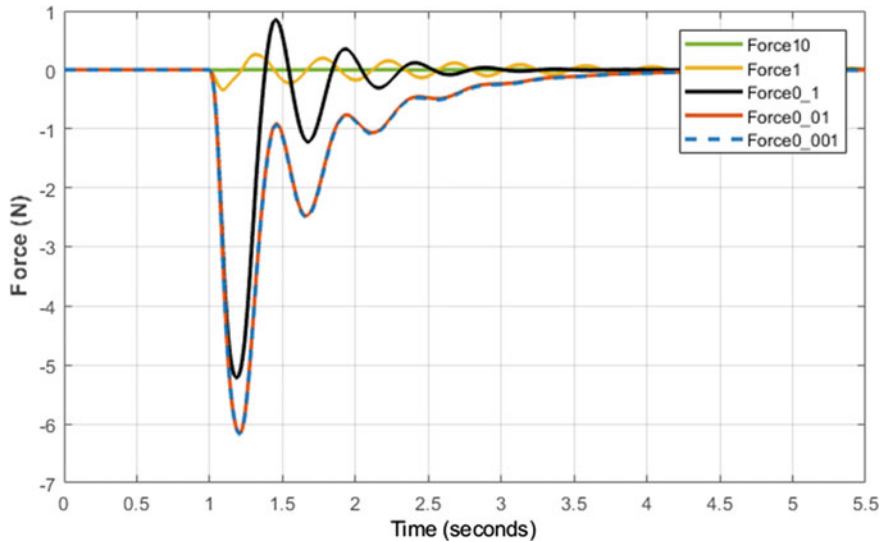


Fig. 9 Variation of actuator force with input weight in MPC

in two areas, namely, actuator force demand and suspension deflection by a significant margin, weights can further be tuned for the input parameter to provide slightly expensive control. This will compensate for the increase in the vertical acceleration that has been observed in the transient response simulation. These results provide a promising insight for further investigation of the LQR and the MPC control using artificial road profiles.

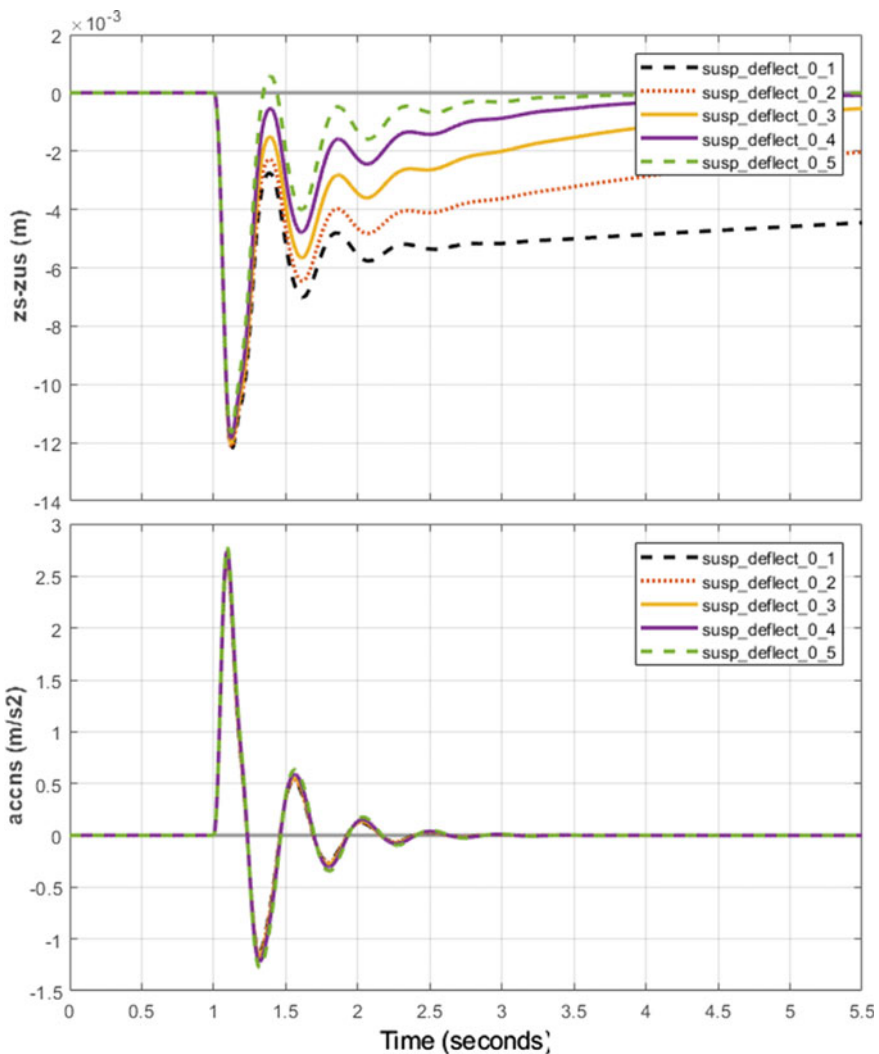


Fig. 10 Variation of vertical acceleration and suspension deflection with output weight for MPC

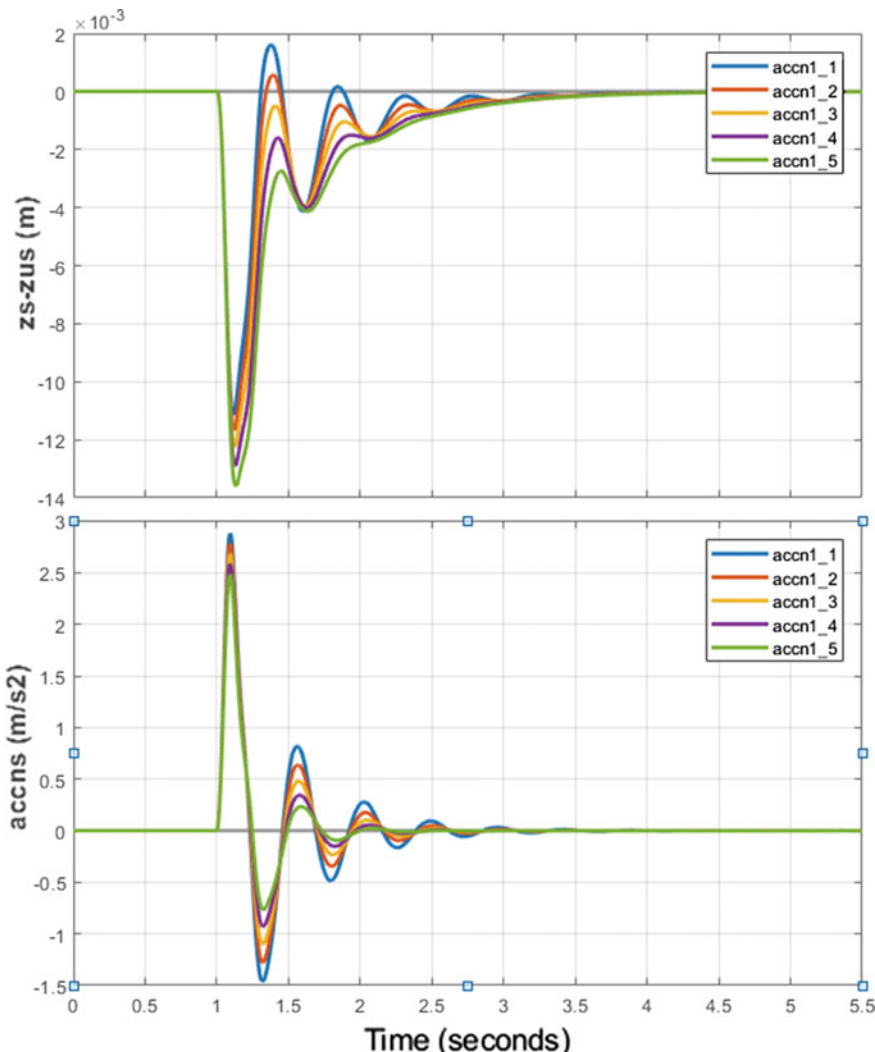


Fig. 11 Variation of suspension deflection and vertical acceleration with output weight (vertical acceleration) in MPC

References

1. Gysen, B.L., van der Sande, T.P., Paulides, J.J., Lomonova, E.A.: Efficiency of a regenerative direct-drive electromagnetic active suspension. *IEEE Trans. Veh. Technol.* **60**(4), 1384–1393 (2011)
2. Gysen, B.L., Paulides, J.J., Janssen, J.L., Lomonova, E.A.: Active electromagnetic suspension system for improved vehicle dynamics. *IEEE Trans. Veh. Technol.* **59**(3), 1156–1163 (2009)
3. Gysen, B.L., Janssen, J.L., Paulides, J.J., Lomonova, E.A.: Design aspects of an active electromagnetic suspension system for automotive applications. *IEEE Trans. Ind. Appl.* **45**(5), 1589–1597 (2009)

4. Lee, S., Kim, W.: Active Suspension Control With Direct-Drive Tubular Linear Brushless Permanent-Magnet Motor. *IEEE Trans. Control Syst. Technol.* **18**(4), 859–870 (2010)
5. C. Görle, A. Wagner, A. Schindler, and O. Sawodny, “Active suspension controller using MPC based on a full-car model with preview information,” in *2012 American Control Conference (ACC)*, 2012: IEEE, pp. 497–502.
6. S. Kashem, R. Nagarajah, and M. Ektesabi, “Control Strategies in the Design of Automotive Suspension Systems,” in *Vehicle Suspension Systems and Electromagnetic Dampers*: Springer, 2018, pp. 9–22.
7. J. Narayan, S. A. Gorji, and M. M. Ektesabi, “Power reduction for an active suspension system in a quarter car model using MPC,” in *2020 IEEE International Conference on Energy Internet (ICEI)*, 2020: IEEE, pp. 140–146.
8. S. Kashem, R. Nagarajah, and M. Ektesabi, “Vehicle Suspension System,” in *Vehicle Suspension Systems and Electromagnetic Dampers*. Singapore: Springer Singapore, 2018, pp. 23–37.
9. M. Tomizuka, Optimum Linear Preview Control With Application to Vehicle Suspension—Revisited, 1976
10. A. Thompson, B. Davis, and C. Pearce, “An optimal linear active suspension with finite road preview,” *SAE Transactions*, pp. 2009–2020, 1980.
11. Pilbeam, C., Sharp, R.: Performance potential and power consumption of slow-active suspension systems with preview. *Vehicle System Dynamics* **25**(3), 169–183 (1996)
12. Senthil, S., Narayanan, S.: Optimal preview control of a two-dof vehicle model using stochastic optimal control theory. *Vehicle system dynamics* **25**(6), 413–430 (1996)
13. Hać, A.: Optimal linear preview control of active vehicle suspension. *Vehicle system dynamics* **21**(1), 167–195 (1992)
14. Prokop, G., Sharp, R.: Performance enhancement of limited-bandwidth active automotive suspensions by road preview. *IEE Proceedings-Control Theory and Applications* **142**(2), 140–148 (1995)
15. Fleming, A.J., Moheimani, S.R., Behrens, S.: Synthesis and implementation of sensor-less active shunt controllers for electromagnetically actuated systems. *IEEE Trans. Control Syst. Technol.* **13**(2), 246–261 (2005)
16. F. Sun and Y. Cui, “Influence of parameter variations on system identification of full car model,” in *World Congress on Engineering 2012. July 4–6, 2012. London, UK.*, 2010, vol. 2189: International Association of Engineers, pp. 839–843.
17. A. AG. (2017, 24–01–2019). *Looking ahead to the new Audi A8: Fully active suspension offers tailor-made flexibility.*
18. Quanser. (11–03–2019). *Quanser active suspension product details.*
19. D. Simon, *Optimal state estimation: Kalman, H infinity, and nonlinear approaches*. John Wiley & Sons, 2006.

Mobility Analysis of Coupled System of Upper Limb Exoskeleton and Human Arm



Macha Vidyaaranya, Sakshi Gupta, and Ekta Singla

1 Introduction

One of the major issues responsible for the rejection of wearable exoskeletons is due to the user discomfort arising from misalignments between the human and the exoskeleton [1]. There are mainly two reasons why misalignments occur: the difference between the kinematics of human and exoskeleton when decoupled and, modified kinematics due to the constraints associated with fixing of the exoskeleton to human. The first problem is alleviated by analyzing the kinematics of human and rendering the same motion to the exoskeleton so that the behavior is similar. For example, the elbow joint is not simply a one DOF revolute joint but it also has translational motion associated with it. So, when the elbow joint of exoskeleton has only one DOF revolute joint, misalignments are prone to occur. Many researchers have tried to compensate for misalignment by utilizing other complex mechanisms (crossed four-bar linkage, five-bar linkage, etc.) or employing redundant DOFs [2]. Introduction of redundant DOFs in the exoskeleton kinematic chain helps to mitigate interaction forces at the harness between human and exoskeleton [3].

Although there is a lot of literature on the kinematic analysis of exoskeleton [4–6] and human arm individually, not much emphasis is given to the kinematic analysis of coupled mechanism between the exoskeleton and the human arm. This paper utilizes the concept of redundant DOF in order to compensate for misalignment

M. Vidyaaranya · S. Gupta (✉) · E. Singla
Indian Institute of Technology Ropar, Punjab 140001, India
e-mail: 2016mez0024@iitrpr.ac.in

M. Vidyaaranya
e-mail: 2016meb1126@iitrpr.ac.in

E. Singla
e-mail: ekta@iitrpr.ac.in

present at the shoulder joint. The primary focus is given to the mobility analysis of the coupled mechanism as it is an important point of concern in the kinematic synthesis of any mechanism. It gives us an idea about the total number of DOF of the mechanism. Chebychev–Grubler–Kutzbach criterion is the most commonly used method for evaluating the DOF of mechanisms. Although the criterion has wide applicability, it fails in the cases of complex mechanisms involving parallel manipulators, redundant joints or closed-loop chains [7]. The criterion breaks down in such cases because it considers virtual constraints as active constraints, which do not restrict any motion or in other words, do not affect the number of DOF of a mechanism. This ultimately results in an incorrect deduction of mobility. In such cases, screw theory can be used for the analysis of spatial mechanisms. The paper is organized into five sections: Sect. 2 discusses the methodology to compute the mobility analysis of coupled mechanism, followed by a brief introduction to screw theory and its implementation. Demonstration of 2-DOF planar configuration with and without redundant joints is given in Sect. 3. Section 4 utilizes screw theory to compute the motion and constraint screw systems as well as the overall mobility of the two mechanisms in consideration. This section also discusses the comparative parameters in order to differentiate between the two mechanisms. In the final section, we conclude the outcome of the paper and discuss the future scope.

2 Methodology

2.1 Basics of Screw Theory

A screw consists of two three-dimensional vectors and is defined by a straight line with a pitch “ h ” associated with it. It is denoted by six homogenous coordinates also known as Plucker coordinates:

$$\$ = \begin{bmatrix} s \\ s_0 + hs \end{bmatrix} \quad (1)$$

where s denotes the direction ratios along the screw axis, h is the pitch of the screw, $s_0 = r \times s$ is the moment of the screw axis about the origin, and r denotes the position of vector a point lying on the screw axis [7]. If the pitch of a screw is zero, it represents a revolute joint. On the other hand, a screw with infinite pitch is associated with a prismatic joint. Fundamentally, we consider two types of screw sets for analysis of rigid body motion: motion screw and constraint screw systems. The first three elements of a motion screw represent rotation about the axis and those of a constraint screw represents a force along the axis. Two screws are considered to be reciprocal to each other when they satisfy:

$$\$^T \begin{bmatrix} 0_3 & I_3 \\ I_3 & 0_3 \end{bmatrix} \$^r = 0 \quad (2)$$

where 0_3 and I_3 are zero and identity matrices of order three, respectively [7]. As in the case of sets, the concept of union and intersection in the case of screw systems are denoted as “ \vee ” and “ \wedge ,” respectively. Moreover, the screw systems satisfy the following properties:

1. $\dim(S_1 \vee S_2) = \dim(S_1) + \dim(S_2) - \dim(S_1 \wedge S_2)$
2. $(S_1 \vee S_2 \dots \vee S_n)^r = (S_1^r \wedge S_2^r \dots \wedge S_n^r)$
3. $(S_1 \wedge S_2 \dots \wedge S_n)^r = (S_1^r \vee S_2^r \dots \vee S_n^r)$
4. $\dim(S) + \dim(S^r) = 6$

The aforementioned properties find their use while calculating the mobility of parallel manipulators [8].

2.2 Mobility Analysis of Parallel Manipulator

A parallel manipulator is composed of a fixed base and a movable base. The two are connected by serial chains which are more than one in number. Suppose, there are a total of p number of serial chains and each serial link is connected by a total of n_i ($i = 1, 2, \dots, p$) number of joints. After establishing a global coordinate system, all the screws associated with joints connected in i th serial chain can be grouped into a matrix S_{bi} (i th branch motion screw system) of size $(n_i \times p)$, where i th row of the matrix is the screw associated with i th joint of the serial chain. Furthermore, S_{bi}^r (i th branch constraint screw system) can also obtain which is nothing but the reciprocal of and can be obtained from Eq. 2 [9]. Based on the above definitions, union and intersections of the branch systems further yield four different types of basic systems as follows [8]:

1. $S_f = S_{b1} \wedge S_{b2} \wedge \dots \wedge S_{bp}$ ($m = \dim(S_f)$)
2. $S^r = S_{b1}^r \vee S_{b2}^r \vee \dots \vee S_{bp}^r$ ($\mu = \dim(S^r)$)
3. $S_m = S_{b1} \vee S_{b2} \vee \dots \vee S_{bp}$ ($d = \dim(S_m)$)
4. $S^c = S_{b1}^r \wedge S_{b2}^r \wedge \dots \wedge S_{bp}^r$ ($\lambda = \dim(S^c)$)

Also, based on the definitions from above, we can clearly see that $S_f \subseteq S_m$ and $S^c \subseteq S^r$. According to the references, [8, 9], there are mainly two criterions for calculating mobility of a parallel mechanism.

Criterion 1: $m = 6 - \mu$, where $\mu = \dim(S^r)$, where m denotes mobility.

Criterion 2: This criterion is used when mechanisms consists of virtual constraints. Each reciprocal screw system can be decomposed as $S_{bi}^r = S^c \vee S_{ci}^r$ where, $S^c \wedge S_{ci}^r = \phi$. In other words, S_{ci}^r is a matrix of screws which is obtained by removing the matrix of screws S^c from S_{bi}^r . Also, from reference [8], $\langle S_c^r \rangle = S_c^r + \langle S_v^r \rangle$ (Note: $\langle \cdot \rangle$ represents multisets and curly brackets $\{\cdot\}$ indicates largest set with unique elements), where $\{S_c^r\}$ is a largest linearly independent set of screws in $\langle S_c^r \rangle$ and

the remaining screws make up the virtual constraint multiset. Combining the relations $S_{bi}^r = S^c \vee S_{ci}^r$ and $\langle S_c^r \rangle = \{S_c^r\} + \langle S_v^r \rangle$ gives us the fundamental constraint screw decomposition:

$$\langle S^r \rangle = \langle S^c \rangle + \{S_c^r\} + \langle S_v^r \rangle \quad (3)$$

The mobility equation is then given as

$$m = d(n - g - 1) + \sum_{i=1}^g f_i + v \quad (4)$$

where, $d = 6 - \lambda$ ($\lambda = \dim(S^c)$), n is the total number of links, g is total number of joints f_i is the DOF of i th joint and $v = \text{card}(\langle S_v^r \rangle)$ (Note: $\text{card}(S)$ is a function that returns the total number of vectors in screw set s) [8].

3 Configuration Selection for Upper Arm Exoskeleton

In this section, we examine and analyze the two configurations of upper-arm exoskeletons that fundamentally differ in the sense that one mechanism comprises redundant joints for misalignment compensation and the other does not.

3.1 *Upper Arm Exoskeleton Without Redundant DOFs (Type I Configuration)*

Figure 1 illustrates the first (Type I) of the two mechanisms taken into consideration. The coupled mechanism consists of two serial chains OGW and EFP connected at two bases OE and WP where OE is the fixed base and WP is the movable base. The serial chain OGW makes up the human limb with joints at O and G as the shoulder and elbow joints, respectively. Kinematic chain EFP can be considered to be the exoskeleton chain. It is also important to notice that the axis of rotation of shoulder and elbow joints are aligned with the joints E and F pertaining to the exoskeleton chain.

3.2 *Upper Arm Exoskeleton with Redundant DOFs (Type II Configuration)*

The shoulder joint of the human arm is a ball and socket joint which consists of three motions: flexion/extension (axis perpendicular to sagittal plane), abduc-

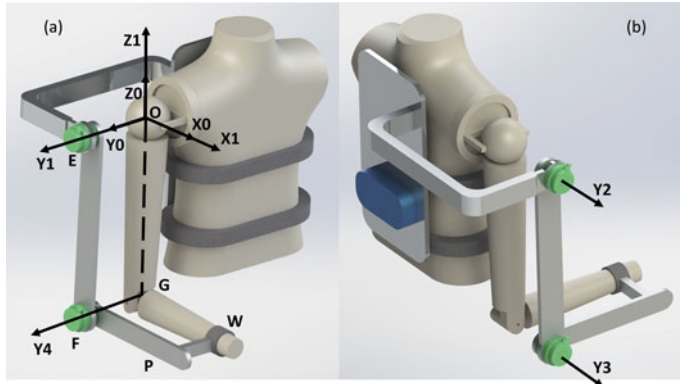


Fig. 1 Type I mechanism where a 2-DOF exoskeleton is attached to the human arm. Rotational axes of joints associated with: **a** Human Arm and **b** Exoskeleton

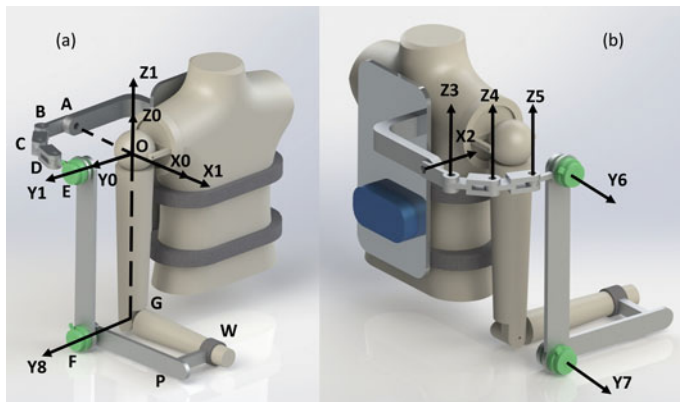


Fig. 2 Type II mechanism where a six DOF (two active and four passive) exoskeleton is attached to human arm. Rotational axes of joints associated with: **a** Human Arm and **b** Exoskeleton

tion/adduction (axis perpendicular to frontal plane), and internal/external (axis perpendicular to transverse plane) rotation. For the design of the exoskeleton, rotational axes of flexion/extension and abduction/adduction can be aligned by placing rotational joints on the rear and the side portions of the body. However, the alignment of the internal/external axis with an external rotational joint restricts the range of motion, and hence in the first prototype, misalignment compensation is provided only for this joint. If we do provide compensation mechanisms for flexion and abduction motions, it would result in added inertia and we intend to reduce it as exoskeleton's inertia has a significant effect on the metabolic cost of the user, and minimizing it should be one of the main objectives in exoskeleton design [10].

The conceptual design of the type II exoskeleton is shown in Fig. 2 where the total number of joints are eight, with one being a spherical joint located at O. The

rest of the joints located at A, B, C, D, E, F, and G are revolute joints. The human arm is represented by the kinematic chain OGW and the points O and G represent shoulder and elbow joints, respectively. The abduction/adduction axis is along the line OA and the line OE represents the flexion/extension axis. The kinematic chain ABCDEF is representative of the exoskeleton and, the human arm (OGW) and the exoskeleton are connected by a rigid link WP. Rotational axes of joints at A and E are along with OA and OE, and these joints provide abduction and flexion motions respectively. The rotational axes of the rest of the joints B, C, and D are perpendicular to the plane formed by OA and OE, i.e., they are oriented along the internal/external rotational axis of the shoulder joint. RRR configuration [1] is achieved by joints B, C, and D which are responsible for misalignment compensation for rotation about the internal/external rotational axis. The rotational axis of joints present at F and G are aligned and are responsible for the flexion/extension motion of the elbow joint.

4 Mobility Analysis of the Two Configurations

4.1 Mobility Analysis of Type I Mechanism

Considering Fig. 1, a global coordinate frame is attached at point O and it is represented by triad $\{X_0, Y_0, Z_0\}$. Rotational axes of the spherical joint present at O are along the directions $\{X_1, Y_1, Z_1\}$. The rotational axes of revolute joints present at E, F, and G are represented by Y_2 , Y_3 , and Y_4 , respectively. The motion screw systems for the exoskeleton chain and the human arm are calculated individually and let them be represented as S_{b1} and S_{b2} , respectively. For obtaining S_{b1} is obtained by a step-by-step calculation of screw vector pertaining to each joint of the exoskeleton is followed:

Joint E: $\omega = [0 \ 1 \ 0]$, $r = [0 \ b_1 \ 0]$, $\$_E = [\omega \ \omega \times r] = [0 \ 1 \ 0 \ 0 \ 0 \ 0]$

Joint F: $\omega = [0 \ 1 \ 0]$, $r = [a_2 \ b_2 \ c_2]$, $\$_F = [\omega \ \omega \times r] = [0 \ 1 \ 0 \ c_2 \ 0 \ -a_2]$

$$S_{b1} = \begin{bmatrix} \$_E \\ \$_F \end{bmatrix} = \begin{bmatrix} 0 & 1 & 0 & 0 & 0 & 0 \\ 0 & 1 & 0 & c_2 & 0 & -a_2 \end{bmatrix} \quad (5)$$

Similarly, the motion screw system S_{b2} is obtained as follows:

$$S_{b2} = \begin{bmatrix} \$O \\ \$G \end{bmatrix} = \begin{bmatrix} 1 & 0 & 0 & 0 & 0 & 0 \\ 0 & 1 & 0 & 0 & 0 & 0 \\ 0 & 0 & 1 & 0 & 0 & 0 \\ 0 & 1 & 0 & c_2 & 0 & -a_2 \end{bmatrix} \quad (6)$$

Reciprocal of screw systems S_{b1} and S_{b2} obtained by using Eq. 2

$$S_{b1}^r = \begin{bmatrix} 0 & 1 & 0 & 0 & 0 & 0 \\ 0 & 0 & 0 & 1 & 0 & 0 \\ 0 & 0 & 0 & 0 & 0 & 1 \\ a_2 & 0 & c_2 & 0 & 0 & 0 \end{bmatrix} \quad (7)$$

$$S_{b2}^r = \begin{bmatrix} 0 & 1 & 0 & 0 & 0 & 0 \\ a_2 & 0 & c_2 & 0 & 0 & 0 \end{bmatrix} \quad (8)$$

The rank of the multiset $\langle S^r \rangle = S_{b1}^r + S_{b2}^r$ is four, as the screws $\{S_{11}^r, S_{21}^r\}$ and $\{S_{14}^r, S_{24}^r\}$ are the same vectors. (Note: S_{ij}^r refers to the j th row of S_{bi}^r matrix).

$$S^r = \begin{bmatrix} 0 & 1 & 0 & 0 & 0 & 0 \\ 0 & 0 & 0 & 1 & 0 & 0 \\ 0 & 0 & 0 & 0 & 0 & 1 \\ a_2 & 0 & c_2 & 0 & 0 & 0 \end{bmatrix}, \mu = \dim(S^r) = 4$$

Mobility of the coupled mechanism can be computed as

Criterion 1: $m = 6 - \mu = 2$. Hence, the coupled mechanism has a total of two DOF. The orientation of these DOF is obtained by calculating S_f (reciprocal of S^r):

$$S_f = \begin{bmatrix} 0 & 1 & 0 & 0 & 0 & 0 \\ 0 & 0 & 0 & c_2 & 0 & -a_2 \end{bmatrix} \quad (9)$$

From S_f , It is observed that the platform has 1 – *DOF* rotation about Y_0 axis and 1 – *DOF* translation in the $X - Z$ plane.

$$\text{Criterion 2 : } S^c = S_{b1}^r \wedge S_{b2}^r = \begin{bmatrix} 0 & 1 & 0 & 0 & 0 & 0 \\ a_2 & 0 & c_2 & 0 & 0 & 0 \end{bmatrix}, \lambda = \dim(S^c) = 1, d = 6 - \lambda = 5$$

This represents every link of mechanism is subjected to a common 1 – *DOF* constraint force along Y -axis and 1 – *DOF* constraint force in the $X - Z$ plane. Quantities $\{S_c^r\}$ and $\langle S_v^r \rangle$ are calculated as follows:

$$\langle S_c^r \rangle = \begin{bmatrix} 0 & 0 & 0 & 1 & 0 & 0 \\ 0 & 0 & 0 & 0 & 0 & 1 \end{bmatrix} \quad (10)$$

The rank of $\langle S_c^r \rangle$ is two, as both the screws $\{S_c^{r,1}, S_c^{r,2}\}$ of the matrix are linearly independent. Hence, $\langle S_c^r \rangle = \{S_c^r\}$, i.e., $\langle S_v^r \rangle = \phi$. Thus $v = \text{card}(\langle S_c^r \rangle) = 0$. Furthermore, number of links (n) = 4, number of joints (g) = 4 and total number of DOF ($\sum_{i=1}^g f_i$) = 6.

$$m = d(n - g - 1) + \sum_{i=1}^g f_i + v = 2 \quad (11)$$

Hence, from both the criteria, the mobility of the mechanism is computed to be two. This implies that the coupled mechanism has only 1 – *DOF* at the shoulder joint and 1 – *DOF* at the elbow joint. The motion is restricted to the sagittal plane only

and other motions of the shoulder joint such as rotation about the internal/external and abduction/adduction rotational axes are not possible.

4.2 Mobility Analysis of Type II Mechanism

Considering Fig. 2, we have a global coordinate frame which is attached at point O and is represented by the triad $\{X_0, Y_0, Z_0\}$. The rotational axes of the spherical joint present at O are along the directions $\{X_1, Y_1, Z_1\}$. The rotational axes of revolute joints present at A, B, C, D, E, F, and G are represented by $X_2, Z_3, Z_4, Z_5, Y_6, Y_7$, and Y_8 , respectively. Similar to the previous case, we have the exoskeleton chain and the human arm represented as S_{b1} and S_{b2} , respectively. For obtaining S_{b1} , we follow step-by-step calculation of screw vector pertaining to each joint of the exoskeleton chain.

Joint A:

$$\omega = [1 \ 0 \ 0], r = [a_1 \ 0 \ 0], \$A = [\omega \ \omega \times r] = [1 \ 0 \ 0 \ 0 \ 0 \ 0]$$

Joint B:

$$\omega = [0 \ 0 \ 1], r = [a_2 \ b_2 \ 0], \$B = [\omega \ \omega \times r] = [0 \ 0 \ 1 \ -b_2 \ a_2 \ 0]$$

Joint C:

$$\omega = [0 \ 0 \ 1], r = [a_3 \ b_3 \ 0], \$C = [\omega \ \omega \times r] = [0 \ 0 \ 1 \ -b_3 \ a_3 \ 0]$$

Joint D:

$$\omega = [0 \ 0 \ 1], r = [a_4 \ b_4 \ 0], \$D = [\omega \ \omega \times r] = [0 \ 0 \ 1 \ -b_4 \ a_4 \ 0]$$

Joint E:

$$\omega = [0 \ 1 \ 0], r = [0 \ b_5 \ 0], \$E = [\omega \ \omega \times r] = [0 \ 1 \ 0 \ 0 \ 0 \ 0]$$

Joint F: The Y-coordinate of joints F and E are same as the two points lie on the same plane parallel to the x-z plane, i.e., $\omega = [0 \ 1 \ 0], r = [a_6 \ b_5 \ c_6], \$F = [\omega \ \omega \times r] = [0 \ 1 \ 0 \ C_6 \ 0 \ a_6]$

$$S_{b1} = \begin{bmatrix} \$A \\ \$B \\ \$C \\ \$D \\ \$E \\ \$F \end{bmatrix} = \begin{bmatrix} 1 & 0 & 0 & 0 & 0 & 0 \\ 0 & 0 & 1 & -b_2 & a_2 & 0 \\ 0 & 0 & 1 & -b_3 & a_3 & 0 \\ 0 & 0 & 1 & -b_4 & a_4 & 0 \\ 0 & 1 & 0 & 0 & 0 & 0 \\ 0 & 1 & 0 & c_6 & 0 & -a_6 \end{bmatrix} \quad (12)$$

S_{b2} is same as the Eq. 6 given in the previous section and reciprocal of screw systems S_{b1}^r and S_{b2}^r is obtained by using Eq. 2

$$S_{b1}^r = \phi, S_{b2}^r = \begin{bmatrix} 0 & 1 & 0 & 0 & 0 & 0 \\ a_6 & 0 & c_6 & 0 & 0 & 0 \end{bmatrix} \quad (13)$$

Here, the rank of S_{b1} is six which means that the reciprocal of S_{b1} i.e., S_{b1}^r is a null set with a rank equal to zero. The rank of the multiset $\langle S^r \rangle = S_{b1}^r + S_{b2}^r$ is two, as the screws $\{S_{21}^r, S_{22}^r\}$ are linearly dependent.

$$S^r = S_{b2}^r = \begin{bmatrix} 0 & 1 & 0 & 0 & 0 & 0 \\ a_6 & 0 & c_6 & 0 & 0 & 0 \end{bmatrix}, \mu = \dim(S^r) = 2$$

Mobility of the coupled mechanism can be computed as

Criterion 1: $m = 6 - \mu = 4$. Hence, the coupled mechanism has a total of four DOF. The orientation of these DOF is obtained by calculating S_f (reciprocal of S^r):

$$S_f = \begin{bmatrix} 1 & 0 & 0 & 0 & 0 & 0 \\ 0 & 1 & 0 & 0 & 0 & 0 \\ 0 & 0 & 1 & 0 & 0 & 0 \\ 0 & 0 & 0 & c_6 & 0 & -a_6 \end{bmatrix} \quad (14)$$

From S_f , we observe that the platform can rotate about the three axes, i.e., $X-axis$, $Y-axis$, and $Z-axis$. It also has 1-DOF translation in the X-Z-plane.

Criterion 2 : $S^c = S_{b1}^r \wedge S_{b2}^r = \text{null}$ (i.e. ϕ), $\lambda = \dim(S^c) = 0$, $d = 6 - \lambda = 6$

This represents every link of mechanism is subjected none common constraint force and constraint couple. Quantities S_c^r and $\langle S_v^r \rangle$ are calculated as follows:

$$\langle S_c^r \rangle = \begin{bmatrix} 0 & 0 & 0 & 1 & 0 & 0 \\ a_6 & 0 & c_6 & 0 & 0 & 0 \end{bmatrix} \quad (15)$$

Rank of $\langle S_c^r \rangle$ is two, as both the screws $\{S_c^{r,1}, S_c^{r,2}\}$ of the matrix are linearly independent. Hence, $\langle S_c^r \rangle = \{S_c^r\}$, i.e., $\langle S_v^r \rangle = \phi$. Thus $v = \text{card}(\langle S_c^r \rangle) = 0$. We also have, number of links (n) = 8, number of joints (g) = 8 and total number of DOF ($\sum_{i=1}^g f_i$) = 10.

$$m = d(n - g - 1) + \sum_{i=1}^g f_i + v = 4 \quad (16)$$

Hence from both the criteria, the mobility of the type II mechanism is computed to be four. This implies that the coupled mechanism has all three rotational degrees of freedom about the axes of the shoulder joint and also an additional degree of freedom at the elbow joint.

Both the coupled configurations are summarized in Table 1. The table consists of a set of comparative parameters to differentiate the performance of the mechanisms. The type II mechanism with redundant DOFs has more mobility at the end-effector and experiences fewer constraint forces/couples.

The results for mobility obtained from Eqs. 11 and 16 represent the maximum mobility possible with the associated configurations. The instantaneous mobility, however, depends on the coordinates of joints pertaining to both the exoskeleton and the human arm. These coordinates are in turn a function of the coupled mechanisms' link lengths, which can be optimized so that no singularities are observed in the mechanisms' workspace, thus enabling the mechanisms to operate with complete mobility.

Table 1 Comparison between both mechanisms based on end-effector motion, constraints and its respective mobilities

Type	Actuator	Mobility	Motion at end-effector	Constraint at mechanism
Coupled system without redundant joint	2-Active	$2 - DOF$	$1 - DOF$ rotation about $Y - axis$ and $1 - DOF$ translation in $X - Z$ plane i.e. sagittal plane	$1 - DOF$ constraint force along $Y - axis$ and $1 - DOF$ constraint force in the $X - Z$ plane
Coupled system with redundant joint	2-Active, 4-Passive	$4 - DOF$	$3 - DOF$ rotation about all axes and $1 - DOF$ translation in $X - Z$ plane i.e. sagittal plane	No common constraint force or couple about any axis is subjected on mechanism

5 Conclusion and Future Work

In this paper, the work presented two variations of upper limb exoskeletons with or without redundant joints, which fundamentally differ by the fact that one has misalignment compensation associated with it and the other does not. A comprehensive analysis of mobility is performed to determine each mechanism's motion and their constraints are studied as well. It is observed that the type II mechanism, i.e., the upper limb exoskeleton with redundant DOFs offers greater mobility than the type I mechanism which restricts motion to the sagittal plane only. The work highlights the approach of computing mobility and constraints of coupled mechanisms between the exoskeleton and the associated human limb. In future, more complicated parallel mechanisms will be investigated where the branches of coupled mechanisms are not just serial chains but may contain loops as well. Furthermore, kinematic and dynamic models of the conceptual design can be formulated. The models will help to realize the concept through simulation and prototype development.

References

1. Naf, M.B., Junius, K., Rossini, M., Rodriguez-Guerrero, C., Vanderborght, B., Lefebvre, D.: Misalignment compensation for full human-exoskeleton kinematic compatibility: state of the art and evaluation. *Appl. Mech. Rev.* **70**(5) (2018). <https://doi.org/10.1115/1.4042523>
2. Kim, H., Lee, C.Y.: Analysis on Kinematics and dynamics of human arm movement toward upper limb exoskeleton robot control part 1: system model and kinematic constraint. *J. Inst. Control Robot. Syst.* **18**(12), 1106–1114 (2012). <https://doi.org/10.5302/J.ICRS.2014.13.0012>

3. Stienen, A.H., Hekman, E.E., Van Der Helm, F.C., Van Der Kooij, H.: Self-aligning exoskeleton axes through decoupling of joint rotations and translations. *IEEE Trans. Robot.* **25**(3), 628–633 (2009). <https://doi.org/10.1109/TRO.2009.2019147>
4. Christensen, S., Bai, S.: Kinematic analysis and design of a novel shoulder exoskeleton using a double parallelogram linkage. *J. Mech. Robot.* **10**(4) (2018)
5. Kim, B., Deshpande, A.D.: An upper-body rehabilitation exoskeleton Harmony with an anatomical shoulder mechanism: design, modeling, control, and performance evaluation. *Int. J. Robot. Res.* **36**(4), 414–435 (2017)
6. Zeiaee, A., Soltani-Zarrin, R., Langari, R., Tafreshi, R.: Design and kinematic analysis of a novel upper limb exoskeleton for rehabilitation of stroke patients. In: 2017 International Conference on Rehabilitation Robotics (ICORR), pp. 759–764. IEEE (2017)
7. Huang, Z., Li, Q., Ding, H.: Basics of screw theory. In: Theory of Parallel Mechanisms, pp. 1–16. Springer, Dordrecht (2013). https://doi.org/10.1007/978-94-007-4201-7_1
8. Dai, J.S., Huang, Z., Lipkin, H.: Mobility of over constrained parallel mechanisms (2006). <https://doi.org/10.1115/1.1901708>
9. Chu, J.S.Z.F., Feng, Z.J.: Mobility of spatial parallel manipulators. In: Parallel Manipulators, towards New Applications. IntechOpen (2008). <https://doi.org/10.5772/5443>
10. Shamaei, K., Cenciarini, M., Adams, A.A., Gregorczyk, K.N., Schiffman, J.M., Dollar, A.M.: Biomechanical effects of stiffness in parallel with the knee joint during walking. *IEEE Trans. Biomed. Eng.* **62**(10), 2389–2401 (2015). <https://doi.org/10.1109/TBME.2015.2428636>

**Pressure Vessels, Acoustics and Noise
Control, Mechanical
and Electro-Mechanical Systems
of Modern Machinery**

AHP Integrated TOPSIS Methodology for Selection of Non-Conventional Machining Process for Micro-Drilling



Pranav Vijay Deosant, Ashish Ravindra Lande,
Anurag Gopal Vishwakarma, and Hemant P. Jawale

1 Introduction

Conventional machining processes have restricted applications for producing complex shapes having required tolerance and surface roughness. Hard materials like tungsten carbide, titanium, ceramics, and refractories are difficult to machine on conventional machining processes. Therefore, these processes are now replaced by non-traditional machining (NTM) processes [1]. In NTM the material is removed by mechanical, thermal, electrical, chemical, or combinations of these energies. In NTM processes, it's not necessary that the tool should be harder than workpiece unlike the conventional machining processes [2]. In most of the NTM processes, there is no direct contact between the tool and the workpiece, so the wear of tool doesn't take place. The NTM processes have high-dimensional accuracy and low surface roughness. The non-traditional machines are expensive and need high power for machining. Their maintenance cost is also high. The selection of optical parametric settings for these machines is also important for achieving maximum efficiency. In some cases, the catalogues and data handbooks are consulted by the manufacturer for achieving maximum efficiency.

P. V. Deosant (✉) · H. P. Jawale

Department of Mechanical Engineering, VNIT, Nagpur, Maharashtra, India

A. R. Lande · A. G. Vishwakarma

Department of Mechanical Engineering, KKWP, Nashik, Maharashtra, India

e-mail: arlande@kkwagh.edu.in

2 Analytical Hierarchy Process (AHP)

AHP is proposed by Saaty in 1980 [3]. It is a measurement theory, based on pairwise contrast and depends mostly on the expert's judgment to gain at priority scales. The expert's judgment may be unstable. AHP is concerned with the improvement of the judgments so as to obtain better consistency. The weights and priorities are gained based on qualitative and quantitative information of multi-objectives. AHP for multi-response improvement has demonstrated an improvement in universal desirability in comparison to the use of equal weights [4]. It is applied in a huge variety of sectors containing planning, selecting the best alternatives, and resolving conflicts. This process is used to find the individual weightage of each criterion. Allotting weights and calculating the performance credits of each alternative can help to select the best alternative.

AHP is of utmost importance for decision-making as it takes into account the strategic goals set in our mind required for the outcome of project. These goals are transformed into a set of weighted criteria that can be used as score for the projects. Thus, our goals can now be prioritized and selected according to our project's needs.

3 Case Study

In this case study, micro-hole drilling operation with minimum diameter to maximum depth is considered. While performing an experiment for the above case study four alternatives have been considered: laser beam machining (LBM), electric discharge machining (EDM), electron beam machining (EBM), and ultrasonic machining (USM). The process parameter considered are hole tolerances, operating volt required, hole depth produced, minimum possible diameter, surface finish, and cost for operation.

Comparisons of capabilities for different parameters with the different NTM processes are shown above. The standard values are reported by [5] except cost, the values of cost for various NTM processes are addressed as shown in Table 1. Elements of Table 1 are presented by a_{ij} .

Table 1 Comparison of capabilities [5]

Parameters(n)	LBM	EBM	USM	EDM
Hole tolerance (mm)	0.05	0.025	0.025	0.025
Operating volt (V)	4500	150,000	220	50
Hole depth (mm)	17.5	7.5	25.0	62.5
Minimum diameter (mm)	0.125	0.025	0.075	0.13
Surface finish (μ)	0.4	0.2	0.25	0.05
Cost	4	5	3	2

Table 2 shows that numerical rating of preferences proposed by Saaty's scale reported by [3].

Table 2 helps the decision-maker to compare the parameters that he/she may be choosing for their outcome of the project. The parameters are compared among themselves by the decision-maker and allotted a numerical rating as per their preference over other parameters. These preferences are recorded for each of the decision maker's parameters. However, the preferences allotted to the parameters are totally dependent on the decision-maker's choice based on their project outcome. By doing so, the decision-maker determines its prioritization over the parameters that had been chosen for the present work.

Table 3 represents the Random Index table given by Saaty [3]. He had performed various experiments on AHP for prioritization while considering the numbers of parameters. He developed this table later, which gives the estimated value of RI for a given number of parameters (n). Table 3 shows values of RI of different parameters (n) which is later useful for the determination of consistency of weights, beneficial and non-beneficial criteria. Ideologies and opinions may clash with each other when a group of mind works together. This does not lead the discussion to any conclusion. However, some solution is still required. Opinions of each decision-maker are still considered and the project is continued, but the errors occurring during the project have to be limited at some point in order to satisfy the demand of each decision-maker. An RI value provides the limitation to this error. Hence for a number of parameters, a RI is the value known which allows only a small amount of error in the whole decision-making process.

Table 2 Saaty's scale [3]

Preference	Numerical rating
Equal importance	1
Moderate importance	3
Strong importance	5
Very strong importance	7
Extreme importance	9
Intermediate values	2, 4, 6, 8
Values for inverse comparison	1/3, 1/5, 1/7, 1/9, 1/2, 1/4, 1/6, 1/8

Table 3 Random index (RI)

n	1	2	3	4	5	6	7	8	9	10
RI	0.00	0.00	0.58	0.90	1.12	1.24	1.32	1.41	1.45	1.49

3.1 AHP for Multi-Criteria Decision-Making (MCDM)

In order to develop the comparison matrix as per the decision-maker's preference for MCDM, AHP is systematically applied. Pairwise comparison matrix for micro-drilling application by considering various parameters is shown in Table 4. In this table, X_{ij} represents the elements of the matrix of 6×6 , as we have considered six parameters, where "i" is for rows and j is for column.

Table 5 shows normalizing the pairwise comparison matrix for calculating weight criteria. The value of each individual cell in the above table is obtained by dividing each cell value of Table 4 by the sum of its corresponding cell column from Table 4.

Mathematically it is given as;

$$\begin{aligned} X_{1ij} &= (a_{ij} / \sum a_{ij}) \\ X_{1ij_{11}} &= (1 / 9.7500) \\ &= 0.1026 \end{aligned} \quad (1)$$

Table 4 Pairwise comparison matrix

Parameter	Hole tolerance	Operating volt	Depth	Min. diameter	SR	Cost
Hole tolerance	1	2	1/3	1/3	1/2	4
Operating volt	½	1	1/5	1/5	½	1
Depth	3	5	1	1	2	4
Min. diameter	3	5	1	1	4	4
SR	2	2	1/2	1/4	1	2
Cost	1/4	1	1/4	1/4	1/2	1
Sum of columns	9.7500	16.0000	3.2833	3.0333	8.5000	16.0000

Table 5 Normalized pairwise comparison matrix

Parameter	Hole tolerance	Operating volt	Depth	Min. diameter	SR	Cost	Criteria weight = Avg. of each row
Hole tolerance	0.1026	0.1250	0.1015	0.1099	0.0588	0.2500	0.1246
Operating volt	0.0513	0.0625	0.0609	0.0659	0.0588	0.0625	0.0603
Depth	0.3077	0.3125	0.3046	0.3297	0.2353	0.2500	0.2899
Min. diameter	0.3077	0.3125	0.3046	0.3297	0.4706	0.2500	0.3292
SR	0.2051	0.1250	0.1523	0.0824	0.1176	0.1250	0.1346
Cost	0.0256	0.0625	0.0761	0.0824	0.0588	0.0625	0.0613

where X_{1ij} represents the element of matrix as shown in the table.

Values of the individual cell of Table 6 can be obtained by multiplying the criteria weight of the parameters with the corresponding elements of Table 4; mathematically, it is given as $X_{2ij} = a_{ij} \times (\text{Criteria weight})_{ij}$, where X_{2ij} represents the elements of matrix Table 6. In this table, terms named as weighted sum value, criteria weight, no of parameters denoted which are by (n), “ λ ” denoting the ratio of weighted sum value to the weight criteria. The average of ratios is calculating as below:

$$\begin{aligned}\lambda_{\text{mean}} &= \text{Average of Ratio } \lambda \\ &= (6.1316 + 6.2172 + 6.2394 + 6.3123 + 6.3462 + 6.1142)/6 \\ \lambda_{\text{mean}} &= 6.2268\end{aligned}$$

From λ_{mean} , the term consistency index (CI) is defined as the ratio of the average weighted sum value and criteria weight to the difference of number parameters:

$$\begin{aligned}CI &= \{(\lambda_{\text{mean}} - n)\}/(n - 1) \\ CI &= (6.2268 - 6)/(6 - 1) \\ CI &= 0.0454\end{aligned}\tag{2}$$

CI gives the information about the logical consistency among the pairwise comparison matrix.

The standard value 0.1 was set by Saaty to compare the index with an appropriate consistency index, known as Random Consistency Index (RI). From CI and RI, consistency ratio is defined as the ratio of CI to RI.

Consistency ratio = (Consistency index/Random Index), for $n = 6$; RI = 1.24 obtained from random index Table 3.

$$\begin{aligned}CI &= 0.0454/1.24 \\ CI &= 0.0366\end{aligned}$$

Since the calculated value of consistency ratio is less than standard ($0.0366 < 0.1$); hence, the decision maker's preferences are consistent and the process is going to be in the right direction. Inconsistency is acceptable if the value of CI is less than or equal to 10%; otherwise, it needs to revise the subjective judgment [6].

Beneficial criteria (B) are those whose larger value is required and non-beneficial criteria (NB) are those lower values that is desired for obtaining the best out of the alternative. Hole tolerance is considered as the non-beneficial criteria because if the lower value is desired for application, the lower will be hole tolerance value more accurate will be the hole as less tolerance. Operating volt is considered as the non-beneficial criteria because we require an alternative which consumes less power for

Table 6 Table for consistency

	Criteria weight	0.1246	0.0603	0.2899	0.3292	0.1346	0.0613	Weighted sum value	Criteria weight	Ratio (λ)
Hole tolerance	0.1246	0.1206	0.0966	0.1097	0.0673	0.2452	0.7640	0.1246	0.1316	
Operating volt	0.0623	0.0603	0.0579	0.0658	0.0673	0.0613	0.3749	0.0603	0.2172	
Depth	0.3738	0.3015	0.2899	0.3292	0.2692	0.2452	1.8088	0.2899	0.2394	
Min. diameter	0.3738	0.3015	0.2899	0.3292	0.5384	0.2452	2.0780	0.3292	0.3123	
SR	0.2492	0.1206	0.1449	0.0823	0.1346	0.1226	0.8542	0.1346	0.3462	
Cost	0.0312	0.0603	0.0724	0.0823	0.0673	0.0613	0.3748	0.0613	0.1142	

Table 7 Decision matrix with beneficial and non-beneficial criteria for selection of best alternative

Criteria	NB	NB	B	NB	NB	NB
Alternatives	Hole tolerances	Operating volt	Depth	Min. diameter	SR	Cost
LBM	0.5000	0.0111	0.2800	0.2000	0.1250	0.5000
EBM	1.0000	0.0003	0.1200	1.0000	0.2500	0.4000
USM	1.0000	0.2273	0.4000	0.3333	0.2000	0.6666
EDM	1.0000	1.0000	1.0000	0.1923	1.0000	1.0000

the operation, thus saving the power and cost for the operation. Depth is considered as the beneficial criteria because its higher value is desired, it requires a hole up to maximum possible depth. Minimum diameter is considered as the non-beneficial criteria because we need a hole of minimum possible diameter for micro-drilling operation. Surface roughness is considered as the non-beneficial criteria because less will be the surface roughness value in microns' smother will be the hole finish. Cost is considered as the non-beneficial criteria because it needs an alternative that is low in cost for economical operation.

Non-Beneficial Criteria each cell value $X_3 = \{(Min\ X_{ij}/ X_{ij})\}$ from each row of Table 1}.

Beneficial Criteria each cell value $X_3 = \{(X_{ij}/ Max\ X_{ij})\}$ from each row of Table 1}.

$X_{3ij} = X_{3ij}$ represents the elements of matrix Table 7.

Values of an individual cell of Table 8 can be obtained by multiplying the corresponding cell of Table 7 with the criteria weight of the parameter calculated in Table 5; mathematically, it is: $X_{3ij} \times (\text{Criteria Weight})_{ij}$. The performance rating of each alternative is the sum of corresponding rows for a given alternative. From the performance rating of Table 8 ($0.7340 > 0.5647 > 0.4315 > 0.2574$), it is noticed that EDM ranks first amongst the other alternatives followed by EBM, then USM, and finally, LBM.

Table 8 Criteria weights allotted to decision matrix

Criteria weights	0.1246	0.0603	0.2899	0.3292	0.1346	0.0613	Performance rating (PR)
Parameters	Hole tolerances	Operating volt	Depth	Min. diameter	SR	Cost	
LBM	0.0623	0.0007	0.0812	0.0658	0.0168	0.0306	0.2574
EBM	0.1246	0.00002	0.0348	0.3292	0.0336	0.0245	0.5467
USM	0.1246	0.0137	0.1159	0.1096	0.0269	0.0408	0.4315
EDM	0.1246	0.0603	0.2899	0.0633	0.1346	0.0613	0.7340

4 Technique for Order of Preference by Similarity to Ideal Solution (TOPSIS)

This method is developed by Hwang and Yoon in 1981. It is ranking method in conception and application. In the standard TOPSIS method, an attempt to choose alternatives simultaneously that have the shortest Euclidean distance positive ideal solution and farthest from a negative ideal solution. This method gives a solution that is not only closest to hypothetical best but also farthest from hypothetical worst [7]. A positive ideal solution maximizes the benefit criteria and minimizes cost criteria, whereas it is vice versa for the negative ideal solution [7].

Table 9 shows the decision matrix for TOPSIS which is obtained by dividing the element of each cell with the square root value of the sum of the square of value of each parameter of Table 1. Mathematically, it is:

$$R_{ij} = \{X_{ij} / [(\sqrt{\sum_{j=1}^n X_{ij}^2})]\} \quad (3)$$

R_{ij} represents the elements of matrix Table 9.

$$\begin{aligned} \text{Considering } R_{11} &= \{0.05 / \sqrt[4]{(0.05^2 + 0.025^2 + 0.025^2 + 0.025^2)}\} \\ R_{11} &= \{0.05 / \sqrt[4]{(0.05^2 + 0.025^2 + 0.025^2 + 0.025^2)}\} \\ R_{11} &= 0.05 / 0.06614 \end{aligned}$$

Individual value of Table 10 is obtained by multiplying the corresponding R_{11j} value from Table 9 to the criteria weight from 5. Ideal best is the smallest value from the column and ideal worst is the largest value from the column considering the beneficial and non-beneficial criteria.

Individual value of Table 11 is obtained by calculating the Euclidean distance for ideal best and ideal worst alternatives. The corresponding values of R_{11j} value from Table 10 are used in positive separation measure and negative separation measure [8]. The formula for calculating the relative closeness from ideal solution to each alternative is given by:

Table 9 Decision matrix for TOPSIS

Parameters	Hole tolerances	Operating volt	Depth	Min. diameter	SR	Cost
LBM	0.7559	0.0299	0.2502	0.6348	0.7770	0.5443
EBM	0.3779	0.9995	0.1072	0.1269	0.3885	0.6804
USM	0.3779	0.0015	0.3574	0.3809	0.4856	0.4082
EDM	0.3779	0.0003	0.8934	0.6602	0.0971	0.2722

Table 10 Allotting criteria to decision matrix

Criteria weights	0.1246	0.0603	0.2899	0.3292	0.1346	0.0613
Parameters	Hole tolerances	Operating volt	Depth	Min. diameter	SR	Cost
LBM	0.0941	0.0002	0.0725	0.2089	0.1046	0.0334
EBM	0.0471	0.0603	0.0311	0.0418	0.0523	0.0417
USM	0.0471	0.00009	0.1036	0.1254	0.0654	0.0250
EDM	0.0471	0.00002	0.2589	0.2173	0.0131	0.0167
Ideal best Vj ⁺	0.0471	0.00002	0.2589	0.0418	0.0131	0.0167
Ideal worst Vj ⁻	0.0942	0.0603	0.0311	0.2173	0.1046	0.0417

Table 11 Calculating the Euclidean distance for ideal best and ideal worst alternatives

Parameter	Positive separation measure(Si ⁺)	Negative separation measure(Si ⁻)	Performance score(PS)
LBM	0.2712	0.0739	0.2141
EBM	0.2402	0.1891	0.4405
USM	0.1842	0.1462	0.4425
EDM	0.0308	0.2583	0.8934

$$Si^+ = [\sum_{j=1}^n (V_{ij} - V_{j+}^+)^2]^{1/2} \text{ Positive Separation Measure} \quad (4)$$

$$Si^- = [\sum_{j=1}^n (V_{ij} - V_{j-}^-)^2]^{1/2} \text{ Negative Separation Measure} \quad (5)$$

$$PS = Si^- / (Si^+ + Si^-) \text{ Relative Closeness to Ideal Measure} \quad (6)$$

$$Si^+ = \{ [(0.0941 - 0.0471)^2 + (0.0002 - 0.00002)^2 + (0.0725 - 0.2589)^2 + (0.2089 - 0.0418)^2 + (0.1046 - 0.0131)^2 + (0.0334 - 0.0167)^2] \}^{1/2}.$$

$$Si^+ = 0.2712.$$

Since $(0.8934 > 0.4425 > 0.4405 > 0.2141)$.

From the above performance score, we noticed that EDM has a higher value so it ranked first followed by USM, EBM, and LBM.

5 Result

In this case study, AHP is proposed to calculate qualitative and quantitative factors using made decision-maker and deployed for determining the weightage criteria of parameter in the given process such as hole tolerances, operating volt, depth, minimum diameter, surface roughness, and cost. For assessment of this criterion, weightage based on decision-maker factor AHP is very useful in industry and social

life. The Final selection of micro-drilling operation considering weightage parameter TOPSIS is applied. It is a precise and simple decision-making method with similarity to ideal solutions. The performance rating values are organized according to priority. The highest relative closeness value is providing for micro-drilling operation in addition to micro-machining process. The relative closeness to the ideal solution gives priority ranking as EDM > USM > EBM > LBM. The most significant micro-drilling process for the present case study of drilling hole of the smallest possible diameter and maximum possible depth is evaluated as EDM by this AHP integrated with TOPSIS methodology with the value of 0.8934. USM and EBM assessed nearby giving a promising nature with a value of 0.4425 and 0.4405 followed by LBM with a value of 0.2141. In this case study, EDM seems to have a ruling power over the other alternatives. The methodology followed in this paper can be used for finding the other possible solution of Micro-machining application.

6 Conclusion

- (1) A joint TOPSIS–AHP method is proposed that helps in the selection of the most appropriate NTM process from among available alternatives. While machining micro-drilling on given work material, the MCDM approach is deployed for identifying various NTM processes, parameters, selection, and its interrelations.
- (2) This approach takes care of quantitative and qualitative attributes which are required for selection and gives a systematic, steady, and logical method for NTM process selection.
- (3) In this paper, promising results are calculated with the consideration of accuracy, tolerances, dimensional stability, and cost. Also taking into account the thoughts and ideologies of person when making the decision in industry or social life problem as well.
- (4) Future scope of this paper can be experimentation and the analysis of our parameters and modifying them as per their needs.

References

1. Shankar, C., et al.: A DoE—TOPSIS method based Meta model for parametric optimization of non-traditional machining processes. *J. Modell. Manage.* **14**, 430–445 (2019)
2. Agarwal, S., et al.: Development of association rules to study the parametric influences in non-traditional machining processes, *Indian Academy of Sciences* **44**, 1–17 (2019)
3. Satty, R.W.: The analytic hierarchy process-what it is and how it is used. *Mathl Modelling* **9**(3–5), 161–176 (1987)
4. Devarasiddappa, D., et al.: Multi performance optimization in wire cut EDM of Inconel 825 using desirability function coupled with analytical hierarchy process. *Materials Today Proceedings* **5**, 11531–11547 (2018)

5. Mohan, S., Shan, H.S.: A review of electrochemical macro- to micro-hole drilling processes, *Int. J. Mach. Tools Manuf.* **45**, 137–152 (2005)
6. Aggeliki, S., et al.: Network selection in a WiMAX–WiFi environment, *Pervasive and Mobile Computing*, Elsevier, **7**, 584–594 (2011)
7. Aghdaie, M.H., Alimardani, M.: Target market selection based on market segment evaluation: a multiple attribute decision making approach. *Int. J. Oper. Res.* **24**(3), 261–278 (2015)
8. Deepa, N., et al.: Predictive mathematical model for solving multi-criteria decision making problems. *Neural Comput. Appl.* **31**, 6733–6746 (2019)

Design and Development of Acoustic Metamaterial and Micro-Perforated Panel by Using 3D Printing



Atharva R. Kshirsagar, D. Job Sandeep Rajprian, and J. Jeyanthi

1 Introduction

Low-mid-frequency noise is common prevailing background noise in urban areas. Vehicles, aircraft, industrial machines, mining explosions, and air conditioning units are a common source of this low-frequency noise. Low-mid-frequency noise problems also occur in the industry presenting a different noise problem to those in homes and offices [1, 2]. The World Health Organization perceives low-frequency noise as an environmental problem [3]. It is more difficult to absorb low-frequency sounds compared to higher frequency sounds.

Metamaterials are artificially designed materials that acquire their properties from internal microstructure than from the chemical composition found in natural materials. These materials are designed to manipulate the propagation of sound much different than it is possible using conventional materials [4, 5]. There are various methods to fabricate the metamaterial, one of which is FDM (fused deposition modeling) is used for the fabrication of core and MPP structures [6].

Sound absorption is the process by which the intensity of sound waves is decreased by the conversion of the sound energy into heat due to the material structure. The sound absorption coefficient, alpha represents the sound-absorbing characteristics of a material. The absorption coefficient (α) ranges from 0 (total reflection) to 1.00 (total absorption) [7]. Frequency variation results in a significant change in the sound-absorbing characteristics of materials.

As a means of noise reduction, sound-absorbing materials have been widely used in interior architecture, transportation, and aerospace engineering. The acoustical effect of the honeycomb structure on the sound-absorbing performance of an MPP sound absorber has been studied by the authors [8, 9]. The honeycomb structure when

A. R. Kshirsagar · D. Job Sandeep Rajprian · J. Jeyanthi (✉)
Vellore Institute of Technology, Chennai Campus, Chennai 600127, India
e-mail: jeyanthi.subramanian@vit.ac.in

coupled with the MPPs acts as Helmholtz resonators and attenuates noise in the low- and medium-frequency bands. These honeycomb structures broaden the frequency band of sound absorption, thereby making it suitable for many applications [9]. Compared to traditional sound absorption materials, MPPs are more durable, environmentally friendly, and plain in structure, so they are suitable for harsh conditions, such as in high-temperature and high-pressure applications [10]. MPPs can be usable in a severe and harsh environment. Also, they are more designable than most of the other sound-absorbing materials [8].

The principle behind using the perforated panel is enhancing the viscous and thermal losses by perforating numerous sub-millimeter diameter holes in the thin panel, leading to the desired acoustic resistance and a reduction in the mass reactance [11].

The sandwich structure comprising a honeycomb core and panels acts as a Helmholtz resonator and therefore exhibits good sound absorption in the low-mid frequency range without the need to increase the thickness of the material. It is lightweight and has excellent mechanical properties and has a high mechanical strength: weight ratio, so it is widely applied in aerospace, railway vehicle, and architectural scenarios [10]. Therefore, these metamaterials provide a lightweight solution in absorbing such low-mid-frequency noise. These can be used in office buildings, residential, and commercial environments. In aircraft, vehicle cabins, and machinery, these materials improve the structural strength and at the same time enhance the absorption frequency range into two or three-octave bands [12, 13].

2 Design and Fabrication

This paper focuses on the honeycomb structure as its lattice structure. Besides, honeycomb structure enhances the effect of the changes in MPP parameters on the sound absorption characteristics [9]. Certain variations were added to the simple hexagonal structure by adding a cylindrical part at the center of the hexagon supported by six vertical faces. To optimize the design, an octagonal structure with a cylinder and supported by eight vertical faces were designed.

The design considerations and the dimensions of the MPP were obtained from the design formulae in [14, 15]. These formulas yielded the parameters that were then used to make the MPPs and the core structures. The MPPs were designed with the following parameters:

Diameter of holes (d): 0.5, 0.6, 0.7, and 0.8 mm.

Distance between holes/perforations (b): 4.5, 5.5, and 10 mm.

The thickness of the plate (t): 1, 1.5, and 2 mm.

Diameter of MPP (D): 99.9 mm.

2.1 Modelling of Core Structures and Micro-Perforated Panels

Three core structures and MPPs were designed in the SOLIDWORKS software by taking into account the parameters in Table 1.

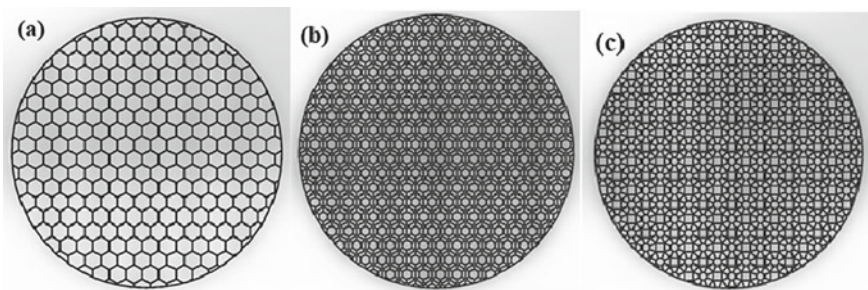


Fig. 1 CAD Model of core structures: **a** hexagonal structure, **b** lined hexagonal structure, **c** octagonal structure

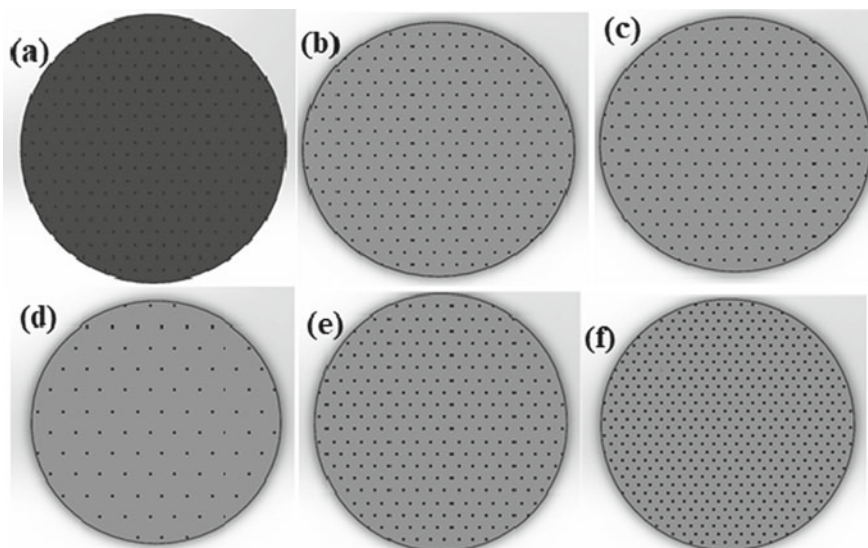


Fig. 2 CAD model Mpp with thickness $t = 1$ mm: **a** $d = 0.5$ mm, **b** $t = 0.6$ mm and, **c** $d = 0.7$ mm; CAD Model of MPPs with $d = 0.8$ mm: **d** $b = 10$ mm, **e** $b = 5.5$ mm, and **f** $b = 4.5$ mm

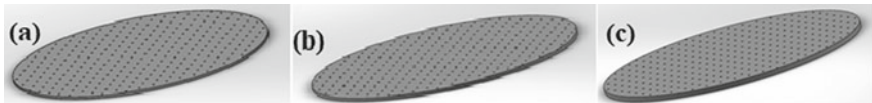


Fig. 3 Solidworks model of 0.8 mm MPP with thickness **a** $t = 1$ mm, **b** $t = 1.5$ mm, and **c** $t = 2$ mm

Table 1 Geometry and specifications of various structures

Structure	Geometry	Specifications
Hexagonal structure		Side of the hexagon: 3 mm Side of the octagon: 3 mm Inner circle radius: 1.36 mm
Modified hexagonal structure		Thickness of the faces and sides: 0.3 mm Thickness of the sample: 30 mm
Octagonal structure		

Fabrication

Fabrication of the core and MPP with sub-millimeter accuracies is a challenge, especially when the holes are in the sizes of 0.5 mm diameter. Fused deposition modeling (FDM) is a type of additive manufacturing technique that is employed in this work to fabricate the required samples. FDM has been proven to be effective in printing structures with sub-millimeter dimensions [16]. The walls of the core structures have a thickness of 0.3 mm, which were printed by an FDM machine, with a 0.3 mm nozzle. PLA (Poly Lactic Acid) is a biodegradable (under the right conditions) thermoplastic derived from renewable resources such as corn starch, or sugarcane was used as the base material. PLA was the material used to print the core structures and the MPPs [17] (Table 2).

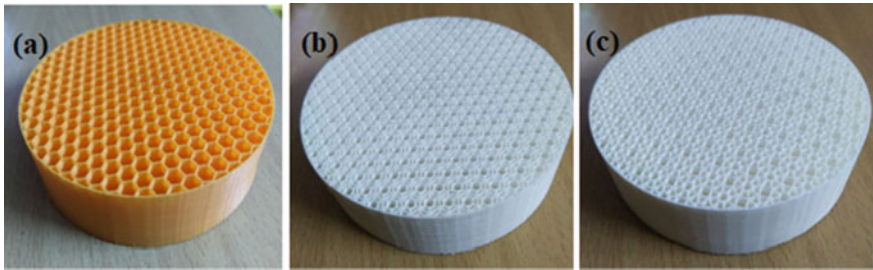


Fig. 4 3D Printed model of **a** Hexagonal core structure (C1), **b** Lined Hexagonal core structure (C2), and **c** Octagonal structure (C3)

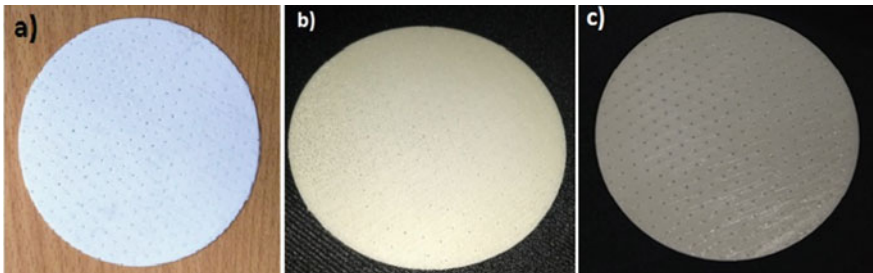


Fig. 5 3D Printed model of MPPs: MPP with **a** $d = 0.5$ mm, **b** $d = 0.6$ mm, **c** $d = 0.7$ mm and fixed $t = 1$ mm and $b = 5.5$ mm

3 Testing and Simulation

3.1 Impedance Tube Test

The sound absorption coefficient of the material is measured using Impedance Tube Apparatus, which is a system consisting of a glass tube containing a speaker at the one end and the material sample whose properties are to be measured at the other end [11].

The system has a pair of 1/2" Microtech Gefell microphones separated by a fixed distance are connected to the glass tube with the help of microphone holders. These microphones are connected to a data acquisition system [11] (Figs. 1, 2, 3, 4 and 5).

A function generator is used to power the speaker in the impedance tube. For the absorption coefficient, a rigid backing is also used [6, 11].

The sound absorption coefficients of the multilayer porous absorber samples were measured with an impedance tube using the transfer function method [6, 11]. The testing setup was established according to ASTM E 1050 and is illustrated in Fig. 6a. The frequency range of interest was 50–1000 Hz.

Table 2 Specifications of impedance tube apparatus

Parameter	Specifications
Impedance tube length	1000 mm
Inside diameter	100 mm
Speaker frequency response range	160–7000 Hz
Signal generator	200–6500 Hz
Sweep in	Automated
Number of microphones	2
Sample holding unit	50 mm
Controls	PC automated measurements
Software	MATLAB

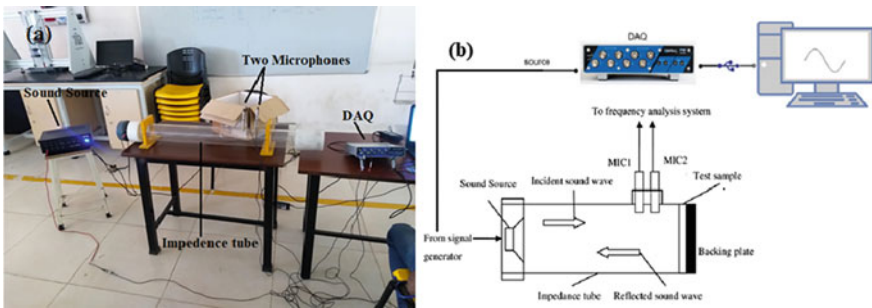


Fig. 6 **a** Experimental setup of Impedance tube setup, **b** Schematic diagram of Impedance tube setup

Simulation

The Absorption coefficient simulation is carried out in the COMSOL 5.5 Multi-physics software. The porous absorber model is solved in the frequency domain and provides the absorption coefficient in a frequency range of 50–1000 Hz in steps of 2 Hz.

The inbuilt model can be used to perform simulations by changing different parameters such as the thickness of the plate, the diameter of holes in the plate, the distance between the holes, and porosity.

Input Parameters:

Model type: Thin Plate (PLA Material); Hole diameter: Varying from 0.5 mm to 0.8 mm; Plate Thickness: 1 mm; Air Domain height: 30 mm; Fluid Material: Air.

4 Results and Discussion

4.1 Impedance Tube Test

The following graph was obtained by experimenting on the samples: C1, C2, C3, C1P, C2P, and C3P. C1P, C2P, and, C3P are C1, C2, and, C3 each coupled with a $d = 0.5$ mm, $t = 1$ mm MPP, respectively.

Figure 7 shows that the core structures C1, C2, and C3 do not offer good acoustic shielding. The sound absorption through a metamaterial is achieved by viscous and thermal losses, through an MPP by resonant behavior. Thus, a wide range of frequencies was absorbed when the MPP was coupled with a porous material. For an MPP with a fixed perforation ratio of 1.1%, Fig. 7 provides a comparison between the three porous structures and their acoustic performance when accompanied by an MPP. These single units (C1P, C2P, and C3P) that behave as Helmholtz resonators are quite effective in broadening the peak over a range of frequencies.

AFoam sample was used as a standard to compare the performance of the test samples. The acoustic performance of C3P was found to be better than C2P, followed by C1P and foam for the frequency range of 400–700 Hz. For instance, at 550 Hz, the value of the absorption coefficient by C3P was 0.756, by C2P was 0.6, and by C1P, it was 0.37. The intricacy of the porous structure contributes to a better acoustic performance that is evident from the octagonal porous structure (C2P) as well.

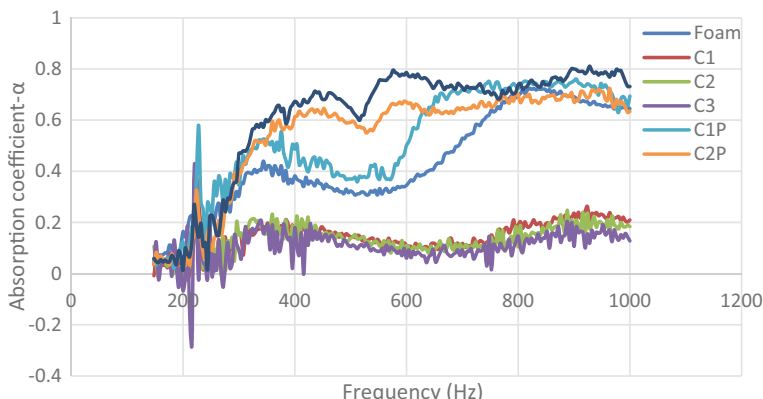


Fig. 7 Comparison of curves of the samples from the sound absorption test

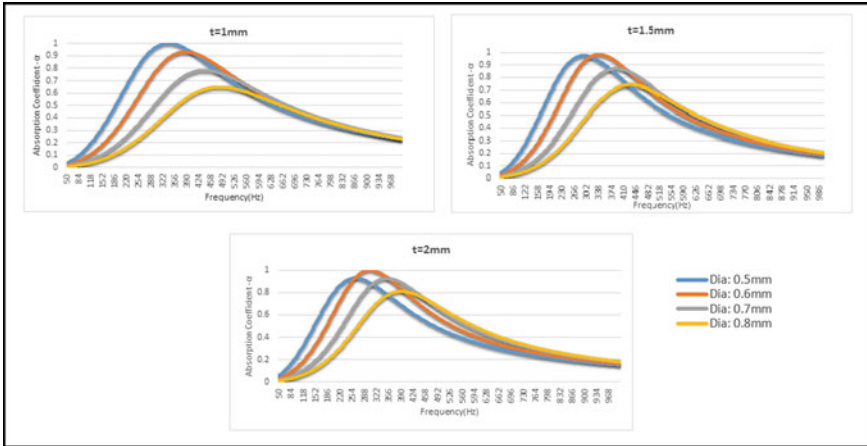


Fig. 8 Comparison of the absorption coefficient with a change in perforation diameter (d) for $t = 1$ mm, $t = 2$ mm, and $t = 3$ mm and a constant pitch, $b = 5.5$ mm

Effect of perforation diameter and plate thickness on the absorption coefficient.

Effect of pitch/number of holes on the absorption coefficient.

From Fig. 8 it can be said that, with the increase in the thickness of the MPP, the absorption coefficient increases and the absorption frequency falls, hence attenuating lower frequencies better.

It can be observed from Fig. 9 that MPPs with shorter pitch absorb a larger frequency range compared to, $b = 10$ mm MPP. With the increase in the diameter of holes, the absorption efficiency of lower pitch MPPs decreases. With the increase in the diameter of holes, the curve for lower pitch MPPs flattens.

The higher pitch boosts the absorption for larger diameter MPPs corresponding to lower frequencies. The MPP with $b = 10$ mm exhibits a high absorption coefficient

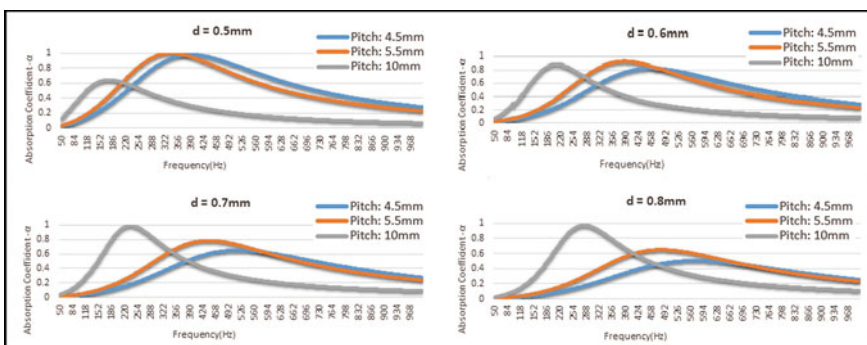


Fig. 9 Comparison of the absorption coefficient with a change in perforation diameter (d) and pitch (b)

(~0.97), but the absorption curve is steep; therefore, a small band of frequencies is absorbed. The objective of the larger diameter MPPs is to absorb the sound in the low-mid-frequency range, which is effectively being done by the low pitch MPP, especially 5.5 mm. Also, as we increase the pitch, the absorption coefficient reaches 0 at the higher end of the low-frequency band, but on the other hand, the lower pitch MPPs have a broad range of absorption.

5 Conclusion

The study showed that the simple hexagonal structured metamaterial when coupled with an MPP exhibited good sound absorption with an absorption coefficient ~0.8. The low-mid-frequency range was absorbed effectively and the absorption coefficient was between 0.6 and 0.8 for this range. The Octagonal structure was found to be better than the modified hexagonal structure in terms of sound absorption.

The simulation study gives the right choice of parameters for fixing the MPP to be coupled with the metamaterial, so that the combination yields maximum absorption coefficient. It can be told that, with the increase in the thickness of the MPP, the absorption coefficient increases, the frequency corresponding to maximum absorption falls, hence attenuating the lower frequencies is better. It is observed that MPP with a higher pitch offered a higher absorption coefficient for different hole diameters, but the curve was steep and therefore attenuating a narrow frequency band. Hence, MPPs with shorter pitch ($b = 5.5, 4.5$ mm) though exhibiting less absorption coefficient are preferable since the frequency band is broader. The design can be improved further to achieve better results.

References

1. Leventhall, G.: Low-frequency noise and annoyance. *Noise Health* **6**(23), 59–72 (2004)
2. Berglund, B., Lindvall, T., Schwela, D.H.: Occupational and Environmental Health Team. Guidelines for Community Noise. World Health Organization (1999)
3. Berglund, B., Hassmén, P., Job, R.S.: Sources and effects of low-frequency noise. *J. Acoust. Soc. Am.* **99**(5), 2985–3002 (1996)
4. Sébastien, G., Movchan, A., Pétursson, G., Ramakrishna, S.A.: Acoustic metamaterials for sound focusing and confinement. *New J. Phys.* **9**(399), 1367–2630 (2007)
5. Bodaghi, M., Damanpack, A.R., Liao, W.: H, Adaptive metamaterials by functionally graded 4D printing. *Mater. Des.* **135**, 26–36 (2017)
6. Valveza, S., Santosa, P., Parentea, J.M., Silvaa, M.P., Reisa, P.N.B.: 3D printed continuous carbon fiber reinforced PLA composites: a short review. *Proc. Struct. Integr.* **25**, 394–399 (2020)
7. Maury, C., Bravo, T., Pinhede, C.: Sound absorption and transmission through flexible micro-perforated structures. *J. Acoust. Soc. Am.* **133**(5), 3309–3309 (2013)
8. Sakagami, K., Yamashita, I., Yairi, M., Morimoto, M.: Sound absorption characteristics of a honeycomb-backed microperforated panel absorber: revised theory and experimental validation. *Noise Control Eng. J.* **58**(2) (2010)

9. Sakagami, K., Yamashita, I., Yairi, M., Morimoto, M.: Effect of a honeycomb on the absorption characteristics of double-leaf microperforated panel (MPP) space sound absorbers Noise Control Eng. J. **59**(4), 363 (2011)
10. Xie, S., Wang, D., Feng, Z., Yang, S.: Sound absorption performance of microperforated honeycomb metasurface panels with a combination of multiple orifice diameters. Appl. Acoust. **158**, 107046 (2020)
11. Yuvaraj, L., Jeyanthi, S.: Acoustic performance of countersunk micro-perforated panel in multilayer porous material. Sage J. Build. Acoust. **27**(1), 3–20 (2019)
12. Putra, A., Ismail, A.Y.: Normal incidence of sound transmission loss from perforated plates with micro and macro size holes. Adv. Acoust. Vib. 1–12 (2014)
13. Pfretzschnner, J., Cobo, P., Simon, F., Cuesta, M., Fernandez, A.: Microperforated insertion units: an alternative strategy to design microperforated panels. Appl. Acoust. **67**(1), 62–73 (2006)
14. Maa, D.Y.: Potential of microperforated panel absorber. J. Acoust. Soc. Am. **104**, 2861 (1998)
15. Maa, D.Y.: Theory and design of microperforated panel sound-absorbing constructions. Scientia Sinica **18**(1), 55–71 (1975)
16. Fernandez-Vicente, M., Calle, W., Ferrandiz, S., Conejero, A.: Effect of infill parameters on tensile mechanical behavior in desktop 3D printing. 3D Print. Addit. Manuf. **3**(3), 183–192 (2016)
17. Carneiro, O.S., Silva, A.F., Gomes, R.: Fused deposition modeling with polypropylene. Mater. Des. **83**, 768–776 (2015)
18. Gupta, M., Sneh, A., Yuvaraj, L., Subramanian, J.: An experimental investigation on the acoustic and thermal properties of copper reinforced sustainable foam. Int. J. Eng. Technol. (IJERT), **08**(08) (2019)

Study of Effect of Angle of Contact and Angle of Extension of Wear Plate on Maximum Stress Induced in Horizontal Pressure Vessel



Aniruddha Nayak and Pravin Singru

1 Introduction

Pressure vessels are tanks that are used to store fluids. Pressure vessels often have a combination of high-pressure and high-temperature fluids in them along with this the fluids might also be highly flammable or poisonous in nature. Because of such hazards, if any accident occurs with pressure vessels, it can cause a large number of fatalities. Because of such risks and hazards, pressure vessels have to follow strict rules and regulations during design process.

Pressure Vessels are classified as Horizontal, Vertical, or Spherical. Horizontal pressure vessels are supported by two saddle supports near its end. One of the saddle supports is sliding in nature to accommodate the changes in the length of the vessel due to the temperature changes in the vessel. Pressure load and self-weight induce membrane stresses, bending stresses, and shear stresses in the shell of the vessel. Pressure vessels are designed based on various International codes to assure their safety in their operating conditions. Common pressure vessel codes used for designing are ASME Boiler and Pressure Vessel Code Section VIII, European committee for Standardization, and British Standards Institution. In this paper, we have used ASME Boiler and Pressure Vessel Code Section VIII [1].

The vessel can be supported by a saddle in two ways: (1) The saddles are welded along the periphery of the vessel. (2) The vessel is freely kept on the saddle support. The prior option is more commonly used. When a vessel is supported by a saddle support, a saddle acts as a stiff support and when the saddle is connected to the vessel

A. Nayak (✉) · P. Singru
BITS, Pilani-K.K. Birla Goa Campus, Goa 403726, India
e-mail: f20180850@goa.bits-pilani.ac.in

P. Singru
e-mail: pmsingru@goa.bits-pilani.ac.in

there is a sudden change in the stiffness as the shell is relatively less stiff as compared to the saddle support. Therefore, we see a stress concentration in the shell of the vessel near the saddle horn. This highest localized stress is termed circumferential stress. There are some methods by which we can reduce this peak stress value at the saddle horn. (1) We can add a wear plate which extends above the saddle between the support and the vessel making the transition from the support to the vessel less intense. (2) In the case of loose-fitting saddle supports we can increase the radius of the saddle slightly than the outer radius of the vessel. This method introduces a gap between the vessel and the saddle at the unloaded condition and when loaded the vessel can deform radially outwards up to some limit and hence the pinching effect of the saddle on the vessel is reduced. (3) Designing saddle supports which are more flexible at the saddle horn. (4) Adding stiffening rings in the vessel near the saddle supports, which increases the stiffness of the shell and thus the stress concentration will be reduced.

2 Literature Review

Zick et al. [2] studied the different stresses in large horizontal cylindrical pressure vessels on two saddle supports. Megysey [3] explained the detailed procedure for designing horizontal pressure vessels and saddle supports. The saddle support should be placed at a distance less than 0.2 times the tangent length from the head to utilize the stiffening effect of the head. Khan [4] studied the variation of the distance of saddle support from the head of the vessel and calculated the maximum stress values. It is found that, when the saddle is placed at a distance of $0.25L$ from the head, it gives the best configuration. He also studied the effect of slenderness ratio (L/R) in this configuration and studied that L/R values below 16 give the minimum value of stress concentration. Ong and Lu [5] performed a parametric study for determining the optimal support radius for loose-fitting saddle support for cylindrical pressure vessel. It was found that the peak localized stress arising from the saddle support can be reduced by using a clearance fit saddle. El-Abbasi et al. [6] performed a three-dimensional finite element analysis study on pressure vessels resting on loose-fitting saddle supports taking into consideration the frictional contact between the saddle and the vessel and using thick shell elements. The results showed that increasing the saddle radius by 1–2% over the vessel radius causes a stress reduction up to 50% in the vessel, also an extension of the wear plate by 5–10 degrees caused stress reduction of 25–40% in the vessel. Seng [7] presented a theory to analyze the effectiveness of incorporating a wear plate at the saddle support of a cylindrical pressure vessel. According to this theory, it is found that peak stresses in the vessel at the saddle horn can be reduced by 15–40% when using a wear plate which has the same thickness as the vessel and it extends 5° or more above the saddle horn. Ong and Lu [8] in their study developed two geometric parameters and then provided a chart with parametric curves to determine the stress reduction caused due to different configurations of the saddle possible.

A detailed FEA study in which the parameters of a saddle support are changed to notice the changes caused in the local maximum stress values is not found in literature. This study is important as this will show the dependence of the maximum stress values for different configurations of the saddle support. Knowing this, selection of the best configuration which passes the ASME code can be made.

3 Problem Statement

A pressure vessel has the function to hold gases or fluids at a substantially higher pressure than the surrounding. A horizontal pressure vessel is supported by two saddle supports and these saddle supports must hold the weight of the vessel plus the weight of the fluid without causing critical stress concentration on the shell of the vessel. A saddle acts as a stiff support and when the saddle is connected to the vessel there is a sudden change in the stiffness as the shell is relatively less stiff as compared to the saddle support. Therefore, there is a stress concentration in the shell of the vessel near the saddle horn. To reduce the effect of this stress concentration, a wear plate is added, which acts as a buffer so that the change in stiffness is not very drastic. It is the surface of the wear plate that is welded to the shell of the vessel. Even after adding the wear plate the stress concentration at the saddle horn still exists but is reduced substantially. The parameters of a saddle support that can be changed in order to change the value of local stress concentration are (1) angle of contact of the saddle, (2) the width of the saddle and wear plate, (3) thickness of the wear plate, and (4) extension of the wear plate over the saddle horn. These parameters directly govern the values and location of maximum local stress concentration in the shell.

A detailed FEA study in which these parameters are changed to notice the changes caused in the local maximum stress values is not yet done. This study is important as this will show us the dependence of the maximum stress values for different configurations of the saddle support, knowing this selection of the best configuration which passes the ASME code can be made.

4 Objective

The objective of the present study is to perform an FEA study and find the trends in local stress concentration in the shell of a pressure vessel for different configurations of saddle. In this study, saddle supports with the angle of contact 120, 130, 140, 150, 160, and 170 degrees is considered. We selected 120° as our lowest angle since according to ASME code requirements, it is the least angle of contact that can be used. Extension of wear plate by 0, 2, 4, 6, 8, 10 degrees on each side is considered for study for the angle of contact of 120, 130, 140, and 150 degrees. In 160° case, 0, 2, 4, 6, 8 degrees of extension on each side and in 170° case 0, 2, 4 degrees of extension on each side are studied as the remaining configurations will lead to a total

angle greater or equal to 180° . The width of the wear plate is kept constant for all configurations.

5 Problem Formulation and Design

The dimensions of the pressure vessel that we considered had an external radius of 2 m, thickness of the vessel was 8 mm, the total length of the pressure vessel from one tangent end to another was 10 m, the head type selected was Elliptical (2:1), the head thickness was 12 mm, the position of the saddle from one tangent end was 1.5 m, width of wear plate was 24 cm, thickness of wear plate was 16 mm, width of saddle support was 20 cm, thickness of rib plates and base plate was 20 mm, thickness of web plate was 30 mm. The material that we selected for the Pressure Vessel; the wear plate was SA 516 Grade 70. The material properties are as follows: Density= 7800 kg/m^3 , Modulus of elasticity = 200 GPa, Poisson's ratio= 0.29, Maximum allowed stress= 260 MPa. The material that we selected for the Web, Rib, and Base plate was IS 2062 Grade A36. The material properties are as follows: Density= 7850 kg/m^3 , Modulus of elasticity= 200 GPa, Poisson's ratio= 0.26, Maximum allowed stress= 260 MPa. These material properties are obtained from ASME Section II Part D [9]. The operating conditions of the pressure vessel were considered as follows. Density of fluid= 1000 kg/m^3 , Temperature of fluid= 298 K, Operating pressure= 1 MPa (Fig. 1).

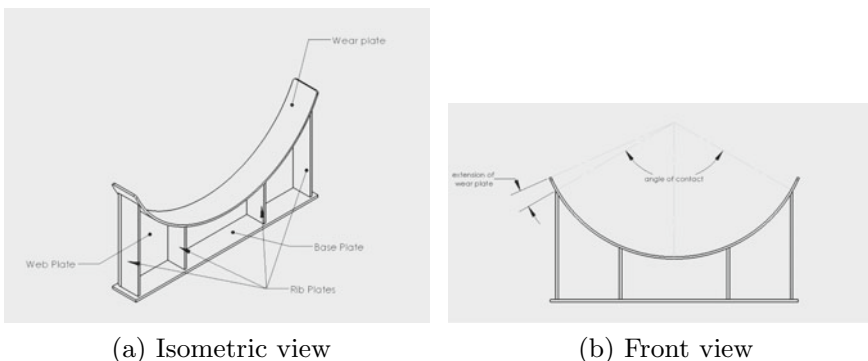


Fig. 1 Views of the saddle support

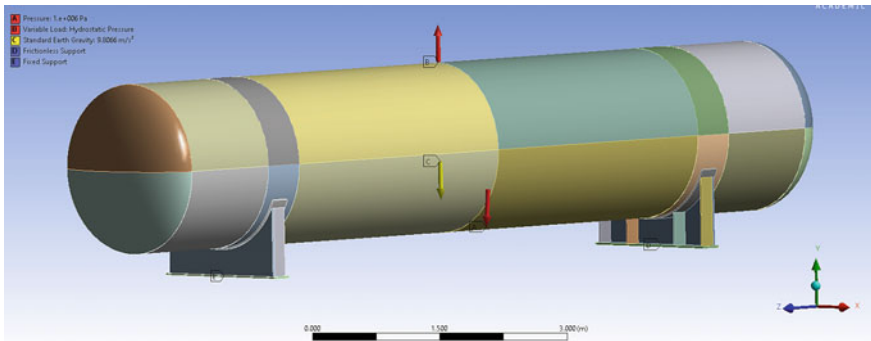


Fig. 2 Sliced Geometry with Loading in the FEA model (120-6 configuration)

6 Methodology

In this study, we kept the width of saddle support a constant and changed the value of angle of contact and angle of extension of wear plate of a saddle and studied the effect on the max stress in the vessel. The aim of this study is to find the most optimum configuration of saddle to pass the ASME requirements according to ASME Section VIII Division-2 [1] (Design by Analysis) while keeping the material costs at the minimum.

The pressure vessel was modeled in SolidWorks 2019 and the 3D FEA analysis study was completed in ANSYS 2020 Release [10]. The loading and boundary condition on pressure vessel is as per Fig. 2. Gravity load due to self-weight, internal hydrostatic pressure, and internal pressure of 1MPa is considered for the study. There is fixed support at one end of saddle and frictionless support at the other end (Sliding end). Solid Shell 190 (SOLSH190) elements, shown in Fig. 3, were used in meshing of the shell and wear plate to give an accurate representation of bending in the thin shell. SOLSH190 is used for simulating shell structures with a wide range of thickness (from thin to moderately thick). The element possesses the continuum solid element topology and features eight-node connectivity with three degrees of freedom at each node: translations in the nodal x-, y-, and z-directions.

It is a 3D solid element free of locking in bending-dominant situations. Unlike shell elements, SOLSH190 (Fig. 3) is compatible with general 3D constitutive relations and can be connected directly with other continuum elements. SOLSH190 utilizes a suite of special kinematic formulations, including the assumed strain method (Bathe and Dvorkin [11] to overcome locking when the shell thickness becomes extremely small. SOLSH190 employs enhanced strain formulations (Simo and Rifai [12], Simo et al. [13] to improve the accuracy in in-plane bending situations. The satisfaction of the in-plane patch test is ensured. Incompatible shape functions are used to overcome the thickness locking. These are the strong reasons to consider SOLSH190 for analysis of the pressure vessels. Three elements were used along the thickness to give an accurate representation of the bending of the shell. The finite element

Fig. 3 Schematic of SOLSH190

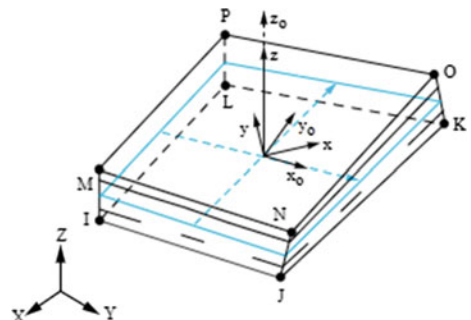


Table 1 Mesh Convergence test results on the 120° angle of contact saddle support with 4° extension of wear plate

Number of elements	Maximum local stress concentration in shell
685554	261.92 MPa
1023768	281.44 MPa
1468242	293.33 MPa
3536219	299.17 MPa
3750086	299.35 MPa

analysis is a numerical technique and a convergence study is required to be done. In this work, convergence study was done on the saddle support and the vessel to confirm the accuracy of the results up to 0.05%. A sample result for one case of the 120° angle of contact saddle support with 4° extension of wear plate is as per Table 1.

7 Results and Discussions

The complete model shown in Fig. 2 is discretized using SOLSH190 with loading and boundary conditions as mentioned in the methodology. The simulation result shown in Fig. 4 is for the case of 120° angle of contact and 4° extension on both

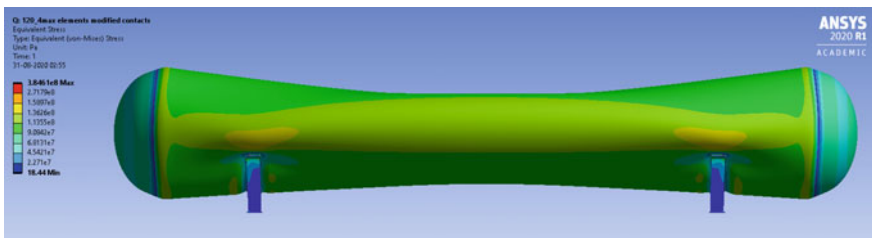
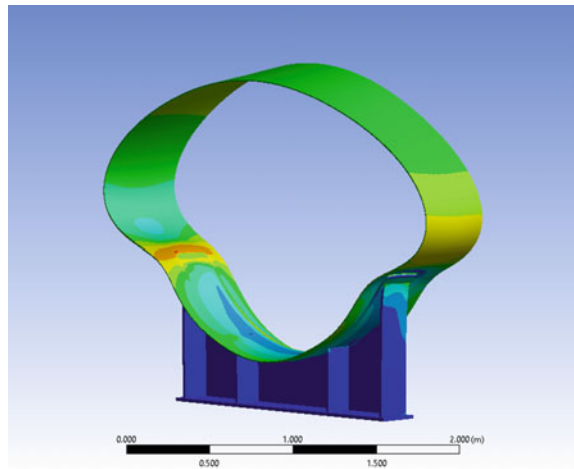


Fig. 4 A simulation image of 120° angle of contact and 4° extension on both sides (deformation is exaggerated)

Fig. 5 Stress distribution of the vessel in the saddle region (deformation is exaggerated)



sides. In Fig. 5, the stress distribution in the vessel in the saddle region is shown. The deformation is exaggerated and it is clear that there is stress concentration is in the vessel at the saddle horn.

The stress distribution in all configurations is similar to that shown in Fig. 4 and the location of the local circumferential stress concentration in all configurations is similar to that shown in Fig. 5 at the saddle horn. Figure 6 shows variation of the max local stress concentration in all the saddle configurations as per FEM simulations. The value of the maximum allowable stress is also plotted as a straight line. All the saddle configurations in which the value of the maximum stress falls below this maximum value are safe and are eligible for use as it passes ASME requirements according to ASME Section VIII Division-2 (Design by Analysis) while keeping the material costs at the minimum.

Seng [7] has derived stress reduction factor at the saddle horn by use of wear plate. The effectiveness of the wear plate (or saddle top plate) in reducing the peak circumferential stress at the saddle horn can be quantified effectively by defining the stress reduction factor K_t as follows:

$$K_t = \frac{\text{Peak stress (with the wear plate)}}{\text{Stress at saddle horn (without the wear plate)}} \quad (1)$$

In this paper, an attempt is made to calculate the same after performing finite element analysis of the vessel under different conditions as discussed in the methodology section. The values of K_t , the stress reduction factor found by Seng [7] and K_f found by FEA is as per Table 2.

It is found that the % difference in the values of K_t and K_f varies from 0 to 8.9%. The practical limits as per ASME Section VIII Division-2 mentions that angle of contact of 120–150° with the angle of extension of 4–8° are advisable in horizontal pressure vessel design to pass the design criteria. The maximum difference in the

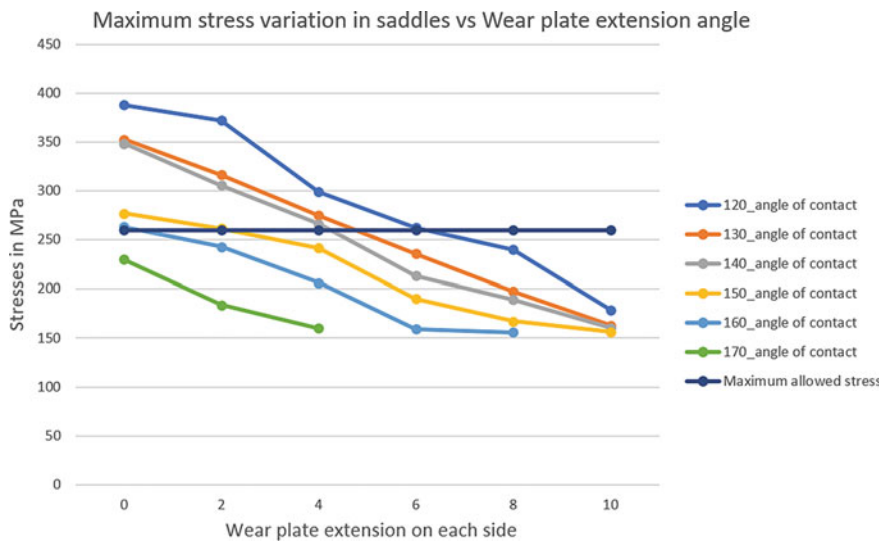


Fig. 6 Plot of the stress concentration values of all the configurations together

Table 2 Comparison of stress reduction factor found by theory and FEA

Angle of extension of wear plate on both sides	4			6			8			10			
	Angle of contact of the saddle support	K _f	K _t	% diff	K _f	K _t	% diff	K _f	K _t	% diff	K _f	K _t	% diff
120		0.77	0.8	3.8	0.68	0.65	-4.62	0.61	0.56	-8.9	0.46	0.44	-4.55
130		0.78	0.8	2.5	0.67	0.65	-3.08	0.56	0.56	0	0.46	0.44	-4.55
140		0.76	0.8	5	0.61	0.65	6.15	0.54	0.56	3.57	0.46	0.44	-4.55
150		0.87	0.8	-8.7	0.68	0.65	-4.62	0.6	0.56	-7.1	0.56	0.44	-27.3

values of K_t and K_f is observed in the case of 150° angle of contact with 10° extension and is equal to 27.3%, but it is observed in the FEA model that the location of the maximum stress value is along the edge of the wear plate and not near the saddle horn. Thus, we can see a higher deviation of the value of K_f from K_t as the K_f is calculated from parametric curves which are accurate if the stress is in the saddle region. This particular case is anyway not important from ASME Section VIII Division-2 requirement. So, we can consider this particular case as an exception for the time being.

8 Conclusions

From the results, we can conclude the following points:

- (1) We can see that as the angle of contact increases from 120° to 170° the value of the maximum stress concentration decreases. There is a 40.8% decrease in maximum stress on the increase of angle of contact from 120° to 170° .
- (2) The increase in wear plate angle also causes the maximum stress concentration to drop. There is an average reduction of 35% in maximum stress concentration on increasing the wear plate angle from 0° to 6° on both sides.
- (3) For our given case, we found that the following configurations are eligible: For angle of contact of 120° configurations with angle of extension of 8° and above, for angle of contact of 130° configurations with angle of extension of 6° and above, for angle of contact of 140° configurations with angle of extension of 6° and above, for angle of contact of 150° configurations with angle of extension of 4° and above, for angle of contact of 160° configurations with angle of extension of 2° and above, and all configurations with 170° angle of contact are eligible.
- (4) For our given case it is found that the saddle configuration with angle of contact 120° and extension of 8° on both sides of the saddle is the best.

References

1. ASME: ASME VIII Division 2—Alternative Rules—Rules for Construction of Pressure Vessels, p. 867 (2017)
2. Zick, L.P.: Stresses in large horizontal cylindrical pressure vessels on two saddle supports. *Press. Vessel. Pip. Des. Anal.* **2**, 959–970 (1972). (September 1951)
3. Megyesy, E.F.: *Pressure_Vessel_Handbook_12th_edition_Eu.pdf* (1973)
4. Khan, S.M.: Stress distributions in a horizontal pressure vessel and the saddle supports. *Int. J. Press. Vessel. Pip.* **87**(5), 239–244 (2010)
5. Ong, L.S., Lu, G.: Optimal support radius of loose-fitting saddle support. *Int. J. Press. Vessel. Pip.* **54**(3), 465–479 (1993)
6. El-Abbasi, N., Meguid, S.A., Czekanski, A.: Three-dimensional finite element analysis of saddle supported pressure vessels. *Int. J. Mech. Sci.* **43**(5), 1229–1242 (2001)
7. Seng, O.L.: Effectiveness of wear plate at the saddle support. *J. Press. Vessel. Technol. Trans. ASME* **114**(1), 12–18 (1992)
8. Ong, L.S., Lu, G.: Stress reduction factor associated with saddle support with extended top plate. *Int. J. Press. Vessel. Pip.* **62**(2), 205–208 (1995)
9. ASME: ASME Section II Part-D (2017)
10. ANSYS: 2020 Release (2020)
11. Bathe, K., Dvorkin, E.N.: A formulation of general shell elements the use of mixed interpolation of tensorial components. *Int. J. Numer. Methods Eng.* **22**(3), 697–722 (1986)
12. Simo, J.C., Rifai, M.S.: A class of mixed assumed strain methods and the method of incompatible modes. *Int. J. Numer. Meth. Eng.* **29**(8), 1595–1638 (1990)
13. Simo, J.C., Armero, F., Taylor, R.L.: Improved versions of assumed enhanced strain tri-linear elements for 3D finite deformation problems. *Comput. Methods Appl. Mech. Eng.* **110**(3–4), 359–386 (1993)

Effect of Number of Stiffening Rings, Their Position and Cross Section on Stress Concentration Near Saddle Support in Horizontal Pressure Vessels



Aniruddha Nayak and Pravin Singru

1 Introduction

Pressure vessels are tanks, vessels that are used to store, transport or receive fluids. Pressure vessels come in any size depending on the requirement but mostly come in three shapes—Horizontal, Vertical and Spherical. Horizontal pressure vessels are supported by two saddle supports near its end. One of the saddle supports is sliding in nature to accommodate the change in length of the vessel due to temperature changes in the vessel. Pressure load, self-weight and other loads due to the different attachments induce membrane stresses, bending stresses and shear stresses in the shell of the vessel.

Pressure vessels often have a combination of high-pressure and high-temperature fluids in them along with this the fluids might also be highly inflammable or poisonous in nature. Because of such hazards, if any accident occurs with pressure vessels, it can cause a large number of fatalities. Because of such risks and hazards, pressure vessels have to follow strict rules and regulations during the process of design. Pressure vessels are designed based on various international codes to assure their safety in their operating conditions, common pressure vessel codes used for designing are ASME Boiler and Pressure Vessel Code Section VIII, European Committee for Standardization and British Standards Institution. For our study, we will be using the ASME Boiler and Pressure Vessel Code Section VIII [1] as it is very commonly used and is accepted in most parts of the world.

A. Nayak (✉) · P. Singru

Birla Institute of Technology and Science, Pilani - K.K. Birla Goa Campus, Goa 403726, India
e-mail: f20180850@goa.bits-pilani.ac.in

P. Singru
e-mail: pmsingru@goa.bits-pilani.ac.in

In case of long pressure vessels, having just two saddle supports is not sufficient to hold the structure. The stiffness of the shell is not enough to withstand the bending force due to self-weight and due to the weight of fluid. When a vessel is supported by a saddle support, a saddle acts as a stiff support and when the saddle is connected to the vessel there is a sudden change in the stiffness as the shell is relatively less stiff as compared to the saddle support. Therefore, we see a stress concentration in the shell of the vessel near the saddle horn. This highest localized stress is termed circumferential stress.

There are some methods by which we can reduce this peak stress value at the saddle horn.

- (1) We can add a wear plate which extends above the saddle between the support and the vessel making the transition from the support to the vessel less intense.
- (2) In the case of loose-fitting saddle supports we can increase the radius of the saddle slightly than the outer radius of the vessel. This method introduces a gap between the vessel and the saddle at the unloaded condition and when loaded the vessel can deform radially outwards up to some limit and hence the pinching effect of the saddle on the vessel is reduced.
- (3) Designing saddle supports which are more flexible at the saddle horn.
- (4) Adding stiffening rings in the vessel near the saddle supports. This will increase the stiffness of the shell and thus the stress concentration will be reduced.

Using stiffening rings, the thickness of the vessel can be further reduced as the stiffening rings increase the combined stiffness of the vessel so that a thinner wall thickness can also withstand the bending and shear forces of the load. Thus, stiffening rings are a popular way of controlling the stress concentration at certain regions in the vessel as they are cost-effective and easy to assemble.

2 Literature Review

Zick [2] studied the different stresses in large horizontal cylindrical pressure vessels on two saddle supports. Megyesy [3] explained the detailed procedure for designing horizontal pressure vessels (with and without stiffening rings) and saddle supports. Also, according to Megyesy, the saddle supports should be placed at a distance less than 0.2 times the tangent length from the head to utilize the stiffening effects of the head. Merlin Thattil and Pany [4] performed FEA analysis on pressure vessels with different head types and found that torispherical heads had lower stress values at the junction between the head and the cylinder as compared to a hemispherical head type. Nitin Bhinde and Rajanarsimha [5] also performed FEA analysis of pressure vessels with Flat, Hemispherical, Ellipsoidal, Conical and Torispherical heads and also came to a conclusion that pressure vessels with torispherical heads had the lowest stress concentration followed by elliptical head, conical head, hemispherical head and finally flat head. Said Golabi et al. [6] performed FEA analysis and found out a new

approach of reducing the head thickness of pressure vessels with internal pressure by attaching a stiffener ring on the head. The pressure vessel with torispherical head was considered and found that a stiffening ring of rectangular cross section is best suitable for this purpose. It was found that using the right dimensions of the stiffening ring and attaching the stiffening ring at the right location would lead to usage of 30% thinner plates as compares to the no stiffening ring case. This method of using stiffener rings on the head is especially more effective in the case of larger head sizes and will lead to a lesser material cost followed by reduced manufacturing costs. Their findings were also verified experimentally. Khot et al. [7] performed an FEA study to quantify the role of stiffening ring in a pressure vessel in presence of a nozzle. A nozzle in the shell of the pressure vessel created instability in that region and add a stiffening ring in the vicinity of the nozzle will balance this instability.

3 Problem Statement

A pressure vessel has the function to hold gases or fluids at a substantially higher pressure than the surrounding. A horizontal pressure vessel is supported by two saddle supports and these saddle supports must hold the weight of the vessel plus the weight of the fluid as well as the weight of any extra attachments on the vessel without causing critical stress concentration in the shell of the vessel. A saddle acts as a stiff support and when the saddle is connected to the vessel there is a sudden change in the stiffness as the shell is relatively less stiff as compared to the saddle support. Therefore, we see a stress concentration in the shell of the vessel near the saddle horn. To reduce the effect of this stress concentration, there is an extended wear plate added, the wear plate acts as a buffer so that the change in stiffness is not very drastic. It is the surface of the wear plate that is welded to the shell of the vessel. In long pressure vessels even after adding the wear plate, there is significant stress concentration in the vessel at the saddle horn region. To reduce this stress value and make the vessel acceptable according to international codes, stiffener rings can be added inside the vessel which makes the entire shell stiffer.

Stiffener rings come in varied shapes and dimensions. The parameters of stiffener rings that can be changed to study their effect on the maximum stress in vessel are (1) The cross-sectional shape of the stiffener ring. (2) The cross-section dimensions of the stiffener ring. (3) The total number of stiffener rings used. (4) The positioning of the stiffener rings. Choosing an appropriate stiffening ring is very crucial.

A detailed FEA study in which these parameters are changed to notice the changes caused in the local maximum stress values is not yet done.

This study is important as this will show us the dependence of the maximum stress values for the different configurations of stiffener rings used. With this knowledge, we can understand the dependences of the different parameters on the overall stress distribution in the vessel and then select the best configuration which passes the ASME code, saving material costs.

4 Objective

The objective of the present study is to do an FEA study and find the trends in local stress concentration in the shell of a pressure vessel for different configurations of stiffener rings.

In this study, we considered stiffening ring of square, rectangular and T-cross section. The square sections selected are 60 mm × 60 mm and 80 mm × 80 mm in dimension. The rectangular cross section had a dimension of 20 mm × 80 mm and 30 mm × 60 mm. The T-section had dimensions of 2 × (20 mm × 80 mm) (Refer Fig. 1). The different configurations that were simulated for all the cross-section shapes were as follows: two stiffener rings (one above each saddle), three stiffener rings (one above each saddle and one placed symmetrically between both the saddles and five stiffener rings (one above each saddle and the remaining three placed symmetrically between both the saddle supports) (Refer Fig. 2). Along with these configurations, we also simulated case of two parallel stiffener rings above the

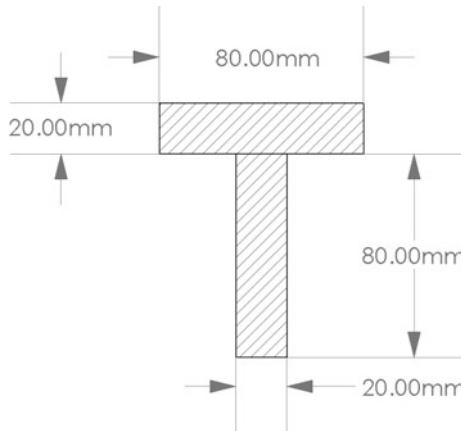


Fig. 1 T cross-section

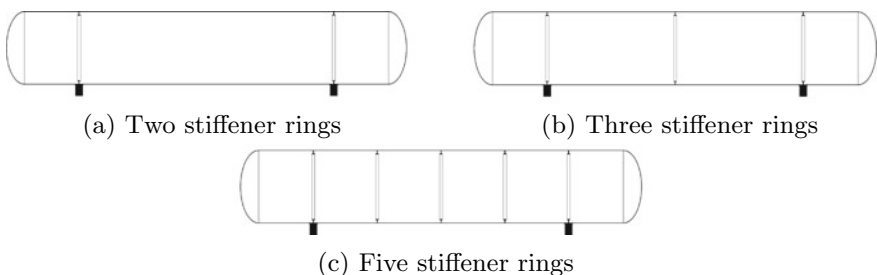


Fig. 2 Different stiffener ring configurations

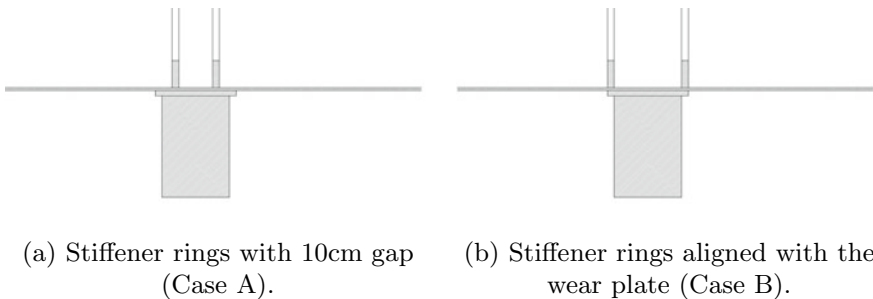


Fig. 3 Different parallel stiffener ring configurations

saddle support for the cross section of $20\text{ mm} \times 80\text{ mm}$ and $30\text{ mm} \times 60\text{ mm}$. For the parallel case, we considered two configurations; first, configuration in which the distance between the inner faces of the two stiffener rings is 10cm (Refer Fig. 3a) and the second configuration in which the external faces of the stiffener rings is aligned with the faces of wear plate (Refer Fig. 3b). For all the configurations, width, extension and thickness of the wear plate are kept constant.

5 Problem Formulation and Design

The dimensions of the pressure vessel that we considered had an external radius of 2 m, thickness of the vessel was 8 mm, the total length of the pressure vessel from one tangent end to another was 10m, the head type selected was Elliptical(2:1), the head thickness was 12 mm, the position of the saddle from one tangent end was 1.5 m, width of wear plate was 24 cm, thickness of wear plate was 16 mm, width of saddle support was 20 cm, angle of contact was 120° , and the extension of wear plate was 6° on each side. The material that we selected for the Pressure Vessel, the wear plate and stiffening ring was SA 516 Grade 55. The material properties are as follows: Density = 7750 kg/m^3 , Modulus of elasticity = 200 GPa, Poisons ratio = 0.29, Maximum allowed stress = 207 MPa. These material properties are obtained from ASME Section II Part D [8]. The operating conditions of the pressure vessel were considered as follows. Density of fluid = 1000 kg/m^3 , Temperature of fluid = 298 K, Operating pressure = 1 MPa.

6 Methodology

In this study, all the saddle support parameters are constant for all the stiffening ring configurations. A saddle support with an angle of contact 120° and an extension of wear plate of 6° on each side was selected. This choice was made because according to ASME requirements a minimum contact angle of 120° is necessary. The aim of

this study is to find the most optimum configuration of saddle to pass the ASME requirements according to ASME Section VIII Division-2 (Design by Analysis) [1] while keeping the material costs at the minimum.

The pressure vessel and stiffening rings were modelled in SolidWorks 2019 and the 3D FEA analysis study was completed in ANSYS 2020R1 [9].

The loading and boundary condition on pressure vessel is as per Fig. 4. Gravity Load due to self-weight, internal hydrostatic pressure and internal pressure of 1MPa is considered for the study. There is fixed support at one end of saddle and frictionless support at the other end (Sliding end). Solid Shell 190 (SOLSH190) elements, shown in Fig. 5, were used in meshing of the shell and wear plate to give an accurate representation of bending in the thin shell. SOLSH190 is used for simulating shell structures with a wide range of thickness (from thin to moderately thick). The element possesses the continuum solid element topology and features eight-node connectivity with three degrees of freedom at each node: translations in the nodal x-, y- and z-directions.

It is a 3D solid element free of locking in bending-dominant situations. Unlike shell elements, SOLSH190 is compatible with general 3D constitutive relations and can be connected directly with other continuum elements. SOLSH190 utilizes a

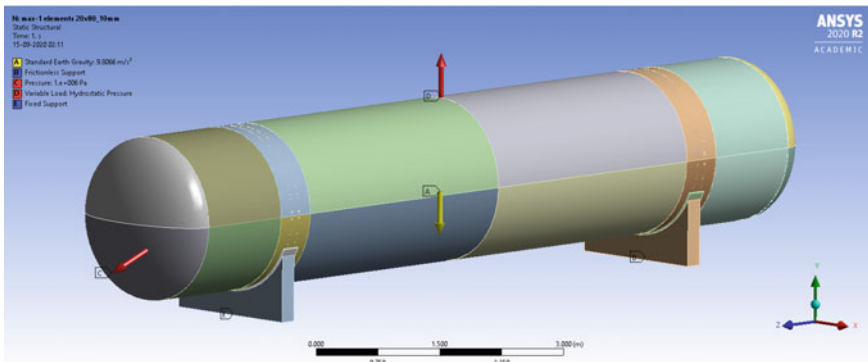
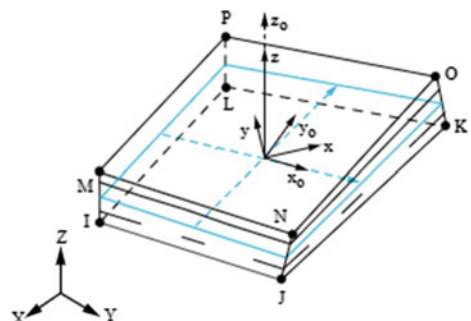


Fig. 4 Sliced Geometry with loading condition in the FEA model

Fig. 5 Schematic of SOLSH190



suite of special kinematic formulations, including the assumed strain method (Bathe and Dvorkin [10]) to overcome locking when the shell thickness becomes extremely small. SOLSH190 employs enhanced strain formulations (Simo and Rifai [11], Simo et al. [12]) to improve the accuracy in in-plane bending situations. The satisfaction of the in-plane patch test is ensured. Incompatible shape functions are used to overcome the thickness locking. These are the strong reasons to consider SOLSH190 for analysis of the pressure vessels. Three elements were used along the thickness to give an accurate representation of the bending of the shell.

The complete model is shown in Fig. 4 is discretized using SOLSH190 with loading and boundary conditions as mentioned in methodology.

The stress distribution in all 2-stiffener ring configurations, 3-stiffener ring configurations and 5-stiffener ring configurations is similar to that shown in Fig. 6a, b and c, respectively. Figure 7a shows the stress concentration at the saddle horn region (no stiffening ring). Figure 7b shows how adding the stiffener rings eliminates the stress concentration at the saddle horn. Mesh convergence study was done on the pressure vessel, stiffener rings and the saddle support to confirm the accuracy of the results up to 0.1% (Table 1).

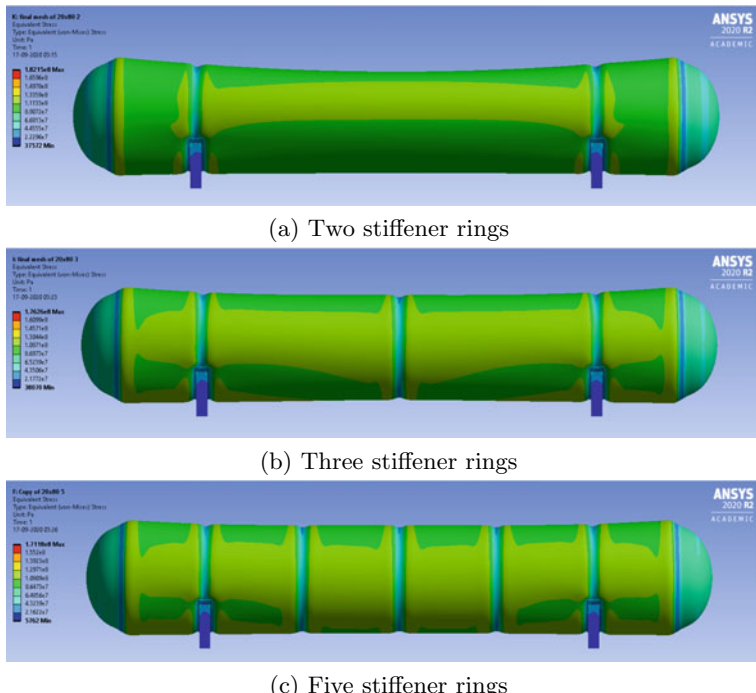
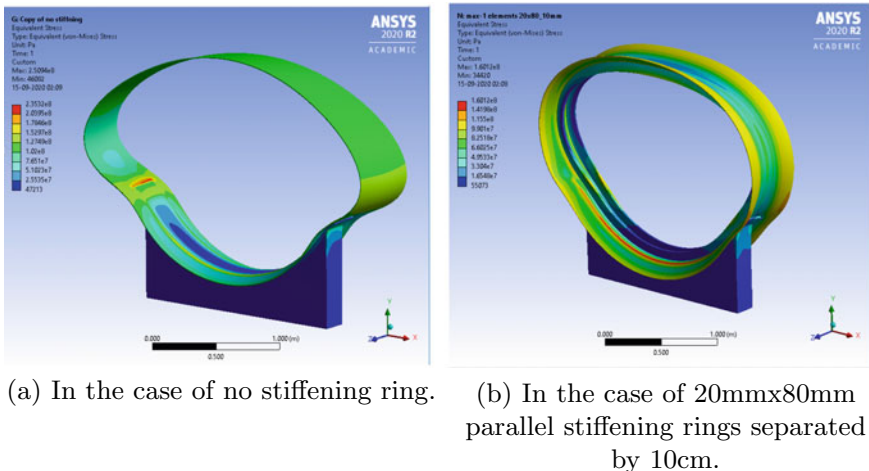


Fig. 6 Simulation images of different $20\text{ mm} \times 80\text{ mm}$ stiffening ring configurations



(a) In the case of no stiffening ring.

(b) In the case of 20mmx80mm parallel stiffening rings separated by 10cm.

Fig. 7 Stress distribution in the saddle region**Table 1** Mesh Convergence test results on the 20 mm × 80 mm parallel stiffening rings separated by 10 cm configuration

Number of elements	Maximum local stress concentration in shell (MPa)
634492	140.53
1849188	155.08
2131398	158.39
2646714	158.55

7 Results

Maximum stress concentration in the pressure vessel with no stiffening ring=235.32MPa. Maximum allowed stress value in pressure vessel = 207 MPa. Table 2 shows maximum local Stress concentration (in MPa) for the different configurations of stiffening rings.

Table 3 shows the maximum local stress concentration (in MPa) for the configurations illustrated by Fig. 3a. In these configurations, there are two parallel stiffener rings on both the saddle supports.

The stress distribution in all the configurations is similar to that as shown in Fig. 6. The location of the local circumferential stress concentration in Fig. 7a is at the saddle horn. Figure 7b shows the stress distribution after adding the stiffener rings. It is clearly observed that the stress concentration near the saddle horn is reduced substantially. It is also seen that there is a new local stress concentration, along the

Table 2 Maximum local Stress concentration (in MPa) for the different configurations of stiffening rings

No. of stiffener rings	2	3	5
Cross section of the stiffener rings			
20 mm × 80 mm	157.89	157.36	156.42
20 mm × 80 mm (T-section)	170.87	168.71	167.24
30 mm × 60 mm	182.61	177.69	174.27
60 mm × 60 mm	202.04	198.14	194.85
80 mm × 80 mm	185.65	183.70	182.29

Table 3 Maximum local Stress concentration (in MPa) for the different configurations of parallel stiffening rings

Position of parallel stiffener rings	Parallel stiffener rings with 10 cm gap in between. (Case A)	Parallel stiffener rings with outer faces aligned with wear plate. (Case B)
Cross section of the stiffener rings.		
20 mm × 80 mm	158.39	179.63
30 mm × 60 mm	160.40	189.63

bottom edge of the stiffening rings in the pressure vessel, but the value of this stress concentration is way less than the value of stress concentration in the no stiffening ring case.

8 Conclusions

From the results, we can conclude the following points.

- (1) All the stiffening ring configurations reduce the maximum local stress concentration under the allowable value. The maximum reduction in stress concentration achieved was equal to 33.5% for the 20 mm × 80 mm and 5 stiffening ring configurations.
- (2) There is no significant decrease in maximum stress concentration if the number of stiffening rings are increased from 2 to 3 and from 3 to 5. So, adding a greater number of stiffening rings is not essential and only two stiffening rings will suffice.
- (3) Increasing the thickness of the stiffening ring also does not help in further reduction in maximum local stress concentration, instead of increasing the thickness of the stiffener ring gives a lesser reduction in maximum stress values.

- (4) In the case of parallel stiffener rings configuration, it is observed that the value of maximum local stress found in Case A is lesser than the maximum local stress values in Case B. Thus, what we can conclude from this point is, it is preferable to contain the parallel stiffeners within the saddle for better stress reduction.
- (5) From the results, we can see that all the stiffening ring configurations have the value of the maximum stress value below the allowable maximum stress value making all configurations eligible for use as they all pass the ASME requirements according to ASME Section VIII Division-2 (Design by Analysis). So the optimum configuration must be selected based on the quantity of material required to manufacture the given configuration to save on material costs. For the given case, it is found that the two 20 mm × 80 mm stiffener ring configuration is the best choice as it has one of the lowest maximum local stress concentration value and also has the least material cost.

References

1. ASME: ASME VIII Division 2 - Alternative Rules - Rules for Construction of Pressure Vessels. ASME, p. 867 (2017)
2. Zick, L.P.: Stresses in large horizontal cylindrical pressure vessels on two saddle supports. Press. Vessel. Pip. Des. Anal. **2**, 959–970 (1972)
3. Megyesy, E.F.: Pressure_Vessel_Handbook_12th_edition_Eu.pdf (1973)
4. Thattil, M.J., Pany, C.: Design and analysis of pressure vessel with different end domes. Int. J. Sci., Eng. Technol. Res. **6**(8), 1225–1233 (2017)
5. Bhinde, D.N., Rajanarsimha, S.: FEA analysis of pressure vessel with different type of end connections. J. Emerg. Technol. Innov. Res. **4**(02), 95–99 (2017)
6. Golabi, S., Ghorbanpour-Arani, A., Zamani, A.: Numerically studying the effect of stiffening rings on reducing the thickness of torospherical heads under pressure on their concave side. Am. J. Appl. Sci. **5**(5), 553–558 (2008)
7. Khot, P., Taji, S., Bawiskar, H.: Design parameters for pressure vessel VI. Modeling of pressure vessel. Int. J. Sic. Eng. Technol. Res. **5**(1) (2016) 332–335
8. ASME: ASME Section II Part-D 2017. ASME (2017)
9. ANSYS: 2020 release (2020)
10. Bathe, K., Dvorkin, E.N.: A formulation of general shell elements the use of mixed interpolation of tensorial components. Int. J. Numer. Methods Eng. **22**(3), 697–722 (1986)
11. Simo, J.C., Rifai, M.S.: A class of mixed assumed strain methods and the method of incompatible modes. Int. J. Numer. Methods Eng. **29**(8), 1595–1638 (1990)
12. Simo, J.C., Armero, F., Taylor, R.L.: Improved versions of assumed enhanced strain tri-linear elements for 3D finite deformation problems. Comput. Methods Appl. Mech. Eng. **110**(3–4), 359–386 (1993)

Water Wave Interaction with Very Large Floating Structures



Kottala Panduranga and Santanu Koley

1 Introduction

In recent years, as the population increases and land becomes more expensive and scarce, various government and private organizations are putting emphasis on land reclamation. In this regard, very large floating structures (VLFSs) are often used and deployed in the nearshore regions. The horizontal dimensions of the VLFSs are large compared to the incident wavelength, and due to this fact, the structural deflection of the VLFS is negligible. Due to this advantage, VLFSs can be used as floating airports, bridges, temporary wave barriers for strategic amphibious military operations, etc. In general, the floating airport is having a length of 5 km, a width of 1 km, and a draft few meters [1], and deployed in shallow and intermediate water depth regions.

In 1970, Japanese researchers and naval architects constructed the world's first floating airport, Kansai international airport, on Osaka Bay (see [2, 3] for details). In 1995, the Japanese government built and studied the hydroelastic behavior of 1km long Mega-floating-type VLFS in Tokyo bay through the Technological Research Association of Megafloat (TRAM) performs usual land airport activities. It was observed that these Megafloat type VLFSs are relatively stable, and the durability of these structures is relatively longer. The analysis of moving loads due to the airplane landing and take-off, mooring requirements, connector system, and anti-corrosion protection due to ocean waves interaction demands a sophisticated mathematical approach to analyze the water wave interactions with VLFS [4, 5].

In this regard, several researchers carried out extensive research to build suitable mathematical models and related efficient solution methodologies to study the hydroelastic responses of the VLFSs, particularly the structural deflection of Mega-floating airport. Kashiwagi [1] and Ohmatsu [6] used the modal expansion method

K. Panduranga (✉) · S. Koley

Department of Mathematics, Birla Institute of Technology and Science-Pilani,
Hyderabad Campus 500078, India

e-mail: p20180027@hyderabad.bits-pilani.ac.in

S. Koley

e-mail: santanu@hyderabad.bits-pilani.ac.in

to study the transient elastic deformation of a pontoon-type VLFS due to the landing and take-off mechanisms of airplanes. The results show that the airplane moves faster during the take-off than the structural waves generated in the early stage. However, as the aircraft's speed decreases to zero, the speed of the structural waves can overtake the aircraft's speed. Similar results are observed during the landing except that the structural waves develop slowly in the early stage. Loukogeorgaki et al. [7] analyzed the hydroelastic behavior of a flexible mat-shaped floating breakwater under the action of oblique wave interactions. Endo [8] studied the deflection of a VLFS during an airplane take-off/landing process. In this study, FEM is used to analyze the structural deflection and Wilson's θ method to analyze the hydrodynamic effects on the VLFS.

In order to prevent the motion of the floating VLFSs due to the drift forces, it is always recommended that the floating structures be connected with the mooring lines. Using the connector's support, [9] studied the hydroelastic responses of flexible VLFSs. It was found that VLFS with a hinge line connector for smaller incident wavelength provides better structural stability than rigid connectors. Karmakar and Soares [10] analyzed the deflection of the elastic plate with the moored lines at the edges, floating over the water domain having finite and shallow depths. It was noticed that, due to the presence of moored lines, the deflection of the floating plate reduced significantly. Moreover, these mooring lines act as wave absorbers. Mohapatra and Guedes Soares [11] analyzed the water wave interaction with the moored floating elastic plate with the submerged flexible membrane. It was observed that the floating plates behave more stable for higher mooring stiffness constants. In the context of the above-outlined state of the art, this paper presents a mathematical model for the oblique wave interactions with VLFS, i.e., mega-floating airport. Here, it is assumed that the length and breadth of floating VLFS are significantly larger than the draft. The hydroelastic response of the floating VLFS is studied using the boundary element method (BEM)-based numerical solution technique. The overall structure of the paper is as follows. Section 2 contains the mathematical formulation of the boundary value problem (BVP) associated with the water wave interactions with VLFS. In Sect. 3, the BVP is solved using the BEM in the water region, and the finite difference scheme is used to discretize the plate equation of motion. Section 4 contains various results associated with the structural deflection of the VLFS. Finally, in Sect. 5, the conclusions of the present study are provided.

2 Mathematical Formulation

In this section, oblique water wave interaction with floating VLFS is studied based on small-amplitude linear water wave theory. The associated BVP is studied in a 3D Cartesian coordinate system with xy -plane being the horizontal plane, and the z -axis is taken vertically upward. Here, it is assumed that floating VLFS occupied the region $0 < x < L$, $-\infty < y < \infty$ with L being the length of floating VLFS. The side edges of the floating VLFS are connected with mooring lines to prevent drift motion due to

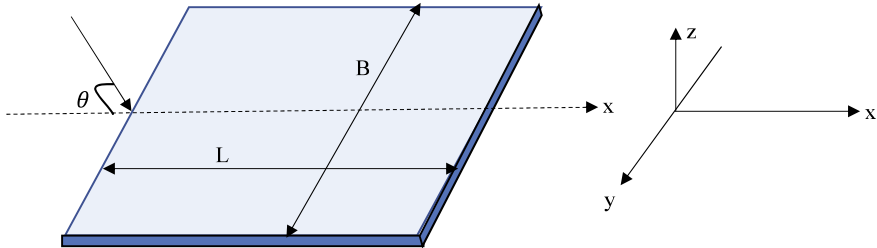


Fig. 1 Top view of the floating VLFS

the incoming waves. Further, assuming that the flow is inviscid, incompressible, and its motion is irrotational and time-harmonic. The heading angle of the incident wave (with the x -axis) is θ as shown in the Fig. 1, so that the fluid motion can be expressed using the velocity potential $\Phi(x, y, z, t) = \text{Re}\{\phi(x, z)e^{i(\beta y - \omega t)}\}$ with ω being the angular frequency and $\beta = k_0 \sin \theta$. Therefore, $\phi(x, z)$ satisfies the reduced wave equation in the fluid region

$$\left(\frac{\partial^2}{\partial x^2} + \frac{\partial^2}{\partial z^2} - \beta^2 \right) \phi = 0. \quad (1)$$

The free surface and bottom boundary conditions (BCs) are expressed as follows:

$$\begin{aligned} \frac{\partial \phi}{\partial z} - \sigma \phi &= 0, & \text{at } z = 0, -\infty < x < 0 \cup L < x < \infty, \\ \frac{\partial \phi}{\partial z} &= 0, & \text{at } z = -h, \end{aligned} \quad (2)$$

where $\sigma = \omega^2/g$, and $g = 9.81 \text{ m/s}^2$. The vertical displacement of the floating elastic VLFS can be represented as $W(x, y, t) = \text{Re}\{w(x)e^{i(\beta y - \omega t)}\}$ with $w(x)$ being the deflection amplitude. Further, the dynamic pressure p_d acting on the floating elastic VLFS is given by [12]

$$EI \left(\frac{d^2}{dx^2} - \beta^2 \right)^2 w - m_p \omega^2 w = p_d, \quad z = 0, \quad 0 < x < L, \quad (3)$$

where EI is the flexural rigidity of the VLFS, and m_p is the mass of the floating VLFS per unit length. Further, the hydrodynamic pressure p_h acting on the surface of the water represented by

$$p_h = i\rho\omega\phi - \rho gw, \quad \text{on } z = 0. \quad (4)$$

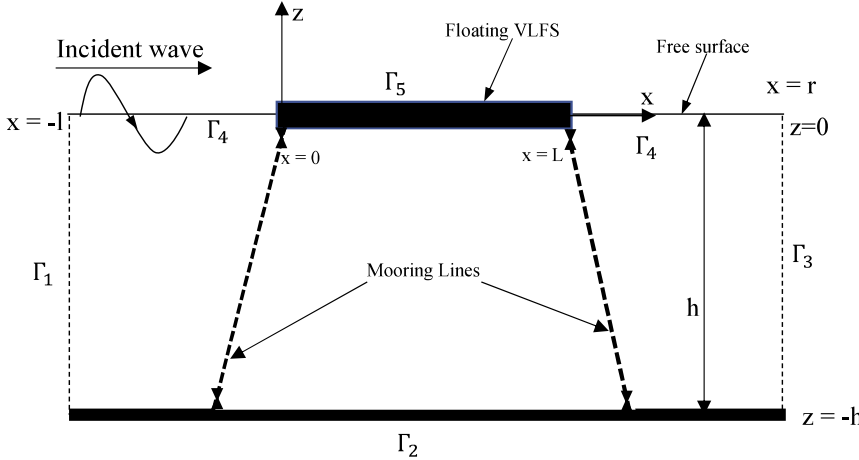


Fig. 2 Side view and computational domain of the physical problem

Assuming $p_d = p_h$ at $z = 0$, Eq. (3) gives

$$EI \left(\frac{d^2}{dx^2} - \beta^2 \right)^2 w + (\rho g - m_p \omega^2) w = i\rho\omega\phi, \quad z = 0, \quad 0 < x < L. \quad (5)$$

The kinematic B.C on the floating plate is given by

$$\frac{\partial \phi}{\partial z} = -i\omega w(x), \quad z = 0, \quad 0 < x < L \quad (6)$$

Assuming that the mooring lines are connected to the floating plate at free edges, as shown in Fig. 2. It is to be noted that within the framework of linear water wave theory, the wake-induced effects on the very large floating structure and the wave breaking phenomena are neglected. The zero shear force and bending moment conditions are represented by [13]

$$EI \frac{\partial}{\partial x} \left(\frac{\partial^2}{\partial x^2} - (2 - \nu)\beta^2 \right) w = q \frac{\partial w}{\partial x}, \quad \left(\frac{\partial^2}{\partial x^2} - \nu\beta^2 \right) w = 0, \quad \text{at } x = 0, L, \quad (7)$$

where q is the mooring stiffness. Here, the edge conditions due to the effect of the mooring stiffness are only considered. Therefore, the hydrodynamic forces acting on the mooring lines and the vortex-induced vibration of the mooring chains are not taken into account. Finally, the far-field radiation conditions are expressed as

$$\begin{cases} \phi = (e^{i\alpha x} + R_0 e^{-i\alpha x}) Z_0(z), & \text{as } x \rightarrow -\infty, \\ \phi = T_0 e^{i\alpha x} Z_0(z), & \text{as } x \rightarrow \infty, \end{cases} \quad (8)$$

where $\alpha = \sqrt{k_0^2 - \beta^2}$ and $Z_0(z) = \left(\frac{-i\pi H}{2\omega} \right) \frac{\cosh k_0(z + h)}{\cosh k_0 h}$ with H being incident wave height and k_0 being the positive real root of the dispersion relation $\sigma = k \tanh(kh)$.

3 Solution Methodology

In this section, the BEM-based numerical solution technique is applied to the water region to determine the velocity potential. On the other hand, the finite difference method (FDM)-based solution scheme is applied to the plate equation to determine the deflection of the floating VLFS. It is to be noted that an appropriate coupling between the BEM and FDM is done at the interface boundary, i.e., at the plate boundary surface.

3.1 Coupled BEM–FDM Solution Technique

Applying Green's second identity to ϕ and the free space Green's function G in the fluid region bounded by $\Gamma = \bigcup_{k=1}^5 \Gamma_k$ as shown in Fig. 2, we get

$$-\frac{1}{2}\phi(x, z) = \int_{\Gamma} \left(\phi \frac{\partial G}{\partial n} - G \frac{\partial \phi}{\partial n} \right) d\Gamma, \quad (x, z) \in \Gamma, \quad (9)$$

where $G(\mathbf{x}, \bar{\mathbf{x}}) = -\frac{1}{2\pi} K_0(\beta r)$, $\frac{\partial G}{\partial n} = \frac{\beta}{2\pi} K_1(\beta r) \frac{\partial r}{\partial n}$ with $\mathbf{x} = (x, z)$ and $\bar{\mathbf{x}} = (x_0, z_0)$ and $r = \text{dist}(\mathbf{x}, \bar{\mathbf{x}})$. Here, K_0 , K_1 are the modified zeroth- and first-order Bessel functions of the second kind, respectively (see [12] for further details). Using the boundary conditions (2), (6), and (8) into (9), we get the following integral equation:

$$\begin{aligned} & -\frac{1}{2}\phi(x, z) + \int_{\Gamma_1} \left(\frac{\partial G}{\partial n} - i\alpha G \right) \phi d\Gamma + \int_{\Gamma_2} \phi \frac{\partial G}{\partial n} d\Gamma + \int_{\Gamma_3} \left(\frac{\partial G}{\partial n} - i\alpha G \right) \phi d\Gamma \\ & + \int_{\Gamma_4} \left(\frac{\partial G}{\partial n} - \sigma G \right) \phi d\Gamma + \int_{\Gamma_5} \frac{\partial G}{\partial n} \phi d\Gamma + i\omega \int_{\Gamma_5} G w d\Gamma \\ & = \int_{\Gamma_1} \left(\frac{\partial \phi_0}{\partial n} - i\alpha \phi_0 \right) G d\Gamma. \end{aligned} \quad (10)$$

To convert the above integral equation (10) into a matrix equation, the entire boundaries of the fluid and plate region are divided into a finite number (say, N) of elements, and the values of ϕ and $\partial\phi/\partial n$ are assumed to be constants over each element. So, Eq. (10) can be written as

$$\sum_{j=1}^{nb1} \left(H^{ij} - i\alpha G^{ij} \right) \phi_j + \sum_{j=1}^{nb2} H^{ij} \phi_j + \sum_{j=1}^{nb3} \left(H^{ij} - i\alpha G^{ij} \right) \phi_j + \sum_{j=1}^{nb4} \left(H^{ij} - \sigma G^{ij} \right) \phi_j + \sum_{j=1}^{nb5} H^{ij} \phi_j + i\omega \sum_{j=1}^{nb5} G^{ij} w_j = \sum_{j=1}^{nb1} \left(\frac{\partial \phi_0}{\partial n} - i\alpha \phi_0 \right) G^{ij}, \quad (11)$$

where the expressions for H^{ij} and G^{ij} are given by

$$H^{ij} = -\frac{1}{2} \delta_{ij} + \int_{\Gamma_j} \frac{\partial G}{\partial n} d\Gamma, \quad G^{ij} = \int_{\Gamma_j} G d\Gamma. \quad (12)$$

In Eq. (11), the deflection of the VLFS w_j 's are unknown. Therefore, to solve Eq. (11), the equation of motion associated with the VLFS deflection (Eq. (5)) has to be discretized. Here, FDM-based numerical solution technique is adopted to discretize the associated plate equation. Applying the central-difference formulae to Eq. (5) over the j th element (see [12] for details), we obtain

$$\left(\frac{w_{j+2} - 4w_{j+1} + 6w_j - 4w_{j-1} + w_{j-2}}{\Delta_j^4} \right) + A' \left(\frac{w_{j+1} - 2w_j + w_{j-1}}{\Delta_j^2} \right) + B' w_j = C' \phi_j, \quad (13)$$

where $A' = -2\beta^2$, $B' = \beta^4 + (\rho g - m_p \omega^2)/EI$ and $C' = (i\rho\omega)/EI$. Now, from Eq. 7, the discretized form of the edge conditions at $x = 0, L$ are given as

$$\begin{cases} \frac{w_{j+1}}{\Delta_j^2} - \left(\frac{2}{\Delta_j^2} + \nu\beta^2 \right) w_j + \frac{w_{j-1}}{\Delta_j^2} = 0, \\ \frac{1}{\Delta_j^3} w_{j+2} - \left[\left(\frac{2}{\Delta_j^3} + \frac{2-\nu}{\Delta_j} \beta^2 \right) + \frac{q}{EI \Delta_j} \right] (w_{j+1} - w_{j-1}) - \frac{1}{\Delta_j^3} w_{j-2} = 0 \end{cases} \quad (14)$$

Now, Eqs. (11), (13) and (14) are solved together to get the required unknowns ϕ_j and w_j 's. With these values of ϕ_j and w_j 's, various physical quantities of interests are evaluated.

4 Results and Discussions

In this section, a number of results are provided to investigate the effects of structural and wave parameters on the deflection of the floating VLFS under the action of the oblique incident wave. In the present analysis, various physical parameters are taken as $h = 15$ m (water depth), $L/h = 10$ (length of the floating VLFS), $E = 6$ GPa (Young's modulus), $\rho_p/\rho = 0.9$ (ρ_p is density of the plate and ρ is the density of the water), $d = 1.0$ m (plate thickness), $\nu = 0.3$ (Poisson's ratio) unless otherwise mentioned.

Figure 3a, b show the variation of VLFS deflection $|w|/H$ for various mooring stiffness q constants and non-dimensional wave numbers $k_0 h$, respectively, for the normal incident wave case. It is noticed that the overall deflection $|w|/H$ of the VLFS decreases for larger values of the mooring stiffness q . The reason is, as the mooring stiffness becomes higher, a higher amount of forces act at the VLFS edges to prevent structural deflection. Figure 3b depicts that the deflection $|w|/H$ of the floating VLFS reduces with a raise in $k_0 h$. This due to VLFS just float in the longwave, whereas the shorter wave interacts much with floating VLFS. Moreover, the VLFS deflection is oscillatory in nature for a higher $k_0 h$, i.e., in the short wave regime.

In Fig. 4a, the deflection $|w|/H$ of the VLFS is plotted for different values of the stiffness q with the angle of incidence $\theta = 30^\circ$. The deflection of the VLFS $|w|/H$ decreases with an increase in the stiffness q of the mooring lines. The reason behind the same is explained in the discussion of Fig. 3a. Further, the pattern of the VLFS deflection $|w|/H$ becomes hump-shaped curves for higher values of the mooring stiffness q . Figure 4b shows that the oscillatory pattern of the VLFS deflection $|w|/H$ diminishes for higher values of the angle of incidence θ . This happens as a normal incident wave impinges on the VLFS with a greater amount of force.

In Fig. 5a, the deflection $|w|/H$ of the floating VLFS is plotted for various values of Young's modulus E of the plate. It is observed that the oscillatory pattern and related

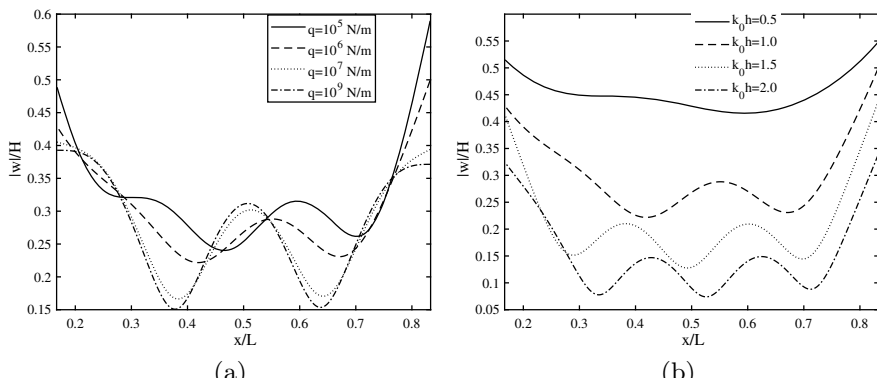


Fig. 3 Variation of the VLFS deflection $|w|/H$ for different **a** mooring stiffness value (q) and **b** non-dimensional wave numbers $k_0 h$ with $\theta = 0^\circ$

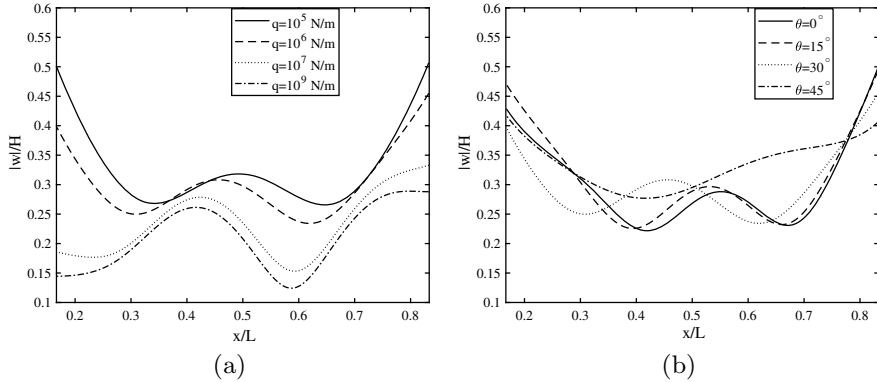


Fig. 4 Variation of VLFS deflection $|w|/H$ for different **a** mooring stiffness q with $\theta = 30^\circ$ and **b** angle of incidence θ with $q = 10^6 \text{ N/m}$

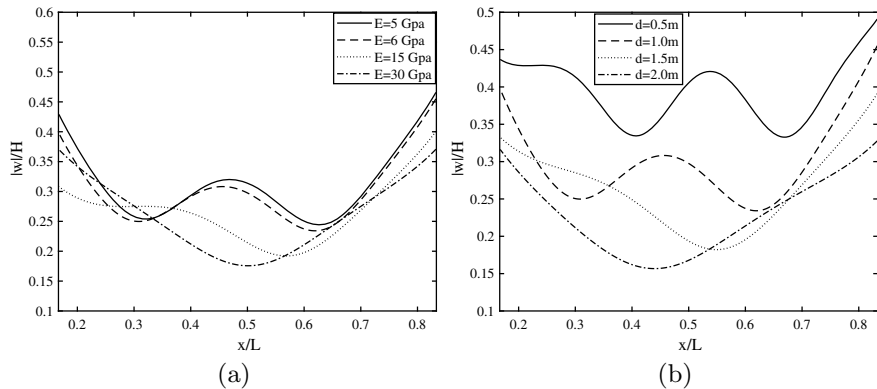


Fig. 5 Variation of the VLFS deflection $|w|/H$ for different **a** Young's modulus E and **b** thickness d of the plate with $\theta = 30^\circ$

amplitude of the plate deflection $|w|/H$ decreases for higher values of Young's modulus E . This happens as the flexible VLFS becomes a rigid plate for higher values of Young's modulus E . In Fig. 5b, the deflection $|w|/H$ of the floating VLFS is plotted for different values of plate thickness d . It is noticed that the plate deflection and related oscillatory pattern diminishes with an increase in the plate thickness. This is because the EI of the VLFS increases with an increase in the plate thickness d , and the flexible plate behaves like a rigid plate.

5 Conclusions

In the present study, oblique water wave interaction with floating VLFS connected with mooring lines is investigated using small-amplitude water wave theory. A coupled BEM-FDM method is used to obtain the velocity potential in the water region and the floating plate deflection. It is observed that increasing the mooring stiffness can significantly reduce the deflection of the VLFS. This is much needed to use the floating VLFS for airplane landing and take-off processes. Further, incident wave angle with the floating VLFS plays an important role in the VLFS deflection. Therefore, the position of the floating VLFS w.r.t the incident waves is crucial to reduce the VLFS deflection. Moreover, higher values of Young's modulus significantly reduces VLFS deflection. However, the wave forces acting on the rigid VLFS will be more compared to the flexible VLFS. So, this will reduce the durability of the VLFS. The deflection of thin VLFS is more than the thick VLFS. However, with an increase in the thickness, the flexible VLFS will act as a rigid VLFS, and the wave impact on the VLFS will be more. In summary, it is concluded that without compromising the durability of the VLFS, suitable combinations of the mooring stiffness and the angle of incidence can reduce the VLFS deflection considerably. The present model can easily be extended to analyze the hydrodynamics of VLFS connected with catenary moorings.

Acknowledgements Santanu Koley acknowledges the financial support received through the DST Project: DST/INSPIRE/04/2017/002460 to pursue this research work. Further, supports were received from BITS-Pilani, Hyderabad Campus through RIG project: BITS/GAU/RIG/2019/H0631 and Additional Competitive Research Grant: BITS/GAU/ACRG/2019/H0631.

References

1. Kashiwagi, M.: Transient responses of a VLFS during landing and take-off of an airplane. *J. Mar. Sci. Technol.* **9**, 14–23 (2004). <https://doi.org/10.1007/s00773-003-0168-0>
2. Wang, C.M., Tay, Z.Y.: Very large floating structures: applications, research and development. *Procedia Eng.* **14**, 62–72 (2011). <https://doi.org/10.1016/j.proeng.2011.07.007>
3. Hideyuki, S.: Overview of megafloat: concept, design criteria, analysis, and design. *Mar. Struct.* **18**(2), 111–132 (2005). <https://doi.org/10.1016/j.marstruc.2005.07.006>
4. Pajalić, T.: Initial design of a mega-floating airport. Diss. Diploma Thesis, University of Zagreb, Zagreb, 2000
5. Andrianov, A.: Hydroelastic analysis of very large floating structures. Doctoral thesis, Delft University of Technology (2005)
6. Ohmatsu, S.: Time domain analysis of hydroelastic behavior of VLFS. *J. Soc. Nav. Arch. Jpn.* **1998**(184), 223–230 (1998). <https://doi.org/10.2534/jjasnae1968.1998.184-223>
7. Loukogeorgaki, E., Michailides, C., Angelides, D.C.: Hydroelastic analysis of a flexible mat-shaped floating breakwater under oblique wave action. *J. Fluids Struct.* **31** (2012). <https://doi.org/10.1016/j.jfluidstructs.2012.02.011>
8. Endo, H.: The behavior of a VLFS and an airplane during takeoff/landing run in wave condition. *Mar. Struct.* **13**(4–5), 477–491 (2000). [https://doi.org/10.1016/S0951-8339\(00\)00020-4](https://doi.org/10.1016/S0951-8339(00)00020-4)

9. Gao, R.P., Tay, Z.Y., Wang, C.M., Koh, C.G.: Hydroelastic response of very large floating structure with a flexible line connection. *Ocean Eng.* **38**(17–18), 1957–1966 (2011). <https://doi.org/10.1016/j.oceaneng.2011.09.021>
10. Karmakar, D., Soares, C.G.: Scattering of gravity waves by a moored finite floating elastic plate. *Appl. Ocean Res.* **34**, 135–149 (2012). <https://doi.org/10.1016/j.apor.2011.09.002>
11. Mohapatra, S.C., Soares, C.G.: Interaction of ocean waves with floating and submerged horizontal flexible structures in three-dimensions. *Appl. Ocean Res.* **83**, 136–154 (2019). <https://doi.org/10.1016/j.apor.2018.10.009>
12. Koley, S.: Water wave scattering by floating flexible porous plate over variable bathymetry regions. *Ocean Eng.* **214** (2020). <https://doi.org/10.1016/j.oceaneng.2020.107686>
13. Cheng, Y., Chunyan, Ji., Gangjun, Z., Gaidai, O.: Hydroelastic analysis of oblique irregular waves with a pontoon-type VLFS edged with dual inclined perforated plates. *Mar. Struct.* **49**, 31–57 (2016).<https://doi.org/10.1016/j.marstruc.2016.05.008>

Annual-Averaged Performance of Oscillating Water Column Wave Energy Converter Devices in Real Sea Conditions



Kshma Trivedi and Santanu Koley

1 Introduction

Due to scarcity of non-renewable resources like crude oil, coal, and natural gases, the global warming arises because of the emission of toxic gases like carbon dioxide in the environment during the process of producing the electricity. To handle this issue, renewable energy sources are contemplated as an alternative source of energy. In this regard, wave energy will play a vital role in the near future. Out of various wave energy converter devices, the concept of the OWC device is the primary and most used technique to transform wave energy into electricity. These devices consist of a submerged collector chamber which is open at both the ends and an axial-flow Wells turbine is situated at the top of the device chamber [1]. Theoretical development on the mathematical modeling of OWC devices started in 1980 by several researchers. Reference [2] used the Galerkin method to analyze the efficiency of an OWC device under the assumption of potential flow theory. Various important parameters related to the efficiency of the OWC devices such as radiation susceptance and radiation conductance, volume flux inside the chamber, and maximum efficiency of the OWC are analyzed for various values of physical parameters associated with the device. Two different resonance mechanisms are highlighted to get maximum efficiency in the OWC device. [3] developed a theoretical model to perform a hydrodynamic analysis of an OWC installed on a steep coast. In this work, the effect of air compressibility on absorbing wave power over a broad range of incident wave frequency was explained. Further, it was shown that the efficiency of the OWC device strongly

K. Trivedi (✉) · S. Koley

Department of Mathematics, Birla Institute of Technology and Science - Pilani,
Hyderabad Campus 500078, India

e-mail: p20190439@hyderabad.bits-pilani.ac.in

S. Koley

e-mail: santanu@hyderabad.bits-pilani.ac.in

depends on the angle of incidence. Reference [4] used the eigenfunction expansions and the BEM to analyze the performance of a dual-chamber OWC device placed over the stepped bottom. It was observed that the existence of bottom steps in front of the OWC device enhances the hydrodynamic performance of an OWC device. Further, the dual-chamber OWC can effectively work in wider frequencies of incoming waves compared to the OWC device having a single chamber. Reference [5] analyzed the performance of an OWC device placed over a sloping bed using a higher-order BEM. It was concluded that the geometric parameters of an OWC device, nonlinearity of the incident waves, and slopes of the bottom bed play a crucial role in the efficiency of the OWC–WEC. Recently, [6] studied the performance of an OWC placed over an undulated bottom bed using the coupled eigenfunction expansion–BEM method. It was reported that for long waves, a protrusion type bed profile could enhance the performance of an OWC device. However, for incident waves having intermediate and short wavelengths, the depression type bed profile is appropriate to enhance the efficiency of the OWC device. Further, the number of ripples and ripple amplitudes of the sinusoidally varying bottom bed has a vital effect on the performance of the OWC device. In the aforementioned research works, the working mechanism of the OWC device is analyzed under the action of the regular incident wave.

However, in real sea conditions, the ocean waves are random in nature. Therefore, to study the OWC device in real sea conditions, often irregular incident waves are considered. Reference [7] presented a theory-based model to simulate the energy conversion of an OWC plant under irregular waves. The model for the air-flow control mechanism to enhance the performance of the OWC device was also provided. It was concluded that the amount of energy production by the plant could be increased substantially using the control valve. Reference [8] developed a stochastic model to investigate the annual-averaged plant efficiency of a rectangular OWC device under random incident waves. It was reported that controlling the rotational speed of the turbine enhanced the efficiency of the device more as compared to the control valve system. Reference [9] used Monte Carlo simulations to analyze the performance of a U-OWC device under random incident waves. It was shown that an appropriate tuning of various parameters associated with the OWC device during the design process could increase the efficiency of the OWC device. Reference [10] investigated the performance of a rectangular OWC device placed over the stepped bottom numerically and experimentally under the irregular incident waves, and it was concluded that incident wave frequency and damping coefficient of the turbine play a crucial role to enhance the efficiency of an OWC device compared to the incident wave height.

The structure of this manuscript is the following. Section 2 consists of boundary value problem and related solution based on BEM. Section 3 contains the expressions related to the performance of the OWC in random waves environment. Sections 4 and 5 contain various results and conspectus of the present study.

2 Boundary Value Problem

Here, the mathematical modeling of a rectangular OWC device placed over a bottom foundation is provided. For the sake of modeling, the 2D Cartesian coordinate system is considered with the horizontal and vertical axes to coincide with the x - and z -axes, respectively (see Fig. 1). The OWC device is made up of a rigid surface-piercing front wall having submergence depth a , and uniform thickness d intersects $z = 0$ at $x = L - b$. Moreover, the rigid rear wall of the device is placed at $x = L$, and the length of the chamber is b . The height of the bottom foundation is b_f with respect to the uniform bottom bed $z = -h$. The total free surface is divided into two parts: (i) internal free surface Γ_4 and (ii) external free surface Γ_6 as shown in Fig. 1. Now, to get a bounded domain for the physical problem, a fictitious boundary Γ_1 is considered at $x = -l$. Further, the boundaries Γ_2 and Γ_3 represent the total bottom boundary and the rear wall of the device, respectively. Moreover, the submerged boundaries of the device are denoted by Γ_5 . The fluid follows the potential flow theory and the motion is assumed to be harmonic in time, the velocity potential is written as $\Phi(x, z, t) = \Re\{\phi(x, z)e^{-i\omega t}\}$. With this background, the governing equation is written as

$$\nabla^2 \phi(x, z) = 0, \quad \nabla \equiv \frac{\partial^2}{\partial x^2} + \frac{\partial^2}{\partial z^2}. \quad (1)$$

It is to be noted that the hydrodynamics effects such as vorticity, separation of flow, and the effect of turbulence are not considered. To solve the aforementioned physical problem, we decompose the total velocity potential ϕ into scattered potential ϕ^S and radiated potential ϕ^R (see [6] for details). Now, the boundary condition (bc) at $z = 0$ is given by

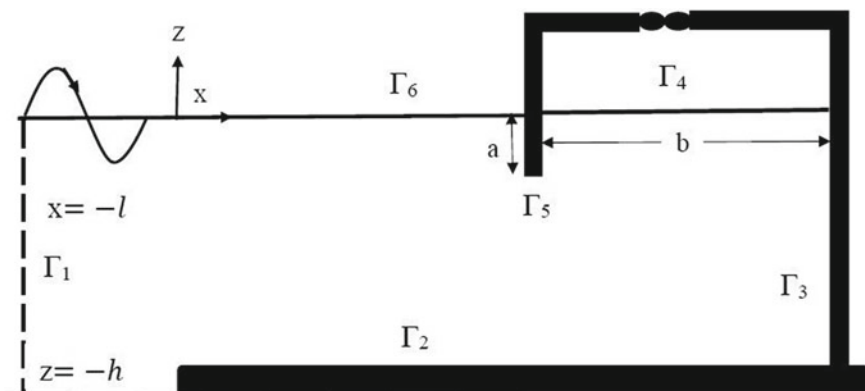


Fig. 1 Schematic diagram

$$\frac{\partial \phi^{S,R}}{\partial n} - K\phi^{S,R} = \begin{cases} \delta, & \text{on } \Gamma_4, \\ 0, & \text{on } \Gamma_6, \end{cases} \quad (2)$$

where $K = \omega^2/g$. Here, $\delta = 1$ for ϕ^R and $\delta = 0$ for ϕ^S , respectively, and $\partial/\partial n$ represents the derivative in the normal direction. Now, the bc on the impermeable boundaries $\Gamma_2 \cup \Gamma_3 \cup \Gamma_5$ is given by

$$\frac{\partial \phi^{S,R}}{\partial n} = 0, \quad \text{on } \Gamma_2 \cup \Gamma_3 \cup \Gamma_5, \quad (3)$$

Finally, the radiation bc on Γ_1 is provided as

$$\frac{\partial \phi^{S,R}}{\partial n} - ik_0\phi^{S,R} = \delta \left(\frac{\partial \phi^I}{\partial n} - ik_0\phi^I \right) \quad \text{on } \Gamma_1, \quad (4)$$

where $\phi^I(x, z) = \left(\frac{-igA}{\omega} \right) \frac{\cosh k_0(h+z)}{\cosh(k_0h)} e^{ik_0x}$ is the incident velocity potential. In Eq. (4), $\delta = 1$ for ϕ^S and $\delta = 0$ for ϕ^R , respectively. Here, k_0 is the real positive root of $\omega^2 = gk \tanh(kh)$ and A represents the amplitude of the incoming wave.

To solve the aforementioned BVP, the BEM is used. In this solution methodology, firstly, we transform the BVP corresponding to the ϕ^R and ϕ^S into the Fredholm integral equations. Now, these integral equations are transformed into the system of equations using the BEM. Green's function $G(x, z; x_0, z_0)$ is given as (see [11] for detailed derivations)

$$G(x, z; x_0, z_0) = \frac{1}{4\pi} \ln((x - x_0)^2 + (z - z_0)^2), \quad (5)$$

Now, applying Green's theorem on $\phi^{R,S}$ and $G(x, z; x_0, z_0)$, and using the boundary conditions (2), (3) and (4), the following integral equations for ϕ^R and ϕ^S are obtained as

$$\begin{aligned} -\frac{1}{2}\phi^R + \int_{\Gamma_1} \phi^R \left(\frac{\partial G}{\partial n} - ik_0 G \right) d\Gamma + \int_{\Gamma_2+\Gamma_3+\Gamma_5} \phi^R \frac{\partial G}{\partial n} d\Gamma + \int_{\Gamma_4} \phi^R \left(\frac{\partial G}{\partial n} - KG \right) d\Gamma \\ + \int_{\Gamma_6} \phi^R \left(\frac{\partial G}{\partial n} - KG \right) d\Gamma = \int_{\Gamma_4} G d\Gamma, \end{aligned} \quad (6)$$

$$\begin{aligned} -\frac{1}{2}\phi^S + \int_{\Gamma_1} \phi^S \left(\frac{\partial G}{\partial n} - ik_0 G \right) d\Gamma + \int_{\Gamma_2+\Gamma_3+\Gamma_5} \phi^S \frac{\partial G}{\partial n} d\Gamma + \int_{\Gamma_4} \phi^S \left(\frac{\partial G}{\partial n} - KG \right) d\Gamma \\ + \int_{\Gamma_6} \phi^S \left(\frac{\partial G}{\partial n} - KG \right) d\Gamma = \int_{\Gamma_1} G \left(\frac{\partial \phi^I}{\partial n} - ik_0 \phi^I \right) d\Gamma. \end{aligned} \quad (7)$$

Now, the BEM is used to transform Eqs. (6) and (7) into the system of equations. In this method, constant boundary elements are used (see [11]). The collocation method is used to get the system of equations in the following matrix form:

$$\begin{aligned} & ([H] - ik_0[G])[\phi^R] \Big|_{\Gamma_1} + [H][\phi^R] \Big|_{\Gamma_2} + [H][\phi^R] \Big|_{\Gamma_3} + ([H] - K[G])[\phi^R] \Big|_{\Gamma_4} \\ & + [H][\phi^R] \Big|_{\Gamma_5} + ([H] - K[G])[\phi^R] \Big|_{\Gamma_6} = [G] \Big|_{\Gamma_4}, \end{aligned} \quad (8)$$

$$\begin{aligned} & ([H] - ik_0[G])[\phi^S] \Big|_{\Gamma_1} + [H][\phi^S] \Big|_{\Gamma_2} + [H][\phi^S] \Big|_{\Gamma_3} + ([H] - K[G])[\phi^S] \Big|_{\Gamma_4} \\ & + [H][\phi^S] \Big|_{\Gamma_5} + ([H] - K[G])[\phi^S] \Big|_{\Gamma_6} = \left(\frac{\partial \phi_j^I}{\partial n} - ik_0 \phi_j^I \right) [G] \Big|_{\Gamma_1}. \end{aligned} \quad (9)$$

These systems of Eqs. (8) and (9) are solved using the standard method to obtain the discrete values of ϕ and its normal derivative over each boundary of the domain.

3 Annual-Averaged Efficiency of the OWC in Irregular Waves

In real sea conditions, incident waves are highly irregular in nature, and the local wave climate is represented by a suitable spectrum along with a number of sea states. The free surface displacement is generated by a Gaussian random process. The instantaneous pressure P , and the volume flux Q^S across the Wells turbine are also assumed to follow the Gaussian process. Therefore, the expression for the chamber pressure standard deviation σ_p is written as (see [10]).

$$\sigma_p^2 = \int_0^\infty S_{inc}(\omega) \left| \frac{p(\omega)}{A_i(\omega)} \right|^2 d\omega, \quad p = (\Lambda + \tilde{D} - i\tilde{C})^{-1} q^S, \quad (10)$$

where $A_i(\omega) = \sqrt{2S_{inc}(\omega_i^{av})\Delta\omega_i}$ is the incident wave amplitude for each regular wave component. Here, S_{inc} represents the incident wave spectrum and the aforementioned model does not take air compressibility into account. Further, q^S represents the volume flux due to the scattered potential, \tilde{C} and \tilde{D} are termed as radiation susceptance and conductance coefficients respectively. The expressions for \tilde{C} and \tilde{D} are given by

$$\tilde{C} = \frac{\omega}{\rho g} \Re\{q^R\}, \quad \tilde{D} = \frac{\omega}{\rho g} \Im\{q^R\}. \quad (11)$$

where q^R is the radiated volume flux. Now, the average efficiency of an OWC is written as

$$\bar{\eta} = \frac{\bar{W}}{\bar{P}}, \quad (12)$$

where \bar{W} and \bar{P} are the averaged available power to the Wells turbine and the average incoming wave energy flux, respectively, along with the expressions $\bar{W} = \Delta\sigma_p^2$ and $\bar{P} = L\rho g \int_0^\infty S_{inc}(\omega)C_g(\omega)d\omega$. Here, C_g is the group velocity of the incoming waves and L represents the chamber width along the y -direction.

The annual-averaged plant efficiency of an OWC is obtained from Eq. (12) by replacing S_{inc} with $S_{inc,ann}$ as following

$$\bar{\eta}_{ann} = \frac{\bar{W}_{ann}}{\bar{P}_{ann}}, \quad (13)$$

where \bar{W}_{ann} and \bar{P}_{ann} are termed as annual-averaged power to the wells turbine and annual-averaged incident wave energy flux, respectively.

4 Results

Now, the efficiency of the OWC device under the random waves is analyzed in a detailed manner. The parameters related with the OWC device configuration and random incident waves are taken as follows: $h = 10$ m, $\rho = 1025$ kg/m³, $g = 9.81$ m/s², $L = 30$ m, $l = 30$ m, $b = 10$ m, $a = 5$ m, $d = 0.5$ m, $b_h = 1$ m, $V_0 = 1050$ m³, $\gamma = 1.4$, $\rho_a = 1.25$ kg/m³, and $p_a = 1.013 \times 10^5$ Pa. For the analysis, the Bretschneider spectrum is considered as the incident wave spectrum and the form for the same is given by

$$S_I(\omega) = 131.5H_s^2T_e^{-4}\omega^{-5}\exp(-1054T_e^{-4}\omega^{-4}), \quad (14)$$

along with the sea states and corresponding frequency of occurrences are taken same as provided in [8].

Figure 2a and b show the variation of the free surface elevation ζ for various values of (a) chamber length b/h and (b) submergence depth a/h , respectively. In Fig. 2a, it is seen that the amplitude of the free surface elevation ζ increases outside the chamber as the chamber length b/h increases. In addition to this, a certain phase change in the free surface elevation ζ occurs with the variation in chamber length b/h . Figure 2b shows that the amplitude of the free surface elevation ζ decreases as the submergence depth a/h becomes higher. For $a/h = 3/4$, the changes in the free surface elevation are very less, and this happens as the submergence depth a/h becomes higher, the OWC device chamber behaves like a closed rectangular tank. As a result, only a

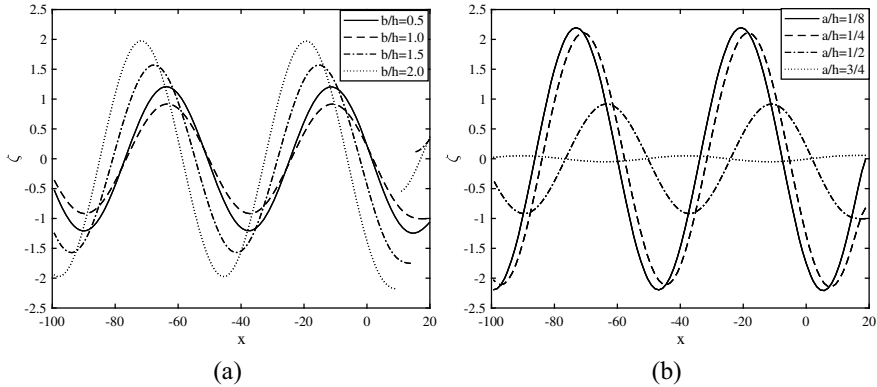


Fig. 2 Variation of ζ for various **a** b/h and **b** a/h with $Kh = 1.0$

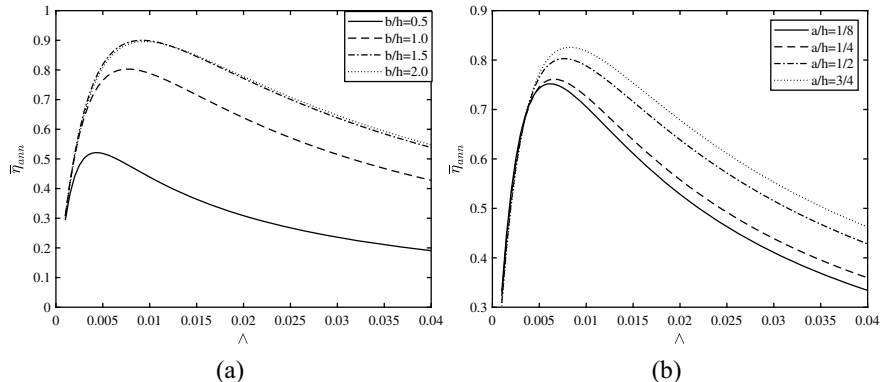


Fig. 3 $\bar{\eta}_{ann}$ versus λ^{\wedge} for various **a** b/h and **b** a/h

small amount of water can enter into the OWC device chamber and therefore reduces the height of the free surface displacement ζ . Further, certain phase changes are also observed for different values of a/h . In Fig. 3a and b, the variation of annual-averaged plant efficiency $\bar{\eta}_{ann}$ are plotted against the turbine damping coefficient λ^{\wedge} for various values of (a) chamber length b/h and (b) submergence depth a/h , respectively. It is observed that the annual-averaged plant efficiency $\bar{\eta}_{ann}$ becomes higher as the chamber length b/h and submergence depth a/h increases. This happens as the chamber pressure standard deviation σ_p becomes higher. Further, it is observed that $\bar{\eta}_{ann}$ attains maximum for moderate values of the turbine damping coefficient $0.005 < \lambda^{\wedge} < 0.01$. This range of turbine damping coefficient λ^{\wedge} is essential to design an efficient OWC device.

In Fig. 4a, the surface plot of annual-averaged plant efficiency $\bar{\eta}_{ann}$ is plotted as a function turbine rotational speed N and rotor diameter D . It is observed that for

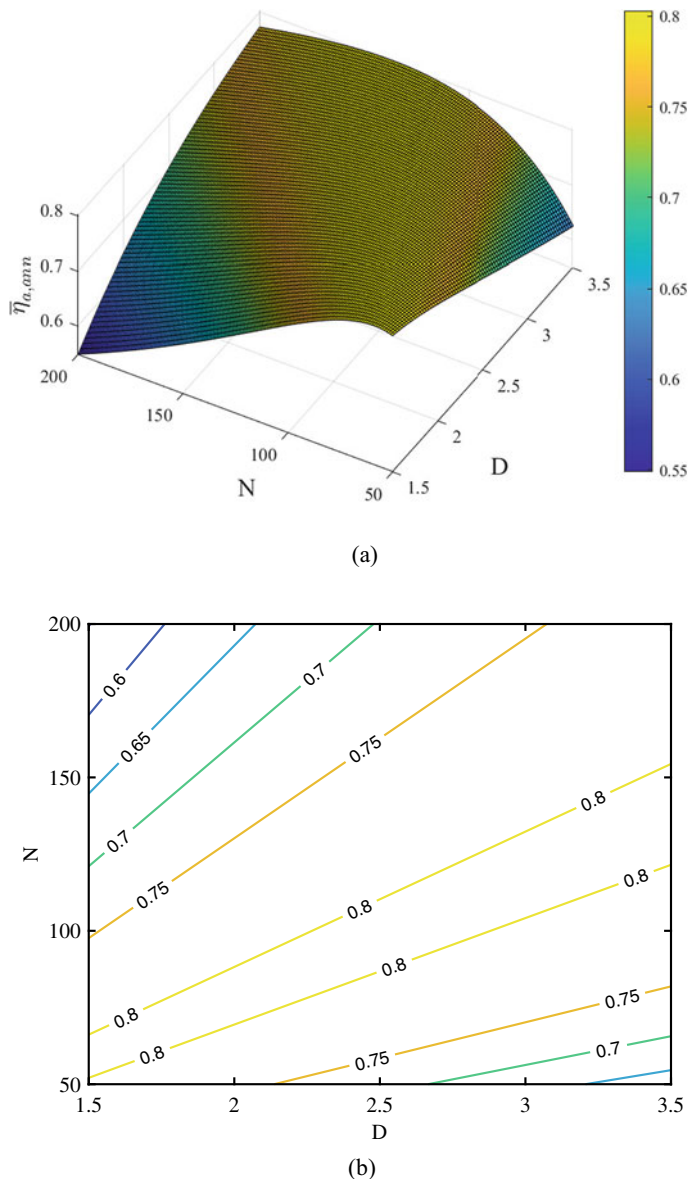


Fig. 4 **a** Surface plot of $\bar{\eta}_{ann}$ versus N and D and **b** Contour plot of $\bar{\eta}_{ann}$ versus N and D

higher values of the turbine rotational speed N , the efficiency $\bar{\eta}_{ann}$ increases with an increase in the rotor diameter D . However, for lower values of N , the efficiency $\bar{\eta}_{ann}$ becomes lower as D takes higher values. On the other hand, for fixed values of D , the efficiency $\bar{\eta}_{ann}$ initially increases with an increase in N , attains maximum, and decreases for further increase in N . To get suitable combinations of rotor diameter D and rotational speed N for maximum efficiency $\bar{\eta}_{ann}$, Fig. 4b shows the contour plot of $\bar{\eta}_{ann}$ as a function of N and D . It is observed that for certain combinations of N and D , annual-averaged plant efficiency $\bar{\eta}_{ann} = 0.8$ can be achieved. For further analysis, we have considered the pair of values (N, D) for which $\bar{\eta}_{ann} = 0.8$. With these values, we have found best-fitted lines:

$$N = 46.3158 D - 4.2632$$

$$N = 34.6667 D - 0.1333$$

to achieve $\bar{\eta}_{ann} = 0.8$.

5 Summary

The annual-averaged performance of a rectangular shape OWC device is studied in real sea conditions. For the analysis, the local wave climate of the OWC plant site Pico, Portugal is taken as the incident wave spectrum. It is observed that the free surface elevation amplitude decreases with an increase in the draft of the seaside wall of the OWC–WEC, and an opposite pattern is observed for larger values of the chamber length. The annual-averaged plant efficiency increases for higher values of submergence depth and chamber length. Further, the annual-averaged plant efficiency attains maximum for moderate values of the turbine damping coefficient $0.005 < \lambda < 0.01$. Moreover, it is found that for appropriate combinations of turbine rotational speed N and rotor diameter D with the relations: $N = 46.3158 D - 4.2632$ and $N = 34.6667 D - 0.1333$, 80% annual-averaged efficiency in the OWC device plant can be achieved. These results are essential to design the appropriate geometry of the OWC device and also helpful to design Wells turbine with relevant turbine parameters. In near future, this model will be extended to incorporate the exact geometry of an OWC plant and the associated numerical results will be validated by comparing them with the experimental results.

Acknowledgements Authors acknowledge the support from DST Project: DST/INSPIRE/04/2017/002460, RIG: BITS/GAU/RIG/2019/H0631, and ACRG: BITS/GAU/ACRG/2019/H0631 grants.

References

1. Antonio, F. de O.: Wave energy utilization: a review of the technologies. *Renew. Sustain. Energy Rev.* **14**(3), 899–918 (2010)
2. Evans, D.V., Porter, R.: Hydrodynamic characteristics of an oscillating water column device. *Appl. Ocean Res.* **17**(3), 155–164 (1995)
3. Martins-Rivas, H., Mei, C.C.: Wave power extraction from an oscillating water column along a straight coast. *Ocean Eng.* **36**(6–7), 426–433 (2009)
4. Rezanejad, K., Bhattacharjee, J., Soares, C.G.: Analytical and numerical study of dual-chamber oscillating water columns on stepped bottom. *Renew. Energy* **75**, 272–282 (2015)
5. Ning, D.Z., Shi, J., Zou, Q.P., Teng, B.: Investigation of hydrodynamic performance of an OWC (oscillating water column) wave energy device using a fully nonlinear HOBEM (higher-order boundary element method). *Energy* **83**, 177–188 (2015)
6. Koley, S., Trivedi, K.: Mathematical modeling of oscillating water column wave energy converter devices over the undulated sea bed. *Eng. Anal. Bound. Elem.* **117**, 26–40 (2020)
7. Falco, A.F. de O., Justino, P.A.P.: OWC wave energy devices with air flow control. *Ocean Eng.* **26**(12), 1275–1295 (1999)
8. de O Falco, A.F., Rodrigues, R.J.A.: Stochastic modelling of OWC wave power plant performance. *Appl. Ocean Res.* **24**(2), 59–71 (2002)
9. Malara, G., Arena, F.: Analytical modelling of an U-Oscillating Water Column and performance in random waves. *Renew. Energy* **60**, 116–126 (2013)
10. Rezanejad, K., Soares, C.G., Lpez, I., Carballo, R.: Experimental and numerical investigation of the hydrodynamic performance of an oscillating water column wave energy converter. *Renew. Energy* **106**, 1–16 (2017)
11. Katsikadelis, J.T.: *The Boundary Element Method for Engineers and Scientists: Theory and Applications*. Academic Press (2016)

Material Handling and Automated Assembly

Inverse Kinematic Model of a Cable-Driven Continuum Manipulator



Vipin Pachouri and Pushparaj Mani Pathak

1 Introduction

The continuum manipulators gained the attention of researchers due to its limitless capabilities like handling variety (shape, size, and material) of objects, highly dexterous and compliance behaviors, safer human-robot interaction, and excellent ability of obstacle avoidance, to name a few. These countless features of continuum manipulators are due to their structure and mechanism of actuation system are inspired from biological life-forms existing in nature like the elephant trunk [1], octopus arms [2, 3], snake's [4] exoskeleton and locomotion, tube feet in starfish, squid, earthworm, etc. The modeling of this new class of robot can be either constant curvature [5] or variable curvature [6] in nature, both giving different levels of capabilities.

Best to the author's knowledge, the first-ever written evidence on continuum manipulators is presented by Anderson et al. in 1970, popularly known as 'Tensor Arm Manipulator' which includes a series of plates which are interconnected by universal joints [7]. Later Robinson and Davies [8] presented a more clear picture of the fundamental difference between discrete, serpentine, and continuum robot. They had also introduced some control issues and the field of application of these 'state of the art' robots. Hannan and Walker [9, 10] proposed a kinematic approach for modeling continuum manipulator by parameterizing a curve in terms of its curvature and arc length followed by a well-proven Denavit–Hartenberg (D–H) procedure. Webster et al. [11] presented a thorough review on the various design principles and

V. Pachouri (✉) · P. M. Pathak

Indian Institute of Technology Roorkee, Roorkee 247667, Uttarakhand, India

e-mail: vpachouri@me.iitr.ac.in

P. M. Pathak

e-mail: pushparaj.pathak@me.iitr.ac.in

kinematic modeling of constant curvature continuum robots. The D–H-based direct kinematic modeling works well for rigid robots consisting of constant link length.

In contrast, for continuum robots, the scenario is different, for these state-of-the-art robotic systems, as links are always bending and follow a curvature, so D–H-based direct kinematic approach does not fit appropriately to continuum robots, whereas if the number of links/frames are increased to a relatively more significant number with a compromise on computation cost, then it seems to be worth noting to represent the kinematics of continuum robots using the D–H approach. Inderjeet et al. [12] proposed the two quantitative approaches based on Newton–Raphson iterative method and damped least square method to solve the IK applicable to compact bionic handling assisted (CBHA) manipulator using the forward kinematic model proposed by Escande et al. [13, 14]. Their approach relies on the initial guess, which goes wrong if hardware in-loop feedback is not available.

This article presents direct and inverse kinematics (IK) of a planar cable-driven continuum manipulator (CDCM) based on the geometry of the manipulator. The same methodology can also be extended for spatial manipulators. Initially, the mathematics for multisection planar CDCM presented briefly followed by the simulation results. Finally, a geometric-based IK model is presented based on a uniform bending assumption. The source of inspiration for the structure and mechanism of the actuation system of the proposed continuum manipulator, obtained by replicating the anatomy of the muscles arrangement in the octopus arm, as shown in Fig. 1. Figure 2a shows the model of the planar CDCM based on the anatomy shown in Fig. 1. These types of robots have numerous applications in industry, agricultural work, navigation in unstructured environments, etc.

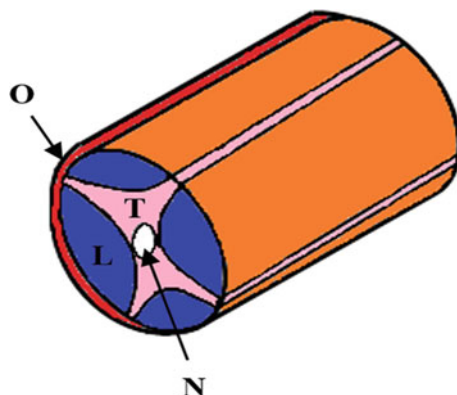


Fig. 1 Schematic of muscle arrangement in the octopus arm inspired from its anatomy (where ‘L’ represents the longitudinal muscle, that extends the octopus arm axially, ‘T’ shows the transverse muscle producing bending and radial contraction described as cables for actuation, ‘O’ represents the oblique muscle responsible for torsional motion, and ‘N’ is the neutral axis, acting as the backbone of continuum manipulator)

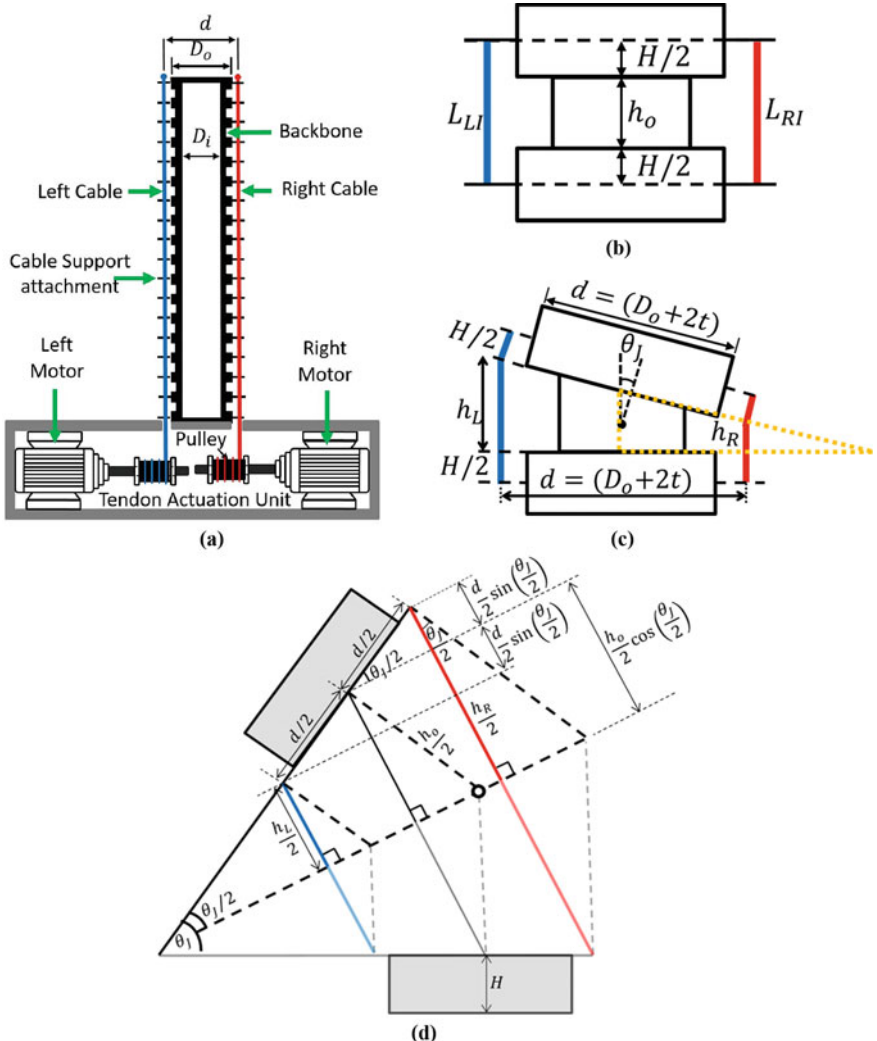


Fig. 2 **a** Schematic of Tendon/Cable actuated planar continuum manipulator, **b** Vertebra at rest, **c** Vertebra after actuation (bending), **d** Geometry of single vertebra after actuation (bending)

2 Forward Kinematics

The initial length of the backbone, right and left cables of continuum robot before bending for a single vertebra at rest represented mathematically as (h_o and H) are geometrical parameters of continuum manipulator shown in Fig. 2(b))

$$L_0 = L_{RI} = L_{LI} = H/2 + h_0 + H/2 = H + h_0 \quad (1)$$

For one section consisting ‘ n ’ vertebrae, the initial length is not only multiplied by n , but a distance of ‘ $H/2$ ’ is added due to the geometry of the robot backbone, as shown in Eq. (2).

$$L_0 = L_{RI} = L_{LI} = n(H + h_0) + H/2 \quad (2)$$

The final cable length for single-section continuum backbone robot having ‘ n ’ vertebrae is

$$\left\{ \begin{array}{l} L_{RF} = n(H + h_R) + H/2 = n(H + h_R) + H/2 \\ L_{LF} = n(H + h_L) + H/2 = n(H + h_L) + H/2 \end{array} \right\} \quad (3)$$

where the values of nh_R and nh_L are calculated for a section consisting ‘ n ’ vertebrae from the geometry of a single vertebra after bending as [15]

$$\left\{ \begin{array}{l} nh_R = n[h_0 \cos(\theta_J/2) + d \sin(\theta_J/2)] \\ nh_L = n[h_0 \cos(\theta_J/2) - d \sin(\theta_J/2)] \end{array} \right\} \quad (4)$$

Using the trigonometric property $[\cos(\frac{\theta_J}{2}) = 1 - 2 \sin^2(\frac{\theta_J}{2})]$, the above expression can be rearranged as

$$\left\{ \begin{array}{l} nh_R = n h_0 + n[d \sin(\theta_J/2) - 2 h_0 \sin^2(\theta_J/4)] = n(h_0 + A) \\ nh_L = n h_0 - n[d \sin(\theta_J/2) + 2 h_0 \sin^2(\theta_J/4)] = n(h_0 - B) \end{array} \right\} \quad (5)$$

where A and B are $[d \sin(\frac{\theta_J}{2}) \mp 2 h_0 \sin^2(\frac{\theta_J}{4})]$ sequentially. The overall length of the right and left cables for ‘ n ’ vertebrae after bending obtained mathematically as (shown in Fig. 2c)

$$\left\{ \begin{array}{l} L_{RF} = L_0 + n[d \sin(\theta_J/2) - 2 h_0 \sin^2(\theta_J/4)] \\ L_{LF} = L_0 - n[d \sin(\theta_J/2) + 2 h_0 \sin^2(\theta_J/4)] \end{array} \right\} \quad (6)$$

where ‘ θ_J ’ and ‘ n ’ are the joint angle of each vertebra and the total number of vertebrae per section, respectively. The relation between joint angle (θ_J) of the vertebra and overall bending angle (θ_R) of the section of a continuum manipulator is obtained by calculating $(L_{RF} - L_{LF})$, i.e.,

$$\theta_R = n \theta_J = 2 n \sin^{-1} \left(\frac{L_{RF} - L_{LF}}{2 n d} \right) \quad (7)$$

The maximum permissible bending angle of each vertebra is restricted based on the geometry of each vertebra after bending as

$$(\theta_{max})_{Joint} = 2 \tan^{-1} \left(\frac{h_0}{d} \right) \quad (8)$$

The right and left cables are actuated via respective motors connected to the pulley of radius ‘ r ’ to bend the backbone of the continuum robot from its initial configuration, as represented in Eq. (9).

$$\begin{cases} \theta_{mR} = r^{-1}(L_{RF} - L_0) \\ \theta_{mL} = r^{-1}(L_{LF} - L_0) \end{cases} \quad (9)$$

2.1 Actuator Space to Configuration Space

The mapping of the actuator space with the configuration space of the planar CDCM is done geometrically as shown in Fig. 3a. The mathematical relation of curvature and bending angle of curvature are expressed in terms of right and left cable lengths. Finally, the curvature of the cables in terms of cable lengths is calculated as shown in Eq. (11).

$$\begin{cases} R_R = R - \frac{d}{2} = \frac{L_R}{\theta_C} \\ R_L = R + \frac{d}{2} = \frac{L_L}{\theta_C} \end{cases}; \quad \begin{cases} \theta_C = \frac{(L_L - L_R)}{d} \\ K = \frac{2}{d} \left(\frac{L_L - L_R}{L_L + L_R} \right) = \frac{1}{R} \end{cases} \quad (10)$$

$$\begin{cases} K_R = \frac{\theta_C}{L_R} = \frac{1}{R_R} = \frac{1}{R-d/2} = \frac{(L_L - L_R)}{dL_R} \\ K_L = \frac{\theta_C}{L_L} = \frac{1}{R_L} = \frac{1}{R+d/2} = \frac{(L_L - L_R)}{dL_L} \end{cases} \quad (11)$$

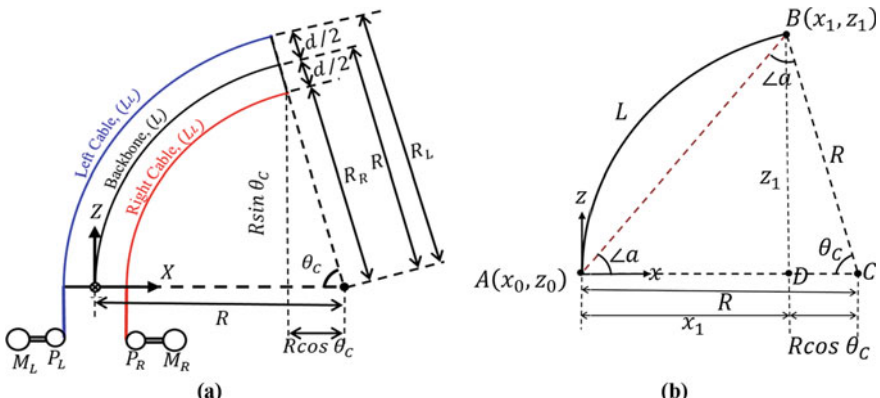


Fig. 3 **a** Geometry of the planar cable-driven continuum section (where $(P_R$ and P_L) represents right and left cables pulleys and $(M_R$ and M_L) represents the right and left motors, respectively), **b** Geometric representation of the continuum robot backbone for inverse kinematic analysis

2.2 Independent Transformation

The coordinates of the tip of the section with respect to the base can be thought of as a rotation about Y-axis by an angle of θ_C followed by translation by an amount of $P, 4$

$$T = \begin{bmatrix} R_Y(\theta_C) & P \\ 0 & 1 \end{bmatrix}; R_Y(\theta_C) = \begin{bmatrix} \cos \theta_C & 0 & \sin \theta_C \\ 0 & 1 & 0 \\ -\sin \theta_C & 0 & \cos \theta_C \end{bmatrix}; P = \begin{bmatrix} R(1 - \cos \theta_C) \\ 0 \\ R \sin \theta_C \end{bmatrix} \quad (12)$$

$$T = \begin{bmatrix} \cos \theta_C & 0 & \sin \theta_C & R(1 - \cos \theta_C) \\ 0 & 1 & 0 & 0 \\ -\sin \theta_C & 0 & \cos \theta_C & R \sin \theta_C \\ 0 & 0 & 0 & 1 \end{bmatrix} \quad (13)$$

3 Workspace and Inverse Kinematics

The workspace is the region of space in which the tip of the robot can maneuver. For workspace, first, a restriction is imposed on the extreme postures of the curvature of the section, which is directly dependent on the geometric parameters of the continuum manipulator. The maximum permissible bending angle of a continuum manipulator is calculated from the allowable joint angle of the section using Eq. (8). Using the permissible joint angle of each vertebra, the maximum and minimum limits of the actuation unit are evaluated. And using this range, the right and left cable lengths can be calculated, as shown in Eq. (14).

$$\begin{cases} L_R = r \theta_{mR} + L_0 \\ L_L = r \theta_{mL} + L_0 \end{cases} \quad (14)$$

The curvature angle of the section is calculated by substituting the cable lengths from Eq. (14) in a different way than that specified in Eq. (10). And the obtained curvature angle is used to calculate the curvature or radius of curvature as shown in Eq. (15).

$$\theta_C = \frac{2(L_L - L)}{d} = \frac{(2L - L_R)}{d}; \quad K = \frac{1}{R} = \frac{\theta_C}{L} \quad (15)$$

where $L = (L_L + L_R)/2$, represents the length of the backbone, calculated using Eq. (14). Finally, the tip coordinates of the backbone of the continuum manipulator are obtained after substituting Eqs. (15) in the transformation matrix as indicated

by Eq. (13). The art of knowing the cable lengths of the section in terms of the position and orientation of center point coordinates of the tip of the backbone is IK. Let (x_1, z_1) and (x_0, z_0) are the coordinates of the tip and base of the manipulator, respectively, shown in Fig. 3b.

From geometry (trigonometrically), the distal end distance with respect to the base coordinate of the manipulator can be calculated as

$$AB = M = \sqrt{(x_1 - x_0)^2 + (z_1 - z_0)^2} \quad (16)$$

From geometry (trigonometrically),

$$\left\{ \begin{array}{l} x_1 = R(1 - \cos\theta_C) \\ z_1 = R\sin\theta_C \end{array} \right\} \quad (17)$$

The sum of angles of triangle ABC (from Fig. 3b), $\angle a + \angle b (= \angle a) + \angle \theta_C = 180^\circ$

$$\angle a = 90 - \frac{\theta_C}{2} \quad (18)$$

From right-angled triangle ADB,

$$\begin{aligned} \tan a &= \left(\frac{z_1}{x_1} \right) = \tan \left(90 - \frac{\theta_C}{2} \right) = \cot \left(\frac{\theta_C}{2} \right) \\ \theta_C &= 2 \cot^{-1} \left(\frac{z_1}{x_1} \right) : \text{Curvature angle of the section} \\ R &= \frac{x_1}{1 - \cos \theta_C} = \frac{x_1}{1 - \cos \left(2 \cot^{-1} \left(\frac{z_1}{x_1} \right) \right)} = \frac{1}{K} : \text{Radius of curvature} \end{aligned} \quad (19)$$

Using the relation of the sum of cable length, the below equations are obtained.

$$\{L_L - L_R = d\theta_C, L_L + L_R = 2L\} \leftrightarrow \left\{ L_R = \frac{(2 - Kd)\theta_C}{2K}, L_L = \frac{(2 + Kd)\theta_C}{2K} \right\} \quad (20)$$

In Eq. (20), the curvature (K) and angle of curvature (θ_C) are only independent variables to determine the cable lengths in terms of desired trajectory having center point coordinates of the tip of the section's backbone. Substituting Eq. (19) in Eq. (20) and finally substituting the obtained resultant in Eq. (9), the desired motor angles are calculated and the objective of the IK model is achieved. Figure 4 portrays the bending profiles of a planar two-section CDCM for inter-vertebral joint angle varying from -4° to -9° . The friction of each inter-vertebral joint is assumed to be identical,

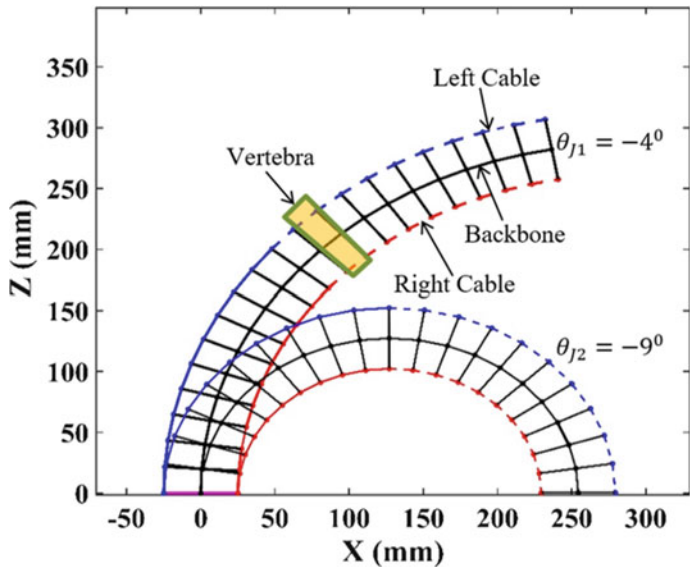


Fig. 4 Bending profile for inter-vertebral joint angle varying from -4° to -9°

which leads to an equal bending angle of each joint of a section due to a change in cable lengths. This is similar to the constant curvature assumption. The IK for a single section is relatively very simple, but for multi-section, the scenario of multiple solutions incorporates complexity as depicted in Fig. 5.

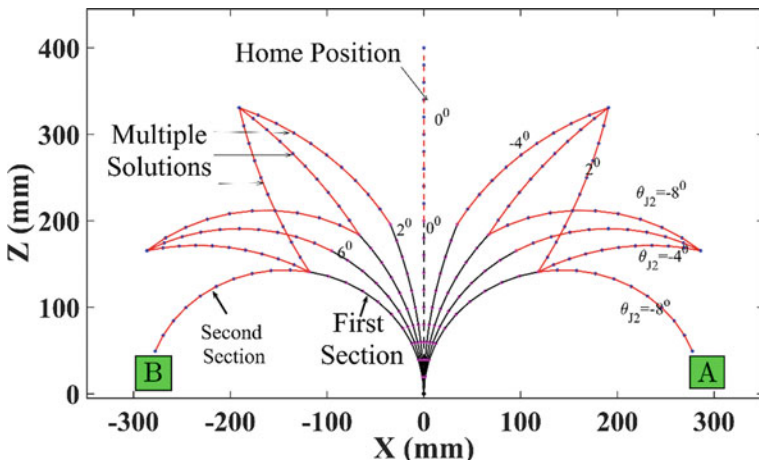


Fig. 5 Portraying multiple inverse kinematic solutions, extreme bending posture (A and B) and home position of multi-section planar CDM

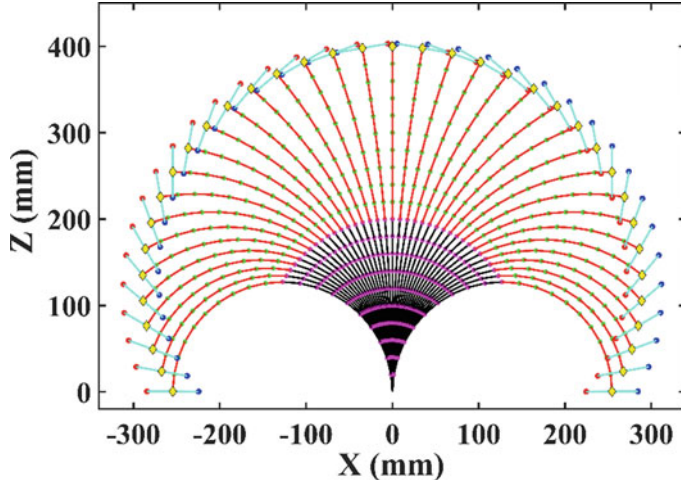


Fig. 6 Bending profile (portrayed by black and red curves) and distal end orientation (cyan line) of planar two-section CDCM for uniform bending of each section (red dot at tip represents the tip of left cable and the blue dot at tip represents the tip of right cable, yellow diamond markers represents the coordinates of desired trajectory)

From Fig. 5, it is clear that the IK of a continuum manipulator has multiple solutions as they belong to the class of under-actuated robotic systems. Due to this property, the unique solution exists rarely except at the maximum bending profile of the manipulator as represented by curves A and B in Fig. 5. But if the entire workspace is observed precisely, then there exist criteria of uniform bending profile that leads to a unique IK solution, compromising on the dexterity of the robotic system. As this research article is mainly focusing on developing a unique geometrical IK solution applicable to a wide variety of multi-section continuum manipulators, so the concern about the dexterity of the manipulator is not given so much consideration and will be addressed in future. Also, the dexterity of continuum manipulators can be enhanced by serially stacking multiple sections over one another. The uniform bending profile assumption leads to the same radius of curvature for each section which simplifies the complexity in solving IK and leads to a unique solution. This assumption is more practical than the closed-form IK solution obtained from knowing the tip coordinates of the individual section separately. The simulation results portrayed in Figs. 6, 7 and 8, validates the proposed IK algorithm.

4 Conclusion

This research article presents a geometrical procedure for obtaining the inverse kinematics of planar multi-section CDCM. Initially, the workspace of the proposed

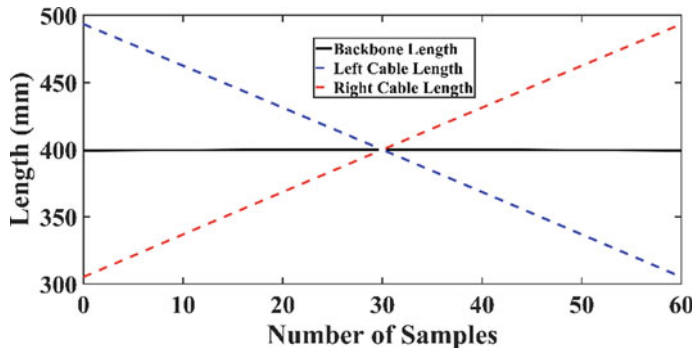


Fig. 7 Backbone length, left and right cable lengths of CDCM under uniform bending assumption following a semi-circular path

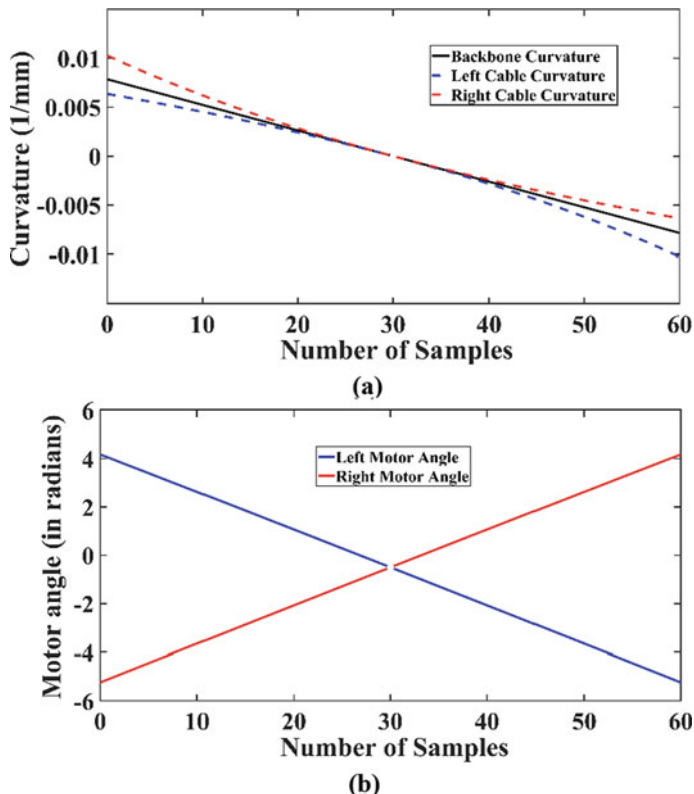


Fig. 8 **a** Backbone Curvature, left and right cable curvature of CDCM for uniform bending assumption following a semi-circular path, **b** Left and right cable motor rotation of CDCM under uniform bending assumption for the tip of manipulator following a semi-circular path

continuum manipulator is calculated using the forward kinematic model of under-actuated CDCM based on the rotation of each vertebra. The upper and lower motor angle limits are set based on the geometric parameters of the vertebrae of the continuum manipulator. These limits restrict the extreme postures of curvature. The shape of the workspace comes out to be circularly symmetric about the home position of the manipulator. Friction on each vertebra joint is set to uniform so that each section follows the constant curvature assumption. To have a unique solution, the uniform bending approach is selected, and based on the proposed IK approach, the tip of the continuum manipulator is shown to follow a semicircular path. In future, the non-uniform bending approach will be investigated for the spatial multi-section CDCM with varying inter-vertebral joint angles. Also in future, the IK proposed in this research article will be used for calculating the initial values for dynamic analysis for these types of continuum manipulators.

References

1. Liu, Y., Ge, Z., Yang, S., Walker, I.D., Ju, Z.: Elephant's trunk robot: an extremely versatile under-actuated continuum robot driven by a single motor. *J. Mech. Robot.* **11**(5) (2019). <https://doi.org/10.1115/1.4043923>
2. Kang, R., Guglielmino, E., Branson, D.T., Caldwell, D.G.: Bio-inspired crawling locomotion of a multi-arm octopus-like continuum system. In: IEEE International Conference on Intelligent Robots and Systems, pp. 145–150 (2012). <https://doi.org/10.1109/IROS.2012.6385954>
3. Guglielmino, E., Tsagarakis, N., Caldwell, D.G.: An octopus anatomy-inspired robotic arm. In: IEEE/RSJ 2010 International Conference on Intelligent Robots and Systems, pp. 3091–3096 (2010). <https://doi.org/10.1109/IROS.2010.5650361>
4. Hirose, S., Mori, M.: Biologically Inspired Snake-like Robots. In: Proceedings of the 2004 IEEE International Conference on Robotics and Biomimetics, pp. 1–7 (2004). <https://doi.org/10.1109/ROBIO.2004.1521742>
5. Jones, B.A., Walker, I.D.: Kinematics for multisection continuum robots. *IEEE Trans. Robot.* **22**(1), 43–55 (2006). <https://doi.org/10.1109/TRO.2005.861458>
6. Mahl, T., Hildebrandt, A., Sawodny, O.: A Variable Curvature Continuum Kinematics for Kinematic Control of the Bionic Handling Assistant. *IEEE Trans. Robot.* **30**(4), 935–949 (2014). <https://doi.org/10.1109/TRO.2014.2314777>
7. Anipulator, T.A.R.M., Horn, R.C.: Tensor arm manipulator (1970)
8. Robinson, G., Davies, J.B.C.: Continuum robots - a state of the art. In: Proceedings - IEEE International Conference on Robotics and Automation, vol. 4, pp. 2849–2854 (1999). <https://doi.org/10.1109/robot.1999.774029>
9. Hannan, M.W., Walker, I.D.: Novel kinematics for continuum robots. In: Advances in Robot Kinematics (2000)
10. Hannan, M.W., Walker, I.D.: Kinematics and the implementation of an elephant's trunk manipulator and other continuum style robots. *J. Robot. Syst.* **20**(2), 45–63 (2003). <https://doi.org/10.1002/rob.10070>
11. Webster, R.J., Jones, B.A.: Design and kinematic modeling of constant curvature continuum robots: a review. *Int. J. Rob. Res.* **29**(13), 1661–1683 (2010). <https://doi.org/10.1177/0278364910368147>
12. Singh, I., Lakhal, O., Amara, Y., Coelen, V., Pathak, P.M., Merzouki, R.: Performances evaluation of inverse kinematic models of a compact bionic handling assistant. In: 2017 IEEE International Conference on Robotics Biomimetics, ROBIO 2017, pp. 264–269 (2018). <https://doi.org/10.1109/ROBIO.2017.8324428>

13. Escande, C., Pathak, P.M., Merzouki, R., Coelen, V.: Modelling of multisection bionic manipulator: application to RobotinoXT. In: 2011 IEEE International Conference on Robotics Biomimetics, ROBIO (2011), pp. 92–97. <https://doi.org/10.1109/ROBIO.2011.6181268>
14. Escande, C., Merzouki, R., Pathak, P.M., Coelen, V.: Geometric modelling of multisection bionic manipulator: experimental validation on robotinoxt. In: 2012 IEEE International Conference on Robotics Biomimetics, ROBIO 2012 - Conference Digest, pp. 2006–2011 (2012). <https://doi.org/10.1109/ROBIO.2012.6491263>
15. Li, Z., Du, R.: Design and analysis of a bio-inspired wire-driven multi-section flexible robot: regular paper. *Int. J. Adv. Robot. Syst.* **10** (2013). <https://doi.org/10.5772/56025>

Task Space Reconstruction in Modular Reconfigurable Manipulation System



Athul Thaliyachira Reji, Anubhav Dogra, Shashi Shekhar Jha,
and Ekta Singla

1 Introduction

Modern robots are designed to be reconfigurable and adaptable to cater to the flexible manufacturing systems of modern industries [4]. The conventional robotic arms are designed to perform a specific task for a specific environment. Such systems have fixed configurations and have workspace limits. For different environments and *non-repetitive* tasks, a robotic arm with alternate attributes is required; thus, a fixed and conventional configuration may not prove effective. Moreover, specially designed manipulators are not economical nor feasible every time. In such scenarios, reconfigurable manipulators are a better fit. Reconfigurability of a mechanism is best achieved using a modular approach [1]. Many researchers have worked on modular robots, mainly on self-reconfigurable robots and manually reconfigurable robots. Modules are designed as link modules, joint modules, and end-effector modules [4, 16]. These modules can be assembled in different ways to get the required configuration of the manipulator. Few researchers have focused on task-based configuration designs [7, 9], but less emphasis is given on the design studies based on cluttered environments.

A. T. Reji (✉) · A. Dogra · S. S. Jha · E. Singla
Indian Institute of Technology Ropar, Punjab, India
e-mail: 2015med1003@iitrpr.ac.in

A. Dogra
e-mail: 2016mez0019@iitrpr.ac.in

S. S. Jha
e-mail: shashi@iitrpr.ac.in

E. Singla
e-mail: ekta@iitrpr.ac.in

Our objective is to provide a framework for task-based customized design of manipulators which can operate in prescribed workspaces. These customized manipulator designs are task-based; thus, automatic reconstruction of the task-space is required to create a virtual model for the integration of the workspace in the design algorithms for task-based customization and design studies. Secondly, it can be integrated with the developed customized robotic systems for demonstrating path planning. An entire workspace cannot be specified by making real-world measurements since it could be out of scale. It might not take into consideration all the obstacles and can consume a lot of time and resources. These challenges will become tougher as the environment gets more complex. Moreover, the preparation of a CAD model every time the workspace undergoes changes is not efficient. Therefore, the process of creating a model of the workspace of a manipulator up to scale is automated in this paper and used for design planning.

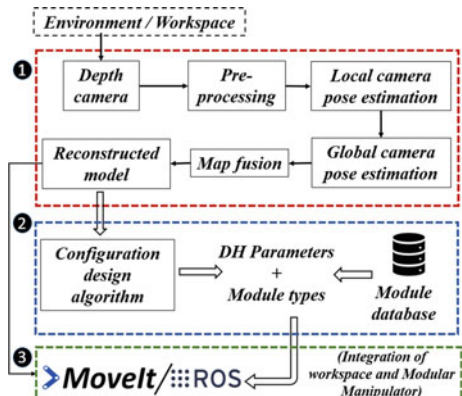
Scene reconstruction techniques are used for creating the model of the workspace accurately [17]. We have utilized RGB-D cameras to capture the color and three-dimensional geometric features of the workspace. Various pre-processing activities like timestamp matching and point cloud generation are performed. Subsequently, camera pose estimation is performed using local image features [14] and RANSAC [6]. The environment is integrated and stored using an efficient and scalable voxel-based representation [5].

The main contributions of the paper can be summarized as follows:

1. A framework for the reconstruction of the cluttered task-space is presented, which is utilized for the configuration synthesis of modular manipulators.
2. Designing a modular library for the realization of modular configurations.
3. Integration of the reconstructed task-space model and modular configuration in Robotic Operating System (ROS)—a framework for quick modeling, visualization, and task execution.

The overall methodology of the work is shown in Fig. 1. The procedure is shown in three phases. Phase one consists of collecting the environmental data using a depth

Fig. 1 Framework is shown in three phases. Phase one consists of collecting the external data and model reconstruction. In phase two, the model environment is integrated with a modular manipulator synthesizer. Finally, in phase three, the reconstructed environment and the resulted modular configuration are integrated using ROS framework for path planning



camera and processing it for the reconstruction of the environment in *STL* format, as explained in Sect. 2. In phase two, the reconstructed model is integrated with the modular manipulator's configuration synthesis algorithm, as described in [10]. In phase three, the reconstructed environment and resulted modular configuration are integrated with *ROS* framework for execution of the tasks defined.

2 Methodology

In this section, various stages of the scene reconstruction pipeline are discussed in detail.

2.1 Pre-processing

Depth cameras or RGB-D cameras are used to record real-world scenes for 3D scene reconstruction. There are mainly two separate and independent components inside a depth camera, viz., the depth measurement module, and the color measurement module, and these work at different frequencies and phases. Hence, the recorded images will have different time sequences and are unsynchronized. Ideally, a set of pairs of color and depth images recorded simultaneously is required for processing the data accurately. However, due to the temporal mismatch, a mechanism is needed for frame associations. We have used the nearest timestamp heuristic to establish associations as the magnitude of the time difference is low (of the order of milliseconds), and the camera won't be able to move much in such a short period of time. In this approach, the color image having the closest timestamp to the available depth image is together taken as an associated pair and assumed to have been recorded at the same time over the same location. Besides, it is made sure that the resolution of the color images and the depth images are the same so that a one-to-one correspondence can be defined over the pixels of the color and the depth images.

Algorithm 1: Registration using Local Image Features and RANSAC

Input: Two-point cloud and RGB image pairs, (P_1, I_1) and (P_2, I_2) measured with respect to frame-1 and frame-2, respectively, the number of local features to detect N , the maximum number of iterations $maxIter$, the number of points in the inlier hypothesis M , the threshold for inliers and outliers θ_1 , the threshold to check the quality of the estimated transformation θ_2 .

Output: The transformation matrix, T_2^1 from frame-2 to frame-1.

```

1  $e_{min} \leftarrow +\infty$ 
2  $T_{2best}^1 \leftarrow null$ 
3  $C_1 \leftarrow \text{findLocalFeatures}(I_1)$ 
4  $C_2 \leftarrow \text{findLocalFeatures}(I_2)$ 
5  $\langle F_1, F_2 \rangle \leftarrow \text{matchFeatures}(N, C_1, C_2, P_1, P_2)$ 
6 for  $i \leftarrow 1$  to  $maxIter$  do
7    $H \leftarrow \phi$                                  $\triangleright$  Hypothetical Inliers
8    $L \leftarrow \phi$                                  $\triangleright$  Consensus Set
9   for  $j \leftarrow 1$  to  $M$  do
10    |    $r \leftarrow \text{randomNumberBetween}(1, N)$            $\triangleright$  r should not repeat
11    |    $H \leftarrow H \cup \{\langle F_r^1, F_r^2 \rangle\}$ 
12   end
13    $S^1 \leftarrow \{F_r^1 : \langle F_r^1, F_r^2 \rangle \in H \text{ where } r \in [1, M]\}$ 
14    $S^2 \leftarrow \{F_r^2 : \langle F_r^1, F_r^2 \rangle \in H \text{ where } r \in [1, M]\}$ 
15    $T_1^2 \leftarrow \text{SVDDMinimization}(S^1, S^2)$ 
16   for  $f^1 \in S^1$  and  $f^2 \in S^2$  do
17    |    $e = \|f^1 - T_1^2 f^2\|_2$ 
18    |   if  $e < \theta_1$  then
19    |     |    $L \leftarrow L \cup \{\langle f^1, f^2 \rangle\}$ 
20    |   end
21   end
22   if  $|L| > \theta_2$  then
23    |    $L \leftarrow L \cup H$ 
24    |    $L^1 \leftarrow \{F_r^1 : \langle F_r^1, F_r^2 \rangle \in L \text{ where } r \in \{1, \dots, |L|\}\}$ 
25    |    $L^2 \leftarrow \{F_r^2 : \langle F_r^1, F_r^2 \rangle \in L \text{ where } r \in \{1, \dots, |L|\}\}$ 
26    |    $T_1^2 \leftarrow \text{SVDDMinimization}(L^1, L^2)$ 
27    |    $e \leftarrow \frac{1}{|L|} \sum_{\langle f^1, f^2 \rangle \in L} \|f^1 - T_1^2 f^2\|_2$ 
28    |   if  $e < e_{min}$  then
29    |     |    $e_{min} \leftarrow e$ 
30    |     |    $T_{2best}^1 \leftarrow T_1^2$ 
31    |   end
32   end
33 end
34 return  $T_{2best}^1$ 
```

2.2 Local Camera Pose Estimation Using Local Image Features and RANSAC

After the successful pre-processing of the depth and color images, local image registrations are performed over the sequence of RGB-D images. Given two RGB-D images recorded at different camera poses with sufficient overlap, the local camera pose estimation's objective is to find the relative transformation matrix that brings one of the RGB-D images into the camera frame of the other image. The fixed camera frame can be selected arbitrarily out of the two choices. The point cloud constructed from the fixed camera frame is called the *modal point cloud* (P^1), and the one to be transformed into the fixed frame is called the *source point cloud* (P^2).

Local image features are used to establish correspondences and create matching pairs of points between the source point cloud and the modal point cloud. In this approach, given a pair of RGB-D images, the local features (such as blobs, edges, corners, and ridges) in the two RGB images (I^1 and I^2) are detected and described using feature detection methods and feature descriptors such as SIFT, SURF, ORB, BRISK, and BRIEF [14] to form a set of ordered pairs of feature vectors and their respective image coordinates: C^1 and C^2 . Each ordered pair of the set C^1 (of feature vectors) is compared with ordered pairs in C^2 , and the pairs having the highest similarity of feature vectors are considered a corresponding pair. This feature matching creates a one-to-one correspondence from C^1 to C^2 .

It is assumed that any pixel in the depth image corresponds to the pixel at the same pixel coordinates in the RGB image, i.e., a one-to-one mapping exists between the pixels of the RGB image and its corresponding paired depth image. This is valid because the timestamps of the RGB image and the depth image only differ by a small magnitude, and the resolution of the depth image and the RGB image is the same. Hence the image coordinates from C^1 and C^2 are used to find the depth values from the corresponding coordinates in the depth images. Only these depth values are then converted to point clouds (F^1 , F^2) instead of the entire depth image. This dramatically reduces the number of computations as the depth images can have over 10^5 pixels. F^1 and F^2 represent the locations of the matched features in 3D space and are a subset of P^1 and P^2 . The size of F^1 and F^2 remains the same and depends on the confidently matched features from C^1 and C^2 . Hence, this procedure results in sampling the point clouds along with matching.

Now that we have a set of sampled points having high correspondence, the next step is to find the optimal relative transformation that best aligns F^1 and F^2 . The objective function (error metric) to be minimized for deriving the transformation is the sum of the squares of Euclidean distances between corresponding points in P^1 and P^2 i.e.:

$$\mathcal{E} = \frac{1}{N} \sum_{i=1}^N \|p_i^1 - \mathbf{T}_2^1 p_i^2\|_2 \quad (1)$$

where $p_i^1 \in F^1$, $p_i^2 \in F^2$ are the corresponding points, N is the number of points in F^1 and F^2 , and \mathbf{T}_2^1 is the relative transformation between the two camera frames. The

objective function (\mathcal{E}) in Eq. 1 is minimized using Singular Value Decomposition (SVD) minimization [15] to find the optimal value of T_2^1 . Here, SVD minimization helps to find the transformation matrix that best minimizes the objective function and thus best aligns the two point clouds in different frames.

RANSAC-Based Outlier Removal The local camera pose estimation method (discussed above) can still result in errors due to outliers or false positive matches. False negative matches do not arise in local camera pose estimation usually because for false-negative matches to occur, a point should be matched to a wrong point in the presence of its correct match, but the algorithm checks for the best match among all possible points making it exhaustive, thus preventing false negative matches. This is caused due to sensor noise, which can distort the image details leading to the wrong description of the local geometry and color. This effect gets compounded by the need to register overlapping images correctly. Thus, in practice, the number of false positives becomes large and can outnumber the number of true positives. Further, using such false positive pairs for calculating the relative transformation, T_2^1 can result in huge errors.

To eliminate such outlier pairs, we employ the RANdom SAmples Consensus (RANSAC) method for outlier detection [6]. The minimum number of pairs of corresponding 3D points required to perform SVD minimization are three. Hence, the set of hypothetical inliers (H) is constructed by randomly sampling three distinct corresponding pairs from F^1 and F^2 . The hypothetical inliers are used to perform SVD minimization to find a hypothetical model, which in this case, is the relative transformation T_2^1 . Next, all the corresponding pairs which are not in the hypothetical inliers are checked to see if they fit with the hypothetical relative transformation T_2^1 given some tolerance level θ_1 . The ones that fit T_2^1 are collected to form the consensus set L . If the number of pairs in the consensus set is more than a threshold θ_2 , then the hypothetical inliers are combined with the consensus set, and the same is used to estimate an improved relative transformation using the SVD minimization procedure. The procedure is repeated for a fixed number of iterations, and the transformation matrix giving the minimum error is chosen as the best model. If no model was found meeting the threshold criteria, the model with the maximum number of inliers is considered the best model.

Algorithm 1 describes the whole process of local camera pose estimation using local image features and outlier removal using RANSAC.

3 Modular Library

The modular library being used consists of the link modules and joint modules, as shown in Fig. 2. The Joint modules are designed to incorporate the actuator and its adjustment in terms of connecting with other modules and the required twist angle. It consists mainly of three components, as shown in Fig. 2a. They are an actuator, an unconventional twist unit, and two casings for the input and output section of the actuator.

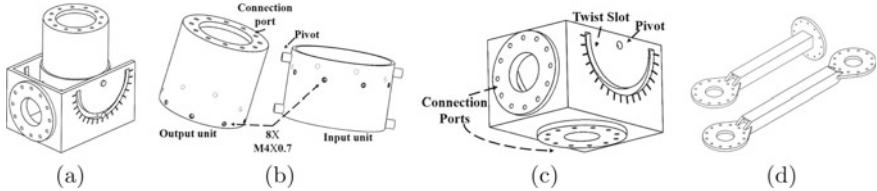


Fig. 2 The modular library consisting of **a** Assembled joint module, **b** actuator, **c** Actuator casings **d** Adaptive twist unit, **e** Link modules

To design the modular joint assembly, *KA-Series* actuators from *Kinova* [3] are used in this work. The KA-series actuators are available in two variants as *KA – 75+* and *KA – 58* and are connected to each other in series using a 20-pin flat flex cable. Each variant of actuator connects in a daisy chain, which makes it perfect for the modular assembly of serial manipulator configurations.

The adaptive Twist Unit is designed to incorporate the twist angles adjustment between the two frames, according to Denavit–Hartenberg (DH) convention. The twist adjustment can be made in two ways. One is the angle between the two adjacent intersecting joint axes, and the other is the angle between two adjacent skew joint axis [10]. In this design, a pivotal extension from the actuator casing, Fig. 2b, is assembled with a pivot of twist adjusting unit, see Fig. 2c. The twist unit has a semi-circular slot with a resolution of 10° ranges from 0 to +90° and -90° in both clockwise and anticlockwise direction, as shown in Fig. 2c. The input unit can rotate about a pivotal axis in the twist unit to adjust the twist angle. Besides, there are two connection ports provided orthogonal to each other and are provided with 12 holes with a resolution of 30° to adjust the twist angle.

3.1 Architecture Validation and Visualization

A *ROS*-based platform is developed to visualize the working of the developed modular manipulators. Here, it is proposed to convert the prescribed DH parameters of modular configurations into the Unified Robot Description File (URDF) formats. *URDF* is an *XML*-based file format that is widely used for the modeling and analysis of robotic systems in software like *ROS*, *v-rep*, *OpenRave*, *Matlab* and so forth. *URDF* describes various elements of a robot, such as links, joints, and frames. It also stores the geometrical and inertial parameters of each link. Each element of the modular library presented in Sect. 3 is converted into *STL* files and are incorporated in *URDFs* for better visualization.

Figure 3 shows the rendered versions of different modular configurations based upon the prescribed DH parameters. Figure 3a shows 2-DoF planar configuration, Fig. 3b shows 3-DoF modular standard configuration and c shows 3-DoF modular

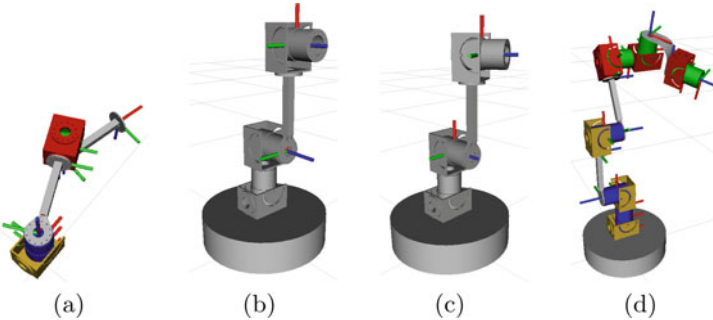


Fig. 3 *URDF* visualization of modular configurations in *ROS*. **a** 2-DoF planar configuration, **b** 3-DoF standard configuration, **c** 3-DoF configuration with twist of 45° in joint 3 and **d** 6-DoF standard configuration

configuration with a twist of 45° , and Fig. 3d shows a 6-DoF standard modular configuration. Through this, the standard and unconventional required set of modular assembly combinations are verified.

4 Results

We have used the TUM dataset [11] as the source of the environment for demonstrating the framework. The parameter values of Algorithm 1 was set to: $N = 100$, $\maxIter = 1000$, $\theta_1 = 0.06$, $\theta_2 = 20$ when it was run on the dataset. SIFT [8] features were used for feature description and detection. Open3D, OpenCV, and Python were used to implement Algorithm 1.

The resultant reconstructed workspace in *STL* format along with the task space locations are taken as input for the configuration design synthesizer. The optimal configuration is obtained by finding the minimum DoF of the manipulator using Lagrangian optimization and simulated annealing [10]. The output from the algorithm is the DH parameters of the modular manipulator. According to these DH parameters and modular assembly sequence, the *URDF* is generated. It is then used with the MoveIt! [12] within the *ROS* environment to integrate the path planning libraries with the modular robot. MoveIt! Setup Assistant provides a GUI interface to generate the specific files for setting up the modular manipulator and workspace in a single framework. MoveIt! configures the simulation by generating the Collision Matrix and configuring the Planning Groups. Moveit uses packages like *ompl* [13] for path planning and *trac-IK* [2] for inverse kinematics computation of the generated robot.

To demonstrate in this paper, a 3-DoF modular manipulator configuration and the reconstructed workspace are integrated into the *ROS* framework are shown in Fig. 4. Two task-space locations are shown as *A* and *B*. Figure 4b is shown in start

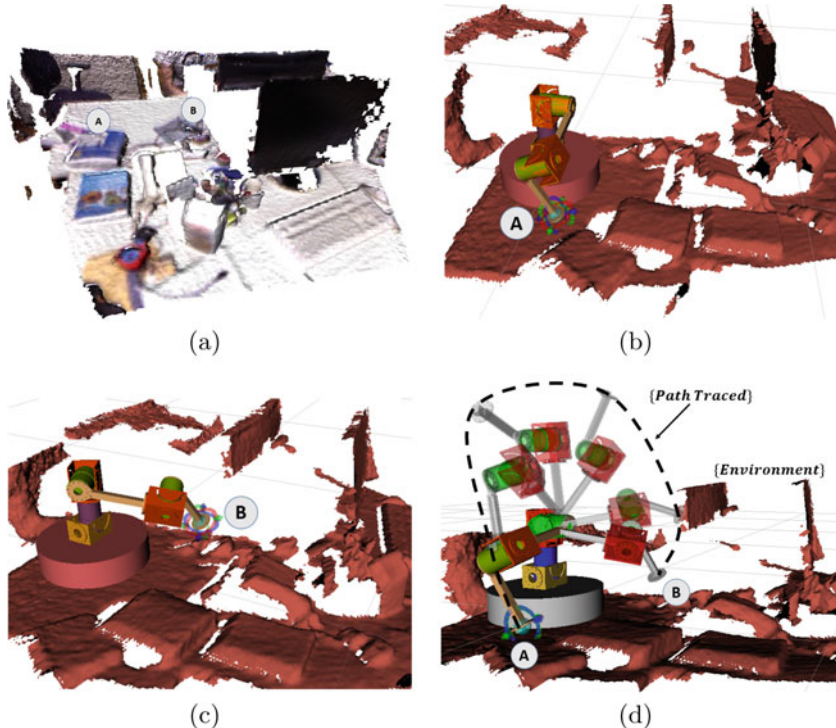


Fig. 4 **a** Reconstructed mesh with color features, **b** modular configuration in developed environment at position *A*, **c** modular configuration in developed environment at position *B*, **d** Planned path of the modular configuration from *A* to *B*

position of the robot with its end-effector at task-location *A* and Fig. 4 c shows the goal position where the robot has to reach. Figure 4d shows the path traced by the end-effector of the 3-DoF modular manipulator while reaching for task-location *B* from *A* by avoiding collisions with obstacles.

5 Conclusion

A framework for reconstructing the workspace of a manipulator and subsequently using it for manipulator design and path planning is delineated in this paper. A scene reconstruction pipeline was used to create the model of the workspace accurately to scale. The resultant model was then used for designing the modular robot. Finally, the modular robot was integrated with the environment model, and the end-effector of the designed robot was moved from one task-location to another in the environment avoiding collisions.

The reconstructed environments can have enormous sizes; thus, it can slow down path planning and other processes. Hence, ways to reduce the size of the model while preserving relevant information should be investigated. The framework could be extended to operate a real-time modular configuration by integrating the hardware controller and the ROS control package.

References

1. Ahmadzadeh, H., Masehian, E., Asadpour, M.: Modular robotic systems: characteristics and applications. *J. Intell. Robot. Syst.* **81**(3–4), 317–357 (2016)
2. Beeson, P., Ames, B.: Tracik: an open-source library for improved solving of generic inverse kinematics. In: 2015 IEEE-RAS 15th International Conference on Humanoid Robots (Humanoids), pp. 928–935 (2015)
3. Campeau-Lecours, A., Lamontagne, H., Latour, S., Fauteux, P., Maheu, V., Boucher, F., Deguire, C., L'Ecuyer, L.-J.C.: Kinova modular robot arms for service robotics applications. In: Rapid Automation: Concepts, Methodologies, Tools, and Applications, pp. 693–719. IGI Global (2019)
4. Chen, I.-M., Yim, M.: Modular robots. In: Springer Handbook of Robotics, pp. 531–542. Springer (2016)
5. Curless, B., Levoy, M.: A volumetric method for building complex models from range images. In: Proceedings of the 23rd Annual Conference on Computer Graphics and Interactive Techniques, pp. 303–312 (1996)
6. Fischler, M.A., Bolles, R.C.: Random sample consensus: a paradigm for model fitting with applications to image analysis and automated cartography. *Commun. ACM* **24**(6), 381–395 (1981)
7. Icer, E., Hassan, H.A., El-Ayat, K., Althoff, M.: Evolutionary cost-optimal composition synthesis of modular robots considering a given task. In: 2017 IEEE/RSJ International Conference on Intelligent Robots and Systems (IROS), pp. 3562–3568. IEEE (2017)
8. Lowe, D.G.: Distinctive image features from scale-invariant keypoints. *Int. J. Comput. Vis.* **60**(2), 91–110 (2004)
9. Moulianitis, V.C., Synodinos, A.I., Valsamos, C.D., Aspragathos, N.A.: Task-based optimal design of metamorphic service manipulators. *J. Mech. Robot.* **8**(6) (2016)
10. Singh, S., Singla, A., Singla, E.: Modular manipulators for cluttered environments: A task-based configuration design approach. *J. Mech. Robot.* **10**(5) (2018)
11. Sturm, J., Engelhard, N., Endres, F., Burgard, W., Cremers, D.: A benchmark for the evaluation of RGB-D SLAM systems. In: 2012 IEEE/RSJ International Conference on Intelligent Robots and Systems, pp. 573–580. IEEE (2012)
12. Sucan, I.A., Chitta, S.: Moveit
13. Sucan, I.A., Moll, M., Kavraki, L.E.: The open motion planning library. *IEEE Robot. Autom. Mag.* **19**(4), 72–82 (2012). <https://ompl.kavrakilab.org>
14. Szeliski, R.: Computer Vision: Algorithms and Applications. Springer Science & Business Media (2010)
15. Umeyama, S.: Least-squares estimation of transformation parameters between two point patterns. *IEEE Trans. Pattern Anal. Mach. Intell.* **4**, 376–380 (1991)
16. Yun, A., Moon, D., Ha, J., Kang, S., Lee, W.: Modman: an advanced reconfigurable manipulator system with genderless connector and automatic kinematic modeling algorithm. *IEEE Robot. Autom. Lett.* **5**(3), 4225–4232 (2020)
17. Zollhöfer, M., Stotko, P., Görlitz, A., Theobalt, C., Nießner, M., Klein, R., Kolb, A.: State of the art on 3d reconstruction with rgb-d cameras. In: Computer Graphics Forum, vol. 37, pp. 625–652. Wiley Online Library (2018)

Design Analysis and Experimental Validation of Modular Handling System for Satellite Ground Application



G. A. Srinivasa, Shashank Srivastava, and Saurabh Chandraker

1 Introduction

The spacecraft's AIT operations involve various assembly processes and testing till the launch of satellite, and all these to be carried out by lifting the spacecraft with the help of spacecraft's handling system which is one of the major applications in MGSEs. For any spacecraft's lifting, the conventional/modular handling systems are used. The MHS is user-friendly with less manpower and less lead time for assembly with provision of variable pitch length adjustment over the conventional handling system as shown in Fig. 1. MHS may consist of two-, three-, four-, or six-point handling system depending on shape and weight of the spacecrafts; Fig. 2 shows four-point MHS and it consists of major and important structural parts which are aluminum (Al) extruded profiles [1] which with sufficient moment of inertia (MI) acts an intermediate member between the spacecraft's assembly and crane with sufficient Factor of Safety (FOS), and this ensures that there are no undue load present on the spacecraft's handling system and other parts of MHS are handling shackle, CG finder, eye end and fork end, and wire rope bracket [2]. The MHS may be used with/without CG finder depending on requirements of the project.

The Finite Element Analysis (FEA) of Al extruded profiles of complex cross-section assembly is extensively studied by Serkan Güler Hira Karagülle in 2016[3]

G. A. Srinivasa (✉) · S. Chandraker

Department of Mechanical Engineering, National Institute of Technology Karnataka, Surathkal,
India

e-mail: srinivasaga86@gmail.com

S. Chandraker

e-mail: schandraker@nitk.edu.in

S. Srivastava

U.R. Rao Satellite Centre, ISRO, Bangalore, Karnataka, India

e-mail: shashank.sig@gmail.com

Fig. 1 Conventional handling

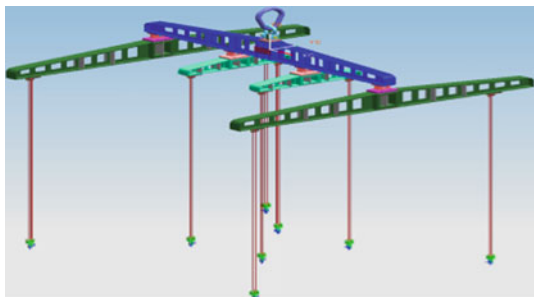
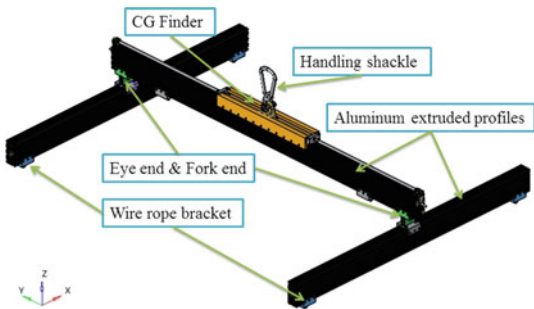


Fig. 2 Modular handling system



with 1D beam element structures for natural frequencies and mode shapes are compared with experiment results, and the complications of 3D meshing of complex cross sections are also noticed. The same Al profiles with bolted joints are studied for some mechanical behaviors like slip, shear, and pull-out experimental tests results are compared with the numerical models by Luigi Fiorino et all in 2014[4]. As there are no research papers found based on these profiles, analysis by 2D shell element method, 1D beam element which is used only for approximate estimation as well as for prediction of failure of structure, and for detailed estimation and analysis 2D/3D elements are used [5], but in our present analysis 2D element method is used because of simple and less solver time compared to 3D element method. 2D shell elements are used for all mid-surfaces in FEA [6, 7] of extruded profiles and other components of MHS assembly analysis for von Mises stress and deflection. The element size is optimized and the peak stress locations are important in FEA because of the singularities [8] present in the model. The extruded profiles' mid-surface extraction and meshing is validated by considering the different cross-section profiles under cantilever beam condition and compare the results of 1D beam, 2D shell element method as well as analytical cantilever beam calculations [9] and finally the von Mises stress and deflection results of MHS assembly from FEA are compared with the experimental results [10] obtained from static analysis of MHS by using the strain gages [11, 12]. The scope of this work is to validate the cross-section profiles for the realization of complete MHS assembly and to optimize the MHS using FEM simulation.

2 Methodology

Here the experimental results used to interpret the results obtained in FEA for static analysis of MHS are discussed and analytical method is used to validate the extruded profile 2D mid-surface meshing under cantilever beam condition.

2.1 Analytical Method

The Al extruded profiles are meshed by using 2D shell elements and 1D beam elements, these are analyzed under simple cantilever beam condition for FEA results, and the results are compared with the analytical calculations by using the following equations:

Deflection equation of cantilever beam with point load and self-weight

$$\delta = \frac{PL^3}{3EI} + \frac{wL^4}{8EI} \quad (1)$$

Von Mises stress equation of cantilever beam with point load and self-weight

$$\sigma = \frac{(wL + P)L}{I} C \quad (2)$$

where P = load applied in N, L = length of the beam in m, E = Young's modulus of the beam material in MPa, I = moment of inertia of c/s in m^4 , w = self-weight of the beam/unit length, and C = extreme surface location from the neutral axis in m.

2.2 Finite Element Analysis (FEA) Method

FEA involves three steps, namely, pre-processing, processing, and post-processing. The first step involves meshing, providing material information, application of boundary conditions and loads, etc.; here, Altair HyperMesh has been used for pre-processing, Optistruct used for solving, and finally for post-processing again Altair HyperMesh is used. Before meshing, the geometry cleanup and mid-surface extraction of all the components of the MHS assembly are done. The geometry cleanup involves removal of small holes, gaps, sharp fillets, etc., which are not necessary for the analysis, and this activity helps in mid-surface creation as well as in obtaining quality mesh. Mid-surface is extracted by dividing individual cross sections of each component by approximating the cross-section profile to match the area moment of inertia and finally assign the properties like thickness and homogeneous, isotropic

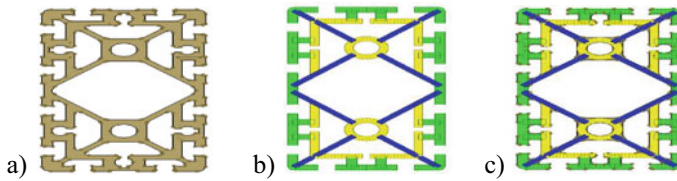


Fig. 3 **a** 90×180 actual 3D profile, **b** 2D shell element approximated profile, and **c** comparison of 2D and actual 3D profiles

material. Figure 3 shows the 90×90 Al extruded profile and Fig. 4 shows the fork end of MHS assembly.

The MHS assembly interconnecting screw joints are done by using Rigid body element (RBE2) shown in Fig. 5a and b which is having one independent node and multiple dependent nodes, the sole purpose of the RBE2 transfers the load in such a way that all the dependent nodes have zero relative deformation after load application.

The Single Point Constraint (SPC) which is number of degrees of freedom of fixed location and the force which is the loading point are specified along with the magnitude and direction as shown in Fig. 5c. Finally, the MHS assembly is analyzed in Optistruct solver for linear static analysis of maximum deflection and von Mises stress.

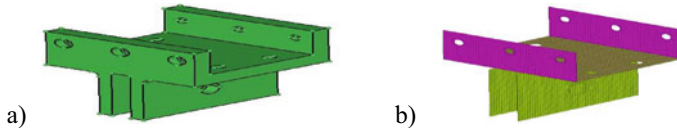


Fig. 4 MHS fork end. **a** 3D part model. **b** 2D shell element model

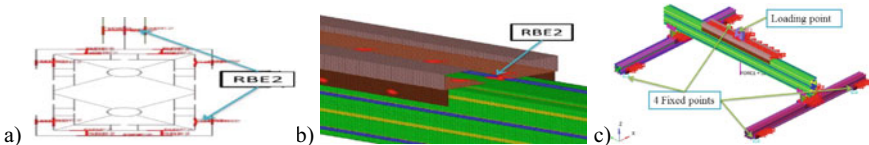


Fig. 5 **a** and **b** MHS RBE2 element connections for joints and **c** MHS loading and fixed constraints representation

2.3 Experimental Method

We need to select the appropriate cross-section profiles for MHS to handle the satellite or panel assembly weight during each AIT operations. The selection of these profiles is strength-based approach [2] where the load factors are considered as follows:

$$(a) \text{ Working Load Limit(WLL)} = \text{Shock factor} \times \text{Safe Working Load(SWL)} \\ = 1.5 \times \text{SWL} \quad (3)$$

$$(b) \text{ Testing load limit (TLL)} = 2 \times \text{SWL} \quad (4)$$

$$(c) \text{ Proof Load Limit (PLL)} = 2 \times \text{WLL} = 3 \times \text{SWL} \quad (5)$$

$$(d) \text{ Design Load Limit (DLL)} = 1.5 \times \text{PLL} = 4.5 \times \text{SWL} \quad (6)$$

The MHS is designed for design load limit by using Eqs. (3), (4), (5) and (6) which are mainly depends on the standard cross section profiles used. The Table 1 shows profile specifications of MHS considered for the experimental test in the present work.

To validate the results obtained from the FEA, we have selected three locations for measuring strains by using three-element rectangular rosette gages [10] as shown in Fig. 6a. At location-1, 2 mm strain gage and at location-2 and 3, 1 mm strain gages are used. The MHS assembly is tested for Testing Load Limit (TLL), and the test setup is shown in Fig. 6b along with the load cell and laser detector. Load cell is used to apply the required load and laser detector is used to measure the deflection of the

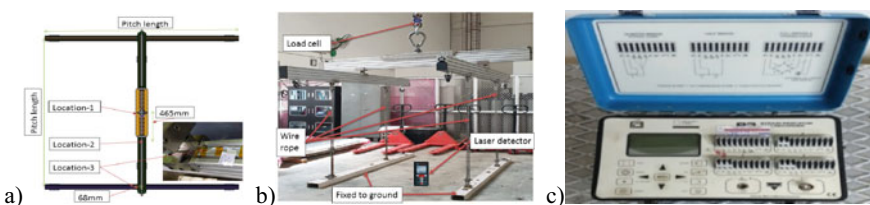


Fig. 6 a Three-element rectangular rosette gages' locations. b MHS experimental setup for load test. c P3 strain indicator and recorder

Table 1 MHS specifications

Sl no.	Type of handling system	Pitch size (mm)	Main beam profile	Auxiliary beam profile
1	MHS-1	1659 × 1250	90 × 180 profile	90 × 90 profile

main beam at the center. The directional strains of each strain gage are recorded with the help of P3 strain indicator and recorder as shown in Fig. 6c.

Principle stresses for linear, isotropic, and homogeneous material are calculated from measured three-directional strains by neglecting the transverse sensitivity of the gages.

$$\sigma_1 = E \left[\frac{(\varepsilon_A + \varepsilon_C)}{2(1 - \mu)} + \frac{1}{2(1 + \mu)} \sqrt{(\varepsilon_A - \varepsilon_C)^2 + (2\varepsilon_B - \varepsilon_A - \varepsilon_C)^2} \right] \quad (7)$$

$$\sigma_2 = E \left[\frac{(\varepsilon_A + \varepsilon_C)}{2(1 - \mu)} - \frac{1}{2(1 + \mu)} \sqrt{(\varepsilon_A - \varepsilon_C)^2 + (2\varepsilon_B - \varepsilon_A - \varepsilon_C)^2} \right] \quad (8)$$

where E = modulus of elasticity in GPa; μ = Poisson's ratio; and $\varepsilon_A, \varepsilon_B$, and ε_C are strain gage readings at $0^\circ, 45^\circ$, and 90° , respectively.

The von Mises stress is calculated from the principle stresses

$$\sigma_{\text{von}} = \sqrt{\sigma_1^2 + \sigma_2^2 - \sigma_1 \sigma_2} \quad (9)$$

The calculated von Mises stress from Eq. (9) is compared with that of the von Mises stress results obtained in FEA with respective locations.

3 Results

The static FEA of MHS assembly is compared with that of experimental results, and before that some cantilever beam analysis for 1D and 2D shell element is carried out to compare with analytical results, one of the cantilever beam deflection and von Mises stress results are verified for convergence test also with different element sizes as plotted in Fig. 7 and the corresponding results are listed in Table 2.

The cantilever beam analysis results with corresponding analytical calculations are shown in Table 2, and by changing the element size the deflection values never

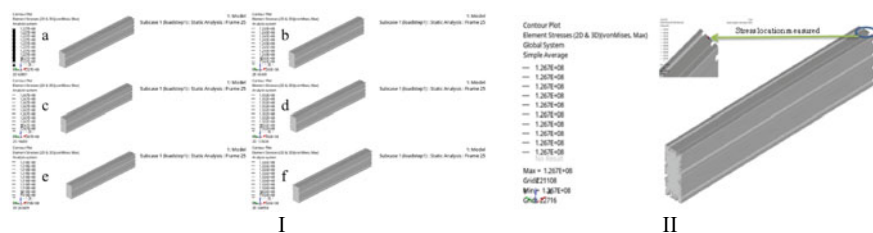


Fig. 7 90 × 180 profile Von Mises stresses (I) Plots of element size. **a** 10 mm. **b** 7.5 mm. **c** 5 mm. **d** 2.5 mm. **e** 1.5 mm. **f** 1 mm. (II) Values measured location in FEA

Table 2 90×180 profile cantilever beam deflection and vonmises stress

Length of the beam $L = 1000$ mm, load applied $P = 30$ KN, 2D profile moment of inertia $I = 2130.16 \text{ cm}^4$, analytical deflection $\delta = 6.7 \text{ mm}$, analytical stress $\sigma = 123.2 \text{ MPa}$

Sl no.	Element size (mm)	FEA deflection (mm)	Error % of deflection	Vonmises stress (MPa)	Error % of vonmises stress
1	10	6.69	0.15	122.7	0.4
2	7.5			124.3	0.9
3	5			126.7	2.8
4	2.5			130.2	5.7
5	1.5			131.8	6.9
6	1			132.6	7.6

deviate but von Mises stress values deviate and never converge because of singularities in the model and single point constraints [8], so to avoid complexity of the model the element size for all the 2D profiles is taken 5 mm based on the convergence results.

After finalizing element size, the deflection and simple average von Mises stress plots for both 1D beam and 2D shell elements of some profiles are shown in Figs. 8 and 9 and the corresponding results with respect to analytical calculations are listed in Table 3.

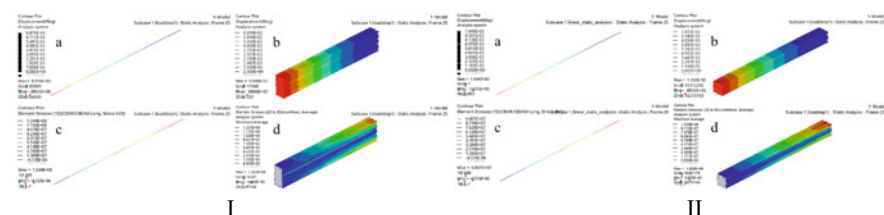


Fig. 8 (I) 90×180 profile and (II) 90×90 profile. **a** 1D beam deflection. **b** 2D shell element deflection. **c** 1D beam von Mises stress. **d** 2D shell element von Mises stress

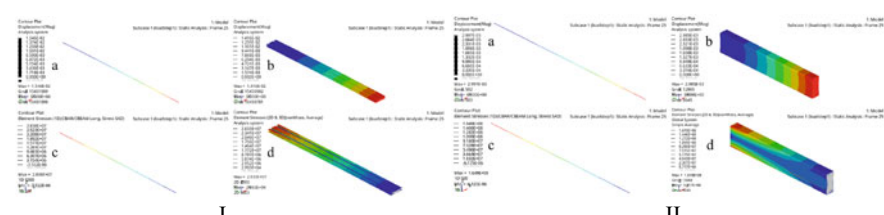


Fig. 9 (I) 90×19 profile and (II) box profile. **a** 1D beam deflection. **b** 2D shell element deflection. **c** 1D beam von Mises stress. **d** 2D shell element von Mises stress

Table 3 Cantilever beam with point load results deflection and vonmises stress comparison table for different cross section profiles

Point load applied and profile						
Result type	Element type	Result type	30 KN and 90 × 180	5 KN and 90 × 90	0.1 KN and 90 × 19	50 KN and box
Deflection in mm	1D	Analytical	MI (cm ³)			
		FEA	2138	6.69	229	10.45
		Error %		2.7%	0.09%	1.2%
Vonmises stress in MPa	2D	Analytical	2130.2	6.72	213.35	3.4
		FEA		6.69	10.3	14.2
		Error %	0.367%	0.44%	6.8%	8.5%
Vonmises stress in MPa	1D	Analytical	2138	125.5	229	99.7
		FEA		124.4	98	28.3
		Error %		0.87%	1.7%	4.4%
Vonmises stress in MPa	2D	Analytical	2130.2	123.2	213.35	3.4
		FEA		132.1	102.5	26.6
		Error %	0.367%	7.2%	6.8%	0.87%

Table 3 shows the percentage of error for all the variants considered in the present work are <8.5% for deflection and <7.2% for average von Mises stress compared with the analytical calculations, which are acceptable range in FEA and the errors are mainly due to the following three major reasons that are observed.

- The MI of the 2D profile and actual 3D profiles itself showing some error.
- For von Mises stress calculations, we have considered only bending stress by neglecting shear stress.
- Method of taking von Mises stress results from FEA tools, here we have considered the simple average method for von Mises stress comparison.

Based on the above results we conclude that these standard extruded profiles can be meshed by using 2D shell elements for further static analysis of MHS assembly.

3.1 Static Analysis of Modular Handling System (MHS)

A four-point MHS with specifications listed in Table 1 is analyzed in FEA for deflection and Von Mises stress but the required von Mises stress from FEA is measured only at specified three locations as shown in Fig. 10 where the strain gages are fixed during experimental static analysis of MHS. Table 4 readings show the strain readings measured from P3 strain indicator at three locations during experimental method.

The von Mises stresses are calculated using Eqs. (7), (8), and (9) and the corresponding values are listed in Table 5, the central deflection of MHS is having 15%

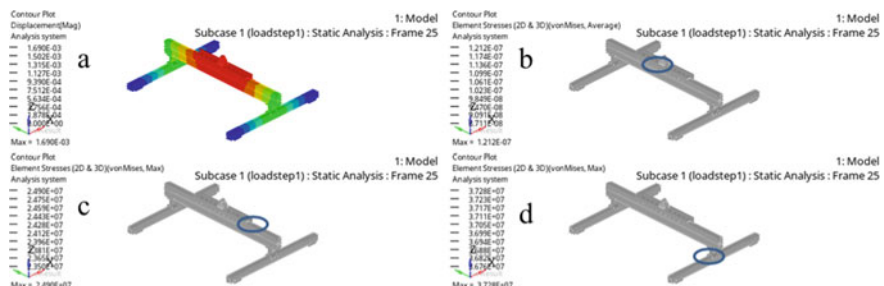


Fig. 10 MHS-1. **a** Overall deflection of system. **b** von Mises stress at location-1. **c** von Mises stress at location-2. **d** von Mises stress at location-3

Table 4 P3 strain indicator reading of strain at 3 locations

Sl no.	Strain gauge readings	Location-1 ($\mu\epsilon$)	Location-2 ($\mu\epsilon$)	Location-3 ($\mu\epsilon$)
1	ε_A 0° angle	102	131	825
2	ε_B 45° angle	49	84	316
3	ε_C 90° angle	162	316	226

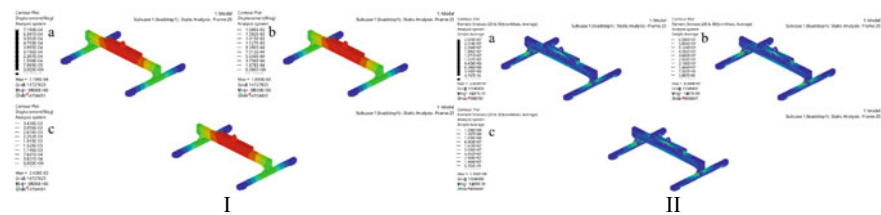


Fig. 11 MHS-1 (1659×1250 mm pitch) (I) Deflection plots and (II) von Mises stress plots. **a** 1200 Kg load, **b** 2700 Kg load and **c** 5400 Kg load

Table 5 FEA and experimental results comparison of deflection and vonmises stress

Type of handling system: MHS-1, pitch size: 1659×1250 mm, testing load applied: 2700 Kg

Sl no.	Central deflection in (mm)	Vonmises stress in MPa						
		Location-1		Location-2		Location-3		
01	FEA	1.69	FEA	1.21×10^{-13}	FEA	24.9	FEA	37.28
	Experimental	2	Experimental	44	Experimental	28	Experimental	41
	Error %	15.5	Error %	100	Error %	11	Error %	9

error and the von Mises stresses are 100%, 11%, and 9% at location-1, 2, and 3, respectively. The FEA von Mises stress value at location-1 is almost zero and the corresponding experimental value is 44 MPa, it is because at location-1 in FEA model used RBE2, so the strain gage placement at this location for experimental method was incorrect, and here the results are compared and concluded based on the location-2 and 3 only.

From the experimental results validation with the FEA results, we conclude that the finite element models with appropriate meshing are used for static analysis and we can design any type of MHS for the specific application of load. Figures 11 and 12 show the deflection and von Mises stress plots for MHS-1 and MHS-2 at SWL, TLL and DLL loads, and the same results are tabulated in Table 6.

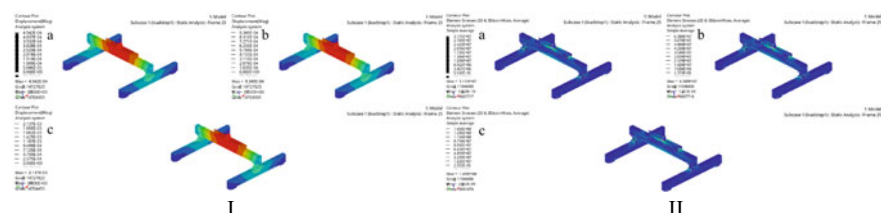


Fig. 12 MHS-2 (1510×1300 mm pitch) (I) Deflection plots and (II) von Mises stress plots. **a** 1425 Kg load, **b** 2850 Kg load and **c** 6415 Kg load

Table 6 Deflection and vonmises stress results

Sl no.	Type of handling system	Pitch size (mm)	C/S used	Load (Kg)	Deflection (mm)	Average vonmises stress (MPa)
01	MHS-1	1659 × 1250	90 × 180 and 90 × 90	SWL = 1200	0.719	28.3
				TLL = 2700	1.69	65.8
				DLL = 5400	3.44	133.6
02	MHS-2	1510 × 1300	90 × 180	SWL = 1425	0.45	31.1
				TLL = 2850	0.93	63.8
				DLL = 6415	2.13	145.8

Table 7 Component level vonmises stress results

Sl no.	Type of handling system	Material	Component showing max stress	Load (Kg)	Designer vonmises stress (MPa)	Yield Stress of the material (MPa)
01	MHS-1	Steel	Eye end	DLL = 5400	198	356
		Al	Auxiliary beam		157	276
02	MHS-2	Steel	Eye end	DLL = 6415	216	356
		Al	Main beam		134	276

From the static analysis results of the MHS-1 and 2, it is observed that the deflection and simple average von Mises stresses are well within the limits for Safe Working Load (SWL), similarly at Testing Load Limit (TLL) and Design Load Limit (DLL), especially the von Mises stresses are less than the yield stress of both the steel and aluminum materials at all load types.

Further, the component-level analysis for aluminum and steel is also carried out and the von Mises stress values are measured based on the designer experience, for MHS-1 and MHS-2, out of the components having steel material the eye end showing the maximum von Mises stress at DLL which is 198 MPa for MHS-1 and 216 MPa for MHS-2 which are less than the yield stress of steel, i.e., 356 MPa. Similarly, for aluminum material in MHS-1, the auxiliary beam showing maximum stress which is 157 MPa and in MHS-2 the main beam showing maximum stress which is 134 MPa, both these stresses are less than the yield stress of aluminum, i.e., 276 MPa as explained in Table 7.

4 Conclusion

This study presents an FEA and experimental approach to investigate the static analysis of the satellite MHS by standard aluminum profiles. These profiles are validated

under cantilever beam case for deflection and von Mises stress by using FEA of 1D beam and 2D mid-surface meshing, and the results are closely matching to the analytical calculations so that 2D mid-surface meshing is used further for all the components of MHS. Based on the agreement of standard aluminum profile results, further these profiles under MHS assembly applications for satellite's handling are considered which helps to select the proper cross-section profiles and required pitch size of MHS assembly for the specific satellite weight requirement. The component-level analysis based on the material yielding, i.e., aluminum and steel help to identify the critical stress locations at design load limit.

References

1. Rexroth Bosch Group: Rexroth profiles catalogue. Bosch Group, MGE 13.1 (2016)
2. Srivatav, S., Sekar, A., Sundaram, N.S., Govinda, K.V.: Modular design of mechanical handling system for spacecraft applications. *ISME J. Mech. Des.* **01**(1), 01–8 (2018)
3. Güler, S., Karagüllü H.: Finite element analysis of structures with extruded aluminum profiles having complex cross sections. *Latin Am. J. Sol. Struct.* 1679–78252755 (2015)
4. Fiorino, L., Macillo, V., Mazzolani, F.M.: Mechanical behaviour of bolt-channel joining technology for aluminium structures. *Constr. Build. Mater.* **73**, 76–88 (2014)
5. Waia, C.M., Rivai, A., Bapokutty, O.: Modeling optimization involving different types of elements in finite element analysis. *Mater. Sci. Eng.* **50**, 012036 (2013)
6. Altair University: Practical Aspects of Finite Element Simulation A Study Guide, 3rd edn. Altair University (2015).
7. Altair University: OptiStruct for Linear Analysis. Altair University (2015)
8. Sönnnerlind, H.: Singularities in Finite Element Models: Dealing with Red Spots. COMSOL Blog (2015)
9. Bansal, R.K.: A Text Book of Strength of Materials, 4th edn. Laxmi Publications (P) Ltd. (2009)
10. Dally, J.W., Riley, W.F.: Experimental Stress Analysis, 3rd edn. McGraw-Hill Inc.
11. TML: Strain Gauges Catalog. pam E-1007C (2017)
12. Calculating Principal Strains using a Rectangular Strain Gage Rosette

Numerical Investigation on Dynamic Stability of a Pick and Place Robot Arm



B. Upendra , B. Panigrahi, K. Singh, and G. R. Sabareesh

1 Introduction

For linear systems, in order to determine the equation of motion, the classical method by mode superposition technique is utilized. This can be used further to explain the general problem of the rotating cantilever beam with tip-mass vibrations. In the case of nonlinear systems, these approaches do not work, as they will customarily be based on the superposition principle. The beam, the Euler–Bernoulli model, was presumed to be for a homogeneous and thin beam. Dynamic analysis of a beam rotating hub has latterly gained a great deal of significance due to numerous practical applications, including flexible manipulator, rotary blades, etc. In most of the literature, the pick and place robot arm with mass holding is modelled as a cantilever beam with a tip mass attached at its free end. However, the dynamic stability of the model is predicted by considering a small amplitude motion. As such linear vibration modelling is proposed, since for small amplitude oscillations, linear equations and boundary conditions can aptly characterize the responses of a deformable body. In varying, as the oscillation amplitude increases, nonlinear effects dominate the dynamic behaviour of the system and the response is completely different from its counterpart

B. Upendra · B. Panigrahi · K. Singh · G. R. Sabareesh

Department of Mechanical Engineering, BITS-Pilani, Hyderabad Campus, Hyderabad 500078, India

e-mail: brajesh@hyderabad.bits-pilani.ac.in

B. Upendra

e-mail: p20190444@hyderabad.bits-pilani.ac.in

K. Singh

e-mail: ksingh@hyderabad.bits-pilani.ac.in

G. R. Sabareesh

e-mail: sabareesh@hyderabad.bits-pilani.ac.in

linear model. In such cases, achieving dynamic stability of the system is cumbersome, and hence it demands a detailed investigation of the nonlinear aspects and its contributing parameters. The fulcrum of the nonlinearities in such systems may be geometric, inertial, material in nature, or from the nonlinear external forces. For a flexible arm, the geometric nonlinearity may be precipitated by nonlinear stretching or large curvatures. Nonlinear stretching of the midplane of a deformable body appends its transverse vibrations if it is supported in such a way as to impede the movement of its ends or edges. The effect of tip mass, excitation in the transverse direction and the stability of the beam are then of prime concern and need to be examined.

To compute the vibration frequencies of a rotating beam with a tip mass, the finite element model is generated and adopted [1]. In the Rayleigh–Ritz method, natural frequencies and mode shapes of a twirled uniform cantilever beam with tip mass are analysed using a collection of beam characteristic orthogonal polynomials [2]. In a subsequent work, the effects of sinusoidal excitation of axial acceleration, speed and displacement on the stability of the revolving beam were then observed [3]. In this analysis, a modal formulation approach is also used to measure the modified angular velocity of a rotating beam where resonance occurs [4]. The high amplitude vibration of the first spatial mode of the Timoshenko beam involving shear deformation and rotary inertia effects was shown [5]. The spinning beam mode forms with a condensed mass are also greatly affected by the two dimensionless parameters [6]. The dynamic performance of the centrifugal cantilever beam with tip mass through theoretical study and modal test under tension state and compression test was recorded [7]. The outcome revealed that the geometric and physical parameters of the tip mass greatly influence the critical values of bifurcation and buckled equilibrium [8]. The effects of the spring–mass mechanism position upon the spinning frequencies of the beam and the direction of the spring have a substantial impact on nonlinear frequencies perceived [9].

An analytical model for an extensive free excitation of an uneven, axially loaded beam that carries a transversely and axially offbeat tip mass was suggested [10]. An iterative technique to catch the nonlinear system behaviour of the spinning FGM Timoshenko beam was discussed [11]. Driven vibration utilizing Ritz process of a revolving composite beam with an associated mass was resolved [12]. In recent papers, the dynamic model was used to predict the dynamic response of a spinning cantilever beam with an offset peak mass [13]. Nonlinear vibration of evenly distributed load and revolving three-dimensional tapered beam was explored [14]. The dynamic stiffness matrix was [15] used to demonstrate the effect of centrifugal stiffening on the dynamic response of a beam.

For the purposes of geometrical nonlinearity, the nonlinear strain–displacement relationships, such as von Karman form, and the related linear stress are implemented in the present Euler–Bernoulli beam model. Nonlinear motion equations, along with related boundary conditions, having tip-mass inertia, are obtained from Hamilton's theorem. This paper aims to present a method, based on the method of multiple scales, which enables us to find the nonlinear response of a transversally exciting pick and place robot arm carrying weight. With the presence of tip mass in the form of weight carried by the robot arm, the excitation in the transverse direction becomes crucial

to the dynamic stability of the robot arm in a transverse direction. Therefore, the study of the possible nonlinear behaviour of such a system will enable the designers to design the system for its dynamical stability.

Nomenclature

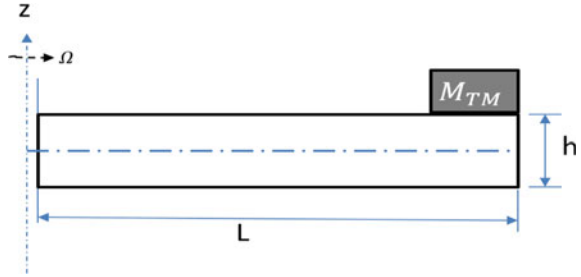
b, h, L	Width, thickness and length of the beam, respectively.
T	Centrifugal force.
t_1, t_2	Two different time instants.
x, y, z	Coordinates along with the length, width and thickness directions, respectively.
A	The cross-sectional area of the beam.
E, ρ	Young's modulus and mass density of beam per unit length, respectively.
M_{TM}	Tip mass.
I	The second moment of area.
T_s	Kinetic energy, strain energy, respectively.
w, \hat{w}	Dimensional and non-dimensional, respectively.
$(\cdot), (\cdot\cdot)$	Single dot and double dots represent single and double time derivatives, respectively.
$(\cdot'), (\cdot'')$	Partial derivatives with respect to single and double x , respectively.
u, w	Axial and transverse displacements, respectively.
ψ	Rotation of the beam cross section due to bending.
r	The radius of gyration of the beam cross section.
$\rho A r^2$	Mass moment of inertia.
N	Axial force.
N_0	Pre-tension in the beam.
ω	The natural frequency of the system.
Ω	The angular speed of rotation of the hub.
R	The radius of the hub.

2 Methodology

In the present work, a flexible arm of a pick and place robot holding the weight is modelled as a beam with a uniform cross section with a tip mass at one end, and the other end is connected to a rotating hub as shown in Fig. 1. Large amplitude motion is modelled by considering the midplane stretching. von Karman nonlinear strain displacement relation is considered as ε_x .

$$\varepsilon_x = \frac{\partial u}{\partial x} + \frac{1}{2} \left(\frac{\partial w}{\partial x} \right)^2 \quad (1)$$

Fig. 1 Rotating beam model with tip mass



In Eq. (1), u and w are the displacement fields in an axial and transverse direction, respectively. Considering the existence of centrifugal stiffening due to the rotation of the beam along with the rotating hub, the load potential due to centrifugal force can be given as

$$V = \frac{1}{2} \int_0^L T u_0 dx \approx \frac{1}{2} \int_0^L T \left(\frac{\partial w}{\partial x} \right)^2 dx \quad (2a)$$

$$T = \int_x^L \rho A \Omega^2 (R + x) dx + M_{TM} \Omega^2 (R + L) \quad (2b)$$

In Eq. (2a), T is the centrifugal force which can be given as in Eq. (2b), where Ω is the angular speed of rotation of the hub, ρ is the density and M_{TM} is the tip mass. Kinetic energy (T_s) and the potential energy (U) of the system are written as

$$\begin{aligned} T_s &= \frac{1}{2} \int_0^L \left[\rho A \left(\frac{\partial u}{\partial t} \right)^2 + \rho A \left(\frac{\partial w}{\partial t} \right)^2 + \rho A r^2 \left(\frac{\partial \psi}{\partial t} \right)^2 \right] dx + \frac{M_{TM}}{2} \left(\frac{\partial w}{\partial t} \right)_{x=L}^2 \\ U &= \frac{1}{2} \int_0^L \left[EI \left(\frac{\partial \psi}{\partial x} \right)^2 + EA \varepsilon_x^2 \right] dx \end{aligned} \quad (3)$$

Applying Hamilton's principle,

$$\int_{t1}^{t2} \delta (T_s - U + W_{ext}) dt = 0$$

Here, W_{ext} will be considered as the load potential V caused by the centrifugal forces. Applying Hamilton's principle, one can obtain

$$EI \left(\frac{\partial^2 \psi}{\partial x^2} \right) - \rho A r^2 \left(\frac{\partial^2 \psi}{\partial t^2} \right) = 0 \quad (4)$$

$$\rho A \left(\frac{\partial^2 w}{\partial t^2} \right) + M_{TM} \left(\frac{\partial^2 w}{\partial t^2} \right)_{x=L} - EA \left[\frac{\partial u}{\partial x} + \frac{1}{2} \left(\frac{\partial w}{\partial x} \right)^2 + \frac{T}{EA} \right] \frac{\partial^2 w}{\partial x^2} = 0 \quad (5)$$

$$\rho A \left(\frac{\partial^2 u}{\partial t^2} \right) - EA \frac{\partial}{\partial x} \left[\frac{\partial u}{\partial x} + \frac{1}{2} \left(\frac{\partial w}{\partial x} \right)^2 \right] = 0 \quad (6)$$

It is a well-known fact that the axial inertia is very small compared to the other directions. Therefore, neglecting axial inertia, an equation can be obtained as

$$EI \left(\frac{\partial^2 \psi}{\partial x^2} \right) - \rho Ar^2 \left(\frac{\partial^2 \psi}{\partial t^2} \right) = 0 \quad (7)$$

$$\rho A \frac{\partial^2 w}{\partial t^2} + M_{TM} \left(\frac{\partial^2 w}{\partial t^2} \right)_{x=L} - N \frac{\partial^2 w}{\partial x^2} = 0 \quad (8)$$

where the N can be given by

$$N = EA \left[\frac{\partial u}{\partial x} + \frac{1}{2} \left(\frac{\partial w}{\partial x} \right)^2 + \frac{T}{EA} \right] = N_0 + \frac{EA}{2L} \int_0^L \left(\frac{\partial w}{\partial x} \right)^2 dx + \frac{T}{L} \int_0^L dx \quad (9)$$

In Eq. (9), N_0 is the pre-tension in the beam. Combining Eqs. (7) and (8), one may obtain

$$EI \frac{\partial^4 w}{\partial x^4} + \rho A \frac{\partial^2 w}{\partial t^2} + M_{TM} \left(\frac{\partial^2 w}{\partial t^2} \right)_{x=L} - \rho Ar^2 \frac{\partial^4 w}{\partial x^2 \partial t^2} - N \frac{\partial^2 w}{\partial x^2} = 0 \quad (10)$$

$$\therefore I = Ar^2$$

$$\frac{\partial^4 w}{\partial x^4} + \frac{\rho}{Er^2} \frac{\partial^2 w}{\partial t^2} + \frac{M_{TM}}{EI} \left(\frac{\partial^2 w}{\partial t^2} \right)_{x=L} - \frac{\rho}{E} \frac{\partial^4 w}{\partial x^2 \partial t^2} - \frac{N}{EI} \frac{\partial^2 w}{\partial x^2} = 0 \quad (11)$$

Non-dimensionalization of the above equations is done considering the following quantities:

$$\hat{t} = \omega t, \quad \hat{x} = \frac{x}{L}, \quad \hat{w} = \frac{w}{L} \quad (12)$$

Substituting these equations in (11) and simplifying, one can obtain the governing equation as mentioned in the (13)

$$\frac{\partial^4 \hat{w}}{\partial \hat{x}^4} + \frac{\rho L^2 \omega^2}{Er^2} \frac{\partial^2 \hat{w}}{\partial t^2} + \frac{M_{TM} L^2 \omega^2}{EI} \left(\frac{\partial^2 w}{\partial t^2} \right)_{x=L} - \frac{\rho L^2 \omega^2}{E} \frac{\partial^4 \hat{w}}{\partial \hat{x}^2 \partial \hat{t}^2} - \frac{N}{EI} \frac{\partial^2 \hat{w}}{\partial \hat{x}^2} = 0 \quad (13)$$

In order to solve Eq. (13), displacement is assumed in variable separable form as mentioned in Eq. (14)

$$w(x, t) = \varphi(x)q(t) \quad (14)$$

In Eq. (14), $\varphi(x)$ is the spatial function for n th mode (nth mode shape) of the corresponding cantilever Euler–Bernoulli beam, which can be taken as mentioned in Eq. (15) as mentioned in [16], which can be completely known with the help of appropriate boundary conditions.

$$\varphi(x) = C_1 \sin \beta x + C_2 \cos \beta x + C_3 \sinh \beta x + C_4 \cosh \beta x \quad (15)$$

Substituting Eq. (14) into Eq. (13) one may derive the equations as

$$q\varphi'''' + \left[\frac{\rho L^2 \omega^2}{Er^2} \varphi + \frac{M_{TM} L^2 \omega^2}{EI} \varphi(L) \right] \ddot{q} - \frac{\rho L^2 \omega^2}{E} \varphi'' \ddot{q} - \frac{N_0}{EI} \varphi'' q - \frac{EA}{2L} q^2 \int_0^1 (\varphi')^2 dx \frac{1}{EI} \varphi'' q - \frac{T}{EI} q \varphi'' = 0$$

Further, simplifying the equations by collecting various coefficients of a different order of q , one can rewrite the above equation, as mentioned in Eq. (16).

$$\left[\frac{\rho L^2 \omega^2}{Er^2} \varphi + \frac{M_{TM} L^2 \omega^2}{EI} \varphi(L) - \frac{\rho L^2 \omega^2}{E} \varphi'' \right] \ddot{q} + \left[\varphi'''' - \frac{N_0}{EI} \varphi'' - \frac{T}{EI} \varphi'' \right] (16)$$

$$\left[\varphi'''' - \frac{N_0}{EI} \varphi'' - \frac{T}{EI} \varphi'' \right] q - \left[\frac{1}{2Lr^3} \varphi'' \int_0^1 (\varphi')^2 dx \right] q^3 = 0$$

Equation (16) can be further simplified by considering the orthogonality of the modes using Galerkin's Method. Multiplying Eq. (16) by $\int_0^1 \varphi dx$, one may deduce the expression as

$$\begin{aligned} & \left[\frac{\rho L^2 \omega^2}{Er^2} f_1 + \frac{M_{TM} L^2 \omega^2}{EI} f_5 - \frac{\rho L^2 \omega^2}{E} f_2 \right] q + \left[f_4 - \frac{N_0}{EI} f_2 - \frac{T}{EI} f_2 \right] q \\ & + \left[-\frac{1}{2Lr^2} f_2 f_3 \right] q^3 = 0 \end{aligned}$$

where

$$\begin{aligned} f_1 &= \int_0^1 \varphi^2 dx, \quad f_2 = \int_0^1 \varphi \varphi'' dx, \quad f_3 = \int_0^1 (\varphi')^2 dx \\ f_4 &= \int_0^1 \varphi \varphi''' dx, \quad f_5 = \int_0^1 \varphi \varphi(L) dx \end{aligned}$$

The equation has now been reduced to general form Duffing's equation as

$$\alpha_1 \ddot{q} + \alpha_2 q + \alpha_3 q^3 = 0 \quad (17)$$

Equation (17) is solved by the multiple-scale analysis given by [17].

Here the coefficients α_i are given by

$$\begin{aligned} \alpha_1 &= \frac{\rho L^2 \omega^2}{Er^2} f_1 + \frac{M_{TM} L^2 \omega^2}{EI} f_5 - \frac{\rho L^2 \omega^2}{E} f_2 \\ \alpha_2 &= f_4 - \frac{N_0}{EI} f_2 - \frac{T}{EI} f_2 \\ \alpha_3 &= -\frac{1}{2Lr^2} f_2 f_3 \end{aligned} \quad (18)$$

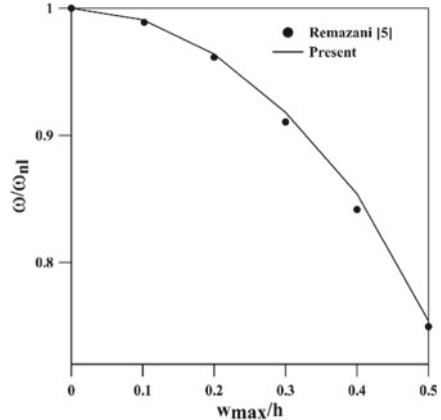
3 Validation

By choosing the appropriate boundary conditions, spatial function φ is determined. For the linear free vibration of cantilever beam, the parameter β , the first characteristic value 1.875 is used [16]. Subsequently, f_i 's ($i = 1, 2, \dots, 5$) and then α_i 's ($i = 1, 2, 3$) are determined for different values of parameters such as length, rotating speed and tip mass. In order to validate the methodology explained earlier firstly, a zero tip mass is considered, and the results obtained from the present methodology are compared with that of Banerjee [15]. Non-dimensional rotational speed (η) is considered as $\eta^2 = \frac{\rho A}{EI} L^4 \Omega^2$. Table 1 insures the accuracy of the results obtained from the present analysis. However, the novelty of the present work focuses on the effect of tip mass

Table 1 Comparison of frequencies with [15]

η	Present	Banerjee [15]
0	3.4798	3.4798
1	3.6450	3.6445
2	4.0981	4.0971
3	4.7563	4.7516
4	5.5385	5.5314
5	6.3951	6.3858

Fig. 2 Comparison of linear-to-nonlinear frequency ratio for various amplitudes of vibration



on the nonlinear behaviour of the vibratory response, which is not considered in the referred articles.

Nonlinear frequencies are compared for zero tip mass and zero rotational speed with that of [5] in Fig. 2. The results show very good agreement with that of the referred results. It is to be noted here that, since the referred results are provided in the form of nonlinear periods, compared results are converted in the ratio of frequencies (linear-to-nonlinear frequencies). Material properties for this comparison and for all subsequent analysis are taken as $E = 70$ GPa, Poisson's ration = 0.3 and $\rho = 2700$ kg/m³. Geometric parameters are taken for beam cross section $A = 256$ mm² and $L/r = 10$.

Figure 3a and b demonstrates the effect of tip mass and rotational velocity on linear-to-nonlinear frequency ratios. From Fig. 3a, it can be identified that with the

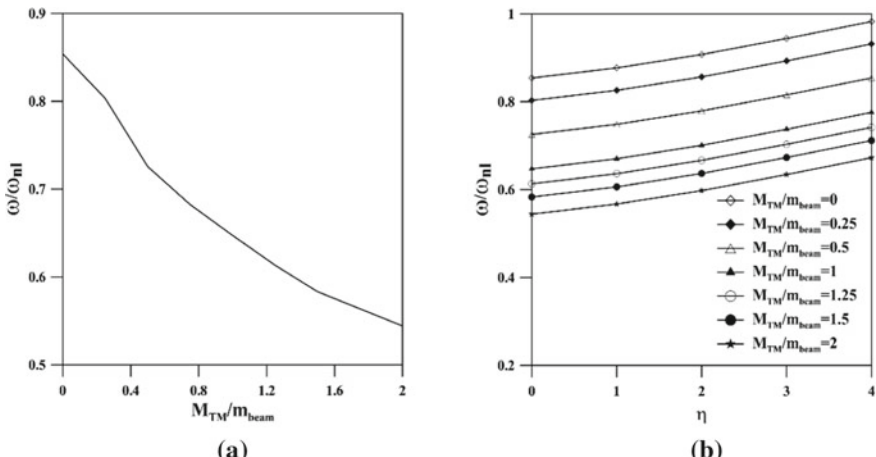


Fig. 3 **a** Frequency ratio versus M_{TM} . **b** Frequency ratio versus η for various M_{TM}/m_{beam}

rise in the tip mass, the ratio decreases significantly. It can also be noticed in Fig. 3b that with the rise in rotational speed, the ratio increases. The truth is that the linear frequency decreases in the case of tip mass with the increase in tip mass. Therefore, the decrement in the ratio of linear-to-nonlinear frequency can be explained quite convincingly. Similarly, due to an increase in rotational speed, the centrifugal stiffening effect is causing an increase of linear frequency and hence the increment in the frequency ratio. Here the results are compared with cantilever Timoshenko beam [5] and rotating non-uniform Timoshenko beam [15].

4 Conclusion

The flexible arm of a pick and place robot with a holding mass is designed as a cantilever beam with a tip mass. It is presumed that the fixed end of the beam is connected to a rotating hub. In the form of Duffing's formula, the nonlinear governing equation of motion of the rotating beam with tip mass is obtained and reduced. The equation is solved using the well-developed multiple-scale analysis. The ratio of linear-to-nonlinear frequency of the system is found to decrease with the increase in tip mass. On the other hand, these ratios are found to increase with an increase in the rotating speed of the hub.

References

1. Hoa, S.V.: Vibration of a rotating beam with tip mass. (1979). [https://doi.org/10.1016/0022-460X\(79\)90542-X](https://doi.org/10.1016/0022-460X(79)90542-X)
2. Bhat, R.B.: Cantilever beam with tip mass as predicted by polynomials in the Rayleigh-Ritz method. **105**, 199–210 (1986)
3. Lee, H.P.: Vibration of an inclined rotating cantilever beam with tip mass. J. Vib. Acoust. **3115**, 241–245 (1993)
4. Engineering, M.: Vibration analysis of rotating cantilever beams. **212**, 807–828 (1998)
5. Ramezani, A., Ghorashi, M.: ESDA2004–58298. 2–7 (2004)
6. Yoo, H.H., Seo, S., Huh, K.: The effect of a concentrated mass on the modal. Proc. Inst. Mech. Eng. Part C: J. Mech. Eng. Sci. (2002). <https://doi.org/10.1243/0954406021525098>
7. Liu, C.: Modal test and analysis of cantilever beam with tip mass. (2015). <https://doi.org/10.1007/BF02487792>
8. Taylor, P., Xiao, S., Chen, B., Du, Q.: mechanics based design of structures and machines: an on dynamic behavior of a cantilever beam with tip mass in a centrifugal field. 37–41 (2004) <https://doi.org/10.1081/SME-200048325>
9. Das, S.K., Ray, P.C., Pohit, G.: Free vibration analysis of a rotating beam with nonlinear spring and mass system **301**, 165–188 (2007). <https://doi.org/10.1016/j.jsv.2006.09.028>
10. Malaekae, H., Moeenfarad, H.: Analytical modeling of large amplitude free vibration of non-uniform beams carrying a both transversely and axially eccentric tip mass. J. Sound Vib. 1–19 (2015). <https://doi.org/10.1016/j.jsv.2015.12.003>
11. Panigrahi, B., Pohit, G.: Nonlinear dynamic analysis of functionally graded timoshenko beam fixed to a rotating hub nonlinear dynamic analysis of functionally timoshenko beam fixed to a rotating hub (2016). <https://doi.org/10.1088/1742-6596/738/1/012115>

12. Aksencer, T., Aydogdu, M.: Vibration of a rotating composite beam with an attached point mass. *Compos. Struct.* **190**, 1–9 (2018). <https://doi.org/10.1016/j.compstruct.2018.02.009>
13. Al-solihiat, M.K., Nahon, M., Behdinan, K.: Three-dimensional nonlinear coupled dynamic modeling of a tip-loaded rotating cantilever (2018). <https://doi.org/10.1177/1077546317753058>
14. Zhou, Y., Zhang, Y., Yao, G.: Nonlinear forced vibration analysis of a rotating three-dimensional tapered cantilever beam (2020). <https://doi.org/10.1177/1077546320949716>
15. Banerjee, J.R.: Dynamic stiffness formulation and free vibration analysis of centrifugally stiffened Timoshenko beams. *J. Sound Vib.* **247**, 97–115 (2001). <https://doi.org/10.1006/jsvi.2001.3716>
16. Meirovitch, L.: Elements of Vibration Analysis, 2nd edn. McGraw-Hill
17. Nayfeh, A.H., Mook, D.T.: Nonlinear Oscillations. Wiley (1979)

A Method for Evaluation of Welding Performance of SMAW Electrodes



Brajesh Asati and Ravi Shanker Vidyarthi

1 Introduction

Shielded Metal Arc Welding (SMAW) is an arc welding process where metals are joined by heat generated from an arc maintained between a flux-coated electrode and the workpiece being welded. The welding current to the arc passes through the core wire and provides metal for the joint being welded. Electrode coating provides stable arc and protects the weld pool from the atmosphere with gases generated from decomposition of the coating under heat produced from the welding arc [1]. The shielding provided, other constituents in the coating and the core steel wire primarily control the mechanical performance, chemistry and metallurgy of the weld zone as well as the welding arc characteristics of the electrode. Composition of the electrode coating depends on the type of electrode, e.g. rutile, cellulose, etc. [2]. EWNR-grade wire rod (complying to BIS 2879) is generally used for production of arc welding stick electrode as per BIS 814—2004 standard. This grade contains low Si (<0.03%), the full specification of which is given in Table 1. However, for low-end applications AWS A5.1 specification is preferred which does not have any chemistry specification for core steel wire. The acceptance is based on all-weld chemical composition, which is specified in Table 2. The accepted Si content in the weld metal is up to 1 wt% for E6013. The common concerns with presence of high Si (more than 0.03%) in electrode core wire are [3] as follows (Table 3):

B. Asati

Research and Development, Tata Steel Ltd., Jamshedpur 831001, India

e-mail: brajesh.asati@tatasteel.com

R. S. Vidyarthi (✉)

Department of Mechanical Engineering, Birla Institute of Technology and Science, Hyderabad Campus, Hyderabad 500078, Telangana, India

e-mail: ravi.vidyarthi@hyderabad.bits-pilani.ac.in

Table 1 Steel chemistry specification (in wt %)

Electrode wire specification	C	Mn	Si	S	P	Al	V	Ti
BIS2879	0.1 max	0.38–0.62 max	0.03 max	0.025 max	0.03 max	0.012 max	0.005 max	0.003 max
EWNR	0.046	0.54	0.025	0.007	0.01	0.005	—	—

Table 2 Chemistry specifications of all-weld as per AWS 5.1 (in wt %)

	C	Mn	Si	P	S	Ni	Cr	Mo	V
E6013	0.20	1.2	1.0	—	—	0.3	0.2	0.3	0.08

Single values are maximum values

- (1) Si increases the electrical resistivity of steel and therefore during welding process overheating of the electrode may take place which in extreme condition would lead to de-bonding of flux from the electrode.
- (2) There is a common concern that Si increases spatter during welding.
- (3) Si is a substitutional alloying element and thereby it strengthens steel. Drawing of high-strength steel would incur more wear in the die and the process would become more expensive.

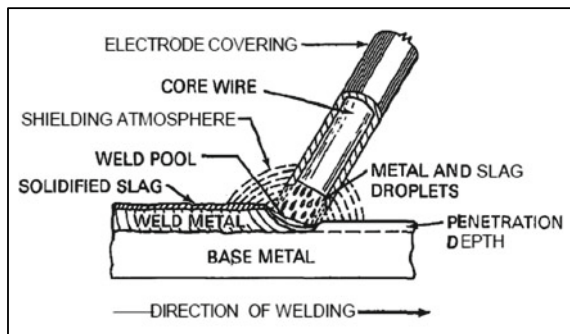
In SMAW, the weld pool is shielded by covering of (a) slag deposited on the surface of the weld bead and (b) non-reactive gases produced from thermal breakdown of coating materials on the core steel wire (Fig. 1). However, type of coating used on the core wire mainly influences the degree of protection of the weld pool. Cellulosic flux generates substantial quantity of inactive gases for weld protection while other fluxes form slag in sufficient quantity to protect the weld pool. The weld pool shielding by means of inactive gases is ineffective due to two reasons: (a) gases produced by thermal breakdown of coating fluxes do not necessarily form protective cover around the arc and weld pool and (b) continuous movable arc and varied arc gap during SMAW process further reduces the usefulness of shielding gas. Therefore, SMAW weld joints are mostly contaminated and not used to develop critical joints [4]. Thickness of the base plate being welded largely controls the welding current used for producing sound weld joints in SMAW process [5]. Generally, thicker plates require more heat input to ensure proper melting, weld penetration and deposition rate. Increased heat input means requirement of more welding current which leads to the use of large diameter electrode. SMAW electrode is commercially available in various sizes and commonly available range is 1–12.5 mm.

This work evaluates the different standard product of the same AWS specification in terms of all-weld chemical composition, all-weld tensile strength, weld spatter measurement and weld bead profiles. Three different E6013 electrodes (Electrodes A, B and C) of diameter 3.15 mm were used for this work. Electrode A was formulated and manufactured indigenously while Electrodes B and C were purchased from market. Core wires of all three electrodes were evaluated for electrical resistivity,

Table 3 Flux composition (in wt %)

Sample	Fe ₂ O ₃	C	CaO	SiO ₂	MgO	MnO	Al ₂ O ₃	TiO ₂	Cr ₂ O ₃	K ₂ O	ZrO ₂	LOI	Na ₂ O
Electrode A	2.97	3.06	2.8	17.09	0.22	7.93	4.38	45.15	0.11	3.4	5.48	9.2	0.31
Electrode B	3.25	3.1	2.66	16.45	0.24	7.4	4.34	43.96	0.16	3.2	5.35	9.2	0.32
Electrode C	2.85	3.14	6.46	21.39	0.23	9.24	6.31	42.84	0.032	3.74	-	-	3.55

Fig. 1 Shielded metal arc welding (SMAW) process



flux composition and tensile strength. All-weld chemical composition and all-weld tensile strength were also evaluated as per AWS A5.1 requirements.

2 Materials and Experimental Procedure

2.1 Electrodes Used and General Characterization of Wire/Wire Rods

Three AWS A5.1 E6013 rutile electrodes were used in this study to carry out the welding performance evaluation. Electrodes B and C are commercially available electrodes from two different manufacturers and purchased from reliable vendor. Electrode A formulation as well as the manufacturing was done in house.

The chemical analysis of the flux was carried out using spectrometer and LECO carbon sulphur analyser. Tensile properties were evaluated employing Instron 5582 testing machine at a cross-head velocity of 5 mm/min with 180 mm total length of wire. Figure 2 represents the tensile properties of the core wires used in different electrodes. Ultimate tensile strength (UTS) and yield strength (YS) values of Electrode B and Electrode C wires are almost similar. However, Electrode A wire has shown slightly lower UTS and YS values than the Electrode B and Electrode C wires. This kind of high strength is obvious with cold-drawn microstructure in these core wires.

2.2 Electrical Resistivity Measurement

For measuring the electrical resistivity of steel wire, a four-probe setup was used (Fig. 3a). A known DC current was passed through the wire using a precise DC power source; the voltage difference was measured across a known length using a

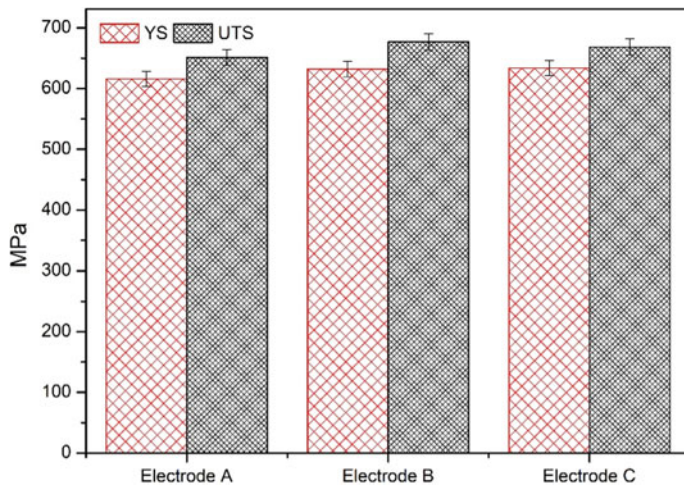


Fig. 2 Represents the tensile properties of the core wires used in different electrodes

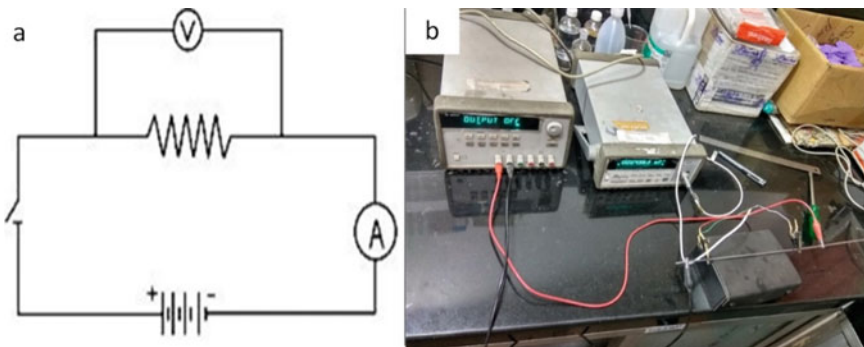


Fig. 3 Schematics show **a** diagram of the four-probe setup. **b** Electrical connections made on the sample; inner leads are for measuring voltage whereas outer lead is for passing current

nanovoltmeter (Agilent). Measuring the diameter of the rod with a Vernier calliper, the resistivity of the sample could be calculated using the following formula:

$$\rho = \frac{VA}{iL} \quad (1)$$

where V = potential difference, A = area of wire rod, i = current and L = length across which potential was measured. Figure 3b depicts the electrical connections on the samples. The inner leads are for measuring voltage drop and the outer leads for applying current. The electrical resistivity measured on the core wires is presented in Table 4. Slight variation can be observed arising out of minute changes in the

Table 4 Resistivity of core wires

Brand	Experimental resistivity ($\mu\Omega\text{-cm}$)
Electrode A	14.66 ± 0.10
Electrode B	14.84 ± 0.21
Electrode C	14.64 ± 0.33

core wires' chemical composition as electrodes were collected from three different sources.

2.3 Spatter Measurement

Welding experiments were carried out on M.S plates having dimensions $300 \times 300 \times 12 \text{ mm}^3$ using Fronius make magic wave 4000 power source. Electrodes were dried in an oven for 1 h at 135°C as per AWS A 5.1 recommendations. To measure the spatter generated during welding experiments, anti-spatter spray was sprayed (Fig. 4a) on M.S Plates before start of welding. Anti-spatter spray helps in easy removal of spatter after welding otherwise spatter sticks to the plate and is difficult to remove. Figure 4b demonstrates the SMAW process on the plate after spraying. And after that welding spatter was collected from the plate. Figure 4c shows the plate after removal of the spatter. Ultrasonic cleaning was done to remove the dirt from the spatter and subsequently the spatter was weighed on weighing balance as shown in Fig. 4d.

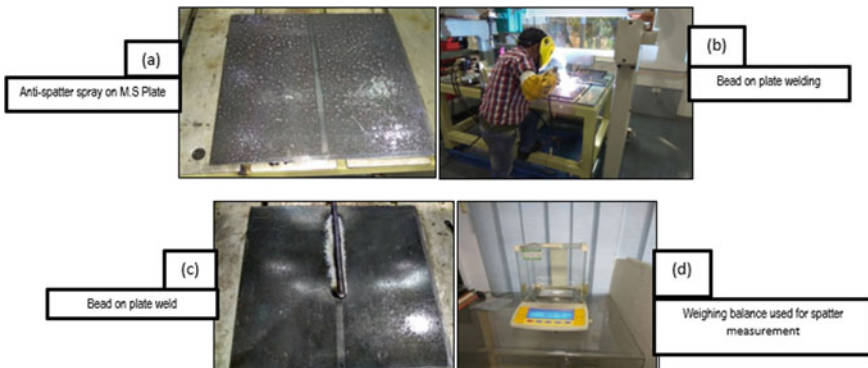


Fig. 4 Welding experiments setup and weighing balance machine

3 Results and Discussions

3.1 Spatter Analysis

Spatter measurement was done after welding as per procedure mentioned in Sect. 2.3. Figure 5a–c shows the spatter loss in DCEP, DCEN and AC power sources, respectively. Spatter values shown here are average spatter at each current level. Three tests were conducted at each current level. Spatter is found increased with increasing welding current irrespective of polarity. At higher welding current, more spatter may be attributed to higher melting rate of electrode [2, 6, 7]. Spatter loss is more in DCEP mode than the AC and DCEN modes. In DCEP mode, electrode melting rate is higher and penetration is higher while in DCEN mode electrode melting rate is slower and penetration is less thus DCEP results in higher spatter loss while DCEN produces lower spatter. In DCEP mode (Fig. 5a), Electrode C produced least spatter while Electrode B produced large spatter among three electrodes. In AC mode (Fig. 5c), Electrode A produced least spatter at both lower and higher currents (110 A, 130 A) while Electrode C wire produced large spatter. In DCEN mode (Fig. 5b) at lower current (110 A), Electrode A produced least spatter and at higher current. Electrodes A and B produced slightly less spatter than the Electrode C. Spatter loss was substantially higher when welding was carried out using DCEP (reverse polarity) and spatter was minimum when DCEN (straight polarity) was used. Spatter amount in AC welding was less than the DCEP but more than DCEN. Electrode A produced

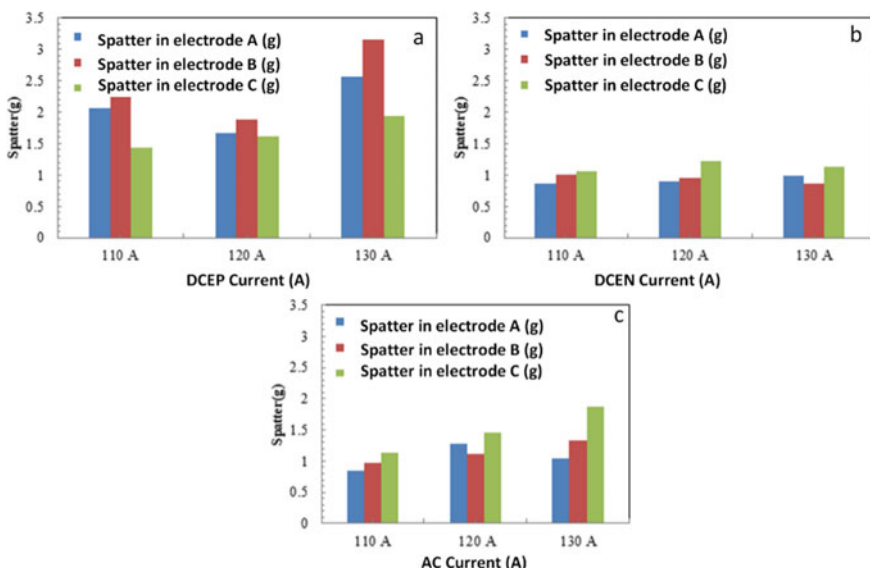


Fig. 5 Schematics show the spatter obtained during welding in **a** DCEP, **b** DCEN and AC current modes

fewer spatters than the Electrode B in almost all current levels. Maximum spattering in DCEP and minimum in DCEN may be attributed to the flow direction and hence striking of electron on electrode in DCEP. This results in higher heat generation on electrode and consequently more melting and spattering from electrode side [8, 9].

3.2 Visual Inspection and Chemical Analysis of the Weld Metal

The gap between the two MS plates has been filled with weld metal using the required electrode. After removing the spattering from the weldments, weld plates were radio-graphed to evaluate the soundness of the weld metal. Once the weldments were confirmed free from any internal and external cavity or crack, the weldments were used for mechanical property study. To determine the chemistry of the weld metal, the electrode is used to prepare a weld metal pad on a mild steel base plate as shown in Fig. 6c. It was subsequently ground to flat and then used for determining the steel chemistry. Weld metal chemistry conforms to AWS A5.1 requirement (Table 5).

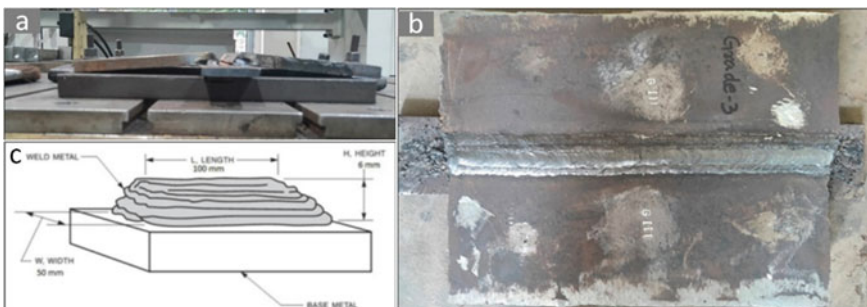


Fig. 6 Schematics show **a** base plate orientation during welding, **b** weldments top surface and **c** weld pad developed for chemical analysis

Table 5 Weld metal chemistry

Sl. no.	Electrode used	C	Mn	Si	S	P
1	AWS A5.1 required	0.2 max	1.2 max	1 max	NS	NS
2	Electrode A	0.054	0.23	0.101	0.019	0.030
3	Electrode B	0.058	0.23	0.101	0.019	0.023
4	Electrode C	0.057	0.23	0.101	0.019	0.025

NS Not specified in AWS A5.1 standard

3.3 Bead Profile Analysis

The cross-sectional view of the weld beads formed using three electrodes with different polarities (viz. AC, DCEP and DCEN) were photographed using a stereo microscope and presented in Figs. 7, 8 and 9. It is evident from these images that the weld beads formed using DCEP mode are showing the maximum depth of penetration when compared to AC and DCEN modes. This is applicable for all three electrodes used in this work. This is because in DCEP mode the arc strikes the substrate rather than hitting the electrode. Hence, more heat is produced in the base metal than the electrode. Thereby the melting rate of base metal is higher than that of the electrode. In case of DCEN mode, the polarity reverses (i.e. the arc strikes the electrode) and electrode melting rate exceeds the base metal melting rate and thereby results in a shallower weld bead. For AC power source, because of alternating polarity, both the base metal and electrodes are melted at equal rate and thereby produces weld bead with moderate penetration. Difference in weld bead geometry during welding in different polarities may be attributed to the current density and distribution [10].

Fig. 7 Macrostructure of the DCEP weldments

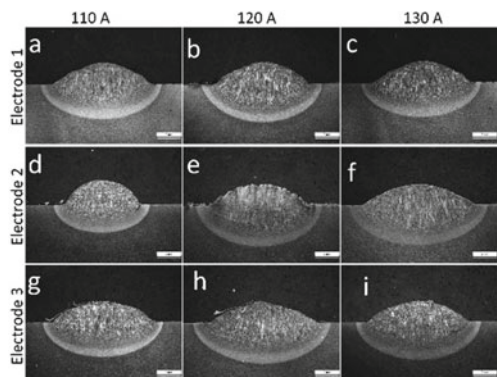


Fig. 8 Macrostructure of the DCEN weldments

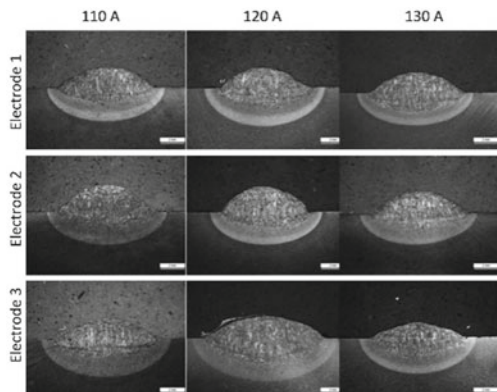
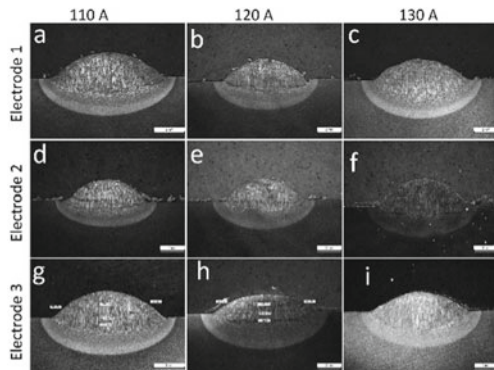


Fig. 9 Macrostructure of the AC weldments



A close examination of these data indicates all the three electrodes produced the similar kind of weld bead when the same mode was used. Hence, it can be concluded from this study that the electrodes under same classification having similar chemical composition do not affect the weld bead profile.

3.4 Tensile Behaviour

Cylindrical tensile samples were machined out of the weld metal as per the ASTM standard. The gauge length, gauge diameter, gripping length and gripping diameter were kept 54 mm, 12.5 mm, 40 mm and 16 mm, respectively. The tensile samples were loaded in an Instron make universal tensile machine using 5 mm/min cross-head speed. From the stress-strain response, the yield strength (YS), ultimate tensile strength (UTS) and ductility were calculated. All the samples were failed from the base metal during tensile testing. Tensile test results along with the tensile sample are shown in Fig. 10. It was observed that tensile strengths of all the weldments (Electrode A, Electrode B and Electrode C) were significantly higher than that of the AWS A5.1 standard requirement. Ultimate tensile strengths (UTS) and yield strengths (YS) of the weldments were too close to compare individually. Minor difference in the UTS and YS among them could be attributed to the chemical composition of the weldments.

4 Conclusions

On the basis of the current work, following conclusions have been drawn:

1. Current setting needs to be done as per recommended setting for the particular electrode since inappropriate current setting will result in either unstable arc or in excessive heating of electrode.

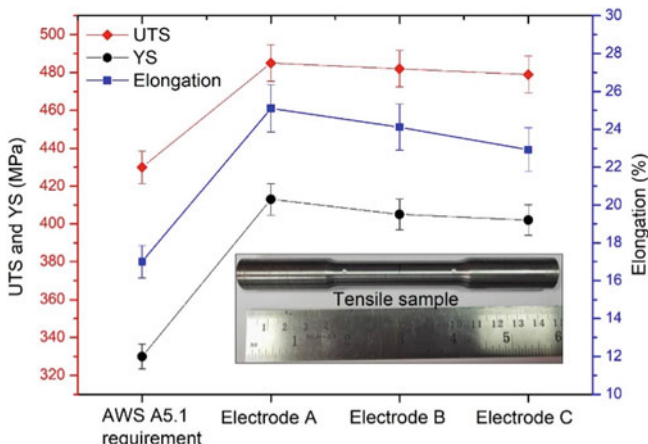


Fig. 10 Schematics shows the tensile test properties and the tensile test sample

2. Selection of appropriate current polarity is important while choosing E6013 electrode for a particular application. DCEN and AC polarities result in less spatter and controlled penetration. DCEP polarity results in more spatter and higher penetration.
3. Occasional problem of spatter experienced by customer may be due to flux composition and baking points that need to be addressed by the electrode manufacturer.
4. All weld chemistry and tensile strength are not significantly influenced for different brand electrodes; however, to achieve higher productivity by means of reduced weld spatter, appropriate weld bead profile, it is recommended to choose the electrode with due diligence.

References

1. Lancaster, J.F.: The physics of fusion welding. Part 2: Mass transfer and heat flow. IEE Proc. B Electr. Power Appl. **134**, 297 (1987). <https://doi.org/10.1049/ip-b.1987.0047>
2. Parmar, R.S.: Welding Processes and Technology (1996)
3. Crespo, A.C., Scotti, A., Pérez, M.R.: Operational behavior assessment of coated tubular electrodes for SMAW hardfacing. J. Mater. Process. Technol. **199**, 265–273 (2008). <https://doi.org/10.1016/j.jmatprotec.2007.07.048>
4. Vimal, K.E.K., Vinodh, S., Raja, A.: Optimization of process parameters of SMAW process using NN-FGRA from the sustainability view point. J. Intell. Manuf. **28**, 1459–1480 (2017). <https://doi.org/10.1007/s10845-015-1061-5>
5. Datta, R., Mukerjee, D., Jha, S., Narasimhan, K., Veeraraghavan, R.: Weldability characteristics of shielded metal arc welded high strength quenched and tempered plates. J. Mater. Eng. Perform. **11**, 5–10 (2002). <https://doi.org/10.1007/s11665-002-0001-7>
6. Sham, K., Liu, S.: Fluxcoating development for SMAW consumable electrode of highnickel alloys. Weld. J. 271–281 (2014)

7. Sowards, J.W., Ramirez, A.J., Dickinson, D.W., Lippold, J.C.: Characterization of welding fume from smaw electrodes—part II. *Weld. J.* **89**, 82–90 (2010)
8. Samardzic, I., Klaric, S., Siewert, T.: Application of an on-line weld monitoring system. *Adv. Technol. Dev. Countr.* 1–6 (2002)
9. Moreno-Uribe, A.M., Bracarense, A.Q., Pessoa, E.C.P.: The effect of polarity and hydrostatic pressure on operational characteristics of rutile electrode in underwater welding. *Materials (Basel)* **13**, 5001 (2020). <https://doi.org/10.3390/ma13215001>
10. A.I.A.S.I.A.S. Institute: Welding of Stainless Steels and Other Joining Methods, pp. 6–11

Modeling and Kinematic Analysis of a Robotic Manipulator for Street Cleaning Applications Using Screw Theory



Neel Gandhi, Garlapati Nagababu, and Janardhan Vistapalli

1 Introduction

Waste management is a major problem in all developing nations. To counter this problem, the Indian Government has introduced Swachh Bharat Abhiyan that involves making India a clean and hygienic nation. Inspired by the mission, portable vacuum cleaners as shown in (Fig. 1a) were made available for instant cleaning of garbage lying on the streets. However, most of them still require human intervention to manipulate its suction hose. The human has to take many precautions since he has to work in highly unsafe conditions, which are not recommended. To address this issue, a robotic manipulator is designed as shown in Fig. 1b, which can be attached to the suction hose of the portable vacuum cleaners as shown in Fig. 1c. Thus providing an integrated solution for waste management without any human intervention.

To realize the proposed robot, the fundamental step is to generate the motion trajectories for the end effector and find the joint angles accordingly. To achieve this, it is necessary to perform the kinematic analysis of the robotic manipulator. Many conventional mathematical techniques such as Denavit–Hartenberg parameters, Euler Angles, quaternions and screw coordinates, etc. can be used to define the kinematics of the robot. Screw coordinates have the advantages of singular free approach and geometric association with the kinematics of robot [1, 2]. Many researchers [3–8] in the recent times have used screw theory to depict the kinematic and dynamic behavior of their robot due to the aforementioned advantages. Screw theory plays a vital role in its implementation for a manipulator as it provides

N. Gandhi · G. Nagababu

School of Technology, Pandit Deendayal Petroleum University, Gandhinagar, India
e-mail: Nagababu.Garlapati@sot.pdpu.ac.in

J. Vistapalli (✉)

School of Engineering and Applied Sciences, SRM University, Andhra Pradesh, India
e-mail: Janardhan.v@srmap.edu

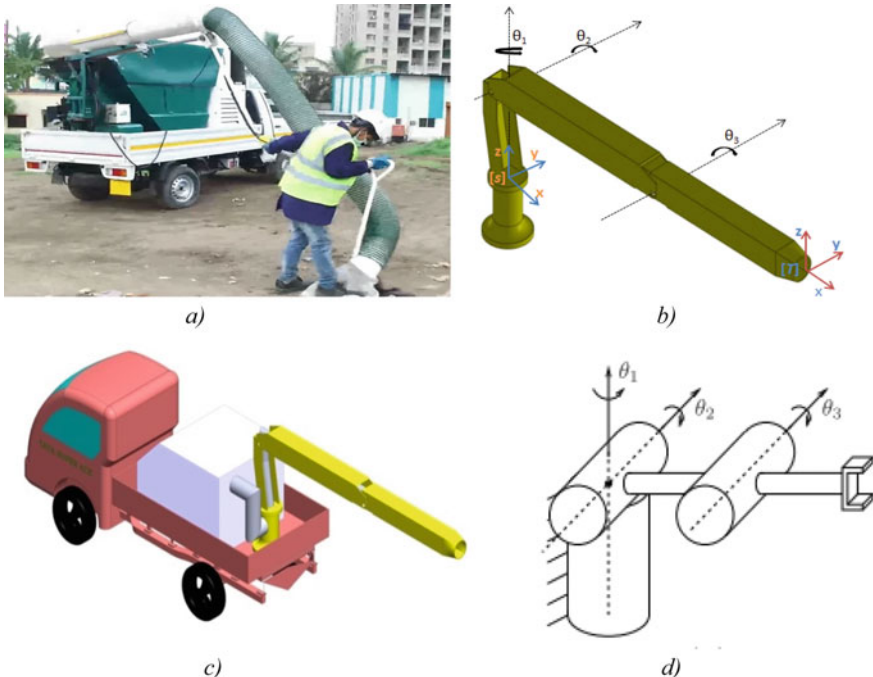


Fig. 1 Street cleaning manipulator anatomy. **a** Practical street cleaning equipment operated by human **b** Proposed robotic manipulator **c** Street cleaning equipment with the robotic manipulator attached **d** Line diagram of the manipulator

compact representation, device-independent features, visualizations, and many more advantages compared to conventional kinematic representation [9, 10].

Forward kinematics of the robot is used to compute the position and orientation of the end effector from specified joint solutions. Inverse kinematics (IK) of the robot is a complex task for a serial link robot as compared to forward kinematics [2]. Here the former one mainly computes the joint solutions given a homogenous transformation matrix (HTM), which encloses the rotation and position of the end-effector frame. Inverse kinematics using the Denavit–Hartenberg approach is mainly implicit and varies for different manipulator designs and thus it cannot be generalized for different manipulator designs. Whereas solving the inverse kinematics of the robot using Paden–Kahan sub-problems which utilizes fundamentals of screw theory leads to an explicit, compact, and precise IK solution [11] for the robot. The most commonly used sub-problems are stated in [2] but they still need to satisfy some pre-requisites to use them. However, there exist manipulators [11–14] that do not satisfy these conditions and thus various researchers over the years have tried to modify these sub-problems to generate IK solutions for them.

On the other hand, the conventional numerical inverse kinematic algorithms are also used to solve the inverse kinematics. They do converge fast to the solution,

Table 1 Description of joints and link lengths for 3-DOF manipulator

Joint	Link, length (meter)	Kinematic constraint	Axis of rotation	Range of motion
Joint-1	Link-1, 0.850	Revolute constraint	Z-axis	-90° to 90°
Joint-2	Link-2, 1.92	Revolute constraint	Y-axis	-45° to 45°
Joint-3	Link-3, 1.66	Revolute constraint	Y-axis	-120° to 120°

based on the condition that the initial guess of joint variables should be close to a true solution [1, 15]. In this article, both the geometrical algorithm and numerical algorithm for the street cleaning manipulator will be portrayed to determine which one is the most effective strategy for the manipulator, along with its mathematical progress.

Section 2 of this paper mainly deals with the design of the manipulator that has been proposed for the street cleaning process. Section 3 mainly approaches to define the mathematical rigor required for obtaining the IK solutions using PK sub-problems. Whereas in Sect. 4 results for the street cleaning manipulator will be discussed, and the methodology used to obtain IK solution for the designed manipulator and its simulation in the V-REP environment will be presented. In Sect. 5, conclusions of this research will be presented.

2 Anatomy of the Street Cleaning Manipulator

The design of the street cleaning manipulator (Fig. 1b) mainly consists of four links with three revolute joints in between and Fig. 1d depicts its line diagram. The specification of the joint along with the rotational axis and link length is shown in Table 1. Link lengths are designed taking into consideration the length of suction pipe for the manipulator, while the range of motion chosen is based on the interference of two links from the Computer-Aided Design (CAD) model.

3 Inverse Kinematics Modeling for 3-DOF Street Cleaning Manipulator

To automate the street cleaning process using portable vacuum cleaners, the manipulator needs to reach the desired location where the garbage lies. To achieve the desired task, the manipulator needs to know two configurations, the current configuration of the robot and the goal configuration from where the garbage picking has to be done. The manipulation task involves two parts: find the goal configuration of the robot and design a suitable trajectory to approach the goal configuration. Once the trajectory is designed, inverse kinematics for the manipulator at each point of

the trajectory needs to be executed to find the joint trajectories corresponding to the desired motion of the end effector.

3.1 3-DOF Street Cleaning Manipulator

The CAD model shown in Fig. 1b is designed using SolidWorks software for automating the garbage collection process. The basic foundation required for acquiring tools to model rigid body system using screw theory can be referred from [2].

As mentioned before, to complete manipulation task, the current configuration or the home configuration of the robot is required. The home configuration of the robot is given denoted as $g_{st}(0)$, which includes orientation and position of the end-effector frame w.r.t the base frame, at the beginning when no joints are actuated. $g_{st}(\theta)$ is found using Product of Exponentials (POE).

$$g_{st}(0) = \begin{bmatrix} 1 & 0 & 0 & 3.580 \\ 0 & 1 & 0 & 0 \\ 0 & 0 & 1 & 0.850 \\ 0 & 0 & 0 & 1 \end{bmatrix} \quad (1)$$

The desired configuration of the end effector is given by Eq. 2 which is known as product of exponentials

$$g_{st}(\theta) = e^{\xi_1} e^{\xi_2 \theta_2} e^{\xi_3 \theta_3} g_{st}(0) \quad (2)$$

where ξ is a six-dimensional vector representing linear and angular velocities for each joint, named as twist. Since there are three joints for 3-DOF Street cleaning manipulator their corresponding twists can be calculated as shown in Eq. 3.

$$\xi_1 = \begin{bmatrix} -\omega_i \times q_i \\ \omega_i \end{bmatrix} \quad (3)$$

where q_i represents point on joint axis and ω_i represents direction of angular velocity. The twists corresponding to the home configuration are given below:

$$\begin{aligned} \xi_1 &= \begin{bmatrix} 0 & 0 & 0 & 0 & 0 & 1 \end{bmatrix}^T, \xi_2 = \begin{bmatrix} -0.8500 & 0 & 0 & 0 & 1 & 0 \end{bmatrix}^T \\ \xi_3 &= \begin{bmatrix} -0.8500 & 0 & 1.9200 & 0 & 1 & 0 \end{bmatrix}^T, q_1 = [0, 0, 0]^T, q_2 = [0, 0, 0.850]^T \\ q_3 &= [1.920, 0, 0.850]^T, \omega_1 = [0, 0, 1]^T, \omega_2 = [0, 1, 0]^T, \omega_3 = [0, 1, 0]^T \end{aligned}$$

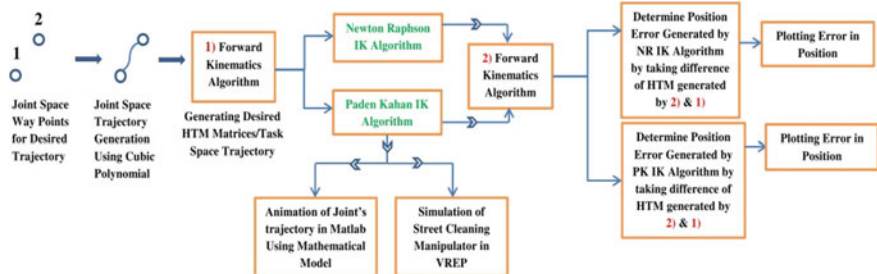


Fig. 2 Flowchart for the paper

Using the twists defined above, the desired configuration to perform forward kinematics can be written as given in Eq. 2 [2]. The desired orientation and position for the forward kinematics corresponding to $g_{st}(\theta)$ are given in Eq. 4. and Eq. 5, respectively.

$$R(\theta) = \begin{bmatrix} \cos(\theta_2 + \theta_3) * \cos(\theta_1) & -\sin(\theta_1) \sin(\theta_2 + \theta_3) * \cos(\theta_1) \\ \cos(\theta_2 + \theta_3) * \sin(\theta_1) & \cos(\theta_1) \sin(\theta_2 + \theta_3) * \sin(\theta_1) \\ -\sin(\theta_2 + \theta_3) & 0 & \cos(\theta_2 + \theta_3) \end{bmatrix} \quad (4)$$

$$P(\theta) = \begin{bmatrix} (\cos(\theta_1) * (83 * \cos(\theta_2 + \theta_3) + 96 * \cos(\theta_2))) / 50 \\ (\sin(\theta_1) * (83 * \cos(\theta_2 + \theta_3) + 96 * \cos(\theta_2))) / 50 \\ 17/20 - (48 * \sin(\theta_2)) / 25 - (83 * \sin(\theta_2 + \theta_3)) / 50 \end{bmatrix} \quad (5)$$

The desired trajectory is formulated as a cubic polynomial function of time based on the break points obtained using the CAD model designed in SolidWorks and flowchart of the paper is shown in Fig. 2.

3.2 Inverse Kinematics of Street Cleaning Manipulator Using Paden–Kahan Sub-Problems

Paden–Kahan sub-problems from mathematical point of view can be studied from [2]. To implement Paden–Kahan sub-problems, the manipulator needs to fulfill some pre-requisites, such as rotation to a given distance for applying sub-problem 3 and rotation about two subsequent axes for sub-problem 2. Satisfying these, the street cleaning manipulator mainly utilizes two sub-problems. The approach to implement Inverse Kinematics (IK) for current robot is as follows.

Once the configurations corresponding to the desired end-effector trajectory is obtained, the Paden–Kahan (PK) sub-problems can be implemented, taking into consideration $gst(\theta)$. To implement PK sub-problems, two points P and Q with

coordinates (3580, 0, 850), (0, 0, 850) in mm are considered from the home configuration. Now let us multiply Eq. 2, with point P on both sides as shown in Eq. 6. Since point P lies on the end-effector frame at its home configuration, and point Q lies on the intersection of the first two joint axis rotation, actuating the first two joints does not change the norm of the vector between points P and Q . Subtracting point Q from both sides of Eq. 6 as given in Eq. 7a and taking its norm in Eq. 7b set a perfect precondition require to execute Paden–Kahan sub-problem 3.

$$e^{\hat{\xi}_1\theta_1} e^{\hat{\xi}_2\theta_2} e^{\hat{\xi}_3\theta_3} P = g_{st}(\theta)g_{st}(0)^{-1} P \quad (6)$$

$$e^{\hat{\xi}_1\theta_1} e^{\hat{\xi}_2\theta_2} e^{\hat{\xi}_3\theta_3} P - Q = g_{st}(\theta)g_{st}(0)^{-1} P - Q \quad (7a)$$

$$\therefore \|e^{\hat{\xi}_3\theta_3} P - Q\| = \|g_{st}(\theta)g_{st}(0)^{-1} P - Q\| \quad (7b)$$

By reviewing [2] and using Eq. 8a, θ_3 can be solved as shown in Eq. 8b.

$$\theta_0 = a \tan 2\left(\omega^T(u' \times v'), u'^T v'\right) \quad (8a)$$

$$\theta_3 = \theta_0 \pm \cos^{-1}\left(\frac{\|u'\|^2 + \|v'\|^2 - \delta'^2}{2\|u'\|\|v'\|}\right) \quad (8b)$$

$$e^{\hat{\xi}_1\theta_1} e^{\hat{\xi}_2\theta_2} e^{\hat{\xi}_3\theta_3} P = g_{st}(\theta)g_{st}^{-1}(0)P \quad (9a)$$

$$\therefore e^{\hat{\xi}_1\theta_1} e^{\hat{\xi}_2\theta_2} P' = R, \text{where } P' = e^{\hat{\xi}_3\theta_3} P, R = g_{st}(\theta)g_{st}^{-1}(0)P \quad (9b)$$

Here u' , v' , and δ' are the projections of vector u ($p-r$), v ($q-r$), and δ ($p-q$) on the plane perpendicular to ω_3 , and r is the point on the axis of rotation. Now since multiple solutions for θ_3 are known. Multiplying P on both sides of Eq. 2 leads to Eq. 9a. Thus forming a base to apply sub-problem 2 and generate multiple joint angle solution for θ_1 , θ_2 which can be analyzed from [2] for the desired goal configuration of the manipulator.

Thus, applying these two sub-problems one can find multiple solutions for joint angles, for any desired end-effector configuration. Using the aforementioned criteria, an algorithm has been developed for solving inverse kinematics of street cleaning manipulator.

4 Results and Discussions

To verify the precision of the Paden–Kahan inverse kinematic algorithm, a random set of joint angles are chosen as

$$\theta_1 = \text{Pi}/3, \theta_2 = \text{Pi}/6, \theta_3 = \text{Pi}/4 \quad (10)$$

Using these joint angles as an input to the products of exponential in Eq. 2, the desired homogenous transformation matrix (HTM) consisting of rotation and position of the end-effector frame w.r.t space frame is generated. Taking this desired configuration as an input to the Paden–Kahan inverse kinematics algorithm, multiple solutions of joints angles are generated as shown in Table 2.

The results generated above show that the second set of joint angles are in good agreement with the joint angle of Eq. 10 which verifies the efficiency and precision of the inverse kinematic algorithm. Furthermore, to verify the performance of the inverse kinematic algorithm and its proficiency in a real-world application, curved trajectory has been designed that has to be traced by the end effector of the manipulator. The trajectory consists of 200 discrete samples of homogenous transformation matrices which represents the goal pose of the end effector at each of these sample points. Applying the Paden–Kahan inverse kinematics algorithm at each of the poses generates a joint trajectory which is taken as an input to the forward kinematics algorithm and Fig. 3 shows its animation in the MATLAB environment. The same set of joint angles generated by the Paden–Kahan IK algorithm is taken as an input in the @V-REP simulation environment for the designed manipulator, as seen in Fig. 4, generates a trajectory that is perfectly aligned with the animation generated by the mathematical model in Fig. 3 thus adding further reliability to the performance of the IK algorithm.

To show the computational efficacy of the Paden–Kahan-based inverse kinematic algorithm, the results are compared with the Newton–Raphson numerical inverse kinematic algorithm. Both the algorithms are used to solve inverse kinematics for the curved trajectory shown in Fig. 3, in the MATLAB environment (Windows 64 bit, Intel Core i3, 2.40 GHz, 4 GB RAM) and computational time was enlisted for solving the given trajectory for 100 times. A comparison of the results obtained can

Table 2 Solution set for inverse kinematics

No.	Joint	θ°
1	1	-120.0000
	2	108.4662
	3	45.0000
2	1	60.0000
	2	30.0000
	3	45.0000
3	1	-120.0000
	2	150.0000
	3	315.0000
4	1	60.0000
	2	71.5538
	3	315.0000

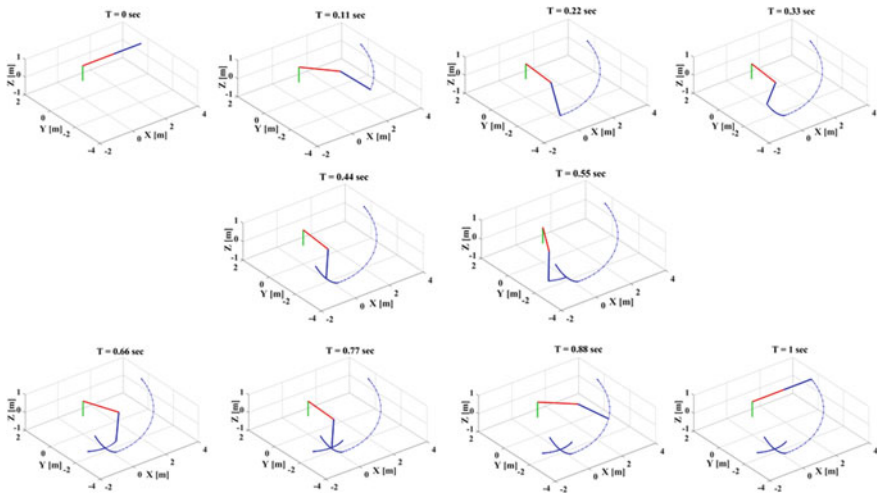


Fig. 3 Mathematical model animation using PK IK joint solutions

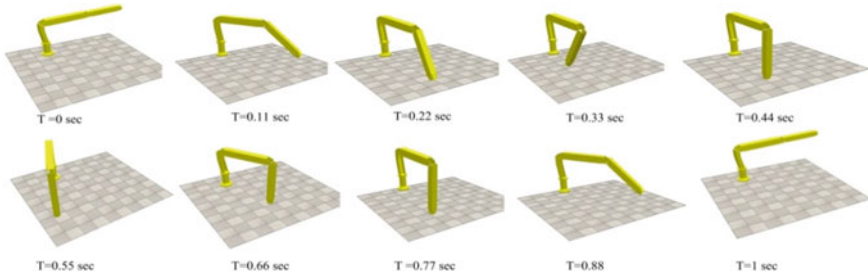


Fig. 4 Simulating trajectory of street cleaning manipulator in V-REP environment

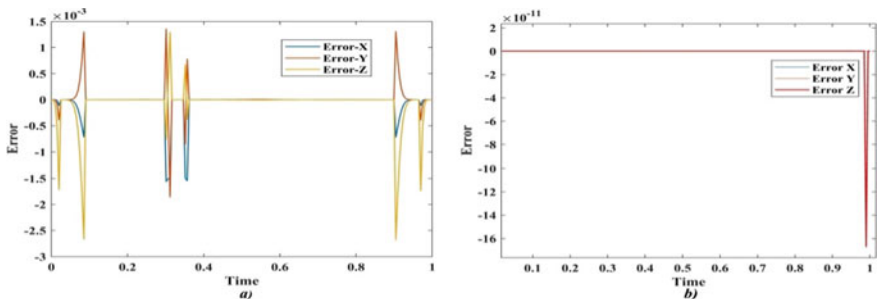


Fig. 5 Difference in Positions of End effector by different algorithms for desired trajectory **a** Error in Position Generated by NR Numerical Algorithm **b** Error in Position Generated by PK IK Algo-rithm

Table 3 Comparison between two algorithms

	Mean time (sec)	Max time (sec)
P-K IK algorithm	0.0396	0.0553
N-R IK algorithm	0.2355	0.3248

be seen in Table. 3. It can be observed that Paden–Kahan-based inverse kinematic algorithm is more potent in determining the solutions compared to a numerical-based inverse kinematic algorithm. As it requires a mean time of 0.0396 s to provide solutions compared to 0.2355 s for the numerical IK algorithm, mainly because of its association with Screw theory which provides geometric characteristics, free of complex matrix computation and precise multiple joint solutions compared to Newton–Raphson IK algorithm which requires complex matrix inverse matrix multiplication. Moreover, the results of the max time computation time also show that the Paden–Kahan inverse kinematic algorithm is preferable than the other one. The difference in the positions of the end effector for the desired and generated trajectory is also found and is depicted as error in Fig. 5. The error for the position in meter as depicted in Fig. 5b is in the range of 10^{-15} for the x- and y-components and in 10^{-11} for the z-component of the positions by Paden–Kahan algorithm. Whereas it is in the range of 10^{-4} in x-component and 10^{-3} for the y- and z-components as shown in Fig. 5a for the Newton–Raphson iterative algorithm. The variance and computational efficiency by Paden–Kahan algorithm is mainly because of its geometrical association provided by screw theory and free from lack of uncertainty to converge as it does not depend on initial guess which all the iterative algorithm like Newton–Raphson do, thus displaying the reliability of the Paden–Kahan Ik algorithm for the current robot.

5 Conclusion

A robotic manipulator attachment for street cleaning applications is proposed in this work. Formulation of forward kinematic for the proposed manipulator is done using screw theory. The joint motion trajectories for the robot are obtained using Paden–Kahan sub-problems for inverse kinematic solutions. The advocated inverse kinematic method using Paden–Kahan sub-problems can generate multiple solutions quickly due to its association with screw theory. Inverse kinematics for street cleaning manipulator can be easily obtained by reducing it into two subsequent sub-problems adding simplicity and getting rid of inverse matrix multiplication. Results obtained from the inverse kinematic algorithm for tracing a curved trajectory by the end effector are computationally efficient and accurate compared to the solutions obtained from numerical techniques like Newton–Raphson method. IK solutions based on Paden–Kahan sub-problems can meet real-time operational requirements. In future, the dynamic behavior of the street cleaning manipulator would be analyzed using

screw theory to design the actuation system and to implement it on the robotic manipulator.

References

1. Lynch, K.M., Park, F.C.: *Modern Robotics*. Cambridge University Press (2017)
2. Murray, Richard M., et al. *A mathematical introduction to robotic manipulation*. CRC press, 1994.
3. Sariyildiz, E., Cakiray, E., Temeltas, H.: A comparative study of three inverse kinematic methods of serial industrial robot manipulators in the screw theory framework. *Int. J. Adv. Rob. Syst.* **8**(5), 64 (2011)
4. Xiao, Q., Cao, Z., Dai, J.S.: Kinematics analysis of a snake robot module using screw theory. *Proc. ASME Des. Eng. Tech. Conf.* **5A-2016**, 1–9 (2016). <https://doi.org/10.1115/DETC2016-59273>
5. Hee Sung et al. "Geometrical kinematic solution of serial spatial manipulators using screw theory." *Mechanism and Machine Theory* 116 (2017): 404–418.
6. Liu, Zhifeng, et al. "Trajectory planning with minimum synthesis error for industrial robots using screw theory." *International Journal of Precision Engineering and Manufacturing* 19.2 (2018): 183–193.
7. Shi, Zhiping, et al. "Formal analysis of the kinematic Jacobian in screw theory." *Formal Aspects of Computing* 30.6 (2018): 739–757.
8. Yang, Bin, et al. "Kinematic modeling and machining precision analysis of multi-axis CNC machine tools based on screw theory." *Mechanism and Machine Theory* 140 (2019): 538–552.
9. Park, F.C.: Computational aspects of the product-of-exponentials formula for robot kinematics. *IEEE Trans. Autom. Control* **39**(3), 643–647 (1994)
10. Rocha, C. R., C. P. Tonetto, and Altamir Dias. "A comparison between the Denavit–Hartenberg and the screw-based methods used in kinematic modeling of robot manipulators." *Robotics and Computer-Integrated Manufacturing* 27.4 (2011): 723–728.
11. Dimovski, Igor, et al. "Algorithmic approach to geometric solution of generalized Paden Kahan Subproblems and its extension International Journal of Advanced Robotic Systems 15.1 (2018): 1729881418755157.
12. Tan YS, Cheng PL, Xiao AP. Solution for a new Sub-problem in Screw Theory and its' Application in the Inverse Kinematics of a Manipulator. In *Applied Mechanics and Materials* 2010 (Vol. 34, pp. 271–275). Trans Tech Publications Ltd.
13. Chen, Q., Zhu, S., Zhang, X.: Improved Inverse Kinematics Algorithm Using Screw Theory for a Six-DOF Robot Manipulator. *Int. J. Adv. Robot. Syst.* **12**(10), 1–9 (2015). <https://doi.org/10.5772/60834>
14. Zhao, Rongbo, et al. "Inverse kinematic solution of 6R robot manipulators based on screw theory and the Paden–Kahan subproblems." *International Journal of Advanced Robotic Systems* 15.6 (2018): 1729881418818297.
15. T Sugihara, Tomomichi. "Solvability-unconcerned inverse kinematics by the Levenberg–Marquardt method." *IEEE Transactions on Robotics* 27.5 (2011): 984–991.

Hybrid Electric Vechicle and Electric Vechicle Mechanisms

Dynamics and Isolation Capabilities of a Magnetic Spring-Based Quasi-Zero Stiffness Vibration Isolation Mechanism for Passenger Vehicle Seat Isolation



Prajapati Brijeshkumar and B. Santhosh

1 Introduction

Vibration at low excitation frequencies (0.5–5 Hz) affects the health of driver and passengers and reduces working efficiency [1]. To improve riders comfort, these low-frequency excitation vibrations need to be isolated. From last few decades, a lot of research have been performed for vibration isolation at low frequencies. Micro- or low-frequency vibration isolation by active, passive, and hybrid techniques was discussed by Liu et al. [2]. The linear isolators are effective for frequency ratio greater than $\sqrt{2}$. By using passive vibration isolation techniques, the vibration isolation at lower frequency is possible using the concept of high-static low-dynamic stiffness (HSLDS). HSLDS can be practically achieved by quasi-zero stiffness (QZS) based on negative stiffness concept. Carella et al. [3] obtained negative stiffness by using two linear springs which are obliquely arranged with respect to a vertical spring. Apart from oblique spring arrangement, buckled beam arrangement and magnetic spring mechanism as negative stiffness correctors were studied both analytically and experimentally [4]. Influence of asymmetry on the performance of QZS-based vibration isolation system was also investigated [5].

The development of QZS-based isolation system using oblique springs or buckled beams has limitation as there is contact between the moving points which lead to friction and thus reduces the performance efficiency. Magnetic spring-based isolation system overcomes the abovementioned difficulty. Ring-type permanent magnets were used to create negative stiffness and attached with mechanical springs and investigated by Zheng et al. [6] for vibration isolation capability.

P. Brijeshkumar · B. Santhosh (✉)

Department of Mechanical Engineering, Amrita School of Engineering, Amrita Vishwa Vidyapeetham, Coimbatore, India
e-mail: b_santhosh@cb.amrita.edu

Passenger seat with passive isolation for better comfort at lower frequency isolation with negative stiffness was investigated by DanhL et al. [7]. This paper proposed a system with two negative stiffness structure (NSS) in parallel with positive stiffness structure. NSS mechanism used with active isolation and parametric study was performed. NSS mechanism is used with active isolation and parametric study was performed by Liang et al. [8]. Magnetic spring can be possible with permanent magnets or electromagnets. Electromagnets are advantageous because the magnetic strength can be changed adaptively.

In this work, the vibration isolation capabilities of a magnetic spring-based negative stiffness isolator to isolate the low-frequency vibrations in a passenger seat are investigated numerically. Human body is modeled as a multi-degree-of-freedom system. The isolation capabilities are investigated using transmissibility plots. The results are compared with that of a conventional linear isolator to bring out the merits of the nonlinear isolator in isolating low-frequency vibrations.

2 Model and Design of Negative Stiffness Magnetic Spring Isolator

2.1 Model Setup

A geometric model of ring-type magnetic spring is shown in Fig. 1a adapted from the earlier study of Zheng et al. [6]. The mechanical spring and magnet arrangement of the model is shown in Fig. 1b. The radial thicknesses are given by T_1 and T_2 , height of magnets are $2L_1$ and $2L_2$, and radius of magnets are R_1 and R_2 for inner and outer magnets, respectively. The relative permeability μ of the magnet is taken as 1.05.

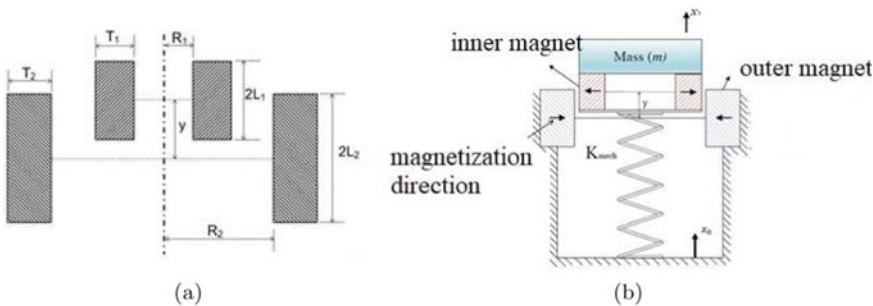


Fig. 1 Magnetic spring isolator **a** geometric parameters of the magnets **b** schematic model [6]

2.2 NSMS Isolator Arrangement for Passenger Seat

The negative stiffness model with two ring-type magnets and a mechanical spring is applied to passenger seat application as shown in Fig. 2. Outer ring-type magnet is fixed with base and the mechanical spring is connected with inner magnet at one end and with base at other magnet. When the base is excited by external excitation, it will displace the mechanical spring, which moves the inner magnet in the upward direction. The magnetic force is exerted due to relative displacement of magnets and it is in a direction opposite to the force generated by mechanical spring achieving low-dynamic stiffness. The seat is assumed to be excited harmonically at the base.

The equation of motion for the model can be expressed as

$$m\ddot{x}_1 + c\dot{y} + ky = F_m(y) \quad (1)$$

where m , c , and k mass, damping, and stiffness of the system. x_1 is the displacement of the seat and $y = x_1 - x_0$ is the relative displacement of the mass with the base.

2.3 Design of Geometric Parameters of NSMS for Passenger Seat Isolator

For applying NSMS isolator in the passenger seat application, geometric parameters are designed as per the procedure outlined in [6]. Linear spring stiffness is considered as 1.5×10^5 N/m in this study. For the condition of QZS, the magnetic stiffness should be near to -1.5×10^5 N/m. Here, negative sign indicates that magnetic spring force is in the opposite direction in relation with mechanical spring force. The effect of magnetic flux density, height, gap, and radial thickness of magnets on the stiffness has been studied in [6]. The geometric parameters and the magnetic strength used in the simulation are given in Table 1.

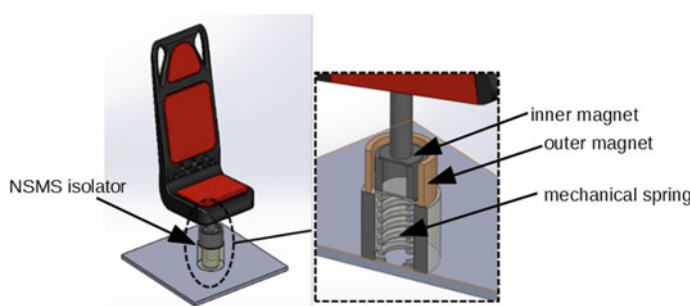
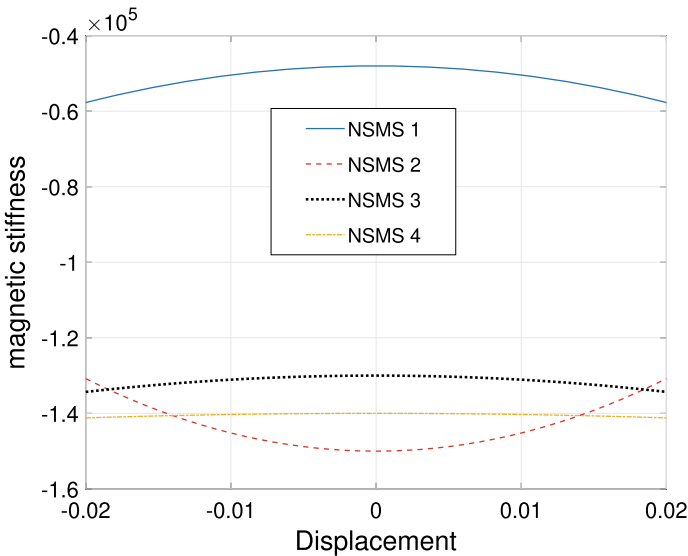


Fig. 2 Passenger seat with negative stiffness isolator

Table 1 Geometric and magnetic parameters used for simulation

	B (T)	R_1 (mm)	T_1 (mm)	T_2 (mm)	L_1 (mm)	L_2 (mm)	G (mm)
NSMS1	3	30	7	7	15	25	6.5
NSMS2	4	30	7	14	15	25	6.5
NSMS3	4	30	7	12	15	25	6
NSMS4	4	30	7	13	15	25	6

**Fig. 3** Magnetic stiffness selection based on geometric parameters

NSMS1 in Fig. 3 is chosen arbitrarily, which has more than the required negative stiffness as shown and not fit to the QZS model. To achieve higher negative stiffness, the flux density and the outer magnet thickness are increased in NSMS2. Magnetic stiffness is close to the required stiffness value but nonlinear in nature. Reducing gap between two magnets and radial thickness of outer magnet give linear magnetic stiffness as shown for NSMS3 in Fig. 3. At final to achieve magnetic stiffness in linear nature and close to mechanical stiffness, radial thickness of outer magnet is changed and stiffness curve for NSMS4 satisfies the required stiffness value for QZS.

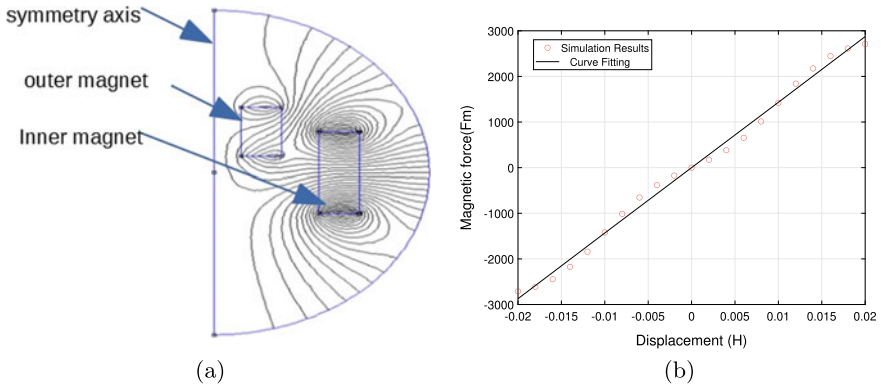


Fig. 4 **a** Magnetic flux lines **b** Magnetic force vs displacement simulation and curve fitting

2.4 Magnetic Simulation and Magnetic Force, Stiffness Equations for NSMS

Geometric parameters of the magnet are designed as given in previous section. Numerical simulations are performed with designed parameters in the software FEM magnetics. Magnet arrangement about axis of symmetry and magnetic flux lines are shown in Fig. 4a. The simulation provides the variation of magnetic force with displacement as shown in Fig. 4b with red circle and cubic curve fitting is used to get the relation of magnetic force with displacement of inner magnet. From simulation results and with curve fitting, magnetic force equation is given by

$$F_m(H) = 10^6 y^3 + 3.7 \times 10^{-10} y^2 + 1.4 \times 10^5 y - 3.7 \times 10^{-14} \quad (2)$$

The magnetic stiffness can be derived from the first derivative of magnetic force. Here, the restoring force produced by magnetic spring is in opposite direction to the magnetic force. The magnetic stiffness for designed NSMS is given in Eq. (3). Quadratic term of magnetic force in Eq. (2) is small and thus it is neglected for further study in this paper. The magnetic stiffness is obtained by differentiating the force equation and is given below:

$$K_m(H) = -3 \times 10^6 y^2 - 7.4 \times 10^{-10} y - 1.4 \times 10^5 \quad (3)$$

3 Results and Discussions

In this section, the magnetic spring-based QZS isolation system is included in a passenger vehicle seat with human body modeling it as a single degree-of-freedom system and also as a five degree-of-freedom system. The transmissibility plots are

obtained and compared with that for a system without QZS isolator to bring out the merits of the nonlinear isolator.

3.1 Single Degree-of-Freedom Modeling

The equation of motion for the system is given by Eq. (1). The magnetic spring force is given by

$$F_m(y) = f_1y + f_2y^3 \quad (4)$$

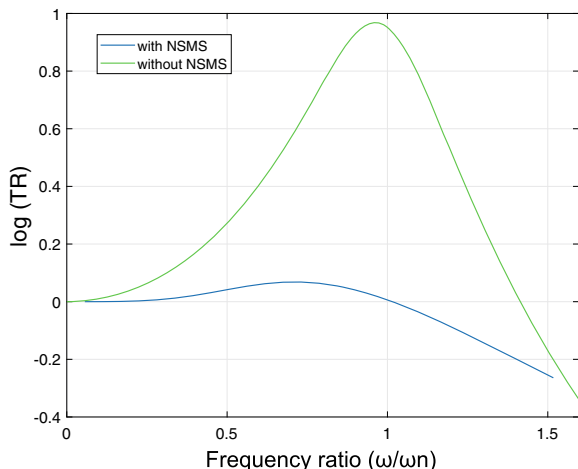
The values of $f_1 = 1.4 \times 10^5$ N/m and $f_2 = 10^6$ N/m³. The human body is modeled as a single degree-of-freedom system and the transmissibility plots are obtained for different values of passenger weights. The closed-form expression for transmissibility is given by [6]

$$TR = \sqrt{1 + U^2 + \frac{2U}{\beta^2}(\beta^2U + U + \frac{3}{4}\delta U^3)} \quad (5)$$

where U is the response amplitude, β is the frequency ratio, and $\delta = -\frac{f_2 X_0}{k - f_1}$ with X_0 is the amplitude of base excitation.

The transmissibility plot for passenger mass of 80 kg with and without NSMS is shown in Fig. 5, and other parameters of isolator are mechanical spring stiffness which is 1.5×10^5 N/m and damping co-efficient which is 1450 Ns/m. The external excitation is considered $0.02 \cos(\omega t)$. It is found that the addition of magnetic stiffness improves the low-frequency vibration isolation.

Fig. 5 Comparison of the transmissibility plots for sdf linear and QZS isolation system



3.2 Human Body Model with QZS Isolator as a Five Degree-of-Freedom System

In this section, the human body along with the QZS isolator system is modeled as a five degree-of-freedom system as shown in Fig. 6. The equations of motion considering the QZS isolator placed between the ground and the seat m_1 are given below:

$$m_1 \ddot{z}_1 + (c_1 + c_2) \dot{z}_1 - c_2 \dot{z}_2 + z_1(k_{QZS} + k_2) - z_2 k_2 - c_1 \dot{z}_0 - k_{QZS} z_0 = 0 \quad (6)$$

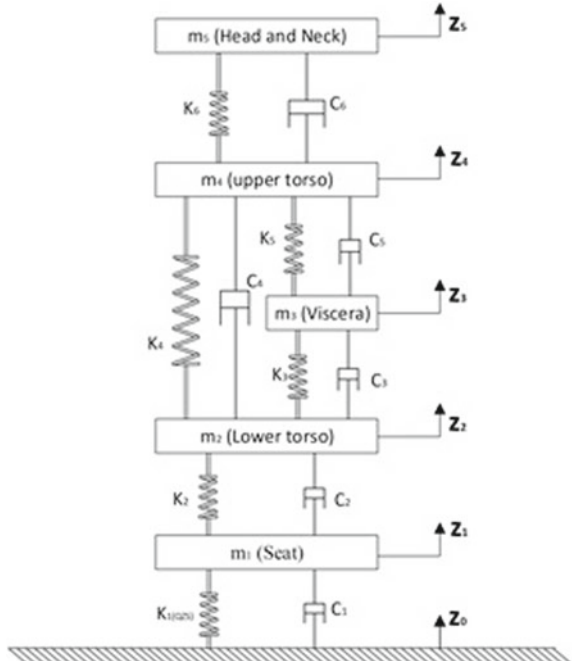
$$\begin{aligned} m_2 \ddot{z}_2 - c_1 \dot{z}_1 + (c_2 + c_3 + c_4) \dot{z}_3 - c_3 \dot{z}_3 - c_4 \dot{z}_4 - k_2 z_1 \\ + (k_2 + k_3 + k_4) z_2 - k_3 z_3 - k_4 z_4 = 0 \end{aligned} \quad (7)$$

$$m_3 \ddot{z}_3 - c_3 \dot{z}_2 + (c_3 + c_5) \dot{z}_3 - c_5 \dot{z}_4 - k_3 z_2 + (k_5 + k_3) z_3 - k_5 z_4 = 0 \quad (8)$$

$$\begin{aligned} m_4 \ddot{z}_4 - c_4 \dot{z}_2 - c_5 \dot{z}_3 + (c_4 + c_5 + c_6) \dot{z}_4 - c_6 \dot{z}_5 \\ - k_4 z_2 - k_5 z_3 + (k_4 + k_5 + k_6) z_4 - k_6 z_5 = 0 \end{aligned} \quad (9)$$

$$m_5 \ddot{z}_5 - c_6 \dot{z}_4 + c_6 \dot{z}_5 - k_6 z_4 + k_6 z_5 = 0 \quad (10)$$

Fig. 6 Human body with QZS isolator system modeled as a five degree-of-freedom system



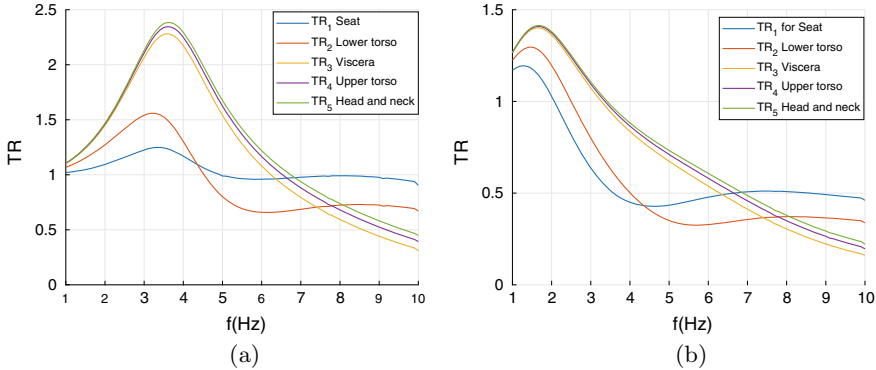


Fig. 7 Transmissibility plots **a** without NSMS **b** with NSMS

In the above equation, k_{QZS} is the quasi-zero stiffness and is given by

$$k_{QZS} = -k + f_1 y - 3f_2 y^2 \quad (11)$$

The equations of motion are integrated numerically and the transmissibility plots for all human parts without negative stiffness magnetic spring (NSMS) and with NSMS are shown in Fig. 7. The following parameters are used in the simulation, $m_1 = 10\text{ kg}$, $m_2 = 36\text{ kg}$, $m_3 = 5.5\text{ kg}$, $m_4 = 15\text{ kg}$, $m_5 = 4.17\text{ kg}$, $k_2 = 49340\text{ N/m}$, $k_3 = 20000\text{ N/m}$, $k_4 = 192000\text{ N/m}$, $k_5 = 10000\text{ N/m}$, $k_6 = 134400\text{ N/m}$, $c_1 = 1450\text{ Ns/m}$, $c_2 = 2475\text{ Ns/m}$, $c_3 = 330\text{ Ns/m}$, $c_4 = 909.1\text{ Ns/m}$, $c_5 = 200\text{ Ns/m}$, and $c_6 = 250\text{ Ns/m}$ [8]. The percentage improvement compared to the linear system is given in Table 2. With NSMS system an improvement of up to 57.29% in the seat and 44.31% in lower torso is observed. There are discomforts due to low-frequency vibration like general discomfort between 4 and 9 Hz, lower jaw symptoms 6–8 Hz, chest pains 5–7 Hz, muscle contraction 4–9 Hz, and abdominal pains 4–10 Hz given in [9]. These discomfort can be eliminated using NSMS isolator. All human body parts are isolated well below the discomfort frequencies as shown in Table 2. Thus, NSMS isolator provides better vibration isolation compared to linear isolator for different parts of human body.

The percentage improvement in the low-frequency vibration isolation when QZS isolator is implemented is shown in Table 2. This study can be further extended by considering more sophisticated models for human body as well as vibration isolation in six directions to completely understand the dynamics.

Table 2 Vibration isolation comparison

Component	Isolation frequency without NSMS with NSMS	% improvement
Seat	4.8 2.05	57.29
Lower torso	4.4 2.4	44.31
Viscera	6.25 3.25	48
Upper torso	6.6 3.35	49.24
Head and neck	6.75 3.45	48.88

4 Conclusions

In this paper, the vibration isolation capability of a quasi-zero stiffness (QZS)-based vibration isolator to isolate the low-frequency vibrations in a passenger seat is investigated numerically. The QZS isolator is obtained by using the negative stiffness magnetic springs (NSMS) in combination with a vertical spring. The seat along with the passenger is first modeled as a single degree-of-freedom and also as a five degree-of-freedom model. The magnetic spring characteristics are obtained by performing simulations in FEMM software and the curve fitting revealed that the stiffness characteristics are cubic in nature. The equations of motions are derived and the transmissibility plots are obtained by numerically integrating the equations. From the transmissibility plots, it is found that the QZS isolator provides better isolation compared to the conventional linear isolator. By modeling human body as a four degree-of-freedom system, it is possible to obtain the transmissibility plots for different body parts. It is found from the simulation results that the passenger seat with QZS isolator is able to isolate all low-frequency vibrations which produce discomfort to the passengers.

References

1. Paddan, G.S., Griffin, M.J.: Evaluation of whole-body vibration in vehicles. *J. Sound Vib.* **253**(1), 195–213 (2002)
2. Liu, C., Jing, X., Daley, S., Li, F.: Recent advances in micro-vibration isolation. *Mech. Syst. Signal Process.* **56**, 55–80 (2015)
3. Carrella, A., Brennan, M.J., Waters, T.P., Shin, K.: On the design of a high-static low-dynamic stiffness isolator using linear mechanical springs and magnets. *J. Sound Vib.* **315**(3), 712–720 (2008)
4. Lan, C.-C., Yang, S.-A., Yi-Syuan, W.: Design and experiment of a compact quasi-zero-stiffness isolator capable of a wide range of loads. *J. Sound Vib.* **333**(20), 4843–4858 (2014)
5. Santhosh, B.: Dynamics and performance evaluation of an asymmetric nonlinear vibration isolation mechanism. *J. Brazilian Soc. Mech. Sci. Eng.* **40**(4), 169 (2018)
6. Zheng, Y., Zhang, X., Luo, Y., Yan, B., Ma, C.: Design and experiment of a high-static low-dynamic stiffness isolator using a negative stiffness magnetic spring. *J. Sound Vib.* **360**, 31–52 (2016)

7. Le, T.D., Ahn, K.K.: A vibration isolation system in low frequency excitation region using negative stiffness structure for vehicle seat. *J. Sound Vib.* **330**(26), 6311–6335 (2011)
8. Liang, C.-C., Chiang, C.-F.: A study on biodynamic models of seated human subjects exposed to vertical vibration. *Int. J. Ind. Ergon.* **36**(10), 869–890 (2006)
9. Rasmussen, G.: Human body vibration exposure and its measurement. *J. Acoustical Soc. Am.* **73**(6), 2229–2229 (1983)

Vertical Vibrations of the Vehicle Excited by Ride Test



Massimo Cavacece, Giorgio Figliolini, and Chiara Lanni

1 Introduction

The influence of a rough road surface on vehicle vertical vibrations and on the driver and passengers is an important research among automotive manufacturers [3]. ISO international standard defines the terminology of vehicle dynamics and road-holding ability. In addition, ISO international standard proposes the test procedures for steady-state circular driving behavior and lateral transient response characteristics against step steering input, sinusoidal steering input, random steering input, and braking in a turn [6]. The standardized test procedure of a double-lane-change test as a severe lane-change maneuver is proposed [2]. In order to estimate the influence of vertical vibration on seated human body, the apparent mass of the human body is evaluated by mechanical lumped models [4]. In this research, a mechanical equivalent model has been developed to characterize the response of the vehicle excited by road profiles. The mechanical equivalent model offers a quantitative evaluation of accelerations of vehicle along vertical axis in terms of natural frequencies and dissipative properties of vehicle. In order to calibrate the mathematical model, an experimental design has been developed by the ride test.

M. Cavacece (✉) · G. Figliolini · C. Lanni

Department of Civil and Mechanical Engineering, University of Cassino and Southern Lazio, Cassino, Italy

e-mail: cavacece@unicas.it

URL: <https://www.unicas.it/>

2 Suspension System

The mass m_s represents the suspended mass (equal to a quarter of the mass of the entire vehicle) (Fig. 1). The unsprung mass associated with the suspension-wheel system is m_u . The variables z_s and z_u represent, respectively, the displacements, with respect to a horizontal reference axis, of the center of gravity of the suspended and unsprung mass. The quantity z_r describes the profile of the road surface. The stiffness constant k_u represents the elasticity of tire. The parameters k_s and c_s are, respectively, the elastic constant and the damping coefficient of the part passive suspension. The rest lengths of the corresponding springs are L_s and L_w . The force generated by the actuator between the wheel and the vehicle is $F(t)$ [1]. The g term is the acceleration of gravity. Model suspension system is described by the following equations:

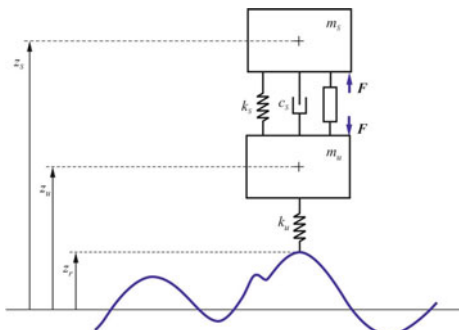
$$\begin{aligned} m_s \ddot{z}_s(t) &= k_s [z_u(t) - z_s(t)] + c_s [\dot{z}_s(t) - \dot{z}_u(t)] + k_s L_s - m_s g + F(t) \\ m_u \ddot{z}_u(t) &= -k_s [z_u(t) - z_s(t)] + c_s [\dot{z}_s(t) - \dot{z}_u(t)] - k_s L_s \\ &\quad + k_u [z_r(t) - z_u(t)] + k_u L_u - m_u g - F(t) . \end{aligned} \quad (1)$$

From the equilibrium equations corresponding to the null values of z_r and F , we obtain

$$\begin{aligned} \bar{z}_s &= L_s + L_u - \left(\frac{m_s}{k_s} + \frac{m_s + m_u}{k_s} \right) g \\ \bar{z}_u &= L_u - \frac{(m_s + m_u)}{k_u} g . \end{aligned} \quad (2)$$

Equation (2) represents the positions of the center of gravity of the suspended mass and of the unsprung mass in static conditions, under the action of gravity. The following notation is introduced:

Fig. 1 Vehicle suspension system



$$\begin{aligned}\delta z_s(t) &= z_s(t) - \bar{z}_s, \\ \delta z_u(t) &= z_u(t) - \bar{z}_u \\ \delta z_r(t) &= z_r(t) - \bar{z}_r = z_r(t).\end{aligned}\quad (3)$$

We obtain the following system of equations:

$$\begin{aligned}m_s \ddot{\delta z}_s(t) &= k_s [\delta z_u(t) - \delta z_s(t)] + c_s [\dot{\delta z}_s(t) - \dot{\delta z}_s(t)] + F(t) \\ m_u \ddot{\delta z}_u(t) &= -k_s [\delta z_u(t) - \delta z_s(t)] - c_s [\dot{\delta z}_s(t) - \dot{\delta z}_s(t)] \\ &\quad + k_u [\delta z_r(t) - \delta z_u(t)] - F(t).\end{aligned}\quad (4)$$

State vectors are defined

$$\mathbf{x}(t) = \begin{Bmatrix} \delta z_s(t) \\ \delta z_u(t) \\ \dot{\delta z}_s(t) \\ \dot{\delta z}_u(t) \end{Bmatrix}, \quad \mathbf{u}(t) = \begin{Bmatrix} \delta z_r(t) \\ F(t) \end{Bmatrix}. \quad (5)$$

The equations become

$$\dot{\mathbf{x}} = \mathbf{Ax}(t) + \mathbf{Bu}(t), \quad (6)$$

with

$$\mathbf{A} = \begin{bmatrix} 0 & 0 & 1 & 0 \\ 0 & 0 & 0 & 1 \\ -\frac{k_s}{m_s} & \frac{k_s}{m_s} & -\frac{c_s}{m_s} & \frac{c_s}{m_s} \\ \frac{k_s}{m_u} & \frac{(k_s + k_u)}{m_s} & \frac{c_s}{m_s} & -\frac{c_s}{m_s} \end{bmatrix}, \quad \mathbf{B} = \begin{bmatrix} 0 & 0 \\ 0 & 0 \\ 0 & \frac{1}{m_s} \\ \frac{k_u}{m_u} & -\frac{1}{m_u} \end{bmatrix}. \quad (7)$$

The model's output variables are the vertical acceleration of the vehicle $a_s(t)$ and the variation of the contact force between the wheel and the road with respect to the force value static contact:

$$\delta F_c(t) = F_c(t) - \bar{F}_c = k_u [\delta z_u(t) - \delta z_r(t)]. \quad (8)$$

with $\bar{F}_c = (m_s + m_u)g$. We obtain

$$y(t) = \begin{Bmatrix} a_s(t) \\ \delta F_c(t) \end{Bmatrix} = \mathbf{Cx}(t) + \mathbf{Du}(t) \quad (9)$$

with

$$\mathbf{C} = \begin{bmatrix} -\frac{k_s}{m_s} & \frac{k_s}{m_s} & -\frac{c_s}{m_s} & \frac{c_s}{m_s} \\ 0 & k_u & 0 & 0 \end{bmatrix} \quad \mathbf{D} = \begin{bmatrix} 1 & 0 \\ \frac{1}{m_s} & -k_u \end{bmatrix}. \quad (10)$$

Equation (10) constitutes a state-space representation of the system. The dynamic system is invariant not strictly proper, of order 4, with two inputs and two outputs (MIMO system model). The first input can be seen as a disturbance, while the second is the control variable.

3 Open-Loop Transfer Functions

Considering the open loop, the inputs are δz_r and F and outputs are a_s and δF_c [1]. The transfer functions between the two inputs and the two outputs are the following relations:

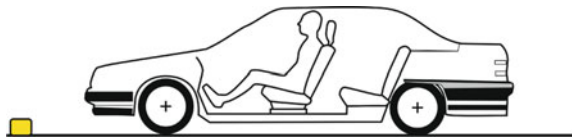
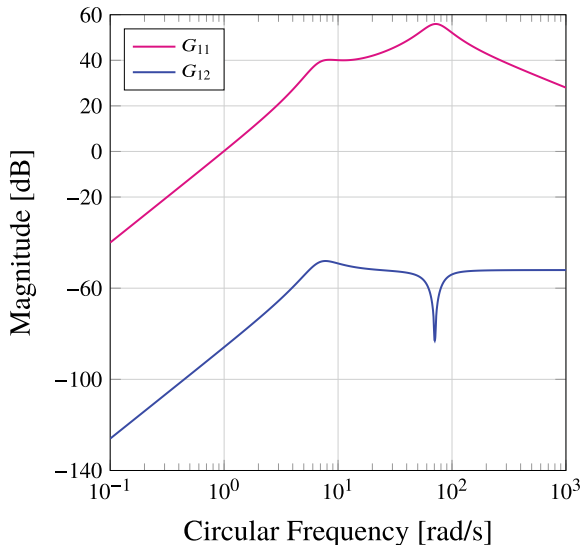
$$\begin{aligned} G_{11}(s) &= \frac{A_s(s)}{Z_r(s)} = \frac{\mu_{11}s^2(1+s\tau_1)}{\left(1 + \frac{2\xi_1 s}{\omega_{n1}} + \frac{s^2}{\omega_{n1}^2}\right)\left(1 + \frac{2\xi_2 s}{\omega_{n2}} + \frac{s^2}{\omega_{n2}^2}\right)} \\ G_{12}(s) &= \frac{A_s(s)}{F(s)} = \frac{\mu_{12}s^2\left(1 + \frac{s^2}{\omega_{n1}^2}\right)}{\left(1 + \frac{2\xi_1 s}{\omega_{n1}} + \frac{s^2}{\omega_{n1}^2}\right)\left(1 + \frac{2\xi_2 s}{\omega_{n2}} + \frac{s^2}{\omega_{n2}^2}\right)} \\ G_{21}(s) &= \frac{F_c(s)}{Z_r(s)} = \frac{\mu_{21}s^2(1+s\tau_1)(1+s\tau_2)}{\left(1 + \frac{2\xi_1 s}{\omega_{n1}} + \frac{s^2}{\omega_{n1}^2}\right)\left(1 + \frac{2\xi_2 s}{\omega_{n2}} + \frac{s^2}{\omega_{n2}^2}\right)} \\ G_{22}(s) &= \frac{F_c(s)}{Z_r(s)} = \frac{\mu_{22}}{\left(1 + \frac{2\xi_1 s}{\omega_{n1}} + \frac{s^2}{\omega_{n1}^2}\right)\left(1 + \frac{2\xi_2 s}{\omega_{n2}} + \frac{s^2}{\omega_{n2}^2}\right)}. \end{aligned} \quad (11)$$

There are two resonance conditions for the system: one at ω_{n1} and another at ω_{n2} . The damping factors associated with the conjugated complex pole pairs are low values. In addition, the functions $G_{11}(s)$, $G_{12}(s)$, $G_{21}(s)$, and $G_{22}(s)$ contain a double derivative action.

The effect of the road profile on vertical acceleration is analyzed, in the absence of control actions. Figure 3 shows the Bode diagram of the magnitude of the $G_{11}(s)$ transfer function. The values of the transfer function $G_{11}(s)$ show high values in the medium- to high-frequency range. The transfer function $G_{11}(s)$ peaks at the natural frequency ω_{n2} . An effective suspension system mitigates the values of peaks.

The vehicle is equipped with passive suspension. Vehicle speed is $v = 10 \text{ km/h} \cong 2.8 \text{ m/s}$ on a rectangular bump. Table 1 shows input data of mathematical modeling and simulation. The profile of the bump is shown in Fig. 2.

The wheel hits the bump at $t = 1 \text{ s}$. The wheel leaves the bump at $t = 3 \text{ s}$. Figure 4 shows the time trends of vertical acceleration and contact force caused by the bump profile. If the road profile presents an irregular appearance, described by a random

Fig. 2 Ride test**Fig. 3** Bode diagram

sign, the trends of accelerations and forces in time domain are proposed in Fig. 5. The Bode diagrams of the function $G_{12}(s)$ express the effect of the input $F(t)$ on the vertical acceleration (Fig. 3).

Two zeros at 0 Hz increase the transfer function $G_{11}(s)$ from 0 to 7 rad/s. Zero at about 10.0 rad/s of the transfer function $G_{11}(s)$ generates 40 dB from 6.92 rad/s to 14 rad/s (Table 2).

4 Experimental Design

In order to evaluate ride performance (Fig. 2), an accelerometer is attached at vehicle floor as shown in figure. An Axivity 6-axis accelerometer is used to measure the vibrations of six components of acceleration at a vehicle floor. The vertical component of the acceleration is utilized. The frequency range is from 0.5 to 1000 rad/s. A rectangular-shaped cleat bar on a road, shown in Fig. 2, is chosen for an impact object driving test [5]. The height and width of rectangular-shaped cleat bar are, respectively, 20 and 20 mm. The test speed is constant at 50 kph while front and rear tires are passing over the cleat bar. The experimental investigations consider the vertical vibrations of the elegant car during four ride tests (Figs. 6, 7, 8, 9, 10, 11,

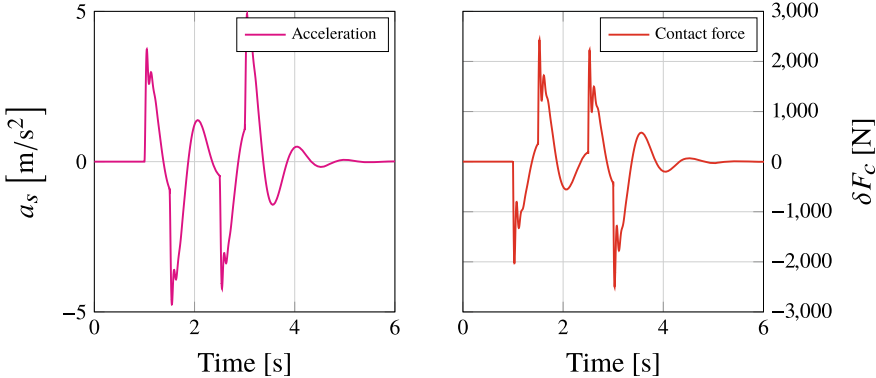


Fig. 4 Vertical accelerations of mass m_s and contact forces of open-loop system with rectangular bump ($v = 10$ km/h)

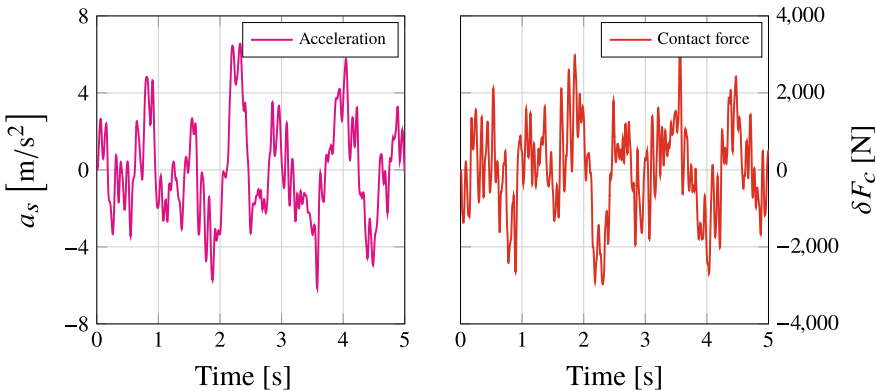


Fig. 5 Vertical accelerations of mass m_s and contact forces of open-loop system with random sign ($v = 10$ km/h)

12, and 13). The car is excited by road profiles. The time interval after impact is considered to estimate the vertical vibrations of vehicle.

5 Discussion

The impact object driving test characterizes the vehicle running over various impact objects. The frequencies of impact ranges from 1.5 to 50 Hz. Experimental investigations indicate relevant movements of the human body during vibration in the range from 4.5 to 7 Hz [5]. The vertical components of accelerations are obtained by ride test. The seat-rail vibrations are analyzed in terms of vertical components of accelerations in time and frequency domains (Figs. 6, 7, 8, 9, 10, 11, 12, and

Fig. 6 Vertical accelerations of mass m_s during Ride Test 1 in time domain

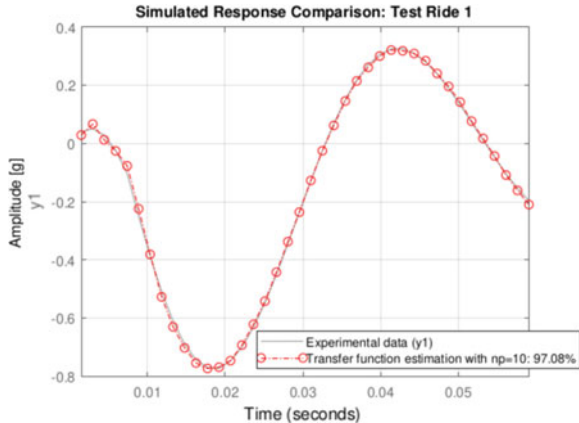
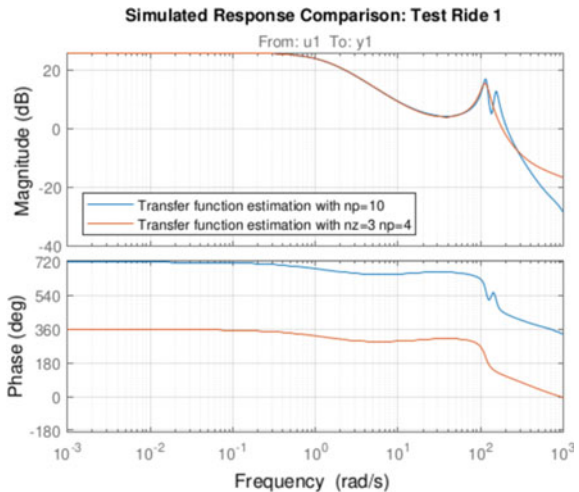


Fig. 7 Vertical accelerations of mass m_s during Ride Test 1 in frequency domain



13). The comparison between acceleration values obtained by mathematical model and ones obtained by experimental investigation is shown in Figs. 6, 8, 10, and 12. The comparison offers a good agreement (84–99%) between acceleration values obtained by mathematical model and ones obtained by experimental investigation in time domain. The mathematical simulation and the experimental investigation concern short and single impact test. The circular frequencies of vertical accelerations of vehicle excited by ride tests lie in three different regions 0–10, 10–20, and 20–80 [rad/s] (Figs. 7, 9, 11, and 13).

If rear tires are passing over the cleat bar, the peak value of the vertical component of vehicle increases. After the impact of rear tires, the vertical component is not easily damped out. One reason for the low damping is that the irregularities of road profile excite the vehicle after the impact between a vehicle and a rectangular-shaped cleat

Fig. 8 Vertical accelerations of mass m_s during Ride Test 1 in time domain

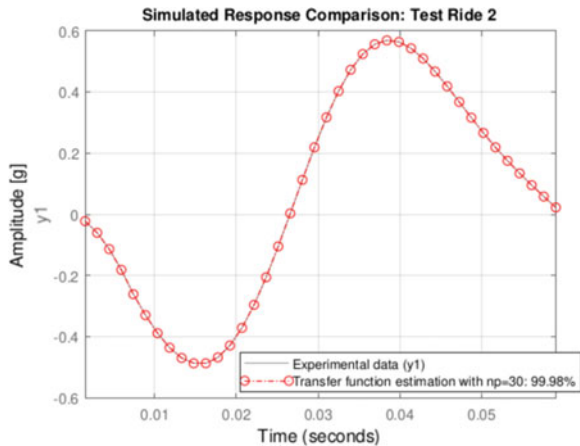
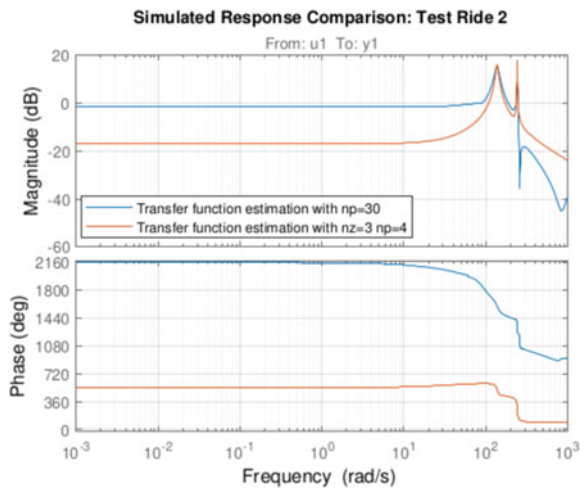


Fig. 9 Vertical accelerations of mass m_s during Ride Test 1 in frequency domain



bar on a road. Figure 14 illustrates damping ratio versus damped frequencies of the vehicle evaluated by ride test.

Table 3 shows the values of the composite weighted level and the fourth power vibration dose VDV for ride test ($v = 50$ km/h).

Fig. 10 Vertical accelerations of mass m_s during Ride Test 2 in frequency domain

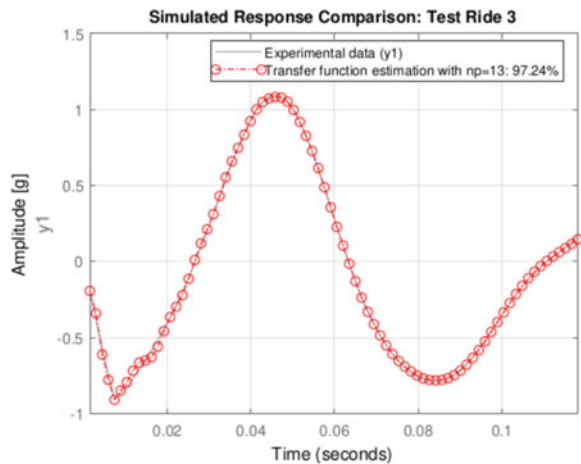


Fig. 11 Vertical accelerations of mass m_s during Ride Test 3 in time domain

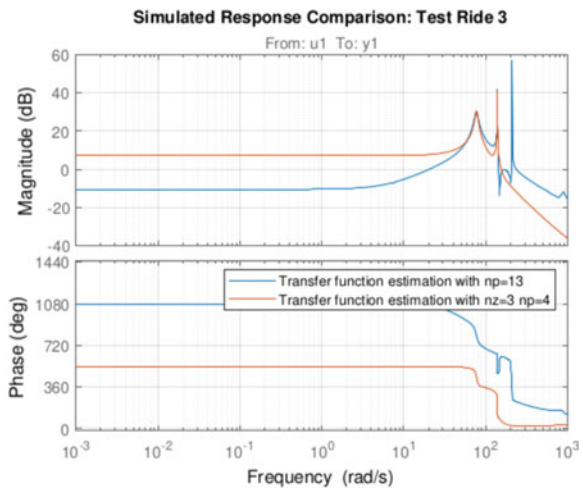


Table 1 Input data

Symbol	Description	Numerical value
m_s	Suspended mass	400 [kg]
m_u	Unsprung mass	50 [kg]
k_u	Elasticity of tire	$2.5 \cdot 10^5 \text{ [N/m]}$
k_s	Stiffness coefficient of the passive suspension	$2 \cdot 10^4 \text{ [N/m]}$
c_s	Damping coefficient of the passive suspension	$2 \cdot 10^3 \text{ [Nsm}^{-1}\text{]}$

Fig. 12 Vertical accelerations of mass m_s during Ride Test 3 in frequency domain

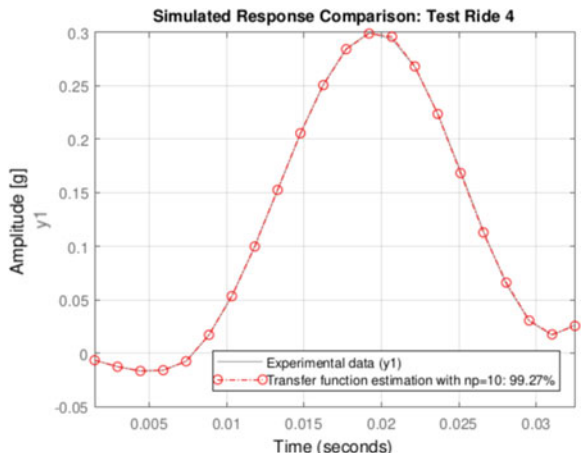


Fig. 13 Vertical accelerations of mass m_s during Ride Test 4 in time domain

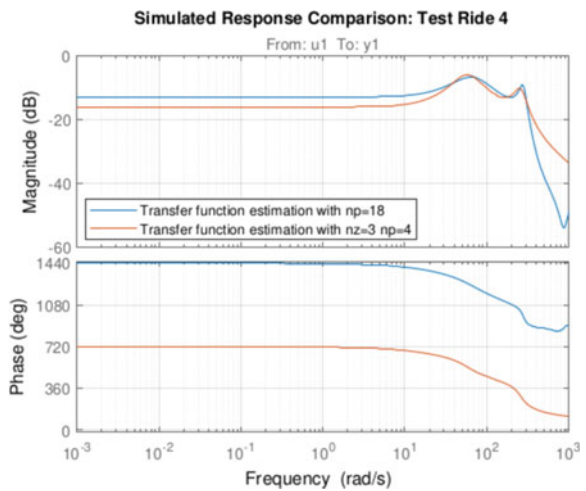
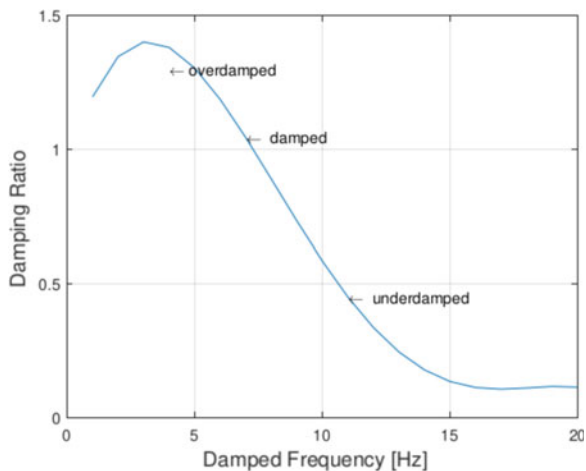


Table 2 Natural frequencies, damping ratio, zeros, gain, and time constant of function G_{11}

Zero	Pole	Damping ratio	Frequency [rad/s]	Time constant [s]
0	$-2.21 \pm i6.56$	0.32	6.92	0.453
-10	$-20.30 \pm i69.40$	0.28	72.30	0.05

Table 3 Composite weighted level AW, fourth power vibration dose VDV for ride test ($v = 50\text{km/h}$)

Description ride test	ID	AW [$\text{m} \cdot \text{s}^2$]	VDV [$\text{m} \cdot \text{s}^{1.75}$]
	1	0.7698	0.6652
	2	0.6432	0.5225
	3	2.376	1.864
	4	0.825	0.6688

Fig. 14 Damping versus damped frequencies**Table 4** Symbols

Symbol	Description
m_s	Suspended mass
m_u	Unsprung mass
nz	Zeros
np	poles
z_s	Displacements of the center of gravity
z_u	Displacement of unsprung mass
z_r	Profile of the road surface
k_u	Elasticity of tire
k_s	Stiffness coefficient of the passive suspension
c_s	Damping coefficient of the passive suspension
L_s, L_w	Rest lengths of the corresponding springs
F	Force generated by the actuator
g	Acceleration of gravity
v	Vehicle speed

6 Conclusion

A mechanical equivalent model has been developed to characterize the response of the vehicle excited by road profiles. The mathematical model is calibrated by the ride test. During the tests, the accelerations represent objective measurement variables to illustrate the vehicle motion variables. The subjective assessment variables can be represented in mathematical formulation. Physical perception variables are related to the vehicle motion variables.

References

1. Bolzern, P., Scattolini, R., Schiavoni, N.: *Fondamenti di Controlli Automatici*. McGraw-Hill, Milano, Italy (2008)
2. ISO, Mechanical vibration and shock: Evaluation of human exposure to whole-body vibration. International Standard, ISO 2631-1:2014, 2014
3. Mastinu, G., Ploechl, M.: *Road and Off-Road Vehicle System Dynamics*, CRC Press (2014)
4. Cavacece, M., Pennestri, E.: Three degree of freedom model for the apparent mass of the seated human body exposed to vertical vibration. In: 51th UK Conference on Human Response to Vibration, Institute of Naval Medecine Gosport (2016). ISBN 978-0-9546028, 19
5. Aghilone, G., Cavacece, M.: Vibration Transmission performance of off-road vehicle seats. In: 53th UK Human Response Vibration, Ascot (UK), pp. 201–208 (2018)
6. Figliolini, G., Lanni, C., Angeles, J.: Kinematic analysis of the planar motion of vehicles when traveling along tractrix curves. ASME. J. Mech. Robot. **12**(5), 054502 (2020). <https://doi.org/10.1115/1.4046509>

Investigation of Dynamic Forces and Moments in the Neck Region of the Driver of a Vehicle



Raj Desai, Anirban Guha, and P. Seshu

1 Introduction

It is widely established that there exist a high risk of health impairment due to prolonged exposure to whole-body vibration [1]. Vehicle occupants commonly experience this situation. So, an understanding of the human body and vehicle dynamics can help in reducing the health risk of vehicle drivers. Vehicle ride comfort is an essential and vital criterion in vehicle dynamics [2]. The comfort experienced by humans varies considerably as different people respond in different ways to the same situation. It has been shown that human body response to vibration depends on posture, excitations (magnitude, frequency and direction) and individual anthropometry. Studies have shown that the effects of vibrations on humans could be quite detrimental and, in some cases, may give rise to physical and psychological health impairments [3]. Research has also revealed that intervertebral disc degeneration [4] and chronic low-back pain as a result of constant exposure to vibrations occur more frequently among drivers than in the general population [5]. However, forces in the neck region are of particular concern since they lead to headache and motion sickness [6, 7]. Thus, study of forces in the neck region and their mitigation should be an important area of research.

Since it is the road roughness which generates the motion to the human body, all the components which are involved in transmission of this motion to the neck region need appropriate modelling. Different kinds of vehicle models have been used to study vehicle dynamics and human body response. Most of these models have lumped parameters and are limited to one-dimensional analysis. For an integrated

R. Desai (✉) · A. Guha

Department of Mechanical Engineering, Indian Institute of Technology, Mumbai, India
e-mail: rajdesai@iitb.ac.in

P. Seshu

Department of Mechanical Engineering, Indian Institute of Technology, Dharwad, India

human-vehicle analysis, it is critical to have a model that is both reasonable in its complexity and accurate enough to demonstrate predictions close to the experimental results. Thus, a two-dimensional human body model is needed to simulate vertical and horizontal forces and rotational moment at different locations of the human body.

This work describes such a model which allows the depiction of the motion of body masses as close as possible to reality for vibration attenuation. Previously developed and validated 12 DoF [8–11] multibody human body and nonlinear cushion contact force models are integrated with a full car model through a multi-compression seat suspension system. This allows accurate prediction of forces in the neck region while keeping modelling complexity within a reasonable level. The damping characteristic of the cushioning material plays an important role in supporting the body, isolating vibration, improving ride quality, and maintaining head-neck posture. Thus, for a better understanding of the dynamic seat performance, the influence of the cushion damping parameter on neck region forces has been studied. Different road classes and vehicle speeds have been investigated.

2 Mathematical Modelling

The detailed formulation, description and numerical data of the human body and nonlinear cushion contact force models used in this study and its integration with the full vehicle model are presented in previous works [12, 13] and are shown in Figs. 1, 2 and 3.

The human body masses are connected with the help of rotational and translational springs and dampers. Each human body mass ($m_1 - m_4$) exhibits three degrees of freedom (vertical displacement, fore-aft displacement and rotational motion).

The Newtonian method is used to formulate the equations of motion [14]. The framework of equations for mass 1 is represented as

$$m_1 \ddot{x}_1 = -f_{1x} - f_{c1x} - f_{c2x} \quad (1)$$

$$m_1 \ddot{z}_1 = -f_{1z} - f_{c1z} - f_{c2z} \quad (2)$$

$$I_1 \ddot{\theta}_1 = f_{1x} l_{1j1v} + f_{1z} l_{1j1h} - f_{c1z} l_{1c1h} - f_{c1x} l_{1c1v} + f_{c2z} l_{1c2h} - f_{c2x} l_{1c2v} - f_{r1} \quad (3)$$

The 12 degree-of-freedom (DoF) two-dimensional multibody human body model ($m_1 - m_4$) and a nonlinear seat human contact force model (F_{cu}) are integrated on a full [15] car vehicle model as represented in Fig. 4 through a seat suspension system. The force developed by the seat suspension framework is represented by F_{SS} . The human body model and nonlinear cushion models are validated using experimental data. The experimental data used for human body model validation was for seat to

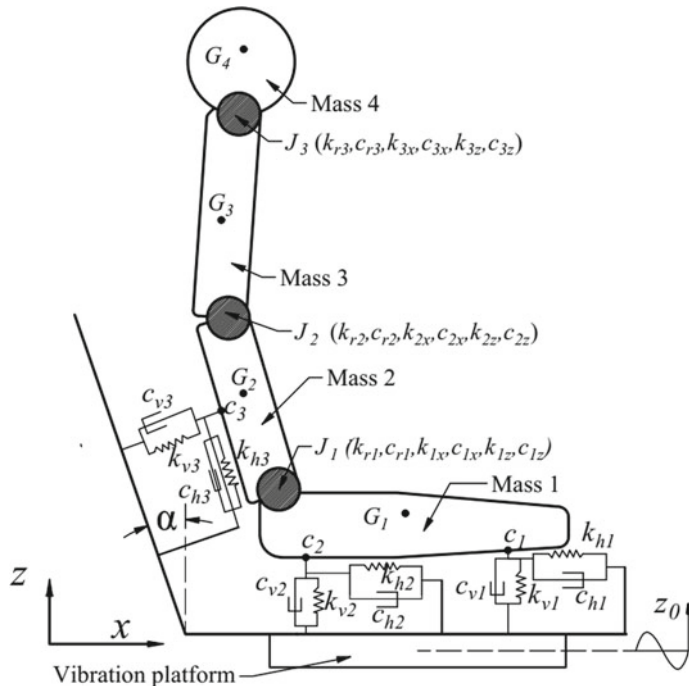


Fig. 1 (DOFs) Backrest supported seated human body

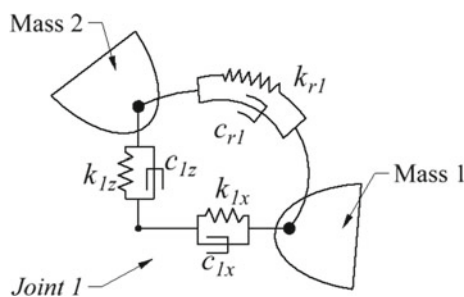


Fig. 2 DOFs joint representation

head transmissibility and for the cushion model, it was contact force corresponding to three different levels of excitation. The road disturbance input is $z_{r1} - z_{r4}$.

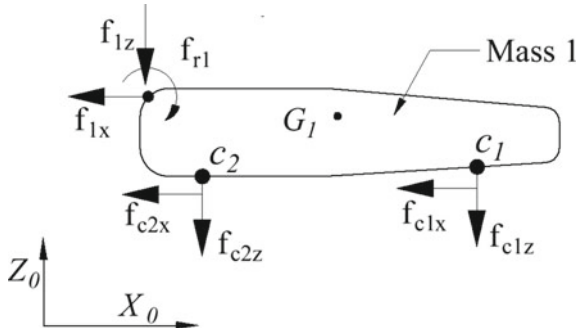


Fig. 3 Free body sketch for Mass 1

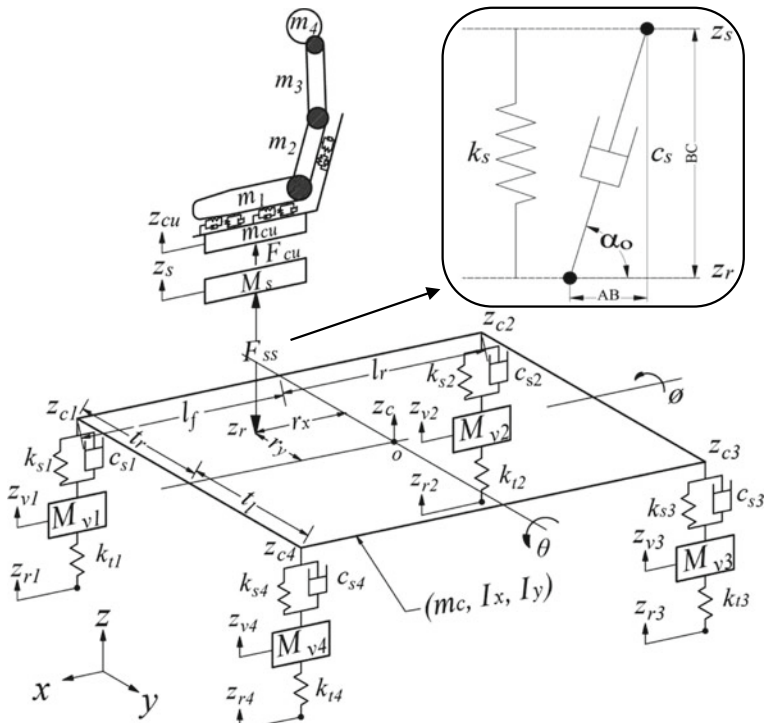


Fig. 4 DoF human-full car vehicle human model integration [10]

3 Road Input Modelling

Vehicles moving on a random irregular profiled road are subjected to vibration generated due to tyre-road interactions and acceleration-braking forces. These are harmful to both the riders and the vehicle. The disturbances observed by the occupant when

a vehicle moves over an irregular and inconsistent road are distinctly different from those notices for an abrupt bump or pothole. These motions not only adversely affect the comfort but also lead to safety issues if the human being loses contact with the seat. As a consequence, the primary function of a better seat suspension system is to ensure good ride comfort to occupants and minimize the seat roll, pitch and yaw motions for a variety of road conditions.

3.1 Random Road Disturbance

Road disturbance is generated using a random process. The road roughness is called a stationary random road in the time domain if the car moves at a constant speed. The mathematical equation for stationary road harshness is given by Eq. (4) and can be simulated in MATLAB-SIMULINK. Random road modelling through numerical simulation was carried out using Eq. (4) [16] in the time domain while the vehicle was running at a constant speed. Figure 5 illustrates the random road profile corresponding to grade C (as per Table 1) and vehicle moving at a constant speed of 72 km/hr.

$$\dot{q}(t) + 2\pi n_0 v q(t) = \sqrt{2\pi G_r v} \omega(t) \quad (4)$$

Here, white noise signal $= \omega(t)$; vehicle velocity $= v$; road roughness $= q(t)$; cutoff spatial frequency $= n_0 = 0.01$ cycle/m.

Fig. 5 Random constant velocity road profile

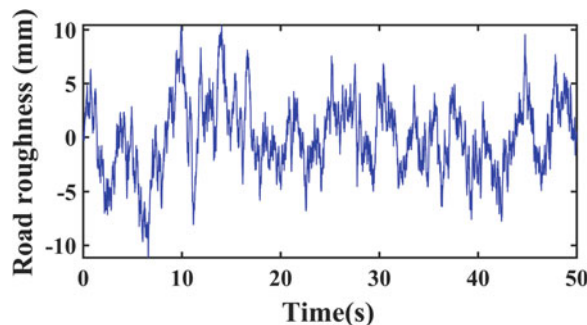


Table 1 Road-roughness coefficients G_r (m^2 /cycle/m) [15, 17]

Road class	A very good	B good	C average	D poor	E very poor
$G_r(10^{-6})$	4	16	64	256	1024

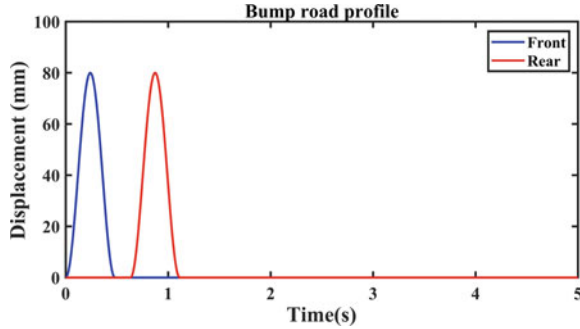


Fig. 6 Bump road profile

3.2 Bump Road Profile

The seat suspension performance is examined for a vehicle moving at a constant speed of $v = 15$ km/hr subjected to single bump road disturbance, as shown in Fig. 6. This road profile is employed to the front and rear wheels with the same peak amplitude but a time delay of $(l_f + l_r)/v$. The plot is generated using Eq. (5) [18]:

$$z_r(t) = \begin{cases} \frac{a}{2}(1 - \cos(\frac{2\pi v}{l}t)) & , 0 \leq t \leq \frac{t}{v} \\ 0 & , t > \frac{t}{v} \end{cases} \quad (5)$$

Here a equals 80 mm for both right and left sides of the vehicle.

4 Neck Region Parameters

The driving of the vehicle leads to vertical and fore-aft forces and rotational joint moments in the neck region, which in turn leads to headache, motion sickness and neck pain [6, 7]. The damping characteristic of cushioning material plays an essential role in supporting, isolating vibration, improving ride quality and head-neck posture [19]. Thus, to improve drive comfort, it is necessary to study the influence of the cushion damping parameter on neck region forces. This section reports such a study for various road classes and vehicle speeds.

4.1 Variation in Road Roughness

The road roughness coefficient is varied in Eq. (4) according to the values presented in Table 1 with the intention of generating different classes of road profiles. The same dataset of white noise has been used in all the cases. Neck region force parameters for

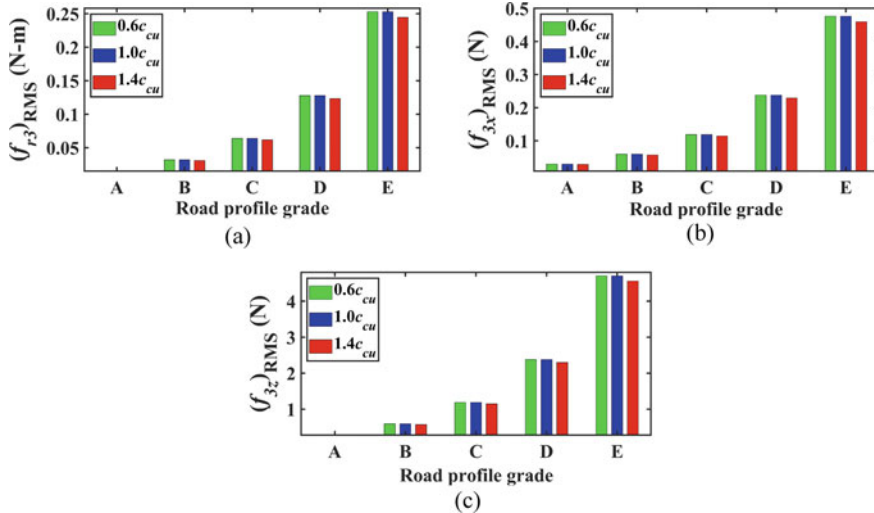


Fig. 7 RMS value of neck region parameters due to variation in road roughness and cushion damping coefficient (speed 72 km/hr): **a** rotational moment, **b** fore-aft and **c** vertical force

different grades of road are presented in Fig. 7. With an increase in road roughness, the moments and forces in the neck region rise continuously. With an increase in cushion damping, the neck region parameters tend to be lower. A cushion with a higher value of damping dissipates a more significant amount of vibrational energy. This will lead to improvement in human comfort. The influence of cushion damping on neck region parameters is more for rough roads than for smooth roads. This may be due to the higher vibrational energy generated in rough roads.

Effect of vehicle speed

The variation in human body parameters (neck region force and moment) for various vehicle speeds for random and bump road profiles is reported in the current subsection (Fig. 8). The study is limited to the random road of class C.

With an increase in vehicle speed, all the parameters rise continuously, leading to deterioration in human comfort. Similar trends are expected for other road profiles. With an increase in cushion damping, neck region parameters tend to be lower, leading to improvement in human comfort. The consequence of variation in cushion damping is more evident at a higher velocity than in lower velocity.

The neck region parameter variation for bump road profile for two different vehicle speeds is presented in Fig. 9. The higher effect of vehicle speed variation for bump road profile is observed on fore-aft forces. Overall, the effect of changes in cushion damping on neck region parameters is similar to those observed for the random road profile.

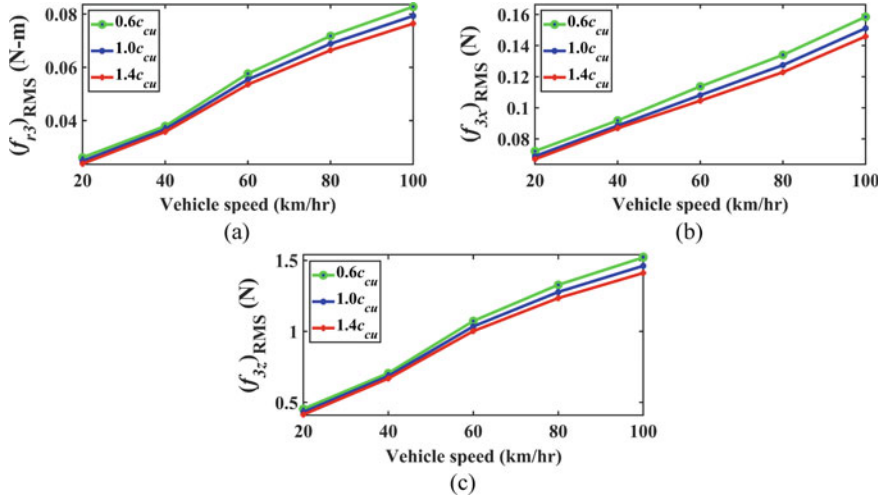


Fig. 8 RMS value of neck region parameters due to variation in vehicle speed and cushion damping coefficient (c-class): **a** rotational moment, **b** fore-aft and **c** vertical force

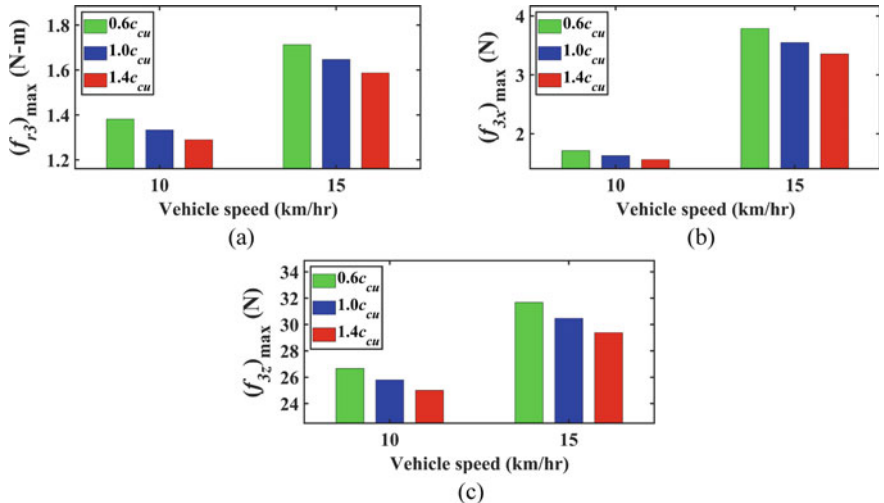


Fig. 9 Maximum value of neck region parameters due to variation in vehicle speed and cushion damping coefficient: **a** rotational moment, **b** fore-aft and **c** vertical force

5 Conclusions

This paper uses an integrated human-cushion-seat suspension-vehicle model to study the neck region forces of a vehicle occupant. The consequences of the variation in cushion damping parameter on neck region moment and forces have been studied

for different grades of roads and vehicle speeds. With the rise in road roughness, the moment and forces in the neck region tend to rise continuously. An increase in cushion damping tends to lower the neck region parameters. The consequence of variation in cushion damping is more apparent at higher velocities. The most significant impact of variation in cushion damping is observed for neck region fore-aft force. For a road bump, a high influence of vehicle speed variation is witnessed on the fore-aft direction force. This detailed analysis of variation of human body neck region parameters due to change in road roughness, vehicle speed and cushion damping parameters can assist seat manufacturers in designing high-performance vibration isolation seats or modifying existing seats for the comfort of drivers.

References

1. Magnusson, M., Pope, M., Wilder, D., Hansson, T.: Vibrations as the cause of low back pain disorders. Professional Drivers Are at Risk, Lakartidningen. **92**, 1711 (1995)
2. G.H.M.A.B.A.M.A. Ghany, Ride comfort enhancement of heavy vehicles using magnetorheological seat suspension. Int. J. Heavy Veh. Syst. **22**, 93–113 (2015)
3. Diyana, M.Y.A., Karmegam, K., Shamsul, B.M.T., Irniza, R., Vivien, H., Sivasankar, S., Syahira, M.J.P.A., Kulanthayan, K.C.M.: Risk factors analysis: Work-related musculoskeletal disorders among male traffic policemen using high-powered motorcycles. Int. J. Ind. Ergon. **74**, 102863 (2019)
4. Hill, T.E., Desmoulin, G.T., Hunter, C.J.: Is vibration truly an injurious stimulus in the human spine? J. Biomech. **42**, 2631–2635 (2009)
5. Bovenzi, M., Hulshof, C.T.J.: An updated review of epidemiologic studies on the relationship between exposure to whole-body vibration and low back pain. J. Sound Vib. **215**, 595–611 (1998)
6. Scutter, S., Türker, K.S., Hall, R.: Headaches and neck pain in farmers. Aust. J. Rural Health. **5**, 2–5 (1997)
7. Fard, M.A., Ishihara, T., Inooka, H.: Dynamics of the head-neck complex in response to the trunk horizontal vibration: modeling and identification. J. Biomech. Eng. **125**, 533–539 (2003)
8. Desai, R., Guha, A., Seshu, P.: Multibody Modeling of Direct and Cross-Axis Seat to Head Transmissibility of the Seated Human Body Supported with Backrest and Exposed to Vertical Vibrations (2021). https://doi.org/10.1007/978-981-15-4477-4_9
9. Desai, R., Guha, A., Seshu, P.: Multibody Biomechanical Modelling of Human Body Response to Vibrations in an Automobile (2019). https://doi.org/10.1007/978-3-030-20131-9_1
10. Desai, R., Guha, A., Seshu, P.: Modelling and simulation of an integrated human-vehicle system with non-linear cushion contact force. Simul. Model. Pract. Theory. 102206 (2020)
11. Desai, R., Guha, A., Seshu, P.: Multibody modelling of the human body for vibration induced direct and cross-axis seat to head transmissibility. In: Proceedings of the Institution of Mechanical Engineers, Part C: Journal of Mechanical Engineering Science (2020). <https://doi.org/10.1177/0954406220967957>.
12. Desai, R., Guha, A., Seshu, P.: Investigation of internal human body dynamic forces developed during a vehicle ride. In: The International Conference of IFToMM ITALY, pp. 85–93. Springer, Berlin (2020)
13. Desai, R., Guha, A., Seshu, P.: Investigations on the human body and seat suspension response using quarter, half and full car models. In: Joint International Conference of the International Conference on Mechanisms and Mechanical Transmissions and the International Conference on Robotics, pp. 507–516. Springer, Berlin (2020)

14. Desai, R., Guha, A., Seshu, P.: Multibody biomechanical modelling of human body response to direct and cross axis vibration. *Procedia Comput. Sci.* **133**, 494–501 (2018)
15. Zuo, L., Nayfeh, S.A.: Structured H₂ optimization of vehicle suspensions based on multi-wheel models. *Veh. Syst. Dyn.* **40**, 351–371 (2003)
16. Zhang, L.-J., Lee, C.-M., Wang, Y.S.: A study on nonstationary random vibration of a vehicle in time and frequency domains. *Int. J. Automot. Technol.* **3**, 101–109 (2002)
17. Nigam, N.C., Narayanan, S.: Applications of Random Vibrations. Springer, Berlin (1994)
18. Du, H., Li, W., Zhang, N.: Integrated seat and suspension control for a quarter car with driver model. *IEEE Trans. Veh. Technol.* **61**, 3893–3908 (2012)
19. Yang, B., Shi, Z., Wang, Q., Xiao, F., Gu, T.-T., Yin, Y.-K., Miao, Z.-L.: Frequency spectrum of the human head--neck to mechanical vibrations. *J. Low Freq. Noise, Vib. Act. Control.* **37**, 611–618 (2018)

Analysis of Design of Head Restraints of Car Seat Considering Indian Anthropometry



Radhika Tekade, Girish Ramteke, and P. V. Kane

1 Introduction

1.1 Why Evaluation of Head Restraint is Important?

The crashes at speeds even as low as 30 miles per hour [1] can generate forces large enough that the mass of the head pulls the neck apart from the body. Due to the physics of the body, the head is likely to lag behind the movement of the torso, causing the neck to bend back and stretch. This motion is commonly called whiplash, and although not life-threatening, it can lead to severe injuries. The primary function of the head restraint is first to support the head and push it forward with the torso and slow the rate of deceleration while coming back, minimizing the sudden jerk on the neck by providing an anchoring point. The effectual head restraint is directly behind the occupant's head that is very close to it and comes at least as high as the occupant's ears. Many head restraints are adjustable to adjust for both short and tall occupants.

R. Tekade · G. Ramteke · P. V. Kane (✉)
Mechanical Engineering Department, VNIT, Nagpur, India

R. Tekade
e-mail: radhikatekade@students.vnit.ac.in

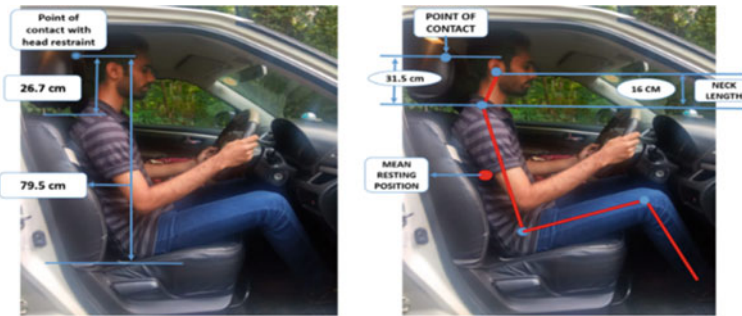


Fig. 1 Anthropometric data of a person sitting on the car seat

2 Methodology

2.1 Candidates Seated in Car Seat for Measurements

For this study, measurements have been taken for the positions of the head and head restraints by asking candidates of different heights as shown in Fig. 1. The study subjects are selected accordingly so that the results and conclusions of the analyses apply to average Indian anthropometric measurements. This data collection leads to understanding, evaluation, and analysis of the following factors: the human posture in the car's driver seat with the help of stick figures, the mean resting position of the individual aid in understanding how the back of the body rests on the seat of the vehicle, and point of contact of the head with a head restraint which is a crucial point for evaluating the position of the head where it will hit the headrest during a rear-end collision. The neck length has also taken into consideration which is used for estimating the whiplash injury due to head extension during rear-end collisions (Fig. 1).

2.2 Car Seat Dimensions

In this study, the measurement of only the car's driver seat is taken into consideration. The following are the attributions used for taking the measurements of the commonly used car seats [2]. As shown in Fig. 2, these attributes are specified as: A—head restraint length (minimum position), B—head restraint length (maximum position), C—insert back length, D—sitting posture length, E—height of seat bottom from the base of the vehicle, and F—sitting posture width.

The following table (Table 1) shows the measurement taken for some commonly used cars in India.

Car models' names are kept anonymous for confidentiality.

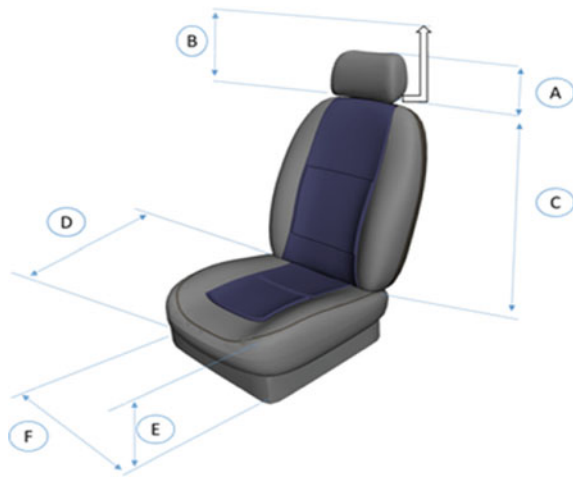


Fig. 2 Car seat measurement attributes

Table 1 Car seat dimensions

Car name	A (cm)	B (cm)	C (cm)	D (cm)	E (cm)	F (cm)
IJK	22	28	60	47	29	43
MN	19	26	61	49	26	45
OPQ	21	27	59	51	30	42
RST	18	25	57	47	28	41
UVW	19	NA	57	48	28	51
XYZ	NA	NA	74	44	17	45
NA—Feature not available						

2.3 Designing Aspect of the Project

Designing car seat

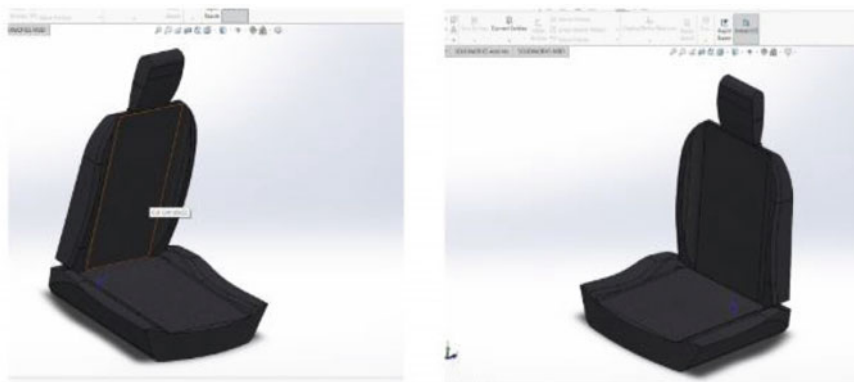
Figure 3 shows the final seat designed in SolidWorks using the car seat dimensions. The following figure shows the solid model for the driver seat with the dimensions of the car seat used in the model of one of the aforementioned cars.

Test Dummy Model

Figure 4 displays the dummy model of a 50th percentile Indian male according to the dimensions given earlier. Three views of the model are shown below for understanding geometry.

Table 2 Results of static analysis of head restraint

Car model	Adjust	Height lock		Tilt lock	
		Down	Up	Back	Front
IJK		No	No	Yes	Yes
LMN		No	No	Yes	Yes
OPQ		No	No	Yes	Yes
RST		No	No	No	No
UVW	X	Yes	No	Fix	Fix
XYZ	X	Fix	Fix	Fix	Fix
Car model	Head restraint down (CM)		Head restraint up (CM)		Overall rating
	HD	VD	HD	VD	
IJK	4	3	4	-3	Good (Zone 1)
LMN	3	5	3	-2	Good
OPQ	7	6	7	0	Acceptable (Zone 2)
RST	9	10	9	3	Marginal (Zone 3)
UVW	6	9	6	X	Marginal
XYZ	8	11	8	X	Poor (Zone 4)

**Fig. 3** Car seat designed in SolidWorks

3 Analysis

3.1 Static Analysis of Head Restraint

The proximity of the head with restraint has been shown in Fig. 5 to help reducing whiplash injury. With that in mind, the Research Council for Automobile Repairs

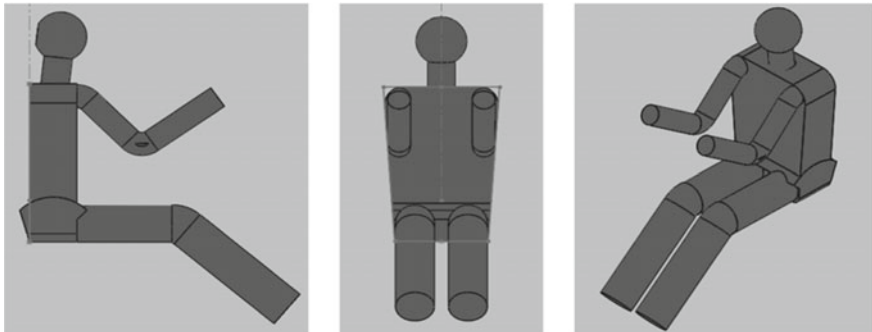


Fig. 4 Test dummy model designed in SolidWorks

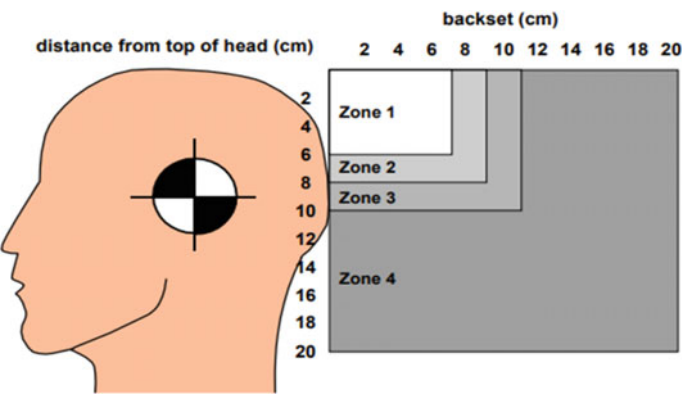


Fig. 5 Head restraint rating zones

(RCAR) has issued a procedure to evaluate head restraints based on geometrical criteria. This procedure applies to these types of head restraints, such as integrated/fixed, adjustable, active, and automatic.

Head Restraint rating overview

Each restraint shall be classified into one of the four geometric zones, as defined by its height and backset measurements. In this classification, Zone 1 is considered a “good” zone where the head restraint is not more than 7 cm from the back of the head and not more than 6 cm down from the top of the head. Zone 2 is regarded as an “acceptable” zone where head restraint is 7 to 9 cm from the back of the head and/or 6 to 8 cm down from the top of the head. Zone 3 is considered “marginal” where it is 9 to 11 cm from the back of the head and/or 8 to 10 cm down from the top of the head. Zone 4 is rated as a “poor” zone that exceeds one or both of the “marginal” measurements as shown in Fig. 5 [3].

According to the head restraint overview given earlier, readings were noted for various cars and their zones of head restraint were devised as our final outcome.

3.2 Dynamic Analysis During Collisions

In this work, ANSYS workbench [4] was used for dynamic modeling analysis of the collision phenomenon. The car seat and the dummy modeled using solid modeling techniques were imported. The material properties were applied to these models. Contact regions and body interactions such as bonded, frictionless, frictional, etc. as per the physics of the problem under study are assigned. The meshing was carried out to avoid errors for solving finite elements solver. Meshing used a patch conforming algorithm with the method of tetrahedrons. Finer meshing was provided at sensitive regions like the neck or chest. Nodes were calculated to be about 11,000 and elements nearly 50,000 for the dummy model with element size ranging from 2 to 8 mm. The initial conditions for collision such as velocity applied to the body, supports (fixed or displacement according to conditions), etc. were applied for simulations. The portion of the seat where the thighs come in contact, once seated, was applied with a fixed contact. The aforementioned conditions were selected after trial-and-error simulations till a convergence in the results was observed relevant to the theorized values. The rest of the body was free to move under the impact forces experienced. Various settings for simulations involve specifying several cycles, end time, etc. The model was simulated and solved to obtain total shear deformations as well as stresses. The results obtained are shown in Figs. 6 and 7.

Results

Figure 6 shows the total deformation of the individual after the impact in front-end collision.

Figures 7 and 8 show equivalent and shear stress acting on the individual during the impact in front-end collision.

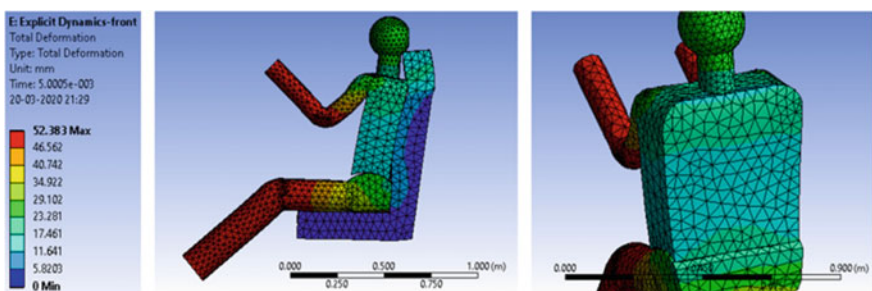


Fig. 6 Total deformation in front-end collision

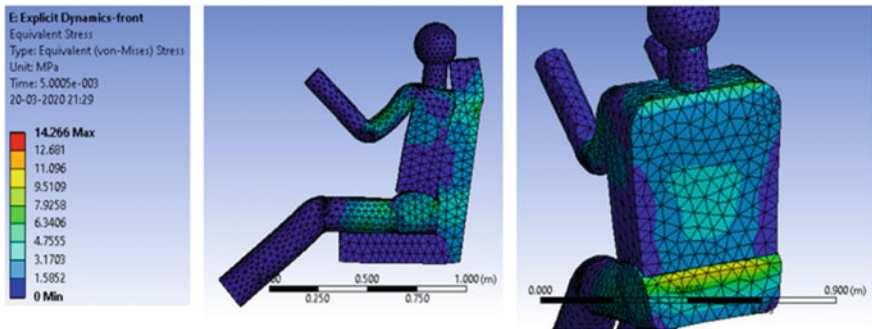


Fig. 7 Equivalent stress in front-end collision

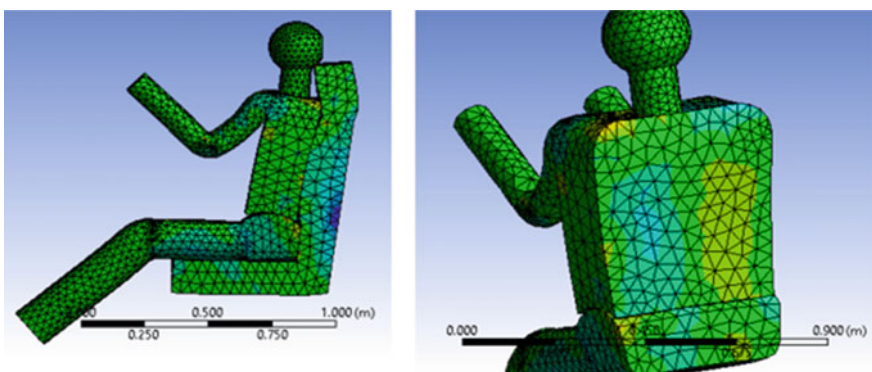


Fig. 8 Shear stress in front-end collision

The results of the rear-end collision are as follows. Figure 9 shows the total deformation of the individual after the impact.

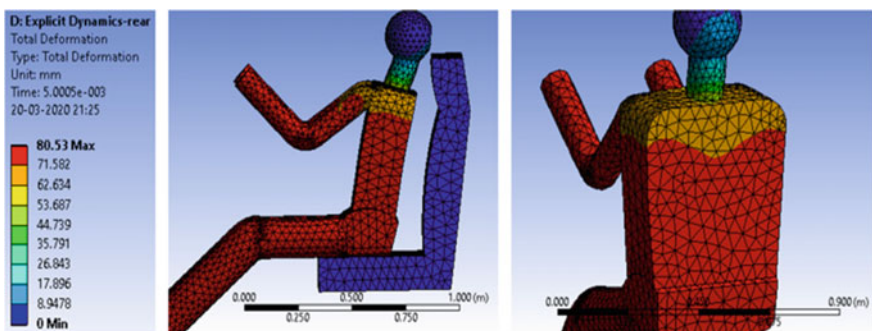


Fig. 9 Total deformation in rear-end collision

Figures 10 and 11 show equivalent and shear stress acting on the individual during the impact.

The dynamic analysis performed revealed maximum stress and deformation regions and also numerical value associated with it. The mentioned numeric values in the images were at a velocity of 20 m/s. 5 milliseconds timespan was used to deduce the total velocity and acceleration undergone by the individual. The value of total velocity change in front-end and rear-end collisions is 10 m/s and 24 m/s, respectively. Similarly, the total acceleration change in front-end and rear-end collisions is 1.5 g m/s^2 and 5 g m/s^2 . Maximum deformation and maximum stress undergone by the body are 52 cm and 14 MPa for front-end collision and 80 cm and 17 MPa for rear-end collision.

The values for rear-end collision are high as compared to front end for the same velocity impact indicating clearly that rear-end collisions are more perilous than front-end collisions. The image (Fig. 10) for equivalent stress in rear-end collision

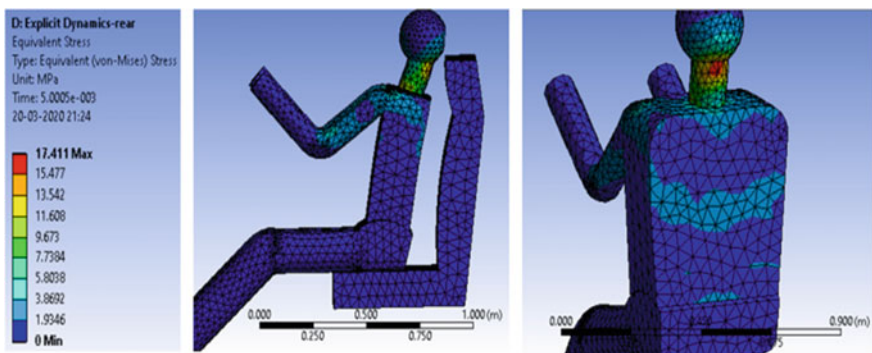


Fig. 10 Equivalent stress in rear-end collision

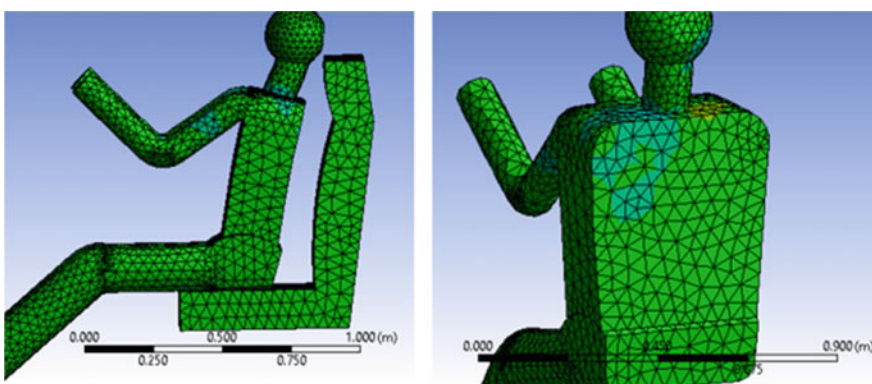


Fig. 11 Shear stress in rear-end collision

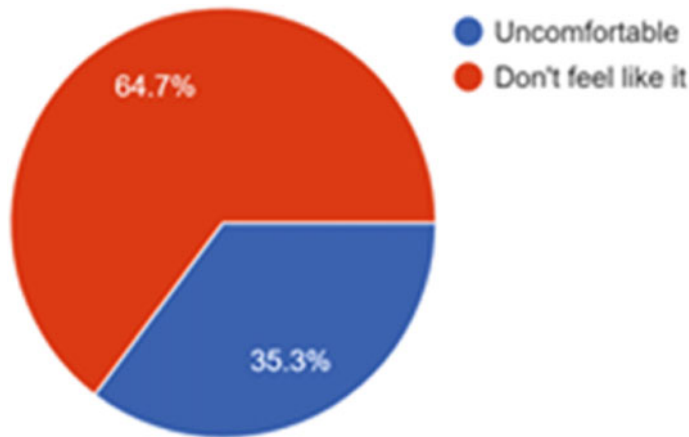


Fig. 12 Responses from individuals not wearing seat belts

shows a red spot on the neck revealing the high-stress values experienced by an individual during whiplash injury that is the major risk during rear-end collisions.

Studies conducted by ARAI and NCAP [5] have revealed that the maximum velocity impact the human body can endure is 25 m/s. It has also been noted that to induce failure stress in the neck (vertebrae—2 MPa) or in the body (femur—17 MPa), a human body has to undergo a sudden velocity impact of 4 to 8 m/s.

The simulations conducted for dynamic analysis of collisions of vehicles did not involve the use of a seat belt. This is because, after static analysis of seat belts, it was clear that the seat belt does not cause harm in wrong positioning. The reason for that is the portion of seat belt length present in car side chassis that smoothens out the effect of sudden momentum during the crash and also helps in adjusting comfortable position during normal driving. The seat belt, if stretched, increases flexibly to the desired length, just enough to direct the head into the center of the airbag which will further assuage the sudden jerk.

The crucial role of the seat belt is to prevent internal injuries by spreading the force of a collision across two of the human body's powerful areas: the pelvis and upper chest. But it came to our realization that a lot many people do not feel comfortable wearing seat belts after surveying the general public (Fig. 12). Hence, the simulations carried out were focused on understanding the effects of collisions on people who were not even incorporating minimal safety devices.

3.3 Head Restraint Rating

A questionnaire was prepared to consist of nearly 20 questions for a quick 5-min survey by the general public. The statistical data collected from about 60 drivers

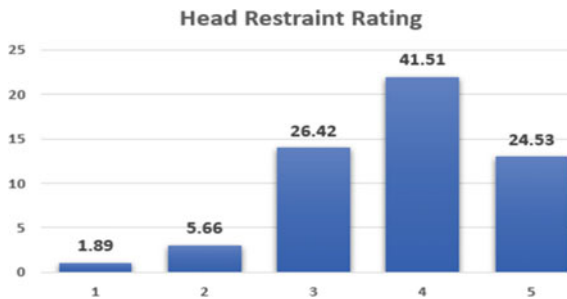


Fig. 13 Survey about head restraint rating

were used to understand the problems of uncomfortableness by the seatbelt, musculoskeletal disorders (MSDs) experienced like lower back or neck pain, the comfort of car seats, etc. One of the questions involved rating of head restraint depending on the support and positioning of a head restraint for seated individuals. Here, a graph (Fig. 13) of rating values (from 1 to 5, where 1 is the worst and 5 being the best) (on X-axis) versus number of people who rated (on Y-axis) is drawn. Bold values above the bars show the percentage of people who rated.

4 Conclusion and Future Scope

Safety devices in cars are beneficial and sometimes essential in both static and dynamic scenarios. For example, the head restraint is necessary at all times, that is, both in static and dynamic conditions. Whereas the seat belt and airbags are pivotal during dynamic circumstances. The project focuses on the rating of the head restraint in static analysis and its responses to front-/rear-end collisions with the help of a simulated environment. It was very clear from the simulation that rear-end collisions are fatal than front-end collisions, though front-end collisions can be equally dangerous at times. This signifies the need to innovate and improve head restraint designs that conform to various anthropometries.

The analysis performed in this project can be taken to a larger extent. More cars can be involved in data collection. The analysis of safety devices can be improved by improving the techniques as well as the software infrastructure for carrying out the analyses.

Considering the derived factors of safety and comfort of the car seat in this work, new improved components can be designed. A standard head restraint design methodology adopted in the market for a range of anthropometry can helpfully reduce the safety-related issues discussed in this study. As the project implied that the Indian anthropometry does not conform to current car seat designs precisely and on a large scale, a similar study can also be conducted in various states or other countries to verify the same.

References

1. Yang, Y., Jeon, E.S.: Design parameters and dynamic analysis of unfolded headrests for vehicles. *Int. J. Mech. Mechatron. Eng.* **18**, 41–45 (2018)
2. Koentjoro Wibowo, R., Soekarno, S., Syuhri, A., Vayendra, D.: Analysis and design of bus chair for economic class using Ergonomic Function Deployment (EFD) method. *Int. J. Adv. Sci. Res. Eng.* **4**, 161–167 (2018)
3. I. I. f. H. S. (IIHS): A procedure for evaluating Motor Vehicle Head Restraints (2008)
4. Ashish, J.: ANSYS Explicit Dynamics. ANSYS Inc. (2011)
5. Amrith, G.S.: Passenger Car Crash Testing (2019)

Novel Method for BSR Test Cycle Generation



K. J. Sarat and C. Lakshmikanthan

1 Introduction

Recently in the automotive industry, there has been a rise in ride comfort by the customers, continuous improvements in the technology combined along with better awareness on safety and comfort that has given the design and analysis process used in the automotive business to an advanced level. Buzz, Squeak, and Rattle are the noises produced in parts, and they are the result of relative motion among the installed parts that interact only sometimes in specific environmental conditions.

Buzz generates from the assembly of the body (above 2000 Hz) Squeak from friction between parts (200 Hz – 10,000 Hz) and Rattle by impact (20 Hz – 2000 Hz). BSR is an eminent cause of risky irritation to the car driver and general observation of the vehicle. BSR sound is noticeable owing to its erratic behavior which comprises a noise of frequency content in which sound covering reduces. An automobile with less BSR is related with high quality and therefore, it is vital for OEMs to attain this. Masking levels are established lesser and lesser, particularly in electric automobiles which also create problems for preventing BSR noises. Material selection, precise tolerance chains, and structural and chassis design are critical parameters to study. Other than them there is also an issue of the frequency content. If the level of vibration is correct, the test won't be qualified not until the frequency content is not correct.

K. J. Sarat · C. Lakshmikanthan (✉)

Department of Mechanical Engineering, Amrita School of Engineering, Ettimadai, Amrita Vishwa Vidyapeetham, Coimbatore 641112, India
e-mail: c_lakshmik@cb.amrita.edu

1.1 Literature Survey

In [1], Chang, Lee, and Hong considered analytical and experimental ways for Squeak and Rattle issues in a door component on how to solve the issues in ways to enhance the Squeak and Rattle performance in a better way. A FE-based procedure was developed using the model of the test setup for inspection of general friction-induced vibration problems. The test outcome exhibited correlations between friction coefficients and the loudness of the sound. The FE-based procedure was used on the door components on both trim and un-trim components. As a conclusion, there were resemblances with the experimental end result which shows that the numerical way of prediction was more supportive in finding the points with protentional S&R issues.

In [2], Rajesh agreed on a code that was developed so that could use in both laboratory and on-road simulated data and also on-road operational data. They concluded that this would assist in decreasing testing and acquisition time but also helps in obtaining good results.

In [3], Tatari, Fard, Naser, and Mahjoob proposed controlling structural dynamics of the seat as this is a strong upfront resolution for enhancing seat in BSR. Dual experimental analysis was done for that. In the primary analysis, a setup was created to distinguish the resonant frequencies of the seat and the equivalent structural mode. The second analysis carried out calculated radiated noise of the seat when the seat is under vibration excitation. The conclusions of both the analysis of experiment proved developed CAE of the model. It revealed both low vibration frequencies (<50 Hz) for major torsion and fore-aft curving structural modes where the structures were more likely to clatter. The conclusion of the analysis and the corresponding CAE model simulation was consonant.

In [4], Vikram. T. Pawar proposed a procedure for charting the service usage with the development of BSR performance vehicle which has to be progressed and successfully executed and observed for decreasing the BSR failure with utilization and toughness with the good value experimental procedure and result for BSR.

In [5], B. P. Naganarayana, S. Shankar, and V. S. Bhattachar proposed FEM-based methods which are used for the analysis discussed and that would result in a better connection around 75 percent between experimental and the analysis results. The results were assessed using FFTs in both the frequency domain and also in the time domain. As a conclusion, high ranking index were created to calculate squeak and rattle. BSR hotspots were found and matched with test locations to prove the software and procedure.

In [6], Nikhil. G. Takalkar and Prof. DR. M. K. Nalawade proposed a method that can be applied to component level in vehicle design to investigate the rattle occurrences also with the help of FEA analysis; also, if the displacement is greater than the allowable gap between the components, the rattle will occur. As the results were obtained, the Displacement versus Time plot is obtained using the same procedure, and the absolute displacement at the tip comes out to be greater than the initial gap between them. Also, in this way, rattle is predicted in the initial stages using FEA, and for the validation of the FEA process, a physical test is conducted. The results

of the test and simulation match with each other. This process can be used to check real parts like panel, lift-gate, doors, etc. as no physical prototype is required, initial development cost also comes down, and the time cycle for the development process is less.

In [7], Su-Hyun Shin and Cheolung Cheong proposed an experiment in which excitation of the jig was devised to produce the argument value without distortion for the roads, and successive experiments were conducted for classifying important BSR hotspots areas according to sound metrics. As a conclusion, in the frequency between 300 to 1200 Hz occurrence of impact and occurrence by slip stick in between the 2 parts, the rattle was more supreme than the squeaks.

In [8], Santosh S Gosavi conducted BSR analysis on a coupled tire road simulator four poster and found the main factor for the process on the four wheels. As a result, the method for charting the development performance of BSR accompanied with vehicle service usage has been progressed plus successfully executed to find and reduce BSR with utilization and toughness and evaluate and implement the BSR-related issues before production.

2 Materials and Method

The following methods were used in sequence to collect the data.

Collection of Road Load Data

The first step was to collect the raw road load data by mounting the tri-axial accelerometer on the vehicle. The sensor was connected with data acquisition systems. The vehicle was driven under different road conditions. The setup used for the trial is shown in Fig. 1. The vehicle was driven at various speeds to simulate diverse road conditions. The driving cycles were selected such that all the frequencies were excited. This includes events like speed breakers, potholes, patchworks, rough roads, concrete roads, etc. The sensor collected the acceleration in all three directions, along with the time. The speed of the vehicle was kept constant.

Pre-Processing of Raw Data

For pre-processing of data, time t is marked as a position for making logical road information data which is related to specific road segments. This information includes vibration data from the road and vehicle speed at which it is driven along that road. The signal collected were filtered based on the time spent by the vehicle over the various road conditions. The data is then combined and repeated to simulate long driving conditions with road conditions that are found normally.

Temporal Analysis

For temporal analysis, common approaches were used. The maximum amplitude for each road condition was found by using a peak-based method. The high amplitude



Fig. 1 Experimental Setup

vibrations which represent the bumps and potholes were detected using the above method.

Spectral Analysis

Wavelet analysis can be used for examining the data which has localized, non-stationary power at dissimilar frequencies. It was appropriate for analyzing vibration data of road as its frequency values could alter according to the existence of the specific road condition. For this study, wavelet function was used with zero mean which is localized in time and frequency spaces. For this purpose, the Morlet wavelet was used. Using the results of the wavelet analysis, max. and avg. power per octave were implemented as spectral features of vibration signals. This hypothesizes that for a specific road anomaly, an equivalent octave(s) is excited or its power is increased.

Road Anomaly Classification

After considering the spectral and temporal characteristics of vibration signals, they were used for road anomaly classification. At first, these characteristics were tested to ensure their statistical meaning. It is done to minimize the no. of features. Later, the road anomaly classification was done considering all external factors.

3 Experimental Setup and Procedure

The complete vehicle or sub systems were placed in a test rig and tested normally by the industries since driving the vehicle for thousands of kilometers to test it for various road load data conditions was difficult, time-consuming, and also an expensive task. Therefore, a typical test cycle data was generated and used in the test rigs. The test

cycles were created using the road load data. In this project, we propose a technique to reduce the test cycle generation time. Normally, a test cycle consists of road load characteristics that were experienced by the vehicle. The parameters collected were minimum and maximum amplitude, short-duration frequencies, long-duration frequencies, and noise level of the signal for a particular road condition. These parameters were used to create a new set of signals. These reconstructed signals would have the complete characteristics of the road load test cycles. A detailed discussion about the experiment to collect the road load data is discussed in the remaining portion of this chapter.

The power supply was given to the data acquisition system, which has a six-channel capacity. The three signals from the three axes of the accelerometer were connected to the first three ports of the data acquisition system. In the driver software, the configurations of the sensor (tri-axial ICP accelerometer) were changed such as channel ON/OFF and channel name type of the sensor, and the sensitivity range was configured. The driver was ready to record the measurements simultaneously since the configuration was completed. A series of tests was conducted once again for different road types.

The collected signals were analyzed using wavelet transform. The results of the analysis clearly showed the difference in the pattern of signals at various road conditions. This method created a new methodology to extract the salient features of the physical data thereby providing an accurate data for increasing the accuracy of the duty cycle.

4 Results and Discussion

BSR studies for the sub systems were conducted as durability tests because a small gap generated between two parts due to wear is one of the major contributors. But all these studies needed a driving cycle to produce the necessary vibrations. These vibrations were getting generated due to the presence of irregularities or features on the surface of the road. As discussed in the previous chapter, the road load data was collected for various features present in a typical rural load. The following results show the key parameters which define and distinguish these features from one another.

A typical rural road consists of smooth, rough, patchwork, stone, and speed breaker as its typical features. Table 1 shows the acceleration values obtained from the experiment for various types of road features.

The above values show that each feature has unique representation in terms of the parameters obtained from them using the experiment. The above phenomenon was noticed in the values obtained by transforming the time domain acceleration signal to the frequency domain. Table 2 shows the amplitude and frequency of the time signals representing the various road features. The following figures show the data of different road conditions.

Table 1 Acceleration values at the door mount for various road features

Smooth road	AXIS	X in m/s ²	Y in m/s ²	Z in m/s ²
Rough road	MIN	-3.87658	-4.4086	-4.33943
	MAX	3.694265	4.020661	3.033008
	AXIS	X	Y	Z
	MIN	-4.3188	-1.92183	-2.4079
Patchwork	MAX	4.120777	2.49874	1.291909
	AXIS	X	Y	Z
Stone road	MIN	-4.35879	-4.4086	-4.33943
	MAX	4.358791	4.408602	4.339432
	AXIS	X	Y	Z
Speed breaker	MIN	-4.35879	-4.4086	-3.79267
	MAX	4.358791	4.408602	4.339432
	AXIS	X	Y	Z
	MIN	-3.32396	-1.89012	-1.41329
	MAX	3.001374	1.533097	1.100397

Table 2 Amplitude and frequency values of various road features

Smooth road	AXIS	X	Y	Z
Rough road	Amplitude in m/s ²	0.187575	0.146171	0.148187
	Frequency in Hz	288	288	288
	AXIS	X	Y	Z
Patchwork	Amplitude in m/s ²	2.104211	0.736514	0.641156
	Frequency in Hz	96	288	192
	AXIS	X	Y	Z
Stone road	Amplitude in m/s ²	2.104211	0.736514	0.641156
	Frequency in Hz	96	288	192
	AXIS	X	Y	Z
Speed breaker	Amplitude in m/s ²	0.201812	0.197792	0.123093
	Frequency in Hz	192	192	288
	AXIS	X	Y	Z
	Amplitude in m/a ²	0.158625	0.632172	0.621398
	Frequency in Hz	96	288	288

Figures 2, 3, 4, 5, and 6 show the typical time signals of the various features of the road. Figure 7 shows the combined signal of all the above signals.

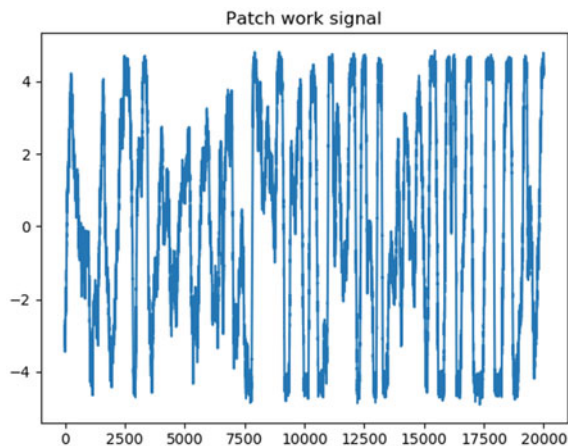
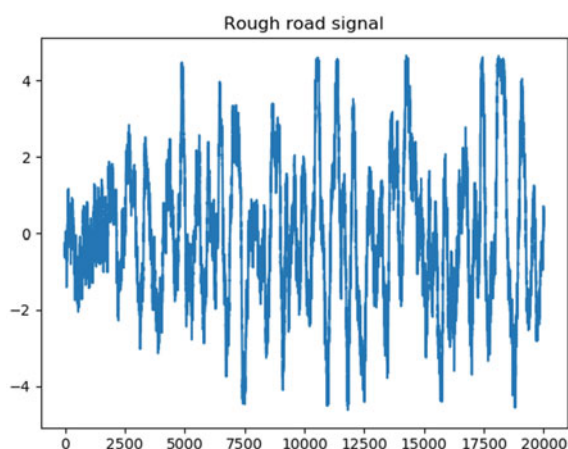
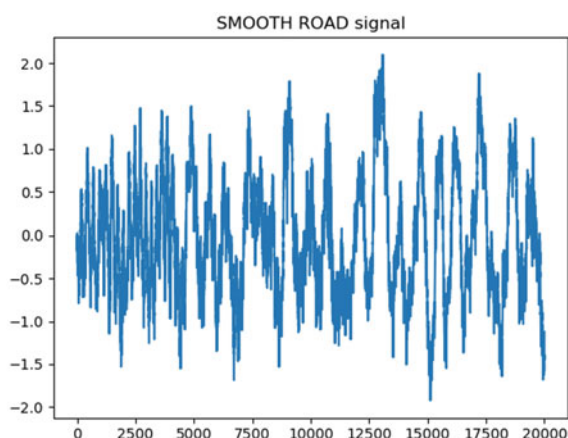
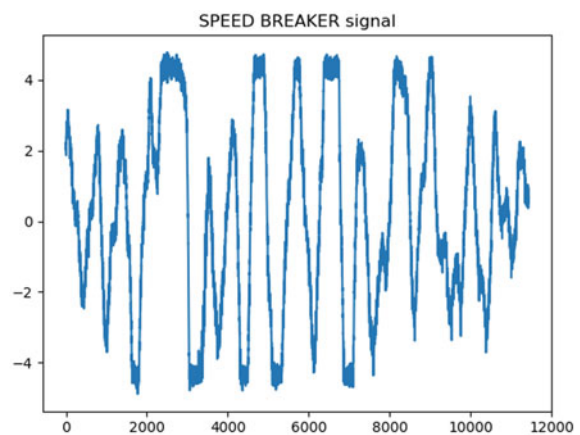
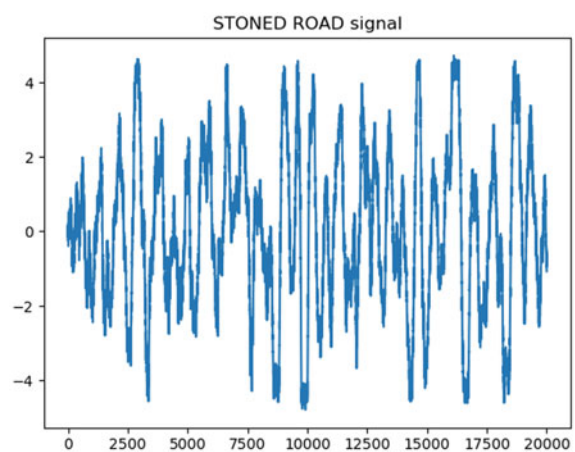
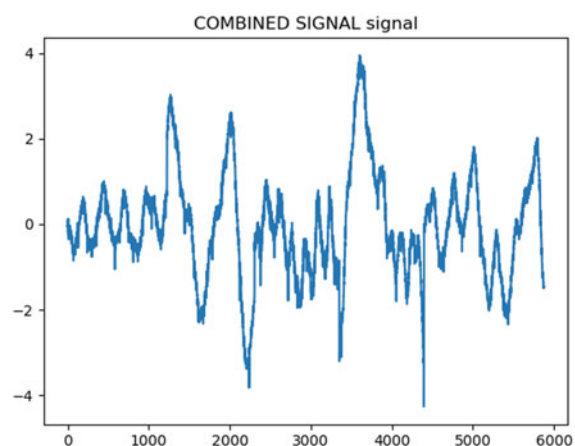
Fig. 2 Patchwork signal**Fig. 3** Rough road signal**Fig. 4** Smooth road signal

Fig. 5 Speed breaker signal**Fig. 6** Stoned road signal**Fig. 7** Combined signal from the above signals

5 Conclusion

The aim of the project was to develop a better methodology for the generation of driving cycles for BSR studies of sub-assemblies. A door assembly of an SUV was selected as sub-assembly to be studied. The measurement location was selected based on the typical mounting location of the assembly. Based on the location selected, accelerometers were mounted. A typical rural road consists of features like smooth section, rough section, patchwork, speed breaker, and stone road. Vehicle mounted with accelerometer was driven through these features. The data collected as time signal was separated as individual features using wavelet transform. The critical parameters which represent a feature uniquely were identified from each feature. Finally, a typical road consisting of all the features was created. The above method can be extended further to create any type of road if the details of the feature are available. This reduces the expensive and time-consuming road profiling.

References

1. Kim, K.C., Lee, S.W., Hong, S.G., Kim, J., Lee, G.J., Choi, J.M., Kim, Y.J.: A case study: application of analytical and numerical techniques to squeak and rattle analysis of a door assembly (No. 2015-01-2257). SAE Technical Paper (2015)
2. Cerrato, G.: Automotive Sound Quality-Accessories, BSR, and Brakes. *Sound Vib.* **43**(9), 10 (2009)
3. Tatari, M., Fard, M., Nasrollahzadeh, N., Mahjoob, M.: CAE characterization and optimization of automotive seat rattle noise. *World J. Eng. Technol.* **2**(03), 201 (2014)
4. Pawar, V.T., Kale, P.R., Jyothish, K.V.: Automotive Buzz, Squeak and Rattle (BSR) Detection and Prevention. *IOSR J. Eng.* **2**(6), 1497–1503 (2012)
5. Naganarayana, B.P., Shankar, S., Bhattachar, V.S., Brines, R.S., Rao, S.R.: N-hance: Software for identification of critical BSR locations in automotive assemblies using finite element models (No. 2003-01-1522). SAE Technical Paper (2003)
6. Shin, S.H., Cheong, C.: Experimental characterization of instrument panel buzz, squeak, and rattle (BSR) in a vehicle. *Appl. Acoust.* **71**(12), 1162–1168 (2010)
7. Gosavi, S.S.: Automotive buzz, squeak and rattle (BSR) detection and prevention (No. 2005-26-056). SAE Technical Paper (2005).
8. Shin, S.H., Cheong, C.: Experimental characterization of BSR noise source in automotive doors using acoustic visualization technique with four post excitation system. In: Proceeding of the 15th ICSV (2008)
9. Kavarana, F., Rediers, B.: Squeak and rattle-state of the art and beyond (No. 1999-01-1728). SAE Technical Paper (1999)
10. Sonie, D.E., Evensen, H.A., Van Karsen, C.D.: A design assessment tool for squeal and rattle performance. In IMAC-XVII. In: A Conference and Exposition on Structural Dynamics, pp. 8–11, Kissimmee, FL (1999)
11. Jay, M., Gu, Y., Liu, J.: Excitation and measurement of BSR in vehicle seats. *SAE Trans.* 1927–1933 (2001)
12. Shin, S.H., Cheong, C., Kim, D.W.: Characteristics of noise for squeak and rattle of vehicle interior module. In Proceedings of the ASK Annual Fall Conference, pp. 152–155 (2009)
13. Broo, R.F., Derico, A.J., Liechty, D.: Silicone Elastomer Reduces Noise, Vibration, and Squeaks in Vehicle Instrument Panels (No. 950635). SAE Technical Paper (1995)

14. Eiss, N., Lee, E., & Trapp, M. (1997). Frictional behavior of automotive interior polymeric material pairs. SAE transactions, 3281–3298.
15. MA, Z.D., Hagiwara, I.: Sensitivity calculation methods for conducting modal frequency response analysis of coupled acoustic-structural systems. JSME Int. J. Ser. 3, Vib., Control Eng., Eng. Ind. **35**(1), 14–21 (1992)
16. Webpage, www.mbdynamics.com/products/squeak-rattle/
17. Webpage, www.sound.eti.pg.gda.pl/srs/psychoacoust.html
18. Textbook Automotive Buzz, Squeak and Rattle 1st Edition, Webpage www.sciencedirect.com/book/9780750684965/automotive-buzz-squeak-and-rattle

Feasibility of Adoption of Double-Crank Inversion of Four-Bar Chain as a Substitute for a Gear Box



Akshay Anant Pachpor , Jayant Pandurang Modak, and Prashant Brajmohan Maheshwary

1 Introduction

The four-bar chain is the basic kinematic chain which forms a basis for the synthesis and development of most of the mechanisms [1]. The double-crank mechanism is one of the inversions of class I type four-bar chain. This inversion can be obtained by fixing the shortest link of the class I type four-bar chain [1].

The literature review indicates that considerable investigations have taken place toward kinematics and dynamics of crank–rocker inversion of four-bar chain. The third inversion double rocker is also done because in many of the six link chains two four-bar chains, namely, crank–rocker and rocker–rocker are in series. In fact, many process units have been developed with these two linkages [2–5]. As compared to crank–rocker and double-rocker mechanism applications of double-crank mechanism are scanty [1]. Some applications of double-crank mechanism are Selective Bell Pepper Harvester [6], Double-Crank External Geneva Mechanism [7], a Simple-type Potted Rice Seedling Transplanting Mechanism [9], Clamping unit with Double Crank [10], etc.

The double-crank linkage is primarily used as a coupling between two parallel non-inline shafts generating nonuniform motion of the driven shaft [11]. However, in the presented research paper, a case of double-crank linkage is graphically investigated for the possibility of generating a uniform circular motion of the driven shaft from the coupler of double-crank linkage. In the forthcoming section, a kinematic analysis of the points of the coupler with predefined dimensions of a double-crank linkage is presented. The analysis justifies the feasibility of the adoption of double-crank mechanism as a substitute of gear box.

A. A. Pachpor · J. P. Modak · P. B. Maheshwary
J D College of Engineering & Management, Nagpur, MH 441501, India

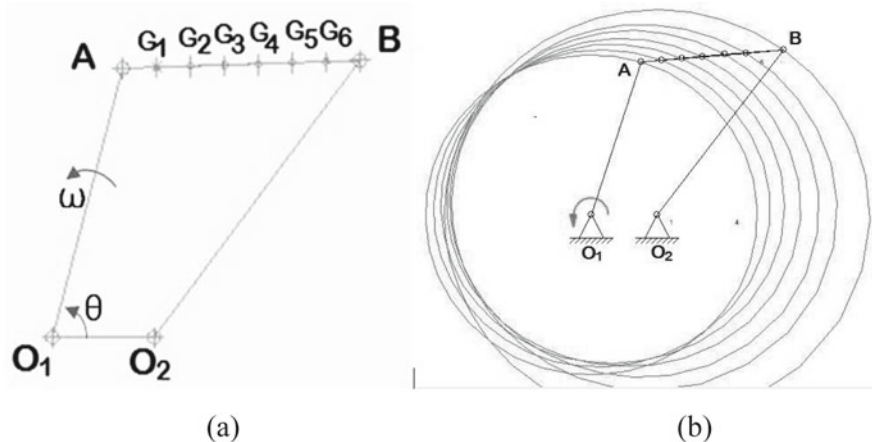


Fig. 1 A double-crank mechanism

2 Kinematic Analysis of Double-Crank Mechanism

2.1 Position Analysis of Coupler Points

In this section, a complete kinematic analysis of coupler points of coupler AB of a double-crank inversion of a four-bar chain O_1ABO_2 is discussed. Figure 1 represents a kinematic linkage O_1ABO_2 , where $O_1O_2 = 15$ cm (fixed link), $O_1A = 40$ cm (input crank), $AB = 35$ cm (coupler link), and $BO_2 = 50$ cm (output crank). For the analysis purpose, consecutive points, viz., G_1, G_2, G_3, G_4, G_5 , and G_6 are considered at a distance of 5 cm, 10 cm, 15 cm, 20 cm, 25 cm, and 30 cm, respectively, from end A of coupler AB.

Let the input crank O_1A be rotating anticlockwise about point O_1 with some constant angular velocity ω rad/s (Fig. 1), and θ be the input crank angle measured in an anticlockwise sense with respect to fixed link O_1O_2 . The kinematic analysis of coupler AB is carried out at 12 different positions of input crank where positions of input crank are defined in terms of input crank angle, such as 1st position at $\theta = 0^\circ$, 2nd position $\theta = 30^\circ$ up to 12th position at $\theta = 330^\circ$. Graphically constructing the configuration of double-crank four-bar mechanism O_1ABO_2 corresponding to these 12 positions of input crank O_1A shows that each point on the coupler traces a circular path (Fig. 1b).

2.2 Velocity Analysis of Coupler Points

Figure 2 shows velocity analysis of the double-crank mechanism at angular velocity $\omega = 1$ rad/s and angular position $\theta = 60^\circ$ of input crank O_1A . The velocity analysis is

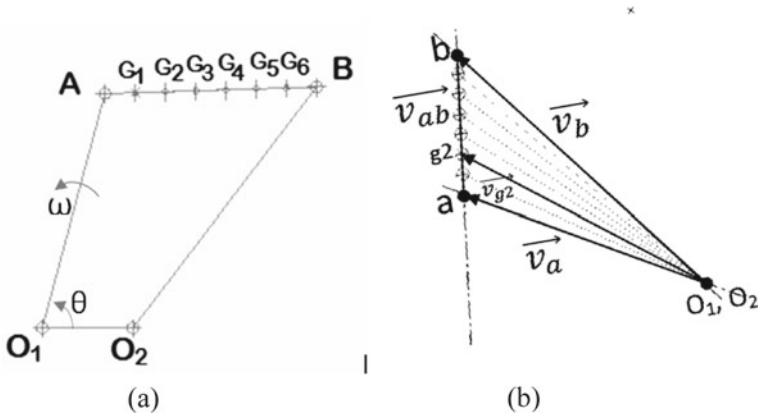


Fig. 2 Velocity analysis of double-crank mechanism at $\theta = 60^\circ$

carried out with the relative velocity method. Let us consider the vectors V_a , V_b , V_{g1} , V_{g2} , V_{g3} , V_{g4} , V_{g5} , and V_{g6} represent the absolute value of the velocity of coupler points A, B, G_1 , G_2 , G_3 , G_4 , G_5 , and G_6 , respectively. The values of these vectors are determined by plotting a velocity vector polygon (Fig. 2b). In the velocity vector polygon velocity vector, V_{g2} is only represented for the sake of simplicity. Likewise, velocities of coupler points A, B, G_1 , G_2 , G_3 , G_4 , G_5 , and G_6 at 12 different angular positions of input crank O_1A is calculated and tabulated under Table 1.

From the velocity analysis of coupler points (Fig. 3), it can be observed that the coupler points are rotating with variable angular velocities. These points exhibit some specific band of angular velocity variation. The maximum percentage variation in

Table 1 Absolute values of velocity of coupler points

Sr. No	Input Crank Angle, θ	V_a mm/s	V_{g1} mm/s	V_{g2} mm/s	V_{g3} mm/s	V_{g4} mm/s	V_{g5} mm/s	V_{g6} mm/s	V_b mm/s
1	0°	400	436.2	482.8	537	596.8	660.6	727.4	796.4
2	30°	400	426.0	455.6	488.2	523.1	560.0	598.54	638.32
3	60°	400	413.2	428.4	445.2	463.6	483.4	504.3	526.2
4	85°	400	406.5	414.7	424.5	435.6	448.1	461.9	476.7
5	120°	400	398.9	399.6	402.2	406.6	412.6	420.3	429.6
6	150°	400	392.1	386.5	383.3	382.4	384.1	388.1	394.5
7	180°	400	384.8	372.6	363.6	358.1	356.2	358.1	363.6
8	210°	400	378.0	359.9	346.2	337.9	334.8	337.4	345.4
9	240°	400	373.0	351.6	336.7	329.3	329.77	338.1	353.8
10	260°	400	371.7	350.7	338.4	335.6	342.6	358.7	383.0
11	300°	400	380.2	374.8	383.5	406.34	440.8	484.41	534.94
12	330°	400	408.2	435.0	477.4	531.6	594.3	663.2	736.6

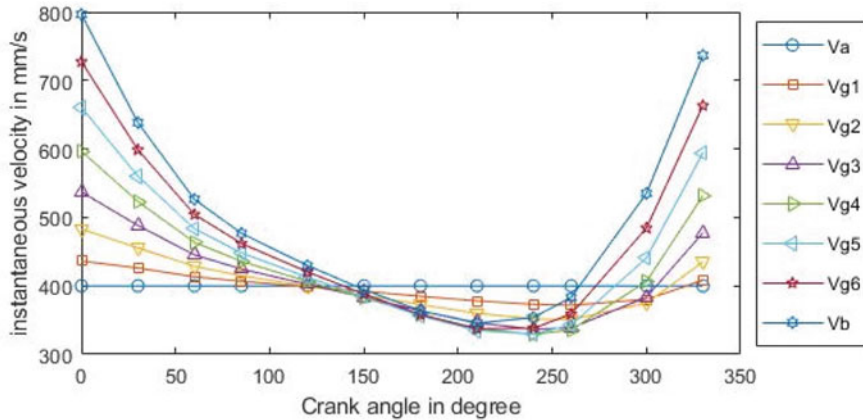


Fig. 3 Graphical representation of velocity variation of coupler points

Table 2 Maximum percentage variation in angular velocity

Absolute Velocity	V _a mm/s	V _{g1} mm/s	V _{g2} mm/s	V _{g3} mm/s	V _{g4} mm/s	V _{g5} mm/s	V _{g6} mm/s	V _b mm/s
% variation	0	8.4	17.29	25.77	33.25	40.59	46.77	51.78

angular velocity of coupler points is found out to be 8.4% at point G₁ to 51.78% at end B of the coupler AB. The values of percentage variation in angular velocity for coupler points are given in Table 2.

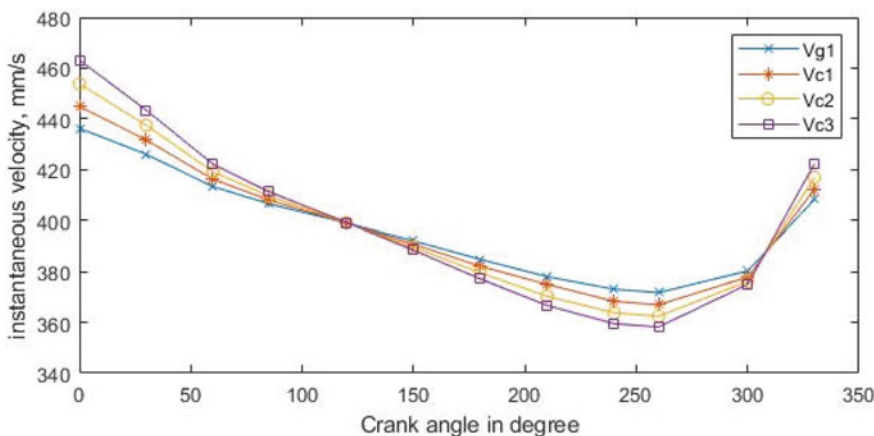
Further, kinematic analysis is carried out by selecting the points on the coupler AB V_{c1}, V_{c2}, and V_{c3} at a distance of 6 cm, 7 cm, and 8 cm, respectively, from end A of coupler AB and corresponding values of velocity of the points are calculated (Table 3). The variation of velocities can be represented graphically as shown in Fig. 4. It can be observed that coupler points V_{g1}, V_{c1}, V_{c2}, and V_{c3} account for the least band of angular velocity variation (Table 4).

3 Double-Crank Mechanism as a Substitute of Gear Box

It is evident from the preliminary kinematic analysis of the coupler AB that each point on the coupler describes a complete circle and performs rotation with some specific band of variation in angular velocity. The analysis shows possibilities of transforming the rotational motion of input crank O₁A to the rotational motion of other links with different angular velocities. The rotational motion of coupler point G₁ can be tapped out by connecting a shaft S₁ to the coupler point G₁ through a link G₁S₁ as shown in Fig. 5. The output speed with a variation of 8.4% in angular velocity (refer Sect. 2) can be obtained from shaft S₁ and, subsequently, shaft S₁ can

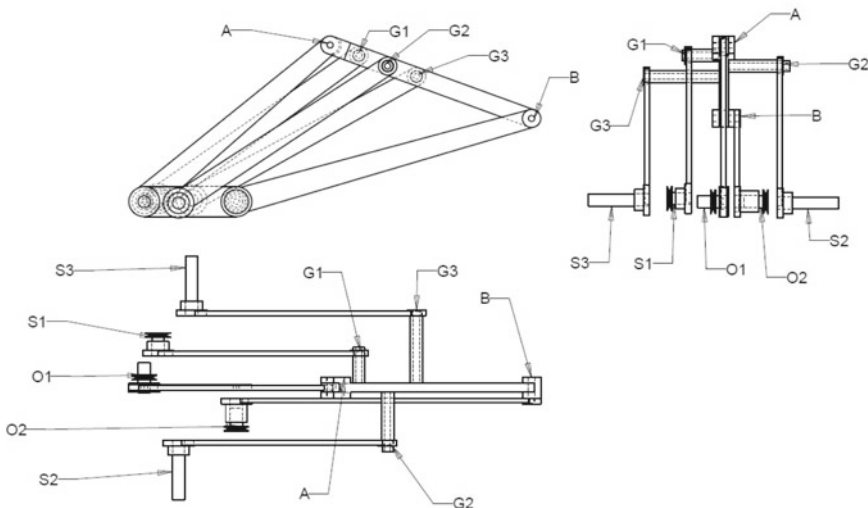
Table 3 Values of absolute velocities of coupler points

Sr. No	Input Crank Angle, θ	V_{g1}	V_{c1}	V_{c2}	V_{c3}
1	0^0	436.25	444.9	453.87	463.21
2	30^0	426.03	431.69	437.48	443.41
3	60^0	413.26	416.15	419.11	422.15
4	85^0	406.56	408.07	409.65	411.29
5	120^0	398.94	398.94	399.02	399.17
6	150^0	392.12	390.81	389.6	388.48
7	180^0	384.84	382.15	379.58	377.13
8	210^0	378.02	374.97	370.28	366.67
9	240^0	373.09	368.33	363.8	359.51
10	260^0	371.76	366.94	362.42	358.21
11	300^0	380.29	377.87	376.13	374.99
12	330^0	408.23	412.19	416.88	422.28

**Fig. 4** Graphical representation of velocity variation**Table 4** Maximum percentage variation in angular velocity

Absolute Velocity	V_{g1}	V_{c1}	V_{c2}	V_{c3}
% variation	8.40	10.17	11.97	13.75

be coupled to some appropriate process unit. Similarly, different output speeds can be obtained from other shafts S_2 , S_3 , and O_2 connected to the coupler points G_2 , G_3 , and B , respectively. This type of linkage configuration with minimum speed variation can be used as a gear box for providing different speed ratios. There are many process units like low-capacity crusher, chopper, cutter, mixer, plastic shredders, etc., [2–5]



Input Link: O_1A ;
 Coupler: AB ;
 Output Link: $BO_2, G_1S_1, G_2S_2, G_3S_3$
 Input Shaft: O_1
 Output Shaft: S_1, S_2, S_3, O_2

Fig. 5 Pictorial representation of three views of double-crank mechanism

where output speed with a very low band of variation of angular velocity could be acceptable. For mechanical energy transmission, such a new concept of gear box can be used instead of a conventional gear box.

4 Conclusion

The literature on double-crank inversion has been very scanty as compared to crank-rocker and rocker-rocker inversions of four-bar chain. Many process units have been developed with crank-rocker and rocker-rocker mechanisms. However, there are applications which involve double-crank linkage as mean for obtaining a nonuniform circular motion.

This paper presents the kinematic analysis of the coupler of a double-crank mechanism. The velocity analysis shows that the path traced out by coupler points is circular and different speed ratios can be obtained by tapping out motion from these points with a percentage variation of 8–54% in angular velocity. The coupler points in the range of 5 cm–8 cm from the crank end of coupler show the least band of variation of about 8.4–13.75% in angular velocity.

With the proper arrangement of links, the assembly could be used as a gear box for the transmission of different speed ratios with minimum variation in output speeds. This concept could possibly eliminate the requirement of synchromesh and toothed gears itself of a conventional gear box.

References

1. Hain, K.: Applied Kinematics, 2nd edn. McGraw-Hill Inc., USA (1967)
2. Johns, F.: Ingenious Mechanisms for Designers and Inventors, vol. 1. 1st edn. Industrial Press Inc., U.S. (1930)
3. Johns, F.: Ingenious Mechanisms for Designers and Inventors, vol. 2, 1st edn. Industrial Press Inc., U.S. (1930)
4. Johns, F.: Ingenious Mechanisms for Designers and Inventors, vol. 3, 1st edn. Industrial Press Inc., U.S. (1930)
5. Johns, F.: Ingenious Mechanisms for Designers and Inventors, vol. 4. 1st edn. Industrial Press Inc., U.S. (1930)
6. Shaw, L.N.: The application of an offset double crank mechanism in a selective bell pepper harvester. In: Transactions of the ASAE, Paper No. 73-15101 (1975)
7. Al-Sabeh, A.K.: Double crank external geneva mechanism. Trans. ASME **115**, 666 (1993)
8. Ju-jiang, C., Yu-qí, W., Ji-, S.: Preliminary research of Crank-group driving mechanism. Appl. Mech. Mater. **229–231**, 555–558 (2012)
9. Xin, L., Lv, Z., Wang, W., Zhou, M., Zhao, Y.: Optimal design and development of a double-crank potted rice seedling transplanting mechanism. Trans. ASABE **60**(1), 31–40 (2017)
10. Wohlrab, W.: Clamping Unit With Double Crank Drive, United States Patent, Patent No.: US 7,445,439 B2 (2008)
11. Bagci, C.: Synthesis of double-crank (drag-link) driven mechanisms with adjustable motion and dwell time ratios. Mech. Mach. Theory **12**, 619–638 (1977)

Structural Synthesis and Classification of Epicyclic Gear Trains: An Acyclic Graph-Based Approach



V. R. Shanmukhasundaram , Y. V. D. Rao , S. P. Regalla ,
D. Varadaraju, and E. Pennestrì

1 Introduction

One of the important steps in the conceptual design stage of mechanical devices/mechanisms is the listing of all the distinct kinematic chains. The synthesis of kinematic chains is performed after knowing the information which includes: type of mechanism, degree of freedom, nature of motion required (planar/spatial), number of links, and pair connections (joints). Graph theory is used to represent the kinematic structure [1]. Precisely, the topology of a graph would convey the information regarding all the links along with their inter-associativity through different joints existing in the kinematic chain. Using graph-based algorithms, an atlas of feasible concepts can be synthesized in the form of representative non-isomorphic graphs [2, 3].

This work deals with the synthesis of epicyclic gear trains (EGTs) which are a class of geared kinematic chains having many applications in modern machinery such as automobile transmissions, machine tool gearboxes, wind energy systems, pulley blocks, harmonic drives, watches, crane hoists, and robotic wrists. EGTs are characterized by the simultaneous presence of turning and gear pair connections in their kinematic structure. A graph model for EGTs was introduced for the first time in the work of Buchsbaum and Freudenstein [4]. In Freudenstein [5], the concepts of rotation graph and displacement graph are detailed.

V. R. Shanmukhasundaram ()
Madanapalle Institute of Technology & Science, Madanapalle, India

Y. V. D. Rao · S. P. Regalla
Birla Institute of Technology and Science, Hyderabad, India

D. Varadaraju
Gayatri Vidya Parishad College of Engineering, Vizag, India

E. Pennestrì
University of Rome Tor Vergata, Rome, Italy

Using the information in a rotation graph, the angular velocity equations can be written with respect to the links of an EGT. Every non-isomorphic rotation graph corresponds to an EGT with a unique kinematic structure. Displacement graphs can be generated from a rotation graph. Basically, with respect to a rotation graph, turning pair edges are labeled in different ways thereby yielding displacement graphs. A displacement graph contains all the information obtainable from a corresponding rotation graph and in addition gives details of the axes levels of the turning pair connections. The turning pair axes levels are necessary so as to sketch an EGT from a certain displacement graph.

For a given number of links and DOF, the task of structural synthesis is aimed at enumerating the complete set of rotation as well as displacement graphs [6–8]. The synthesis problem of EGTs necessarily involves detection and elimination of isomorphic graphs as well as those graphs containing degenerate structure/s [9, 10].

For enumerating rotation graphs, there exist two different approaches, namely, recursive and non-recursive schemes. The recursive method builds candidate graphs through addition of graph components to predecessor EGTs [11]. But the drawback with this method is that the enumerated solution is not complete (i.e., combinatorially). Technically, only a non-recursive scheme can enumerate the complete set of rotation graphs [12]. The conventional non-recursive scheme is not only hard to execute on a computer, but also computationally demanding with too many parent graphs [13, 14]. Experience suggests that it is particularly difficult to enumerate EGTs with more than 6-link complexity because of the above-mentioned reasons. So, there is a need for a simpler non-recursive method which enumerates the entire set of rotation graphs and in turn displacement graphs.

In this work, rotation graphs for a certain number of links and DOF are enumerated using a method involving the usage of acyclic graphs of same number of vertices (i.e., as that of links), as parent structures. This method is non-recursive in nature. The correspondence between an edge-labeled tree and an acyclic graph is exploited here. Since the edge labels are apparent in an acyclic graph, therefore, all feasible circuits containing the gear pair connections can be derived. Upon combining the circuits, rotation graphs are generated. It is a fact, that, the entire collection of these acyclic graphs, for a certain number of vertices (links), is an exhaustive set of edge labeled trees. Therefore, it is justified that, with the usage of all the distinct acyclic graphs for generation, thereby ultimately leads to the enumeration of rotation graphs that are combinatorially complete.

This paper is organized in the following manner. Section 2 deals with the basis of graph structures, namely, acyclic graphs. Later the proposed method is explained with examples followed by a classification scheme for rotation graphs. Section 3 is devoted to a discussion, highlighting the advantages of the proposed method in comparison to that of conventional non-recursive scheme. Finally, some conclusions are drawn in Sect. 4.

2 Non-Recursive Scheme Using Acyclic Graphs as Parents

In the graph of an EGT, vertices correspond to links and edges to that of pair connections. Some characteristics are mentioned in the graph-theoretical framework [4, 5], which need to be satisfied by the graph of an EGT and those are summarized here.

- The edges are colored to distinguish turning and gear pairs.
- The turning pair edges are labeled with axes levels.
- The edge set of turning pairs are connected and constitute a spanning tree with respect to the graph of EGT.
- Further, the same labeled edges must not be disjoint in the graph.
- Every gear pair gives rise to a fundamental circuit (FC). The FC comprises a walk of turning pair edges connecting the either ends of the gear pair edge.
- The turning pair edges within every FC possess any one of the two different labels existing in the circuit. A transfer vertex (TV) in the FC separates the two differently labeled components.
- The DOF of an EGT is numerically equal to the difference between the number of turning and gear pair edges.

A rotation graph will contain the information regarding all the gear pairs along with their respective TVs. The remainder of this section will deal with acyclic graphs and its usage in enumerating rotation graphs.

2.1 Trees, Edge Labeled Trees, and Acyclic Graphs

Trees are geometric combinatorial structures consisting of vertices and edges. Let T be a tree with v vertices. T possesses the following properties:

- (1) Any two vertices of T are connected by one and precisely one path.
- (2) T contains $(v-1)$ edges.
- (3) Whenever any two arbitrary vertices of a tree are joined by an edge, the resulting enlarged graph has a unique cycle or circuit.

By applying the last property, it is possible to derive the FCs of EGT graphs derivable from a tree. In order to form a FC, the path of a tree needs to be closed with a gear paired edge.

In a tree, every pair of vertices is connected by means of a path. The number of paths of an N -vertex tree is therefore equal to C_N^2 . Among these, paths of length 1 (i.e., only one edge) need to be excluded as connecting these would cause the formation of loops which are incapable of forming a FC. Therefore, the number of paths capable of forming FCs is $C_N^2 - (N - 1)$. Now, every one of these paths may not give rise to an FC. This is because the set of turning pair edges constituting the FC must possess exactly two labels separated by a TV. This cannot be ascertained unless all of the turning pair edges are labeled. For this reason, every edge labeling

possibility of a tree needs to be determined. Some guidelines for labeling the edges of a spanning tree, for it to correspond to an EGT are as follows:

Statement 1

The minimum and maximum bound for the number of edge labels of the spanning tree corresponding to any EGT graph is given by, $2 \leq \text{Edgelabels} \leq (N - 1)$.

The minimum number of edge labels to which the edge set of any N -vertex tree can be distributed to must be two. This is because to form any fundamental circuit requires at least two different labels. Therefore, in an edge-labeled spanning tree with only 2 edge labels, the same pair of edge labels is common for all the fundamental circuits derivable from the same. The maximum number of edge labels, the edge set of a tree can be distributed to is $(N - 1)$, in which case every edge of the tree has assigned to it, a different label. Hence, none of the fundamental circuits have the same pair of edge labels separated by their transfer vertices.

Statement 2

Any like labeled set of edges cannot be disjoint and is therefore a tree in itself. All like labeled edges are therefore a single component subgraph of the spanning tree.

This statement comes as an offshoot of the concept of pseudo isomorphism in EGTs [4, 8]. Turning pair edges possessing the same labels are also connected as a tree and vertices of such a tree imply coaxial links of an EGT chain.

Statement 3

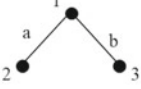
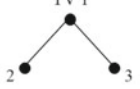
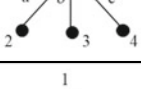
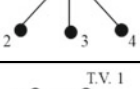
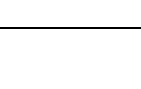
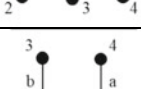
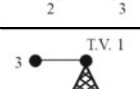
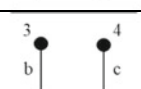
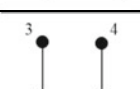
For a certain number of vertices (N), the set of all edge-labeled trees can be represented in the form of corresponding acyclic graphs.

The usage of acyclic graphs was introduced in the works of Hsu and others [15, 16], for representing the displacement graphs of EGTs. In the acyclic graph representation, the edge labeling of turning pair edges is affected by using single edges and/or polygons. A polygon is used to denote a connected graph component, all of whose edges are labeled alike. The order of polygon being numerically equal to number of vertices of the tree containing all the like labeled edges. The number of distinct labels existing in the acyclic graph is equal to the number of single edges and/or polygons.

The advantage of using an acyclic graph is that there is no need for labeling the axes level on each edge. All exhaustive labeling possibilities of the tree of turning pair edges of an EGT can be replaced by an acyclic graph of same number of vertices (i.e., as that of the spanning tree of EGT graph). In fact, these acyclic graphs can be synthesized in a systematic manner [17].

Table 1 shows the distinct trees for 3 and 4 vertices along with the edge labeling possibilities. In the last column, equivalent acyclic graphs are given also indicating possible TVs, from which FCs can be generated with the connection of a gear pair edge. Once FCs are generated, rotation graphs can be synthesized by combining them in different ways. This is explained in the subsequent sections.

Table 1 Trees and their edge labeling possibilities along with acyclic graph equivalents

Number of vertices	Tree	Edge labeling possibilities	Equivalent acyclic graph
3			
4			
			
			
			

2.2 Generation of Rotation Graphs

The equivalence of acyclic graph with edge labeled trees was discussed previously. Therefore, given an acyclic graph, all the vertex pairs for addition of gear pair connections can be established. One thing which is apparent from an acyclic graph is transfer vertices (TVs). Any vertex of an acyclic graph incident with at least two single edges or two polygons or combinations of single edges and polygons is a plausible TV of fundamental circuits (FCs) derivable from the same [16]. Through each of these TVs, the set of feasible paths for FCs can be determined. The process of generation of N -link, F-DOF rotation graphs of an EGT is equivalent to that of choosing $(N - F - 1)$ FCs at a time from the set of determined feasible paths through all the TVs.

The number of rotation graphs derivable from a given N -vertex acyclic graph,

$$= C_{\text{Number of feasible through all the plausible TVs of the given acyclic graph}}^{(N-F-1)\text{FCs corresponding to as many feasible paths}} \quad (1)$$

The chosen set of $(N - F - 1)$ FCs must consist of all the vertices belonging to the vertex set of the acyclic graph. This is a problem in combinations, and it is illustrated with an example.

Example—Generation of 7-link, 1 DOF rotation graphs from acyclic graph.

For the 7-vertex acyclic graph given in Fig. 1, the plausible TVs are vertex-1, vertex-2, and vertex-3. At each 3 TVs, the pairs of vertices suitable for gear pair edge addition are tabulated in Table 2. There exist a total of 6 possible pairs of vertices across the 3 TVs that give rise to fundamental circuits (FCs). In order to generate 7-link EGTs of 1 DOF, the corresponding rotation graphs are obtained by combining 5 FCs at a time from among the 6 possible pairs of vertices. The C_6^5 (i.e., 6) rotation graphs are shown in Fig. 2.

Out of these generated graphs, some are eliminated because the vertex set does not contain all the 7 vertices of the original acyclic graph taken in this example. The

Fig. 1 A 7-vertex acyclic graph

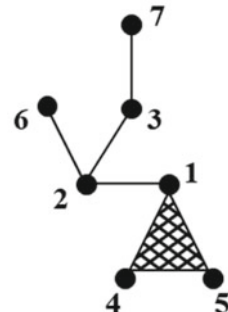


Table 2 The gear pairs giving rise to FCs with respect to acyclic graph of Fig. 1

Single edges and polygons incident at a particular TV	Vertex pairs for addition of gear pair edges	Fundamental circuit
	(2, 4)	1-2-4
	(2, 5)	1-2-5
	(1, 3)	2-1-3
	(1, 6)	2-1-6
	(3, 6)	2-3-6
	(2, 7)	3-2-7

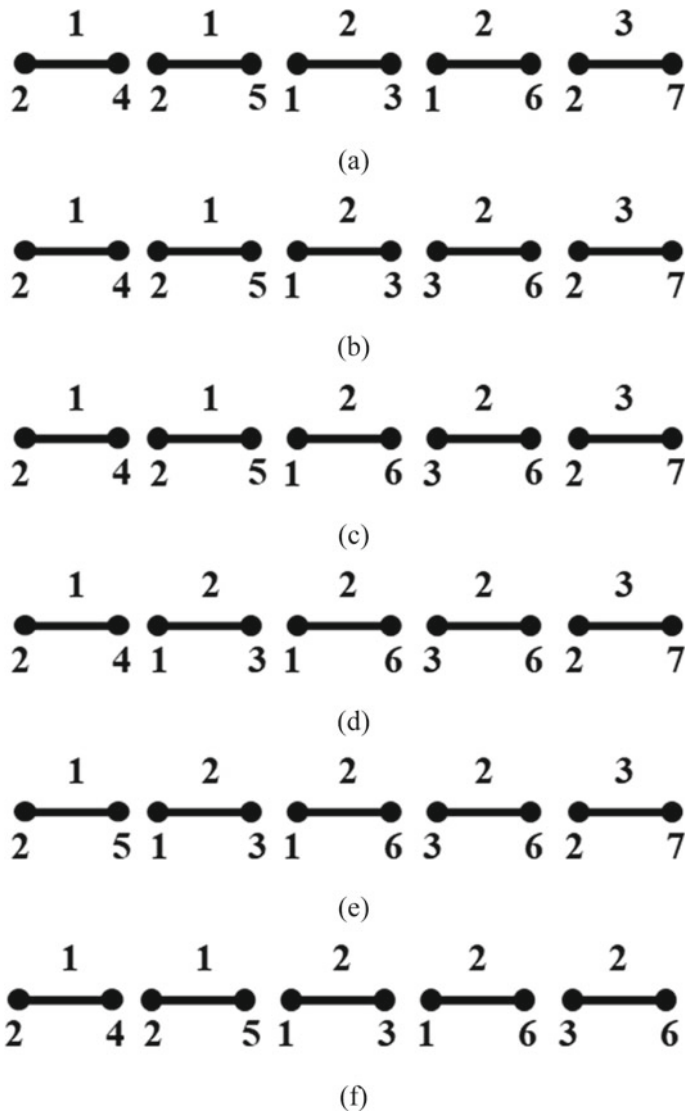


Fig. 2 The 6 rotation graphs of 1 DOF derived from the acyclic graph of Fig. 1

rotation graphs in Fig. 2d–f must be eliminated because their vertex set does not contain all the 7 vertices of the original acyclic graph.

2.3 Grouping of Acyclic Graphs into Classes

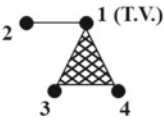
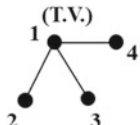
For a general structural synthesis problem, it may seem that rotation graphs need to be generated from all the acyclic graphs followed by test for isomorphism thereby resulting in the generation of the complete set of candidates. But instead of utilizing all the acyclic graphs as parents, the acyclic graphs can be grouped into classes such that a representative from each class is enough for carrying out the generation of all the rotation graphs, some of which are as well obtainable from remaining acyclic graphs of the same class. This way, the computational efficiency of the overall synthesis procedure can be reduced.

As an example, considering the two acyclic graphs for 4 vertices shown in Table 3 alongside with their possible vertex pairs for addition of gear pair edges, both of them have vertex-1 as the TV. The acyclic graph with three different labels for the edges 1–2, 1–3, and 1–4 has all those vertex pairs for addition of gear pair edges which are also obtainable from the other acyclic graph (i.e., possessing two different labels for edge 1–2 and polygon 1–3–4). Therefore, the former acyclic graph (with three different labels) is a representative of the two. As a result, a representative acyclic graph has the potential of enumerating all those rotation graphs as its subset, which are also obtainable from the remaining acyclic graphs belonging to the same class.

In order for different acyclic graphs to fall in the same class, they must necessarily possess the same number of TVs. Having said that, all acyclic graphs possessing the same number of TVs need not fall under the same class.

For a particular number of vertices, all the maximum labeled acyclic graphs correspond to the non-isomorphic tree topologies. All these maximum labeled acyclic graphs can be considered as independent class representatives in themselves. The acyclic graphs having polygons which are associated with single TV only are a subset of the maximum labeled acyclic graphs (trees). Figure 3a is a maximum labeled graph. The acyclic graphs in Fig. 3b–e are all subset of the graph of Fig. 3a. This is because the polygons present in the graphs are associated with only one TV. A simple practice is to number the vertices of the graphs and verify that the vertex

Table 3 Two acyclic graphs for 4 vertices belonging to the same class

The two 4-vertex acyclic graphs possessing a single TV	Vertex pairs for addition of gear pair edges
	$\{(2, 3); (2, 4)\}$
	$\{(2, 3); (2, 4); (3, 4)\}$

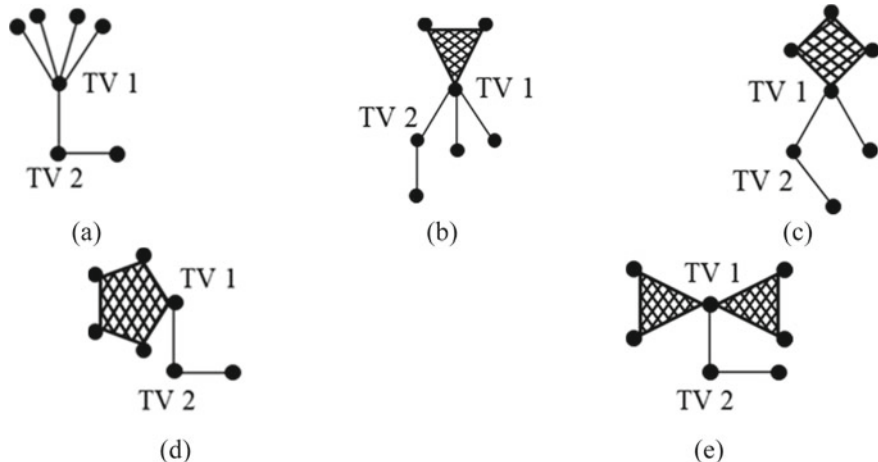
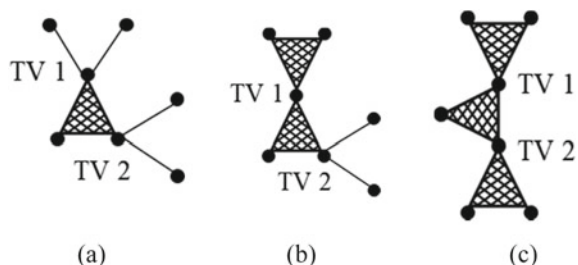


Fig. 3 A maximum labeled 7-vertex acyclic graph; **b–e** It's subset acyclic graphs each having polygon/s common to only one TV

pairs (for gear pair addition) that can be obtained from graph of Fig. 3a is a superset of all those derivable by the rest (Fig. 3b–e). Hence, rotation graphs that can be generated from acyclic graph of Fig. 3a can also be generated from the other graphs in Fig. 3b–e.

The remaining acyclic graphs (i.e., having polygons common to more than one TV) can be grouped into different classes. The criterion for different acyclic graphs to belong to a common class is that, all of them have 1:1 correspondence between their respective TVs, precisely, each TV must be incident with the same number of edges (for the case of n -vertex polygon, an equivalent of $(n - 1)$ edges can be considered). The representative of a class of acyclic graphs is the one which possesses the most number of edge labels. As an example, Fig. 4a–c shows 3 acyclic graphs having one or more polygons common to more than one TV and at each TV there exists 1:1 correspondence among the graphs and therefore all the 3 graphs belong to a common class. These 3 graphs cannot be represented by any maximum labeled acyclic graph as seen in the case of Fig. 3. Of these, Fig. 4a has more labels (precisely 5) than

Fig. 4 Examples of acyclic graphs possessing at least one polygon associated with more than one TV; with the graph in (a) possessing more labels and therefore it is “representative” of graphs of (b) and (c)



those of Fig. 4b, c (4 and 3 labels, respectively). Therefore, the graph of Fig. 4a is representative of the other two.

In Table 4, all 5-vertex acyclic graphs are grouped into 4 different classes. In class 1, all the acyclic graphs have vertex-1as TV with each of them incident with 4 edges (or equivalent polygons). Among these, the one with maximum labeled having all the 4 edges labeled differently is chosen as the representative. Similarly, for class 2, both the acyclic graphs have same number of edges incident at TV 1 and TV 2. Of these two, the one having all its edges labeled differently is chosen as the representative for the class 2. For classes 3 and 4, there is only one graph and therefore they are the respective class representatives. In this manner, out of the 8 acyclic graphs, just four of them originating from as many classes are sufficient for carrying out the enumeration of rotation graphs.

Tables 5 and 6, respectively, contain the 6-vertex and 7-vertex acyclic graphs grouped into classes. All the 21 acyclic graphs for 6 vertices are grouped into 10 classes and all the 58 acyclic graphs for 7 vertices are grouped into 25 different classes. The enumeration of 6-link and 7-link rotation graphs can be proceeded by making use of 10 and 25 representative acyclic graphs, respectively, as parents.

3 Summary of Generation of Rotation Graphs Using Method of Acyclic Graphs

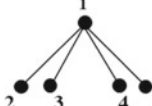
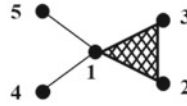
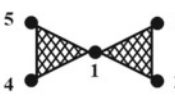
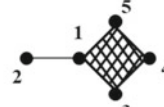
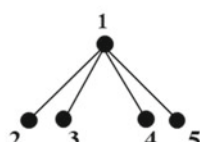
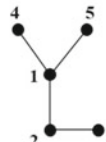
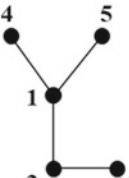
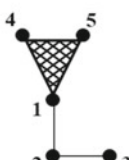
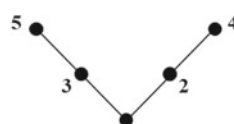
The following steps were executed in order to enumerate rotation graphs of N-link and F-DOF EGTs:

- (1) Enumerate the set of all acyclic graphs for N-vertices.
- (2) Classify acyclic graphs into classes and determine representative for every class.
- (3) From every acyclic graph (representative of a class), determine all the possible pairs of vertices capable of giving rise to FCs along with their respective TVs.
- (4) Obtain combinations of $(N - 1 - F)$ FCs thereby giving rise to rotation graphs.
- (5) Perform step 3 and 4 for all the representatives determined in step 2.
- (6) Detect isomorphism among all the generated graphs so as to arrive at the set of rotationally non-isomorphic graphs.

In this work, all rotationally non-isomorphic graphs with up to 7 links are enumerated. The topological information was stored in the form of vertex-vertex adjacency matrices which are square and symmetric and whose elements are given by:

$$A(i, j) = \begin{cases} 1, & \text{If transfer vertex } i \text{ is associated with a vertex } j \text{ belonging to a gear pair edge} \\ 2, & \text{Vertex } i \text{ and vertex } j \text{ are connected by a gear pair edge} \\ 0, & \text{Otherwise (including } i = j\text{)} \end{cases} \quad (2)$$

Table 4 The 5-vertex acyclic graphs grouped into 4 classes with “representative” mentioned

Class	Acyclic graphs	Vertex pairs for addition of gear pair edges	Representative
1		$\{(2, 3); (2, 4); (2, 5); (3, 4); (3, 5); (4, 5)\}$	
		$\{(2, 4); (2, 5); (3, 4); (3, 5); (4, 5)\}$	
		$\{(2, 4); (2, 5); (3, 4); (3, 5)\}$	
		$\{(2, 3); (2, 4); (2, 5)\}$	
2		$\{(1, 3); (4, 5); (2, 4); (2, 5)\}$	
		$\{(1, 3); (2, 4); (2, 5)\}$	
3		$\{(2, 3); (1, 5); (1, 4)\}$	

(continued)

Table 4 (continued)

4		$\{(1, 5); (3, 5); (2, 4); (3, 4)\}$	
---	--	--------------------------------------	--

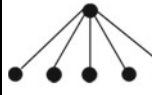
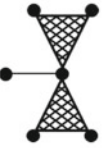
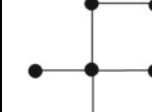
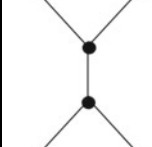
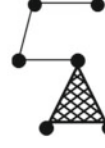
Figure 5a shows a 5-link rotation graph, and its topological information using adjacency matrix is given alongside in Fig. 5b. Spectral method involving the usage of eigenvalues and eigenvectors was used to detect isomorphism [18]. Degeneracy testing was also performed to discard those rotation graphs containing immobile sub-chains.

4 A Basis for Classification of Rotation Graphs Using Structural Similarities

Recalling that a rotation graph contains the information of gear pair edges along with their respective TVs. A rotation graph can therefore have a minimum of one TV associated with all its gear pairs and a maximum number of TVs equaling the number of gear pairs in which case every gear pair will have a unique TV. For the case of N-link 1 DOF EGTs, the number of TVs can be 1, 2, 3..... ($N - 2$). TV implies the carrier link of EGT, and this can be used as a classification criterion. As illustrated in Table 7, the 5-link rotation graphs can be classified as 1-carrier system, 2-carrier system, and 3-carrier system based on whether they contain 1 TV, 2 TVs, and 3 TVs, respectively.

As a second level of classification, for all the rotation graphs having same number of TVs, another criterion can be enforced as to how many FCs are associated with each TV. This is nothing but the number ways of integer partitioning the gear pair edges with the partitioning integer numerically equal to the number of TVs. For example, 2-carrier system rotation graphs for 6-link 1 DOF EGTs can be classified into 2 categories: Out of the 4 gear pairs or FCs, each of the 2 TVs associated with two FCs; 3 FCs having a common TV and the other TV associated with another FC. In this manner, all the 27 6-link rotation graphs of 1 DOF are classified in Table 8. The ID numbers of the non-isomorphic graphs are used same as in the work of Tsai [11].

Table 5 The 6-vertex acyclic graphs grouped into 10 classes with “representative” mentioned

Class	Acyclic graphs			Representative
1				
				
2				
3				
4				
5				

(continued)

Table 5 (continued)

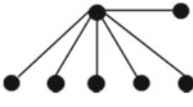
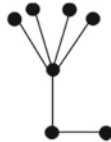
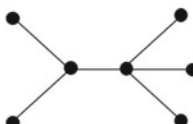
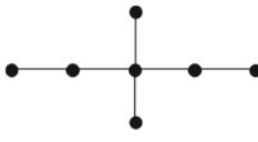
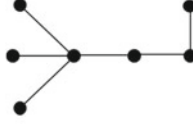
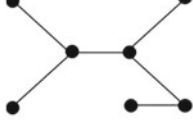
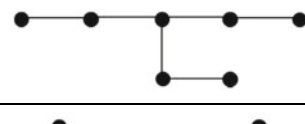
6		
7		
8		
9		
10		

5 Comparison of Proposed Scheme with Conventional Method

In the literature, the usage of acyclic graphs in the synthesis of EGTs was limited to only the generation of displacement graphs [16]. However, in the previous sections, it was shown that acyclic graphs can also be used as parent structures for enumerating rotation graphs. This method is computationally simpler than the conventionally used non-recursive scheme.

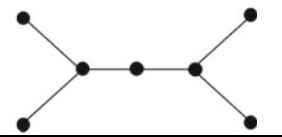
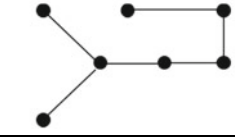
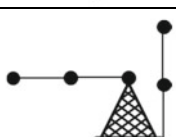
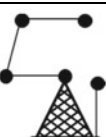
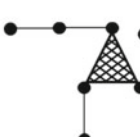
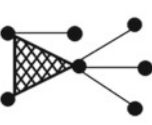
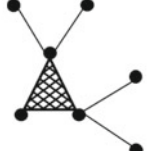
The conventional non-recursive method involves the steps as mentioned in Table 9. Firstly, all the parent graphs are synthesized. The parent graphs have N -vertices (same as links of EGT to be enumerated) and edges equal to the sum of turning and gear pairs. The number of turning and gear pair connections is calculated based on the required DOF, using Gruebler's equation. In the second step gear pair, edges are distributed in different ways in the parent graph. At this stage, the geared graphs that do not meet the fundamental rules of the EGT graph are discarded. In the final step, TVs are identified for each circuit, thereby leading to generation of rotation graphs.

Table 6 The 25 class representatives for 58 acyclic graphs of 7 vertices

Class	Representative acyclic graph
1	
2	
3	
4	
5	
6	
7	
8	

(continued)

Table 6 (continued)

9	
10	
11	
12	
13	
14	
15	
16	

(continued)

Table 6 (continued)

17	
18	
19	
20	
21	
22	
23	
24	
25	

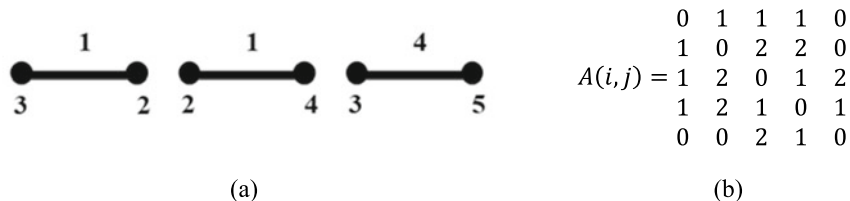


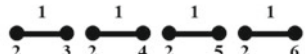
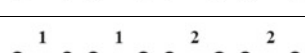
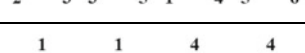
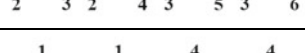
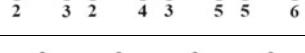
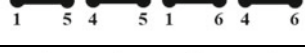
Fig. 5 **a** A 5-link rotation graph; **b** Its adjacency matrix

Table 7 The 6 rotation graphs for 5-link EGTs classified based on number of carriers

Classification based on number of TVs	ID No. as in Tsai (1987)	5-link rotation graphs
1-carrier system: {TV-1 (3 FCs)}	5201	
	5301	
2-carrier system: {TV-1 (1 FC); TV-2 (2 FCs)}	5103	
	5101	
3-carrier system: {TV-1 (1 FC); TV-2 (1 FC); TV-3 (1 FC)}	5302	
	5102	

One of the difficulties encountered in writing a computer program for executing the conventional non-recursive method is the problem of identifying TV for each FC. This decision-making is generally difficult to automate. However, in the new non-recursive scheme developed herein, the TVs can be easily interpreted from an acyclic graph and given as input. An algorithm can then generate all feasible circuits from every TV, followed by combining them in groups so as to generate rotation graphs. This way, the generation process automation becomes simple.

Table 8 The 27 rotation graphs for 6-link EGTs classified based on number of carriers

Classification type	ID No. as in Tsai (1987)	Rotation graphs
1-carrier system: {TV-1(4 FCs)}	6401	
	6503	
	6601	
	6201	
	6203	
	6206	
	6306	
	6403	
	6506	
	Ravisankar & Mruthyunjaya graph (1985)	
2-carrier system: {TV-1 (1 FC); TV-2 (3 FCs)}	6101	
	6103	
	6301	
	6305	

(continued)

Table 8 (continued)

	6402	
	6404	
	6501	
	6502	
3-carrier system: {TV-1 (1 FC); TV-2 (1 FC); TV-3 (2 FCs)}	6102	
	6202	
	6205	
	6302	
	6303	
4-carrier system: {TV-1 (1 FC); TV-2 (1 FC); TV-3 (1 FC); TV-4 (1 FC)}	6304	
	6504	
	6505	
	6204	

In Figs. 6 and 7, acyclic graphs are given. For the 5-vertex acyclic graph in Fig. 6a, vertex-3 is the transfer vertex, and therefore it is the carrier link. If we consider vertex-2 as planet link, and vertices: 1, 4, and 5 as suns then we end up with the rotation graph in Fig. 6b and whose schematic is the commonly known transmission, namely, “Minuteman cover drive”. Similarly, the generation of the “Simpson Gear Train” transmission from a 6-vertex acyclic graph is shown in Fig. 7. Therefore, the

Table 9 Illustration of the conventional scheme through generation of 4-link rotation graphs

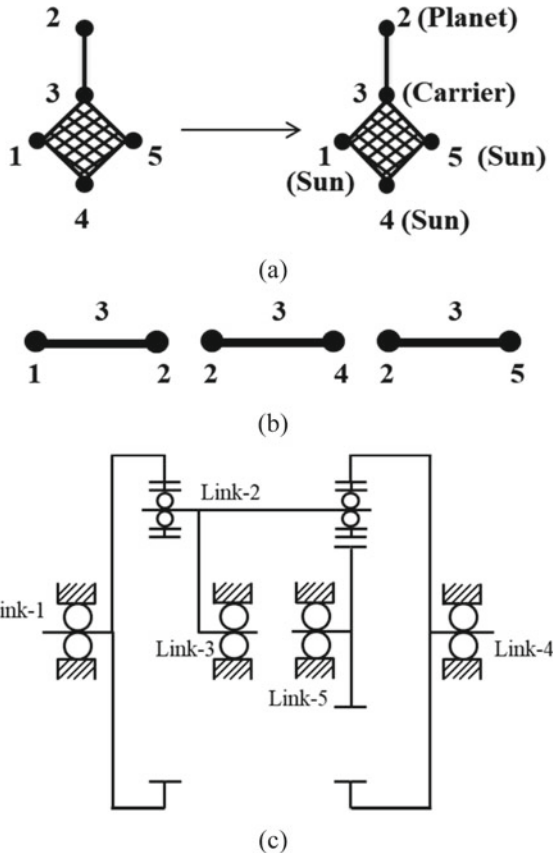
Step	Illustration
Parent graphs: Set of Non colored graphs	
Distribution of gear edges in the parent graph	
Determination of the transfer vertex for fundamental circuits and generation of rotation graphs	

proposed scheme is a new direction for synthesizing EGTs while also envisaging the structural features intended by an EGT designer.

In Table 10, first column, the details for number of parent graphs employed in Yang and Ding [6] using the conventional scheme is given. In column 2 of the same table, the total number of distinct acyclic graphs is given. As per the new scheme, the number of acyclic graphs required for enumerating the complete set of rotation graphs can be pruned from the total number of distinct acyclic graphs, based on the concept of “representative classes” as explained earlier and it is mentioned in column 3. It can be seen that, as the number of links increases, the parent graphs required according to the conventional scheme simply proliferates; whereas the total number of acyclic graphs is much lesser and in fact these numbers can be pruned further. In this work, we applied the proposed method and obtained 27 and 152 rotation graphs for 6-link and 7-link 1 DOF EGTs. The results are in agreement with existing works [6, 8].

Structures such as Baranov trusses and Assur groups are popular in mechanisms community for their usage in the synthesis of basic kinematic chains [19, 20]. Likewise, acyclic graphs and their potential for synthesizing EGTs of higher number of links is a topic worth exploring by future works. The total number of acyclic graphs with up to 8 links is verified with that of Hsu and Hsu [16]. Our result of 494 9-link acyclic graphs is new and can be verified by other researchers. The atlas of all the acyclic graphs can be found in the doctoral thesis of the first author [21].

Fig. 6 **a** A 5-vertex acyclic graph; **b** Its derived rotation graph of 1 DOF; **c** Corresponding schematic “Minuteman cover drive”



6 Conclusions

The main advantage of going for a non-recursive scheme for synthesizing the kinematic structure of EGTs is because in principle it is capable of obtaining all the combinatorially possible concepts (graphs). In this regard, there exists a non-recursive method in the literature for generating the rotation graphs of EGTs, given the number of links and DOF. This has been applied by many scientific works during the last 50 years. In this work, a new non-recursive scheme is offered which utilizes acyclic graphs of a certain number of vertices (same number as links of the EGTs derivable from same) as parent graphs. In the first step, all the feasible pairs of vertices for addition of a gear pair edge are determined from an acyclic graph. Each of these gear pair edges gives rise to a unique FC with respect to the acyclic graph, in accordance with the graph-theoretic framework for EGTs. When the plausible FCs (determined in the first step) are combined in different ways, they yield rotation graphs. The number of circuits to be combined depends on the DOF of the EGT to be synthesized.

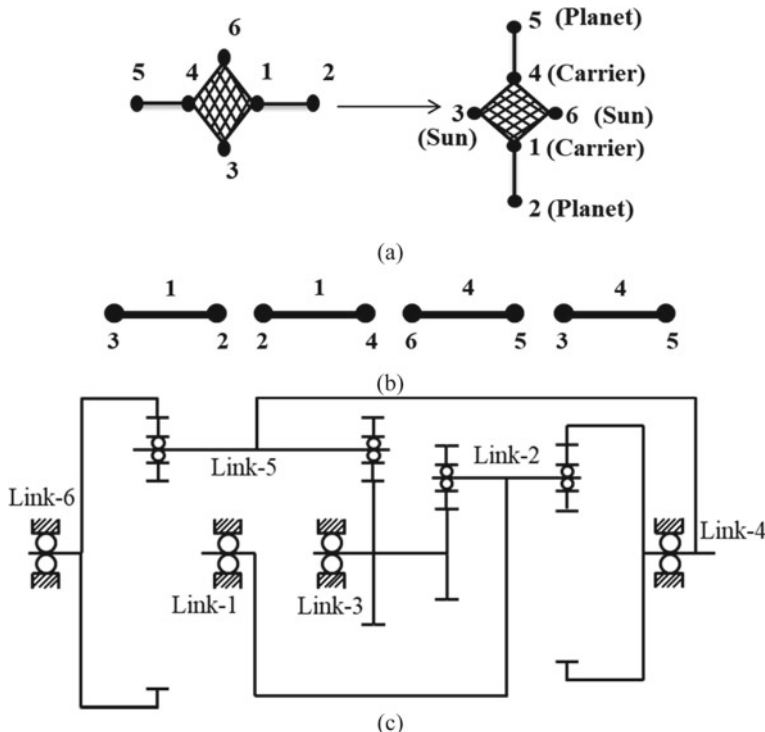


Fig. 7 **a** A 6-vertex acyclic graph; **b** Its derived rotation graph of 1 DOF; **c** Corresponding schematic “Simpson gear train”

Table 10 Comparison of parent graphs used by conventional method and with the new scheme

Number of links	Parent graphs required according to conventional non-recursive method	Number of acyclic graphs	Parent acyclic graphs used according to newly proposed non-recursive method in this work (after pruning into representative classes)
3	1	1	1
4	1	3	2
5	3	8	4
6	14	21	10
7	82	58	25
8	780	164	Not attempted in this work
9	9983	494	Not attempted in this work

In addition to the simple nature of the outlined synthesis steps, a significant feature of the discussed approach is that, it uses lesser number of parent graphs than the conventional non-recursive method, in order to enumerate the complete set of rotation graphs. Therefore, by using this method, enumeration of EGTs with 8 or more number of links can be carried out in a computationally efficient manner.

Further, it was shown that the catalogue of rotation graphs of same number of links and DOF can be classified. This classification will benefit the EGT designer in enabling him/her to recognize particular structural features in the graph of an EGT. This can, for instance, pave way for selectively enumerating EGTs sharing similar structural characteristics. Interestingly, this can actually be realized by generating EGTs using a certain class of parent acyclic graphs.

References

1. Freudenstein, F., Dobrjanskyj, L.: On a theory for the type synthesis of mechanisms. In: Görller, H. (ed.) Applied mechanics, pp. 420–428. Springer, Berlin, Heidelberg (1966)
2. Pennestri, E., Belfiore, N.P.: On Crossley's contribution to the development of graph based algorithms for the analysis of mechanisms and gear trains. *Mech. Mach. Theory* **89**, 92–106 (2015)
3. Pennestri, E., Valentini, P.P.: Kinematics and enumeration of combined harmonic drive gearing. *J. Mech. Des.* **137**(12) (2015)
4. Buchsbaum, F., Freudenstein, F.: Synthesis of kinematic structure of geared kinematic chains and other mechanisms. *J. Mech.* **5**(3), 357–392 (1970)
5. Freudenstein, F.: An application of boolean algebra to the motion of epicyclic drives. *J. Eng. Ind.* **93**(1), 176–182 (1971)
6. Yang, W.J., Ding, H.F.: The complete set of one-degree-of-freedom planetary gear trains with up to nine links. *J. Mech. Des.* **141**(4), 043301 (2018)
7. Yang, W., Ding, H., Kecskeméthy, A.: Automatic structural synthesis of non-fractionated 2-DOF planetary gear trains. *Mech. Mach. Theory* **155**, 104125 (2019)
8. Shanmukhasundaram, V.R., Rao, Y.V.D., Regalla, S.P.: Enumeration of displacement graphs of epicyclic gear train from a given rotation graph using concept of building of kinematic units. *Mech. Mach. Theory* **134**, 393–424 (2019)
9. Shanmukhasundaram, V.R., Rao, Y.V.D., Regalla, S.P.: Algorithms for detection of degenerate structure in epicyclic gear trains using graph theory. *J. Braz. Soc. Mech. Sci. Eng.* **41**(11), 496 (2019)
10. Morlin, F.V., Carboni, A.P., de Souza, M.B., Martins, D.: Degeneracy detection in epicyclic gear trains using a matroid-based algorithm. In: International Symposium on Multibody Systems and Mechatronics, pp. 11–18. Springer, Cham (2020)
11. Tsai, L.W.: An application of the linkage characteristic polynomial to the topological synthesis of epicyclic gear train. *ASME J. Mech. Trans. Autom. Des.* **109**(3), 329–336 (1987)
12. Ravisankar, R., Mruthyunjaya, T.S.: Computerized synthesis of the structure of geared kinematic chains. *Mech. Mach. Theory* **20**(5), 367–387 (1985)
13. Souza, M.B.D., Vieira, R.D.S., Martins, D.: Enumeration of kinematic chains with zero variety for epicyclic gear trains with one and two degrees of freedom. In: International Symposium on Multibody Systems and Mechatronics. Springer, Cham (2017)
14. Souza, M.B.D., Vieira, R.D.S., Martins, D.: Synthesis of epicyclic gear trains with one and two degrees of freedom from kinematic chains belonging to minimal sets. *Int. J. Mech. Robot. Syst.* **4**(4), 383–400 (2018)

15. Hsu, C.H., Lam, K.T.: A new graph representation for the automatic kinematic analysis of planetary spur-gear trains. *ASME J. Mech. Des.* **114**(1), 196–200 (1992)
16. Hsu, C.H., Hsu, J.J.: An efficient methodology for the structural synthesis of geared kinematic chains. *Mech. Mach. Theory* **32**(8), 957–973 (1997)
17. Shamukhasundaram, V.R., Rao, Y.V.D., Regalla, S.P.: Review of structural synthesis algorithms for epicyclic gear trains. In: Sen, D., Mohan, S., Ananthasuresh, G. (eds.) *Mechanism and Machine Science* (2021)
18. Sunkari, R.P., Schmidt, L.C.: Reliability and efficiency of the existing spectral methods for isomorphism detection. *ASME J. Mech. Des.* **128**(6), 1246–1252 (2006)
19. Morlin, F.V., Martins, D.: Reconciling enumeration contradictions: Complete list of Baranov chains with up to 15 links with mathematical proof. *J. Mech. Des.* (2020)
20. Huang, P., Ding, H.: Structural synthesis of baranov trusses with up to 13 links. *J. Mech. Des.* **141**(7) (2019)
21. Shamukhasundaram, V.R.: Number synthesis and structure based rating of multilink epicyclic gear trains satisfying gruebler's degree of freedom equation. Doctoral Thesis, BITS Pilani – Hyderabad Campus, India (2020)

Fuel Economy and Drivability Trade-Off for Mild Hybrid Electric Vehicle Architectures



Neeraj Shidore, Norman Bucknor, and Madhusudan Raghavan

1 Introduction

Hybrid vehicle technology is considered as a bridge to develop affordable electric vehicles. Especially, hybrid vehicle technologies that retain key components of the conventional powertrain, i.e., electrify the conventional powertrain, are especially attractive as low-cost solutions to improving fuel economy. ‘Mild’ hybrid vehicles, wherein the engine is the main source of traction power, are examples of such hybrids.

Propulsion system architectures (for any type of powertrain, i.e., conventional, hybrid, and electric) have an impact on three important customer-facing features. These features are—cost, fuel economy, and drive quality, i.e., customer perception of how the vehicle responds to accelerator pedal, brake pedal, and steering inputs from the driver. Among these, fuel economy and drive quality are strictly functions of propulsion system architecture, component sizing, vehicle control and calibration. These factors will be the focus of this paper, for mild hybrid powertrains. It should be noted that all the plots showing time axis data and numerical results in the paper are based on simulation results. The simulations were undertaken for the study that culminated in this research paper.

N. Shidore · N. Bucknor · M. Raghavan (✉)
General Motors, Warren, MI 48092, USA
e-mail: Madhu.raghavan@gm.com

N. Shidore
e-mail: neeraj.shidore@gm.com

N. Bucknor
e-mail: norman.k.bucknor@gm.com

1.1 Common Mild Hybrid Architectures

Hybrid architectures are commonly described in terms of the location of the motor on the driveline, relative to the location of the engine and the transmission [1, 2]. Figures 1 and 2 show some of the most frequently used locations for the motor (M/G in the figure) on the driveline, in P0, P1, and P2 hybrid architectures. In a P0 architecture, the motor is inserted in the place of the alternator and interacts with the engine via the accessory drive belt, for executing functions such as engine start/stop and regenerative braking/torque boosting. Such a system is also referred to as a Belted Alternator Starter (BAS). In a P1 architecture, the motor is located between the engine and transmission and is generally geared or directly coupled to the engine, so that they always move together. The motor can perform engine start/stop and hybrid functions like regenerative braking/torque boosting. In a P2 architecture, the motor is located between the engine and transmission with one or more additional

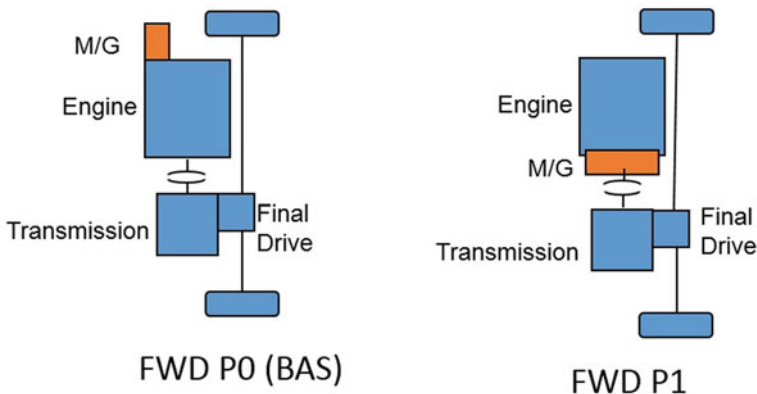


Fig. 1 P0 and P1 hybrid vehicle architecture for Front-Wheel Drive (FWD)

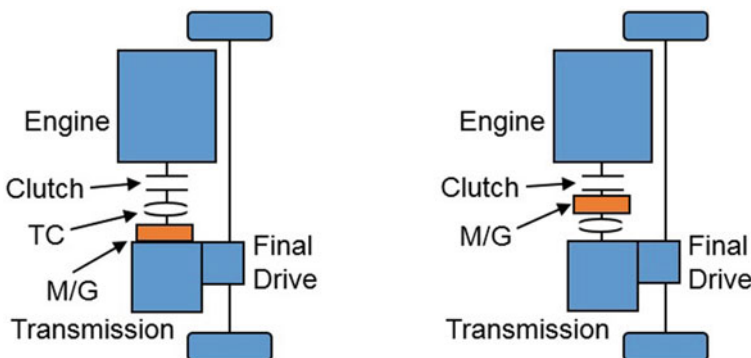


Fig. 2 P2 hybrid architecture for FWD

clutches so that it can be selectively attached to the engine or transmission or both. Figure 2 shows two possible variations. The left figure shows the motor attached to the transmission downstream of the torque converter (TC). The right figure shows the motor located upstream of the torque converter, with a clutch to connect/disconnect it to/from the engine.

2 Hybrid Operation and Impact of Powertrain Architecture on Fuel Economy Benefits

2.1 Hybrid System Power Level

The hybrid system power level determines capability and system cost. For the vehicle considered in this study, Fig. 3 shows the cumulative braking energy, binned by axle power, during decelerations on different drive cycles used for fuel economy (FTP City, Highway, and US06) or fuel consumption certification (MVEG, WLTP) [3]. The data in Fig. 3 is based on a vehicle system simulation. The simulation model has been validated with actual vehicle test data. The cumulative energy (shown positive for clarity) is a measure of the total energy that can be recuperated via regenerative braking on each drive cycle below a given braking power magnitude. The plot shows that US06 decelerations requiring more than 50 kW of braking power do not add significant additional energy, providing an approximate upper limit for regenerative

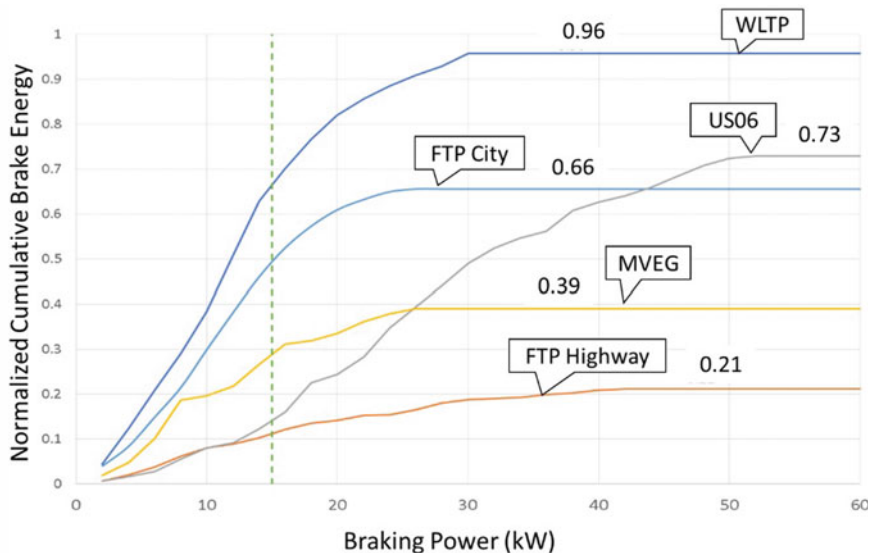


Fig. 3 Normalized cumulative axle energy during deceleration for various drive cycles

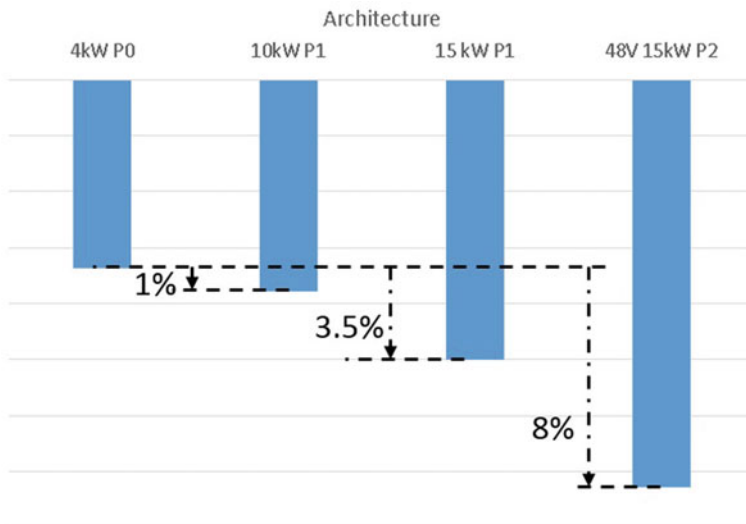


Fig. 4 P1 and P2 hybrid architecture fuel consumption reduction relative to a P0

braking system capability; the effects of system losses in the power-transfer path between the axle and the battery pack are neglected. This is a suitable power level for a ‘strong’ hybrid but generally requires higher system voltage and significant motor power. Looking at the EPA City Cycle (UDDS), up to 30 kW of braking power is needed. With a 15 kW hybrid system, all the energy to the left of the dashed line is potentially recoverable by regenerative braking. For the City Cycle, 76% of the total braking energy available can be recuperated. On the MVEG and WLTP cycles, the percentages are 67% and 72% respectively. With the exception of the US06 cycle, a 15 kW system can, therefore, potentially recover a significant amount of vehicle kinetic energy.

2.2 Architecture Impact on Fuel Economy

The fuel consumption reduction for the P1 and P2 architecture relative to a P0 baseline is shown in Fig. 4 for a small CUV. The data for Fig. 4 is derived from system simulation of the different powertrain architectures. The systems shown are a 4 kW P0, a 10 kW P1 and a 15 kW P2. The difference in power level between the systems is for purposes of illustrating the difference in benefit due to system power level rather than an inherent physical constraint.¹ P2 systems can be strong hybrids but the maximum power level that can be considered is a trade-off between system

¹Typically, P0 is a belt-driven unit on the front end of the engine, P0 is usually limited by the power that can be transmitted through the belt.

Table 1 Hybrid operating feature by architecture

Operating feature	S/S	P0	P1	P2
No engine idle	Y	Y	Y	Y
Regenerative braking	N	Y	Y	Y
Engine torque assist	N	Y	Y	Y
Launch vehicle with engine off	N	N	N	Y
Engine disconnect during decel	N	N	N	Y
Electric-only cruising	N	N	N	Y

voltage, cost, and fuel consumption benefit. As discussed in the previous section, a 15 kW power level allows the system to achieve a significant degree of kinetic energy recuperation on most cycles. The hybrid operating features available for each system are described in Table 1. The P2 hybrid controls are configured to maximize the hybrid system benefit consistent with the drivability constraints discussed in Sect. 3. With all operating features enabled, the P2 can achieve approximately 8% additional fuel consumption reduction, when compared to a P0. In principle, the engine could also be downsized to maintain overall system power (engine + battery) to gain a further reduction on the 10 and 15 kW systems. The difference between the 15 kW P1, which has no electric-only driving and the P2 is approximately 4.5%.

Figures 5 and 6 are courtesy of our colleagues Derek Lahr and Farzad Samie. These figures show schematics of possible modular add-ons of a traction motor to a conventional planetary front-wheel drive transmission. Figure 5 shows a belt connection to the torque converter. This arrangement would require a dual tensioner on the belt to ensure proper tension during regeneration and torque boosting modes. Figure 6 shows a schematic of an alternative possible modular add-on of a traction motor to a conventional planetary front-wheel drive transmission using a geartrain to connect the motor to the turbine shaft. Suitable bearing supports must be designed for NVH mitigation [4, 5].

3 P2 Architecture, Drive Quality, and Impact on Fuel Economy

3.1 Tip-In Response

As stated in the prior section, in a P2 architecture, the engine can be disconnected from the rest of the drivetrain. This improves fuel economy, since during vehicle deceleration and coasting conditions, the motor and battery can recuperate more energy from regenerative braking. This is because the engine drag is eliminated by disconnecting the engine from the drivetrain [6–9]. To maintain a balanced battery State of Charge (SOC) for a charge sustaining hybrid, this recuperated energy is

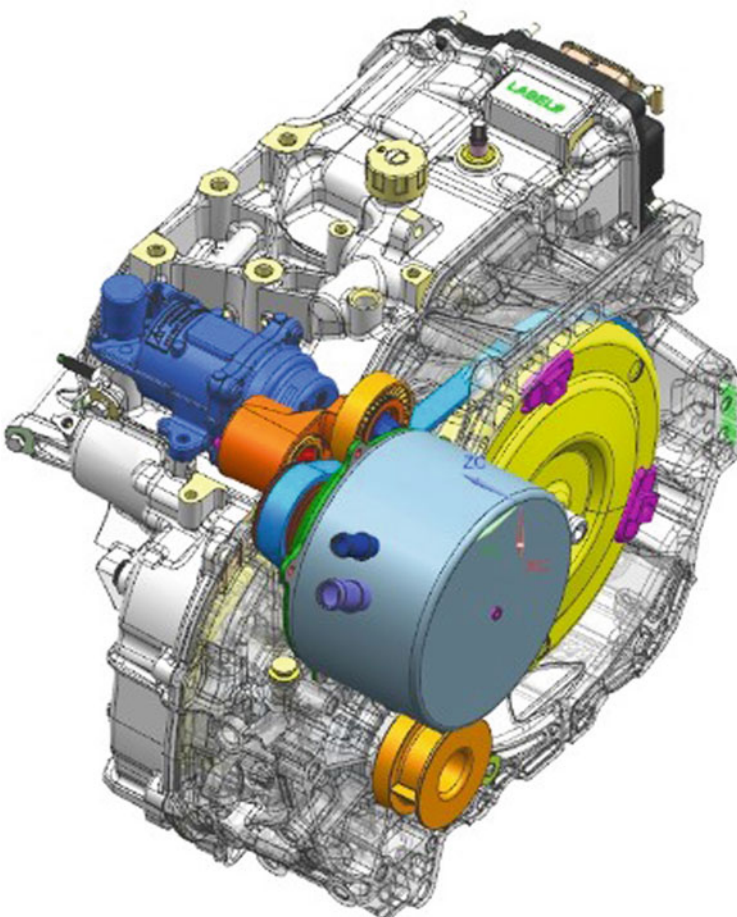


Fig. 5 Modular add-on of a traction motor to a planetary transmission via belt

used to propel the vehicle in electric mode with the engine disconnected. This occurs under certain conditions, as described below:

1. At vehicle launch, i.e., when the vehicle accelerates from zero speed, the hybrid motor is typically used to launch the vehicle, and the engine is subsequently connected to the driveline as the vehicle power demand or requested torque exceeds the capability of the electrical system.
2. When the vehicle is coasting at constant speed (for example, on the highway), the engine is disconnected from the driveline and the electric motor torque is used to balance resistive forces such as wind and road friction.
3. When the vehicle is decelerating, the engine may be disconnected from the driveline and the electric motor absorbs braking energy.

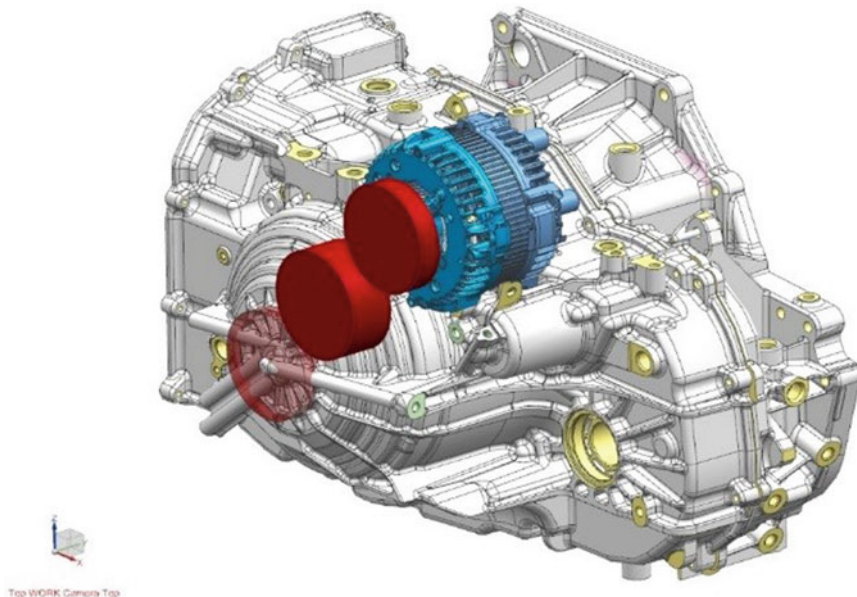


Fig. 6 Modular add-on of a traction motor to a planetary transmission via Geartrain

A sudden aggressive pedal tip-in, during situations (2) or (3) above, where the vehicle is slowing down or coasting at constant speed, is referred to as a “change of mind.” Figure 7 (simulation data) shows the change of mind scenarios as dotted lines that “branch off” from the vehicle speed trace during the coasting or regenerative braking (regen) event. Note that engine power is zero during both tip-ins, i.e., vehicle is in electric-only (EV) mode. The driver expects rapid vehicle acceleration in response to a sudden, aggressive accelerator pedal tip-in.

3.2 Control Philosophy for Satisfactory P2 Tip-In Response

In order to mitigate the potentially sluggish tip-in response due to a P2 architecture featuring engine connects/disconnects, three key components have to be considered synergistically. They are the following:

1. Power limits of the on-board electrical system (i.e., battery/motor power at any instance of time),
2. System response (i.e., time for the engine to start and connect to the driveline, based on driveline speed),
3. Knowledge of what constitutes a “good tip-in response” as perceived by the driver.

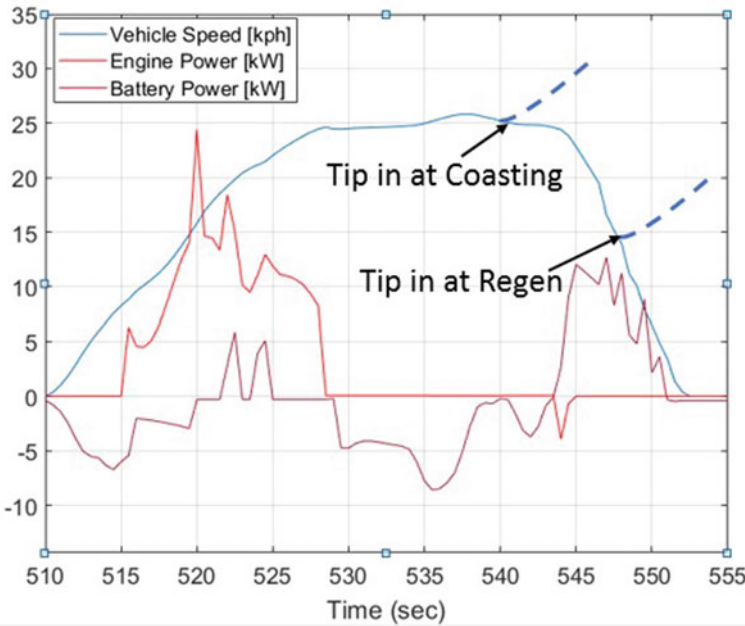
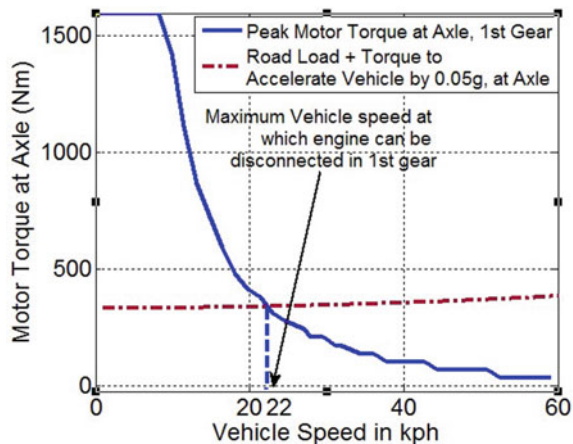


Fig. 7 Potential tip-in scenarios during EV driving

Among many factors that constitute a good tip-in response, a key element is the initial acceleration that can be achieved as soon as the accelerator pedal is depressed. This initial acceleration, for the P2 system, is provided by the electrical motor. Therefore, in the case of a sudden tip-in, the electric motor should be able to provide at least, as a rule of thumb, 0.05 g of delta acceleration. Since the vehicle is already operating in EV mode at tip-in, the electric motor is also providing torque to meet road load demand. Therefore, the electric motor should be able to provide road load torque + torque for 0.05 g of acceleration for a good tip-in response. Figure 8 shows motor torque capability at the axle for a given gear state (solid blue line), as a function of vehicle speed. The dotted brown line shows the road load torque, with the additional torque required for 0.05 g acceleration. The velocity at which the brown line intersects the blue line is, theoretically, the maximum speed at which the demand for (0.05 g + road load) can be satisfactorily met by the system, while in EV mode. This velocity is 22 kph in Fig. 8. Therefore, the engine is always turned on above 22 kph, to avoid a situation where the electrical system cannot meet the initial acceleration requirement during tip-in.

Fig. 8 Speed limit beyond which EV operation cannot meet requirements for a satisfactory tip-in response



3.3 Trade-Off Between Drive Quality and Fuel Consumption for a P2

As described in the section above, EV operation in a P2 is limited to a certain kph, to meet drive quality requirements. For hybrid vehicles, fuel consumption improvement is achieved by using as much electrical energy as possible to propel the vehicle, by maximizing EV operation within the battery SOC charge balancing constraints. Curtailment of EV operation, due to drive quality considerations, therefore, reduces the fuel consumption benefits of a P2, and there is a trade-off between the two. A strong hybrid architecture, wherein the electrical system is sufficiently powerful to meet drive quality requirements, does not have such a trade-off. This, however, comes with a significant cost increase to the customer.

Figure 9 shows the theoretically achievable fuel consumption with a mild hybrid P2 (without drive quality consideration) with EV driving permitted up to 50 kph, compared to the fuel consumption when EV operation has been curtailed for drive quality reasons. The results shown in the figure are from simulations. As the maximum allowed vehicle speed in EV mode is reduced, the engine re-starts sooner, regardless of the acceleration demand. In addition, the ability to do electric cruising on the highway, is essentially removed once the maximum permitted EV speed drops below 30 kph. Based on the maximum allowed EV speed, the drive quality penalty for the P2 is in the range of 2 to 3%. Fast starters [10] are key to enabling acceptable drive quality during operation with frequent engine re-starts.

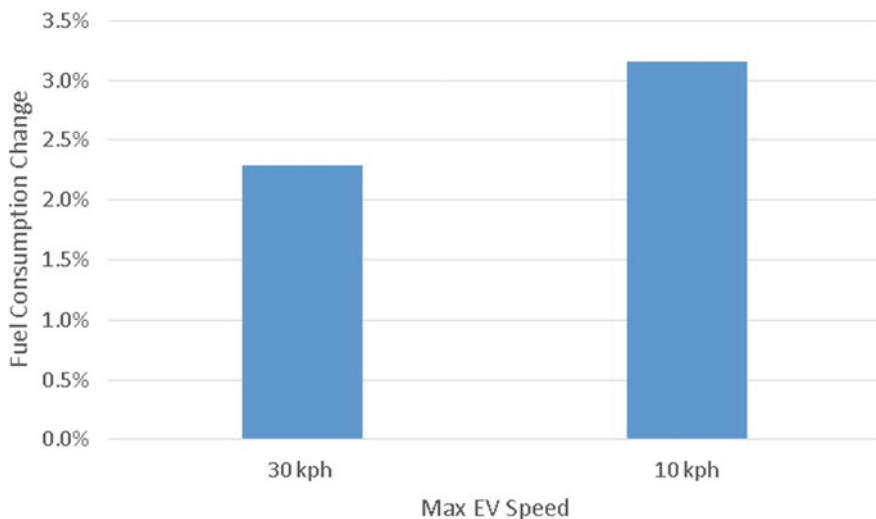


Fig. 9 Change in FTP combined unadjusted fuel consumption due to reduction in maximum EV driving speed from 50 kph

4 Summary

This paper compares different mild hybrid powertrain configurations for their fuel consumption benefits. Tip-in response is an important drive quality metric for the longitudinal acceleration of a vehicle. The trade-off between fuel consumption and drive quality for the P2 is discussed. A 15 kW mild hybrid with a P2 architecture, can achieve about 8% improvement in fuel consumption over a P0 system, when drive quality concerns are neglected in the analysis. In order to ensure that the P2 architecture offers a good tip-in response, the EV operation is curtailed, which results in a 2 to 3% reduction in fuel consumption.

References

1. Morra, E., Spessa, E., Ciraavino, C., Vassallo, A.: Analysis of various operating strategies for a parallel-hybrid diesel powertrain with a belt alternator starter. *SAE Int. J. Alt. Power* **1**(1) (2012). <https://doi.org/10.4271/2012-01-1008>.
2. Conlon, B., Barth, M., Hua, C., Lyons, C., Nguy, D., Palardy, M.: Development of Hybrid-Electric Propulsion System for, : Chevrolet Malibu. *SAE International Journal of Alternative Powertrains* **5**(2), 259–271 (2016)
3. <https://www.epa.gov/vehicle-and-fuel-emissions-testing/dynamometer-drive-schedules>.
4. Lahr, D.F., Samie, F., Bucknor, N.K., Lee, C.J. et al.: Hybrid Powertrain System. United States Patent US 10,017,044 B2.
5. Lahr, D.F., Samie, F., Lee, C.J., Li, D., Bucknor, N.K.: Powertrain and a Vehicle. United States Patent US 10,583,728 B2.

6. Guang, Wu., Zhang, X., Dong, Z.: Powertrain Architectures of electrified vehicles: Review, classification, and comparison. *J. Franklin Inst.* **352**(2), 425–448 (2015)
7. Moawad, A., Kim, N., Shidore, N., Rousseau, A.: Assessment of vehicle sizing, energy consumption and cost through large scale simulation of advanced vehicle technologies, No. ANL/ESD-15/28. Argonne National Lab.(ANL), Argonne, IL (United States) (2016)
8. Onori, S., Serrao, L., Rizzoni, G.: *Hybrid Electric Vehicles: Energy Management Strategies*. Springer, London (2016)
9. Lu, X., Chen, H.: Design of model predictive controller for anti-jerk during tip-in/out process of vehicles, In: *Proceedings of the 30th IEEE Chinese Control Conference*. Yantai, China.
10. Hao, L., Shidore, N., Brushless fast starter for automotive engine start/stop application. *IEEE Trans. Ind. Appl.* <https://doi.org/10.1109/TIA.2020.3012930>.